THE ELECTROMAGNETIC PERFORMANCE OF BRUSHLESS PERMANENT MAGNET DC MOTORS - WITH PARTICULAR REFERENCE TO NOISE AND VIBRATION

ZI-QIANG ZHU, B.Eng., M.Sc., MIEEE

A thesis submitted for the degree of Doctor of Philosophy

in the Department of Electronic and Electrical Engineering,

University of Sheffield

May, 1991

TO

My Motherland - P.R. of China

ACKNOWLEDGEMENTS

I should like to extend my sincere thanks to everyone who contributed to making this thesis possible, in particular:

- My supervisor, Professor D. Howe, for his continuous encouragement, advice, and ideas throughout the project, as well as for making it possible for me to pursue research in his group;
- Professors D. Z. Xu and Y. X. Chen, Zhejiang University, China;
  Dr S. J. Yang, Heriot-Watt University;
  Drs T. S. Birch and W. F. Low, University of Sheffield; and
  Dr B. Ackermann, Philips GmbH Forschungslaboratorium, Aachen, Germany,
  for their invaluable encouragement and discussions;
- All members of the Electrical Machines and Drives Group at Sheffield for all their help and many useful discussions;
- Miss J. A. Brookfield for her patience in typing this thesis;
- The University of Sheffield and DGXII of the European Commission for making it possible for me to work on a BRITE research project, without which this work would not have been possible;
- Finally my parents, wife, and daughter, for their continued love and consistent encouragement.

ABSTRACT

The research focuses on the electromagnetic performance of brushless permanent magnet DC motors, with particular reference to acoustic noise and vibration, but spanning issues such as the prediction of the magnetic field distribution under any specified operating condition, the calculation of force and torque components, and the dynamic simulation of drive systems.

A comprehensive analytical technique is developed for predicting the instantaneous magnetic field distribution in radial-field, surface-mounted permanent magnet brushless DC motors under any load condition and commutation strategy. It is based on a 2-dimensional analysis in polar coordinates and accounts implicitly for the corresponding stator winding current waveforms and the effect of stator slot openings. In addition, a 2-dimensional analytical method for calculating the back-emf waveform is presented, whilst the analytical technique is applied to the prediction of the cogging torque waveform and the calculation of the self- and mutual-winding inductances.

Also developed and validated is an analytical model for predicting the steady-state dynamic performance of a 3-phase brushless DC drive, by exploiting the periodicity in the stator winding voltage and current waveforms, with due account of the influence of commutation events in the inverter bridge, the back-emf waveform, current limiting, and commutation timing etc. The model is developed further to couple with the motion equation of the rotor to enable the transient and steady-state dynamic performance of brushless DC drives to be predicted.

The effect of end-shields on the vibrational behaviour of stators is investigated by the modern modal analysis technique, and new formulae for the calculation of the acoustic power radiated by a cylindrical stator of finite length, using an analytical method, are presented. A technique which combines the finite element method and Fourier analysis to account for the effects of end-shields on the acoustic radiation is developed, and the spherical acoustic radiation model of motors has been improved by the application of finite elements. Finally, a systematic analytical approach to the estimation and analysis of the acoustic noise from a radial-field, internal rotor, brushless DC motor is presented.

CONTENTS

Acknowledgements

Abstract

Chapter 1 General introduction **1**

1.1 Introduction 1

1.2 Literature review of electromagnetic noise and vibration 2

1.3 Review of previous work on vibrational behaviour 10

1.4 Review of previous work on acoustic behaviour 15

1.5 Main research and features in the thesis 18

Chapter 2 Effects of end-shields and rotor on natural frequencies and modes of stator of small electrical machines, by modal analysis **26**

2.1 Introduction 26

2.2 Modern experimental modal analysis technique 27

2.3 Experimental method 30

2.4 Modal analysis 32

2.4.1 Measured results 32

2.4.2 Natural frequencies and modes of stator 33

2.4.3 Effects of end-shields 34

2.4.4 Effect of rotor 35

2.4.5 Effect of running condition 35

2.5 Conclusions 36

2.6 Appendix - Electromagnetic spectral analysis 37

Chapter 3 Study of acoustic field and power radiation from electrical machines by analysis of finite cylinder model **47**

Chapter 5 Analytical calculation of open-circuit magnetic field distribution in permanent magnet motors accounting for the effect of slotting **101**

5.1 Introduction 101

5.2 Brief description of calculation method 103

5.2.1 A simple 1-d model 103

5.2.2 A refined 1-d model 105

5.2.3 A 2-d model 106

5.3 Magnetic field produced by magnets 109

5.3.1 In polar coordinates 112

5.3.1.1 Internal rotor motors 112

5.3.1.2 External rotor motors 119

5.3.2 In rectangular coordinates 123

5.4 Effects of slotting 125

5.4.1 Effect of slotting on the effective flux 125

5.4.2 Effect of slotting on the field distribution - the relative permeance calculation 127

5.5 Comparison with finite element calculations 133

5.5.1 Magnetic field produced by surface mounted magnets 134

5.5.2 Relative permeance models 141

5.5.3 Open-circuit field calculation 149

5.6 Conclusions 150

5.7 Appendix - Determination of the magnetisation M_n 151

Chapter 6 Analytical prediction of cogging torque in permanent magnet motors based on the calculation of tooth lateral forces **158**

6.1 Introduction 158

6.2 Methods of reducing cogging torque and limitations of existing methods of calculation 159

3.1 Introduction 47

3.2 Derivation of formulae 49

3.3 Comparison of relative sound intensity coefficients 53

3.4 Measurement and calculation of acoustic field 54

3.5 Conclusions 57

3.6 Appendix - S.J. Yang's formula for calculating radiated acoustic power 57

Chapter 4 Finite element analysis of the acoustic power radiated by electrical machines 67

4.1 Introduction 67

4.2 Calculation of acoustic power 68

4.2.1 Three-dimensional finite element analysis of acoustic radiation 68

4.2.2 Planar and axisymmetric fields 73

4.2.3 Harmonic axisymmetric acoustic field 75

4.2.4 Element matrices and acoustic power in different fields using triangular elements 80

4.2.4.1 Planar acoustic field 81

4.2.4.2 Axisymmetric acoustic field 82

4.2.4.3 Harmonic axisymmetric acoustic field 83

4.3 Effects of far-field boundary conditions on the calculation of the radiated acoustic power 84

4.4 Experimental verifications 90

4.5 Investigation of spherical model 92

4.6 Conclusions 95

4.7 Appendices 95

4.7.1 Acoustic field radiated by an electrical machine and its boundary conditions 95

4.7.2 Three-dimensional isoparametric elements 98

4.7.3 Detection of standing waves and travelling waves 99

6.3 Methodology of analytical prediction 161

6.3.1 Basic concept for predicting cogging torque based on the calculation of the tooth lateral force 161

6.3.2 Relative permeance calculation 163

6.3.3 Calculation of magnetic field produced by magnets 166

6.3.4 Magnet shifting 169

6.3.5 Uneven distribution of slots 173

6.4 Validations 173

6.4.1 Finite elment calculations 174

6.4.2 Comparisons 184

6.4.2.1 Internal rotor motor 184

6.4.2.2 External rotor motor 187

6.5 Conclusions 190

6.6 Appendices - Torque calculation by energy method 192

6.6.1 Torque produced in an electromagnetic device 192

6.6.2 Energy stored in a magnetic field 193

6.6.3 Input electrical energy 196

Chapter 7 Analytical simulation of dynamic performance of brushless DC drives 197

7.1 Introduction 197

7.2 System model and its symmetry 199

7.3 Mathematical models 205

7.3.1 Back-emf and commutation 205

7.3.2 Drive circuit 207

7.3.3 Voltage equations 208

7.3.4 Calculation of phase currents 211

7.3.5 Conducting time of freewheeling diodes 214

7.3.6 Torque, terminal current, and efficiency 215

7.3.7 Numerical integration 216

7.4 Validation of mathematical models 217

7.4.1 Radial-field brushless DC motors 217

7.4.2 Axial-field brushless DC motor 226

7.5 Incorporation the rotor motion equation into steady-state models 229

7.5.1 Idealised state variables 229

7.5.2 State-variable equations 234

7.5.3 Numerical integration of state-variable equations 238

7.6 Comparison of predictions from different approaches 240

7.7 Effects of commutation and temperature on dynamic performance 249

7.7.1 Commutation effects 251

7.7.2 Temperature effects 259

7.8 Conclusions 262

Chapter 8 Magnetic field analysis in brushless DC motors on load 263

8.1 Introduction 263

8.2 Analytical calculation of armature reaction field in brushless DC motors 265

8.2.1 Magnetic field of a single conductor 265

8.2.2 Magnetic field of one coil 268

8.2.3 Effect of airgap length 271

8.2.4 Effect of slot opening 273

8.2.5 Effect of current harmonics - analytical spectral analysis 277

8.2.6 Armature reaction field of 3-phase windings in brushless DC motors 281

8.2.7 Comparison of predictions with finite element calculations 285

8.3 Back-emf induced in windings of a brushless DC motor 293

8.4 Resultant magnetic field on load 296

8.4.1 Relative positions of open-circuit field, armature reaction field, and permeance function 297

8.4.2 Instantaneous field distributions 302

8.4.3 Comparison of predictions with finite element calculations 304
8.5 Extension to the calculation of self- and mutual-inductances 305
8.6 Conclusions 307

Chapter 9 Estimation and analysis of electromagnetic force, vibration, and acoustic power of brushless DC motors 324

9.1 Introduction 324
9.2 Spatial and time dependent radial force calculation 326
9.2.1 Radial force density wave 326
9.2.2 Relative permeance 329
9.2.3 Magnetic field produced by magnets 330
9.2.4 Magnetic field produced by windings 331
9.3 Analytical model for vibrational response estimation 332
9.3.1 Vibrational response of the stator 332
9.3.2 Effect of the frame 333
9.3.3 Lumped stiffness and mass of the stator 335
9.4 Analytical model for acoustic power level prediction 337
9.5 Validations 337
9.5.1 Description of experiments 338
9.5.2 Comparison of natural frequencies of stators 343
9.5.3 Calibration for noise measurement 348
9.5.4 Sound pressure level measurement 354
9.5.5 Analysis of acoustic power radiated by the test motor 357
9.6 Conclusions 363

Chapter 10 General conclusions 364

10.1 Introduction 364
10.2 Magnetic fields in brushless DC motors 366
10.2.1 Effect of stator slotting 366

10.2.2 Open-circuit magnetic field 367

10.2.3 Armature reaction field 367

10.2.4 Instantaneous magnetic field on load 368

10.2.5 Back-emf and winding inductances 369

10.3 Cogging torque and dynamic performance of brushless DC motors 369

10.3.1 Cogging torque 369

10.3.2 Dynamic simulation 370

10.3.3 Dynamic performance 371

10.4 Vibrational and acoustic behaviour 372

10.4.1 Modal analysis of vibrational behaviour 372

10.4.2 Analytical acoustic model 373

10.4.3 Finite element analysis of acoustic behaviour 374

10.5 Acoustic noise of brushless DC motors 375

10.5.1 Vibrational response model 375

10.5.2 Acoustic noise of brushless DC motors 375

10.6 Possible future work 376

References **378**

Appendices **393**

1 Chapter contents of the book entitled " Analysis and control of noises from electrical machines " 393

2 Abstract and chapter contents of the thesis " CAD of electrical machines - A study of electromagnetic, vibrational, and acoustic behaviour " 394

3 Publications from the research in the thesis 398

CHAPTER 1

GENERAL INTRODUCTION

1.1 Introduction

In the foreword of the well known book entitled " Low noise electrical motors " written by Dr. S.J. Yang and published by Oxford University Press, Oxford, 1981, Professor A.J. Ellison is quoted as saying that research on noise from electrical machines has " spanned electric power, energy conversion, mechanical vibration, physics especially acoustics, electronics, and mathematics ". Indeed, this thesis is further proof of this statement.

The main research issues which are covered in the thesis range from the open-circuit, armature reaction, and load magnetic fields, the calculation of force and torque, the dynamic performance simulation of drives, and mechanical vibration and acoustic radiation of brushless permanent magnet DC motors. The work which is reported is a further extension to the candidate's book entitled " Analysis and control of noises from electrical machines " which was first published in 1987 and whose chapter contents are given in Appendix 1, and a previous thesis entitled " CAD of electrical machines - A study of electromagnetic, vibrational, and acoustic behaviour " which was completed in 1989 and presented to Zhejiang University (China), and whose abstract and chapter contents are given in Appendix 2.

The brushless permanent magnet DC motor is arguably the most important emerging category of machine for a wide spectrum of motion control applications, many of which are noise sensitive. The vast majority of brushless permanent magnet DC motors have surface-mounted magnet rotors which leads to a large effective airgap, whilst, unlike more traditional machine formats such as induction motors, the armature reaction field results from phase current waveforms which contain significant harmonics as a consequence of electronic commutation, and rotates in incremental steps between commutation events. In this thesis the research focuses on the

electromagnetic performance of brushless permanent magnet DC motors - with particular reference to their noise and vibration. This task represents completely original, and to some extent speculative research, since no such investigations on brushless permanent magnet motors have been reported before.

In this chapter a general literature review on the noise and vibration of electrical machines, as well as their vibrational and acoustic behaviour, is presented, whilst a discussion of particular issues is given at the beginning of the following chapters. The main features of the research to be described in the thesis are also outlined at the end of this chapter.

1.2 Literature Review of Electromagnetic Noise and Vibration

Nowadays, since people expect a quiet and comfortable environment both at home and work, acoustic noise from electrical machines is an important environmental issue, and the maximum permissible emitted noise level is usually cited as a parameter in the design specification. By controlling the radiated acoustic noise and vibration level of electrical machines, their commercial potential is enhanced, as is that of the products for which they provide the drive. However, in order to achieve this and be capable of designing low noise electrical machines, it is necessary to understand and analyse the physical mechanisms of noise generation. As a consequence, a considerable amount of research continues to be carried out both by industrial organisations and academic institutions in many countries, in particular the United States, Germany, the United Kingdom, Czechoslovakia, Canada, the Soviet Union, Japan, Belgium, and even in China, and standards for noise level limitation and noise measurement from electrical machines have been established in most industrial countries.

In general, the noise emitted from an electrical machine originates from three major sources, viz, electromagnetic, mechanical, and aerodynamic [1.1]-[1.15]. In this thesis, however, the investigation focuses on the electromagnetically generated noise.

The process of electromagnetic noise generation in an electrical machine is illustrated in Fig.1.1 [1.7]-[1.15]:

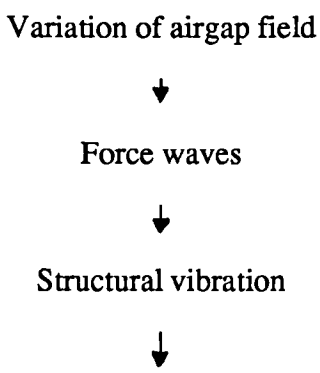

Fig.1.1 Generation of electromagnetic noise

Hence the important aspects can be classified as follows:

a) Airgap field and electromagnetic force waves;

b) Vibrational behaviour and corresponding dynamic response;

c) Acoustic behaviour;

d) Methods of noise measurement, standards for noise level limitation and noise measurement;

e) Identification and control of noise;

f) Estimation of noise level and design of low noise motors.

Numerous papers have been published on the subject of noise from electrical machines, and these are summarised in excellent bibliographies by Ellison and Moore [1.1] up to 1967 and by Yang [1.8] up to 1980 for electromagnetically, mechanically and aerodynamically induced noise. In addition, some particular aspects, such as the vibration of the end-windings of large electrical machines, which although largely unrelated to noise generation are important as regards vibrations, have been throughly researched. However such subjects are out of the range of the work reported in this thesis, and this literature survey is confined to a brief review of the work done on electromagnetic noise over the last ten years or so.

The emitted electromagnetic noise spectrum varies with the type of electrical machine, typical features relating to the frequencies and modes being:

Brushed direct-current machines (commutator machines) [1.16]-[1.19]: The frequencies are directly proportional to number of armature slots and the rotational speed, whilst the mode orders are related to the ratio of the armature slot number to pole number as well as the ratio of the width of the magnet pole-arc to the armature slot pitch.

Asynchronous machines (induction motors) [1.20]-[1.28]: The frequencies depend not only on the slot number of the rotor, the pole number, and the slip, but are also proportional to the supply frequency. The mode orders are determined by the order of the field harmonics, especially that of the slot harmonics of the stator and rotor.

Synchronous machines [1.29]-[1.35][1.11]: The frequencies are integer multiples of twice-supply-frequency. The mode orders are related to the harmonics due to the slot openings and armature windings on the stator and the harmonics exhibited in the main field on the rotor.

The noise frequencies of a DC machine or an asynchronous machine vary with the load as the speed of the rotor changes, whilst those of a synchronous machine are independent of the load condition. Therefore, when a variation of load occurs,for example, from no-load to full-load, the change in acoustic power level for a synchronous machine is determined only by the field distribution, and hence the force distribution, irrespective of the vibrational and the acoustic behaviour of the structure [1.11].

Early research concentrated on establishing basic rules for the noise spectra of different types of machine, and these are now quite well known for conventional machine topologies. The generalised analysis of the noise spectrum, though restricted to asynchronous machines, can be found in the textbook "Low-noise Electrical Motors" written by Yang [1.8]. For other classes of

machine such an analysis is given in the author's book entitled "Analysis and Control of Noises from Electrical Machines" [1.11].

In order to understand the spectral behaviour of the noise and also to predict the most important components in the spectrum, a detailed analysis of the airgap field and force waves, as well as the vibrational responses and their acoustic radiation, is required.

Methods for field analysis include both analytical and numerical techniques. Analytical methods, which range from conformal transformation and Fourier series analysis to those based on the concepts of permeance and mmf, are often used interactively. However,by their very nature these necessarily imply some idealisation in the representation of a machine, On the other hand, numerical methods, such as finite elements, are more generally applicable. However,difficulties exist with the application of pure numerical methods to noise analysis since the field analysis required for the prediction of the noise spectrum is concerned not only with the spatial variable, but also with the time variable [1.36]. Field analysis also involves the calculation of harmonic fields containing a wide spread of components of different pole numbers and different rotational speeds [1.37]. Therefore, the most practical method as far as accuracy and convenience is concerned is the method of Fourier series analysis .

The electromagnetic vibrational forces or torques include axial, tangential, and radial components.

Axial vibrational forces cause the end-shields to vibrate and to radiate acoustic noise. In addition the vibration of the bearings may be affected by the induced end-shield vibration. The axial forces are usually generated due to skewed slots, magnetic unbalance in the radial and axial plane, as well as by ventilating fans [1.38]-[1.42].

Tangential vibrational forces (torques) can be separated into two kinds according to their manner of vibration,viz, **oscillating torques** - which are independent of the spatial angular

position, and **bending vibrational torques** which are functions of the spatial angular position and are zero when the torques are integrated around the whole circumference. In general the vibrations which are induced by the oscillating torques are negligible due to their direction being perpendicular to the normal direction of the radiating surface. Therefore they are not the main exciting source as far as the noise of a motor is concerned. However, the vibrations may be amplified and transmitted through coupling parts to linked structures and cause them to vibrate and even resonate. Hence a large radiated noise level may be observed in the equipment for which a motor provides the drive [1.43]-[1.48]. In addition, such kinds of vibrational torques will affect the electrical performance [1.49]. They become large, and hence important, when three-phase asynchronous and synchronous machines are started as well as under some fault conditions, such as a short-circuit or open-circuit, and in single-phase induction motors in which the rotating field is usually unsymmetrical [1.50]-[1.54]. Bending vibrational torques act on the teeth or poles. Their effects on the vibration and noise are determined by the relative stiffness of the teeth or poles to the core and the frame of the stator. Generally speaking, however, in the case of asynchronous and synchronous machines they are not as important as the radial vibrational forces. However in a machine with a stator which has convex poles, such as in DC commutator motors, bending vibrational torques are almost as important as the radial vibrational forces [1.16][1.10][1.11].

Radial vibrational forces are the main source of electromagnetic noise. Due to the non-linear response of the human ear to noise, and from the analysis of the magnetic field in the airgap of an asynchronous machine, it is the low order force waves produced by the interaction of the slot harmonics of the stator and the rotor which are usually responsible for the principle components of the electromagnetic noise [1.10][1.11]. However in a synchronous machine, it is the interaction of the first-order slot harmonic component of the armature winding mmf with the first-order slot harmonic component of permeance due to the slot opening on the stator which produces the resultant first order slot harmonic component. The important force waves which dominate the electromagnetic noise spectrum are produced by the interaction of this resultant first order slot harmonic component with two or three harmonic components exhibited in the rotor main field

in which the pole pairs of the harmonics are the closest to the slot number of the stator [1.11]. A similar situation exists in direct-current machines where the force waves produced by the interaction of the main field harmonics of the stator with the first-order slot harmonic components of the armature are the main contributors to electromagnetic noise. However, the stored magnetic energy, and hence the energy variation, is mainly in the airgap under the stator magnetic poles[1.10]. It is the resultant forces or torques acting on the poles of a DC machine that cause the stator to vibrate [1.11].

The effects of magnetic saturation, magnetic asymmetry of the stator and/or rotor, e.g., static/dynamic eccentricity of the rotor, elliptic inner surface of the stator and elliptic outer surface of the rotor etc., have been the subject of a number of studies [1.26][1.11]. Furthermore, the effect of dynamic eccentricity of the rotor on noise is not only a popular concern for investigation, but high accuracy has been achieved in its numerical calculation [1.55].

In the last few years electronic drive systems based around AC machines have been widely adopted for adjustable speed drives [1.56]. However one consequence is that the phase current waveforms are then no longer pure sinusoidal waveforms but contain significant harmonics. These greatly increase the possibility of resonances between the exciting forces and the structure, as well as the total level of acoustic noise [1.57]-[1.64]. Therefore, studies of noise emitted from electrical machines cannot be restricted to the motor itself but must consider the whole system including the electronic drive [1.65]. By proper drive design not only can the electrical performance be improved but also the noise can be reduced, by current injection for example [1.66][1.67]. Although this aspect has been researched recently, much remains to be studied since, to date, only the component identification on the spectrum has been investigated. More recently, electronic commutation has been employed increasingly to replace the traditional mechanical commutator of brushed DC machines, leading to brushless DC machine drives [1.68][1.69]. Whilst the removal of the commutator reduces the mechanical noise at the same time it has tended to increase the electromagnetic noise. With the advent of brushless DC drives, with surface mounted magnet rotors, the slot harmonic fields have been alleviated because of

their large effective airgap. However for a wide range of motion control applications, such as computer floppy disc drives and spindle drives for VCR's etc., many of which are extremely noise sensitive, noise level reduction remains a major concern particularly since the use of brushless DC drive results in significant time harmonics in the winding phase current waveforms. Furthermore the use of a brushless DC drive may result in significant torque ripples due to commutation events as well as cogging, which will induce tangential vibration of the machine [1.70][1.71].

By monitoring or simulating the spectral behaviour of noise and vibration abnormal conditions in a machine may be identified, e.g., rotor eccentricity, or electrical faults such as short-circuited stator windings, broken squirrel-cage bars etc.[1.72]-[1.77]. Advanced digital signal analysis techniques, such as the analysis of the the coherence function between the noise and the vibration signals [1.77][1.78] and the order trace analysis of the rotor vibration, are now used extensively to identify noise sources in electrical machines.

Usually the noise level of an electrical machine is judged by its acoustic power level. Corresponding international and national standards for noise level limitation and noise measurement have been established and improved from time to time. Both reference standards and national standards are available for noise measurement in free-field, semi-free-field, reverberant-field and semi-reverberant-field [1.79]. Ellison and Yang [1.80][1.81] have applied the analysis of statistics in the study of the relationships between measured results and the number of machines and measurement points. Near-field measurement techniques such as sound intensity measurement [1.82] have also progressed over the last few years.

Since electromagnetic noise is closely related to the slot combination of the stator and rotor, the effects of slot combinations on the noise level in asynchronous machines have been studied extensively [1.83][1.84]. The early studies concentrated mainly on magnetic field analysis and experimental investigations [1.85][1.86]. As a consequence many favourable slot combinations have been proposed. However the subject of slot combinations is very complex since it is related

to almost all aspects of the electromagnetic performance, as well as to vibrational and acoustic behaviour. However as far as the noise is concerned, a good slot combination depends on the resultant force waves, the mechanical structure, and the acoustic behaviour. However, the natural frequencies of the machine stators over a range of power ratings and structures are different [1.87]. Hence it is impossible for a slot combination that is preferred in a low noise sense for small machines to be ideal for large machines. Also it is impossible for one slot combination to be the most suitable for any running condition from starting, to no-load and full-load. A good slot combination should increase the minimum order of the force waves produced by the airgap field and avoid resonances between the important force waves and the stator structure within a certain speed range, whilst the stator should be designed to have an acoustic radiation efficiency (relative sound intensity) much smaller than unity for the dominating vibrational components [1.88]. Clearly this is not a simple task and requires a full knowledge of electromagnetic, vibrational, and acoustic aspects.

In respect of noise control and the design of low noise electrical motors, the so-called Active Noise Control technique has been of particular interest in the last few years [1.89].

Active Noise Control requires a machine designer to control the noise level from the source itself. From the physical mechanism of noise generation shown in Fig.1.1, the possible techniques include reducing the vibrational forces and the mechanical response of the vibrating structure, and lowering the acoustic radiation [1.90][1.91][1.92][1.11].

Methods of reducing the vibrational forces include both minimising the number of force components and the amplitude of the more important components by, for example,

a) Ensuring symmetry in both electrical and magnetic aspects and avoiding any asymmetry which might be introduced during construction [1.93][1.11];
b) Using auxiliary windings or special connections of windings to compensate for magnetic asymmetry [1.55];

c) Using damping windings to alleviate the variation of harmonic field etc.

Methods of reducing the mechanical response of the vibrating structure include:

a) Avoiding mechanical resonances,which requires the selection of an appropriate slot combination as well as structural design parameters, and the accurate prediction of the exciting frequencies of the force waves and the natural frequencies and modes of the structure;
b) Increasing the order of the force waves, which can be achieved along the circumference by selecting a proper stator/rotor slot (or pole) combination, or along the axis by skewing either the slots or poles;
c) Increasing the damping of the structure;
d) Reinforcing the stiffness of the structure and
e) Employing elastic mountings or couplings etc.

In order to reduce the acoustic radiation it is necessary to reduce the acoustic radiation efficiency, i.e., to make less than unity the relative sound intensity coefficients which the most important vibrational components possess. This can be achieved by:

a) Selecting an appropriate stator/rotor slot combination;
b) Reducing the effective radius of acoustic radiation;
c) Increasing the mode order of the vibration (force) wave either on the circumference or on the axis;
d) Reducing the aspect ratio of the machine,i.e., the axial length to diameter ratio.

1.3 Review of Previous Work on Vibrational Behaviour

Studies of the natural frequencies and modes of the stators of electrical machines can be divided into several groups depending on the type of stator, e.g. single-ring type [1.94]-[1.95], double-ring type [1.97][1.98], encased type [1.99]-[1.108], asymmetrical type [1.109], and

square-frame type [1.110] etc. Further, the methods which have been used in the analysis may be divided into analytical, Fourier series analysis, finite elements (numerical), and the experimental modal analysis technique etc.

The analytical method utilises both the theory of elastic mechanics and the technique of electromechanical analogues. Early studies often employed this approach since the analytical formulae obtained were simple and easy to use in design. However, it is restricted to thin single-ring type stators,for example, the core only. Moreover, the effects of the teeth and windings can be taken into account only by a modification factor. Nevertheless, in many engineering applications the natural frequencies of single-ring cores have been calculated to an acceptable accuracy by modifying the thickness of the core yoke. Typical examples are: Den Hartog [1.111] who studied the effect of the feet mounting on the natural frequencies of a single-ring type stator; Jordan [1.94], Frohne [1.95],Uner [1.96] et al who accounted for the effects of shear energy, rotating energy, as well as the effects of teeth and windings; Voronetskii [1.112], Lubcke [1.113] who modified the analytical formulae by experimental factors; and Seidal and Erdelyi [1.114] who investigated the effect of the thickness of the core yoke; whilst the author [1.115][1.116] employed the electromechanical analogue technique and obtained analytical formulae which are capable of analysing the vibration of encased type and double-ring type stators.

Fourier series analysis based on the energy principle has been used to study not only single-ring type stator cores but also the effects of the frame, teeth, and windings. However the method itself, whilst convenient for analysing stators having a symmetrical structure, is difficult to apply to asymmetrical stators such as those with magnetic poles, mounting feet, or a square-frame. In principle the method is no different to the analytical method mentioned above. Erdelyi [1.9][1.97] modelled the stator as two thin rings which were linked by ribs. He studied the natural frequencies and mechanical response of a stator of a machine having a medium size power rating; Later Ellison and Yang [1.98] modelled the stator as a thin frame and a thick core with teeth and windings which were linked by ribs. They studied the effects of various components of the energy on the accuracy of the calculated natural frequencies. Holtzmann [1.109] studied the

asymmetrical stator of a direct-current machine, whilst Verma and Girgis [1.99]-[1.108] systematically studied the natural frequencies and modes of encased type stators. Based on a three-dimensional theory they investigated the natural frequencies and their relationship with the non-uniform longitudinal modes. Furthermore they investigated not only the natural frequencies corresponding to the modes in which the radial component dominates the vibration but also those dominated by tangential vibrations or axial vibrations. However the natural frequencies associated with the latter two kinds of modes are of much less importance than the first kind of mode.

More recently the finite element technique has been applied to the analysis of the vibrational behaviour of electrical machines. Yang [1.117] calculated the natural frequencies and modes of the asymmetrical stator of a DC motor; the author [1.118]-[1.121][1.110] studied the effects of swallow-tail slots, teeth/slots, magnetic poles, ribs and the frame etc., and the natural frequencies of stators of the single-ring type, asymmetrical type, encased type, double-ring type,as well as stators having a square-frame structure; Watanabe et al [1.122] and Noda et al [1.123] investigated the effects of swallow-tail slots and windings on the vibrational behaviour of the cores of medium and low power machines. Belmans et al [1.124][1.125] have explored the possibility of using three-dimensional finite elements. However in their calculation the stator core was constrained to have the same axial length as the frame. Furthermore, as in the three-dimensional Fourier series analysis used by Verma and Girgis, they did not consider the effects of end-shields on the calculation of the natural frequencies of the non-uniform longitudinal modes. Nevertheless, the finite element method has been proved to be very suitable for the analysis of the vibrational behaviour of machines since it can account for the irregular shape of machine stators and can easily deal with magnetic poles, mounting feet and ribs etc.with a high accuracy.

Due to the complexity of the stator structure, experimental modal analysis has always played an important role in the study of vibrational behaviour. Baudry [1.126] et al investigated the natural frequencies of a generator stator by model experiment, Verma and Girgis [1.100] found, by a

sinusoidal signal exciting technique, that the natural frequencies of the non-uniform longitudinal modes depend on the axial length of the core and the frame, whilst those of the uniform longitudinal modes are almost independent. Similar conclusions were obtained by the author [1.118] from model experiments when the finite element model was established. Meanwhile, Verma and Girgis [1.101] have experimentally studied the effects of the teeth, windings, frame, and the silicon sheet on the stator vibrational behaviour. The author [1.127] has also studied the effect of the siting of the exciting and picking-up points on the measured natural frequencies.

With the advance of the modern experimental modal analysis technique based on dynamic signal analysis [1.128], its application to the study of the vibrational behaviour of machines has been extensive [1.129][1.130]. However all investigations are restricted to the validation of existing conclusions. Nevertheless the author [1.131] has used the technique to study the effects of the end-shields, the rotor, and machine running conditions on the natural frequencies and modes of the stator.

To date only experimental investigations on the damping behaviour of stators have been reported. Hubner and Yang [1.7], for example, measured the damping ratios of the stator in medium and low power machines. It is interesting that their measured results of cores with windings are almost identical, particularly since Yang [1.8] found that the damping ratio of a stator core without windings is much lower than when carrying windings. The difference is most likely caused by the additional energy dissipation in the winding-to-core friction and in the windings themselves. On the other hand Girgis and Verma [1.101] found that the damping of a laminated stator structure was significantly greater than that of an equivalent solid steel structure. The effects of laminations on the vibrational behaviour have also been studied [1.132].

Usually the calculation of the dynamic response to the electromagnetic vibration is composed of two significant steps, the static radial deflection of the stator core being calculated first. Subsequently a dynamic amplifier factor, which is determined by the exciting force frequency of a given mode, the natural frequency of a particular stator mode, and the damping ratio is

introduced to obtain the dynamic radial deflection [1.13][1.8]. In such an analysis only the stator core is considered, and it is assumed to be a thin single-ring, the stiffness of the teeth and windings as well as the restriction of mounting feet and end-shields being neglected. Based on the electromechanical analogue analysis that has been proposed by the author [1.88] the vibrational response of encased-type stators can be calculated according to an analytical model consisting of two thin rings, accounting for the damping ratios of the stator core and the frame respectively according to the predicted natural frequencies and Hubner and Yang's measured results of damping ratios. Since in this method the effects of the teeth and windings are approximated by an additional mass to the stator core and the effects of the thickness of the core and the frame yokes are neglected in the calculation of the vibrational response, it necessitates a modification to the stiffness of the stator by comparing the natural frequencies from an analytical prediction with those from a finite element calculation or from measurements.

In the control and analysis of electromagnetically induced noise, of most importance is the study of the vibrational behaviour of the stator when the vibration is uniform along the longitudinal axis.

Since the stator structure is complex, due to the existence of teeth/slots and windings etc, a large number of elements and interations are required in a finite element analysis. Therefore special considerations are required in its application to the study of the vibrational behaviour of stators. In [1.120] from the point of view of routine engineering design, which requires a rapid means of prediction, the possibilities of using a lumped mass matrix which results in a diagonal matrix and high order curved isoparametric elements and initial values from analytical solutions, instead of using a consistent mass matrix,and ordinary first-order triangular elements and generalised initial values, are considered. A special technique for forming the lumped mass matrices for various high-order curved isoparametric element is introduced. By analysing the functional characteristics of the stiffness and mass matrices the error introduced due to the finite element discretisation has been partially compensated for by employing the reduced-order integration technique, whose effectiveness is validated by a case study.

For the resonances between the exciting forces and the stator structure, nowadays it is possible to predict the frequencies of the more important exciting forces produced by the harmonic field in the airgap. However a significant amount of work remains to be done as regards accurately predicting the natural frequencies of stators, especially for asymmetrical stators which are generally the case in electrical machines. "Dual resonance" frequencies existing in the measured transfer function of the stators cannot be calculated or measured with confidence. The methods proposed by some authors are applicable only when the stator has a special structure, whilst the finite element discretised region and its corresponding boundary conditions need to be determined. Therefore, in [1.121] the concept of a generalised tooth/slot is introduced. According to this concept the finite element discretised region is determined by utilising the perpendicularity between the components of the vibrational displacements. Principles for selecting the exciting/picking-up points have been established and validated both theoretically and experimentally [1.127]. As a consequence the effects of teeth/slots on the core, the magnetic poles on direct-current machine stators, the ribs in the double-ring type and square-frame type stators, the ventilating ribs on encased type stators, the swallow-tail slots in the core, and the mounting feet on the frame etc have been systematically studied as to their effect, taking into account the effects of the windings and the frame.

1.4 Review of Previous Work on Acoustic Behaviour

The noise level of a machine is judged not by its sound pressure but by its emitted acoustic power since the acoustic power, unlike the sound presure, has a unique value for a given motor operating under a given condition, regardless of the location of the measuring surface.

From a knowledge of the surface vibration there are two kinds of analytical models with which to analyse and calculate the sound field and radiated acoustic power. One is based on a spherical model, whilst the other assumes a cylindrical model.

The spherical model was first introduced by Carter [1.133]. However due to an undetermined constant his solution cannot give quantitative results. Whilst the method derived by Jordan [1.134] gives reasonably accurate predictions for motors whose axial length and diameter are similar, i.e., aspect ratio = 1, especially for small machines, its main advantage is that it yields results for the acoustic power. On the other hand the method presented by Ellison and Moore [1.135] allows the variation of the sound pressure along the axial direction and the calculation of the total acoustic power to be obtained. Again, however, their analysis is restricted to machines having an aspect ratio of around unity. However, further investigations on such a model, by finite element analysis, have shown that the method is either improper or inconvenient for the direct calculation of the radiated acoustic power [1.136]. As mention earlier, it is common to employ a Fourier series expression to describe the airgap field distribution, and hence the radial vibrational forces, as well as to obtain the vibrational mechanical response. Whilst this approach enables the acoustic power to be predicted, the solution is in the form of a Legendre series. Therefore, in order to calculate accurately the acoustic power, it is necessary to convert the expression for the vibration from a Fourier series to a Legendre series, which is usually inconvenient.

A cylindrical model of infinite length was first introduced by Alger [1.137] and is widely used to calculate the sound pressure distribution of machines [1.13][1.15]. However at that time the sound pressure, and not the acoustic power, was used to estimate the noise level. Subsequently, it has been found by analysis [1.138] that Alger's method is not suitable for calculating the acoustic power since it neglects the phase difference between the sound pressure and the particle velocity. Therefore it can be improved by accounting for this phase difference in the acoustic power calculation.

In the cylindrical model of finite length, which was proposed by Erdelyi [1.9][1.139], the ends of the machine were replaced by infinitely long cylindrical stiffening baffles, such that the vibration of the stator would not be trasmitted into the extensions. Once the vibrational mode and frequency, together with the dimensions of the stator are specified, the sound pressure level

at any point around the machine can be calculated, and used to estimate the noise. However, Erdelyi did not present a method for calculating the radiated acoustic power. This was done subsequently by Ellison and Yang [1.140][1.141], using the same model, by calculating the acoustic power according to the sound pressure and the particle velocity in the air on the surface of the stator by the "p-v" conjugation method [1.140]. Furthermore, the effect of the length to diameter ratio on the acoustic power was studied [1.141]. Unfortunately, since their formulae for the calculation of acoustic power is in terms of Bessel functions and modified Hankel functions and includes generalised integrations they are inappropriate for routine use in the course of design. However this disadvantage has been overcome by utilising the surface vibration of the stator and employing a much simpler formula for the relative sound intensity [1.142] which has eliminated the necessity of calculating the sound pressure and particle velocity distribution around the machine in the acoustic power estimation as was required in Ellison and Yang's method.

In addition, experimental methods are also available for the determination of the acoustic power, such as the sound intensity method [1.82], acoustic vibrational measurement etc [1.143].

In the analysis of acoustic radiation from structural vibrations, the results obtained from research carried out by the acoustic society using both analytical [1.144][1.145] and numerical methods [1.146][1.147], such as the boundary integration, finite difference, and finite element techniques, are of considerable reference value to the study of acoustic radiation from electrical machines. In [1.148], the acoustic radiation of a cylindrical model with non-uniform vibrations along its longitudinal axis has been studied, and results show that, similar to the increase of the vibration mode order along the circumference, the relative sound intensity coefficients, i.e., the normalised acoustic resistance, decrease with the increase of the vibration mode order along the longitudinal axis. In [1.144], solutions for the sound pressure distribution from a cylindrical model of finite length with two semi-infinite length stiffening baffles were obtained similar to those given in [1.9][1.140]. However, in general, the results obtained from theoretical acoustics cannot be applied directly to the analysis of noise from electrical machines since the sound pressure

distribution etc. is of more concern in theoretic acoustics, whilst it is the acoustic power which is of most interest in the study of noise from electrical machines. On the other hand, results from numerical predictions are usually applicable only to the acoustic power radiated by oscillating or impulsive vibration models, whilst in the aspect of noise from electrical machines it is more important to study the acoustic power radiated by higher order vibration models, e.g., vibration mode order equal to 2 or 3.

1.5 Main Research and Features in the Thesis

Following a review of previous work on the noise and vibration of electrical machines in this Chapter, the research is concentrated on the vibrational and acoustic behaviour, and electromagnetic field, force, torque, dynamic performance, and noise of radial-field brushless permanent magnet DC motors.

Existing investigations on the vibrational behaviour concern only the stator itself, neither the end-shields nor the rotor and the running conditions have been taken into account, which is the case even for experimental investigations and three-dimensional analysis. Therefore, in Chapter 2 the effects of end-shields, the rotor, and the running conditions on the natural frequencies and modes of the stator are investigated, for the first time, by the modern modal analysis technique, the results of which should be the foundation to establish more detailed vibrational and acoustic models.

Another important aspect in the analysis and control of noise from electrical machines is the acoustic radiation efficiency (relative sound intensity coefficient) which is studied in the thesis, both analytically and numerically in Chapters 3 and 4. Based on the cylindrical model of finite length, in Chapter 3 the analytical prediction of acoustic power has been extended further on the basis of research carried out by Erdelyi, Alger, Ellison and Yang. By utilising the surface vibration of the stator a new formula for the relative sound intensity has been obtained. Compared

with existing methods, it has eliminated the neccessity of calculating the sound pressure and particle velocity distribution around an machine. Hence the computing time is greatly reduced. Also it has the advantage of a much simpler form, making it easier to use for routine design. In addition the sound pressure distribution has been investigated, and its variation in three-dimensions has been calculated and measured.

Existing analytical models for acoustic radiation assume that the stator has a unity aspect ratio, or infinite axial length and infinite stiffening baffles. Hence they cannot account for the effects of the end-shields. A technique, which combines the finite element method and Fourier series analysis, to include the effects of end-shields on the acoustic radiation has been developed in Chapter 4. Based on this technique a suite of planar, axisymmetric, and harmonic axisymmetric finite element programs, which are capable of calculating the radiated acoustic field and power in a three-dimensional field, have been developed and validated against results from a test motor. Furthermore, the spherical model for the acoustic radiation of motors has been improved by the application of finite elements, and has overcome the inconvenience and inaccuracy in Jordan's method.

Following the study of the vibrational and acoustic behaviour of electrical machines, the research focuses on the analysis and prediction of noise from permanent magnet brushless DC motors, for which no quantitive research work has been carried out before. Hence this study represents completely original work.

Firstly improved analytical models are established in Chapter 5 to calculate the open-circuit magnetic field distribution of permanent magnet motors. They cater for slotless and slotted, and internal and external rotor, radial-field motors modelled in either polar or rectangular coordinate systems. The technique is based on a 2-dimensional analytical model to calculate the magnetic field produced by the magnets in the airgap/magnet regions. In the calculation the concept of 2-dimensional permeance function is utilised to account for the induced harmonics due to the presence of slot openings, which are analysed by the conformal transformation method.

Therefore the open-circuit magnetic field distributions in all topologies of radial-field permanent magnet motor can be solved analytically. The predicted results have been compared with predictions from finite element calculations.

Cogging manifests itself in a permanent magnet motor by the tendency of the rotor to align in a number of stable positions even when unexcited. Under dynamic conditions the resultant pulsating torque, of zero net value, can cause undesirable speed pulsations, and can be transmitted to the coupling devices, through the stator frame or the rotor and induce tangential vibrations, resonances, and noise. However the prediction of cogging torque in a permanent magnet motor by finite element analysis is a rather time consuming task since the periodic wave length of the cogging torque waveform is usually less than one slot pitch, and therefore a very fine spatial discretisation is necessary to catch its peak value. Existing analytical methods are successful only in some particular cases, and fail in others,e.g.,they fail when the magnet pole-arc is unity. Furthermore accuracy is another problem which exists in both numerical and analytical predictions. In Chapter 6 an analytical method for predicting the cogging torque is presented and validated. It is based on the analytical calculation of the magnetic field distribution as described in Chapter 5 and the lateral force which acts on teeth. The technique is capable of predicting the cogging torque in internal and external rotor motors, in either a rectangular or a polar coordinate system. Also it is able to deal with motor topologies in which the magnets are shifted, have an uneven slot distribution etc., design features which are sometimes employed in an attempt to reduce the cogging torque.

Since a brushless DC motor system integrates a permanent magnet motor with its electronic drive, the phase current waveform contains significant time harmonics which may increase the emitted noise level . An analytical model for predicting the steady-state dynamic performance of a 3-phase brushless DC drive has been developed and validated in Chapter 7. In the model, which assumes a constant speed and takes the back-emf and cogging torque waveforms as input functions, the initial conditions which yield the steady-state solution are generated directly by exploiting the periodicity in the stator winding voltage and current waveforms. With due account

of the influence of the inverter bridge and commutation events, the model provides a rapid means of assessing the important features of the motor and drive performance during the early stages of design, such as the influence of the back-emf waveform, current limiting, as well as commutation timing etc.. The model is then developed further to couple in the equation of motion of the rotor to enable the transient and steady-state dynamic performance of brushless DC drives to be predicted. The drive circuit is idealised into two states which depend on whether the freewheel diode is conducting or not, and are described by two groups of state equations and solved by the Runge-Kutta integration method. The dynamic performance is obtained by introducing a relationship between the state variable and the stator winding currents. Using the developed technique, the effects of commutation and winding temperature on the dynamic performance, including the level of harmonics in the current and torque waveforms and the linearity of the torque-speed curve etc., are investigated.

In Chapter 8 a comprehensive analytical technique is presented for predicting the airgap field distribution in radial-field, internal/external rotor, brushless DC motors under any load condition, acounting implicitly for the corresponding stator winding current waveforms and the effect of stator slot openings. It is based on a 2-dimensional analytical analysis in polar coordinates of the airgap /magnet regions, and combines an analytical calculation of the armature reaction field with the analytical prediction of the current waveforms from Chapter 7 and the open-circuit magnetic field produced by the magnets from Chapter 5, to permit the instantaneous field distribution and hence the radial force distribution to be predicted under any load condition and specified commutation strategy. The analytically predicted open-circuit, armature reaction, and load field distributions have been compared with finite element analyses. In addition, a 2-dimensional analytical method for calculating the back-emf waveforms in the windings of a brushless permanent magnet DC motor is developed. Futhermore, the developed analytical technique for predicting the armature reaction field is applied to the calculation of the self- and mutual winding inductances, again with due account of the relatively large effective airgap.

In Chapter 9, a systematic analytical approach to the prediction of the acoustic power level of a permanent magnet brushless DC motor is presented and validated on a prototype motor. The model can estimate the noise level of internal rotor, encased type motors. Its vibrational response model differs from conventional ones in that it can consider not only the iron core but also the frame, as well as their damping effects, the damping ratios from Yang's and Frohne's measurement being directly utilised. The modifing effects of the end-shields on the stiffness of the stator are considered by experiment, although in the future this may be carried out by three-dimensional finite element calculation.

Conclusions are presented in Chapter 10 on the various aspects of the research, viz. magnetic field, torques, forces, dynamic performance, vibrational and acoustic behaviour, as well as the noise from radial-field brushless permanent magnet DC motors.

The main elements of the research described in the thesis are summarised in Figs. 1.2, 1.3, and 1.4. Fig. 1.2 shows the strategies for noise prediction of brushless permanent magnet DC motors/drives, whilst the flow-chart and features for the analytical electromagnetic analyses are illustrated in Figs. 1.3 and 1.4. The various models developed for the prediction of magnetic field distribution, force, vibration, and acoustic noise are integrated into a single CAD package.

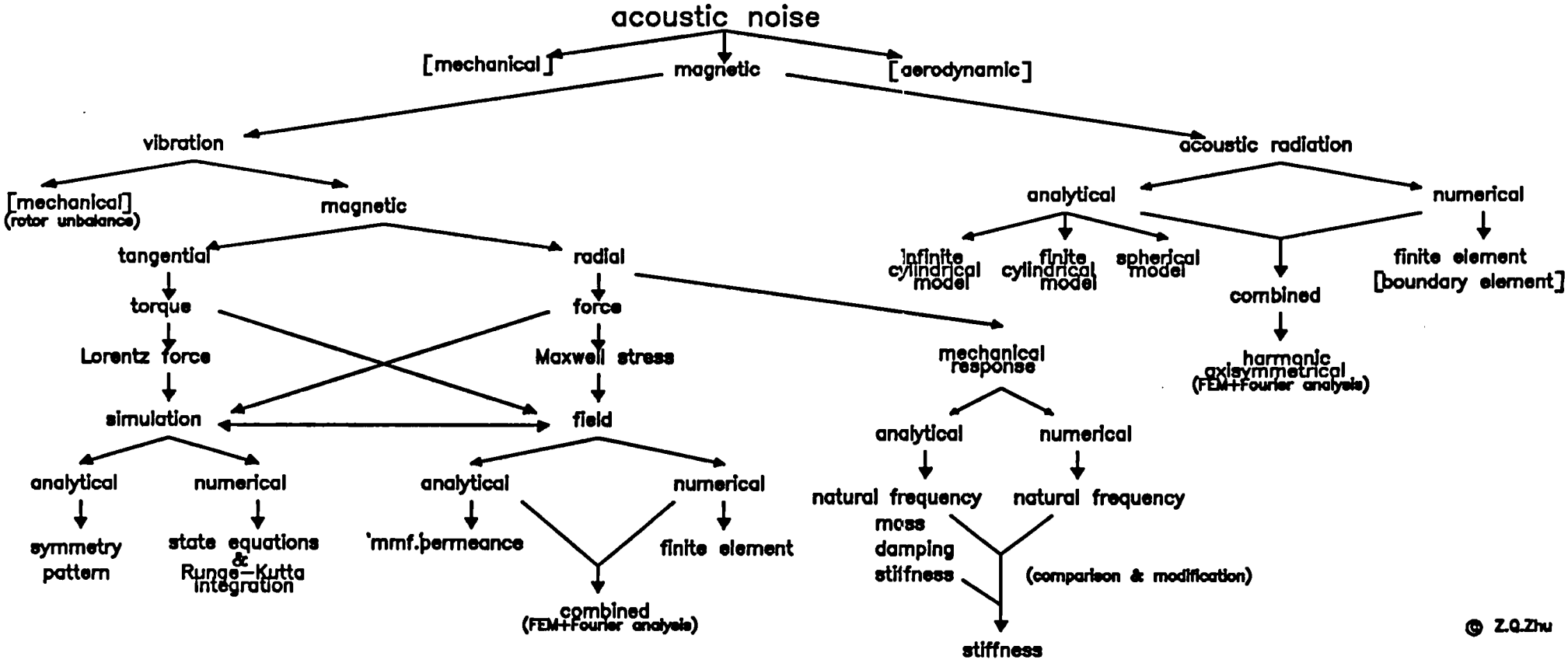

Fig. 1.2 Strategies for noise prediction of a brushless permanent magnet DC motor

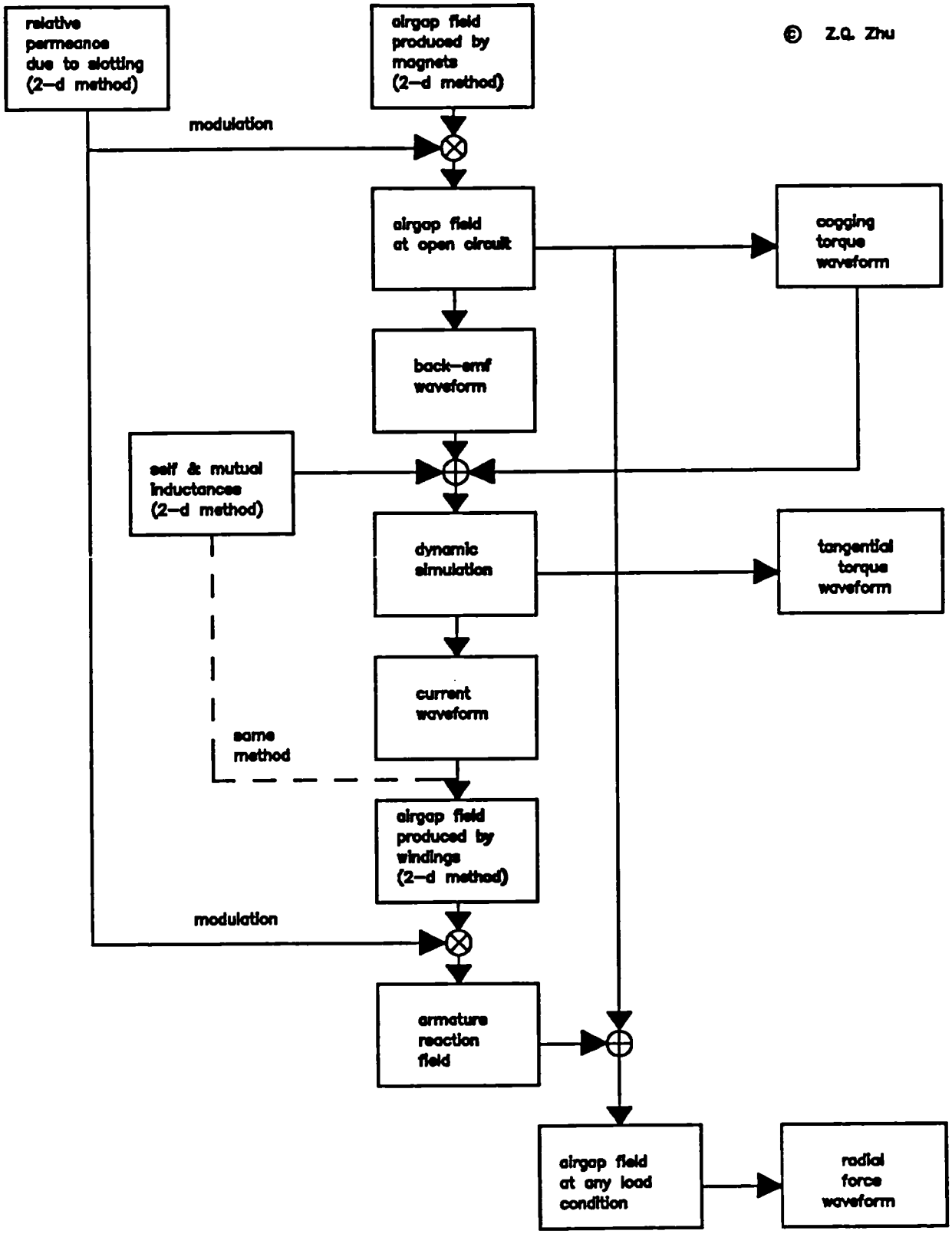

Fig. 1.3 Flow-chart for analytical electromagnetic analyses

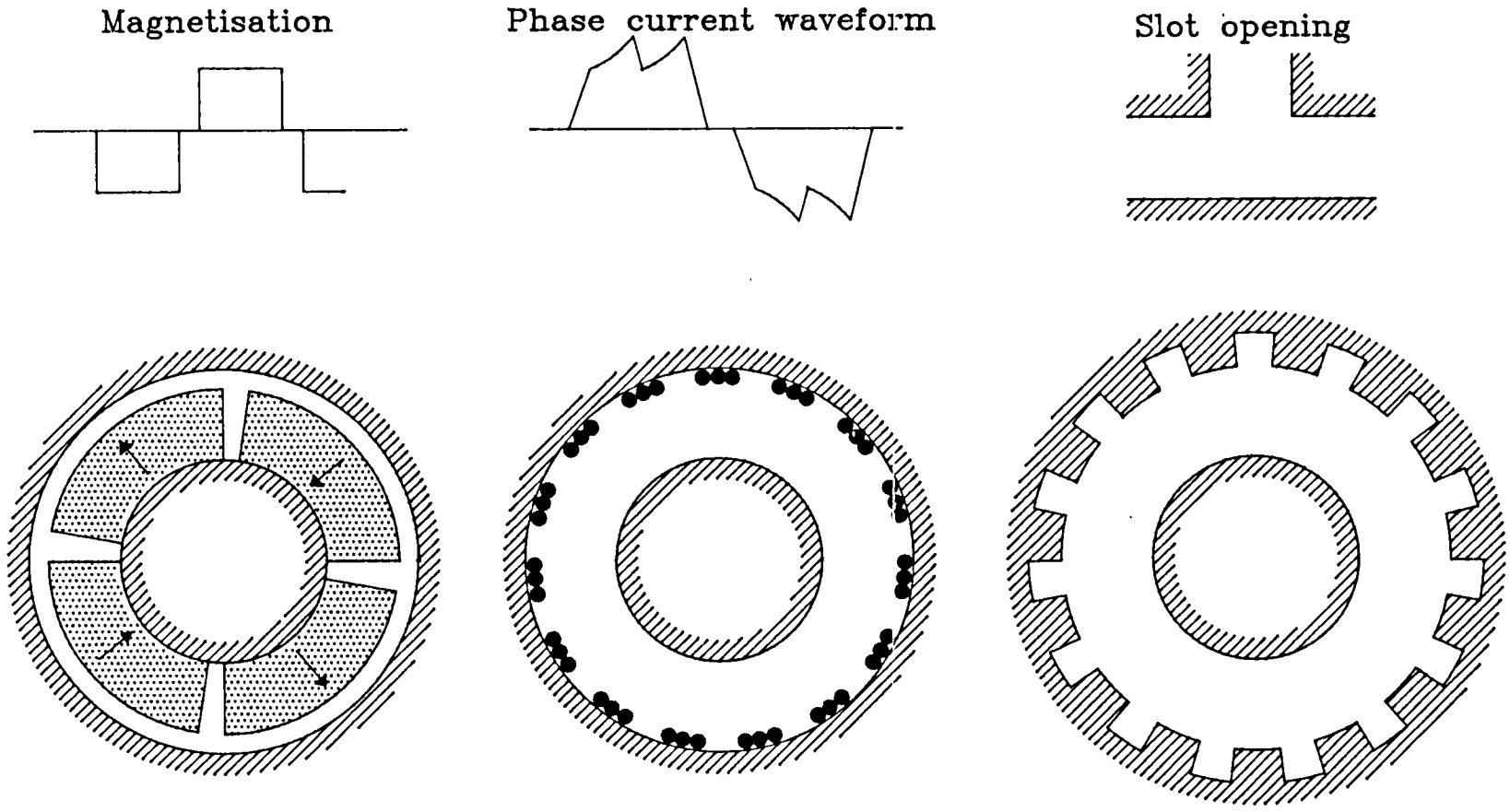

(a) Model for calculating magnetic field produced by magnets

(b) Model for calculating magnetic field produced by windings

(c) Model for calculating relative permeance

Fig. 1.4 Features of analytical models for electromagnetic analyses

CHAPTER 2

EFFECTS OF END-SHIELDS AND ROTOR ON NATURAL FREQUENCIES AND MODES OF STATOR OF SMALL ELECTRICAL MACHINES, BY MODAL ANALYSIS

2.1 Introduction

As has already been shown in chapter 1 a knowledge of the natural frequencies and modes of the stator of an electrical machine is essential to avoid resonances between the stator and the impressed exciting force [2.1], as well as for establishing its acoustic radiation model [2.2]. The finite element and the modern experimental modal analysis techniques provide a means for their prediction and measurement. However due to computing limitations it is not feasible for a finite element model to account for all the detailed features of a machine structure, which consists of the stator itself, end-shields, bearings, the rotor etc. Nevertheless finite element analysis can be used to predict the vibration behaviour of the stator at the design stages. Modal analysis on the other hand, can be used only when the machine is available. It does, therefore, compliment the finite element method, by experimentally validating predicted results and justifying essential simplifications to theoretical models.

Many papers have been published on the natural frequencies and modes of stators, reporting both theoretical and experimental studies. Baudry et al [2.3] investigated the vibration of an a. c. generator stator by model test, whilst Verma and Girgis [2.4] investigated the influence of the main dimensions of encased stators on their non-uniform axial vibration, the effects of teeth, windings, frame and laminations on the natural frequencies and modes, and dual resonances. Erdelyi and Horvay [2.6], and Ellison and Yang [2.7], have studied the vibration modes of double ring type stators, and, more recently, Watanabe et al [2.8] and Noda et al [2.9] have reported the influence of the windings on the natural frequencies of stator cores. However all investigations have been restricted to the stator itself. None has considered the effects of the end-shields and

the rotor, or actual running condition, this is the case even in the three-dimensional studies of the natural frequencies related to the non-uniform longitudinal mode by finite elements as reported by Belmans et al [2.10][2.11], and the Fourier series analysis of Verma et al [2.12][2.13][2.14].

In small machines, such as brushless permanent magnet DC motors and small induction motors, the length-to-diameter ratio of the stator is usually not very large. As a consequence their end-shields, which are bolted to the stator frame, have a relatively large stiffness. The rotor, which is supported by the end-shields and the bearings, will also restrict and affect the vibrational behaviour of the stator. As a further contribution to the subject, therefore, an investigation by the modal analysis technique into the effects of end-shields, the rotor, and the running condition on the natural frequencies and modes of the stator of a small 3-phase induction motor whose stator is identical to that of a brushless permanent magnet DC motor was undertaken under the following condition:

(a) stator, with frame, core and winding only
(b) with end-shields added to (a)
(c) with rotor included in (b)
(d) as (c), but under no load operation

2.2 The Modern Experimental Analysis Technique

If a vibrating system is expressed in the form of a discretised system having n degrees of freedom, it can approximated by a set of second-order linear differential equations:

$$[M]\{\ddot{y}(t)\}+[C]\{\dot{y}(t)\}+[K]\{y(t)\}=\{p(t)\} \qquad (2.1)$$

which are coupled by inertial, damping and elastic terms, and where [M], [C] and [K] are mass, damping and stiffness matrices, (n x n); $\{\ddot{y}(t)\}$, $\{\dot{y}(t)\}$, and $\{y(t)\}$ are acceleration, velocity and displacement vectors, (n x 1); {p(t)} is the exciting force vector (n x 1).

Modal analysis is a process by which the coordinates are transformed to a modal description through the application of a natural mode matrix $\{\psi\}$. The equations then become uncoupled, the transformation simultaneously diagonalising the coefficient matrices, i. e. mass, damping and stiffness.

Basically the technique involves the application of a known exciting force to the structure and the measurement of resulting response, to obtain the transfer function between the exciting signal and the response signal by digitising and applying the Fast Fourier Transformation (FFT). Whilst the natural frequencies can be obtained from only one transfer function curve, to determine the vibration modes it is necessary to fix either the reference accelerometer and excite all the measurement points or to fix the reference exciting force site and move the accelerometer to every measurement point selected on the surface of the structure, and repeat the transfer function measurement for each condition. The measured transfer functions are in the form of discretised data from which the resonant frequencies, damping ratio, and vibration modes etc can be obtained by curve fitting.

By taking the Laplace transform of the system equations (2.1) and assuming zero initial condition, they can be written in the form:

$$\{y(s)\} = [H(s)]\{p(s)\} \tag{2.2}$$

from which the transfer function can be expressed as:

$$[H(s)] = ([M]s^2 + [C]s + [K])^{-1} \tag{2.3}$$

According to complex modal theory if [M], [C] and [K] are all symmetric , i. e. if the system satisfies structural reciprocity, which simply states that the motion of point A, resulting from a force at point B, is identical to that of point B, resulting from the same force applied at point A, [H(s)] is a symmetrical transfer function matrix (n x n). Every element in [H(s)] is a transfer function $H_{ap}(s)$, that is

$$[H(s)] = \sum_{k=1}^{n} \left\{ \frac{[A_k]}{s - s_k} + \frac{[A_k]^*}{s - s_k{}^*} \right\}$$

$$= \sum_{k=1}^{n} \left\{ \frac{\{\psi_k\}\{\psi_k\}^T}{\gamma_k (s - s_k)} + \frac{\{\psi_k{}^*\}\{\psi_k{}^*\}^T}{\gamma_k{}^* (s - s_k{}^*)} \right\} \qquad (2.4a)$$

and

$$H_{ap}(s) = \sum_{k=1}^{n} \left\{ \frac{A_{kap}}{s - s_k} + \frac{A_{kap}{}^*}{s - s_k{}^*} \right\}$$

$$= \sum_{k=1}^{n} \left\{ \frac{\psi_{ka}\,\psi_{kp}}{\gamma_k (s - s_k)} + \frac{\psi_{ka}{}^*\,\psi_{kp}{}^*}{\gamma_k{}^* (s - s_k{}^*)} \right\} \qquad (2.4b)$$

represents the transfer function between the points "a" and "p" on the structure, "a" being a response point and "p" an exciting point. By evaluating at s = j ω, the transfer function in the frequency domain is obtained. In equation (2.4) $A_{kap} = \Psi_{ka}\Psi_{kp} / \gamma_k$ is the one element of the residue matrix $[A_k]$ of the kth mode related with the complex root or pole s_k, $\{\psi\}$ is the mode vector, Ψ_{ka} and Ψ_{kp} are elements in $\{\psi\}$, γ_k is the complex scaling from the *k* th mode, and * denotes the complex conjugate.

According to complex modal theory, if a single driving point is excited and response measurements processed at each test point, one column of [H(s)] is obtained, whilst if the response at a single test point is measured as the driving point is moved around the structure one row of [H(s)] can be obtained. In practice only one column or one row of [H(s)] needs to be determined in order to solve for all the unknowns, viz. poles (s_k) and residues (A_{kap}). In a stable system, a pole $s_k = \zeta_k \omega_k + j\, \omega_k \sqrt{1 - \zeta_k^2}$, where ζ_k represents the damping ratio and ω_k the natural frequency for the *k* th mode. The residue matrix $[A_k]$, formed by residues A_{kap}, describes the vibrational behaviour in space, i. e. the *k* th mode vibration.

2.3 Experimental Method

2.3.1 Experimental Machine

A 180w, 6-pole, 3-phase encased type induction motor was used throughout the investigation. Its main dimensions are shown in Fig 2.1 and listed below:

Outer/inner diameters of stator core	120/71 mm
Outer/inner diameters of rotor core	70. 5/18 mm
Axial lengths of stator core/rotor core	55/55 mm
No of slots on stator/rotor	36/33
outer/inner diameter of frame	130/120 mm
Axial length of frame	124 mm
Total axial length (frame + end-shields)	180 mm

Both the stator and rotor cores are of 0. 5mm laminations. The frame and end-shields are cast aluminium, and a small hole of diameter 8 mm is provided in the frame for connections to the windings.

2.3.2 Experimental Apparatus

A schematic of the experimental system, which is based around a Hewlett-Packard 5423A Structural Dynamic Analyser is shown in Fig. 2.2.

2.3.3 Experimental Conditions

The measurements were made with the motor elastically suspended from a tripod under the conditions shown in Table 2.1

Table 2.1 Measurement Condition

Condition number	Conditions				Measurements	
	Stator (frame+core with winding)	End-shields	Rotor	No-load running	Transfer function	Modes
(a)	/				/	/
(b)	/	/			/	
(c)	/	/	/		/	/
(d)	/	/	/	/	/	vibration

2.3.4 Selection of Measurement Points

Considerable care is required in the selection of points at which to apply the excitation force and at which to measure the response. In particular points which coincide with the nodes of the vibration modes must be avoided, otherwise they cannot be excited or will not be detected [2.15]. Since the experiment machine was a small motor whose resonant frequencies are relatively high, random white noise generated by a permanent magnet shaker was used as the exciting force signal. Care was taken to ensure that the exciting force was not applied at the nodes of axial modes of order 0 or 1. An accelerometer was used to monitor the vibrations at the points shown in Fig. 2.2.

2.3.5 Other Measurement Considerations

1) In carrying out modal analysis it is assumed that:
   a) the vibration of the frame is in a radial direction, and that tangential and axial vibrations can be neglected;
   b) the vibration of the end-shields is in an axial direction, and that radial and tangential vibrations can be neglected.

2) The modal analysis of the stator (i. e. frame + core + winding) is selected as a reference for the investigation. The stator exhibits both circumferential symmetrical and anti-symmetrical modes [2.15], but these are not studied independently. Thus the exciting point is maintained at a single site.
3) Since the measurement of transfer functions is the key to modal analysis, the ordinary coherence functions [2.16] between the exciting force and the response acceleration is measured to estimate the reliability of the measurement.
4) In carrying out the measurements the force signal and acceleration signals are sampled and discretised. In order to reduce discretisation error an upper frequency limitation of 3. 2 kHz was selected, which covers the range of natural frequencies of interest. "Hanning windows" are used, both for the exciting signal and the response signal, to reduce the bias and leakage errors of the finite sample.

2.4 Modal Analysis

2.4.1 Measured Results

Both Figs 2.3 and 2.4 show the measured modes of both the motor under conditions (a) and (c) respectively. The structure of the motor and the site of the excitation are marked in order to show clearly the relative displacement and modes. Fig 2.5 shows the transfer functions between the exciting force and the response at a given point but under the four different conditions of Table 2.1. The transfer function curves show that there are three or four low frequency resonant peaks, albeit much lower than the natural frequencies of the motor, which are caused by the mounting of the shaker and its connection with the impedance head. The values of the related coherence functions are low.

When the transfer functions are measured under a no-load running condition, the coherence functions become worse due primarily to the disturbing effect of electro-magnetic vibrations as well as mechanical vibrations associated with the bearings. Fortunately, however, despite

sampling errors slightly reducing the coherence functions at the resonant frequencies, the amplitude of the coherence functions is nearly 1, as shown in Fig 2.6, which confirms that the measurement of the transfer function is reliable. Fig 2.5 also compares the measured vibration power spectrum for no-load operation with the transfer functions under the different conditions cited in Table 1, whilst the measured natural frequencies under different conditions are listed in Tables 2.2 and 2.3. As a further illustration of the measurements, Fig 2.7 shows the coherence function, the transfer function together with its real and imaginary parts, as well as the Nyquist plot for condition (c).

Table 2.2 Measured Results under conditions (a) and (b)

Conditions	Natural frequencies (Hz)					
(a)	1154	1373	1487	1820	2426	2972
(b)	1162.5	1400	1788			

Table 2.3 Comparison of Natural Frequencies of mode (n x m) under different conditions

Conditions	1 x 0	2 x 0	2 x 1	3 x 0
(a)		1487	1820	2972
(b)		1788	>3200	>3200
(c)	644	1838	>3200	>3200
(d)	650	1825	>3200	>3200

Note: 3200Hz is the upper-limit of the measured frequency

2.4.2 Natural Frequencies and Modes of Stator

Fig 2.3 shows that modes of natural frequencies 1487 Hz, 1820 Hz, 2972 Hz are very regular and that their mode orders are n x m = 2 x 0, 2 x 1, 3 x 0 respectively. The displacements of these modes indicate that the vibration of the stator is much larger at one end than that at the other. The test motor is one of a range of three phase induction motors, rated from 180 W - 550 W [2.17] which were designed by the author to a low noise specification, and all utilise the same frame, end-shields and laminations. The only significant difference is in the windings and the

axial length of the cores. However, as a consequence the core is not located centrally in the frame, being much closer to the back end-shield, as illustrated on Fig 2.1. As a consequence the stator stiffness near the front end-shield is much lower than that near the back end-shield, which accounts for the increased level of vibration.

In addition to the natural frequencies referred to above, other natural frequencies, viz. 1154 Hz, 1373 Hz and 2426 Hz, are observed, Fig 2.2, where it will be seen that the mode associated with the 2426 Hz natural frequency has a circumferential order of two and an axial order of one, but that its displacement is not as regular as that of the (2 x 1) mode associated with 1820 Hz. Around the region of the feet the displacement is more or less uniform whereas it varies significantly elsewhere, which suggests that the probable cause is the feet.

As to the 1154 Hz and 1373 Hz vibrations since the exciting point is located close to a node of the vibrational mode, the resonance peaks are small, and a relatively large error is introduced into the modal analysis.

2.4.3 Effects of End-Shields

When the end-shields are affixed to the stator its stiffness is increased significantly as are the values of the natural frequencies. As will be seen on the transfer function curve of Fig 2.5, and Tables 2.2 and 2.3, the natural frequency of mode order n x m = 2 x 0 is increased from 1487 Hz to 1788 Hz, whilst the natural frequencies of mode orders n x m = 2 x 1, and n x m = 3 x 0, which were previously 1820 Hz and 2972 Hz respectively are now beyond the high frequency limitation of the measurement 3.2 kHz. However the circumferential variation of the radial displacement has not changed significantly, Fig 2.4. It will also be seen that since it is the stator which is being excited radially the axial vibration of the end-shields is much smaller than the radial vibration of the stator. This suggests that in an acoustic radiation model of a machine the vibration of the end-shields can be neglected when the electro-magnetic noise is assumed to be produced by radial forces alone.

It will be noted on Fig 2.4 that axial vibration of the front end-shield is smaller than that of the back end-shield. This was subsequently diagnosed as being caused by one of the three securing bolts for the front end-shield being loose, which inhibited the transmission of the vibrations to that end-shield.

By comparing the displacement of each mode on Figs 2.3 and 2.4, it is seen that without the end-shields the vibration of the frame near the front end is larger than that near the back end. When the shields are attached the vibration is more or less similar at both ends due to the restricting effect of end-shields. However, the amplitude of the radial displacement near the back end-shield of mode 1838 Hz still varies, due to the exciting point and the stator core being in closer proximity.

2.4.4 Effect of Rotor

Although the rotor is supported in the end-shields by rolling bearings its addition does not significantly increase the stiffness of the stator. Therefore, by comparison with the end-shields the rotor has a much smaller effect on the values of the natural frequencies and the shape of the mode. For example, the natural frequency of mode order n x m = 2 x 0 is only changed from 1788 Hz to 1838 Hz. However the rotor does create important new frequencies, in particular the n x m = 1 x 0 mode, is produced. For example, a new natural frequency 644 Hz of mode order n x m = 1 x 0, as shown in Fig 2.4, is introduced, an effect which has been measured by the author on other machines. It results from the fact that it is only when the rotor is inserted or when the feet are fixed, that such a mode is possible.

2.4.5 Effect of Running Condition

It will be seen in Fig 2.5 and in Table 2.3 that the modifying effects under the no-load running condition are negligible, since from standstill to rated no-load speed, the natural frequencies of mode order n x m = 1 x 0 and 2 x 0 change only slightly, from 644 Hz and 1838 Hz to 650 Hz and 1825 Hz respectively.

The measured vibration power spectrum of the motor on no-load is shown on Fig 2.5. The frequencies of the three pronounced peaks are 550Hz, 650 Hz and 1750 Hz, and have been shown to correspond to mode orders of three, the 550 Hz and 650 Hz components being produced by the first-order slot harmonics of the stator and the rotor, and the 1750 Hz component being produced by the third-order slot harmonics, whose electromagnetic spectral analysis is given in Appendix 2.6. Although these two electro-magnetic vibrational frequencies are close to the natural frequencies of 650 Hz and 1825 Hz, though their mode orders are different, when the natural frequencies were measured the amplitude of the exciting force was adjusted to make its response much bigger than the electro-magnetic vibration, thus minimising the effect of electro-magnetic vibration on the transfer function measurement.

2.5 Conclusions

The effects of allowing for the end-shields, the rotor, and the running condition on the natural frequencies and modes of the stator of a small electrical machine have been investigated by the modern experimental modal analysis technique. It has been shown that:

1) Because of their restricting effects, the end-shields significantly increase the values of the natural frequencies of the stator.
2) By comparison the effect of the rotor is much smaller. However the rotor does cause important new natural frequencies to be introduced, in particular the first-order mode.
3) The modifying effects under a no-load condition are negligible, as is likely to be the case up to rated load.
4) The study has provided data which should assist further investigations, particularly in regard to the effects of the mounting feet on the natural frequencies and modes of stators, in developing vibrational models based on finite elements, as well as acoustic models.

More investigations on a brushless DC motor will be described in Chapter 9.

2.6 Appendix - Electromagnetical Spectral Analysis

As described in section 2.3.1, the test motor is a three-phase, 6-pole induction motor, whose stator and rotor slot combination is 36/33. Hence p=3, Q_s=36, Q_r=33, the slip $s \cong 0$ at no-load. the radial electromagnetic force waves, vibrational frequencies and orders are analysed and listed in Tables 2.4 and 2.5 according to the technique described in [2.18]. The most important components of electromagnetic noise in this particular motor are those frequencies related to mode order 3, viz. 550 Hz, 650 Hz, and 1750 Hz, all of which are due to the interaction of the slot harmonics of the stator and the rotor.

Table 2.4 Radial Electromagnetic Force Waves

	k_1	-1	+1	-2	+2	-3	+3
k_2	$\mu\backslash\nu$	-33	39	-69	75	-105	111
-1	-30	3^-					
+1	36	3^+	3^-				
-2	-63			6^-			
+2	69			0^+	6^-		
-3	-96						
+3	102					3^+	

where $\nu = k_1 Q_s + p$, $\mu = k_2 Q_r + p$

Frequencies of vibrational forces are

$f = f_1 [k_2 Q_s (1 - s)/p + 2]$ for $n^+ = \mu + \nu$

$f = f_1 [k_2 Q_s (1 - s)/p + 0]$ for $n^- = \mu - \nu$

Table 2.5 Vibrational frequencies and orders

μ	-30	36	36	-63	69	69	102
ν	-33	-33	39	-69	-69	75	-105
n	3^-	3^+	3^-	6^-	0^+	6^-	3^+
f (Hz)	***550***	***650***	***550***	1100	1200	1100	***1750***

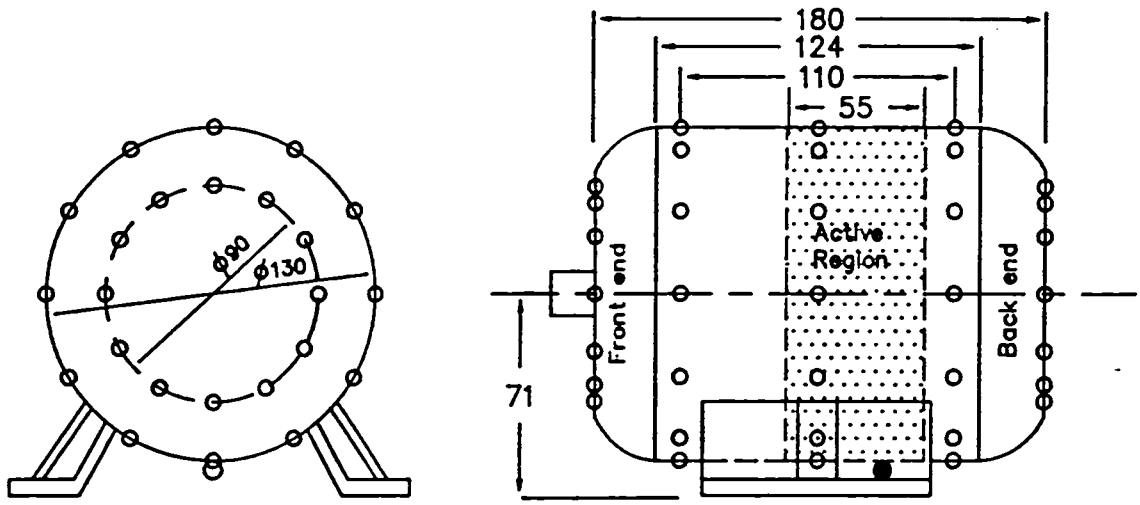

Fig.2.1 Test motor and measurement point distribution

Exciting point ●; picking-up point o

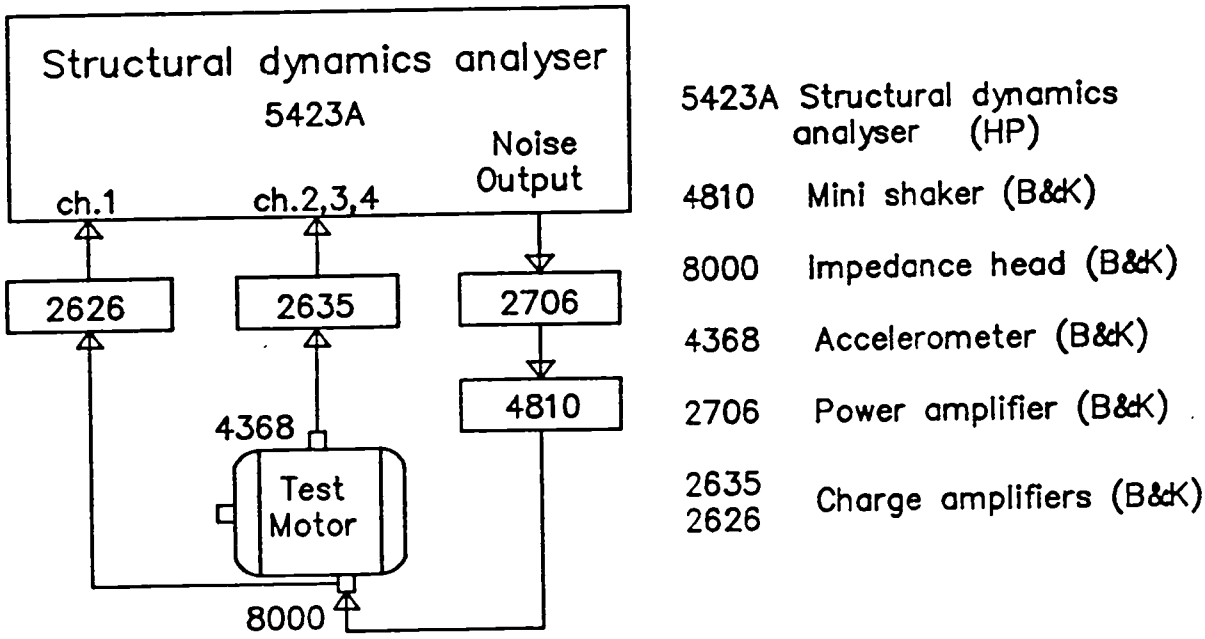

Fig.2.2 Experimental system

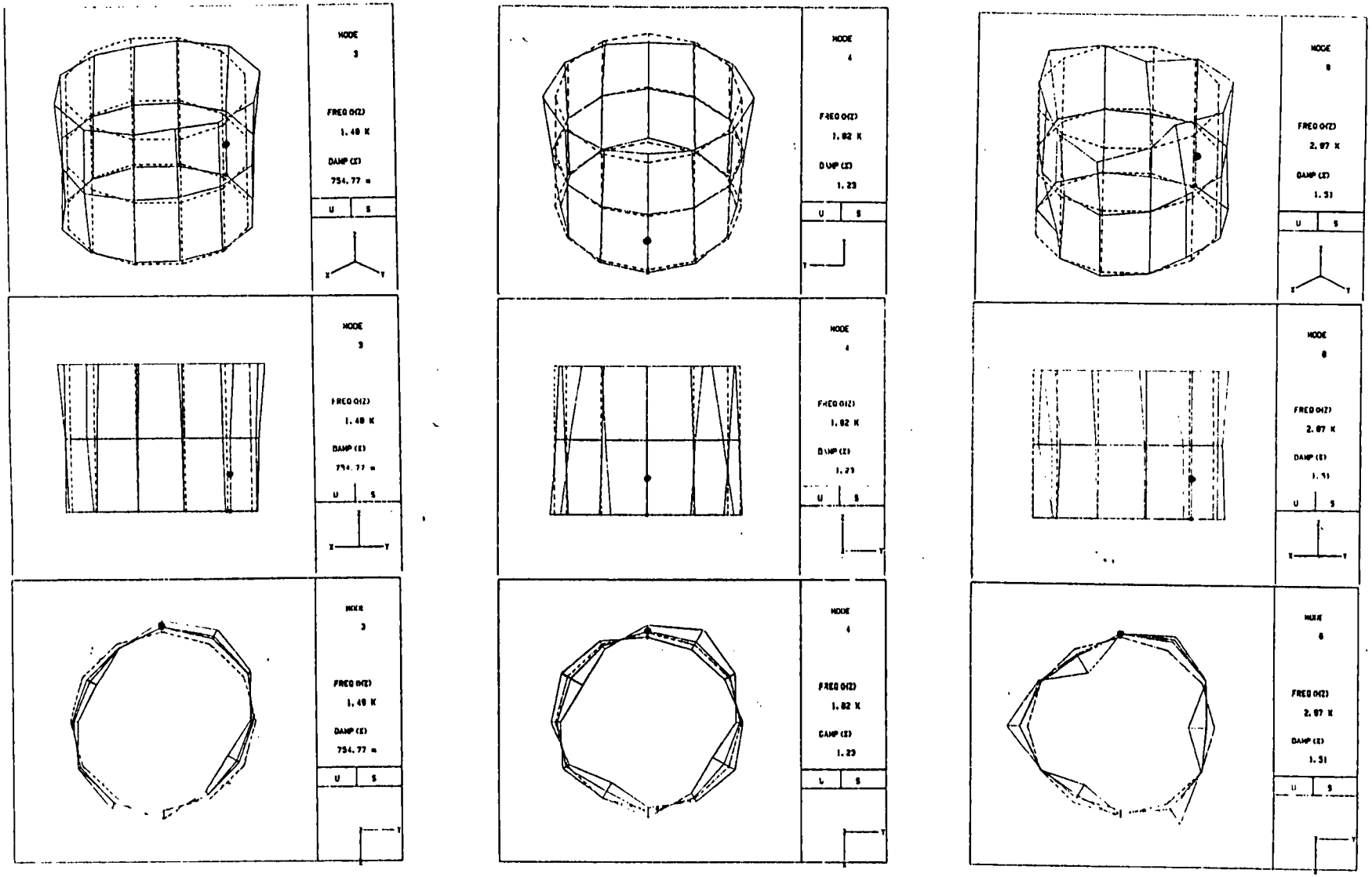

FREQ(HZ) 1.49K
DAMP(%) 754m

FREQ(HZ) 1.82K
DAMP(%) 1.23

FREQ(HZ) 2.97K
DAMP(%) 1.51

Fig.2.3a Modes under condition (a)

Exciting point ●; structure of motor.....; mode shape _____

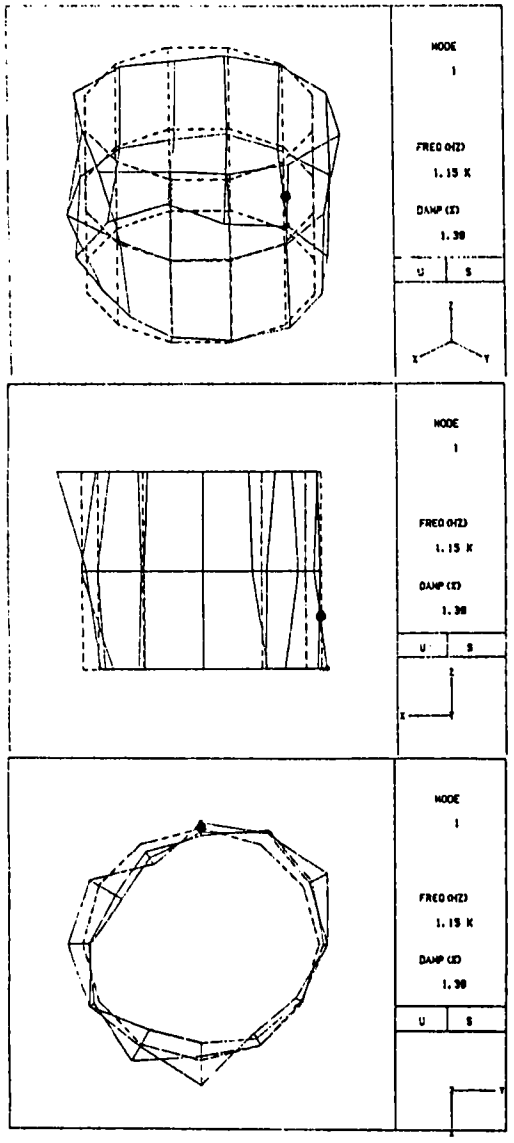

FREQ(HZ) 1.15K
DAMP(%) 1.39

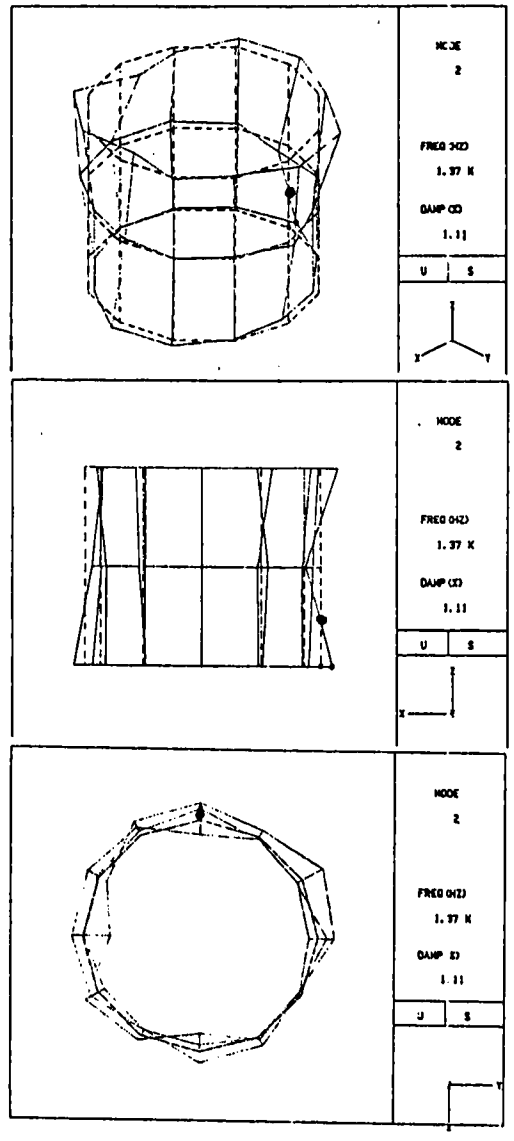

FREQ(HZ) 1.37K
DAMP(%) 1.11

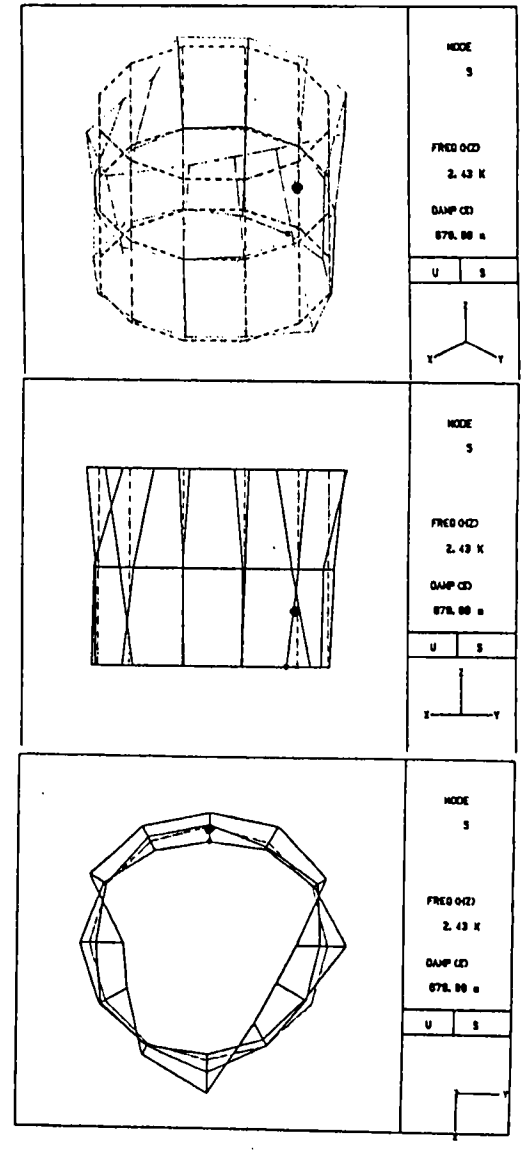

FREQ(HZ) 2.43K
DAMP(%) 679m

Fig.2.3b Modes under condition (a)

Exciting point ●; structure of motor.....; mode shape _____

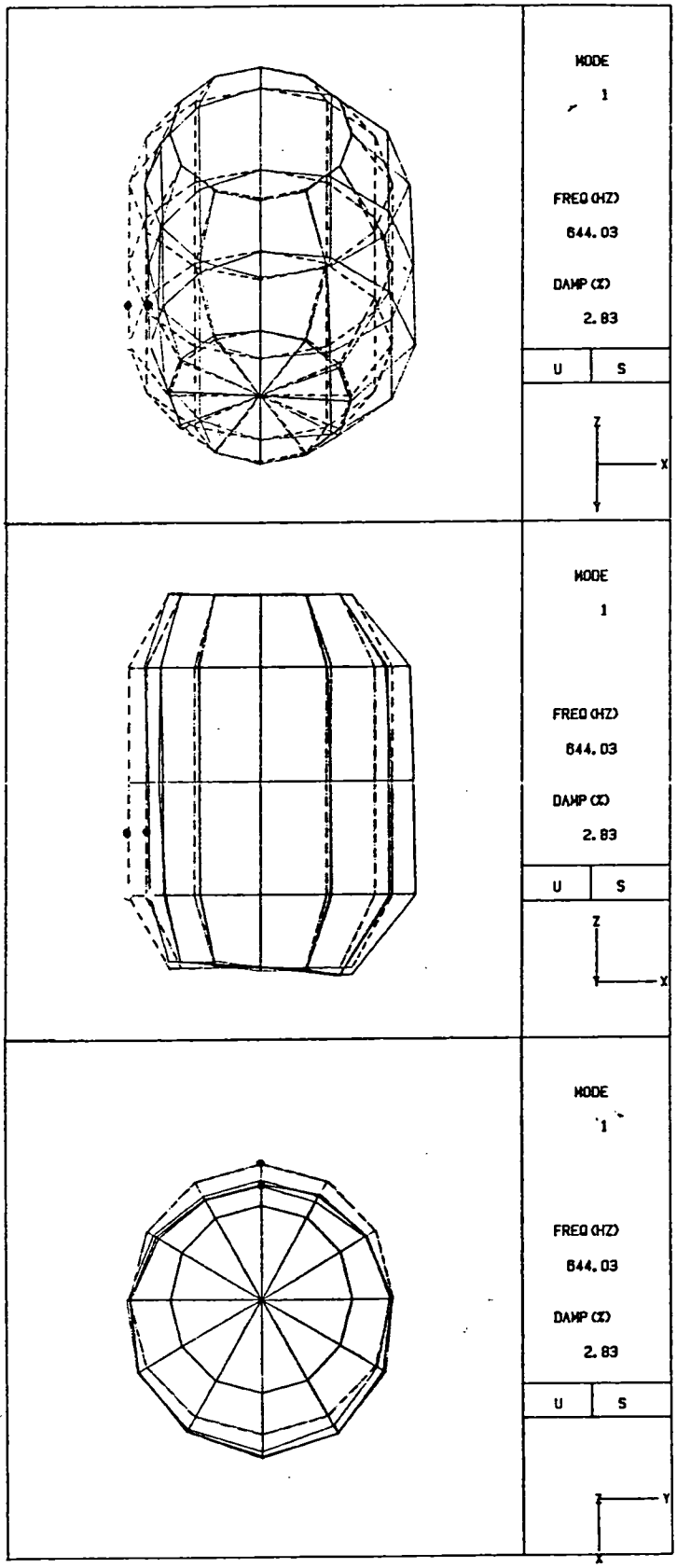

FREQ(HZ) 644.03
DAMP(%) 2.83

Fig.2.4a Modes under condition (c)

Exciting point ●; structure of motor.....; mode shape _____

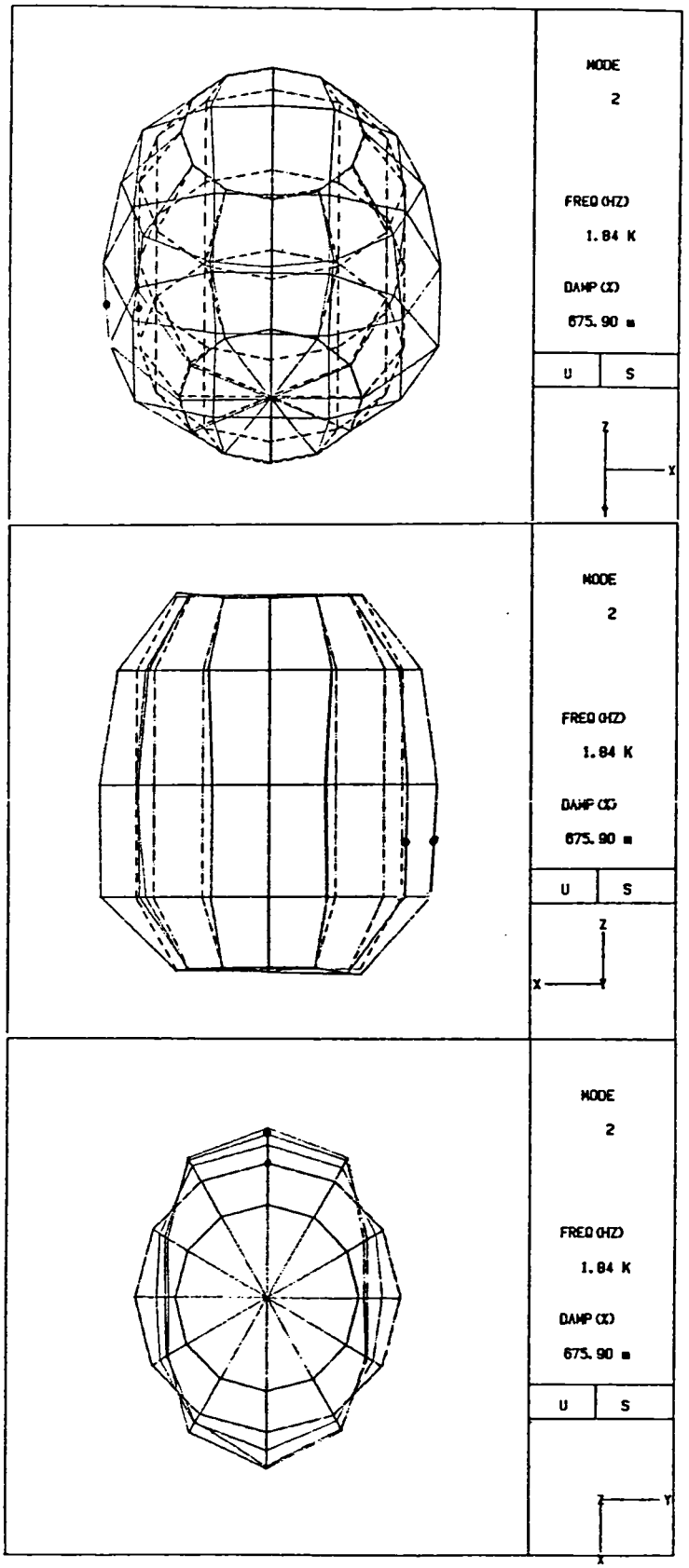

FREQ(HZ) 1.84K
DAMP(%) 675m

Fig.2.4b Modes under condition (c)

Exciting point ●; structure of motor.....; mode shape _____

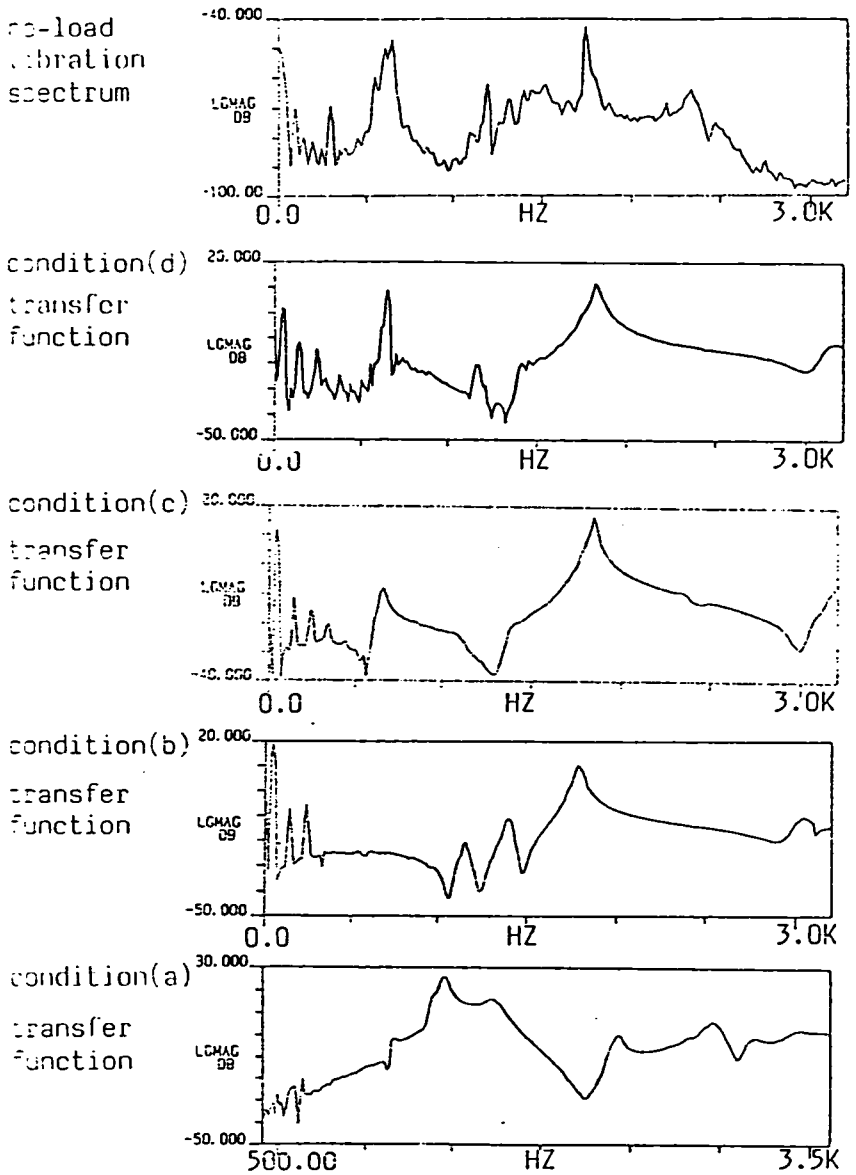

Fig.2.5 Comparison of measured results under different conditions

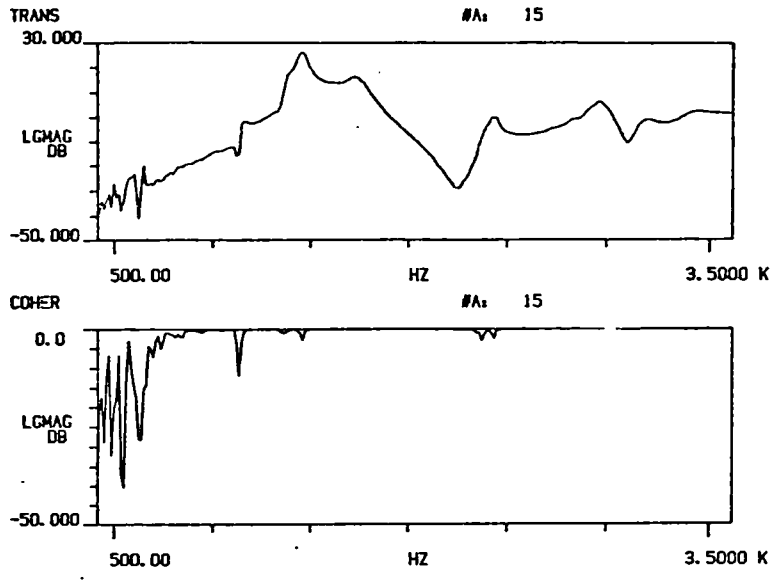

condition(a)

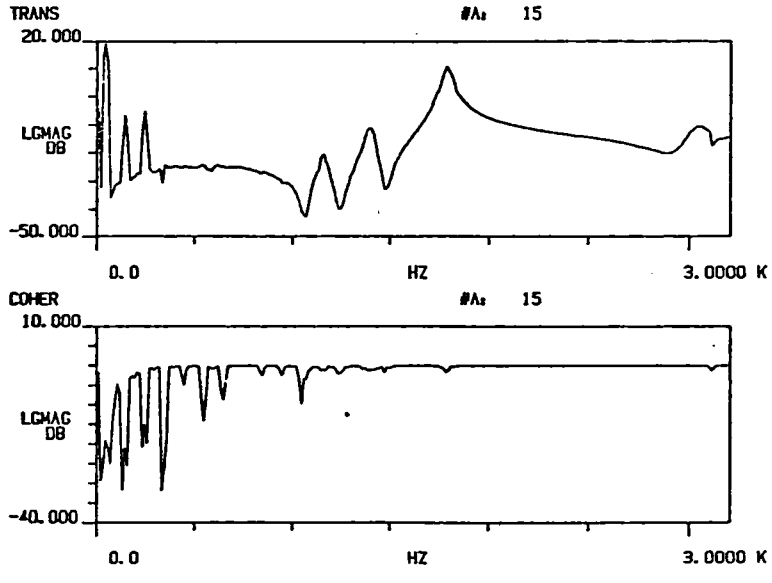

condition(b)

Fig.2.6a Transfer and coherence functions under different measurement conditions

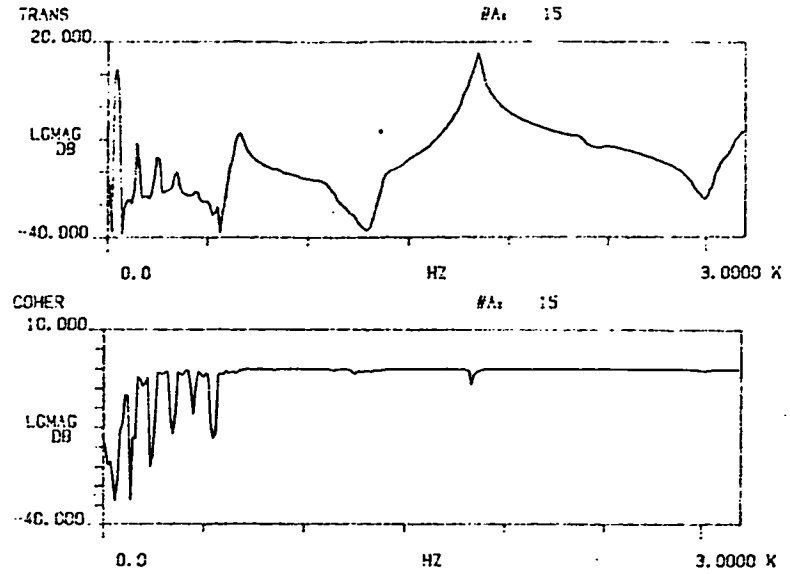

condition(c)

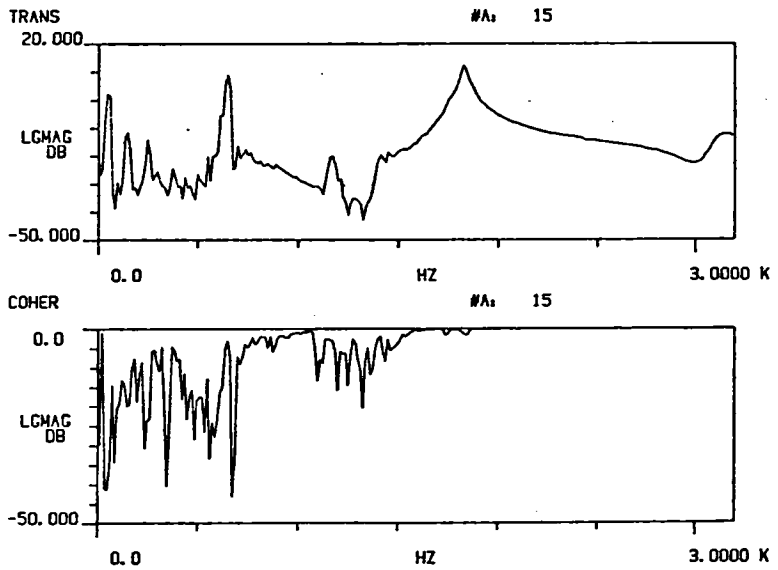

condition(d)

Fig.2.6b Transfer and coherence functions under different measurement condition

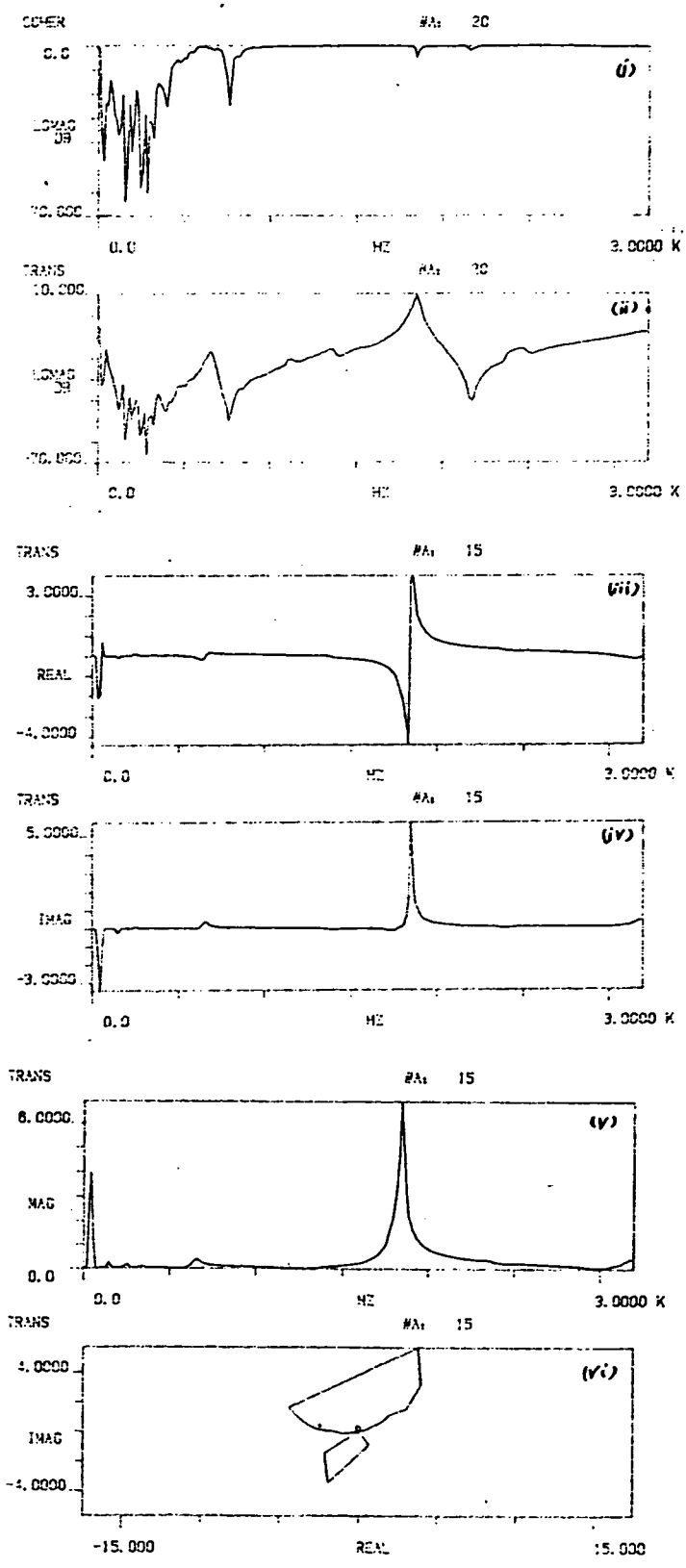

Fig.2.7 Measured results under condition (c)

Coherence function (i); Transfer function amplitude (ii);

Real part (iii); Imaginary part (iv);Nyquist plot (vi)

CHAPTER 3

STUDY OF ACOUSTIC FIELD AND POWER RADIATED FROM ELECTRICAL MACHINES BY ANALYSIS OF FINITE CYLINDER MODEL

3.1 Introduction

It is well known that harmonic magnetic fields in the airgap of electrical machines generate forces acting on the stator core and the end shields, which in turn cause the stator and the end-shields to vibrate and consequently to radiate acoustic noise. From a knowledge of the surface vibrations together with the machine dimensions, the radiated acoustic field and power can be calculated from the relationship between the vibration and noise.

There are two main kinds of model for calculating the radiated acoustic power, one being based on a spherical model whilst the other assumes a cylindrical model.

The spherical model was suggested by Carter [3.1], and developed by Jordan [3.2], Ellison and Moore et al [3.3]. The acoustic power radiated by radial vibrations of a machine stator can be calculated by Jordan's method [3.2], whilst the effect of a longitudinal variation of the radial vibrations can be determined from Ellison and Moore's method. The model, however, is suitable only for short machines, having an aspect ratio of axial length-to-diameter nearly equal to unity.

The cylindrical model was developed by Alger [3.4][3.5], Erdelyi [3.6][3.7], Ellison and Yang et al [3.8][3.9]. However Alger [3.5][3.6] considered the machine as an infinitely long cylinder, so that he could not account for the effect of the aspect ratio. Erdelyi [3.7] on the other hand treated the machine as a finite length cylinder with infinitely long cylindrical stiffening baffles at each end, thus enabling the effect of the length-to-diameter ratio to be studied. Physically this model neglects the effect of the ends and prevents the vibration of the stator from being

transmitted into the extensions. This artifice can be represented by an infinitely long cylinder vibrating only in an infinite length, as shown in Fig 3.1.

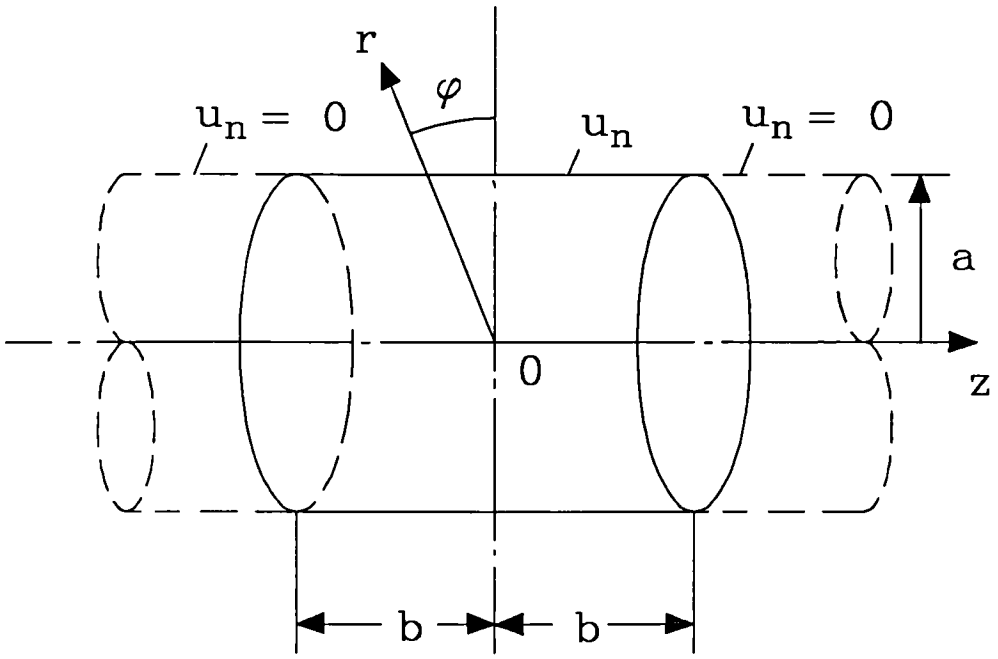

Fig 3.1 Acoustic radiation model of finite cylinder

Initially it was the sound pressure level and not the acoustic power level that was used to estimate the noise emitted from an electrical machine. The sound pressure at any point around the machine can be calculated, once the vibrational mode, frequency, and dimensions of the stator have been specified. Erdelyi [3.6] did not present a method for calculating the radiated acoustic power. This was done subsequently by Ellison and Yang in 1971 and 1975, using the same model on both occasions, by calculating the acoustic power according to the sound pressure and the particle velocity in the air on the surface of the stator by the "p-v" conjugation method [3.8]. In addition, they studied the effect of the length-to-diameter ratio on the acoustic power [3.9]. Unfortunately, since their formulae for the calculation of the acoustic power are in terms of Bessel functions and modified Hankel functions and also include generalised integrations they are not particularly convenient for routine use during the course of designing a machine.

Nevertheless the main dimensional characteristics of electrical machines are included in the cylindrical model of finite length as far as electromagnetic noise is concerned. In addition the effect of the axial length-to-diameter ratio can be considered, whilst the solutions are obtained analytically. Consequently as the first stage of the current research, as well as for the further extension of Erdelyi, Ellison and Yang's work, the same model for calculating the acoustic power is used. However, the technique which is developed eliminates the need for calculating the sound pressure and particle velocity distribution around a machine as was required in Ellison and Yang's method. Instead it utilises the surface vibration of the stator, and a much simpler formula for the relative sound intensity is obtained. Subsequently the sound pressure distribution is investigated, and its variation in three-dimensions is calculated and measured.

3.2 Derivation of Formulae

When the acoustic radiation model of the electrical machine shown in Fig 3.1 is adopted the problem can be expressed as follows, with the assumption that the pressure, p, is a harmonic function of time:

$$(\nabla^2 + k^2)p = 0 \tag{3.1}$$

where ∇^2 is the Laplacian operator; $k = \omega/c$; c is the speed of sound; ω is the angular frequency.

If the mode number of the surface vibration is n and the magnitude of the travelling vibration wave along a longitudinal axis of the stator surface is constant, the surface vibrating radial velocity can be expressed as*

$$u_n(\varphi, z, t) = \begin{cases} -j\omega A_{rd} e^{j(n\varphi - \omega t)} & \text{for} \quad -b < z < +b \\ 0 & \text{for} \quad z < -b \quad or \quad z > +b \end{cases} \tag{3.2}$$

where A_{rd} is the amplitude of the surface vibratory displacement. r, φ, z, b, etc ar shown in Fig 3.1.

**Note : It is worth noting that in Ellison and Yang's papers [3.8][3.9][3.10] they did not specify whether their acoustic radiation model was the same as Erdelyi's model or not, viz. for the surface vibrating radial velocity given in equation (3.2) they only described the first part within - b < z < + b, whilst ignoring the second part at z < - b or z > + b which refers to the infinitely long extensions in Fig 3.1. However, independant analysis has shown that their results can be obtained only with the infinitely long stiffening baffles. Therefore, as mentioned in section 3.1, their acoustic radiation model is the same as Erdelyi's.*

Close to the surface of the machine, the particle velocity $v_n(a, \varphi, z, t)$ of the air is assumed to be equal to the stator vibration velocity $u_n(\varphi, z, t)$.

$$v_n(r, \varphi, z, t)\Big|_{r=a} = u_n(\varphi, z, t) \tag{3.3}$$

Whilst by Newton's law the relationship between the pressure and the radial particle velocity is

$$v_n(r, \varphi, z, t) = \frac{1}{j\omega\rho}\frac{\partial p_n(r, \varphi, z, t)}{\partial r} \tag{3.4}$$

where ρ is the density of the medium.

Therefore from equations (3.2), (3.3) and (3.4) the boundary condition of equation (3.1) is:

$$\frac{\partial p_n(r, \varphi, z, t)}{\partial r}\Big|_{r=a} = \begin{cases} -\omega^2 \rho A_{rd} e^{j(n\varphi - \omega t)} & \text{for} \quad -b < z < +b \\ 0 & \text{for} \quad z < -b \quad or \quad z > +b \end{cases} \tag{3.5}$$

Combining equations (3.1) and (3.5), the pressure around the surface is found as

$$p_n(r, \varphi, z, t) = \frac{A_{rd}\,\omega^2 \rho\, b}{\pi} e^{j(n\varphi - \omega t)} (Q_{pr} + j Q_{pm}) \tag{3.6}$$

where Q_{pr} and Q_{pm} are given in Appendix 3.6.

It is an important assumption that the particle velocity of the air on the stator surface of the machine is equal to the stator vibration velocity at the surface. This assumption is reasonable only when the radial vibration of the stator is considered. When the frame is made of cast iron

or cast aluminium, and is sufficiently thick enough the coupling between the acoustic radiation and the structural vibration can be neglected, ie. the acoustic radiation and the structural vibration can be studied independantly.

The acoustic power radiated by a machine is calculated according to the sound pressure and the stator vibration velocity at the surface by the "p-v" conjugate method, which is very similar to one of the sound intensity measurement methods, in which the surface vibration is measured by an accelerometer, the pressure is measured by a microphone, and then the sound intensity is obtained [3.11].

Therefore, the radiated acoustic power is:

$$
\begin{aligned}
W &= \int_s \frac{1}{2} \mathrm{Re}\{ p_n v_n{}^* \} ds \\
&= \int_{-b}^{b} \int_0^{2\pi} \frac{1}{2} \mathrm{Re}\{ p_n u_n{}^* \} a \, d\varphi \, dz \\
&= 2 \rho c \pi^2 f^2 A_{rd}{}^2 . 4 \pi a b . I_l
\end{aligned}
\tag{3.7}
$$

where * means "conjugate"; s is the total surface area enclosing the machine; and I_l is the relative sound intensity coefficient.

Therefore

$$
\begin{aligned}
W &= \int_{-b}^{b} \int_0^{2\pi} \frac{1}{2} \mathrm{Re}\{ p_n u_n{}^* \} a \, d\varphi \, dz \\
&= \int_{-b}^{b} \int_0^{2\pi} \frac{1}{2} \mathrm{Re}\left\{ \frac{A_{rd} \, \omega^2 \rho \, b}{\pi} e^{j(n\varphi - \omega t)} (Q_{pr} + j Q_{pm}) [-j \omega A_{rd} \, e^{j(n\varphi - \omega t)}]^* \right\} a \, d\varphi \, dz
\end{aligned}
$$

$$= \int_{-b}^{b} \int_{0}^{2\pi} \frac{1}{2} \mathrm{Re} \left\{ \frac{A_{rd}{}^2 \omega^3 \rho a b}{\pi} j (Q_{pr} + j Q_{pm}) \right\} d\varphi \, dz$$

$$= - A_{rd}{}^2 \omega^3 \rho a b \int_{-b}^{b} Q_{pm} \, dz$$

$$= - A_{rd}{}^2 \omega^3 \rho a b \int_{-b}^{b} \int_{-k}^{k} \frac{2 \sin b h}{b h \sqrt{k^2 - h^2}} \left(\frac{Q_b Q_c - Q_a Q_d}{Q_c{}^2 + Q_d{}^2} \right) dh \, dz \qquad (3.8)$$

For simplicity, $J_n (a \sqrt{k^2 - h^2})$ is simply written as J_n and similarly for Y_n. Hence, from the expressions for Q_a, Q_b, Q_c, and Q_d in Appendix 3.6,

$$\begin{aligned} Q_b Q_c - Q_a Q_d &= (Y_n \cos h z + J_n \sin h z) (J_{n-1} - J_{n+1}) \\ &\quad - (J_n \cos h z - Y_n \sin h z) (Y_{n-1} - Y_{n+1}) \\ &= \cos h z \, [(Y_n J_{n-1} - J_n Y_{n-1}) + (J_n Y_{n+1} - Y_n Y_{n+1})] \\ &\quad + \sin h z \, [Y_n (Y_{n-1} - Y_{n+1}) + J_n (J_{n-1} - J_{n+1})] \end{aligned} \qquad (3.9)$$

and by the recurrence formula for Bessel functions

$$Q_b Q_c - Q_a Q_d = \frac{-4}{\pi a \sqrt{k^2 - h^2}} \cos h z + 2 \sin h z \, (Y_n Y_n{}' + J_n J_n{}') \qquad (3.10)$$

and

$$Q_c{}^2 + Q_d{}^2 = 4 (J_n{}'^2 + Y_n{}'^2) \qquad (3.11)$$

Therefore by replacing equation (3.8) by equation (3.10)(3.11), and noting that the integration of the odd function sin bz becomes zero when the variable z is integrated from -b to b, equation (3.8) simplifies to:

$$\begin{aligned} W &= \frac{1}{2} \rho c (\omega A_{rd})^2 . 4 \pi a b . I_l \\ &= 2 \rho c \pi^2 f^2 A_{rd}{}^2 . 4 \pi a b . I_l \end{aligned} \qquad (3.12)$$

in which the relative sound intensity coefficient I_l is given by

$$I_l = \frac{2\,k\,a\,b}{\pi^2} \int_{-k}^{+k} \frac{\dfrac{1}{a^2(k^2-x^2)}}{J_n{}'^2(a\sqrt{k^2-x^2}) + Y_n{}'^2(a\sqrt{k^2-x^2})} \left(\frac{\sin b\,x}{b\,x}\right)^2 dx \tag{3.13}$$

When the infinitely long cylindrical stator model is considered [3.13] the calculation of the acoustic power is obtained by setting the axial length b to infinity in equation (3.13), giving

$$I_{l\infty} = \frac{2}{\pi\,k\,a\,(J_n{}'^2(ka) + Y_n{}'^2(ka))} \tag{3.14}$$

where J_n, Y_n, J_n', Y_n' are Bessel functions of the first and second kinds, and their derivatives respectively.

3.3 Comparison of Relative Sound Intensity Coefficients

It can be seen from equation (3.13) that the relative sound intensity coefficient obtained by this analysis is much simpler than that given by S J Yang (see Appendix 3.6). As a consequence it is much more convenient to use in that it takes significantly less time to evaluate since it has eliminated the need for calculating the sound pressure and particle velocity distributions around a machine. The predicted numerical results are the same as those calculated from Yang's method, as can be seen in [3.8][3.9].

Fig 3.2 shows a comparison of the calculated results of the relative sound intensity by equations (3.3)(3.4), and by formulae derived by Alger and Jordan for n = 0 and n = 2. Alger's results are much larger than the others since the phase difference between the pressure and the particle velocity is not considered in the calculation of the radiated acoustic power in his infinitely long cylindrical model. When the phase difference is considered, the results can be expressed by equation (3.14) and are shown by curve c which is coincident with Jordan's and Yang's results. It can also be seen that the relative sound intensity coefficient for the stator with infinite axial length is almost the same as that for the stator with a length-to-diameter ratio equal to 4 as

calculated by equation (3.13), ie. when the length-to-diameter ratio is near to 4, the machine can be treated as an infinitely long cylindrical model.

For different aspect ratios of axial length-to-diameter the variation of the relative sound intensity coefficient with the vibration mode is shown in Fig 3.3.

3.4 Measurement and Calculation of Acoustic Field

It is useful to know the sound pressure distribution around a machine for the purpose of noise control as well as for the measurement of acoustic power, viz. the selection of the number of measurement points and their location. In addition it can assist in the near-field measurement of the acoustic power, such as by the sound intensity method - which is of increasing interest due to the availability of "on-line" acoustic power measurement equipment. The measurement and calculation of the sound pressure distribution variation in three-dimensions, viz. in the radial, axial, and circumferential directions, have been made on a three-phase, 4-pole encased type induction motor whose main parameters are:

Rated power	0.8 kW
Rated speed	1380 rpm
Outer diameter of frame	0.14 m
Axial length of frame	0.174 m
Stator and rotor slot combination	24/22

The measurement was separated into two steps. In the first the ventilating fan was removed from the motor, so that aerodynamic noise could be neglected. The sound pressure and vibration spectra of the machine on no-load were then measured in a quiet laboratory using a signal analyser (B & K 3348). The measured results and the theoretical analysis of the vibrational force waves, which are similar to those described in section 2.6, show that in this particular motor, the noise level was dominated by components of frequency 550 Hz andf 1750 Hz, these being larger than

any other components by more than 13dB. Therefore, the vibration and noise spectrum of this motor was considered to consist only of these two components. However, by switching off the power supply when the machine was running on no-load and observing the variation in the vibration and noise spectra, as well as from a theoretical prediction of bearing noise and vibration frequencies, it was deduced that the 1750 Hz component was pure electromagnetic noise, whilst the 550 Hz component was composed of both electromagnetic noise as well as mechanical noise from the ball-bearings. The mode order of the 550 Hz and 1750 Hz electromagnetic components was two, and was produced by the interaction of slot harmonics. In addition, the measurement of end-shield vibrations showed that compared with the radial vibration of the stator their axial vibration was small enough to be neglected.

The sound pressure distribution around the test motor was then measured in an anechoic chamber. The measurement equipment was a B & K 7501 1/3 band frequency spectrum analyser. The machine was placed on an elastic mounting and the measurement was made on no-load, which satisfies the noise measurement standard. However in order to simplify the measurement, the ventilating fan and its shield were again removed so as to minimise aerodynamic noise. The location of the measurement points in the radial, axial, and circumferential directions is shown in Fig 3.4.

The measurements were made at points along a circumference of radius 1 metre in the r-z plane, the sound level transducer being maintained horizontal at the same height as the machine axis, as was also the case when the measurements were made in the axial and radial directions. In addition the transducer was aligned with the outer surface of the machine axis, as was also the case when measurements were made in the axial and radial directions. In addition the transducer was aligned with the outer surface of the machine (excluding the ventilating ribs) when the variation of the sound pressure was measured along its longitudinal axis. As has been pointed out already, the test motor had two dominant components of noise of frequencies 550 Hz and 1750 Hz. An equivalent measured sound pressure level of the 550 Hz component was calculated from the sound pressure levels at two adjacent frequency bands whose band centre frequencies

were 500 Hz and 630 Hz respectively. Similarly an equivalent measured sound pressure level of the 1750 Hz component was calculated from the sound pressure level at two adjacent frequency bands whose band centre frequencies were 1600 Hz and 2000 Hz respectively. The measured results are shown in Fig 3.5 together with predicted results which are obtained from the method described in this chapter by neglecting the ventilating ribs, power supply connection box, and the mounting feet, as well as the effect of the end-shields, and the effect of ball-bearing noise in the 550 Hz component.

In general the comparison of the predicted and measured variation of sound pressure in the three-dimensions shows good agreement. This confirms the suitability of the finite length cylindrical acoustic radiation model with infinitely long stiffening baffle extensions for studying the sound pressure variation. The results also show that the attentuation of the sound pressure with radial distance as predicted from a finite length cylindrical model is more pronounced that predicted from an infinitely long cylindrical model. In addition, for this particular test motor the sound pressure at its mid-plane ($\theta = 0^{o}$) is much larger than at its axis ($\theta = 90^{o}$), which again confirms that the electromagnetic noise induced by radial vibrations of the stator is dominant, whilst the emitted noise contributed by the end-shield is small. However, on comparing the predicted and measured variation of sound pressure along the circumferential and axial directions, it is seen that near the region of the end-shields excellent agreement is achieved for the 1750 Hz component, whilst the difference is relatively larger for the 550 Hz component. Furthermore, the predicted results are smaller than the measured results for this component. This tendency was also evident when measurements were made at circumferences of radius 1.0, 0.7 and 0.4 metre, further confirming the existence of mechanical noise due to ball-bearing vibration in the 550 Hz component.

Further comparisons are given in the next chapter.

3.5 Conclusions

An improved technique for calculating the acoustic power radiated by an electrical machine has been presented. It is based on the sound pressure and the stator vibration velocity at the vibrating surface and results in a much simpler formula for calculating the relative sound intensity, and eliminates the need for calculating the sound pressure and the particle velocity distributions around a machine. The results obtained, viz. the relative sound intensity coefficients, as illustrated on Figures 3.6 are eminantly suitable for routine design purposes.

Appendix 3.6 S J Yang's Formula for Calculating of Radiated Acoustic Power

The formula for calculating the acoustic power radiated by an electrical machine as quoted in references [3.8], [3.9], [3.10] and [3.12] by Yang is as follows:

$$W = 2\rho c \pi^2 f^2 A_{rd}{}^2 . 4\pi a b . I_l$$

$$= \int_0^b \frac{2 A_{rd}{}^2 \omega^3 \rho a b^2}{\pi} (Q_{pr}{}^2 + Q_{pm}{}^2)(Q_{vr}{}^2 + Q_{vm}{}^2) \cos\theta \, dz$$

where

$$\theta = \frac{\pi}{2} + tg^{-1}\left(\frac{Q_{pm}}{Q_{pr}}\right) - tg^{-1}\left(\frac{Q_{vm}}{Q_{vr}}\right)$$

$$Q_{pr} = \int_{-k}^{k} \frac{2 \sin b h}{b h \sqrt{k^2 - h^2}} \left(\frac{Q_a Q_c + Q_b Q_d}{Q_c{}^2 + Q_d{}^2}\right) dh$$

$$- 4 \int_0^{\infty} \cos\left(\sqrt{k^2 + \frac{x^2}{a^2}}\, z\right) \frac{\sin\left(\frac{b}{a}\sqrt{a^2 k^2 + x^2}\right)}{\frac{b}{a}(a^2 k^2 + x^2)} \frac{K_n(x)}{K_{n-1}(x) + K_{n+1}(x)} dx$$

$$Q_{pm} = \int_{-k}^{k} \frac{2 \sin b h}{b h \sqrt{k^2 - h^2}} \left(\frac{Q_b Q_c - Q_a Q_d}{Q_c{}^2 + Q_d{}^2}\right) dh$$

$$Q_{vr} = \int_{-k}^{k} \frac{2 \sin b h}{b h \sqrt{k^2 - h^2}} \left(\frac{E_a Q_c + E_b Q_d}{Q_c{}^2 + Q_d{}^2}\right) dh$$

$$+\int_0^{\infty} \frac{2\pi}{a} \cos\left(\sqrt{k^2+\frac{x^2}{a^2}}\, z\right) \frac{\sin\left(\frac{b}{a}\sqrt{a^2 k^2+x^2}\right)}{\frac{b}{a}\left(a^2 k^2+x^2\right)} dx$$

$$Q_{vm} = \int_{-k}^{k} \frac{2 \sin b\, h}{b\, h \sqrt{k^2-h^2}} \left(\frac{E_b Q_c - E_a Q_d}{{Q_c}^2+{Q_d}^2}\right) dh$$

$$Q_a = \cos(h\,z)\, J_n\left(a\sqrt{k^2-h^2}\right) - \sin(h\,z)\, Y_n\left(a\sqrt{k^2-h^2}\right)$$

$$Q_b = \cos(h\,z)\, Y_n\left(a\sqrt{k^2-h^2}\right) + \sin(h\,z)\, J_n\left(a\sqrt{k^2-h^2}\right)$$

$$Q_c = J_{n-1}\left(a\sqrt{k^2-h^2}\right) - J_{n+1}\left(a\sqrt{k^2-h^2}\right)$$

$$Q_d = Y_{n-1}\left(a\sqrt{k^2-h^2}\right) - Y_{n+1}\left(a\sqrt{k^2-h^2}\right)$$

$$E_a = \sqrt{k^2-h^2}\cos(h\,z)\, J_n'\left(a\sqrt{k^2-h^2}\right) - \sqrt{k^2-h^2}\sin(h\,z)\, Y_n'\left(a\sqrt{k^2-h^2}\right)$$

$$E_b = \sqrt{k^2-h^2}\cos(h\,z)\, Y_n'\left(a\sqrt{k^2-h^2}\right) + \sqrt{k^2-h^2}\sin(h\,z)\, J_n'\left(a\sqrt{k^2-h^2}\right)$$

where $K_n(x)$, $K_{n-1}(x)$, $K_{n+1}(x)$ are the n^{th}, $n-1^{th}$, and $n+1^{th}$ modified Bessel functions.

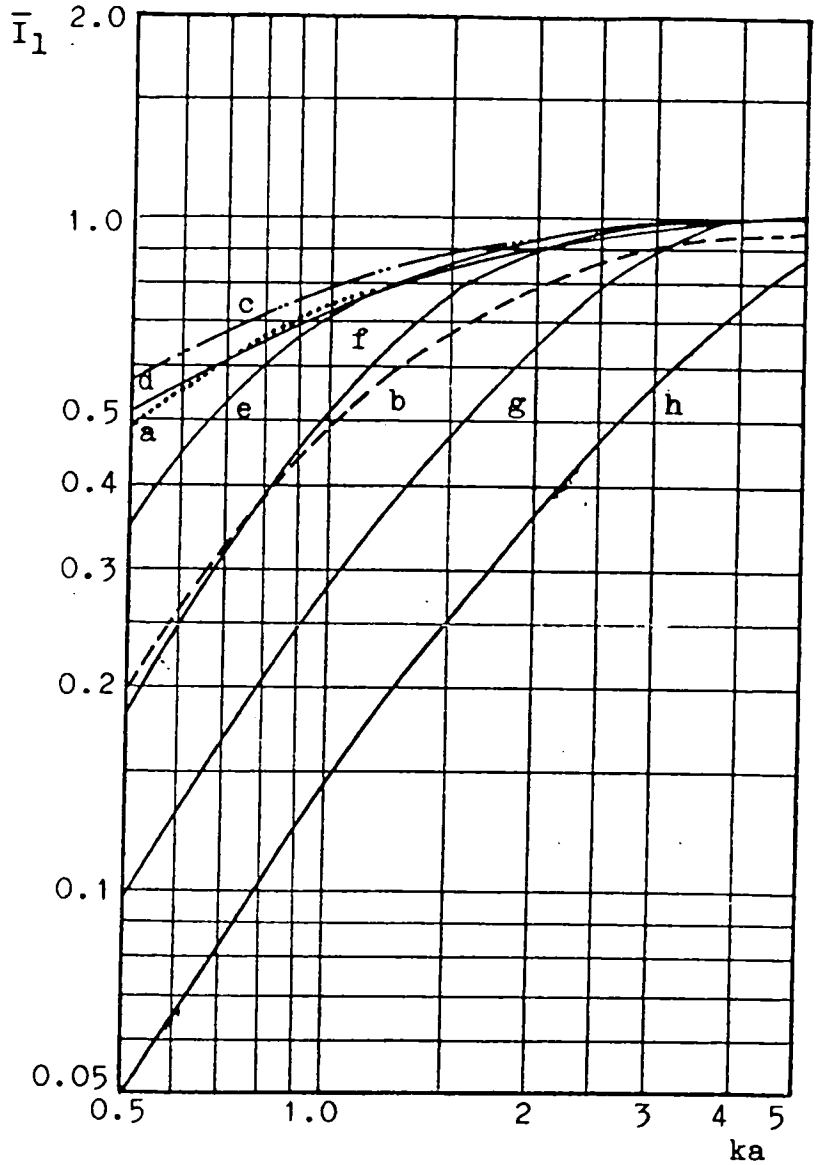

Fig 3.2a Relative sound intensity coefficient

(a): Alger's result (b): Jordan's result (c): Equation (3.14) (d) - (h): Equation (3.13)

(d): b/a=4.0 (e): b/a=2.0 (f): b/a=1.0 (g): b/a=0.5 (h): b/a=0.25

b/a is the ratio of length to diameter

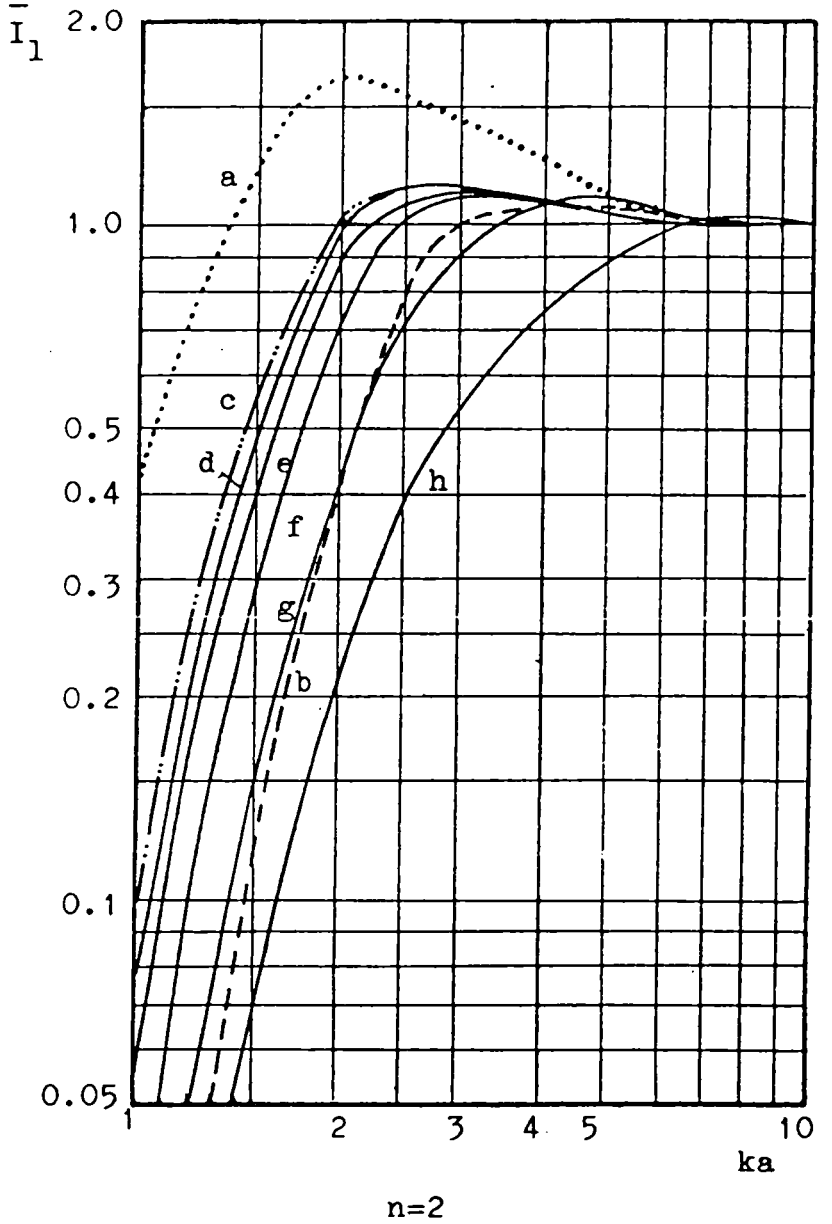

Fig 3.2b Relative sound intensity coefficient

(a): Alger's result (b): Jordan's result (c): Equation (3.14) (d) - (h): Equation (3.13)

(d): b/a=4.0 (e): b/a=2.0 (f): b/a=1.0 (g): b/a=0.5 (h): b/a=0.25

b/a is the ratio of length to diameter

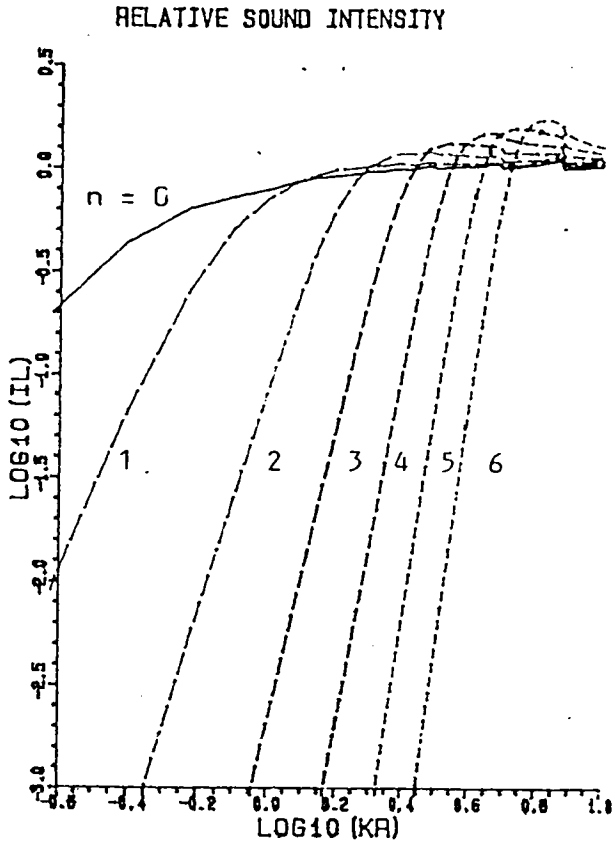

(a) b/a=4

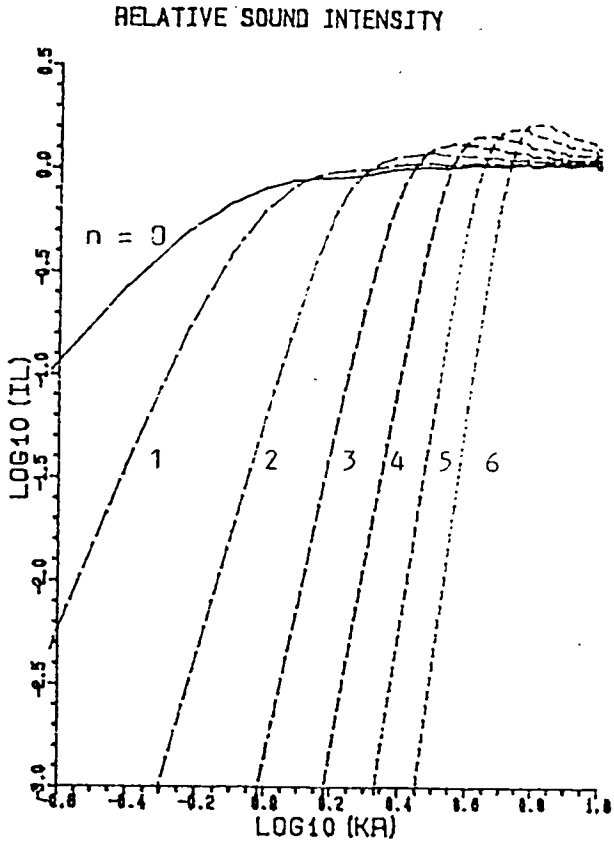

(b) b/a=2

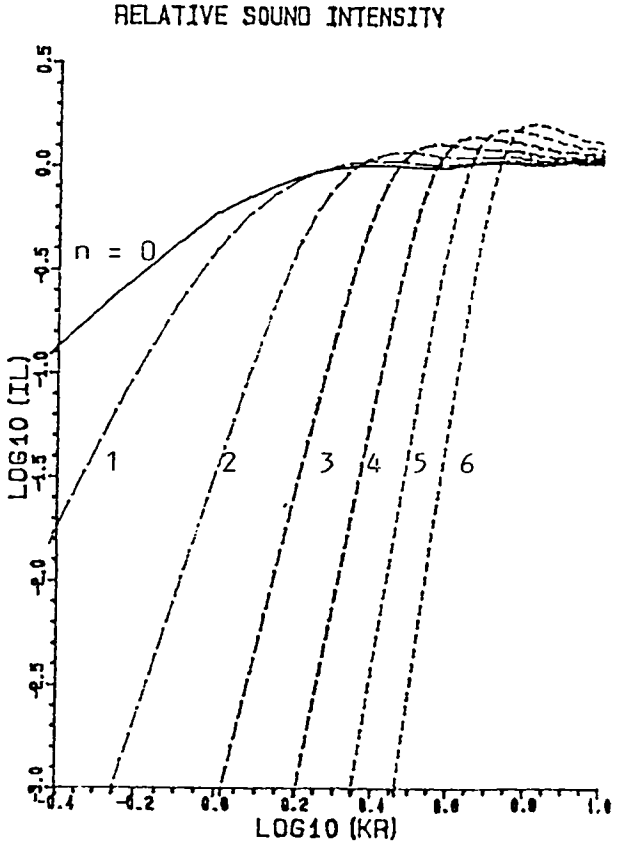

(c) b/a=1

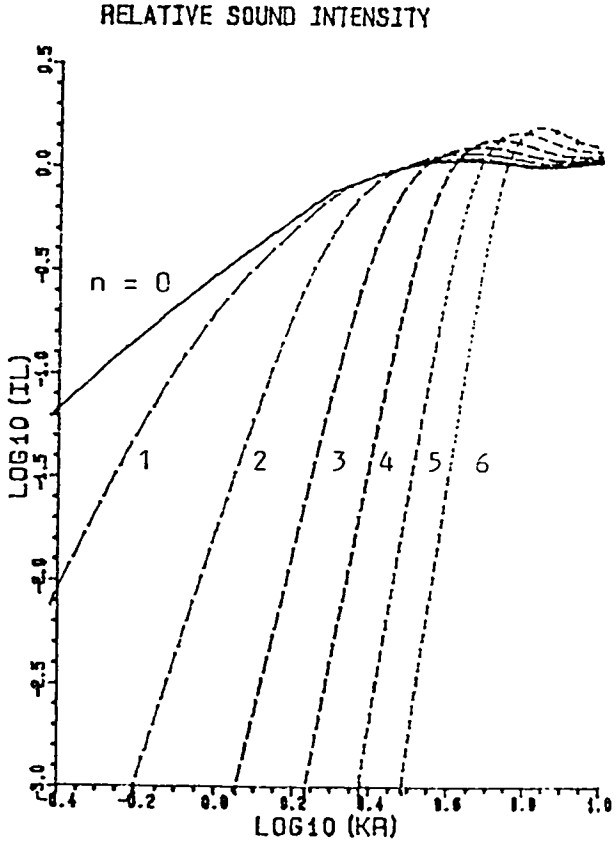

(d) b/a=0.5

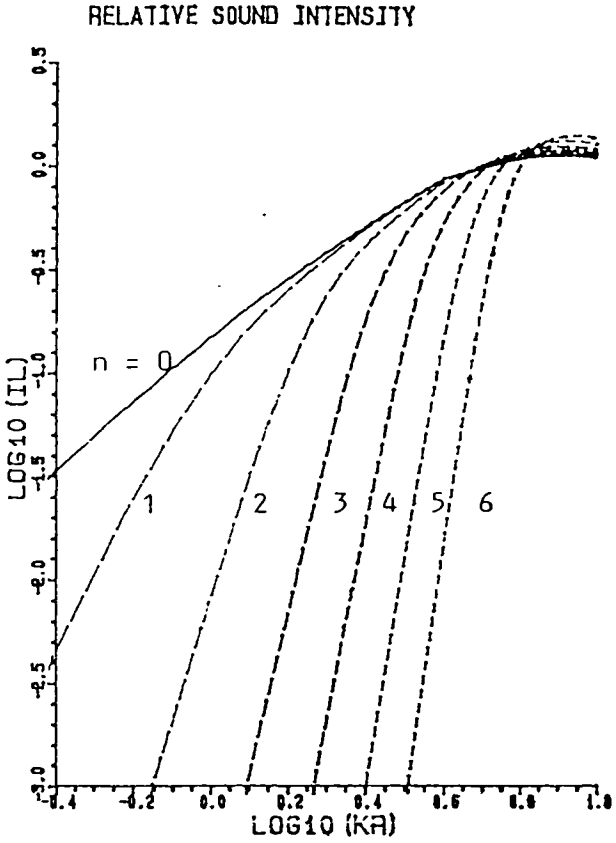

(e) b/a=0.25

Fig 3.3 Variation of the relative sound intensity with vibration mode for different ratios of axial length-to-diameter

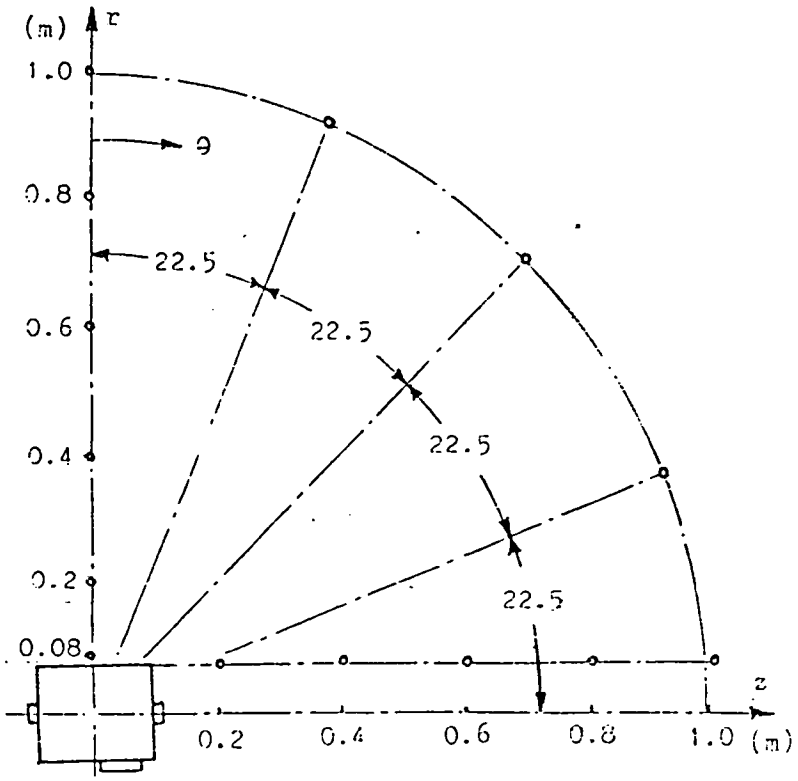

Fig 3.4 Measurement points

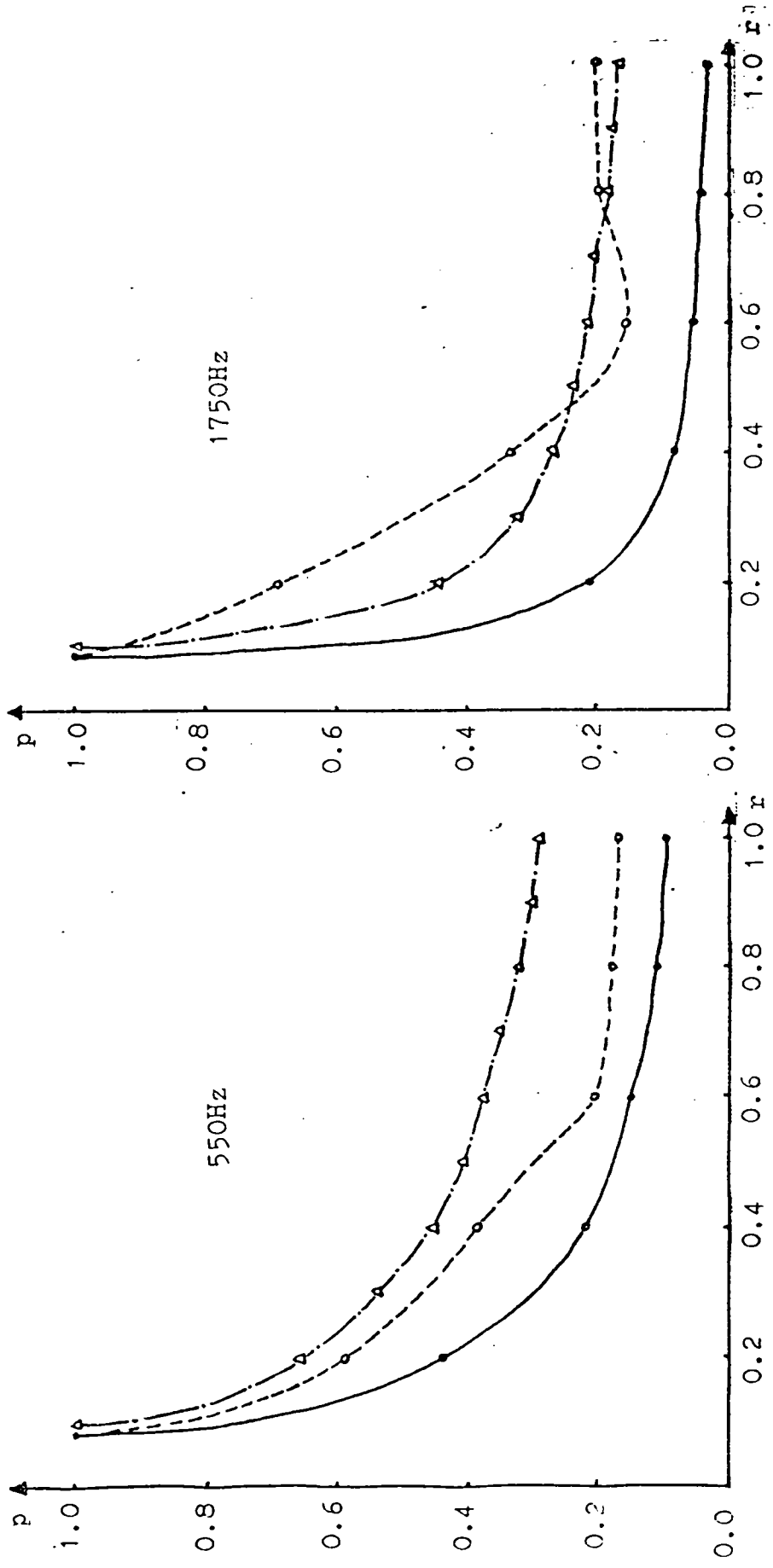

(a) Variation of sound pressure with radial distance

Fig 3.5 Variation of sound pressure around the machine

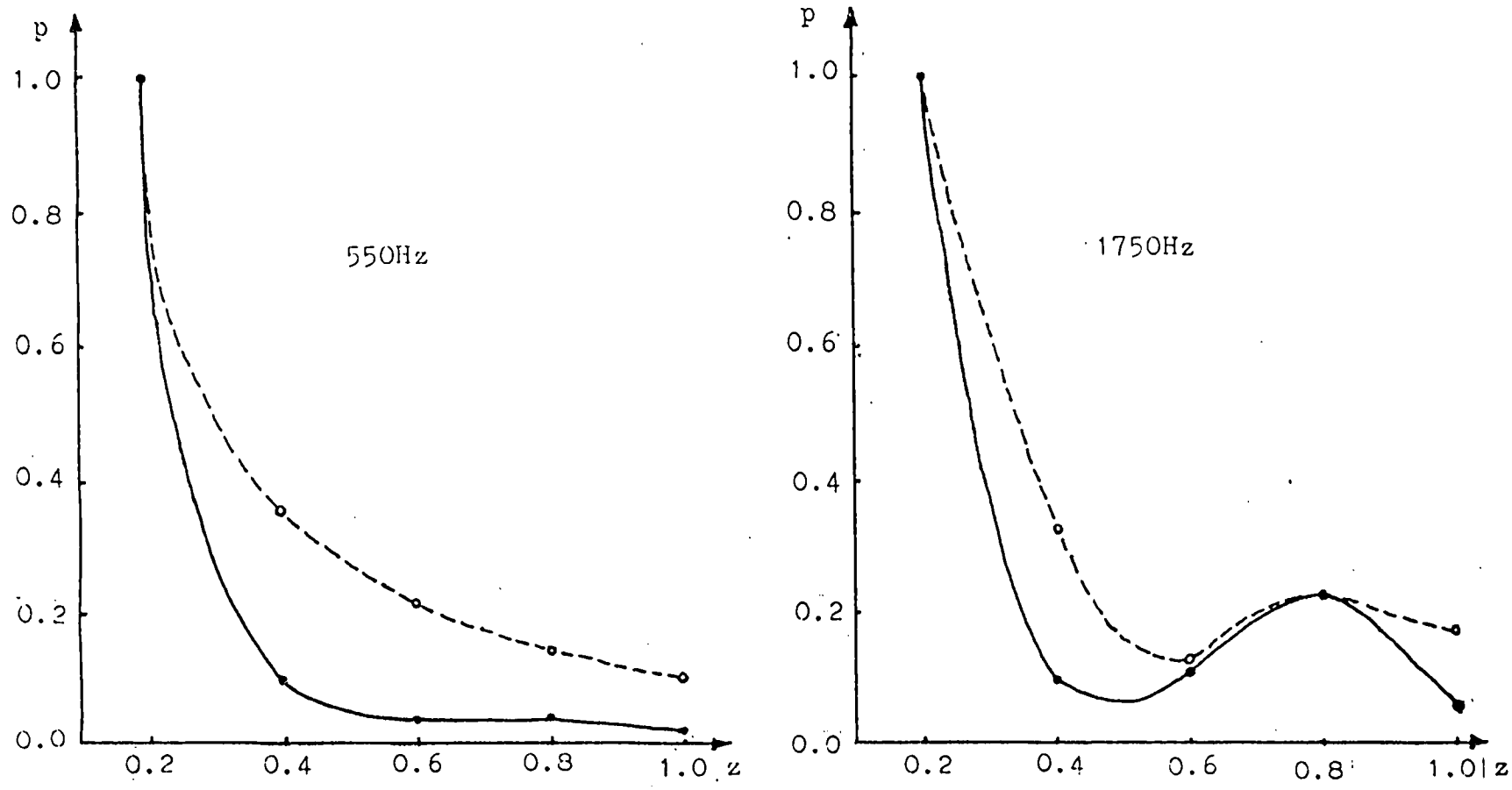

(b) Variation of sound pressure with axial distance

Fig 3.5 Variation of sound pressure around the machine

predicted ----- measured ----- calculated from infinite cylindrical model

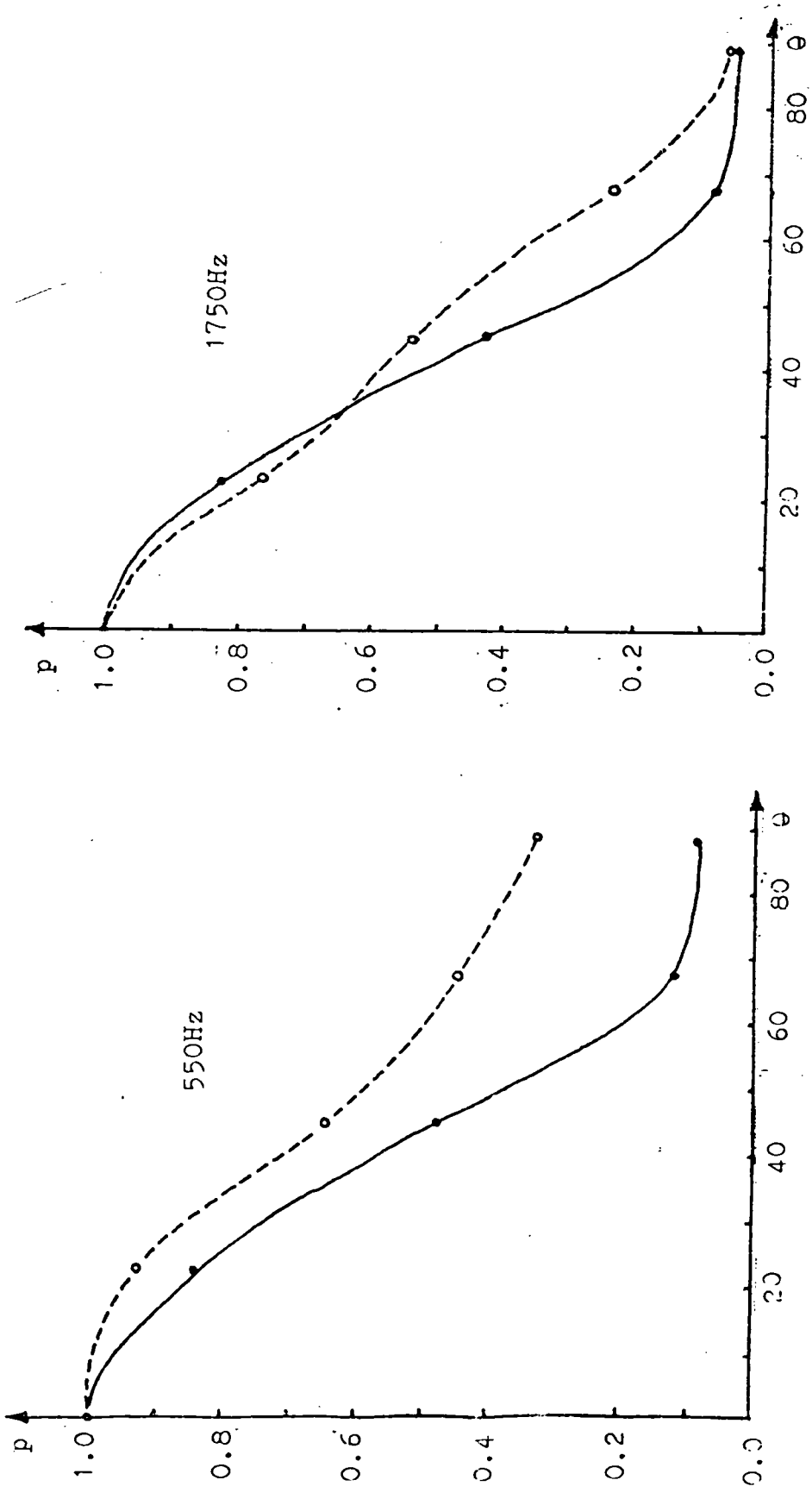

(c) Variation of sound pressure with circumferential angle

Fig 3.5 Variation of sound pressure around the machine

—●— predicted ----●---- measured ----◀---- calculated from infinite cylindrical model

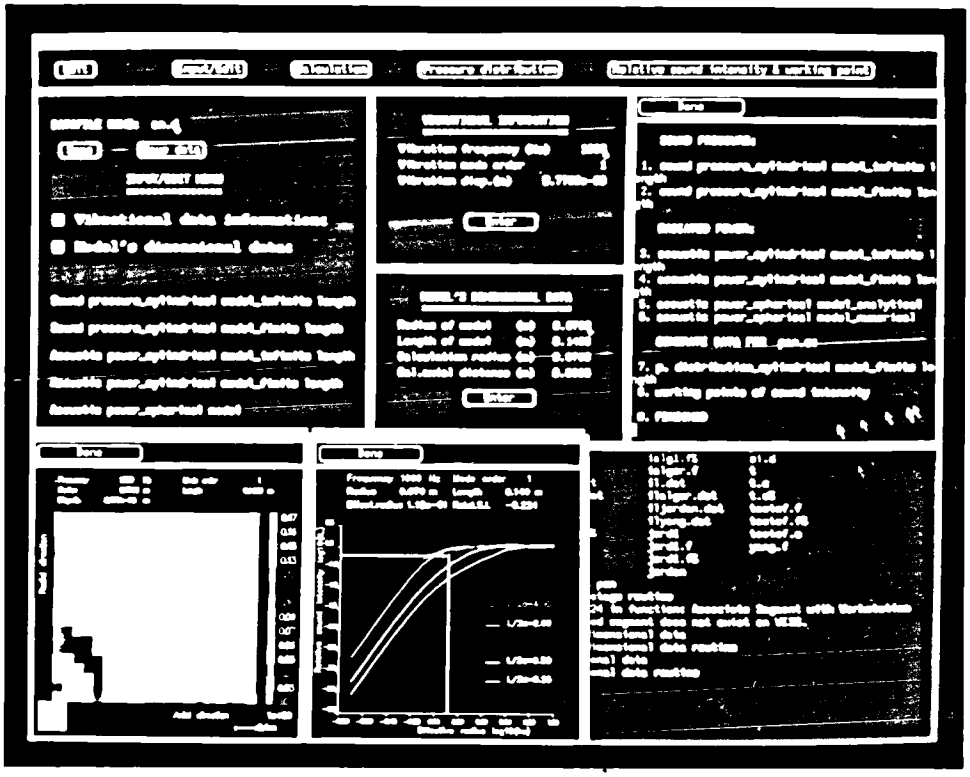

Fig 3.6 Acoustic radiation calculations

CHAPTER 4

FINITE ELEMENT ANALYSIS OF THE ACOUSTIC POWER RADIATED BY ELECTRICAL MACHINES

4.1 Introduction

A knowledge of the relationship between the vibration and noise of an electrical machine is critical to the calculation of its acoustic power [4.1]. However analytical methods, such as those described in Chapter 3, for predicting the acoustic radiation are applicable only to idealised models having a regular shape, eg. spherical or cylindrical, and cannot account for the effect of end-shields or cater for all topologies of motor, eg. axial-field or square frame. Even finite length cylindrical motors cannot be solved analytically unless they are assumed to have infinite stiffening baffles at each end [4.2].

Whilst the finite element method has been applied to analyse the modes of acoustic cavities, comparatively few papers have been published on its application to acoustic radiation [4.3]. Furthermore, it is usually restricted to a radiator of mode order zero or one (extensive or impulse type vibration). The main difficulty in the application of the finite element method to acoustic radiation is in dealing with the far-field boundaries, which must be well represented otherwise the resulting accuracy will be very poor. This arises from the fact that the sound pressure level is low at the far-field boundary, whilst the acoustic power radiated by a vibrating structure, such as an electrical machine, should be independant of the enclosing surface used for the calculation. Whilst some authors use the finite element method in the near-field and an analytical method in the far-field, both being combined to solve for the radiated sound pressure distribution [4.4], others use the finite element in the near-field and the infinite element in the far-field [4.5][4.6].

Nevertheless, limitations still exist with the application of finite elements to the analysis of high frequency and/or large acoustic radiation fields, such as emanate from electrical machines.

The boundary element method provides an approach which inherently accounts for the characteristics of the far-field, and makes it unnecessary to deal with the far-field boundaries, and also reduces the field dimension by one. However, whilst these two advantages should make the method ideal for solving acoustic radiation problems, at the natural frequencies (or characteristic frequencies) of the related interior field the equations obtained by the ordinary boundary element method lead to ill-conditioned equations or a non-unique solution. As a consequence special boundary element methods must be used [4.7][4.8].

In this chapter, the finite element method is used to study the acoustic power radiated by electrical machines with particular emphasis on those having an axisymmetric construction. It is combined with a Fourier series analysis, the Fourier series being used to represent the r- θ variation of the sound pressure, whilst finite elements are used to interpolate and discretise the variation in the r-z plane. The combination of both methods allows the acoustic radiation of electrical machines to be predicted with due account of the effect of end-shields, which would not be possible with existing analytical methods. Calculation methods for the acoustic power using finite elements in various acoustic fields, from two-dimensional and axisymmetric to three-dimensional, are described, and corresponding formulae deduced. The effects of the far-field boundary condition on the calculation is studied. Predictions of the acoustic power from the harmonic axisymmetric finite element method are validated against measurements on a three-phase induction motor. The technique is then applied to the spherical model of acoustic radiation.

4.2 Calculation of Acoustic Power

4.2.1 Three-dimensional Finite Element Analysis of Acoustic Radiation

The acoustic field of radiation is described by the Helmholtz equation together with specified Dirichlet and Neumann boundary conditions, viz:

$$\nabla^2 p + k^2 p = f \qquad v \qquad (4.1a)$$

$$p = \bar{p} \qquad \Sigma_1 \qquad (4.1b)$$

$$\frac{\partial p}{\partial n} + j\,k\,h_n\,p = j\,\rho\,c\,k\,g_n\,v_n \qquad \Sigma_2 \qquad (4.1c)$$

where $\Sigma_1 + \Sigma_2$ are the boundaries of the region v to be analysed. In order to simplify the study of the noise from electrical machines the above expression for the Neumann boundary Σ_2 has been used, with the constants $\bar{p}$, h_n, g_n, and v_n being given values which are described in Appendix 4.7.1.

Similar to the vibrational problem, the acoustic field is discretized into N isoparametric elements, the interpolation function being given by:

$$p = \sum_{i=1}^{n} N_i\,p_i \qquad (4.2)$$

where

p_i is the value of the sound pressure p at node i of the element;

n is the node number of the element;

N_i is the shape function, which is a function of the coordinates

If the residue between the approximate solution p given by the interpolation function and the exact solution is R(p), then

$$R(p) = \nabla^2 p + k^2 p - f \qquad v \qquad (4.3)$$

In the weighted residual method, the product of R(p) and the weighting function We should be zero, ie.

$$<W_e, R> = \int_v W_e R(p)\, dv = \sum_{e=1}^{N} \varepsilon_e = 0 \tag{4.4}$$

where

$$\varepsilon_e = \int_{v_e} W_e R(p)\, dx\, dy \tag{4.5}$$

$W_e = N_i$ is the weighting function applied to element e.

Therefore

$$\int_{v_e} N_i (\nabla^2 p + k^2 p - f)\, dv = \varepsilon_i \qquad i = 1, 2, ..., n \tag{4.6}$$

After some deduction, a system of equations, in discretized finite element form, is obtained as:

$$-\left[K_{ij}^e\right]_{nxn} \left\{p_i^e\right\}_{nx1} + k^2 \left[M_{ij}^e\right]_{nxn} \left\{p_i^e\right\}_{nx1} - j\,k \left[C_{ij}^e\right]_{nxn} \left\{p^e\right\}_{nx1}$$
$$+\left[F_i^e\right]_{nx1} + j\,\rho\,c\,k \left[G_i^e\right]_{nx1} = \left[\varepsilon_i^e\right] \equiv \varepsilon_e \tag{4.7}$$

where

$$K_{ij}^e = \int_{v_e} \left(\frac{\partial N_i}{\partial x}\frac{\partial N_j}{\partial x} + \frac{\partial N_i}{\partial y}\frac{\partial N_j}{\partial y} + \frac{\partial N_i}{\partial z}\frac{\partial N_j}{\partial z} \right) dv$$

$$= \int_{-1}^{1}\int_{-1}^{1}\int_{-1}^{1} \left(\frac{\partial N_i}{\partial x}\frac{\partial N_j}{\partial x} + \frac{\partial N_i}{\partial y}\frac{\partial N_j}{\partial y} + \frac{\partial N_i}{\partial z}\frac{\partial N_j}{\partial z} \right) |J|\, d\xi\, d\eta\, d\zeta \tag{4.8}$$

$$M_{ij}^e = \int_{v_e} N_i N_j\, dv$$

$$= \int_{-1}^{1}\int_{-1}^{1}\int_{-1}^{1} N_i N_j |J|\, d\xi\, d\eta\, d\zeta \tag{4.9}$$

$$C_{ij}^e = \int_{\Sigma_{2e}} h_n N_i N_j\, d\Sigma$$

$$= \int_{-1}^{1}\int_{-1}^{1} h_n N_i N_j \sqrt{EG - F^2}\,|_{\xi=1}\; d\eta\, d\zeta \tag{4.10}$$

$$F_i^e = \int_{v_e} f N_i \; dv$$

$$= \int_{-1}^{1}\int_{-1}^{1}\int_{-1}^{1} f N_i \; |J|\, d\xi\, d\eta\, d\zeta \tag{4.11}$$

$$G_i^e = \int_{\Sigma_{2e}} v_n g_n N_i \; d\Sigma$$

$$= \int_{-1}^{1}\int_{-1}^{1} v_n g_n N_i \; \sqrt{EG - F^2}\,|_{\xi=1}\; d\eta\, d\zeta \tag{4.12}$$

i,j=1,2,...,n

where |J|, E, F, G are given in Appendix 4.7.2 and the boundary Σ_2 is assumed to be on the surface of $\xi = 1$ in the element.

By assembling all the elements

$$\sum_{e=1}^{N} \varepsilon_e = 0 \tag{4.13}$$

The global system equation for the sound pressure is obtained as

$$\{[K] - k^2\,[M] + j\,k\,[C]\}\{p\} = \{F\} + j\,\rho\,c\,k\,\{G\} \tag{4.14}$$

whilst the particle velocity in the air medium is given by

$$\vec{v} = v_x \vec{i} + v_y \vec{j} + v_z \vec{k} = \frac{1}{j\,\rho\,\omega}\,\nabla p$$

$$v_x = \frac{1}{j\,\rho\,\omega}\,\frac{\partial p}{\partial x}$$

$$v_y = \frac{1}{j\,\rho\,\omega}\,\frac{\partial p}{\partial y}$$

$$v_z = \frac{1}{j\rho\omega}\frac{\partial p}{\partial z} \tag{4.15}$$

The acoustic power is calculated by the conjugation method of the surface vibration of the machine and the sound pressure distribution on the surface, as described in Chapter 5. Hence

$$\begin{aligned} W &= \int_{S_a} p\,\vec{v}.\,d\vec{\Sigma} \\ &= \sum_{e=1}^{N_s} W_e \\ W_e &= \int_{S_e} p\,\vec{v}.\,d\vec{\Sigma} \\ &= \frac{1}{2}\mathrm{Re}\int_{S_e} p\,v_n^*\,d\Sigma \\ &= \frac{1}{2}\mathrm{Re}\int_{-1}^{1}\int_{-1}^{1}\left(\sum_{i=1}^{n} N_i p_i\right) v_n^*\sqrt{EG-F^2}\,|_{\xi=1}\,d\eta\,d\zeta \end{aligned} \tag{4.16}$$

where S_a, S_e are the vibrating surface and the discretized element respectively, and v_n is the normal vibrational velocity of the element.

If the reference acoustic power is chosen as

$$\begin{aligned} W_o &= \frac{1}{2}\int_{S_a} \rho c\,|v_n|^2\,d\Sigma \\ &= \sum_{e=1}^{N_s} W_{eo} \\ W_{eo} &= \frac{1}{2}\int_{S_e} \rho c\,v_n v_n^*\,d\Sigma \\ &= \frac{1}{2}\mathrm{Re}\int_{-1}^{1}\int_{-1}^{1} |v_n|^2\sqrt{EG-F^2}\,|_{\xi=1}\,d\eta\,d\zeta \end{aligned} \tag{4.17}$$

the relative sound intensity coefficient is then calculated from

$$I = \frac{W}{W_o} \tag{4.18}$$

4.2.2 Planar and Axisymmetric Fields

When the field is invariant in the axial direction it simplifies to a two-dimensional problem. The system of discretized finite element equations is still given by

$$\{[K] - k^2 [M] + j\, k\, [C]\}\{p\} = \{F\} + j\, \rho\, c\, k \{G\} \tag{4.19}$$

However the coefficients in the element matrices are now given by:

$$K_{ij}^e = \int_{S_e} \left(\frac{\partial N_i}{\partial x} \frac{\partial N_j}{\partial x} + \frac{\partial N_i}{\partial y} \frac{\partial N_j}{\partial y} \right) t_e \, ds$$

$$= \int_{-1}^{1} \int_{-1}^{1} \left(\frac{\partial N_i}{\partial x} \frac{\partial N_j}{\partial x} + \frac{\partial N_i}{\partial y} \frac{\partial N_j}{\partial y} \right) |J| \, t_e \, d\xi \, d\eta \tag{4.20}$$

$$M_{ij}^e = \int_{S_e} N_i N_j \, t_e \, ds$$

$$= \int_{-1}^{1} \int_{-1}^{1} N_i N_j \, |J| \, t_e \, d\xi \, d\eta \tag{4.21}$$

$$C_{ij}^e = \int_{\Gamma_{2e}} h_n N_i N_j \, t_e \, d\Gamma$$

$$= \int_{-1}^{1} h_n N_i N_j \sqrt{\left(\frac{\partial x}{\partial \eta}\right)^2 + \left(\frac{\partial y}{\partial \eta}\right)^2}\Big|_{\xi = 1} t_e \, d\eta \tag{4.22}$$

$$F_i^e = \int_{S_e} f N_i \, t_e \, ds$$

$$= \int_{-1}^{1} \int_{-1}^{1} f N_i \, |J| \, t_e \, d\xi \, d\eta \tag{4.23}$$

$$G_i^e = \int_{\Gamma_{2e}} v_n \, g_n \, N_i \, t_e \, d\Gamma$$

$$= \int_{-1}^{1} v_n \, g_n \, N_i \sqrt{\left(\frac{\partial x}{\partial \eta}\right)^2 + \left(\frac{\partial y}{\partial \eta}\right)^2}\Big|_{\xi=1} t_e \, d\eta \tag{4.24}$$

where Γ_{2e} corresponds to Σ_{2e} in the three-dimensional field and is assumed to be on the side $\xi = 1$ of the element. t_e is the axial length of the element.

The particle velocity is then given by

$$\vec{v} = v_x \vec{i} + v_y \vec{j} = \frac{1}{j \rho \omega} \nabla p$$

$$v_x = \frac{1}{j \rho \omega} \frac{\partial p}{\partial x}$$

$$v_y = \frac{1}{j \rho \omega} \frac{\partial p}{\partial y} \tag{4.25}$$

The radiated acoustic power is again calculated according to the conjugation of the surface vibration of the machine and the sound pressure distribution on the surface, ie.

$$W = \int_{s_a} p \, \vec{v} . d\vec{s} = \sum_{e=1}^{N_s} W_e$$

$$W_e = \int_{s_e} p \, \vec{v} . d\vec{s} = \frac{1}{2} \mathrm{Re} \int_{s_e} p \, v_n^* \, t_e \, d\Gamma$$

$$= \frac{1}{2} \mathrm{Re} \int_{-1}^{1} \left(\sum_{i=1}^{n} N_i \, p_i \right) v_n^* \sqrt{\left(\frac{\partial x}{\partial \eta}\right)^2 + \left(\frac{\partial y}{\partial \eta}\right)^2}\Big|_{\xi=1} t_e \, d\eta \tag{4.26}$$

The reference acoustic power is given by

$$W_o = \frac{1}{2} \int_{s_a} \rho \, c \, |v_n|^2 \, ds = \sum_{e=1}^{N_s} W_{eo}$$

$$W_{eo} = \frac{1}{2} \int_{s_e} \rho \, c \, v_n \, v_n^* \, d\Gamma$$

$$= \frac{1}{2} \mathrm{Re} \int_{-1}^{1} |v_n|^2 \sqrt{\left(\frac{\partial x}{\partial \eta}\right)^2 + \left(\frac{\partial y}{\partial \eta}\right)^2}\Big|_{\xi=1} t_e \, d\eta \tag{4.27}$$

Therefore the relative sound intensity coefficient for the acoustic radiation of an electrical machine becomes

$$I = \frac{W}{W_o} \tag{4.28}$$

In the case of an axisymmetric acoustic field, the system of discretized finite element equations is exactly the same as that for a three-dimensional formulation. However because of the axisymmetry, the sound pressure p is independant of the circumferential angular variable θ . Hence if the axial variable z and the radial variable r are represented by x and y respectively, the integration becomes

$$dv = 2\,\pi\, y\, ds \tag{4.29}$$

$$d\Sigma = 2\,\pi\, y d\Gamma \tag{4.30}$$

where

$$y = \sum_{i=1}^{n} N_i\, y_i$$

Therefore when an axisymmetric acoustic field is to be solved, it is necessary only to change the axial length t_e of the element to $2\pi y$ in the integration of the various coefficients for a two-dimensional element. Similarly, t_e is replaced by $2\pi y$ when the acoustic power is being calculated.

4.2.3 Harmonic Axisymmetric Acoustic Field

It is well known that the noise which results from electromagnetically induced vibrations consists not only of an axisymmetric component (circumferential mode order n = 0), but also higher order harmonics (n > 0), whose sound pressure varies with the circumferential angular position. In electrical machines the latter are the most important, because

i) the vibration produced by a harmonic airgap field usually has a comparatively higher spatial mode order due to the presence of slots and teeth

ii) the natural frequencies of the stator for a circumferential mode of order zero are usually higher than those for the higher order modes of interest.

However, neither planar or axisymmetric finite elements can solve the acoustic field if the sound pressure varies around the circumference. To cater for this a 3-d representation is necessary. However a 3-d finite element analysis would be impractical because of the necessarily large number of elements which would be required to model the finite free-field and the high vibration frequency of the machine. The combination of finite element and Fourier series analyses on the other hand provides a feasible approach to the calculation of the acoustic power radiated by an electrical machine, since it is based on the:

i) Finite element discretisation of an r-z plane of a machine, and a
ii) Fourier series representation of the circumferential variation of the sound pressure radiated by the machine, as indicated in Fig 4.1.

The main advantage of the technique is that the dimension of the field is reduced by one, so that the 3-d field is calculated by a 2-d method.

For a harmonic axisymmetric field, the Helmholtz equation and relevant boundary conditions are:

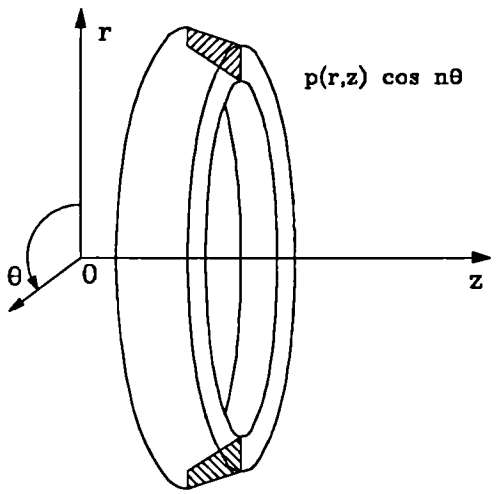

Fig 4.1 Illustration of Element

$$\frac{1}{r}\frac{\partial}{\partial r}\left(r\frac{\partial p}{\partial r}\right)+\frac{1}{r^2}\frac{\partial^2 p}{\partial \theta^2}+\frac{\partial^2 p}{\partial z^2}+k^2 p=f, \quad in\ v$$

$$p=\sum_{n=0}^{\infty}\bar{p}_o(r,z)\cos n\theta\, e^{-j\omega t}, \qquad on\ \Omega_1$$

$$\frac{\partial p}{\partial n}+jkh_n p=j\rho c k\sum_{n=0}^{\infty}v_{no}g_n\cos n\theta\, e^{-j\omega t}, \qquad on\ \Omega_2 \tag{4.31}$$

letting

$$v_n=\sum_{n=0}^{\infty}v_{no}\cos n\theta\, e^{-j\omega t} \tag{4.32}$$

$$f=\sum_{n=0}^{\infty}f_o(r,z)\cos n\theta\, e^{-j\omega t} \tag{4.33}$$

$$\text{and} \quad p(r,\theta,z,t)=\sum_{n=0}^{\infty}p_o(r,z)\cos n\theta\, e^{-j\omega t} \tag{4.34}$$

where, for simplicity, the term sin nθ in the Fourier series has been neglected since it has no effect on the calculation of acoustic power.

$$\frac{1}{r}\frac{\partial}{\partial r}\left(r\frac{\partial p_o}{\partial r}\right)+\frac{\partial^2 p_o}{\partial z^2}+\left[k^2-\left(\frac{n}{r}\right)^2\right]p_o=f_o, \quad in\ s$$

$$p=\bar{p}_o, \qquad on\ \Omega_1$$

$$\frac{\partial p_o}{\partial n}+jkh_n p_o=j\rho c k\, v_{no}g_n, \qquad on\ \Omega_2 \tag{4.35}$$

where the surface S, and its boundaries Γ_1 and Γ_2 are formed by the intersection between region V, and its boundaries Ω_1 and Ω_2 and the r-z plane respectively; $h_n=\left(1+\frac{1}{jkR}\right)$; R is the radius of the far-field boundary, $g_n = 1$; v_{no} is the vibrational velocity of the machine; ρc is the sound resistance; $k = \omega/c$; ω is the vibrational angular velocity; and c is the speed of sound.

By letting $k^2 = k^2 - \left(\frac{n}{r}\right)^2$ it can be shown that the above equations have the same form as those for an axisymmetric formulation. In other words, the harmonic axisymmetric field has been transformed into the ordinary axisymmetric field. Letting $x \equiv z$ and $y \equiv r$ gives

$$dv = 2\pi y\, ds\,; \quad \text{and} \quad d\Omega = 2\pi y\, d\Gamma \tag{4.36}$$

where

$$y = \sum_{i=1}^{n} N_i y_i \tag{4.37}$$

is the shape function, n is the node number of an element.

Hence the element matrices are given by

$$K_{ij}^e = \int_{s_e} \left(\frac{\partial N_i}{\partial x}\frac{\partial N_j}{\partial x} + \frac{\partial N_i}{\partial y}\frac{\partial N_j}{\partial y}\right) 2\pi y\, ds$$

$$= \int_{-1}^{1}\int_{-1}^{1} \left(\frac{\partial N_i}{\partial x}\frac{\partial N_j}{\partial x} + \frac{\partial N_i}{\partial y}\frac{\partial N_j}{\partial y}\right) |J|\, 2\pi y\, d\xi\, d\eta \tag{4.38}$$

$$M_{1ij}^e = \int_{s_e} N_i N_j\, 2\pi y\, ds$$

$$= \int_{-1}^{1}\int_{-1}^{1} N_i N_j\, |J|\, 2\pi y\, d\xi\, d\eta \tag{4.39}$$

$$M_{2ij}^e = \int_{s_e} N_i N_j \left(\frac{1}{y^2}\right) 2\pi y\, ds$$

$$= \int_{-1}^{1}\int_{-1}^{1} N_i N_j\, |J| \frac{2\pi}{y}\, d\xi\, d\eta \tag{4.40}$$

$$C_{ij}^e = \int_{\Gamma_{2e}} h_n N_i N_j\, 2\pi y\, d\Gamma$$

$$= \int_{-1}^{1} h_n N_i N_j \sqrt{\left(\frac{\partial x}{\partial \eta}\right)^2 + \left(\frac{\partial y}{\partial \eta}\right)^2}\Big|_{\xi=1} 2\pi y \, d\eta \tag{4.41}$$

$$F_i^e = \int_{s_e} f N_i \, 2\pi y \, ds$$

$$= \int_{-1}^{1}\int_{-1}^{1} f N_i \, |J| \, 2\pi y \, d\xi \, d\eta \tag{4.42}$$

$$G_i^e = \int_{\Gamma_{2e}} v_{no} \, g_n N_i \, 2\pi y \, d\Gamma$$

$$= \int_{-1}^{1} v_n \, g_n N_i \sqrt{\left(\frac{\partial x}{\partial \eta}\right)^2 + \left(\frac{\partial y}{\partial \eta}\right)^2}\Big|_{\xi=1} 2\pi y \, d\eta \tag{4.43}$$

and the corresponding assembled equations are:

$$\{[K] + n^2 [M_2] - k^2 [M_1] + j k [C]\}\{p_o\} = \{F\} + j \rho c k \{G\} \tag{4.44}$$

It will be noted that compared to an axisymmetric formulation the equations have an extra term, n^2 [M2] , which results from the circumferential vibration mode order n.

The particle velocity is calculated from

$$\vec{v} = v_r \vec{i} + v_\theta \vec{j} + v_z \vec{k} = \frac{1}{j \rho \omega} \nabla p \tag{4.45}$$

$$v_r = \frac{1}{j \rho \omega} \frac{\partial p}{\partial r} \equiv \frac{1}{j \rho \omega} \frac{\partial p_o}{\partial y} \cos n\theta \, e^{-j\omega t}$$

$$v_z = \frac{1}{j \rho \omega} \frac{\partial p}{\partial z} \equiv \frac{1}{j \rho \omega} \frac{\partial p_o}{\partial x} \cos n\theta \, e^{-j\omega t}$$

$$v_\theta = \frac{1}{j \rho \omega} \frac{\partial p}{\partial \theta} \equiv \frac{1}{j \rho \omega} \frac{n}{y} p_o \cos n\theta \, e^{-j\omega t}$$

By the method of conjugation between the surface vibration of the machine and the sound pressure distribution on the surface, the radiated acoustic power is calculated from

$$W = \int_{s_a} p\,\vec{v}.\,d\vec{s} = \sum_{e=1}^{N_s} W_e$$

where

$$W_e = \int_{s_e} p\,\vec{v}.\,d\vec{s} = \frac{1}{2}\,\mathrm{Re}\int_0^{2\pi}\int_{s_e} p\,v_n^*\,y\,d\Gamma$$

$$= \frac{\varepsilon_n}{2}\,\mathrm{Re}\int_{s_e} p_o\,v_{no}^*\,2\pi\,y\,d\Gamma$$

$$= \frac{\varepsilon_n}{2}\,\mathrm{Re}\int_{-1}^{1}\left(\sum_{i=1}^{n'} N_i\,p_i\right) v_{no}^*\sqrt{\left(\frac{\partial x}{\partial \eta}\right)^2+\left(\frac{\partial y}{\partial \eta}\right)^2}\,\Big|_{\xi=1}\,2\pi\,y\,d\eta \qquad (4.46)$$

where

$$\varepsilon = \begin{cases} 1 & n=0 \\ \dfrac{1}{2} & n\neq 0 \end{cases} \qquad (4.47)$$

and N is the total number of elements on the machine surface.

The reference acoustic power and relative sound intensity coefficient are calculated similarly.

4.2.4 Element Matrices and Acoustic Power in Different Fields Using Triangular Elements

It has been shown in the previous sections that the planar finite element, the axisymmetric finite element, and the harmonic axisymmetric finite element methods are all variants of an essentially two-dimensional formulation. If planar triangular elements are used, their shape function is given by

$$N_i = \frac{1}{2\Delta^e}(a_i + b_i\,x + c_i\,y) \qquad i = 1,2,3 \qquad (4.48)$$

where: $a_1 = x_2\,y_3 - x_3\,y_2 \quad b_1 = y_2 - y_3 \quad c_1 = x_3 - x_2$

$a_2 = x_3\,y_1 - x_1\,y_3 \quad b_2 = y_3 - y_1 \quad c_2 = x_1 - x_3$

$a_3 = x_1\,y_2 - x_2\,y_1 \quad b_3 = y_1 - y_2 \quad c_3 = x_2 - x_1$

where Δ^e is the area of the triangular element "e".

Therefore

$$\frac{\partial N_i}{\partial x} = \frac{1}{2\,\Delta^e} b_i$$

$$\frac{\partial N_i}{\partial y} = \frac{1}{2\,\Delta^e} c_i \qquad i = 1, 2, 3 \tag{4.49}$$

Meanwhile the acoustic power radiated by a machine can be calculated in the free-field just as if it was being measured in an anechoic chamber. To represent the fact that there is no other sound source in the field, f and {F} are set to zero in the previous equations. The element matrices and the formulae radiated for the acoustic power are then deduced and given by:

4.2.4.1 Planar Acoustic Field

$$\left[K^e\right]_p = \frac{t_e}{4\Delta^e}\begin{bmatrix} b_1 b_1 + c_1 c_1 & b_1 b_2 + c_1 c_2 & b_1 b_3 + c_1 c_3 \\ b_2 b_1 + c_2 c_1 & b_2 b_2 + c_2 c_2 & b_2 b_3 + c_2 c_3 \\ b_3 b_1 + c_3 c_1 & b_3 b_2 + c_3 c_2 & b_3 b_3 + c_3 c_3 \end{bmatrix} \tag{4.50}$$

$$\left[M^e\right]_p = \frac{t_e\,\Delta^e}{12}\begin{bmatrix} 2 & 1 & 1 \\ 1 & 2 & 1 \\ 1 & 1 & 2 \end{bmatrix} \tag{4.51}$$

$$\left[C^e\right]_p = h_n \frac{t_e\,S_{23}}{6}\begin{bmatrix} 0 & 0 & 0 \\ 0 & 2 & 1 \\ 0 & 1 & 2 \end{bmatrix} \tag{4.52}$$

$$\left[G^e\right]_p = v_n\,g_n \frac{t_e\,S_{23}}{2}\begin{bmatrix} 0 \\ 1 \\ 1 \end{bmatrix} \tag{4.53}$$

where S_{23} is the distance between nodes 2 and 3 of an element "e" which are assumed to lie on the surface of the machine. If the vibration velocity is assumed to be constant v_{neo} over S_{23} the acoustic power can be deduced as

$$W_p = \sum_{e=1}^{N} \mathrm{Re}\left\{\frac{t_e\,S_{23}\,v_{neo}^*}{4\,\Delta^e}\left(A_2^e\,p_2 + A_3^e\,p_3\right)\right\} \tag{4.54}$$

where v_{neo} is the normal vibrational velocity of the element on the surface of the machine and nodes 2 and 3 of the element "e" are on the vibrational surface.

$$A_2^g = a_2 + b_2 \frac{x_2 + x_3}{2} + c_2 \frac{y_2 + y_3}{2}$$

$$= x_2 \frac{y_3 - y_1}{2} + x_3 \frac{y_1 - y_2}{2} + x_1 \frac{y_2 - y_3}{2}$$

$$= \frac{1}{2} (x_1 b_1 + x_2 b_2 + x_3 b_3) \tag{4.55}$$

$$A_3^g = a_3 + b_3 \frac{x_2 + x_3}{2} + c_3 \frac{y_2 + y_3}{2}$$

$$= y_2 \frac{x_1 - x_3}{2} + y_3 \frac{x_2 - x_1}{2} + y_1 \frac{x_3 - x_2}{2}$$

$$= \frac{1}{2} (y_1 c_1 + y_2 c_2 + y_3 c_3) \tag{4.56}$$

If the vibrational velocity varies linearly from v_{ne2} to v_{ne3} over S_{23} the acoustic power is deduced as

$$W_p = \sum_{e=1}^{N} \mathrm{Re} \left\{ \frac{t_e S_{23}}{4 \Delta^e} \left[v_{ne2}^* (A_2^1 p_2 + A_3^1 p_3) + v_{ne3}^* (B_2^1 p_2 + B_3^1 p_3) \right] \right\} \tag{4.57}$$

$$A_2^1 = \frac{1}{2} a_2 + b_2 \left(\frac{2 x_2 + x_3}{6} \right) + c_2 \left(\frac{2 y_2 + y_3}{6} \right) \tag{4.58}$$

$$A_3^1 = \frac{1}{2} a_3 + b_3 \left(\frac{2 x_2 + x_3}{6} \right) + c_3 \left(\frac{2 y_2 + y_3}{6} \right) \tag{4.59}$$

$$B_2^1 = \frac{1}{2} a_2 + b_2 \left(\frac{x_2 + 2 x_3}{6} \right) + c_2 \left(\frac{y_2 + 2 y_3}{6} \right) \tag{5.60}$$

$$B_3^1 = \frac{1}{2} a_3 + b_3 \left(\frac{x_2 + 2 x_3}{6} \right) + c_3 \left(\frac{y_2 + 2 y_3}{6} \right) \tag{4.61}$$

4.2.4.2 Axisymmetric Acoustic Field

When the field is axisymmetric, y is approximated by

$$\bar{y}_e = \frac{1}{3} (y_1 + y_2 + y_3) \tag{4.62}$$

Therefore the element matrices are given by

$$\left[K^e\right]_a = \frac{2\pi \bar{y}_e}{t_e}\left[K^e\right]_p \tag{4.63}$$

$$\left[M^e\right]_a = \frac{2\pi \bar{y}_e}{t_e}\left[M^e\right]_p \tag{4.64}$$

$$\left[C^e\right]_a = h_n \frac{2\pi S_{23}}{12}\begin{bmatrix} 0 & 0 & 0 \\ 0 & 3y_2+y_3 & y_2+y_3 \\ 0 & y_2+y_3 & y_2+3y_3 \end{bmatrix} \tag{4.65}$$

$$\left[G^e\right]_a = v_n g_n \frac{2\pi S_{23}}{6}\begin{bmatrix} 0 \\ 2y_2+y_3 \\ y_2+2y_3 \end{bmatrix} \tag{4.66}$$

Similarly if the vibration velocity is assumed to be a constant v_{neo} over S_{23} the acoustic power can be deduced as

$$W_a = \sum_{e=1}^{N} \mathrm{Re}\left\{\frac{2\pi \bar{y}_e' S_{23} v_{neo}^*}{4\Delta^e}\left(A_2^g p_2 + A_3^g p_3\right)\right\} \tag{4.67}$$

where

$$\bar{y}_e' = \frac{1}{2}(y_2+y_3) \tag{4.68}$$

However if the vibrational velocity various linearly from v_{ne2} to v_{ne3} over S_{23} the acoustic power is deduced as

$$W_a = \sum_{e=1}^{N} \mathrm{Re}\left\{\frac{2\pi \bar{y}_e' S_{23}}{4\Delta^e}\left[v_{ne2}^*(A_2^1 p_2 + A_3^1 p_3) + v_{ne3}^*(B_2^1 p_2 + B_3^1 p_3)\right]\right\} \tag{4.69}$$

4.2.4.3 Harmonic Axisymmetric Acoustic Field

In a similar manner to the axisymmetric field the element matrices are obtained as

$$\left[K^e\right]_{ha} = \left[K^e\right]_a \tag{4.70}$$

$$\left[M_1^e\right]_{ha} = \left[M^e\right]_a \tag{4.71}$$

$$\left[M_2^e\right]_{ha} = \frac{1}{\overline{y}_e^2}\left[M^e\right]_a \tag{4.72}$$

$$\left[C^e\right]_{ha} = \left[C^e\right]_a \tag{4.73}$$

$$\left[G^e\right]_{ha} = \left[G^e\right]_a \tag{4.74}$$

and the radiated acoustic power is

$$W_{ha} = \varepsilon_n W_a \tag{4.75}$$

4.3 Effect of Far-Field Boundary Conditions on the Calculation of the Radiated Acoustic Power

In theory the region of finite element analysis of the acoustic radiation from an electrical machine in free-space should extend to infinity. However as has been pointed out in the introduction one of the important aspects in solving the acoustic radiation problem in an infinite region is the bounding of the far-field. If the far-field boundary is located too far from the machine, the discretized finite element region becomes very large, which then leads to rather slow computation since the discretisation should be as fine as possible in order to achieve the required accuracy. On the other hand, if the far-field boundary is too close, the radiation boundary conditions at the far-field boundary cannot be satisfied, which leads to an inaccurate solution.

Consequently the effects of the far-field boundary conditions on the calculation of the radiated acoustic power have been investigated by case studies on spherical and cylindrical acoustic radiation models.

Table 4.1 shows a comparison of the relative sound intensity coefficients for the infinite cylindrical model of acoustic radiation for two locations of the far-field boundary. Due to the

use of harmonic axisymmetric elements, it is convenient to apply the local planar wave as the far-field boundary condition on the r-z plane. It will be seen that when the effective radius of the machine kR is relatively small and the radius of the vibrating surface is fixed at 0.1m, the relative sound intensity coefficients calculated by setting the radius of the far-field boundary at 0.75m are of higher accuracy than those when the radius is set at 0.5m. However with an increase of vibrational mode order and an increase of effective radius kR , the radiated sound pressure decreases more rapidly with distance from the vibrating surface, whilst the phase difference between the sound pressure and the particle velocity decreases with an increase of distance from the vibrating surface. As a consequence, when the vibrational mode order is relatively high and the effective radius of the machine is large the radiation boundary condition is well-fitted at either of the radii 0.5m or 0.75m. However in the following calculation the far-field boundary is chosen as a surface 7.5 times the outer radius of the machine.

Table 4.2 shows the effect of the far-field boundary condition on the acoustic power radiated by an infinite cylindrical model. It shows that when the far-field boundary condition is chosen as a local planar wave for the infinite cylindrical model the results from the finite element calculation using either planar elements or harmonic axisymmetric elements agree well with the exact values. The error becomes larger when the far-field boundary condition is represented by a local spherical wave since the far-field radiated by an infinite cylindrical model is not consistent with such a boundary condition.

Table 4.3 compares the effect of the far-field boundary condition on the acoustic power radiated by a spherical model. It shows that in contrast to the case for the infinite cylindrical model it is the local spherical wave that best represents the far-field boundary condition. A relatively large error exists when the far-field boundary condition is imposed by a local planar wave, especially when the effective radius kR is small. It also shows that differences in the calculation of the radiated acoustic power are negligible when an nth-order spherical wave boundary condition is imposed at the far-field, viz. using the radiation impedance of the nth-order spherical model in equation (4.84).

$$Z_{\sigma o} = \frac{-j\rho c k R}{n - kR \dfrac{h_{n+1}(kR)}{h_n(kR)}}$$

where h_n is the nth-order of the spherical Hankel function, instead of imposing a o-order spherical wave boundary condition at the far-field which is represented by the radiation impedance of o-order spherical mode, viz.

$$Z_{\sigma o} = \frac{\rho c}{1 + \dfrac{1}{jkR}}$$

This is due to the fact that when the radius of the far-field is large enough the difference between the impedances $Z_{\sigma o}$ and $Z_{\sigma nR}$ is very small.

In summary, the far-field boundary has an effect on the calculation of the acoustic power. However, the investigation has shown that, in general, the far-field boundary for electrical machines can be an enclosing spherical surface of 7.5 x the outer radius of the machine and on which a zero-order spherical wave boundary condition can be imposed in the finite element calculation.

Table 4.1 Effect of the Radius of the Far-Field Boundary

on the Radiated Acoustic Power for an Infinite Cylindrical Model

kR_0	Relative sound intensity											
	n=0		n=1		n=2		n=3		n=4		n=5	
0.1	0.151	0.153	0.005	0.002					Calculated result 1		Exact value	
	0.210		0.008									
1.0	0.796	0.792	0.731	0.739	0.098	0.100	0.003	0.003	Calculated result 2			
	0.726		0.795		0.113		0.002					
2.0	0.907	0.925	0.980	0.988	1.076	1.025	0.279	0.270	0.019	0.016		
	0.931		0.975		0.983		0.310		0.017			
3.0	0.947	0.963	0.988	1.004	1.133	1.138	1.271	1.217	0.461	0.437	0.048	0.042
	0.994		1.039		1.172		1.202		0.482		0.046	
4.0	0.972	0.978	0.995	1.005	1.077	1.093	1.262	1.264	1.428	1.367	0.632	0.591
	0.965		0.993		1.092		1.291		1.402		0.628	
5.0	0.973	0.986	0.989	1.004	1.045	1.062	1.171	1.178	1.410	1.374	1.541	1.492
	0.982		0.997		1.047		1.153		1.364		1.561	
10.0	1.018	0.996	1.013	1.001	0.997	1.016	0.980	1.043	0.981	1.083	1.030	1.142
	1.033		1.039		1.057		1.087		1.125		1.168	

Note:

1. In the finite element calculation:

   the radius of the vibrating surface R_0 = 0.1m; along the radius beetween the outer surface of the machine R_σ and the far-field boundary whose radius R_σ is chosen as 0.5m or 0.75m, there are 128 triangular elements.

2. The boundary condition at the far-field boundary is chosen as the local planar wave.

3. The calculated results 1 and 2 from finite element analysis correspond to radii of the far-field boundary of 0.75m and 0.5m respectively.

4. The exact value is calculated according to equation (3.9).

Table 4.2 Effect of Far-Field Boundary Condition on the Radiated Acoustic Power for an Infinite Cylindrical Model

kR_o (n=0)	Relative sound intensity							
	0.1	0.5	1.0	2.0	3.0	4.0	5.0	10.0
Exact value	0.157	0.574	0.797	0.922	0.961	0.984	0.994	1.000
Calculated 1	0.151	0.621	0.796	0.907	0.947	0.972	0.973	1.020
Calculated 2	0.151	0.621	0.796	0.906	0.947	0.973	0.989	0.995
Calculated 3	0.095	0.527	0.790	0.947	0.988	1.005	1.012	1.008
Average of 2 & 3	0.123	0.574	0.793	0.927	0.968	0.989	1.001	1.001

Note:

1. In the finite element calculation:

   radius of vibrating surface $R_o = 0.1$m; radius of far-field boundary $R_\sigma = 0.75$m; number of triangular elements along a radius between the outer surface of the machine R_o and the far-field boundary R_σ : 128.

2. Exact value is calculated according to equation (3.9).
3. Calculated value 1 is obtained by using harmonic axisymmetric triangular elements and assuming the far-field boundary condition to be a local planar wave.
4. Calculated value 2 is obtained by using planar triangular elements and assuming the far-field boundary condition to be a local planar wave.
5. Calculated value 3 is obtained by using planar triangular elements and assuming the far-field boundary condition to be a local spherical wave.

Table 4.3 Effect of Far-Field Boundary Condition on the Radiated Acoustic Power for a Spherical Model

kR_o	Relative sound intensity									
	n=0		n=1		n=2		n=3		n=4	
0.1	0.010	0.010					Calculated 1		Exact value	
	0.020									
0.5	0.204	0.200	0.010	0.015			Calculated 2			
	0.263		0.057							
1.0	0.506	0.500	0.367	0.200	0.049		0.002			
	0.560		0.411		0.043		0.002			
2.0	0.804	0.800	0.816	0.800	0.689		0.165		0.012	
	0.791		0.832		0.727		0.156		0.013	
3.0	0.905	0.900	0.930	0.953	0.994		0.923		0.300	
	0.873		0.906		1.012		0.947		0.292	
4.0	0.952	0.941	0.972	0.985	1.034		1.135		1.108	
	0.921		0.942		1.017		1.161		1.114	
5.0	0.977	0.962	0.992	0.994	1.039		1.126		1.260,	
	0.952		0.966		1.014		1.120		1.292	
10.0	0.994	0.990	0.996	1.000	1.003		1.023		1.066	
	0.981		0.983		0.992		1.015		1.065	

Note:

1. In the finite element calculation the vibration of the machine is expressed in the form of a Fourier series:

   radius of vibrating surface R_o = 0.1m; radius of far-field boundary R_σ = 0.75m; number of triangular elements along a radius between the outer surface of the machine R_o and the far-field boundary R_σ :128.

2. Exact values for n = 0 and n = 1 are calculated according to equation (4.77), when $n \geq 2$ no exact value exists, as is discussed in section 4.5.

3. The calculated values 1 and 2 correspond to far-field boundary conditions in the harmonic axisymmetric triangular element calculation, viz. local spherical and local planar waves.

4.4 Experimental Verification

Table 4.4 shows a comparison between the results calculated by finite elements and measurements on a 3-phase, 4-pole induction motor whose main parameters were: FL rating : 0.8kW, 1380rpm; encased type stator, outside diameter/axial length of the stator = 0.14m/0.17m; stator/rotor slot number = 24/22. The prototype motor is the same machine as used in Chapter 3. The vibrational acceleration was the average value of measured results made at 24 points uniformly distributed over the stator surface. The acoustic power was measured on no-load in an anechoic chamber by measuring the sound pressure at 8 points over an imaginary hemispherical surface of radius 1 metre enclosing the machine.

Table 4.4 Comparison between Predicted and Measured Results

	550Hz	1750Hz	LwA Calculated from Lw550Hz,Lw1750Hz	LwA from direct measurement
Amplitude of acceleration (m/s^2)	1.70	7.76		
Measured results (8 points) (dB)	64.3	68.2	69.85	70.6
Calculated results (Finite element)(dB)	60.6	68.3	69.0	
Analytical prediction (dB)	61.7	69.1	70.4	

Vibration measurements on the stator and end-shields confirm that the vibration of the end-shields is negligible compared with that of the stator. Therefore in the finite element calculation the vibration of the end-shields is set to zero, although there is no assumption of infinite cylindrical stiffening baffles at the end-shields as is usually the case in analytical cylindrical models of acoustic radiation. The machine exhibits two dominant vibration components, of frequencies 550 Hz and 1750 Hz, which were larger than other components by more than 13dB. Therefore, the vibration and noise spectrum of this machine can be considered as consisting only of these two components, which was confirmed further by comparing the measured acoustic power with/without other components included, Table 4.4, which showed a difference of < 1 dB. By measuring the sound pressure distribution and analysing the electromagnetic and the mechanical noise spectras, as well as by identifying the components from the spectra before/after the power supply was switched off, it was shown that the 1750 Hz

component is pure electromagnetic noise, whilst the 550 Hz component is composed of both electromagnetic noise as well as mechanical noise from the ball-bearings. The mode orders of the 550 Hz and 1750 Hz electromagnetic components are two, and are produced by the interaction of slot harmonics. The 550 Hz component was dominated by noise produced by the ball-bearings and exhibited a relatively unstable amplitude on a spectrum display of a real-time signal analyser. Therefore, the 1750 Hz component was calculated according to the circumferential mode order two, whilst the 550 Hz was calculated according to circumferential mode order zero by assuming the probability of radial vibration along the circumference to be constant. The calculation used 8-node isoparametric elements and 50 divisions along the radius between the outer surface of the machine and the far-field boundary - which was a spherical surface of radius 7.5 times the radius of the machine. The calculated relative sound intensity coefficients were $I_{550Hz} = 0.305$ and $I_{1750Hz} = 0.819$, and the corresponding calculated acoustic powers are shown in Table 4.4. Good agreement was achieved, especially for the 1750 Hz component. The 550 Hz component results confirm that the assumption of circumferential mode order zero for the ball-bearing noise was quite acceptable. It should be noted that the acoustic power measurements were from the sound pressure, and thus do not consider the phase difference between the sound pressure and the particle vibrational velocity. Therefore the measured results in Table 4.4 are only reference values. Further comparisons would require more accurate measurements, of the sound intensity, for example.

A comparison of the predicted acoustic power level from the finite cylindrical model of acoustic radiation described in Chapter 3 is also given in Table 4.4. Again as was the case for the finite element calculation, the 1750 Hz component was calculated according to circumferential mode order two, whilst the 550 Hz was calculated according to circumferential mode order zero. The calculated relative sound intensity coefficients are $I_{550Hz} = 0.395$ and $I_{1750Hz} = 0.985$ respectively. As was mentioned earlier the vibration of the end-shields in this prototype motor was negligible, therefore there is a very good agreement between results from the analytical finite cylindrical model of acoustic radiation and those from the finite element calculation.

4.5 Investigation of Spherical Model

The vibration of an electrical machine can be approached from that of a sphere [4.10] in which the radiated sound waves can be approximated by spherical waves radiated by a vibrating sphere. The vibrational velocity of the stator of the machine can be expressed as a Legendre series

$$v(\theta) = \sum_{n=0}^{\infty} v_n P_n(\cos\theta)\, e^{-j\omega t} \qquad r = a \tag{4.76}$$

where v is the vibrational velocity, v_n is its amplitude, n is the mode order, P_n is a Legendre function, a is the ouside radius. The relative sound intensity coefficients are obtained, by solving Helmholtz equation, as:

$$I_b = \frac{1}{(ka)^2} \frac{1}{j_n'^2(ka) + n_n'^2(ka)} \tag{4.77}$$

where j_n' and n_n' are the differential of the first and second spherical Bessel functions. Therefore if the vibration of a machine is known, the radiated acoustic power can be calculated from the relative sound intensity.

$$W = \frac{2}{2n+1} \rho c \pi^2 v_n^2 I_b \tag{4.78}$$

This method has the following features:

(i) The model is suitable only for analysing the noise of electrical machines having a length-to-diameter ratio approaching unity;

(ii) The vibrations produced by the machine must be expressed in the form of Legendre series;

(iii) The reference for the relative sound intensity coefficient is not the acoustic power of a planar wave when the vibration is expressed in the form of Fourier series, which is the usual convention, but the acoustic power calculated from the sound wave with its sound pressure and particle velocity in phase and expressed in the form of Legendre series.

However, since the vibrations and hence the radiated noise are caused by electromagnetic forces produced by harmonic fields in the airgap it is much easier to employ Fourier series to describe both the airgap field distribution and the radially excited vibrational forces, and hence the vibration of the stator. Comparing the general forms of Fourier (cos nθ) and Legendre (P_n(cos θ)) series, they are different except for n = 0 and n = 1. Therefore in order to predict noise it is necessary to convert the Fourier series into the form of a Legendre series, a difficult and sometimes impossible task.

For the above reasons, many papers employ the relative sound intensity coefficient directly but use the vibration expressed in the form of a Fourier series to calculate the radiated acoustic power.

$$W = \frac{1}{2}\ \rho\, c\, V_n^2\, I_b\, S_a \tag{7.79}$$

where S_a is the surface area of the machine.

As a consequence errors are introduced because of the mismatching between the model and the calculation method. In order to highlight this the finite element method was applied to the spherical model of acoustic radiation, which is still widely used to analyse the noise of electrical machines having a length-to-diameter ratio of 1.0.

Fig 4.2 compares the calculated relative sound intensity coefficients of the spherical model obtained from finite element analysis (I_{b2}) when the vibration of the machine is expressed in the form of a Fourier series with Jordan's results (I_{b1}) [4.10]. It shows that when the mode order is 0 or 1, the relative sound intensity coefficients from the two methods are identical, whilst for higher mode orders $I_{b1} > I_{b2}$. Hence the acoustic power from I_{b1} is less than that calculated from I_{b2}, if the same reference is used.

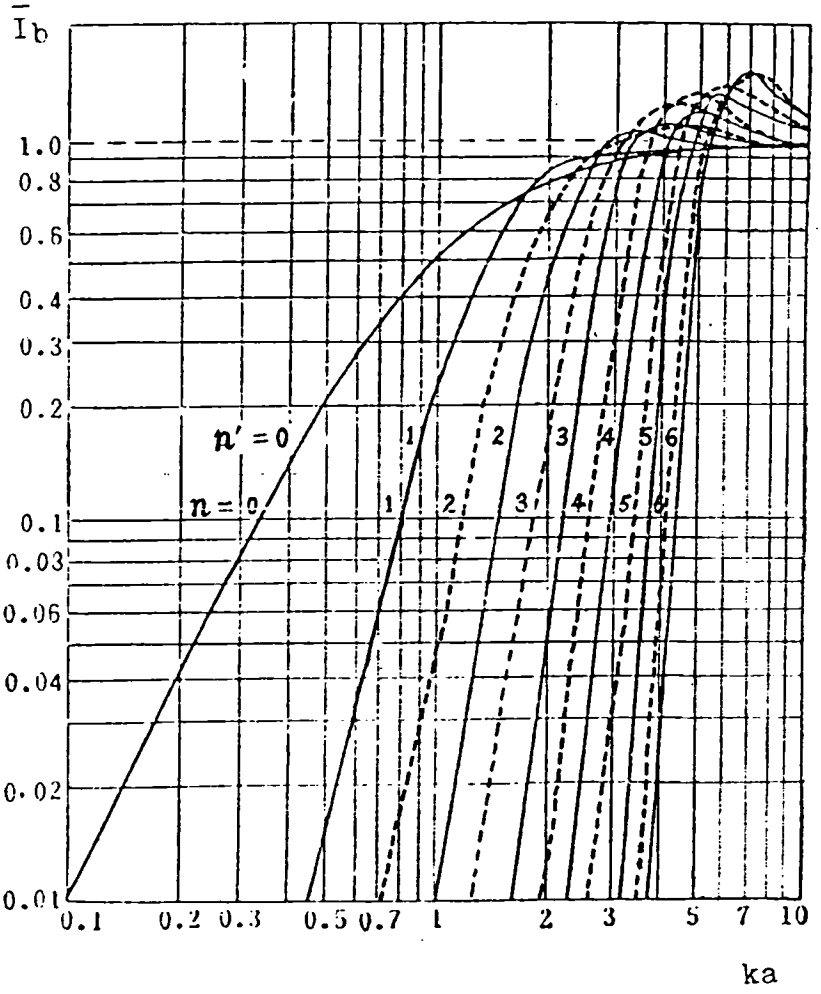

Fig 4.2 Relative Sound Intensity Coefficients of Spherical Model

When $n \geq 2$ dashed line is the results obtained in the paper

(vibration expressed in Fourier series),

solid line is Jordan's results (vibration expressed in Legendre series)

when n = 0 or 1, both are identical.

4.6 Conclusions

A technique has been presented which combines finite element and Fourier series analyses to calculate the acoustic power radiated from an electrical machine, for which predictions are validated against measurements on a 3-phase induction motor. The technique is capable of accounting for the effect of end-shields on the sound radiation, which would not be possible with existing analytical methods. The application of the finite element method to the spherical model of acoustic radiation has shown that when Jordan's method is used to calculate the radiated acoustic power, it is necessary to express the vibrations of the machine in the form of a Legendre series, otherwise large errors are introduced. The relative sound intensity coefficients of the spherical model, in which the vibration of the machine is expressed in the form of a Fourier series, have been obtained by finite element analysis which makes it possible to use Fourier series analysis throughout.

4.7 Appendices

4.7.1 Acoustic Field Radiated by an Electrical Machine and Its Boundary Conditions

The noise level of an electrical machine is estimated by it's acoustic power level which is a constant value irrespective of the background noise. Therefore the finite element calculation can be done in a free-space field. Due to the non-existence of other noise source, the term f in equation (4.1a) is zero.

Considering an electrical machine with vibrating surfaces, the finite element analysis of the infinite region is restricted to a finite region which is completely enclosed by a spherical boundary surface S. The radius of the surface σ is chosen to be large enough that the boundary condition can be represented by equation (4.81) by applying the radiation conditions of Sommerfield [4.2]. Therefore the boundary conditions are

$$\frac{\partial p}{\partial n} = j \rho c k v_n \qquad s \tag{4.80}$$

$$\frac{\partial p}{\partial n} = -j \rho c k \frac{p}{Z_\sigma} \qquad \sigma \tag{4.81}$$

where v_n is the normal velocity of the vibrating surface, and Z_σ is the acoustic impedance over the surface σ.

If the radius of the sphere is large enough then the waves crossing σ can be assumed to be approximated by planes waves, viz.

$$Z_\sigma = \rho c \tag{4.82}$$

that is

$$\frac{\partial p}{\partial n} + j k p = 0 \qquad \sigma \tag{4.83}$$

If the waves crossing σ are assumed as spherical waves, a smaller sphere can be used, which gives

$$Z_\sigma = \frac{\rho c}{1 + \frac{1}{j k R}} \tag{4.84}$$

that is

$$\frac{\partial p}{\partial n} + \left(\frac{1}{R} + j k \right) p = 0 \qquad \sigma \tag{4.85}$$

where R is the radius of σ.

Therefore, for $p = p_0 e^{-j\omega t}$ the acoustic field of an electrical machine and its boundary conditions are given by:

$$\nabla^2 p + k^2 p = f \qquad v$$

$$p = \bar{p} \qquad \Sigma_1$$

$$\frac{\partial p}{\partial n} = j \rho c k v_n \qquad \Sigma_2'$$

$$\frac{\partial p}{\partial n} + j k p = 0 \qquad \Sigma_2''$$

$$\text{or} \quad \frac{\partial p}{\partial n} + \left(\frac{1}{R} + j k\right) p = 0 \qquad \Sigma_2'' \tag{4.86}$$

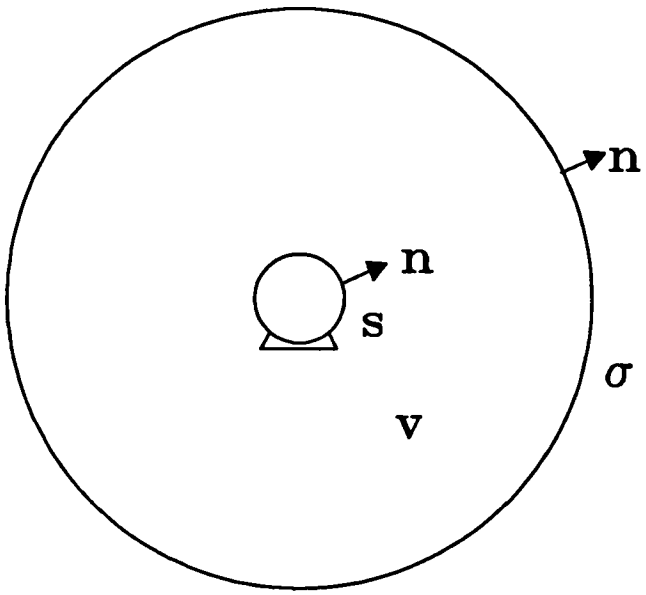

Fig 4.3 Field and boundary of an electrical machine

In the analysis of noise emitted by an electrical machine the first kind of boundary condition $p = \bar{p} = 0$ is used only when the symmetry of the field distribution is utilised. A comparison of equations (4.86) and (4.1) leads to

$$f = 0$$

$$h_n = 0 \,,\; 1 \,,\; or \quad \left(1 + \frac{1}{j k R}\right)$$

$$g_n = 0 \quad or \quad 1 \tag{4.87}$$

4.7.2 Three-dimensional Isoparametric Elements

In a similar manner to the vibrational two-dimensional isoparametric elements, the three-dimensional acoustic element, the sound pressure, and coordinates are approached by shape functions and the nodal values.

$$
\begin{aligned}
p &= \sum_{i=1}^{n} N_i p_i \\
x &= \sum_{i=1}^{n} N_i x_i \\
y &= \sum_{i=1}^{n} N_i y_i \\
z &= \sum_{i=1}^{n} N_i z_i
\end{aligned}
\tag{4.88}
$$

In the local coordinate system, the shape function is dependant on the local coordinate variables (ξ, η, ζ), viz.

$$N_i = N_i(\xi, \eta, \zeta) \tag{4.89}$$

The relationship between the local coordinates and the global coordinates is given by

$$
\begin{bmatrix} \frac{\partial}{\partial \xi} \\ \frac{\partial}{\partial \eta} \\ \frac{\partial}{\partial \zeta} \end{bmatrix} = [J] \begin{bmatrix} \frac{\partial}{\partial x} \\ \frac{\partial}{\partial y} \\ \frac{\partial}{\partial z} \end{bmatrix}
\tag{4.90}
$$

where

$$[J] = \begin{bmatrix} \frac{\partial x}{\partial \xi} & \frac{\partial y}{\partial \xi} & \frac{\partial z}{\partial \xi} \\ \frac{\partial x}{\partial \eta} & \frac{\partial y}{\partial \eta} & \frac{\partial z}{\partial \eta} \\ \frac{\partial x}{\partial \zeta} & \frac{\partial y}{\partial \zeta} & \frac{\partial z}{\partial \zeta} \end{bmatrix} \tag{4.91}$$

$dv = dx\, dy\, dz = |J|\, d\xi\, d\eta\, d\zeta$

$d\Sigma = | \vec{r_\eta}\, d\eta \times \vec{r_\zeta}\, d\zeta | = | \vec{r_\eta} \times \vec{r_\zeta} |\, d\eta\, d\zeta$

(assuming Σ is on the surface of $\xi = 1$)

$| \vec{r_\eta} \times \vec{r_\zeta} | = \sqrt{EG - F^2}$

$$E = \left(\frac{\partial x}{\partial \eta}\right)^2 + \left(\frac{\partial y}{\partial \eta}\right)^2 + \left(\frac{\partial z}{\partial \eta}\right)^2$$

$$G = \left(\frac{\partial x}{\partial \zeta}\right)^2 + \left(\frac{\partial y}{\partial \zeta}\right)^2 + \left(\frac{\partial z}{\partial \zeta}\right)^2$$

$$F = \frac{\partial x}{\partial \eta}\frac{\partial x}{\partial \zeta} + \frac{\partial y}{\partial \eta}\frac{\partial y}{\partial \zeta} + \frac{\partial z}{\partial \eta}\frac{\partial z}{\partial \zeta} \tag{4.92}$$

In the case of two-dimensions, the isoparametric elements are exactly the same as those in the analysis of vibrational behaviour.

4.7.3 Detection of Standing Waves and Travelling Waves

When the vibration of an electrical machine is in the form of standing waves, its vibration can be expressed as

$$a = A \cos (\omega t + \alpha_t) \cos (n \theta + \alpha_\theta) \tag{4.93}$$

The signals detected by two transducers at circumferential positions θ_1 and θ_2 are then given by

$$a_1 = A \cos (\omega t + \alpha_t) \cos (n \theta_1 + \alpha_{\theta 1}) \tag{4.94}$$

$$a_2 = A \cos (\omega t + \alpha_t) \cos (n \theta_2 + \alpha_{\theta 1}) \tag{4.95}$$

Therefore their relative amplitude is

$$\left| \frac{\cos (n \theta_1 + \alpha_{\theta 1})}{\cos (n \theta_2 + \alpha_{\theta 2})} \right| \qquad (4.96)$$

which is related to the positions of the transducers. If one transducer is fixed at θ_2 , its value varies according to cos $n\theta$.

The relative phase difference depends on whether the values of $\cos (n \theta_1 + \alpha_{\theta 1})$ and $\cos (n \theta_2 + \alpha_{\theta 2})$ have the same or opposite signs. If the signs are the same, then the phase difference is 0^o, otherwise the phase difference is 180^o.

When the vibration of an electrical machine is in the form of travelling waves, its vibration can be expressed as

$$a = A \cos (\omega t - n \theta + \alpha) \qquad (4.97)$$

Then the signals detected by two transducers at circumferential positions θ_1 and θ_2 are

$$a_1 = A \cos (\omega t - n \theta_1 + \alpha) \qquad (4.98)$$

$$a_2 = A \cos (\omega t - n \theta_2 + \alpha) \qquad (4.99)$$

Therefore their relative amplitude is unity.

The relative phase difference $n (\theta_2 - \theta_1)$ depends on the positions of the transducers, being n times the geometric angle between the positions of the two transducers.

CHAPTER 5

ANALYTICAL CALCULATION OF OPEN-CIRCUIT FIELD DISTRIBUTION IN PERMANENT MAGNET MOTORS, ACCOUNTING FOR THE EFFECT OF SLOTTING

5.1 Introduction

A general analytical technique for predicting the open-circuit magnetic field distribution in radial-field brushless permanent magnet motors is a pre-requisite for force calculations - for the purpose of acoustic noise and vibration predictions [5.1]; for the prediction of back-emf waveforms [5.2] - for both use in steady-state and transient dynamic simulations; for the calculation of torque-speed performance curves [5.3], as well as for the prediction of cogging torque waveforms [5.4].

G Eid and A Mouilett [5.5] proposed an analytical model for predicting the field distribution of internal rotor motors having a cylindrical permanent magnet with uniform magnetisation over its cross-section. In addition they and Q Gu and H Gao [5.6] employed the separation of variables method to study the airgap field of a multi-pole permanent magnet motor modelled in a rectangular coordinate system. N Boules [5.7] also presented a multi-pole permanent magnet model in rectangular coordinates but used an equivalent magnet width to account for the fact that in a cylindrical machine the magnet width generally varies with radius. In [5.8] Boules also applied two-dimensional field theory formulated in polar coordinates to determine the flux density distribution at the stator and rotor surfaces of permanent magnet machines by utilising the concept of equivalent current carrying coils. Hence it was suitable for investigating the flux focussing effect of the magnet, as well as the influence of the direction of magnetisation, ie. radial or diametric, on the useful flux per pole and the shape of the flux density waveform. G Xiong and S A Nasar [5.9] analysed the field in a permanent magnet linear synchronous machine by employing the concept of magnet charge, whilst Q Gu and H Gao [5.10] and C Kramer [5.11]

used a "sub-region" method by using a Fourier series expansion in the slot, airgap, and magnet regions, applying continuity boundary conditions between the sub-regions and solving the resultant equations to determine the coefficients of the Fourier series. They established a model for calculating the effective airgap flux (Carter coefficient) for slotted permanent magnet motors. By using a similar technique and a segmented permanent magnet model, Q Gu and H Gao [5.12] predicted the fringing flux distribution along the axial length of a permanent magnet motor.

In summary, an accurate knowledge of the airgap flux density waveform on open-circuit is essential for the accurate prediction of various aspects of a motors performance. However whilst numerical methods for field computation, such as finite elements, provide an accurate means of determining the flux density distribution with due account of saturation etc they are time-consuming and do not provide nearly as much insight as analytical solutions into the underlying principles. On the other hand, existing analytical methods have not accounted effectively for the effects of slotting on the airgap field distribution which in a permanent magnet motor is critical to the prediction of noise and vibration, cogging torque, iron loss etc. In addition existing analytical methods have approximated the relative recoil permeability of the permanent magnets, ie μ_R, as unity, which can cause an error in the calculation of flux density, of up to around 20% for $\mu_R = 1.2$ [5.8].

In this chapter improved analytical models are established for the calculation of the open-circuit airgap field distribution of permanent magnet excited motors. They cater for slotted and slotless stators, and internal and external rotor radial-field topologies modelled in either rectangular or polar coordinate systems. The technique is based on the two-dimensional analytical model cited in Chapter 1, Fig 1.4, and utilises the concepts of permeance and mmf, ie. the field produced by the magnets and a relative permeance function. It involves the solution of the governing Laplacian/quasi-Poissonian field equation in the airgap/magnet regions without the assumption of unity relative recoil permeability of the magnet, but with due account for the presence of stator slot openings by the application of the conformal transformation method and the introduction of

a "2-d" relative permeance function. The results of the analysis of various radial-field motors are reported and compared with predictions from corresponding finite element analyses.

5.2 Brief Description of Calculation Method

Although the method employed is based on a two-dimensional analytical field calculation, the following 1-d methods are included in order to illustrate the strategy of the calculation.

5.2.1 A Simple 1-D Model

From a simple 1-d magnetic circuit analysis, as shown in Fig 5.1, if flux leakage is neglected and the permeability of the stator and rotor iron is assumed to be infinite, then for magnets mounted adjacent to the airgap, ie. $A_m = A_g$, where A_m and A_g are the cross-sectional areas of the magnet and the airgap respectively, the airgap flux density is given by:

$$B_g = \frac{\mu_o M_o}{1 + \mu_R \frac{g}{h_m}} \tag{5.1}$$

$$\text{therefore} \quad B_g = \frac{B_R}{1 + \mu_R \frac{g}{h_m}} = \frac{B_R}{g + \frac{h_m}{\mu_R}} \frac{h_m}{\mu_R} = \left(\frac{\mu_o}{g'}\right)\left(H_c\, h_m\right) \tag{5.2}$$

where B_g is the airgap flux density; M_o is the magnetisation; B_R is the remanence; H_c is the normal coercivity, assuming a linear demagnetisation curve; μ_R is the relative recoil permeability of the magnet; g is the length of the airgap; h_m is the thickness of the magnet.

$$\text{and} \quad g' = g + \frac{h_m}{\mu_R} \quad \text{is an effective airgap.} \tag{5.3}$$

If the mmf F is defined as:

$$F = H_c\, h_m = \frac{B_R}{\mu_o\, \mu_R} h_m \tag{5.4}$$

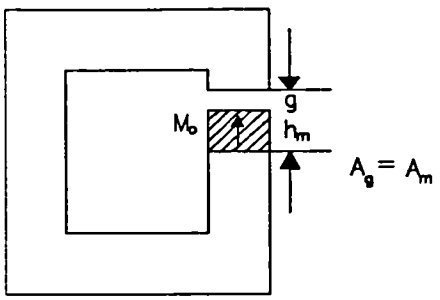

Fig 5.1 Simple "1-d" model

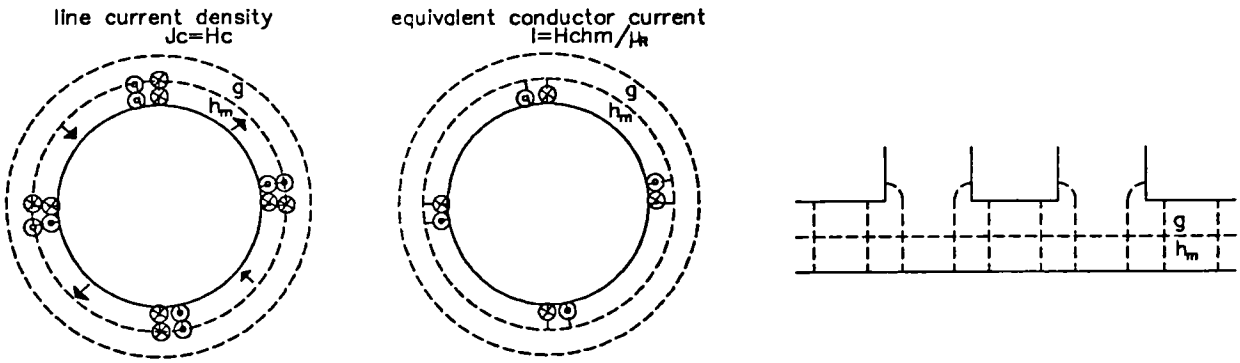

(a) Physical model (b) "1-d" mmf model (c) "1-d" permeance model

Fig 5.2 "1-d" model

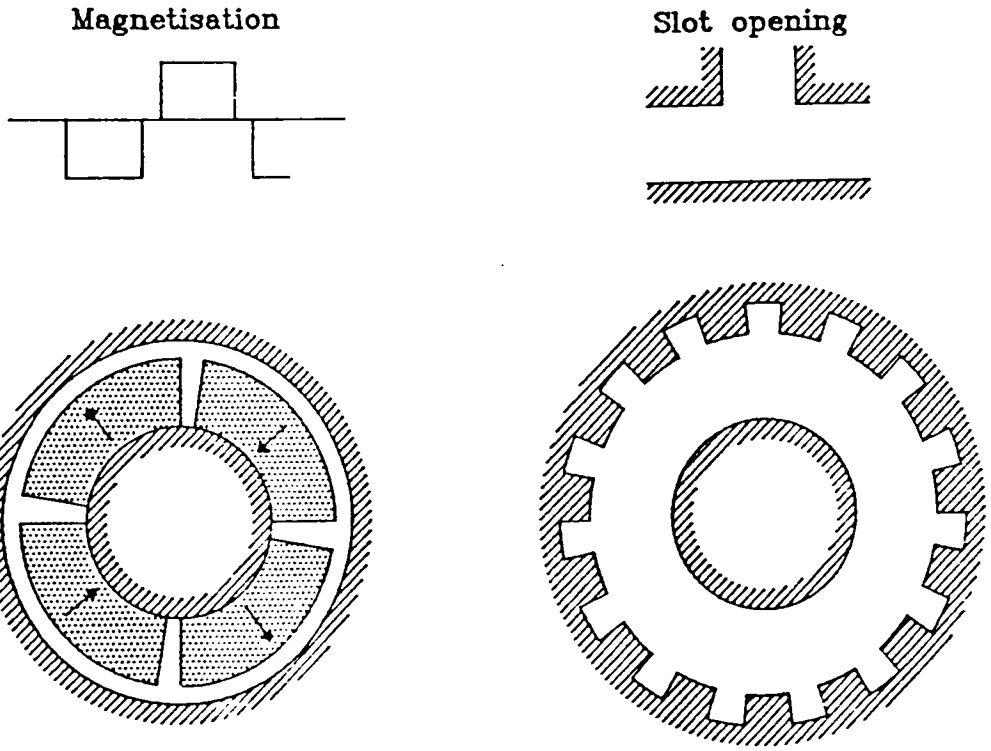

(a) "2-d" model for calculating the field produced by magnets

(b) "2-d" model for calculating the relative permeance

Fig 5.3 Open-circuit field calculation

and the permeance is defined as:

$$\Lambda = \frac{\mu_o}{g'} \tag{5.5}$$

Then the airgap flux density is given by the product of the permeance and the mmf, ie.

$$B_g = F\,\Lambda \tag{5.6}$$

Considering the fact that ($H_c h_m$) is an equivalent current source whilst g' is an equivalent effective airgap, the above definitions are consistent with the more conventional definitions applied to induction motors [5.1].

5.2.2 A Refined 1-D Model

If the airgap field in a permanent magnet motor is assumed to vary only with the circumferential coordinate,α, and depend on the angle of rotation of the rotor, α_{ma}, as shown in Fig 5.2, then from one-dimensional field theory, the airgap field is given by:

$$B_g = \frac{\mu_o M(\alpha, \alpha_{ma})}{1 + \mu_R \dfrac{g(\alpha)}{h_m}}$$

$$= \left[\frac{M(\alpha, \alpha_{ma})}{\mu_R}\, h_m\right]\left[\frac{\mu_o}{g(\alpha) + \dfrac{h_m}{\mu_R}}\right] = F\,\Lambda \tag{5.7}$$

where the mmf

$$F = \frac{M(\alpha, \alpha_{ma})}{\mu_R}\, h_m \tag{5.8}$$

can be calculated by conventional 1-d methods, such as those applied to the wound induction motor, according to the equivalent model shown in Fig 5.2(b). In Fig 5.2(b) the magnets are modelled by surface current sheets and are converted into equivalent current carrying conductors distributed around the surface of the rotor.

The permeance is

$$\Lambda = \frac{\mu_o}{g'(\alpha)} \tag{5.9}$$

$$\text{where } g'(\alpha) = g(\alpha) + \frac{h_m}{\mu_R} \tag{5.10}$$

If the magnetic flux paths are assumed to be straight lines across the airgap/magnet region and circular trajectories in the slot region, as shown in Fig 5.2(c), the airgap length is then calculated from

$$g(\alpha) = g_o \tag{5.11a}$$

$$\text{for } (k-1)\alpha_\tau + \frac{\alpha_o}{2} \le \alpha \le \alpha_\tau - \frac{\alpha_o}{2}, \quad k = 1, 2, ..., Q_s$$

and

$$g(\alpha) = g_o + \frac{\pi}{2} R_i \left\{ \frac{\alpha_o}{2} - [\,|\alpha| - (k-1)\alpha_\tau\,] \right\} \tag{5.11b}$$

$$\text{for } (k-1)\alpha_\tau - \frac{\alpha_o}{2} \le \alpha \le (k-1)\alpha_\tau + \frac{\alpha_o}{2}, \quad k = 1, 2, ..., Q_s$$

where

$\alpha_o = \frac{b_o}{R_i}$; $\alpha_\tau = \frac{\tau_t}{R_i}$; b_o is the slot opening; τ_t is the slot pitch; R_i is the radius of the stator surface adjacent to the airgap; Q_s is the number of slots; g_o is the airgap length in the equivalent slotless stator motor which equals the airgap length under the teeth in the slotted motor.

5.2.3 A 2-D Model

In the above 1-d model the magnet is modelled by a constant mmf source. However, in practice in a multi-pole permanent magnet motor, because of the low magnet permeability and interpolar flux leakage, the magnet mmf is no longer constant, but varies over the pole-arc. Hence, as

mentioned in [5.7], the simplifying assumption of concentrating the magnet mmf between the magnet and airgap can lead to a significant error.

Therefore in the ensuing analysis instead of using the earlier mmf and permeance models, the magnetic field B is expressed as the magnetic field B_m produced by the rotor magnets but then modulated by the relative permeance λ due to the stator slotting, ie. the field is calculated from the product of the field produced by the magnets and the relative permeance function,

$$B = B_m \lambda \tag{5.12}$$

With this definition the equations (5.4 - 5.6) for the simple 1-d model are now re-written as:

$$B_g = B_m \lambda \tag{5.13a}$$

$$\text{where } B_m = \frac{B_R}{1 + \mu_R \frac{g}{h_m}} \tag{5.13b}$$

$$\text{and } \lambda = 1 \tag{5.13c}$$

whilst equations (5.7 - 5.9) for the refined 1-d model become

$$B_g = B_m \lambda \tag{5.14a}$$

$$\text{where } B_m = \frac{\mu_o M(\alpha, \alpha_{ma})}{1 + \mu_R \frac{g_o}{h_m}} \tag{5.14b}$$

$$\text{and } \lambda = \frac{g_o + \frac{h_m}{\mu_R}}{g(\alpha) + \frac{h_m}{\mu_R}} \tag{5.14c}$$

Clearly for these 1-d models the results for the field calculation remain the same as before.

However in the 2-d model of a permanent magnet motor, the calculation of the magnet field B_{magnet}, the relative permeance λ, and the open-circuit field $B_{open-circuit}$, are as follows:

i) Calculation of $B_{magnet}(r, \alpha, \alpha_{ma})$

$B_{magnet}(r, \alpha, \alpha_{ma})$ is calculated as the radial component of an equivalent slotless stator motor, as shown in Fig 5.3(a). The motor can have either an external or internal rotor topology. Its steady-state magnetic field is solved from the governing 2-d Maxwell equations framed in a polar coordinate system. However at present, the permanent magnets are assumed to be radially magnetised and to have a linear demagnetisation characteristic. In addition end-effects are ignored, and the permeability of the rotor and stator iron is assumed to be infinite.

NOTE : It will be possible to extend the analysis to cater for diametrically magnetised permanent magnets and to account for saturation of the back-iron and teeth of the stator and rotor.

ii) Calculation of $\tilde{\lambda}(r, \alpha)$

The permeance $\lambda(r, \alpha)$ is calculated from the magnetic field $B'(r, \alpha)$ in the magnet and airgap regions produced by a unit difference in magnetic potential between the stator and rotor iron, as shown in Fig 5.3(b). Since $\tilde{\lambda}(r, \alpha)$ is defined as the relative permeance with a unity maximum value, the relative permeance is obtained from the calculated field divided by a reference permeance. From a previous definition (eqn (5.12)), the reference permeance is equal to the one-dimensional permeance of an equivalent slotless stator motor, ie.

$$\Lambda_{ref} = \Lambda_o = \frac{\mu_o}{g + \frac{h_m}{\mu_R}} \tag{5.15}$$

Therefore

$$\tilde{\lambda}(r, \alpha) = \frac{\lambda(r, \alpha)}{\Lambda_{ref}} \tag{5.16}$$

$$\text{where } \lambda(r, \alpha) = B'(r, \alpha) \tag{5.17}$$

It will be shown in the following sections that, due to the large effective airgap in permanent magnet motors, it is necessary to employ a 2-d permeance model in order to account for the effect of the slot openings.

iii) Calculation of $B_{open-circuit}\,(r, \alpha, \alpha_{ma})$

The open-circuit magnetic field $B_{open-circuit}\,(r, \alpha, \alpha_{ma})$ at any point in the magnet/airgap region is calculated from the corresponding magnetic field produced by the magnets, multiplied by the corresponding value of relative permeance, ie.

$$B_{open-circuit}\,(r, \alpha, \alpha_{ma}) = B_{magnet}\,(r, \alpha, \alpha_{ma})\,\lambda\,(r, \alpha) \qquad (5.18)$$

5.3 Magnetic Field Produced by Magnets

In this section expressions are derived in terms of rectangular and polar coordinates for the magnetic field produced by the permanent magnets in external and internal rotor slotless motors. The effect of slotting is accounted for in the subsequent section 5.4.

For any magnetic field without a distributed current source,

$$div\,\vec{B} = 0 \qquad (5.19)$$

and

$$curl\,\vec{H} = 0 \qquad (5.20)$$

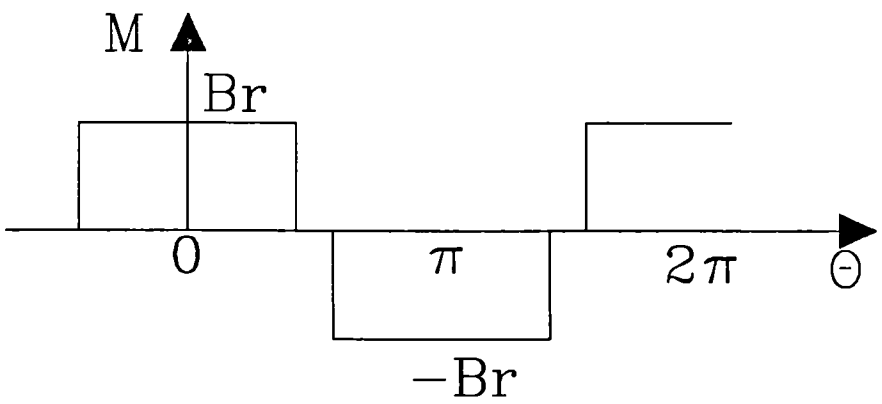

Fig 5.4 Radial magnetisation (for the case of the magnet pole arc < pole-pitch).

which are coupled by the fundamental relationships

$$\vec{B_I} = \mu_o \vec{H_I} \quad \text{in airspaces;} \tag{5.21}$$

$$\vec{B_{II}} = \mu_o \vec{H_{II}} + \vec{M} \quad \text{in a permanent magnet} \tag{5.22}$$

where $\vec{M}$ is the magnetisation, whose distribution is given in Appendix 5.1 and shown in Fig 5.4 for the case of a multipole radially magnetised machine.

The variable " θ " which is used in the cylindrical model, is with reference to the centre of a magnet pole.

If the scalar magnetic potential ϕ is introduced

$$\vec{H} = -\nabla \varphi \tag{5.23}$$

Therefore

$$\nabla^2 \varphi_I = 0 \quad \text{in the airgap} \tag{5.24}$$

and

$$\nabla^2 \varphi_{II} = \frac{div \vec{M}}{\mu_m} \quad \text{in the magnet} \tag{5.25}$$

$$\text{where} \quad \mu_m = \mu_o \mu_R \tag{5.26}$$

In rectangular coordinates since the magnetisation $\vec{M}$ is given by

$$\vec{M} = M_x \vec{i} + M_y \vec{j} \tag{5.27}$$

$$\text{where} \quad M_x = 0 \tag{5.27a}$$

$$\text{and} \quad M_y = M = \sum_{n=1,3,5,\ldots}^{\infty} M_n \cos n \frac{\pi}{\tau_p} x \tag{5.27b}$$

where τ_p is the pole-pitch

$$\text{therefore} \quad div\vec{M} = \frac{\partial M_x}{\partial x} + \frac{\partial M_y}{\partial y} = 0 \tag{5.28}$$

Therefore the scalar magnetic potential in both the airspace and permanent magnet regions is described by the Laplacian equation

$$\frac{\partial^2 \varphi}{\partial x^2} + \frac{\partial^2 \varphi}{\partial y^2} = 0 \tag{5.29}$$

which is related to the components of the magnetic intensity $\vec{H}$ by

$$H_x = - \frac{\partial \varphi}{\partial x} \tag{5.31a}$$

$$H_y = - \frac{\partial \varphi}{\partial y} \tag{5.31b}$$

In polar coordinates, however, since the magnetisation $\vec{M}$ is given by

$$\vec{M} = M_r \vec{r} + M_\theta \vec{\theta} \tag{5.32}$$

$$\text{where} \quad M_r = \sum_{n=1,3,5,\ldots}^{\infty} M_n \cos n p \theta \tag{5.32a}$$

$$\text{and} \quad M_\theta = 0 \tag{5.32b}$$

where p is the number of pole-pairs,

$$div\, \vec{M} = \frac{M_r}{r} + \frac{\partial M_r}{\partial r} + \frac{1}{r} \frac{\partial M_\theta}{\partial \theta} = \frac{M_r}{r} \tag{5.33}$$

Therefore, whilst the scalar magnetic potential distribution in the airspace is again governed by the Laplacian equation, in the permanent magnet regions it is governed by the Poissonian equation, ie

$$\frac{\partial^2 \varphi_I}{\partial r^2} + \frac{1}{r} \frac{\partial \varphi_I}{\partial r} + \frac{1}{r^2} \frac{\partial \varphi_I^2}{\partial \theta^2} = 0 \qquad \text{in the airspace} \tag{5.34a}$$

and

$$\frac{\partial^2 \varphi_{II}}{\partial r^2} + \frac{1}{r}\frac{\partial \varphi_{II}}{\partial r} + \frac{1}{r^2}\frac{\partial \varphi_{II}^2}{\partial \theta^2} = \frac{M_r}{r\,\mu_m} \qquad \text{in the permanent magnet} \tag{5.34b}$$

where both ϕ_I and ϕ_{II} are related to the components of $\vec{H}$ by

$$H_r = -\frac{\partial \varphi}{\partial r} \tag{5.35a}$$

$$H_\theta = -\frac{1}{r}\frac{\partial \varphi}{\partial \theta} \tag{5.35b}$$

5.3.1 In Polar Coordinates

5.3.1.1 Internal Rotor Motors

For an internal rotor motor, such as that shown in Fig 5.5, the scalar magnetic potential distribution in the airspace I and the magnets II is governed by the partial differential equations

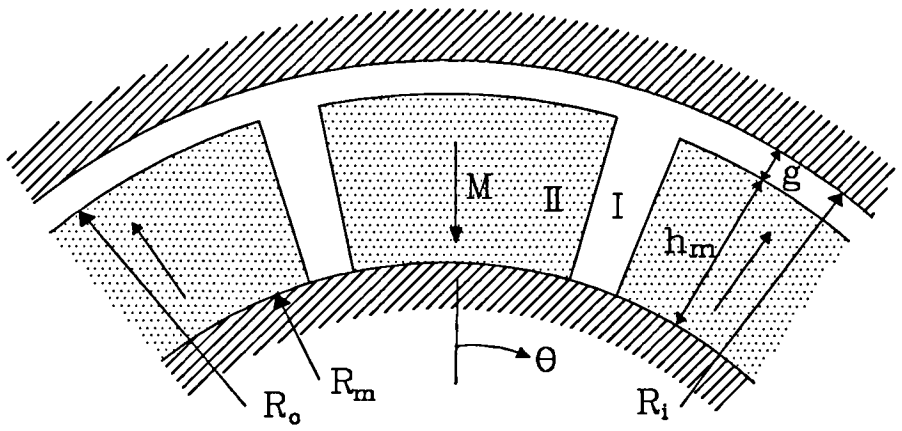

Fig 5.5 Internal rotor motor.

(5.34(a)) and (5.34(b)), for which the general solution has the following form:

$$\varphi(r,\theta) = \sum_{n'=1}^{\infty} (A_{n'} r^{-n'} + B_{n'} r^{-n'})(C_{n'} \cos n'\theta + D_{n'} \sin n'\theta)$$
$$+ (A_o \ln r + B_o)(C_o \theta + D_o) \tag{5.36}$$

However due to the periodicity of the field, the general solution of the corresponding homogeneous equation for both the airspace and magnet regions becomes

$$\varphi(r,\theta) = \sum_{n=1}^{\infty} (A_n r^{-np} + B_n r^{-np}) \cos np\,\theta \tag{5.37}$$

In the magnets since

$$\nabla^2 \varphi_{II} = \frac{M_r}{r\,\mu_m} = \frac{1}{r\,\mu_m} \sum_{n=1,3,5,\ldots}^{\infty} M_n \cos np\,\theta \tag{5.38}$$

then by assuming the specific solution of the form:

$$\varphi'_{II} = \sum_{n=1,3,5,\ldots}^{\infty} C_1\, r \cos np\,\theta \tag{5.39}$$

and substituting it into equation (5.38), the constant C_1 is obtained as:

$$C_1 = -\frac{1}{(np)^2 - 1}\,\frac{M_n}{\mu_m} \tag{5.40}$$

Therefore

$$\varphi'_{II} = \sum_{n=1,3,5,\ldots}^{\infty} \frac{M_n}{\mu_m\,[1-(np)^2]}\, r \cos np\,\theta \tag{5.41}$$

However this solution is not valid for the particular case of np = 1. Hence for np = 1, by letting $r = e^t$, equation (5.38) becomes

$$\frac{\partial^2 \varphi_{II}}{\partial t^2} + \frac{\partial^2 \varphi_{II}}{\partial \theta^2} = \frac{M_1}{\mu_m}\, e^t \cos\theta \tag{5.42}$$

Now assuming $\varphi'_{II} = C_2\, t\, e^t \cos\theta$ (5.43)

and substituting it into equation (5.42) the constant C_2 is obtained as

$$C_2 = \frac{1}{2}\,\frac{M_1}{\mu_m} \tag{5.44}$$

Therefore for np = 1

$$\varphi'_{II} = \frac{1}{2}\,\frac{M_1}{\mu_m}\, t\, e^t \cos\theta = \frac{1}{2}\,\frac{M_1}{\mu_m}\, r \ln r \cos\theta \tag{5.45}$$

Therefore the general solutions of equations (5.34(a)) and (5.34(b)) are obtained as

$$\varphi_I(r,\theta) = \sum_{n=1,3,5,\ldots}^{\infty} (A_{nI}\, r^{-np} + B_{nI}\, r^{-np}) \cos np\,\theta \quad \text{in the airspace} \tag{5.46}$$

and

$$\varphi_{II}(r,\theta) = \sum_{n=1,3,5,\ldots}^{\infty} (A_{nII}\, r^{-np} + B_{nII}\, r^{-np}) \cos np\,\theta + \sum_{n=1,3,5,\ldots}^{\infty} \frac{M_n}{\mu_m\,[1-(np)^2]}\, r \cos np\,\theta \quad \text{for} \quad np \neq 1 \tag{5.47a}$$

$$\text{or} \quad \varphi_{II} = (A_{1II}\, r + B_{1II}\, r^{-1}) \cos\theta + \frac{1}{2}\,\frac{M_1}{\mu_m}\, r \ln r \cos\theta \quad \text{for} \quad np = 1 \tag{5.47b}$$

in the magnets.

The boundary conditions for the model of Fig 5.5 and the magnetisation distribution M, which is shown in Fig 5.4, are defined by

1) $H_{\theta I}(r,\theta)|_{r=R_i} = 0$, *ie.* $\varphi_{II}|_{r=R_i} = 0$ (5.48)

2) $H_{\theta II}(r,\theta)|_{r=R_m} = 0$, *ie.* $\varphi_{II}|_{r=R_m} = 0$ (5.49)

3) $B_{rI}(r,\theta)|_{r=R_o} = B_{rII}(r,\theta)|_{r=R_o}$ (5.50)

4) $H_{\theta I}(r,\theta)|_{r=R_o} = H_{\theta II}(r,\theta)|_{r=R_o}$ (5.51)

5) $M = \sum_{n=1,3,5,\ldots}^{\infty} M_n \cos np\,\theta$ as derived in Appendix 5.1 (5.52)

where $R_o = R_i - g$

and $R_m = R_i - g - h_m$

Hence the complete solution for the magnetic field components in the airgap/magnet regions is deduced as:

(i) when $np \neq 1$

In the airspace

$$B_{rI}(r,\theta) = \sum \frac{M_n}{\mu_R} \frac{np}{(np)^2 - 1} R_o^{-(np-1)} \cdot \left\{ \frac{(np-1)R_o^{2np} + 2R_m^{np+1} R_o^{np-1} - (np+1)R_m^{2np}}{\frac{\mu_R+1}{\mu_R}\left[R_i^{2np} - R_m^{2np}\right] - \frac{\mu_R-1}{\mu_R}\left[R_o^{2np} - R_i^{2np}(R_m/R_o)^{2np}\right]} \right\} \cdot \left[r^{np-1} + R_i^{2np} r^{-(np+1)} \right] \cos np\,\theta \quad (5.53)$$

$$B_{\theta I}(r,\theta) = \sum \frac{(-M_n)}{\mu_R} \frac{np}{(np)^2 - 1} R_o^{-(np-1)} \cdot \left\{ \frac{(np-1)R_o^{2np} + 2R_m^{np+1} R_o^{np-1} - (np+1)R_m^{2np}}{\frac{\mu_R+1}{\mu_R}\left[R_i^{2np} - R_m^{2np}\right] - \frac{\mu_R-1}{\mu_R}\left[R_o^{2np} - R_i^{2np}(R_m/R_o)^{2np}\right]} \right\} \cdot \left[r^{np-1} - R_i^{2np} r^{-(np+1)} \right] \sin np\,\theta \quad (5.54)$$

In the magnets

$$B_{rII}(r,\theta) = \sum M_n \frac{np}{(np)^2 - 1} R_o^{-(np-1)} \cdot \left\{ \frac{\left(np - \frac{1}{\mu_R}\right)R_o^{2np} + \left(1 + \frac{1}{\mu_R}\right)R_m^{np+1} R_o^{np-1} - \left(np + \frac{1}{\mu_R}\right)R_i^{2np} - \left(1 - \frac{1}{\mu_R}\right)(R_m/R_o)^{np+1} R_i^{2np}}{\frac{\mu_R+1}{\mu_R}\left[R_i^{2np} - R_m^{2np}\right] - \frac{\mu_R-1}{\mu_R}\left[R_o^{2np} - R_i^{2np}(R_m/R_o)^{2np}\right]} \right\}$$

$$\cdot\left[r^{np-1} + R_m^{2np}\, r^{-(np+1)}\right] \cos np\,\theta$$

$$+ \sum M_n \frac{np}{[(np)^2 - 1]} \left(\frac{R_m}{r}\right)^{np+1} \cos np\,\theta$$

$$+ \sum M_n \frac{(np)^2}{[(np)^2 - 1]} \cos np\,\theta \qquad (5.55)$$

$$B_{\theta II}(r,\theta) = \sum(-M_n) \frac{np}{(np)^2 - 1} R_o^{-(np-1)}$$

$$\cdot\left\{\frac{\left(np - \frac{1}{\mu_R}\right)R_o^{2np} + \left(1 + \frac{1}{\mu_R}\right)R_m^{np+1} R_o^{np-1} - \left(np + \frac{1}{\mu_R}\right)R_i^{2np} - \left(1 - \frac{1}{\mu_R}\right)(R_m/R_o)^{np+1} R_i^{2np}}{\frac{\mu_R + 1}{\mu_R}[R_i^{2np} - R_m^{2np}] - \frac{\mu_R - 1}{\mu_R}\left[R_o^{2np} - R_i^{2np}\,(R_m/R_o)^{2np}\right]}\right\}$$

$$\cdot\left[r^{np-1} - R_m^{2np}\, r^{-(np+1)}\right] \sin np\,\theta$$

$$+ \sum M_n \frac{np}{[(np)^2 - 1]} \left(\frac{R_m}{r}\right)^{np+1} \sin np\,\theta$$

$$- \sum M_n \frac{np}{[(np)^2 - 1]} \sin np\,\theta \qquad (5.56)$$

(ii) when np = 1

In the airspace

$$B_{rI}(r,\theta) = \frac{M_1}{2\mu_R}\left\{\frac{\left(\frac{R_o}{R_i}\right)^2 - \left(\frac{R_m}{R_i}\right)^2 + \left(\frac{R_m}{R_i}\right)^2 \ln\left(\frac{R_o}{R_m}\right)^2}{\frac{\mu_R + 1}{\mu_R}\left[1 - \left(\frac{R_m}{R_i}\right)^2\right] - \frac{\mu_R - 1}{\mu_R}\left[\left(\frac{R_o}{R_i}\right)^2 - \left(\frac{R_m}{R_o}\right)^2\right]}\right\}$$

$$\cdot\left[1 + \left(\frac{R_i}{r}\right)^2\right] \cos\theta \qquad (5.57)$$

$$B_{\theta I}(r,\theta) = \frac{(-M_1)}{2\mu_R}\left\{\frac{\left(\frac{R_o}{R_i}\right)^2 - \left(\frac{R_m}{R_i}\right)^2 + \left(\frac{R_m}{R_i}\right)^2 \ln\left(\frac{R_o}{R_m}\right)^2}{\frac{\mu_R + 1}{\mu_R}\left[1 - \left(\frac{R_m}{R_i}\right)^2\right] - \frac{\mu_R - 1}{\mu_R}\left[\left(\frac{R_o}{R_i}\right)^2 - \left(\frac{R_m}{R_o}\right)^2\right]}\right\}$$

$$\cdot\left[1 - \left(\frac{R_i}{r}\right)^2\right] \sin\theta \qquad (5.58)$$

In the magnets

$$B_{rII}(r,\theta) = \frac{M_1}{2}\left\{\frac{\left(\frac{R_o}{R_i}\right)^2 - 1 + \ln\left(\frac{R_o}{R_m}\right)\left[\frac{\mu_R+1}{\mu_R}\left(\frac{R_m}{R_i}\right)^2 - \frac{\mu_R-1}{\mu_R}\left(\frac{R_m}{R_o}\right)^2\right]}{\frac{\mu_R+1}{\mu_R}\left[1-\left(\frac{R_m}{R_i}\right)^2\right] - \frac{\mu_R-1}{\mu_R}\left[\left(\frac{R_o}{R_i}\right)^2 - \left(\frac{R_m}{R_o}\right)^2\right]}\right\}$$

$$\cdot\left[1+\left(\frac{R_m}{r}\right)^2\right]\cos\theta + \frac{M_1}{2}\left[1 - \ln\left(\frac{r}{R_o}\right) + \left(\frac{R_m}{r}\right)^2 \ln\left(\frac{R_o}{R_m}\right)\right]\cos\theta \qquad (5.59)$$

$$B_{\theta II}(r,\theta) = \frac{(-M_1)}{2}\left\{\frac{\left(\frac{R_o}{R_i}\right)^2 - 1 + \ln\left(\frac{R_o}{R_m}\right)\left[\frac{\mu_R+1}{\mu_R}\left(\frac{R_m}{R_i}\right)^2 - \frac{\mu_R-1}{\mu_R}\left(\frac{R_m}{R_o}\right)^2\right]}{\frac{\mu_R+1}{\mu_R}\left[1-\left(\frac{R_m}{R_i}\right)^2\right] - \frac{\mu_R-1}{\mu_R}\left[\left(\frac{R_o}{R_i}\right)^2 - \left(\frac{R_m}{R_o}\right)^2\right]}\right\}$$

$$\cdot\left[1-\left(\frac{R_m}{r}\right)^2\right]\sin\theta + \frac{(-M_1)}{2}\left[-\ln\left(\frac{r}{R_o}\right) - \left(\frac{R_m}{r}\right)^2 \ln\left(\frac{R_o}{R_m}\right)\right]\sin\theta \qquad (5.60)$$

Further it will be shown in the next section that the above solutions are also valid for external rotor motors, provided that the variables R_o and R_m are correctly re-defined.

For internal rotor motors ($np \neq 1$) since

$$R_o = R_i - g$$

$$R_m = R_i - g - h_m$$

hence $R_i > R_o > R_m$

Therefore the expressions for the field vectors B_r and B_θ can be re-written in the following forms in order to ease their numerical computation:

In the airspace: $R_o < r < R_i$

$$B_{rI}(r,\theta) = \sum \frac{M_n}{\mu_R}\,\frac{np}{(np)^2-1}$$

$$\cdot\left\{\frac{(np-1) + 2\left(\frac{R_m}{R_o}\right)^{np+1} - (np+1)\left(\frac{R_m}{R_o}\right)^{2np}}{\frac{\mu_R+1}{\mu_R}\left[1-\left(\frac{R_m}{R_i}\right)^{2np}\right] - \frac{\mu_R-1}{\mu_R}\left[\left(\frac{R_o}{R_i}\right)^{2np} - \left(\frac{R_m}{R_o}\right)^{2np}\right]}\right\}$$

$$\cdot\left[\left(\frac{r}{R_i}\right)^{np-1}\left(\frac{R_o}{R_i}\right)^{np+1} + \left(\frac{R_o}{r}\right)^{np+1}\right]\cos np\,\theta \qquad (5.62)$$

$$B_{\theta I}(r,\theta) = \sum \frac{(-M_n)}{\mu_R} \frac{np}{(np)^2 - 1}$$

$$\cdot\left\{\frac{(np-1) + 2\left(\frac{R_m}{R_o}\right)^{np+1} - (np+1)\left(\frac{R_m}{R_o}\right)^{2np}}{\frac{\mu_R+1}{\mu_R}\left[1 - \left(\frac{R_m}{R_i}\right)^{2np}\right] - \frac{\mu_R-1}{\mu_R}\left[\left(\frac{R_o}{R_i}\right)^{2np} - \left(\frac{R_m}{R_o}\right)^{2np}\right]}\right\}$$

$$\cdot\left[\left(\frac{r}{R_i}\right)^{np-1}\left(\frac{R_o}{R_i}\right)^{np+1} - \left(\frac{R_o}{r}\right)^{np+1}\right] \sin np\,\theta \qquad (5.63)$$

In the magnets: $R_m < r < R_o$

$$B_{rII}(r,\theta) = \sum M_n \frac{np}{(np)^2 - 1}$$

$$\cdot\left\{\frac{\left(np - \frac{1}{\mu_R}\right)\left(\frac{R_o}{R_i}\right)^{2np} + \left(1 + \frac{1}{\mu_R}\right)\left(\frac{R_m}{R_o}\right)^{np+1}\left(\frac{R_o}{R_i}\right)^{2np} - \left(np + \frac{1}{\mu_R}\right) - \left(1 - \frac{1}{\mu_R}\right)\left(\frac{R_m}{R_o}\right)^{np+1}}{\frac{\mu_R+1}{\mu_R}\left[1 - \left(\frac{R_m}{R_i}\right)^{2np}\right] - \frac{\mu_R-1}{\mu_R}\left[\left(\frac{R_o}{R_i}\right)^{2np} - \left(\frac{R_m}{R_o}\right)^{2np}\right]}\right\}$$

$$\cdot\left[\left(\frac{r}{R_o}\right)^{np-1} + \left(\frac{R_m}{R_o}\right)^{np-1}\left(\frac{R_m}{r}\right)^{np+1}\right] \cos np\,\theta$$

$$+ \sum M_n \frac{np}{[(np)^2 - 1]}\left(\frac{R_m}{r}\right)^{np+1} \cos np\,\theta$$

$$+ \sum M_n \frac{(np)^2}{[(np)^2 - 1]} \cos np\,\theta \qquad (5.64)$$

$$B_{\theta II}(r,\theta) = \sum (-M_n) \frac{np}{(np)^2 - 1}$$

$$\cdot\left\{\frac{\left(np - \frac{1}{\mu_R}\right)\left(\frac{R_o}{R_i}\right)^{2np} + \left(1 + \frac{1}{\mu_R}\right)\left(\frac{R_m}{R_o}\right)^{np+1}\left(\frac{R_o}{R_i}\right)^{2np} - \left(np + \frac{1}{\mu_R}\right) - \left(1 - \frac{1}{\mu_R}\right)\left(\frac{R_m}{R_o}\right)^{np+1}}{\frac{\mu_R+1}{\mu_R}\left[1 - \left(\frac{R_m}{R_i}\right)^{2np}\right] - \frac{\mu_R-1}{\mu_R}\left[\left(\frac{R_o}{R_i}\right)^{2np} - \left(\frac{R_m}{R_o}\right)^{2np}\right]}\right\}$$

$$\cdot\left[\left(\frac{r}{R_o}\right)^{np-1} - \left(\frac{R_m}{R_o}\right)^{np-1}\left(\frac{R_m}{r}\right)^{np+1}\right] \sin np\,\theta$$

$$+ \sum M_n \frac{np}{[(np)^2 - 1]}\left(\frac{R_m}{r}\right)^{np+1} \sin np\,\theta$$

$$- \sum M_n \frac{np}{[(np)^2 - 1]} \sin np\,\theta \qquad (5.65)$$

5.3.1.2 External Rotor Motors

For external rotor motors, such as the one shown in Fig 5.6, the scalar magnetic potential distribution in the airspace I and the magnets II is given by equations (5.34(a)) and (5.34(b)) respectively, whilst their general solutions are given by equations (5.46) and (5.47), which are exactly the same as those for internal rotor motors.

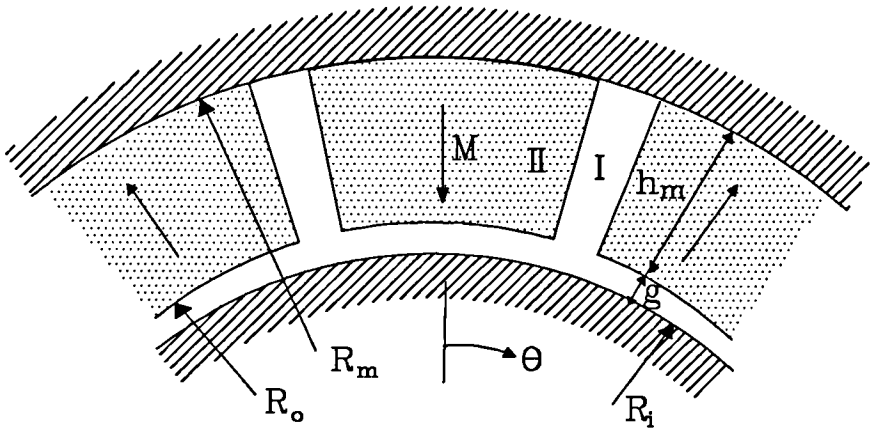

Fig 5.6 External rotor motor.

However the boundary conditions and the magnetisation distribution M are now defined by:

1) $H_{\theta I}(r,\theta)|_{r=R_i} = 0$, *ie.* $\varphi_{II}|_{r=R_i} = 0$ (5.66)

2) $H_{\theta II}(r,\theta)|_{r=R_i+g+h_m} = 0$, *ie.* $\varphi_{II}|_{r=R_i+g+h_m} = 0$ (5.67)

3) $B_{rI}(r,\theta)|_{r=R_i+g} = B_{rII}(r,\theta)|_{r=R_i+g}$ (5.68)

4) $H_{\theta I}(r,\theta)|_{r=R_i+g} = H_{\theta II}(r,\theta)|_{r=R_i+g}$ (5.69)

5) $M = \sum_{n=1,3,5,\ldots}^{\infty} M_n \cos np\theta$ as derived in Appendix 5.1 (5.70)

Again it will be noted that if

$R_o = R_i + g$

$R_m = R_i + g + h_m$ (5.71a)

then the boundary conditions and magnetisation for external rotor motors, ie. equations (5.66) - (5.70), have the same forms as those for internal rotor motors. Therefore, if equation (5.71(a)) replaces equation (5.61), the solutions for the magnetic field distribution in the airspace/magnet regions of external rotor motors will also be given by equations (5.53) - (5.60), which were derived for internal rotor motors.

However, for an external rotor motor,

$$R_i < R_o < R_m \tag{5.71b}$$

Therefore in order to enable numerical computation, for the case of $np \neq 1$, the solutions, ie. equations (5.53 - 5.56) and (5.71(a)), are re-written as:

For $np \neq 1$

In the airspace: $R_i < r < R_o$

$$B_{rI}(r,\theta) = \sum \frac{(-M_n)}{\mu_R} \frac{np}{(np)^2 - 1} \cdot \left\{ \frac{(np-1)\left(\frac{R_o}{R_m}\right)^{2np} + 2\left(\frac{R_o}{R_m}\right)^{np-1} - (np+1)}{\frac{\mu_R+1}{\mu_R}\left[1 - \left(\frac{R_i}{R_m}\right)^{2np}\right] - \frac{\mu_R-1}{\mu_R}\left[\left(\frac{R_i}{R_o}\right)^{2np} - \left(\frac{R_o}{R_m}\right)^{2np}\right]} \right\} \cdot \left[\left(\frac{r}{R_o}\right)^{np-1} + \left(\frac{R_i}{R_o}\right)^{np-1}\left(\frac{R_i}{r}\right)^{np+1}\right] \cos np\,\theta \tag{5.72}$$

$$B_{\theta I}(r,\theta) = \sum \frac{M_n}{\mu_R} \frac{np}{(np)^2 - 1} \cdot \left\{ \frac{(np-1)\left(\frac{R_o}{R_m}\right)^{2np} + 2\left(\frac{R_o}{R_m}\right)^{np-1} - (np+1)}{\frac{\mu_R+1}{\mu_R}\left[1 - \left(\frac{R_i}{R_m}\right)^{2np}\right] - \frac{\mu_R-1}{\mu_R}\left[\left(\frac{R_i}{R_o}\right)^{2np} - \left(\frac{R_o}{R_m}\right)^{2np}\right]} \right\} \cdot \left[\left(\frac{r}{R_o}\right)^{np-1} - \left(\frac{R_i}{R_o}\right)^{np-1}\left(\frac{R_i}{r}\right)^{np+1}\right] \sin np\,\theta \tag{5.73}$$

In the magnets: $R_o < r < R_m$

$$B_{rII}(r,\theta) = \sum (-M_n)\frac{np}{(np)^2-1}$$
$$\cdot\left\{\frac{\left(np-\frac{1}{\mu_R}\right)+\left(1+\frac{1}{\mu_R}\right)\left(\frac{R_i}{R_o}\right)^{np+1}\left(\frac{R_i}{R_m}\right)^{np-1}-\left(np+\frac{1}{\mu_R}\right)\left(\frac{R_i}{R_o}\right)^{2np}-\left(1-\frac{1}{\mu_R}\right)\left(\frac{R_o}{R_m}\right)^{np-1}}{\frac{\mu_R+1}{\mu_R}\left[1-\left(\frac{R_i}{R_m}\right)^{2np}\right]-\frac{\mu_R-1}{\mu_R}\left[\left(\frac{R_i}{R_o}\right)^{2np}-\left(\frac{R_o}{R_m}\right)^{2np}\right]}\right\}$$
$$\cdot\left[\left(\frac{r}{R_m}\right)^{np-1}\left(\frac{R_o}{R_m}\right)^{np+1}+\left(\frac{R_o}{r}\right)^{np+1}\right]\cos np\,\theta$$
$$-\sum M_n\frac{np}{[(np)^2-1]}\left(\frac{r}{R_m}\right)^{np-1}\cos np\,\theta$$
$$+\sum M_n\frac{(np)^2}{[(np)^2-1]}\cos np\,\theta \qquad (5.74)$$

$$B_{\theta II}(r,\theta) = \sum M_n\frac{np}{(np)^2-1}$$
$$\cdot\left\{\frac{\left(np-\frac{1}{\mu_R}\right)+\left(1+\frac{1}{\mu_R}\right)\left(\frac{R_i}{R_o}\right)^{np+1}\left(\frac{R_i}{R_m}\right)^{np-1}-\left(np+\frac{1}{\mu_R}\right)\left(\frac{R_i}{R_o}\right)^{2np}-\left(1-\frac{1}{\mu_R}\right)\left(\frac{R_o}{R_m}\right)^{np-1}}{\frac{\mu_R+1}{\mu_R}\left[1-\left(\frac{R_i}{R_m}\right)^{2np}\right]-\frac{\mu_R-1}{\mu_R}\left[\left(\frac{R_i}{R_o}\right)^{2np}-\left(\frac{R_o}{R_m}\right)^{2np}\right]}\right\}$$
$$\cdot\left[\left(\frac{r}{R_m}\right)^{np-1}\left(\frac{R_o}{R_m}\right)^{np+1}-\left(\frac{R_o}{r}\right)^{np+1}\right]\sin np\,\theta$$
$$+\sum M_n\frac{np}{[(np)^2-1]}\left(\frac{r}{R_m}\right)^{np-1}\sin np\,\theta$$
$$-\sum M_n\frac{np}{[(np)^2-1]}\sin np\,\theta \qquad (5.75)$$

Hence solutions for the magnetic field distribution in the airspace and and magnet regions have been obtained for both internal and external rotor motors. However whilst these can provide useful information for the field distribution, such as its radial and circumferential components, it is the radial component of the open-circuit flux density distribution at the surface of the stator which is of most significance, for example, in the calculation of the induced back-emf waveform in Chapter 8, and in the prediction of cogging torque which is considered in Chapter 6.

At the stator surface, ie. r = R_i , the general expression for the radial component of flux density in internal and external rotor motors become:

when $np \neq 1$

$$B_{rI}(\theta) = \sum 2\frac{M_n}{\mu_R}\frac{np}{(np)^2-1}\left(\frac{R_i}{R_o}\right)^{np-1} \cdot \left\{\frac{(np-1)R_o^{2np} + 2R_m^{np+1}R_o^{np-1} - (np+1)R_m^{2np}}{\frac{\mu_R+1}{\mu_R}[R_i^{2np} - R_m^{2np}] - \frac{\mu_R-1}{\mu_R}\left[R_o^{2np} - R_i^{2np}(R_m/R_o)^{2np}\right]}\right\}\cos np\,\theta \quad (5.76)$$

and when np=1

$$B_{rI}(\theta) = \frac{M_1}{\mu_R}\left\{\frac{\left(\frac{R_o}{R_i}\right)^2 - \left(\frac{R_m}{R_i}\right)^2 + \left(\frac{R_m}{R_i}\right)^2 \ln\left(\frac{R_o}{R_m}\right)^2}{\frac{\mu_R+1}{\mu_R}\left[1 - \left(\frac{R_m}{R_i}\right)^2\right] - \frac{\mu_R-1}{\mu_R}\left[\left(\frac{R_o}{R_i}\right)^2 - \left(\frac{R_m}{R_o}\right)^2\right]}\right\}\cos\theta \quad (5.77)$$

For numerical computation the expression for $np \neq 1$ may also be written as:

Internal rotor motor ($np \neq 1$)

$$B_{rI}(\theta) = \sum 2\frac{M_n}{\mu_R}\frac{np}{(np)^2-1}\left(\frac{R_o}{R_i}\right)^{np+1} \cdot \left\{\frac{(np-1) + 2\left(\frac{R_m}{R_o}\right)^{np+1} - (np+1)\left(\frac{R_m}{R_o}\right)^{2np}}{\frac{\mu_R+1}{\mu_R}\left[1 - \left(\frac{R_m}{R_i}\right)^{2np}\right] - \frac{\mu_R-1}{\mu_R}\left[\left(\frac{R_o}{R_i}\right)^{2np} - \left(\frac{R_m}{R_o}\right)^{2np}\right]}\right\}\cos np\,\theta \quad (5.78)$$

External rotor motor ($np \neq 1$)

$$B_{rI}(\theta) = \sum 2\frac{(-M_n)}{\mu_R}\frac{np}{(np)^2-1}\left(\frac{R_i}{R_o}\right)^{np-1} \cdot \left\{\frac{(np-1)\left(\frac{R_o}{R_m}\right)^{2np} + 2\left(\frac{R_o}{R_m}\right)^{np-1} - (np+1)}{\frac{\mu_R+1}{\mu_R}\left[1 - \left(\frac{R_i}{R_m}\right)^{2np}\right] - \frac{\mu_R-1}{\mu_R}\left[\left(\frac{R_i}{R_o}\right)^{2np} - \left(\frac{R_o}{R_m}\right)^{2np}\right]}\right\}\cos np\,\theta \quad (5.79)$$

5.3.2 In Rectangular Coordinates

When modelled in rectangular coordinates, as shown in Fig 5.7, for which the governing Laplacian equation is given by equation (5.29) the boundary conditions and the magnetisation distribution $\vec{M}$ are given by:

1) $H_{xII}|_{y=0} = 0, ie.\ \varphi_{II}|_{y=0} = 0$ (5.80)

2) $H_{xI}|_{y=g+h_m} = 0, ie.\ \varphi_{II}|_{y=g+h_m} = 0$ (5.81)

3) $H_{xI}|_{y=h_m} = H_{xII}|_{y=h_m}$ (5.82)

4) $B_{yI}|_{y=h_m} = B_{yII}|_{y=h_m}$ (5.83)

5) $M = \sum_{n=1,3,5,\ldots}^{\infty} M_n \cos n\frac{\pi}{\tau_p} x$, as derived in Appendix 5.1 (5.84)

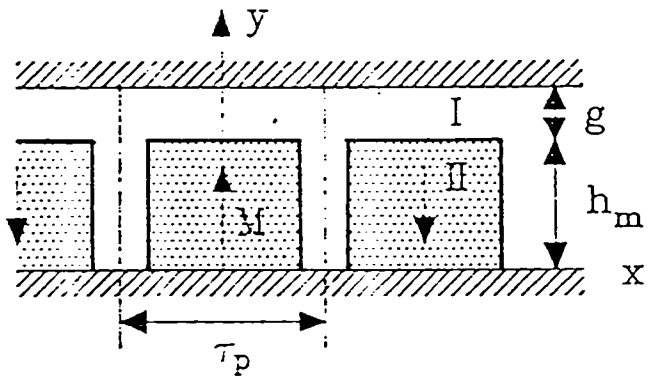

Fig 5.7 Model for calculating magnetic field produced by magnets in rectangular coordinates

The general solution for the scalar magnetic potential distribution is:

$$\varphi(x,y) = \sum_{n=1}^{\infty} \left(A_n \cosh n\frac{\pi}{\tau_p} y + B_n \sinh n\frac{\pi}{\tau_p} y\right) \cos n\frac{\pi}{\tau_p} x \quad (5.85)$$

whilst the following solutions for the field components in the airgap/magnet regions are obtained:

$$B_{xII}(x,y) = \sum_{n=1,3,5,\ldots}^{\infty} \mu_R M_n \frac{\sinh n\frac{\pi}{\tau_p} g}{\sinh n\frac{\pi}{\tau_p}(g+h_m)} \sinh n\frac{\pi}{\tau_p} y \quad \sin n\frac{\pi}{\tau} p\, x \tag{5.86}$$

$$B_{yII}(x,y) = -\sum_{n=1,3,5,\ldots}^{\infty} \mu_R M_n \frac{\sinh n\frac{\pi}{\tau_p} g}{\sinh n\frac{\pi}{\tau_p}(g+h_m)} \cosh n\frac{\pi}{\tau_p} y \quad \cos n\frac{\pi}{\tau_p} x$$

$$+ \sum_{n=1,3,5,\ldots}^{\infty} M_n \cos n\frac{\pi}{\tau_p} x \tag{5.87}$$

$$B_{xI}(x,y) = \sum_{n=1,3,5,\ldots}^{\infty} M_n \frac{\sinh n\frac{\pi}{\tau_p} h_m}{\sinh n\frac{\pi}{\tau_p}(g+h_m)} \sinh n\frac{\pi}{\tau_p}(g+h_m-y) \quad \sin n\frac{\pi}{\tau_p} x \tag{5.88}$$

$$B_{yI}(x,y) = \sum_{n=1,3,5,\ldots}^{\infty} M_n \frac{\sinh n\frac{\pi}{\tau_p} h_m}{\sinh n\frac{\pi}{\tau_p}(g+h_m)} \cosh n\frac{\pi}{\tau_p}(g+h_m-y) \quad \cos n\frac{\pi}{\tau_p} x \tag{5.89}$$

Again for ease of numerical computation, the formulae may be re-written as:

$$B_{xII}(x,y) = \sum_{n=1,3,5,\ldots}^{\infty} \mu_R M_n \frac{1-e^{-2n\frac{\pi}{\tau_p} g}}{1-e^{-2n\frac{\pi}{\tau_p}(g+h_m)}}$$

$$\frac{e^{n\frac{\pi}{\tau_p}(y-h_m)} - e^{-n\frac{\pi}{\tau_p}(y+h_m)}}{2} \sin n\frac{\pi}{\tau_p} x \tag{5.90}$$

$$B_{yII}(x,y) = -\sum_{n=1,3,5,\ldots}^{\infty} \mu_R M_n \frac{1-e^{-2n\frac{\pi}{\tau_p} g}}{1-e^{-2n\frac{\pi}{\tau_p}(g+h_m)}}$$

$$\frac{e^{n\frac{\pi}{\tau_p}(y-h_m)} + e^{-n\frac{\pi}{\tau_p}(y+h_m)}}{2} \cos n\frac{\pi}{\tau_p} x \quad + \sum_{n=1,3,5,\ldots}^{\infty} M_n \cos n\frac{\pi}{\tau_p} x \tag{5.91}$$

$$B_{xI}(x,y) = \sum_{n=1,3,5,\ldots}^{\infty} M_n \frac{1-e^{-2n\frac{\pi}{\tau_p} h_m}}{1-e^{-2n\frac{\pi}{\tau_p}(g+h_m)}}$$

$$\frac{e^{n\frac{\pi}{\tau_p}(h_m-y)} - e^{-n\frac{\pi}{\tau_p}(2g+h_m-y)}}{2} \sin n\frac{\pi}{\tau_p}x \tag{5.92}$$

$$B_{yI}(x,y) = \sum_{n=1,3,5,\ldots}^{\infty} M_n \frac{1-e^{-2n\frac{\pi}{\tau_p}h_m}}{1-e^{-2n\frac{\pi}{\tau_p}(g+h_m)}}$$

$$\frac{e^{n\frac{\pi}{\tau_p}(h_m-y)} + e^{-n\frac{\pi}{\tau_p}(2g+h_m-y)}}{2} \cos n\frac{\pi}{\tau_p}x \tag{5.93}$$

The flux density distribution, B_{yI}, on the stator surface $y = g + h_m$ is obtained as:

$$B_{yI}(x) = \sum_{n=1,3,5,\ldots}^{\infty} M_n \frac{1-e^{-2n\frac{\pi}{\tau_p}h_m}}{1-e^{-2n\frac{\pi}{\tau_p}(g+h_m)}} e^{-n\frac{\pi}{\tau_p}g} \cos n\frac{\pi}{\tau_p}x \tag{5.94}$$

5.4 Effect of Slotting

Slotting affects the magnetic field in two different ways. Firstly the airgap flux will be reduced compared with the flux when unslotted. Such effects can be accounted for by introducing the Carter coefficient into the calculation, ie. by modifying the effective airgap length in the calculation of the magnetic field produced by the magnets. Secondly, slotting will affect the magnetic field distribution in both the airgap and the magnets.

5.4.1 Effect of Slotting on the Effective Flux

When the stator is slotted, an appropriate Carter coefficient K_c can be included and instead of g and R_i effective values g_e and R_{ie} are used in the calculation of the magnetic field produced by the magnets to account for the reduction in the effective flux.

For example, in an internal rotor motor:

$$g_e = g + (K_c - 1)\, g' \tag{5.95}$$

$$R_{ie} = R_i + (K_c - 1)\, g' \tag{5.96}$$

where $g' = g + h_m / \mu_R$ is the effective airgap;

K_C is the Carter coefficient and can be approximated by:

$$K_C = \frac{\tau_t}{\tau_t - \gamma g'} \tag{5.97}$$

where

$$\tau_t = \frac{2 \pi R_i}{Q_s}$$

$$\gamma = \frac{4}{\pi} \left\{ \frac{b_o}{2 g'} \tan^{-1}\left(\frac{b_o}{2 g'}\right) - \ln \sqrt{1 + \left(\frac{b_o}{2 g'}\right)^2} \right\} \tag{5.98}$$

and b_o is the slot opening.

Similarly, in an external rotor motor:

$$g_e = g + (K_C - 1) g' \tag{5.99}$$

$$R_{ie} = R_i - (K_C - 1) g' \tag{5.100}$$

whilst in rectangular coordinates if the stator is slotted, a Carter coefficient may be used again with g_e used instead of g, where

$$g_e = g + (K_C - 1) g' \tag{5.101}$$

However due to the large effective airgap, which equals the physical airgap length plus magnet height, in a permanent magnet motor the ratio of slot opening to the effective airgap is small, hence the Carter coefficient $K_C \approx 1$, a typical calculation showing that K_C is around 1.01. Therefore the effect of slotting on the effective flux reduction in a permanent magnet motor is negligible, except when a very large slot opening is employed, such as may be the case for reducing the cogging torque.

5.4.2 Effect of Slotting on the Field Distribution - the Relative Permeance Calculation

The permeance of a slotted airgap/magnet region can be calculated by the conformal transformation method with unity magnetic potential applied between the stator and rotor iron surfaces and no magnet present, as shown in Fig 5.8 in which infinitely permeable stator and rotor iron surfaces and an infinitely deep rectilinear stator slot are assumed. For permanent magnet motors which have a small number of slots, a single-slot model is acceptable for the calculation of the relative permeance, and even when the ratio of the airgap to slot pitch is large the calculation of the airgap flux density distribution by a single-slot model may still be acceptable. In this case, however, errors may arise if the flux density does not attain its maximum value before the centre of the teeth [5.13]. Hence a model consisting of a continuous series of slots can be used [5.13].

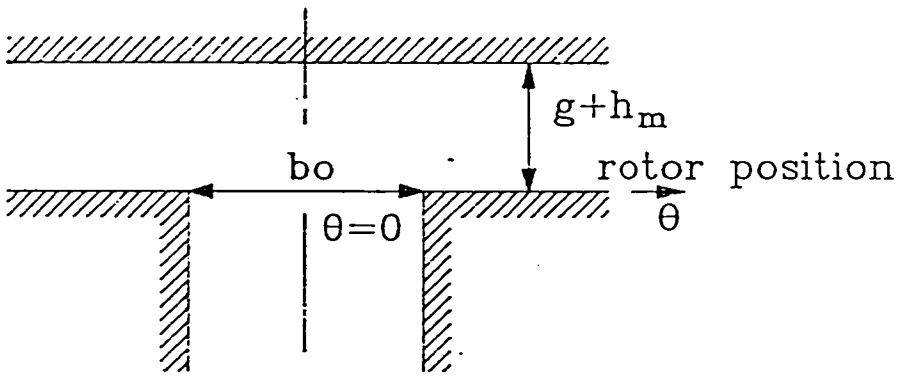

Fig 5.8 Permeance calculation model.

Based on a single-slot model, the interior of the airgap region in the z-plane is transformed to the upper half of the w-plane and subsequently to the t-plane, as shown in Fig 5.9.

The transformations are given by:

$$z = \frac{b_o}{\pi}\left\{ \arcsin\frac{w}{a} + \frac{g'}{b_o}\ln\left[\frac{\sqrt{a^2-w^2}+\frac{2g'}{b_o}w}{\sqrt{a^2-w^2}-\frac{2g'}{b_o}w}\right]\right\} \qquad (5.102)$$

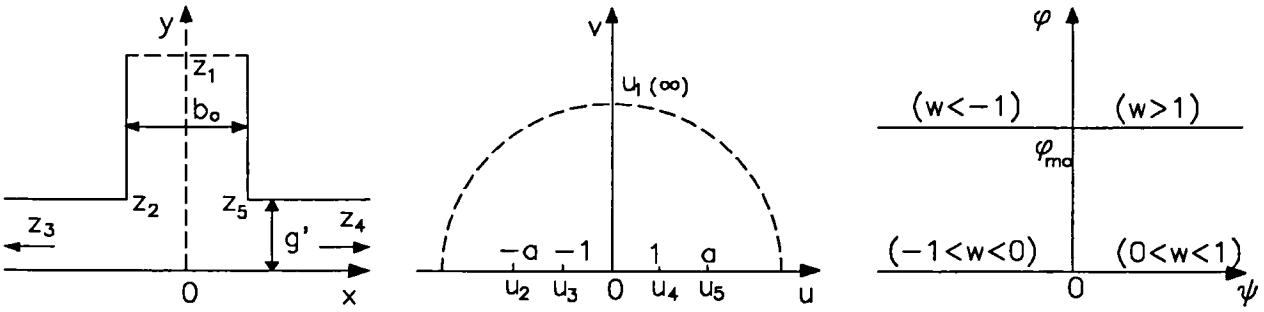

(a) z - plane (b) w - plane (c) t - plane

($g' = g + h_m/\mu_R$)

Fig 5.9 Conformal transformation

which after some deduction becomes:

$$z = \frac{b_o}{\pi}\left\{\frac{j}{2}\ln\left[\frac{1-j\dfrac{w}{\sqrt{a^2-w^2}}}{1+j\dfrac{w}{\sqrt{a^2-w^2}}}\right]+j\frac{2g'}{b_o}\arctan\left[\frac{-j\,2g'\,w}{b_o\sqrt{a^2-w^2}}\right]\right\} \tag{5.103}$$

where j is the complex operator, $j = \sqrt{-1}$

$$a = \sqrt{1+\left(\frac{2g'}{b_o}\right)^2} \tag{5.104}$$

and $$t = \frac{\varphi_{mo}}{\pi}\ln\frac{1+w}{1-w} \tag{5.105}$$

The corresponding flux density in the airgap region is given by:

$$B = \mu_o H = \mu_o \left|\frac{dt}{dz}\right| = \mu_o \left|\frac{dt}{dw}\right| \left|\frac{dw}{dz}\right|$$

$$= \mu_o \frac{\varphi_{mo}}{g'} \frac{1}{\sqrt{1+\left(\frac{b_o}{2g'}\right)^2 - \left(\frac{b_o}{2g'}w\right)^2}} \tag{5.106}$$

where $\varphi_{mo} = \frac{B_R}{\mu_o \mu_R} h_m$ (5.107)

Therefore by letting w = 1, the maximum flux density B_{max} is obtained as

$$B_{max} = \mu_o \frac{\varphi_{mo}}{g'} \tag{5.108}$$

The variation of the flux density against the circumferential angular position shows it to have a minimum value at the central axis of the slots. The value depends on the radius (or y) and is obtained by letting w = jv, ie.

$$B_{min} = \mu_o \frac{\varphi_{mo}}{g'} \frac{1}{\sqrt{1+\left(\frac{b_o}{2g'}\right)^2 + \left(\frac{b_o}{2g'}v\right)^2}} = B_{max} \frac{1}{\sqrt{1+\left(\frac{b_o}{2g'}\right)^2 (1+v^2)}} \tag{5.109}$$

$$\text{and } \beta = \frac{B_{max} - B_{min}}{2B_{max}} = \frac{1}{2}\left[1 - \frac{1}{\sqrt{1+\left(\frac{b_o}{2g'}\right)^2 (1+v^2)}}\right] \tag{5.110}$$

v can be determined by solving equation (5.103) and letting

$$\text{and } z = j\,y \qquad w = j\,v \tag{5.111}$$

ie.

$$jy = \frac{b_o}{\pi}\left\{\frac{j}{2}\ln\left[\frac{1-j\dfrac{jv}{\sqrt{a^2+v^2}}}{1+j\dfrac{jv}{\sqrt{a^2+v^2}}}\right]+j\frac{2g'}{b_o}\arctan\left[\frac{-j2g'(jv)}{b_o\sqrt{a^2+v^2}}\right]\right\}$$

$$y\frac{\pi}{b_o} = \frac{1}{2}\ln\left[\frac{\sqrt{a^2+v^2}+v}{\sqrt{a^2+v^2}-v}\right] + \frac{2g'}{b_o}\arctan\frac{2g'}{b_o}\frac{v}{\sqrt{a^2+v^2}} \qquad (5.112)$$

where y is given by:

$$y = \begin{cases} r-(R_i-g-h_m) = r-R_i+g' & \text{for } \textit{internal rotor motor} \\ (R_i+g+h_m)-r = R_i+g'-r & \text{for } \textit{external rotor motor} \\ y & \text{for } \textit{rectangular coordinate} \end{cases} \qquad (5.113)$$

At the rotor surface B_{min} can be determined by letting v = 0, ie.

$$B_{min} = B_{max}\frac{1}{\sqrt{1+\left(\dfrac{b_o}{2g'}\right)^2}} \qquad (5.114)$$

$$\text{Hence} \quad \beta = \frac{1}{2}\left[1-\frac{1}{\sqrt{1+\left(\dfrac{b_o}{2g'}\right)^2}}\right] \qquad (5.115)$$

It is worth mentioning that in induction motors due to their small airgap, typically 0.25 - 0.3 mm, the minimum flux density varies only a little in passing on a radius through the mid-point of the slot opening from the stator surface to the rotor surface. In other words, the effect of slotting on the magnetic field distribution is almost independant of radius. Therefore the radial variation in the flux density is often ignored in the analysis of harmonic fields in induction motors [5.1], equation (5.114) being used to approximate the minimum flux density because of its simplicity. However, in the case of permanent magnet motors with surface-mounted magnets, as shown in Figs 5.5 and 5.6, although the actual airgap g is also relatively small, the equivalent airgap

$g' = g + h_m/\mu_R$ is relatively large since the recoil permeability of the magnet is very close to that of air. As a consequence, at the central axis of the slots, the flux density varies from a value, typically around half of the maximum flux density, at the mid-point of a slot opening on the stator surface to a value very close to the maximum flux density at the mid-point of a slot opening on the rotor surface. This indicates that in a permanent magnet motor the effect of stator slotting on the magnetic field distribution at the rotor iron surface is negligible, whilst at other radii, such as at the stator or magnet surfaces, equation (5.112) must be solved by iteration in order to determine the minimum flux density.

In summary, the field distribution in a permanent magnet motor can be determined from equation (5.106). However, since it is a two-dimensional field problem and the flux density is implicit to the coordinate variables in the solution, ie. equation (5.106), the calculation is very complicated and time-consuming. Therefore, in order to simplify the analysis, the airgap/magnet field variation in the circumferential direction is assumed to be similar to that in an asynchronous induction machine [5.1], whilst the variation of the maximum and minimum flux density along any radius is determined by the conformal transformation method, ie. from equations (5.108), (5.109), and (5.112), viz:

If the stator is slotted the airgap flux density is assumed to be:

$$B(r,\alpha) = \begin{cases} B_{\max}\left(1-\beta-\beta\cos\dfrac{\pi}{0.8\,\alpha_o}\alpha\right) & \text{for } 0 \le \alpha \le 0.8\ \alpha_o \\ B_{\max} & \text{for } 0.8\,\alpha_o \le \alpha \le \alpha_d/2 \end{cases} \qquad (5.116)$$

$$\text{where } \alpha_o = \frac{b_o}{R_i} \ ; \ \alpha_d = \frac{\tau_t}{R_i} \ ; \ \frac{\alpha_o}{\alpha_d} = \frac{b_o}{\tau_t} \qquad (5.117)$$

and β depends on the ratio of (b_o/g') and the radius (or y) .

With unit magnetic scalar potential, ie. $\varphi_{mo} = 1$, the variation of the permeance will be the same as that of the airgap flux density

$$\lambda(r,\alpha) = \begin{cases} \frac{\mu_o}{g'}\left(1-\beta-\beta\cos\frac{\pi}{0.8\,\alpha_o}\alpha\right) & \text{for } 0 \le \alpha \le 0.8\ \alpha_o \\ \frac{\mu_o}{g'} & \text{for } 0.8\,\alpha_o \le \alpha \le \alpha_d/2 \end{cases} \tag{5.118}$$

If the permeance is expressed in the form of a Fourier series, it becomes:

$$\lambda(r,\alpha) = \sum_{\mu=0}^{\infty} \Lambda_\mu(r)\cos\mu Q_s(\alpha-\alpha_o) \tag{5.119}$$

where $\alpha = 0$ is at the centre of slot openings and α_o depends on the relative position of the stator and the rotor, and will be discussed in Chapter 8, the coefficients being determined from:

$$\Lambda_o(r) = \frac{\mu_o}{g'}\left(1-1.6\,\beta\frac{b_o}{\tau_t}\right) \tag{5.120}$$

$$\Lambda_\mu(r) = \frac{2}{\alpha_d}\int_{-\alpha_d/2}^{\alpha_d/2} \lambda(r,\alpha)\cos\mu Q_s\alpha\, d\alpha$$

$$= \frac{\mu_o}{g'}\frac{4}{\alpha_d}\left\{\int_0^{0.8\,\alpha_o}\left(1-\beta-\beta\cos\frac{\pi}{0.8\,\alpha_o}\alpha\right)\cos\frac{2\pi}{\alpha_d}\mu\alpha\, d\alpha + \int_{0.8\,\alpha_o}^{0.5\,\alpha_d}\cos\frac{2\pi}{\alpha_d}\mu\alpha\, d\alpha\right\}$$

$$= -\frac{\mu_o\beta}{g'}\frac{4}{\pi\mu}\left[0.5+\frac{\left(\mu\frac{b_o}{\tau_t}\right)^2}{0.78125-2\left(\mu\frac{b_o}{\tau_t}\right)^2}\right]\sin\left(1.6\,\pi\,\mu\frac{b_o}{\tau_t}\right) \tag{5.121}$$

Therefore by definition, ie. equations (5.15)-(5.17), the relative permeance is determined from

$$\Lambda(r,\alpha) = \frac{\lambda(r,\alpha)}{\Lambda_{ref}} = \frac{\lambda(r,\alpha)}{\mu_o/g'} = \frac{B(r,\alpha)}{B_{\max}} \tag{5.122}$$

$$\text{ie.} \quad \Lambda(r,\alpha) = \sum_{\mu=0}^{\infty} \Lambda_\mu(r)\cos\mu Q_s(\alpha-\alpha_o) \tag{5.123}$$

$$\text{where} \quad \Lambda_o(r) = \frac{1}{K_c}\left(1-1.6\beta\frac{b_o}{\tau_t}\right) \tag{5.124}$$

$$\Lambda_\mu(r) = -\beta\, G_\mu\left(\frac{b_o}{\tau_t}\right) \tag{5.125}$$

$$G_\mu\left(\frac{b_o}{\tau_t}\right) = \frac{1}{\mu}\frac{4}{\pi}\left[0.5+\frac{\left(\mu\frac{b_o}{\tau_t}\right)^2}{0.78125-2\left(\mu\frac{b_o}{\tau_t}\right)^2}\right]\sin\left(1.6\pi\mu\frac{b_o}{\tau_t}\right) \tag{5.126}$$

NOTE: In equation (5.124), a Carter coefficient K_c has been included to account for the increase in effective airgap, referred to in section (5.4.1).

5.5 Comparison with the Finite Element Calculations

In this section the analytical models developed for the open-circuit field calculation are validated by comparing the analytical prediction with finite element calculations. For an internal rotor motor, firstly results for the magnetic field produced by the magnets are compared, secondly the relative permeance model is validated, and thirdly the results for the open-circuit magnetic field are compared. The comparison includes not only the circumferential variation of flux density, but also the radial variation in both the airgap and magnet regions. Comparisons are also made for an external rotor motor, as well as for the models formulated in rectangular coordinates.

The internal rotor 3-phase brushless DC motor has the parameters listed in Table 5.1.

Table 5.1 Parameters of an internal rotor motor.

pole number	$2p = 2$ or 4
slot number	$Q_s = 12$
pole-arc/pole-pitch ratio	$\alpha p = 1.0$
airgap length	$g = 0.00075$m
height of magnet	$h_m = 0.0045$m
internal radius of stator	$R_i = 0.02975$m
slot-opening	$b_o = 0.00205$m
remanence	$B_R = 0.38$T
relative recoil permeability	$\mu_R = 1.05$

The main parameters of the external rotor 3-phase brushless DC motor, with either a 6- or 12-pole rotor, are listed in Table 5.2, whilst the corresponding parameters of a planar model are given in Table 5.3.

Table 5.2 Parameters of an external rotor motor

pole number	$2p = 6$ or 12
slot number	$Q_s = 9$
pole-arc/pole-pitch ratio	$\alpha_p = 1.0$
airgap length	$g = 0.00043$m
height of magnet	$h_m = 0.00187$m
radius of stator near airgap	$R_i = 0.0207$m
slot opening	$b_o = 0.0014$m
remanence	$B_R = 0.25$T
relative recoil permeability	$\mu_R = 1.02$

Table 5.3 Parameters of an external rotor motor in rectangular coordinates

pole-pitch	$\tau_p =$ 0.045m (6-poles) or 0.0225m (12-poles)
slot-pitch	$\tau_t = 0.015$m
pole-arc/pole-pitch ratio	$\alpha_p = 1.0$
airgap length	$g = 0.00043$m
height of magnet	$h_m = 0.00187$m
slot-opening	$b_o = 0.0014$m
remanence	$B_R = 0.25$T
relative recoil permeability	$\mu_R = 1.02$

5.5.1 Field Produced by the Magnets

Fig 5.10 shows a comparison of the field distributions predicted by both the finite element and developed analytical techniques. In order to eliminate the effects of saturation and slotting, the

internal rotor motor has been idealised as one pole-pitch of a model consisting of magnets and airgap and backed by infinitely permeable rotor and stator iron.

By applying the half-periodic boundary condition and natural Neuman boundary conditions at both the stator and rotor iron surfaces of the finite element model, the predicted flux density distribution at the stator surface is obtained. It will be recalled that the analytical expressions for the case np = 1 differs from those for higher pole numbers due to the singularity. Comparisons have also been made for both 2- and 4-pole internal rotor motors whose parameters are the same. It will be seen that there is excellent agreement between the results obtained from the analytical prediction and the finite element calculation.

Further comparisons have been made for the 4-pole motor, Fig 5.11 showing the finite element discretisation and flux distribution over one pole-pitch of an idealised model in which the slots have been neglected and the stator iron has again been idealised in order to emphasise the magnetic field due to the magnets. Fig 5.12 compares the field distribution produced by the magnets at different radii in the magnet/airgap region. Since at any radius the finite element results are derived from layers of elements, upper and lower, as shown in Fig 5.13, the analytical predictions are calculated for two radial positions. The radii used in the analytical calculations are given in Table 5.4.

Table 5.4 Computation radii and regions

Symbol for radius	Calculation radius (m)	region
$r = R_i^-$	0.02975	airgap
	0.02950	
$r = R_i - g^+$	0.02925	airgap
	0.02900	
$r = R_i - g^-$	0.02900	magnet
	0.027825	
$r = R_i - g - h_m^+$	0.025475	magnet
	0.0243	

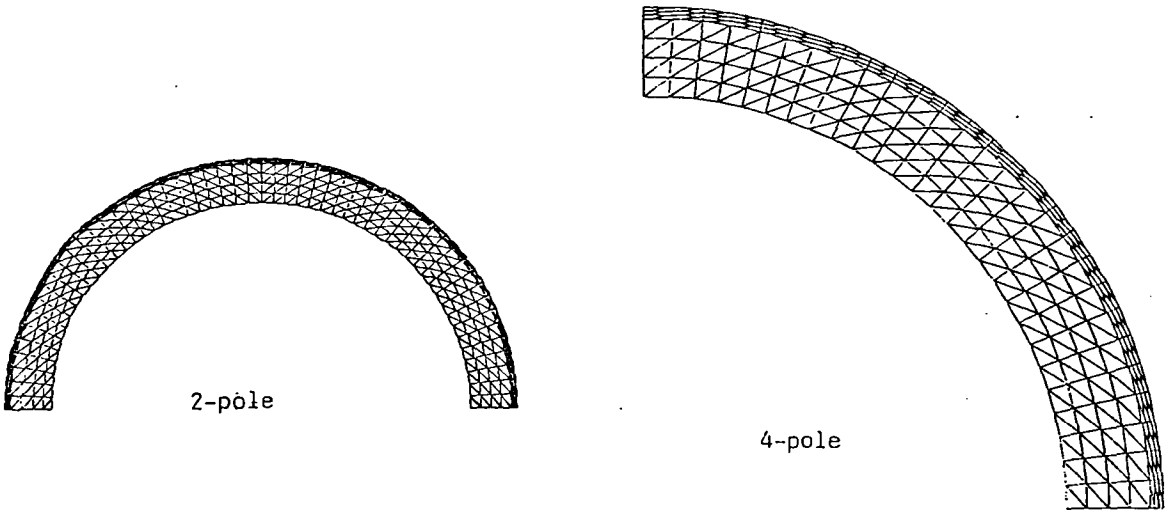

(a) Mesh

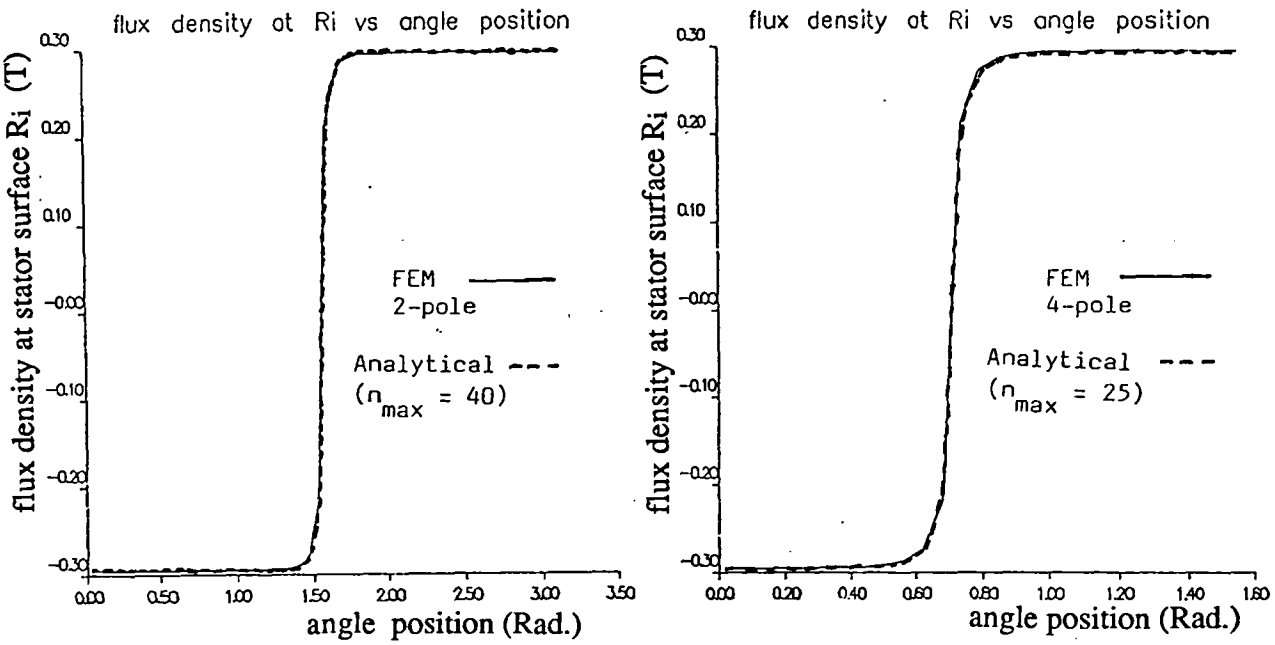

(b) Field distribution

Fig 5.10 Comparison of field distribution predicted by finite element and analytical techniques

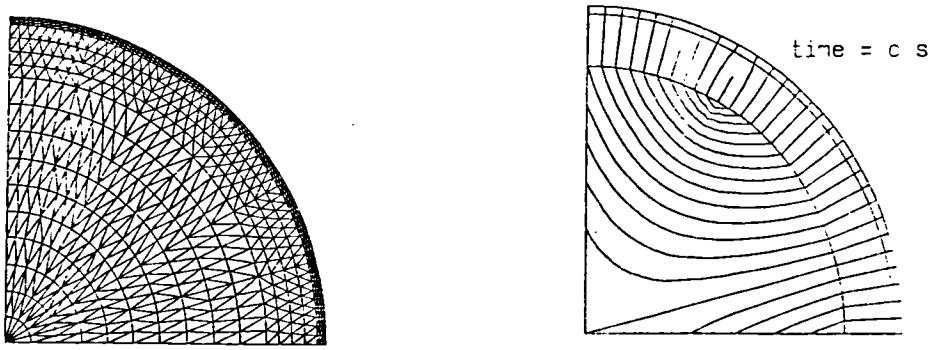

(a) Mesh

(b) Flux distribution

Fig 5.11 Finite element mesh and flux distribution due to the magnets alone

From Fig 5.12 it is observed that:

i) Both the finite element and analytical predictions show that at a radius which passes through the magnets, the magnetic field at the edges of the magnet is higher due to inter-pole leakage, whilst at a radius which passes through the airgap the magnetic field near the edges of the magnet is weaker.

ii) Oscillations exist on the field distribution predicted from the finite element calculation due to plotting the value in the upper/lower layers of elements. However the oscillation is much lower in the airgap since a finer discretisation in the radial direction was employed.

iii) The oscillation in the analytical predicted field distribution is due to the use of a finite number of terms in the Fourier series. In the calculation those harmonics whose amplitudes are smaller than 1/500 of the harmonic component having the maximum amplitude have been neglected.

iv) The predictions from the analytical technique are in good agreement with those from the finite element calculations, not only along the circumferential direction but also in the radial direction, as shown in Fig 5.14.

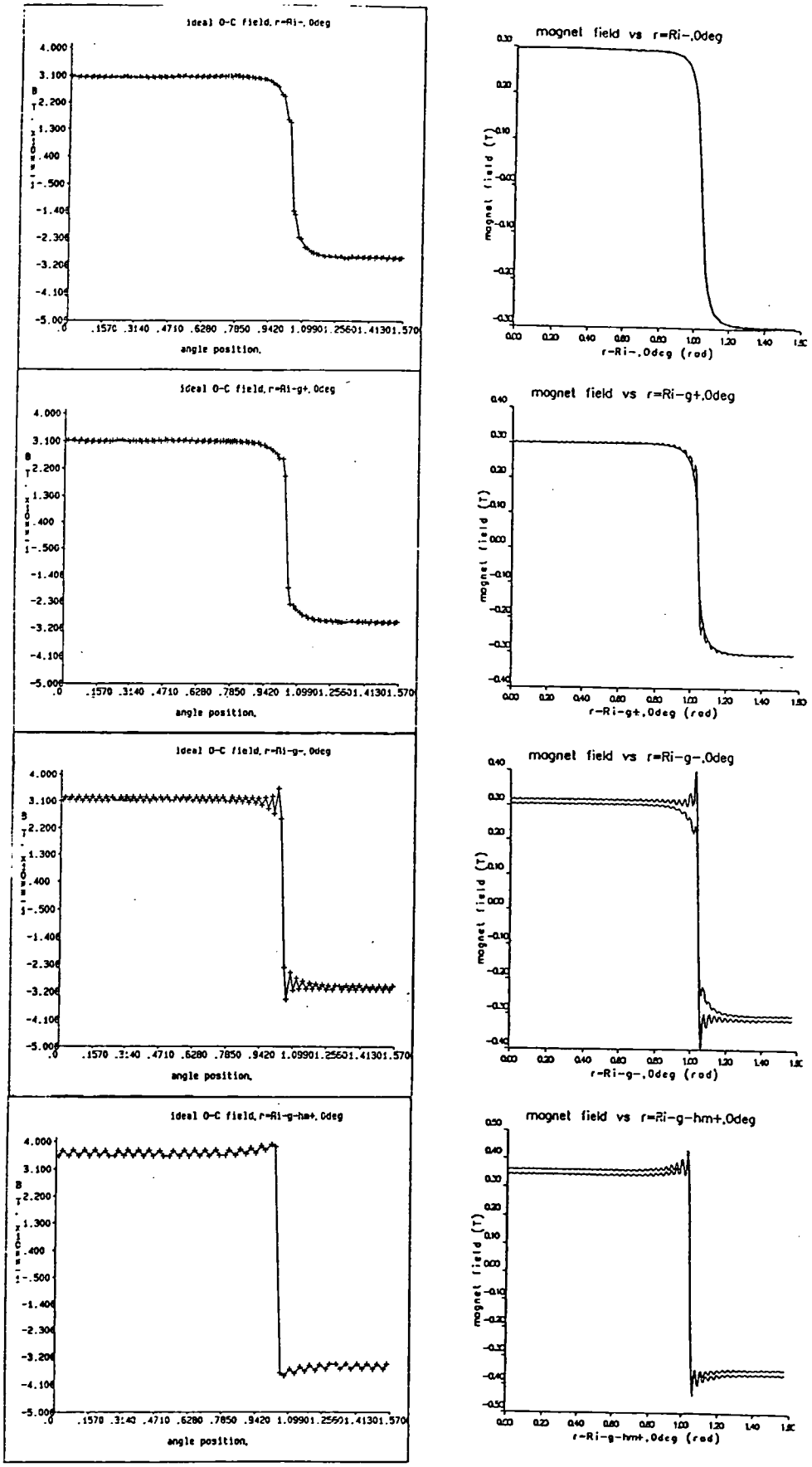

FEM calculation Analytical prediction

Fig 5.12 Comparison of field distribution produced by the magnets at different radii, time = 0 s

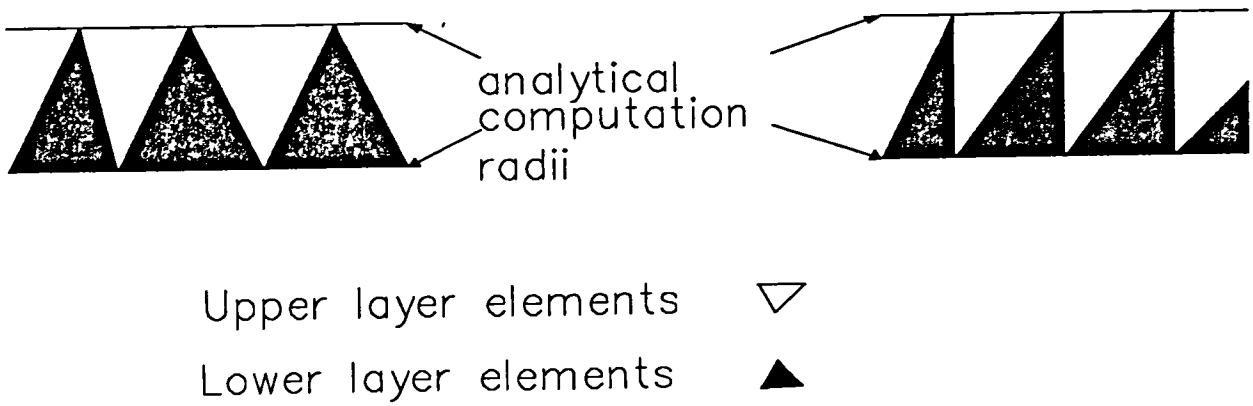

Fig 5.13 Effect of discretisation

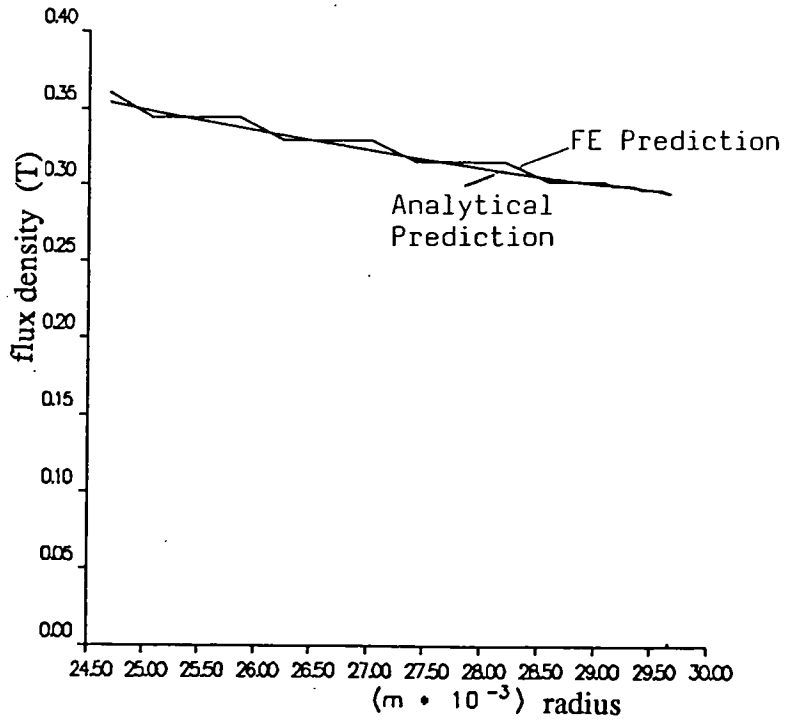

Fig 5.14 Variation of field along the pole axis due to magnets alone

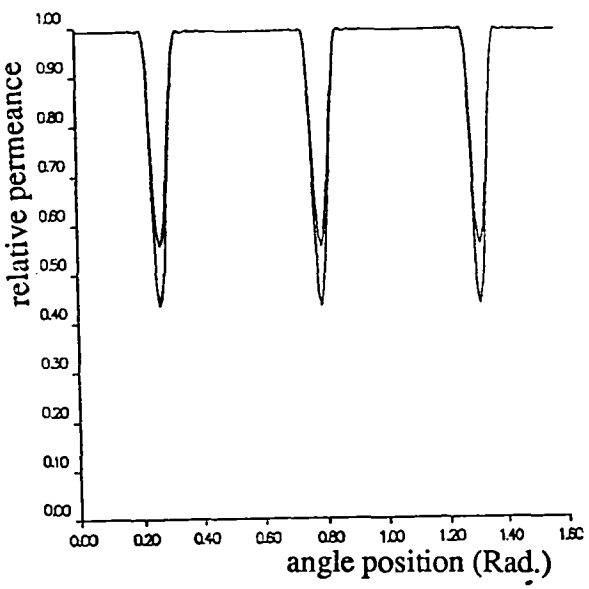

(a) $r = R_i^-$

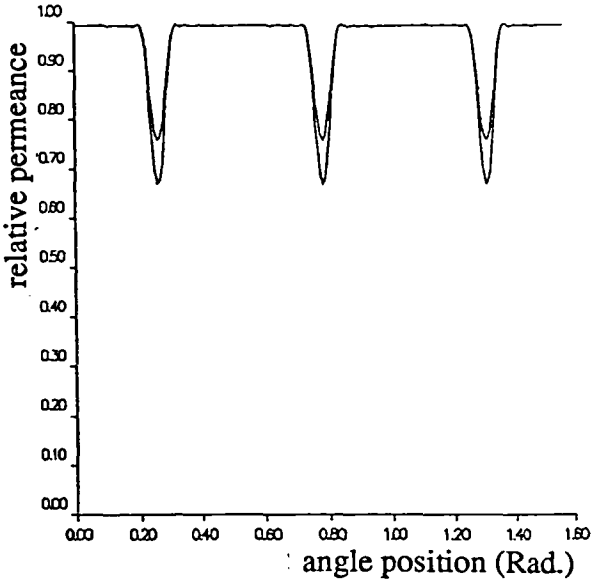

(b) $r = R_i - g^+$

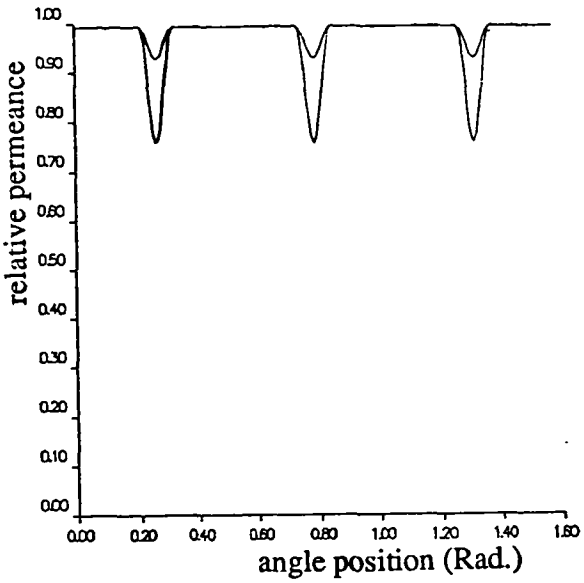

(c) $r = R_i - g^-$

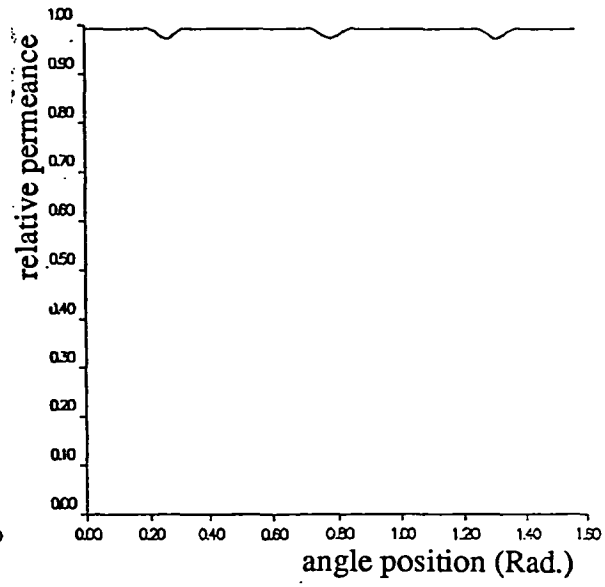

(d) $r = R_i - g - h_m^+$

Fig 5.15 Variation of relative permeance waveform with radius

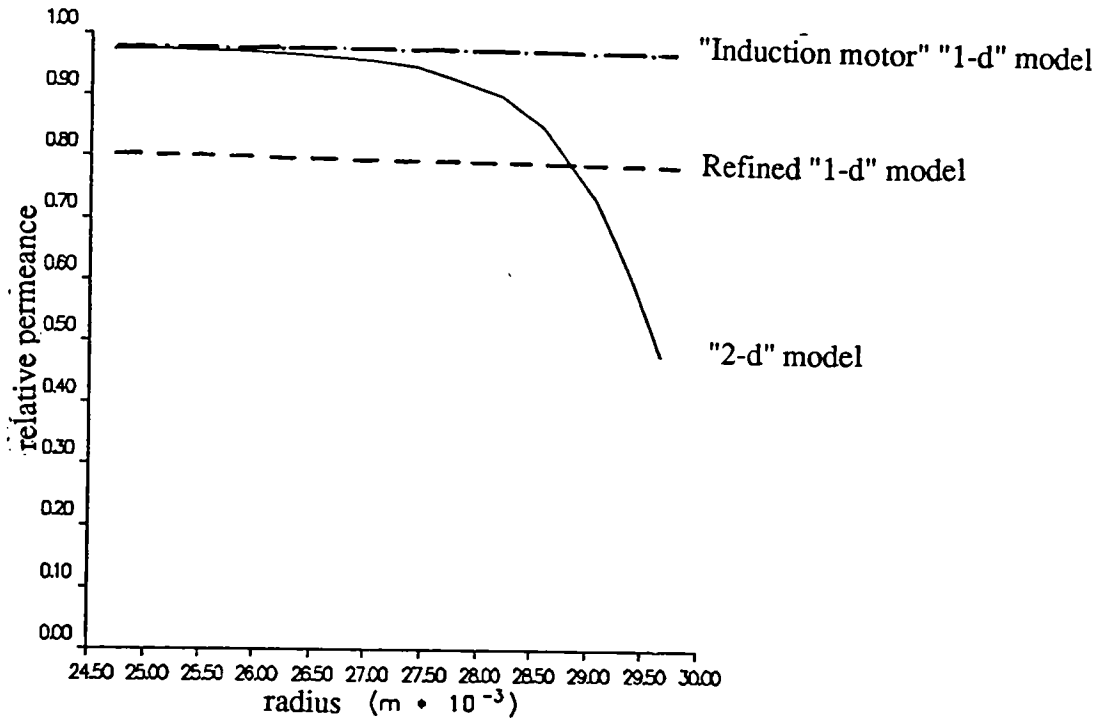

Fig 5.16 Variation of the minimum permeance with radius

5.5.2 Relative Permeance Models

In this section the relative permeance predicted from the finite element and analytical techniques are compared. The variation of the permeance with radius as predicted from the proposed "2-d" relative permeance model is also investigated. In addition, different permeance models are compared, and their merits discussed.

Based on the "2-d" relative permeance model, Fig 5.15 shows the variation of the relative permeance waveform with the radius for the internal rotor 4-pole motor, whilst Fig 5.16 shows the variation of the minimum relative permeance (at the slot centres) with radius. Clearly, stator slotting has a significant effect on the permeance waveform at the stator surface, whilst at the rotor surface its effect is negligible due to the large effective airgap. For comparison Fig 5.16 also shows the relative permeance calculated from the refined "1-d" model described in section

5.2.2, as well as the result calculated from the one-dimensional permeance model which is widely used for induction motors [5.1], which can be obtained from equation (5.123) by setting β to a fixed value given by equation (5.115).

It is observed that the most significant difference between the "2-d" and "1-d" models is that whilst in the "2-d" model the minimum value of the relative permeance decreases as the radius increases, ie. as the slots are approached, the minimum value of the relative permeance predicted from the "1-d" models is independent of the radius. Meanwhile the permeance model of the induction motor always understates the slotting effect in a permanent magnet motor since it utilises the value on the smooth rotor iron surface. Hence this confirms that the permeance model which is used in induction motors [5.1] is unsuitable for application to permanent magnet motors. However another permeance model which is the combination of refined "1-d" model and "2-d" models is possible if for the refined "1-d" permeance model equation (5.14) is re-written as:

$$\tilde{\lambda} = \begin{cases} \dfrac{g + h_m/\mu_R}{g + h_m/\mu_R + \dfrac{\pi}{2}\left(\dfrac{b_o}{2} - r_s\right)} & \textit{in the region of the slot openings} \\ 1 & \textit{in the region of the tooth tips} \end{cases} \qquad (5.127)$$

where b_o is the slot-opening and r_s , ($0 \le r_s \le b_o/2$), is the distance from the axis through the centre of a slot, as shown in Fig 5.17(a).

Clearly

$$\tilde{\Lambda}_{max} = 1 \qquad (5.128)$$

$$\tilde{\Lambda}_{min} = \frac{g + h_m/\mu_R}{g + h_m/\mu_R + \dfrac{\pi}{2}\dfrac{b_o}{2}} \qquad (5.129)$$

which is the same at different radii. Hence the circumferential variation of the relative permeance is identical at all radii. In order to overcome this disadvantage in the "1-d" model, the length of the flux path in Fig 5.17(a) is modified to the one shown in Fig 5.17(b) in which instead of

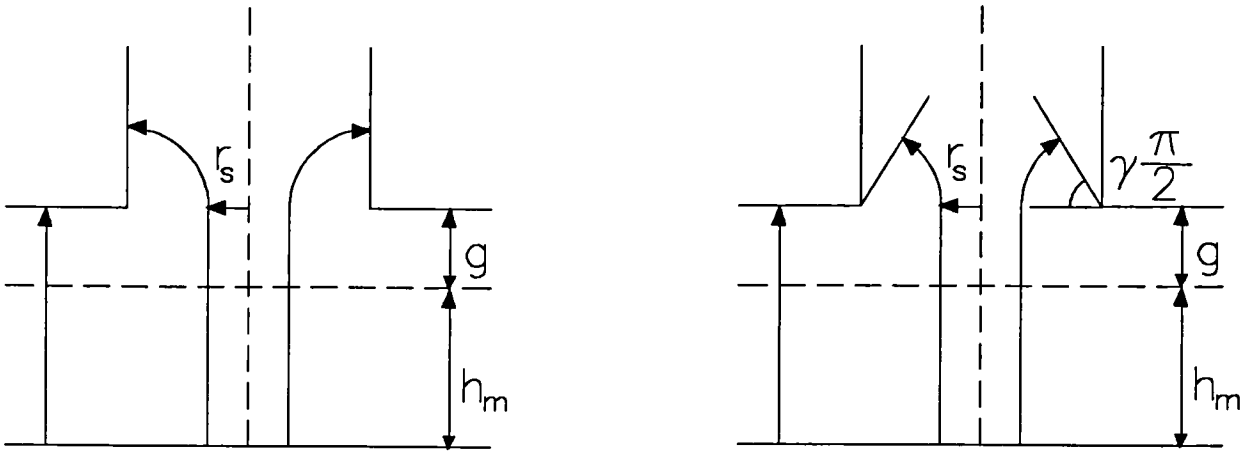

(a) Refined "1-d" model (b) Modified model

Fig 5.17 Modification of permeance model

assuming a circular path it makes use of a modification factor γ. The relative permeance of this modified model is then calculated from

$$\bar{\lambda} = \begin{cases} \dfrac{g + h_m/\mu_R}{g + h_m/\mu_R + \gamma\,\dfrac{\pi}{2}\left(\dfrac{b_o}{2} - r_s\right)} & \textit{in the region of the slot openings} \\ 1 & \textit{in the region of the tooth tips} \end{cases} \qquad (5.130)$$

This modified permeance model is essentially the same as the permeance model used in the analysis of stepping motors [5.14]. However instead of using a fixed value of γ (around 1 to 1.1) for all radial positions as in stepping motors [5.14], γ is now determined from the 2-d conformal transformation method. The calculation method is as follows:

Utilising the result of $B_{min}/B_{max} = \bar{B}$ calculated from equation (5.110), ie.

$$\bar{B} = \frac{B_{min}}{B_{max}} = 1 - 2\beta \qquad (5.131)$$

Since $\bar{\lambda}_{min}$ now is given by

$$\bar{\lambda}_{min} = \frac{g + h_m/\mu_R}{g + h_m/\mu_R + \gamma \frac{\pi}{2} \frac{b_o}{2}} \tag{5.132}$$

and $\bar{\lambda}_{max} = 1$

Therefore γ is determined from

$$\frac{\bar{\lambda}_{min}}{\bar{\lambda}_{max}} = \frac{B_{min}}{B_{max}} \tag{5.133}$$

ie. $$\frac{g + h_m/\mu_R}{g + h_m/\mu_R + \gamma \frac{\pi}{2} \frac{b_o}{2}} = \bar{B} \tag{5.134}$$

$$\gamma = \frac{g + h_m/\mu_R}{\pi\, b_o/4} \left(\frac{1}{\bar{B}} - 1 \right) \tag{5.135}$$

Fig 5.18 compares the relative permeance and the open-circuit field using the refined "1-d" model and this modified model, whilst Fig 5.19 compares the magnetic field produced by the magnets, when the effects of slotting are neglected, and the open-circuit field, predicted from a finite element calculation and the analytical techniques, viz. the "2-d" permeance model and modified permeance model given by equation (5.130). They show that predictions from both permeance models are in very good agreement with those from the finite element calculation.

In conclusion, therefore:

i) The 1-d permeance model can be modified by the method presented in this section.

ii) The Bmin/Bmax ratio calculated from the 2-d method is acceptable compared with the ratio obtained from finite element calculations.

iii) Although the difference between the 2-d model and the modified 1-d model is in the assumption of the permeance waveform, both can be used in future analyses.

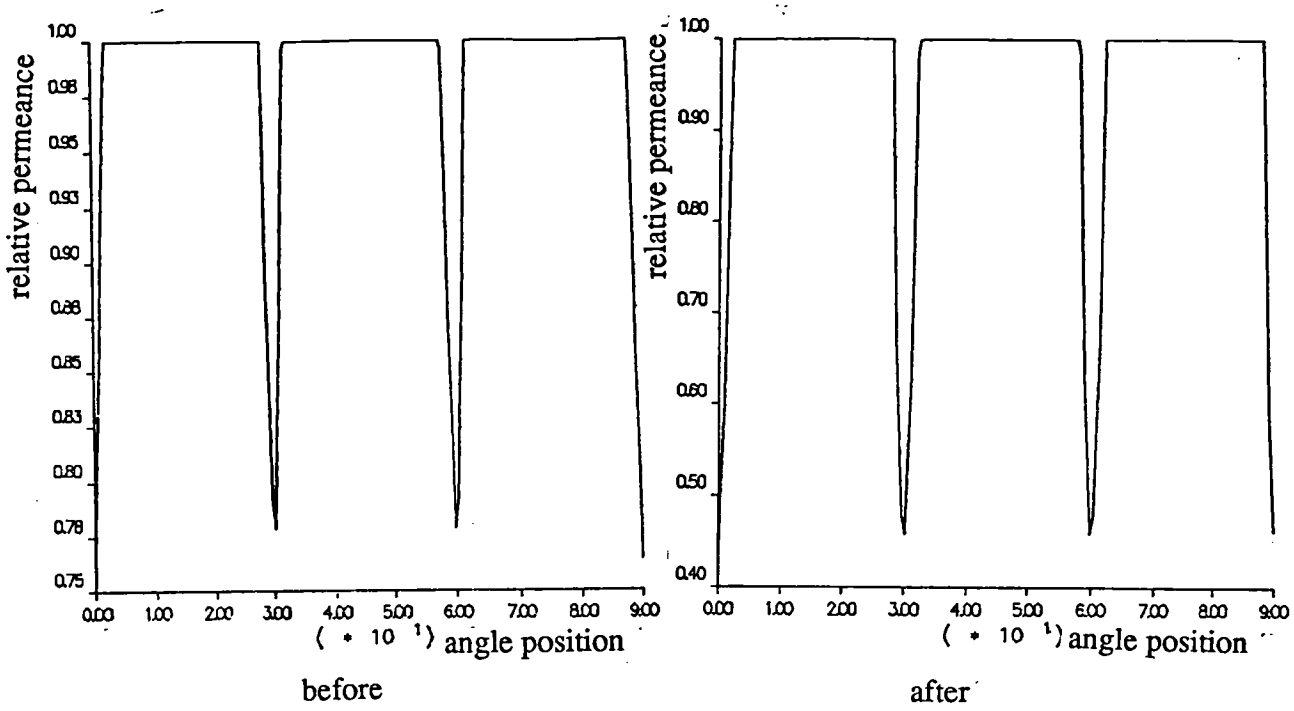

(a) Relative permeance

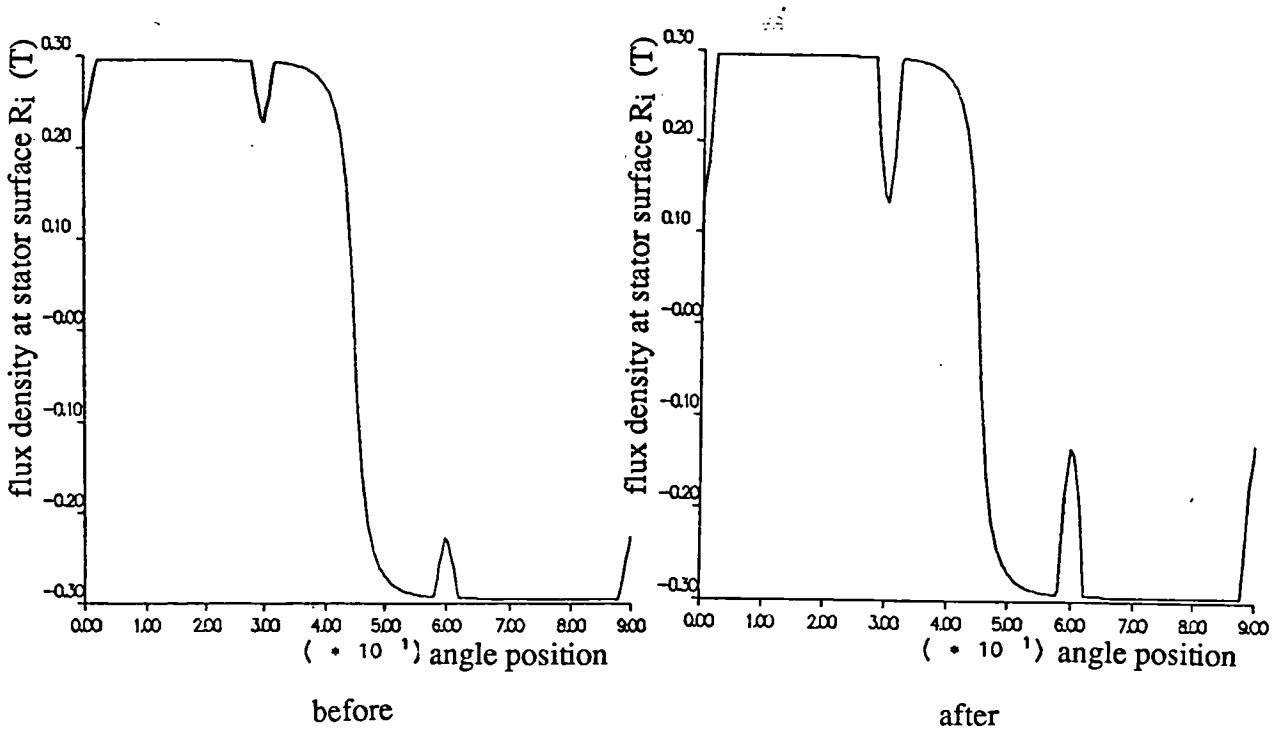

(b) Open-circuit field

Fig 5.18 Comparison of refined "1-d" model before/after modification

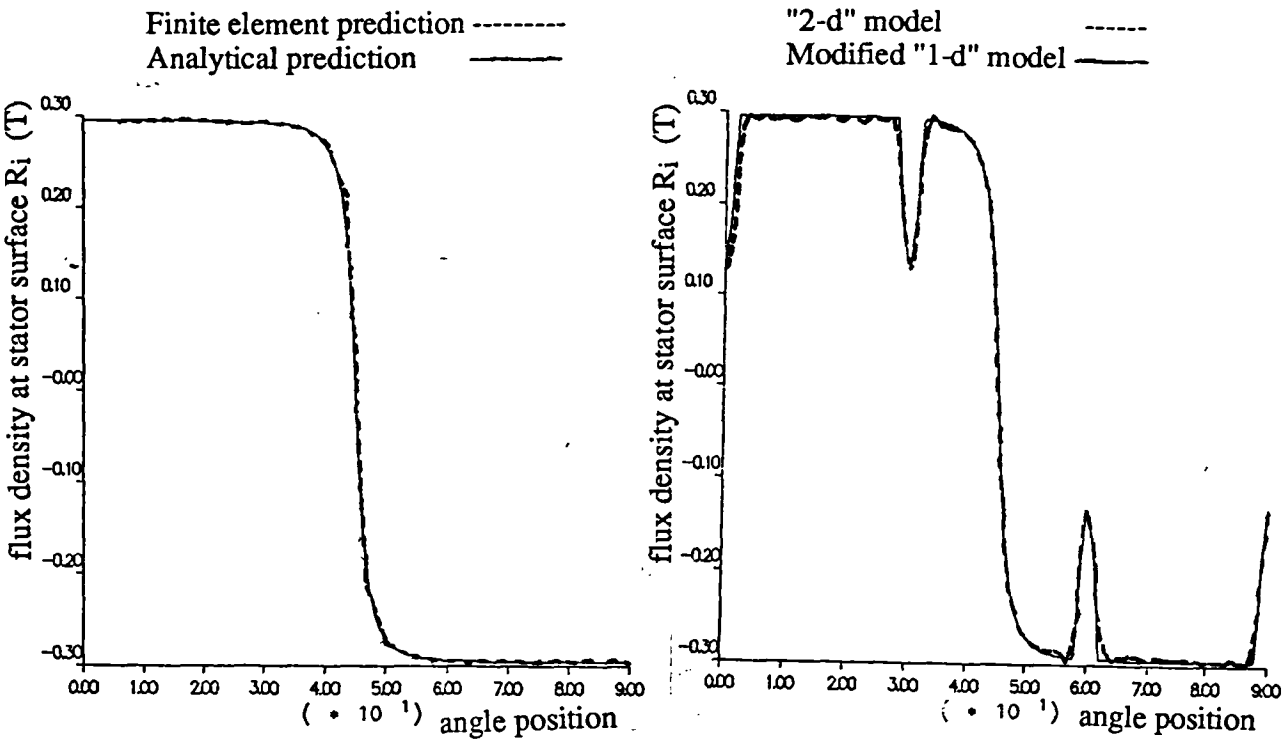

(a) Magnetic field produced by the magnets alone

(b) Open-circuit field distribution from analytical prediction

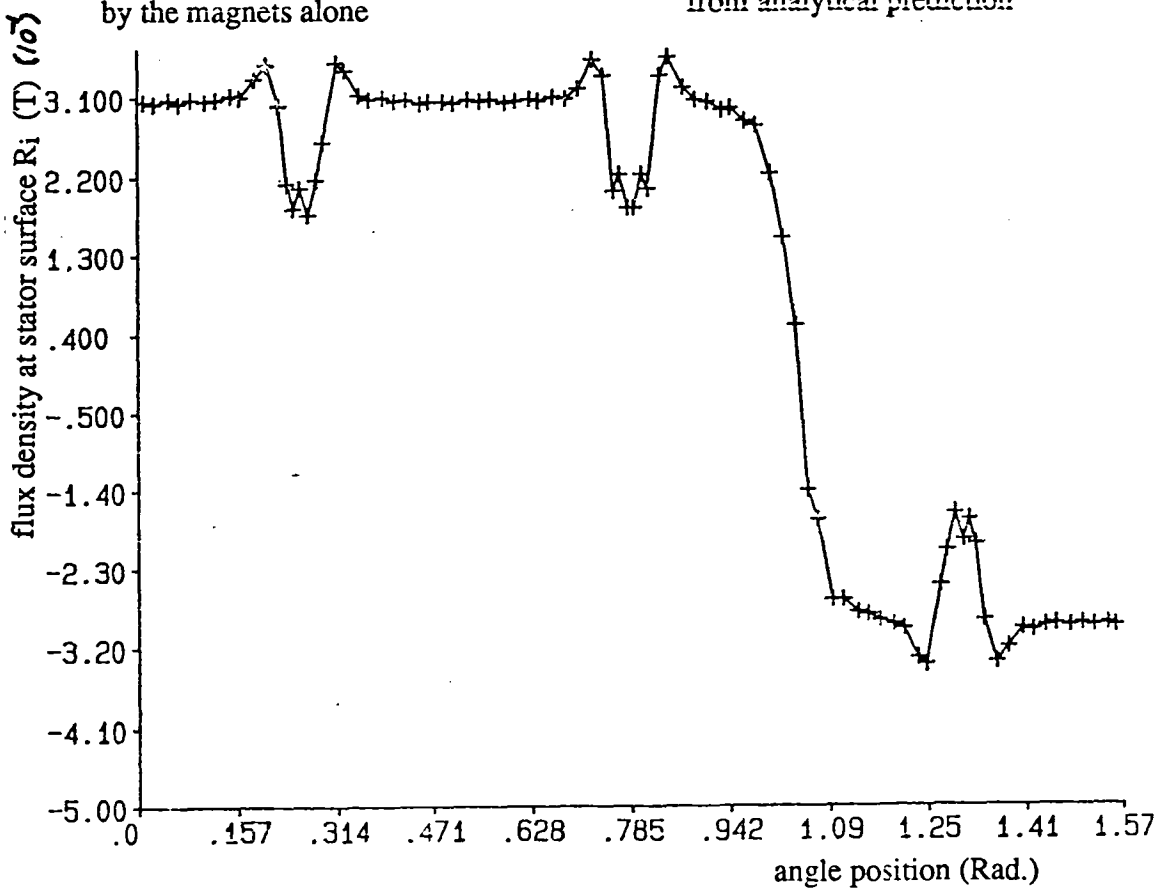

(c) Open-circuit field distribution from finite element calculation

Fig 5.19 Comparison of predictions at the stator surface from different models

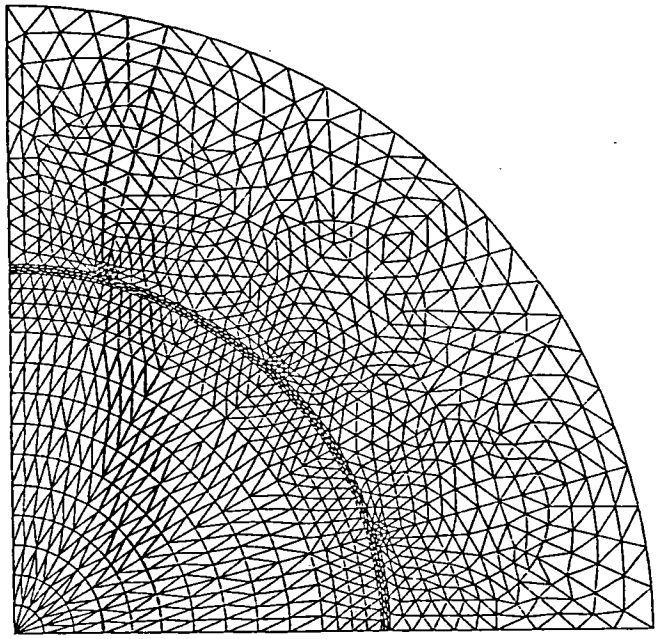

(a) Mesh

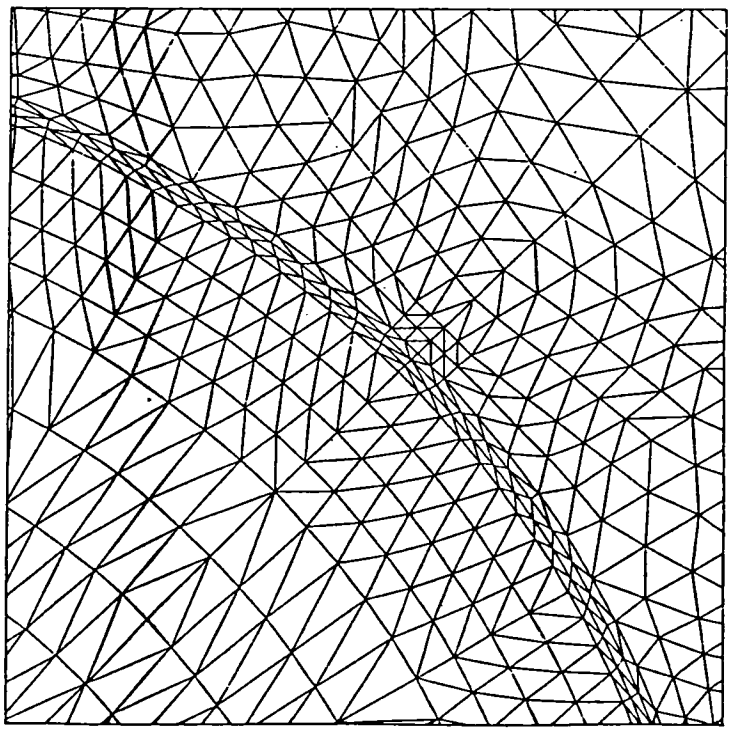

(b) Zoom of mesh

Fig 5.20 Finite element mesh

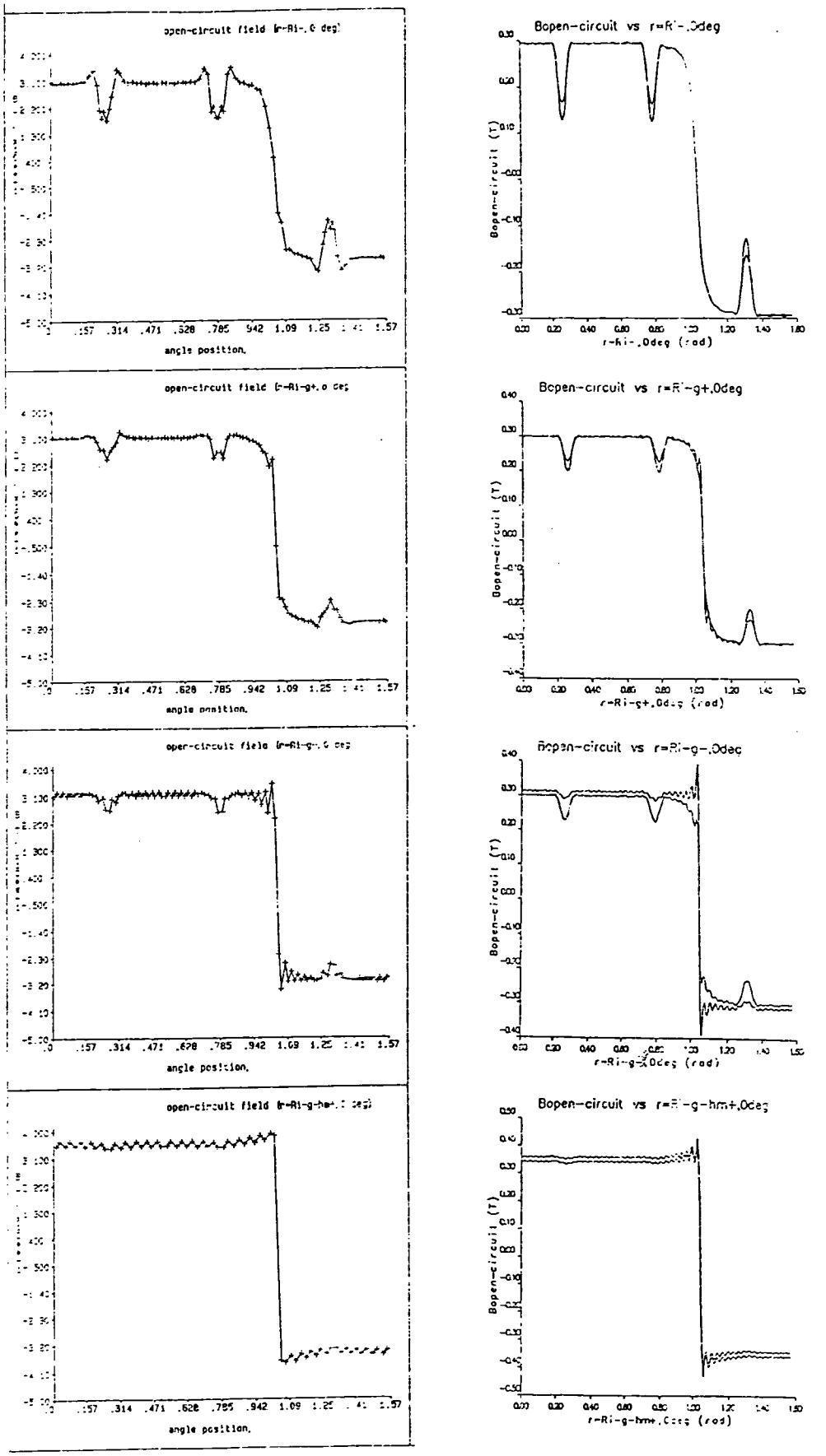

Fig 5.21 Comparison of open-circuit field distribution at different radii, time = 0s

5.3.3 Open-circuit Field Calculation

In this section the open-circuit field in both internal and external rotor motors, as well as a rectangular coordinate model, are calculated and compared with finite element calculations.

Fig 5.20 shows the finite element discretisation of the internal rotor motor, whilst Fig 5.21 compares the predicted open-circuit flux density distribution at different radii in the magnet/airgap regions. Fig 5.22 compares the variation of the flux density with radius under a tooth. The discussions in section 5.5.1, as well as those in section 5.5.2 are still valid for the open-circuit field calculation.

Fig 5.23 compares analytical and finite element calculations of the airgap flux density waveform for both 6- and 12-pole external rotor motors when the effect of stator slot-openings is neglected, whilst Figs 5.24 and 5.25 show similar comparisons in the presence of stator slots. In Figs 5.26

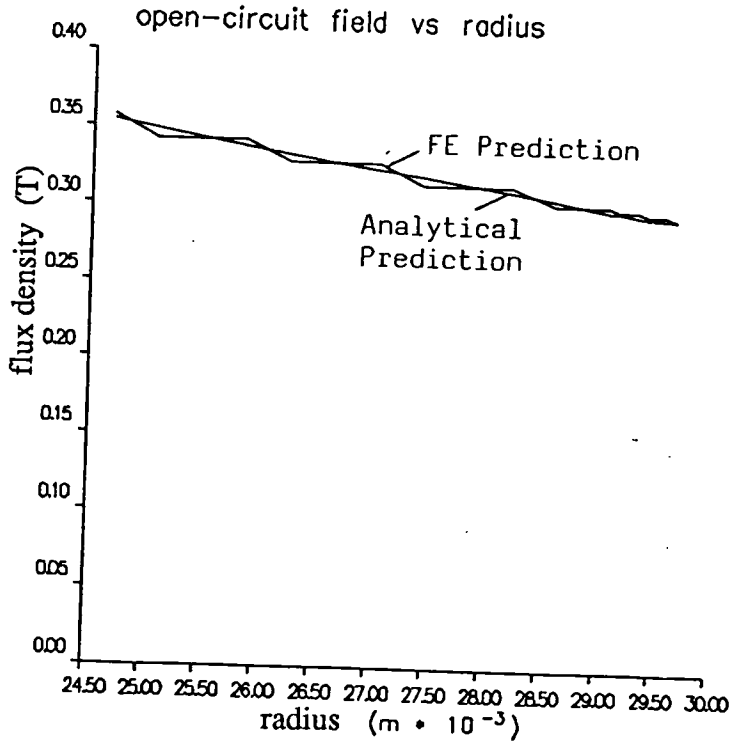

Fig 5.22 Variation of open-circuit field along pole axis

and 5.27 the models of the external rotor motors have been simplified, by modelling them in rectangular coordinates and assuming the permeability of the iron to be infinite, whilst the slot shape is assumed to be rectangular. As a consequence improved agreement with predictions from the analytical model can be expected since the effect of saturation has been eliminated. The main cause of the difference between the analytical and finite element results is due to the neglect of saturation, which is more pronounced in the 6-pole motor, as shown in Fig 5.25(b), in which the stator back-iron is highly saturated. However, this could be taken into account by the introduction of a saturation factor, ie. the analytically predicted waveform of the field distribution could be multipied by the saturation factor. However as to the more subtle effects of saturation, further investigation is required.

Overall the results from the analytical technique and the finite element method, both internal and external rotor motors modelled in either polar and rectangular coordinates, are in good agreement, both in amplitude and waveform. However whilst the analytically predicted results follow the finite element variation of flux density against radius in the angular position corresponding to a slot-opening, along a radius from the rotor to the edge of a stator tooth the finite element calculation predicts an increase in flux density at the tooth tips, because of their flux concentrating effect, whilst this is absent from the results of the analytical model, due primarily to the fact that the permeance calculation assumes a simple permeance waveform in order to simplify the computation. The analytical calculation could be improved by using a more realistic permeance distribution delivered from the conformal transformation method, that is by relaxing the waveform assumption of equation (5.116) in section 5.4.2 and calculating the field distribution waveform directly from equation (5.106). However this would increase the computing time significantly, and, in most cases, is not likely to be critical.

5.6 Conclusions

On the basis of a two-dimensional analytical technique for calculating the magnetic field produced by the magnets and the concept of relative permeance, a general analytical method for obtaining the open-circuit field distribution in all topologies of radial-field permanent magnet

motors has been established and compared with the finite element calculation. It embraces slotted and slotless, and internal and external rotor configurations, modelled in either polar or rectangular coordinates, and accounts for the effect of slotting on the field distribution by introducing a "two-dimensional" relative permeance function.

The model will allow the induced back-emf waveform to be predicted for subsequent use in a dynamic simulation of a brushless DC drive so as to obtain the stator current waveforms, and thereby allow the stator winding magnetic field, ie. armature reaction field, to be determined, as will be described in Chapter 8. The net field will then be utilised for predicting the acoustic noise and vibration from the motors by obtaining the time/spatial dependent magnetic field under any load, as will be discussed further in Chapter 9.

5.7 Appendix - Determination of the Magnetisation M_n

For the radial-field motors having either an internal or external rotor, the magnets are assumed to have a uniform magnetisation throughout their cross-section as shown in Fig 5.28, which can be expressed in the form of a Fourier series.

For internal and external rotor motors modelled in a cylindrical coordinate system:

$$M = \sum_{n=1,3,5,\ldots}^{\infty} M_n \cos n p \theta \tag{5.136}$$

$$M_n = \frac{4 M_o}{n \pi} \sin \frac{n \pi \alpha_p}{2} = 2 M_o \alpha_p \frac{\sin \frac{n \pi \alpha_p}{2}}{\frac{n \pi \alpha_p}{2}} \tag{5.137}$$

whilst in a rectangular coordinate system:

$$M = \sum_{n=1,3,5,\ldots}^{\infty} M_n \cos n \frac{\pi}{\tau_p} x \tag{5.138}$$

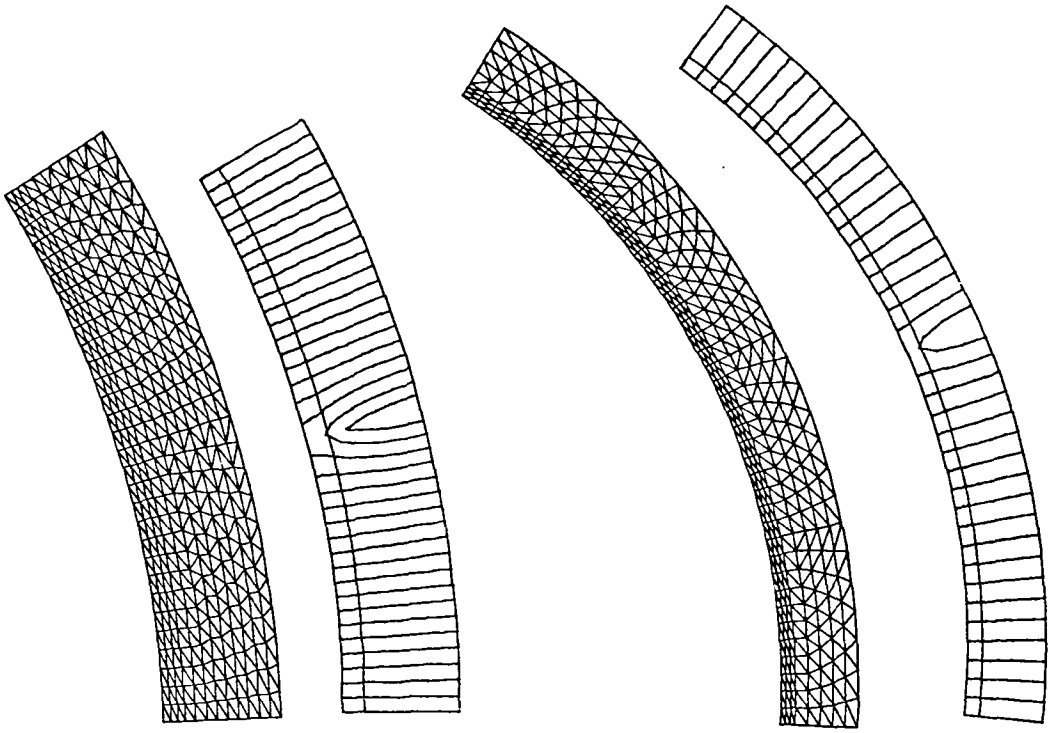

12-pole 6-pole

mesh and equi-potential distribution

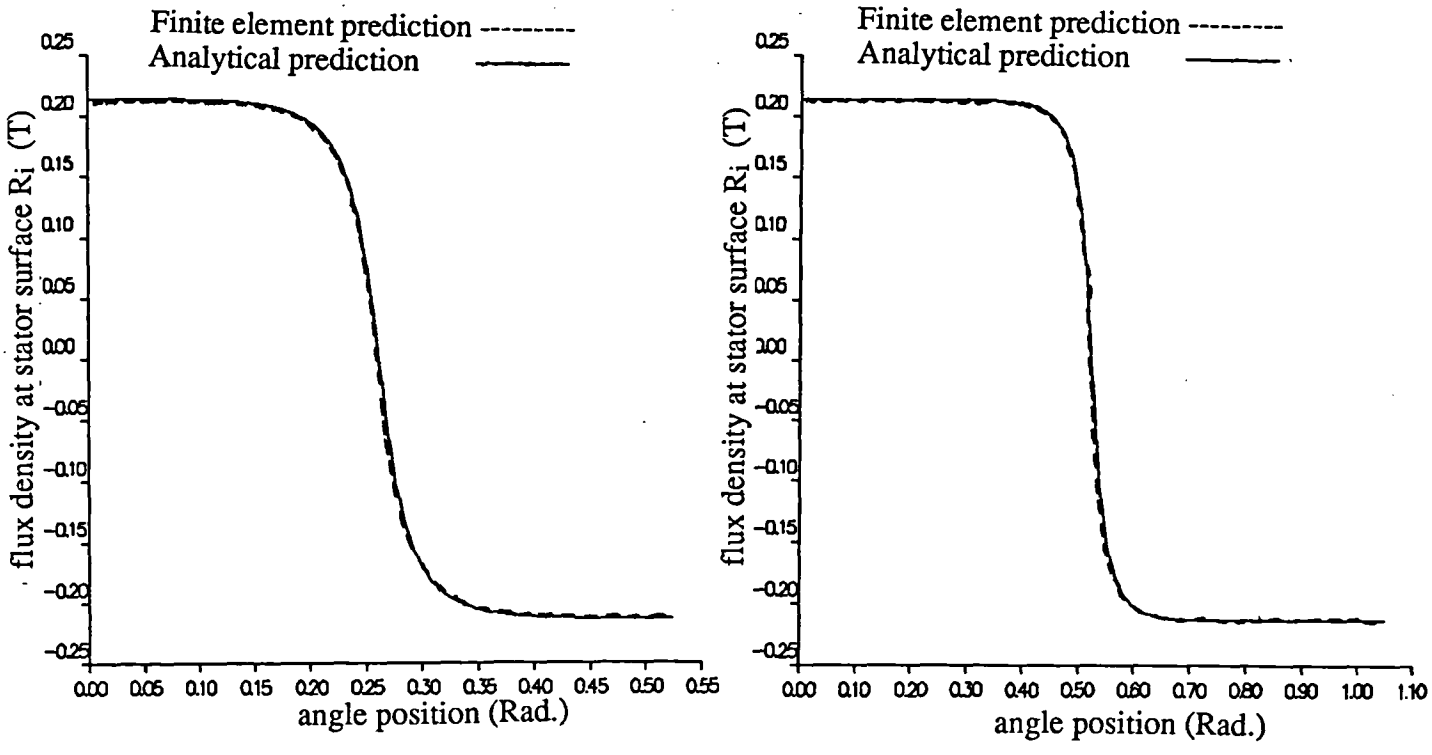

12-pole 6-pole

airgap field

Fig 5.23 Mesh and airgap field of idealised models for external rotor motors

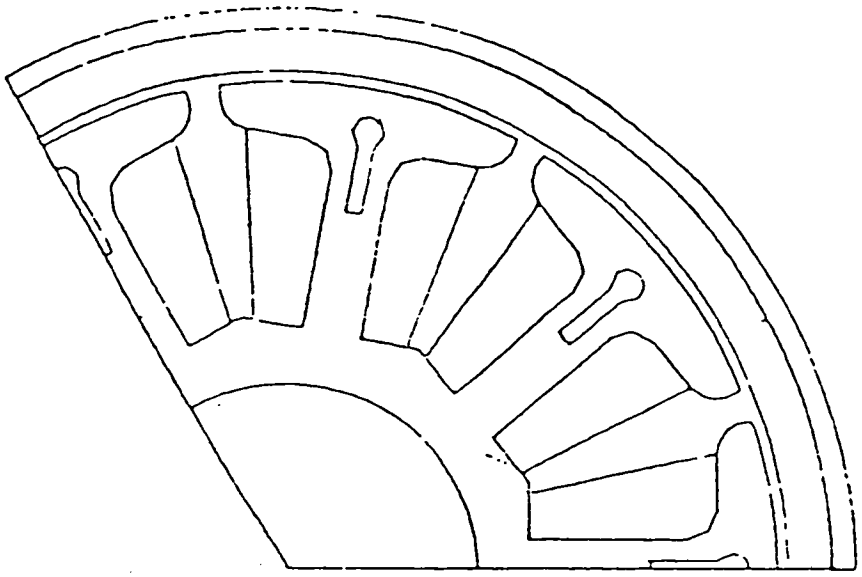

(a) Outline

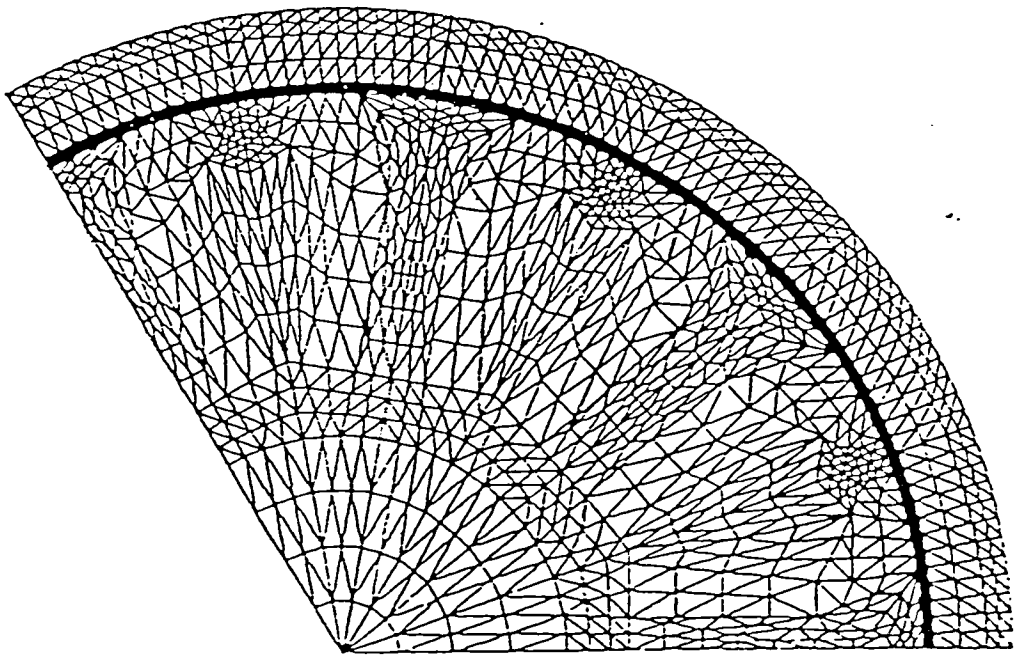

(b) Finite element discretisation

Fig 5.24 Outline and mesh for external rotor motors

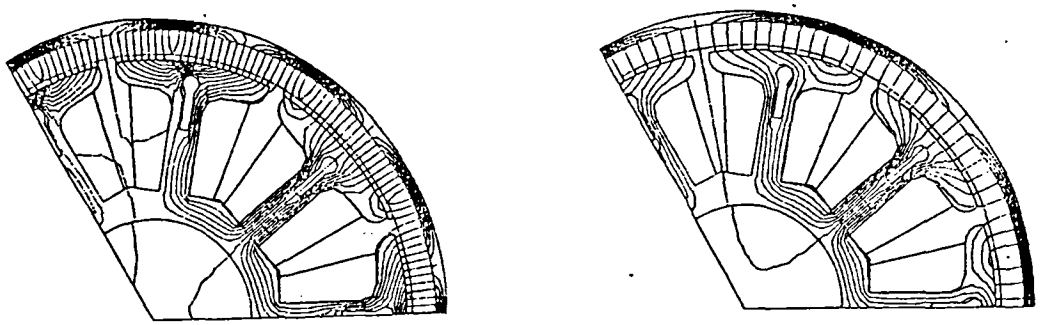

(a) Mesh

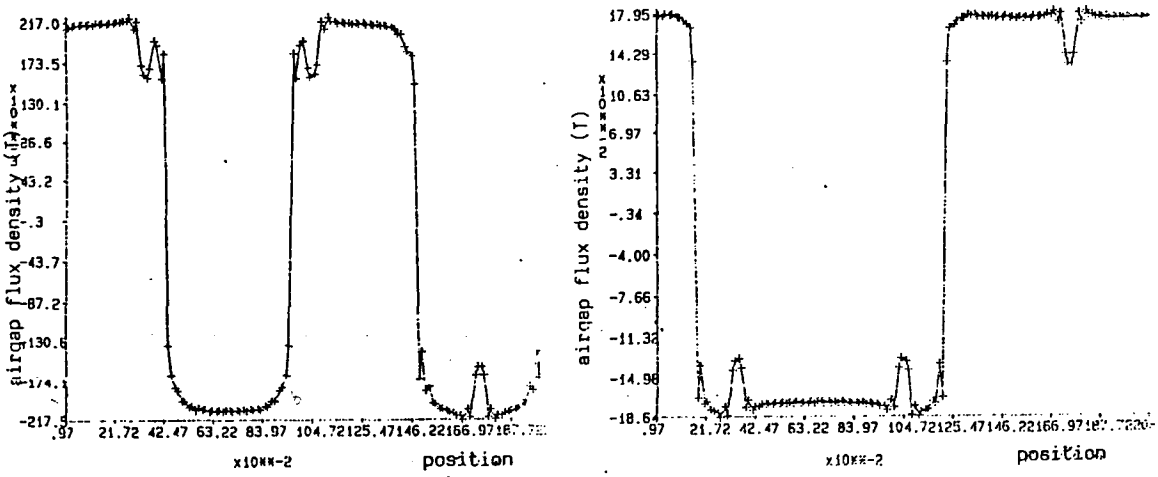

(b) Finite element prediction

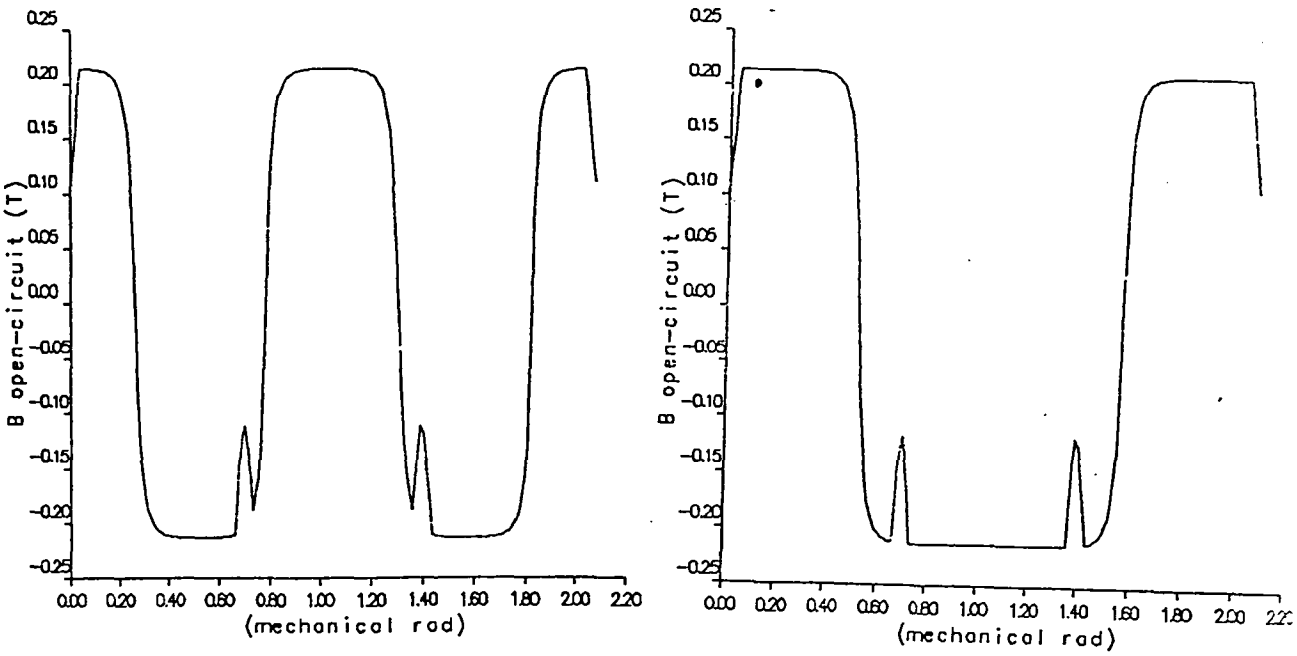

(c) Analytical prediction

12-pole 6-pole

Fig 5.25 Airgap flux density distribution of external rotor motors

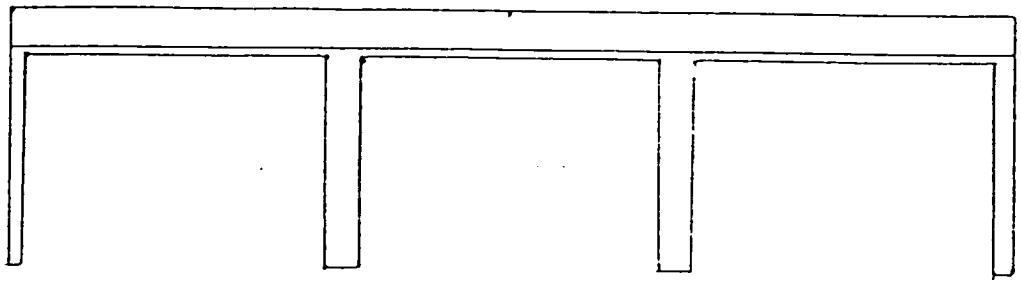

(a) Outline

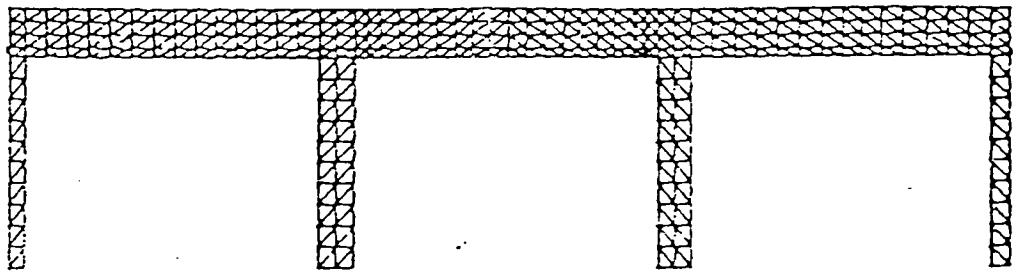

(b) Finite element discretisation

Fig 5.26 Outline and mesh for the idealised model in rectangluar coordinates

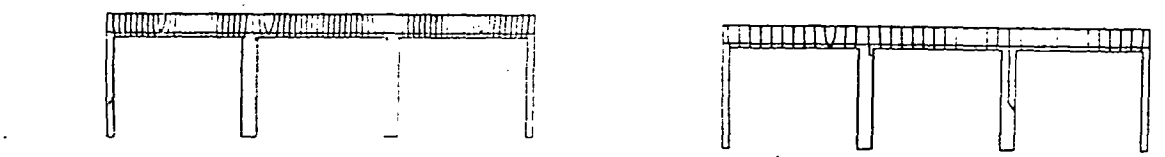

(a) Mesh

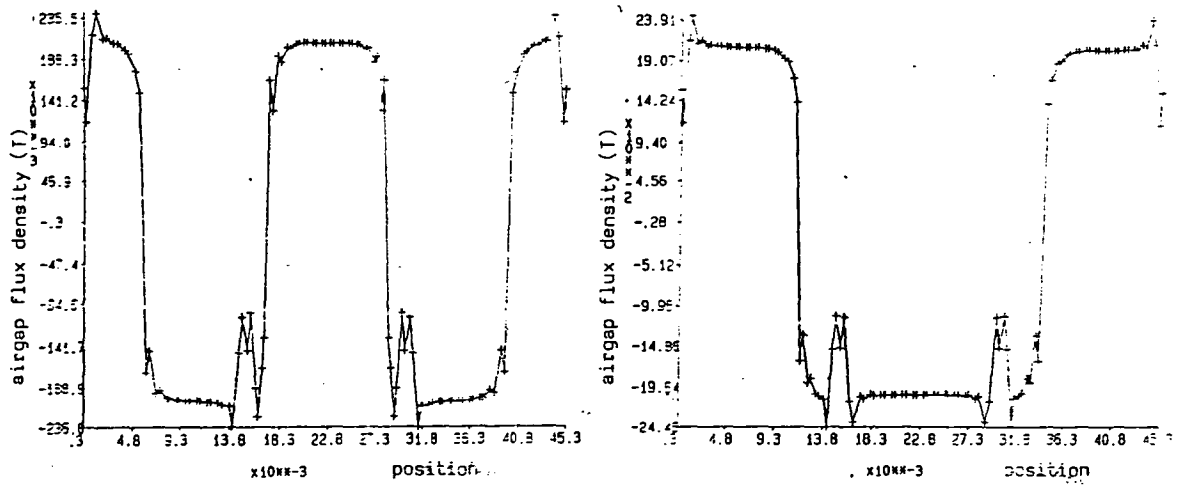

(b) Finite element prediction

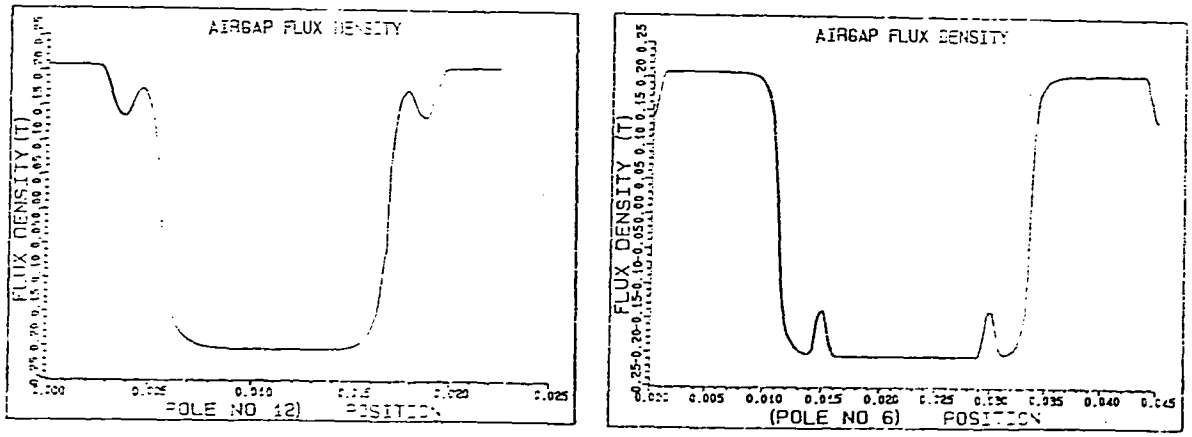

(c) Analytical prediction

12-pole 6-pole

Fig 5.27 Airgap flux density distribution of finite element calculation and analytical prediction on the idealised models

$$M_n = 2 M_o \alpha_p \frac{\sin \frac{n \pi \alpha_p}{2}}{\frac{n \pi \alpha_p}{2}} = as\ above \tag{5.139}$$

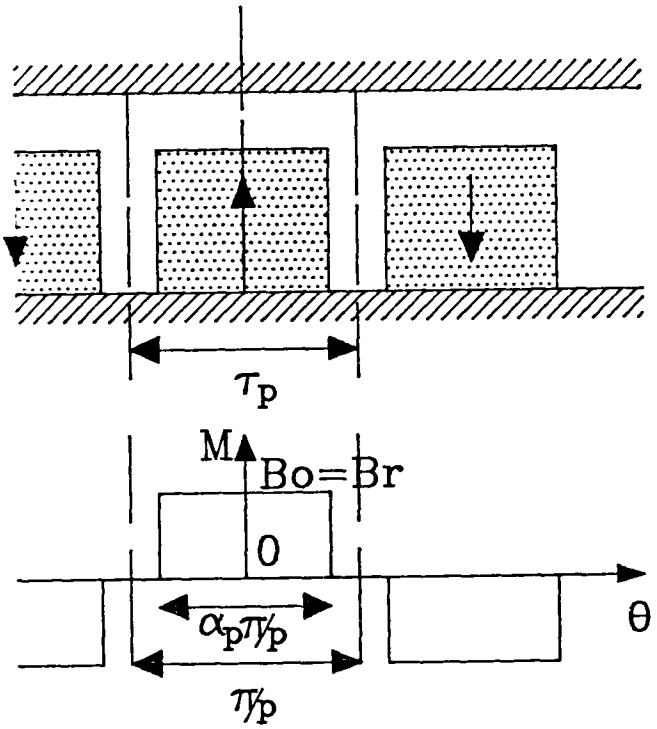

For cylindrical coordinate

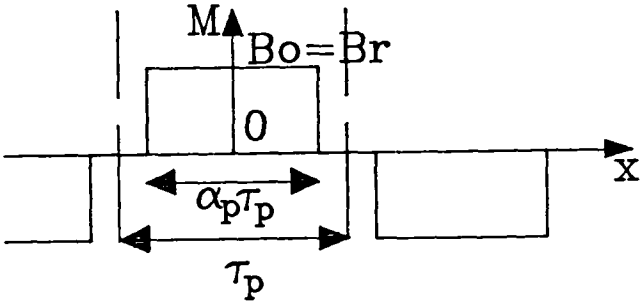

For rectangular coordinate

Fig 5.28 Magnetisation

CHAPTER 6

ANALYTICAL PREDICTION OF COGGING TORQUE IN PERMANENT MAGNET MOTORS BASED ON THE CALCULATION OF THE TOOTH LATERAL FORCE

6. 1 Introduction

Cogging arises from the interaction of the mmf harmonics and the airgap permeance harmonics. Hence it exists in almost all types of motor in which the airgap permeance is not constant. Cogging manifests itself in a permanent magnet machine by the tendency of the rotor to align in a number of stable positions even when unexcited. Under dynamic conditions the resultant pulsating torque, of zero net value, can cause undesirable speed pulsations, and can be transmitted to the coupling devices, through the stator frame or the rotor, and induce vibration, resonance and noise.

Because of the sensitivity to speed pulsations of many applications for which permanent magnet motors now provide the drive, eg. video cassette recorders, and because the emergence of high-energy permanent magnets, such as NdFeB, tends to aggravate the problem given the preference to employ unskewed slots or poles in order to fully utilise the flux produced by the magnets, cogging effects remain a major concern. Hence a reliable means of estimating the likely level of cogging and its dependance on the motor design parameters was required.

The numerical prediction of the cogging torque in a permanent magnet motor can be rather time-consuming since the wavelength of the cogging torque waveform is usually less than one stator slot-pitch, and therefore a very fine spatial discretisation in the circumferential direction is necessary if the peak value is to be captured. Existing analytical methods are successful only in certain circumstances, and fail in others, eg. when the magnets have a full pole-arc [6.1].

However in this chapter an analytical method for predicting the cogging torque, based on the analytical calculation of the field distribution and the lateral forces acting on the teeth, is developed and validated. The technique is capable of predicting the cogging torque in both internal and external rotor motor topologies, modelled in either rectangular or polar coordinate systems. Also it can cater with variants to the basic motor topologies, eg. having the magnets shifted (ie. spaced unevenly) or an uneven stator slot distribution etc, which may be employed in an attempt to reduce the cogging torque.

6.2 Methods of Reducing Cogging Torque and Limitations of Existing Methods of Calculation

The following is a comprehensive list of possible methods for reducing the cogging torque:

(i) Optimise the pole-arc to pole-pitch ratio [6.2][6.3].

(ii) Optimise the tooth-width to slot-opening ratio [6.1][6.3].

(iii) Rotate pairs of poles relative to each other [6.3].

(iv) Introduce auxiliary slots or teeth [6.4][6.5].

(v) Select a suitable combination of slot number and pole number.

(vi) Skew the slots or the magnetisation pattern.

(vii) Use a slotless topology.

(viii) Use an uneven distribution of slots.

Clearly all the above methods of reducing cogging torque are closely related to the electromagnetic performance of the motor as well as to the complexity of manufacture.

Existing methods for predicting the cogging torque employ either analytical [6.6][6.7][6.8][6.9] or numerical [6.10][6.11] techniques. The energy method is widely used in both analytical and numerical approaches [6.1]~[6.11]. Of course other methods, such as Maxwell stress, have also been used in the numerical approach [6.10][6.11]. However it is surprising to observe that

in the calculation of energy many papers, eg. [6.1], [6.2], [6.7], [6.8], [6.9], neglect the component of energy stored inside the magnets themselves, and yet still claim that good agreement has been achieved between predicted and measured results, since in the author's experience [6.6] the neglect of the energy stored inside the magnets can introduce an error of, typically, around 50% into the global results obtained from a finite element calculation.

In analytical approaches using the energy method the greatest difficulty is found in accounting for the tangential components of flux density in both the magnets and the airgap region, which arise due to the fringing of the field, leakage directly between the magnets, and at the slot-openings. These components are as important as the radial components of the flux density since although the absolute value of the energy may be small its rate of change with rotor position in localised regions, such as the magnet edges and tooth tips, may be at least as large as that due to the radial component. Clearly it is impossible for an analytical method to account for all the geometrical complexities associated with the airgap region. As a consequence it is found that whilst one analytical method may be adequate in one particular case it may fail in another.

As regards numerical methods, because of the short wavelength of the cogging torque waveform a fine spatial discretisation is required for a finite element mesh, typically less than 1 degree mech being required for a numerical energy calculation if the peak value of the cogging torque is to be captured. However in the energy method, in which the torque is calculated from the derivative of coenergy the calculation is approximated by performing two finite element analyses at two rotor positions dispaced by a finite angle. This in itself may result in a large numerical error due to the small change of energy with rotor position. Equally in a Maxwell stress calculation the results can be extremely dependant on the local discretisation of the mesh, which again necessitates a fine spatial discretisation. It is found that in general the Maxwell stress method is usually accurate for determining normal forces but tends to be inaccurate for torques and tangential forces [6.10][6.12][6.13].

6.3 Methodology of Analytical Prediction

6.3.1 Basic Concept for Predicting Cogging Torque based on the Calculation of the Tooth Lateral Force

Due to the difficulties cited in the previous section in the analytical calculation of energy, in this section an alternative approach, based on the calculation of the lateral force acting on the teeth, is proposed to predict the cogging torque.

However in order to simplify the field calculation the following assumptions are made:

a) the permeability of the iron is infinite, ie $\mu_{Fe} = \infty$;

b) the slot is simplified to a rectangular shape;

c) the field distribution can be determined from the magnetic field produced by the magnets and relative permeance, as described in Chapter 5;

d) the magnetic field developed by the magnets can be calculated by assuming a smooth stator surface, ie slotting is neglected, as shown in Fig 6.1;

e) the magnetic field distribution at the surface of the stator is obtained from a two-dimensional solution given in Chapter 5;

f) the relative permeance can be calculated according to the assumed field pattern shown in Fig 6.2, in which flux crosses the magnet and airgap in a straight line where the magnet faces a tooth and in a circular path, centred about the corner of a tooth, where the magnet faces a slot opening.

The lateral force acting on the stator teeth, and hence the cogging torque at any rotor position, is calculated by assuming that the circumferential flux density distribution on the sides of the teeth is equal to the radial flux density distributions at the adjacent slot openings at the radius of the stator surface. Therefore, along a circular flux path in a slotted region, centred at the corner of an adjacent tooth as shown in Fig 6.3, the flux density is assumed to be the same at corresponding points on the side of the tooth and at the slot opening, ie. $B_{\theta b1'} = B_{rb1}$ etc.

The cogging torque developed by an internal rotor/external rotor motor, at any rotor position, is then calculated from:

$$T_c = \sum_{k=1}^{Q_s} l_a \int_{toothside} \left(\frac{B_1'^2 - B_2'^2}{2\mu_o} \right) r_t \, dy$$

$$= \sum_{k=1}^{Q_s} l_a \int_{0}^{\frac{b_o}{2}} \left(\frac{B_1^2 - B_2^2}{2\mu_o} \right) r_t \, dy \qquad (6.1)$$

where $r_t = R_i + r_s$ for an internal rotor topology

$R_i - r_s$ for an external rotor topology

Note:

$$f(x) = \frac{(B_{at R_i})^2}{2\mu_o} \qquad N/m \qquad (6.2)$$

where $B_{atRi} = B_{magnet} \lambda$ (6.3)

The calculation of the magnetic field produced by the magnets (B_{magnet}) and the relative permeance (λ) for motors having different topologies and modelled in different coordinate systems has already been described in Chapter 5 and will be summarised in subsequent sections. However a simple numerical evaluation procedure is:

$$T_c = T_1 - T_2 \qquad (6.4)$$

where

$$T_1 = \sum_{k=1}^{Q_s} \sum_{i=1}^{N_p} f(x_i)(l_a \Delta x) r_t \qquad \text{for } (k-1)\tau_t - \frac{b_o}{2} \le x_i \le (k-1)\tau_t \qquad (6.5a)$$

and

$$x_i' = -(i-1)\Delta x$$

$$x_i = (k-1)\tau_t + x_i'$$

$$r_s = \frac{b_o}{2} - |x_i'|$$

$$\Delta x = \frac{b_o/2}{N_p} \tag{6.6a}$$

N_p is the number of discretisation integration points over a half-slot opening.

and

$$T_2 = \sum_{k=1}^{Q_s} \sum_{i=1}^{N_p} f(x_i)\,(l_a \Delta x)\, r_t \qquad \text{for } (k-1)\,\tau_t \le x_i \le (k-1)\,\tau_t + \frac{b_o}{2} \tag{6.5b}$$

where

$$x_i' = +\,(i-1)\,\Delta x$$

$$x_i = (k-1)\,\tau_t + x_i'$$

$$r_s = \frac{b_o}{2} - |\,x_i'\,| \tag{6.6b}$$

6.3.2 Relative Permeance Calculation

In accordance with Fig 6.2 the permeance can be calculated from

$$\lambda = \begin{cases} \dfrac{\mu_o}{g + \dfrac{h_m}{\mu_R} + \dfrac{2\pi r_s}{4}} & \text{for } (k-1)\,\tau_t - \dfrac{b_o}{2} \le x_i \le (k-1)\,\tau_t + \dfrac{b_o}{2} \qquad (6.7a) \\ \dfrac{\mu_o}{g + \dfrac{h_m}{\mu_R}} & \text{for } (k-1)\,\tau_t + \dfrac{b_o}{2} \le x_i \le \tau_t - \dfrac{b_o}{2} \qquad (6.7b) \end{cases}$$

where $k = 1, 2, \ldots\ldots Q_s$

whilst the relative permeance is calculated from

$$\bar{\lambda} = \frac{\lambda}{\left(\dfrac{\mu_o}{g + \dfrac{h_m}{\mu_R}}\right)} \tag{6.7c}$$

$$r_s = \frac{b_o}{2} - |\,x_i'\,|$$

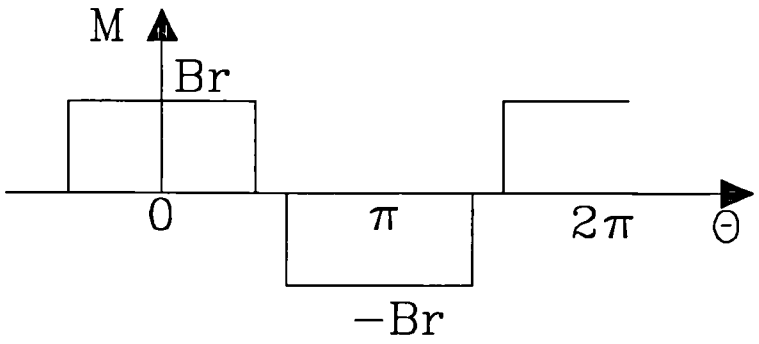

(a) Magnetisation

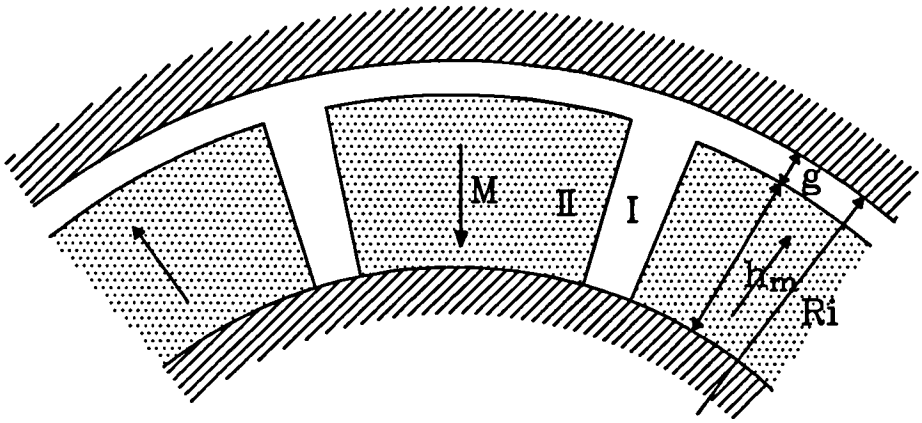

(b) Internal rotor motor

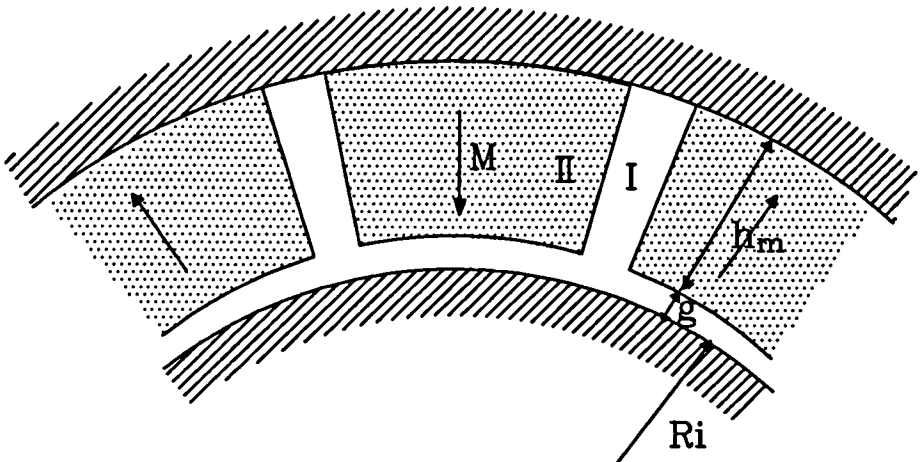

(c) External rotor motor

Fig.6.1 Magnetisation distribution

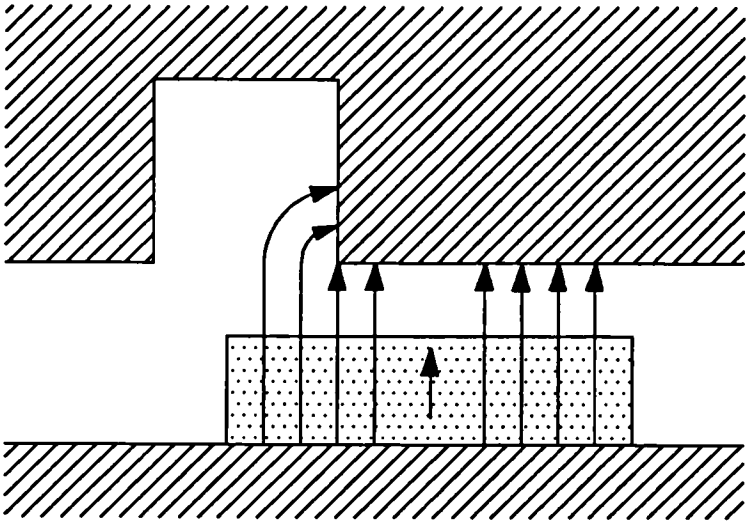

Fig.6.2 Idealised flux distribution used for calculating the permeance

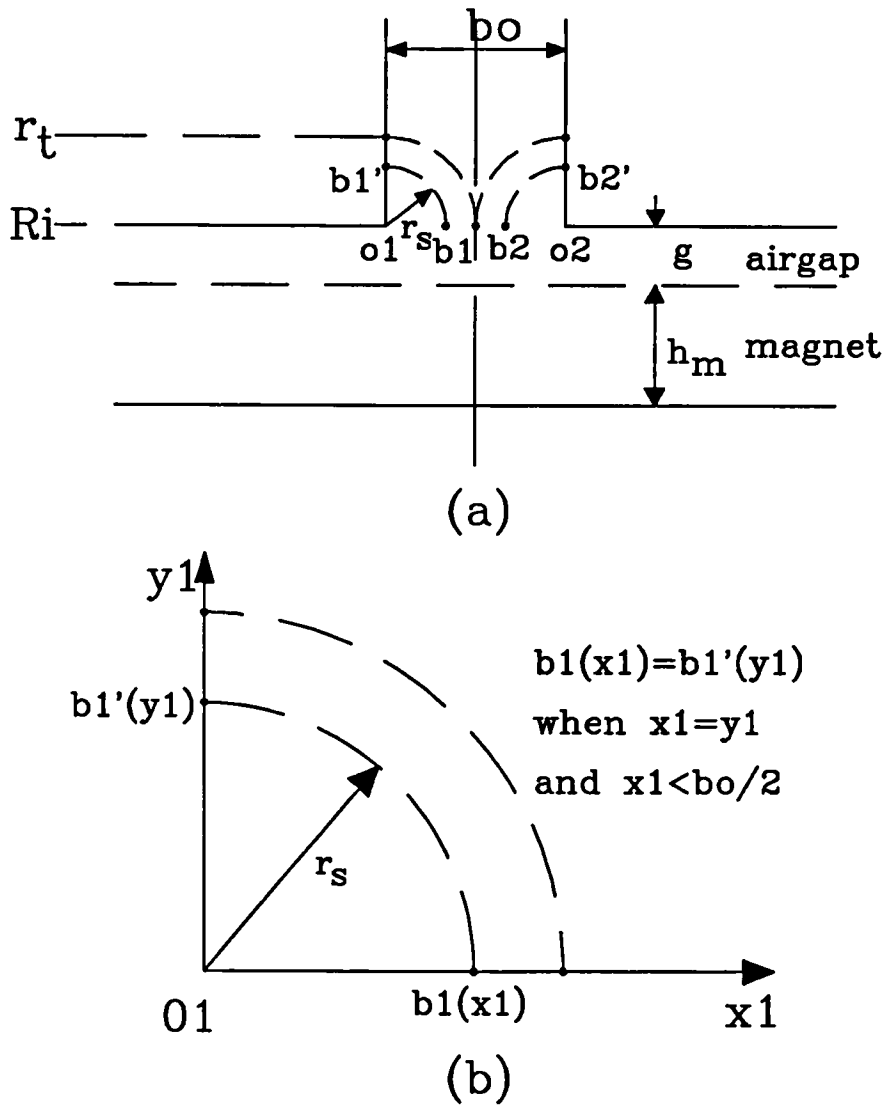

Fig.6.3 Circumferential force calculation

$$x_i = (k-1)\,\tau_t + x_i'$$

$$x_i' = \begin{cases} -(i-1)\,\Delta x & \text{for } (k-1)\,\tau_t - \dfrac{b_o}{2} \le x_i \le (k-1)\,\tau_t \\ +(i-1)\,\Delta x & \text{for } (k-1)\,\tau_t \le x_i \le (k-1)\,\tau_t + \dfrac{b_o}{2} \end{cases}$$

and Δx is as before. However in the calculation of the cogging torque the flux density, and hence the permeance, is required only in the slot-opening regions. Therefore only equation (6.7a) is used in the calculation.

6.3.3 Calculation of Magnetic Field Produced by Magnets

The calculation of magnetic field produced by the magnets is based on the field calculation described in Chapter 5 and is summarised as follows:

a) In a rectangular coordinate system the magnetisation can be expressed as:

$$M = \sum_{n=1,3,5,\ldots}^{\infty} 2\,M_n' \cos n\frac{\pi}{\tau_p}x \tag{6.8a}$$

where

$$M_n' = B_R\ \alpha_p\ \frac{\sin\dfrac{n\,\alpha_p\,\pi}{2}}{\dfrac{n\,\alpha_p\,\pi}{2}} \tag{6.8b}$$

Since

$$B_{yI}(x,y) = \sum_{n=1,3,5,\ldots}^{\infty} 2\,M_n'\ \frac{1-e^{-2n\frac{\pi}{\tau_p}h_m}}{1-e^{-2n\frac{\pi}{\tau_p}(g+h_m)}}$$

$$\frac{e^{n\frac{\pi}{\tau_p}(h_m-y)} + e^{-n\frac{\pi}{\tau_p}(2g+h_m-y)}}{2}\cos n\frac{\pi}{\tau_p}x \tag{6.9}$$

Therefore the flux density distribution produced by the magnets on the stator surface, ie. at $y = g + h_m$, is used to calculate the cogging torque:

$$B_{magnet} = B_{yI}(x,y)|_{y=h_m+g} = \sum_{n=1,3,5,\ldots}^{\infty} 2M_n' \frac{1-e^{-2n\frac{\pi}{\tau_p}h_m}}{1-e^{-2n\frac{\pi}{\tau_p}(g+h_m)}} e^{-n\frac{\pi}{\tau_p}g} \cos n\frac{\pi}{\tau_p}x \tag{6.10}$$

b) In a polar coordinate system

(1) In internal rotor motors the magnetisation is given by:

$$M = \sum_{n=1,3,5,\ldots}^{\infty} 2M_n' \cos np\theta \tag{6.11}$$

where M'n is the same as in equation (6.8b).

since when $np = 1$ the airgap field distribution is given by:

$$B_{rI}(r,\theta) = \frac{M1'}{\mu_R} \left\{ \frac{\left(\frac{R_o}{R_i}\right)^2 - \left(\frac{R_m}{R_i}\right)^2 + \left(\frac{R_m}{R_i}\right)^2 \ln\left(\frac{R_o}{R_m}\right)^2}{\frac{\mu_R+1}{\mu_R}\left[1-\left(\frac{R_m}{R_i}\right)^2\right] - \frac{\mu_R-1}{\mu_R}\left[\left(\frac{R_o}{R_i}\right)^2 - \left(\frac{R_m}{R_o}\right)^2\right]} \right\} \left[1+\left(\frac{R_i}{r}\right)^2\right] \cos\theta \tag{6.12a}$$

and when $np \neq 1$ it is given by:

$$B_{rI}(r,\theta) = \sum \frac{2M_n'}{\mu_R} \frac{np}{(np)^2-1} \left\{ \frac{(np-1)+2\left(\frac{R_m}{R_o}\right)^{np+1} - (np+1)\left(\frac{R_m}{R_o}\right)^{2np}}{\frac{\mu_R+1}{\mu_R}\left[1-\left(\frac{R_m}{R_i}\right)^{2np}\right] - \frac{\mu_R-1}{\mu_R}\left[\left(\frac{R_o}{R_i}\right)^{2np} - \left(\frac{R_m}{R_o}\right)^{2np}\right]} \right\} \left[\left(\frac{r}{R_i}\right)^{np-1}\left(\frac{R_o}{R_i}\right)^{np+1} + \left(\frac{R_o}{r}\right)^{np+1}\right] \cos np\theta \tag{6.12b}$$

where $R_o = R_i - g$

and $R_m = R_i - g - h_m$ (6.12c)

Therefore at the stator surface, ie. $r = R_i$ the magnetic field produced by the magnets is given by:
when np=1

$$B_{magnet} = \frac{2\,M_1'}{\mu_R}\left\{\frac{\left(\frac{R_o}{R_i}\right)^2 - \left(\frac{R_m}{R_i}\right)^2 + \left(\frac{R_m}{R_i}\right)^2 \ln\left(\frac{R_o}{R_m}\right)^2}{\frac{\mu_R+1}{\mu_R}\left[1 - \left(\frac{R_m}{R_i}\right)^2\right] - \frac{\mu_R-1}{\mu_R}\left[\left(\frac{R_o}{R_i}\right)^2 - \left(\frac{R_m}{R_o}\right)^2\right]}\right\}\cos\theta \qquad (6.13a)$$

and when $(np \neq 1)$

$$B_{magnet} = \sum \frac{4\,M_n'}{\mu_R}\,\frac{np}{(np)^2 - 1}\left(\frac{R_o}{R_i}\right)^{np+1}$$

$$\left\{\frac{(np-1) + 2\left(\frac{R_m}{R_o}\right)^{np+1} - (np+1)\left(\frac{R_m}{R_o}\right)^{2np}}{\frac{\mu_R+1}{\mu_R}\left[1 - \left(\frac{R_m}{R_i}\right)^{2np}\right] - \frac{\mu_R-1}{\mu_R}\left[\left(\frac{R_o}{R_i}\right)^{2np} - \left(\frac{R_m}{R_o}\right)^{2np}\right]}\right\}\cos np\,\theta \qquad (6.13b)$$

(2) In external rotor motors the magnetisation is again given by equation (6.11)

since when $np = 1$ the airgap field distribution is given by:

$$B_{rI}(r,\theta) = \frac{M_1'}{\mu_R}\left\{\frac{\left(\frac{R_o}{R_i}\right)^2 - \left(\frac{R_m}{R_i}\right)^2 + \left(\frac{R_m}{R_i}\right)^2 \ln\left(\frac{R_o}{R_m}\right)^2}{\frac{\mu_R+1}{\mu_R}\left[1 - \left(\frac{R_m}{R_i}\right)^2\right] - \frac{\mu_R-1}{\mu_R}\left[\left(\frac{R_o}{R_i}\right)^2 - \left(\frac{R_m}{R_o}\right)^2\right]}\right\}$$

$$\cdot\left[1 + \left(\frac{R_i}{r}\right)^2\right]\cos\theta \qquad (6.14a)$$

and when $np \neq 1$ it is given by:

$$B_{rI}(r,\theta) = \sum \frac{(-2\,M_n')}{\mu_R}\,\frac{np}{(np)^2 - 1}$$

$$\cdot\left\{\frac{(np-1)\left(\frac{R_o}{R_m}\right)^{2np} + 2\left(\frac{R_o}{R_m}\right)^{np-1} - (np+1)}{\frac{\mu_R+1}{\mu_R}\left[1 - \left(\frac{R_i}{R_m}\right)^{2np}\right] - \frac{\mu_R-1}{\mu_R}\left[\left(\frac{R_i}{R_o}\right)^{2np} - \left(\frac{R_o}{R_m}\right)^{2np}\right]}\right\}$$

$$\cdot\left[\left(\frac{r}{R_o}\right)^{np-1} + \left(\frac{R_i}{R_o}\right)^{np-1}\left(\frac{R_i}{r}\right)^{np+1}\right]\cos np\,\theta \qquad (6.14b)$$

where $R_o = R_i + g$

and $R_m = R_i + g + h_m$ (6.14c)

Therefore at the stator surface, ie. $r = R_i$ the magnetic field produced by the magnets is given by:

when np=1

$$B_{magnet} = \frac{2M_1}{\mu_R}\left\{\frac{\left(\frac{R_o}{R_i}\right)^2 - \left(\frac{R_m}{R_i}\right)^2 + \left(\frac{R_m}{R_i}\right)^2 \ln\left(\frac{R_o}{R_m}\right)^2}{\frac{\mu_R+1}{\mu_R}\left[1-\left(\frac{R_m}{R_i}\right)^2\right] - \frac{\mu_R-1}{\mu_R}\left[\left(\frac{R_o}{R_i}\right)^2 - \left(\frac{R_m}{R_o}\right)^2\right]}\right\}\cos\theta \qquad (6.15a)$$

and when ($np \neq 1$)

$$B_{magnet} = \sum \frac{(-4M_n')}{\mu_R}\frac{np}{(np)^2-1}\left(\frac{R_i}{R_o}\right)^{np-1}$$
$$\left\{\frac{(np-1)\left(\frac{R_o}{R_m}\right)^{2np} + 2\left(\frac{R_o}{R_m}\right)^{np-1} - (np+1)}{\frac{\mu_R+1}{\mu_R}\left[1-\left(\frac{R_i}{R_m}\right)^{2np}\right] - \frac{\mu_R-1}{\mu_R}\left[\left(\frac{R_i}{R_o}\right)^{2np} - \left(\frac{R_o}{R_m}\right)^{2np}\right]}\right\}\cos np\,\theta \qquad (6.15b)$$

6.3.4 Magnet Shifting

When one pair of magnet poles is rotated relative to an adjacent pair, whilst the permeance will remain unchanged the mmf distribution will be modified since the magnetisation is no longer a symmetrical pattern (cos np θ terms only) but a combination of symmetrical components (cos np θ terms) and anti-symmetrical components (sin np θ terms). This can be seen in Fig 6.4, where the magnetisation pattern after shifting is decomposed into a symmetrical pattern, which is the same as before, and an anti-symmetrical pattern.

If the distance by which one pole-pair is shifted relative to another pole-pair is dx_m the magnetisation pattern will be as shown in Table 6.1 where it is compared against a normal symmetrical pattern.

In a rectangular coordinate system the resultant magnetisation is:

$$M = \sum_{n=1,2,3,\ldots}^{\infty} M_n'\{[1+(-1)^{n+1}\cos n\frac{\pi}{\tau_p}\,dx_m]\cos n\frac{\pi}{\tau_p}x$$

$$+[(-1)^n \sin n\frac{\pi}{\tau_p} d x_m] \sin n\frac{\pi}{\tau_p} x\} \tag{6.16}$$

where

$$M_n' = B_R \alpha_p \frac{\sin \frac{n\alpha_p \pi}{2}}{\frac{n\alpha_p \pi}{2}} \tag{6.8b}$$

Table 6.1 Comparison of magnetisation pattern before and after magnet shifting

M	Normal	Shifted by dx_m
$-B_R$	$-\tau_p \le x \le -(\tau_p - \frac{\alpha_p}{2}\tau_p)$	$-\tau_p \le x \le -(\tau_p - \frac{\alpha_p}{2}\tau_p) - d x_m$
0	$-(\tau_p - \frac{\alpha_p}{2}\tau_p) \le x \le -\frac{\alpha_p}{2}\tau_p$	$-(\tau_p - \frac{\alpha_p}{2}\tau_p) - d x_m \le x \le -\frac{\alpha_p}{2}\tau_p$
B_R	$-\frac{\alpha_p}{2}\tau_p \le x \le \frac{\alpha_p}{2}\tau_p$	$-\frac{\alpha_p}{2}\tau_p \le x \le \frac{\alpha_p}{2}\tau_p$
0	$\frac{\alpha_p}{2}\tau_p \le x \le \tau_p - \frac{\alpha_p}{2}\tau_p$	$\frac{\alpha_p}{2}\tau_p \le x \le \tau_p - \frac{\alpha_p}{2}\tau_p - d x_m$
$-B_R$	$\tau_p - \frac{\alpha_p}{2}\tau_p \le x \le \tau_p$	$\tau_p - \frac{\alpha_p}{2}\tau_p - d x_m \le x \le \tau_p$
Note: Condition: $\lvert d x_m \rvert \le (1-\alpha_p)\tau_p$		

Hence the magnetic field produced by the magnets is obtained as:

$$B_{magnet} = \sum_{n=1,3,5,\ldots}^{\infty} M_n' \frac{1 - e^{-2n\frac{\pi}{\tau_p} h_m}}{1 - e^{-2n\frac{\pi}{\tau_p}(g+h_m)}} e^{-n\frac{\pi}{\tau_p} g}$$

$$[\cos n\frac{\pi}{\tau_p} x + (-1)^{n+1} \cos n\frac{\pi}{\tau_p}(x - d x_m)] \tag{6.17}$$

Similarly for internal and external rotor motors the magnetic field distributions produced by the magnets when one pole-pair is shifted by dx_m with respect to another are:

Internal rotor motor:

when np=1

$$B_{magnet} = \frac{M_1'}{\mu_R} \left\{ \frac{\left(\frac{R_o}{R_i}\right)^2 - \left(\frac{R_m}{R_i}\right)^2 + \left(\frac{R_m}{R_i}\right)^2 \ln\left(\frac{R_o}{R_m}\right)^2}{\frac{\mu_R+1}{\mu_R}\left[1 - \left(\frac{R_m}{R_i}\right)^2\right] - \frac{\mu_R-1}{\mu_R}\left[\left(\frac{R_o}{R_i}\right)^2 - \left(\frac{R_m}{R_o}\right)^2\right]} \right\}$$

$$\left[\cos\frac{\pi}{\tau_p}x + \cos\frac{\pi}{\tau_p}(x - d\,x_m)\right] \qquad (6.18a)$$

and when ($np \neq 1$)

$$B_{magnet} = \sum \frac{2M_n'}{\mu_R} \frac{np}{(np)^2 - 1}\left(\frac{R_o}{R_i}\right)^{np+1}$$

$$\left\{ \frac{(np-1) + 2\left(\frac{R_m}{R_o}\right)^{np+1} - (np+1)\left(\frac{R_m}{R_o}\right)^{2np}}{\frac{\mu_R+1}{\mu_R}\left[1 - \left(\frac{R_m}{R_i}\right)^{2np}\right] - \frac{\mu_R-1}{\mu_R}\left[\left(\frac{R_o}{R_i}\right)^{2np} - \left(\frac{R_m}{R_o}\right)^{2np}\right]} \right\}$$

$$\left[\cos n\frac{\pi}{\tau_p}x + (-1)^{n+1}\cos n\frac{\pi}{\tau_p}(x - d\,x_m)\right] \qquad (6.18b)$$

External rotor motor:

when np=1

$$B_{magnet} = \frac{M_1'}{\mu_R} \left\{ \frac{\left(\frac{R_o}{R_i}\right)^2 - \left(\frac{R_m}{R_i}\right)^2 + \left(\frac{R_m}{R_i}\right)^2 \ln\left(\frac{R_o}{R_m}\right)^2}{\frac{\mu_R+1}{\mu_R}\left[1 - \left(\frac{R_m}{R_i}\right)^2\right] - \frac{\mu_R-1}{\mu_R}\left[\left(\frac{R_o}{R_i}\right)^2 - \left(\frac{R_m}{R_o}\right)^2\right]} \right\}$$

$$\left[\cos\frac{\pi}{\tau_p}x + \cos\frac{\pi}{\tau_p}(x - d\,x_m)\right] \qquad (6.19a)$$

and when ($np \neq 1$)

$$B_{magnet} = \sum \frac{(-2M_n')}{\mu_R} \frac{np}{(np)^2 - 1}\left(\frac{R_i}{R_o}\right)^{np-1}$$

$$\left\{ \frac{(np-1)\left(\frac{R_o}{R_m}\right)^{2np} + 2\left(\frac{R_o}{R_m}\right)^{np-1} - (np+1)}{\frac{\mu_R+1}{\mu_R}\left[1 - \left(\frac{R_i}{R_m}\right)^{2np}\right] - \frac{\mu_R-1}{\mu_R}\left[\left(\frac{R_i}{R_o}\right)^{2np} - \left(\frac{R_o}{R_m}\right)^{2np}\right]} \right\}$$

$$\left[\cos n\frac{\pi}{\tau_p}x + (-1)^{n+1}\cos n\frac{\pi}{\tau_p}(x - d\,x_m)\right] \qquad (6.19b)$$

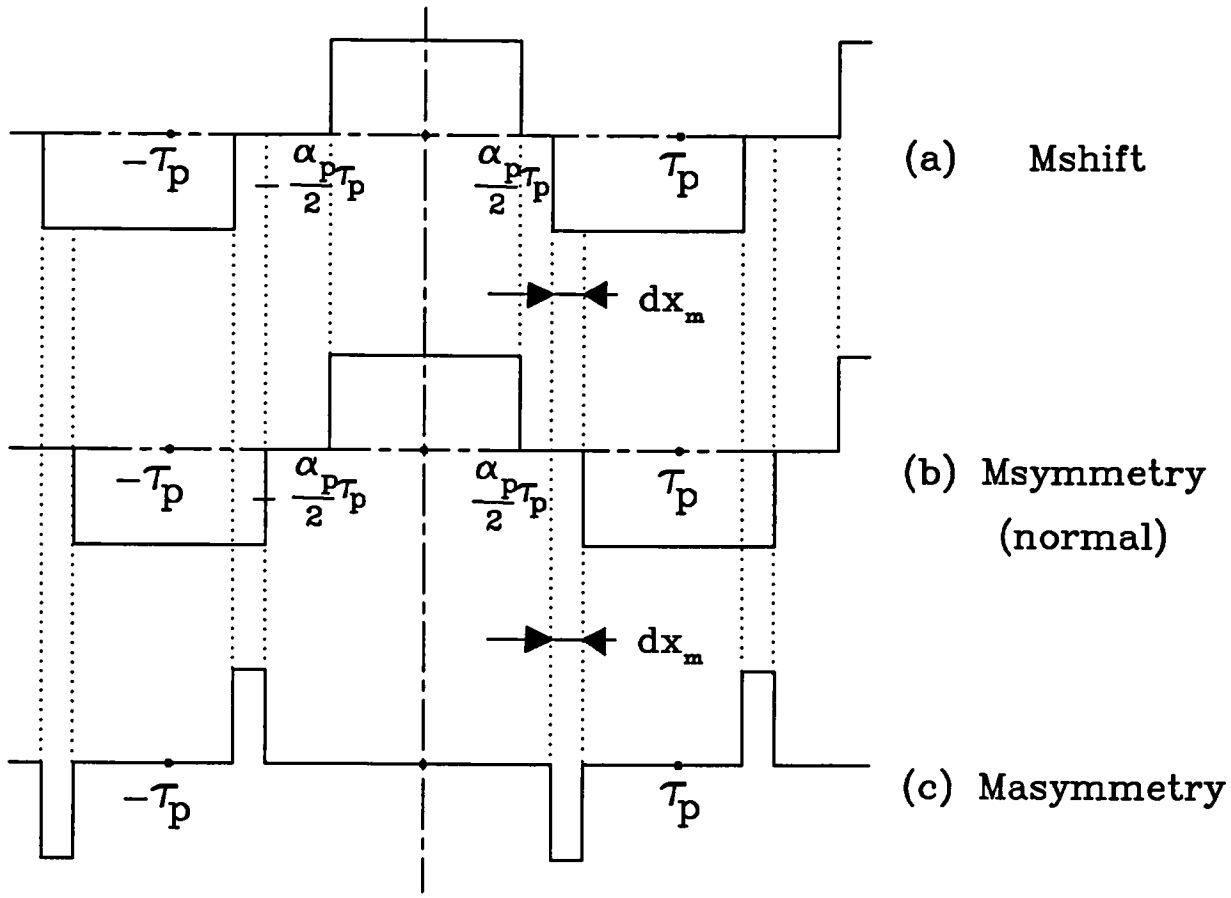

Fig.6.4 Relationship of magnetisation between shifted and normal magnet arrangements

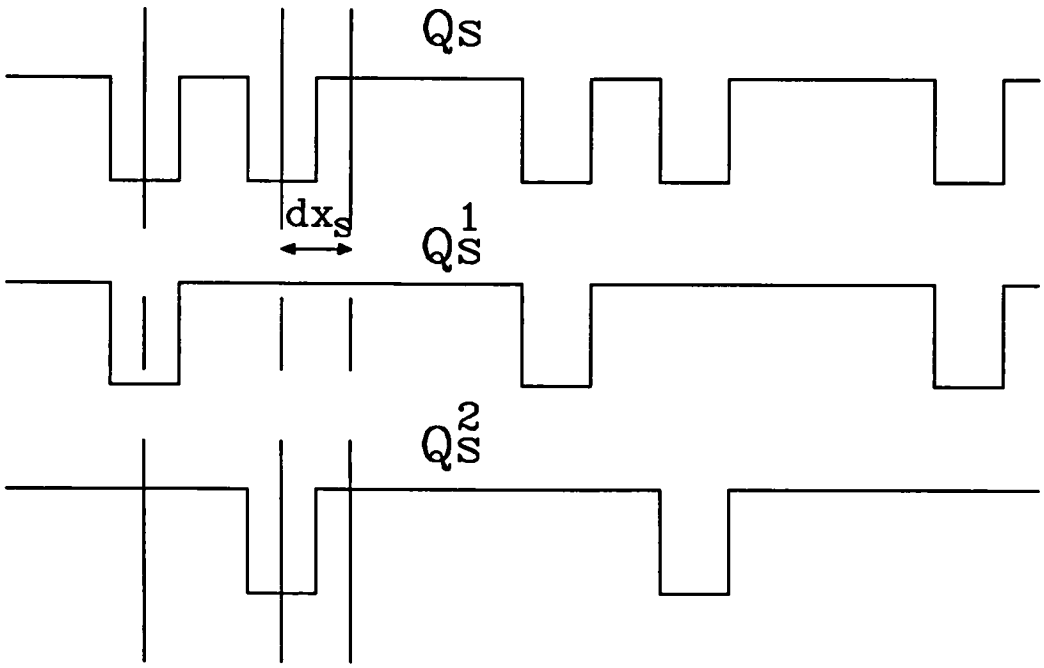

Fig.6.5 Uneven slot distribution

where $\frac{\pi}{\tau_p} x = p\,\theta$ and $x = x_s - x_{sr}$, $\theta = \varphi_s - \varphi_{sr}$

φ_s is the angular position with respect to the stator reference;

φ_{sr} is the angle between the stator and the rotor reference positions;

x_s, x_{sr} are similarly defined.

6.3.5 Uneven distribution of slots

The use of unevenly distributed stator slots offers another alternative method for reducing the cogging torque. Again by utilising the idea of superposition the resultant cogging torque can be calculated by the technique developed in this chapter. For example, if the slot distribution is as shown in Fig 6.5 where alternate slots are displaced by dx_s from the position which they could occupy with uniform slotting, then if

$$Q_s^1 = Q_s^2 = Q_s/2 \tag{6.20}$$

the resultant cogging torque is given simply by

$$T_c = T_c^1 + T_c^2 \tag{6.21}$$

If all the slot-openings are identical then

$$T_c(x) = T_c^1(x) + T_c^1(x + dx_s) \tag{6.22}$$

6.5 Validations

Validations of the cogging torque waveform and its variation with slot opening have been made against finite element predictions for two prototype motors whose main parameters are listed in Table 6.2.

Table 6.2 Parameters of prototype motors

Parameters	Motor 1 (internal rotor)	Motor 2 (external rotor)
2p	12	8
B_R	0.56	0.245
μ_R	1.05	1.05
α_p	1.0	0.8
R_i	0.7327×10^{-1}	0.1325×10^{-1}
g	0.13×10^{-2}	0.5×10^{-3}
h_m	0.91×10^{-2}	0.3×10^{-2}
b_o	0.38×10^{-2}	Variable
Q_s	36	6
l_a	0.95×10^{-1}	0.8×10^{-2}

6.5.1 Finite Element Calculations

In this section the finite element method is used to calculate the cogging torque by both the Maxwell stress integration and the energy methods which are described in Appendix 6.7. As indicated earlier the calculation of the cogging torque by both of these methods necessitates a very fine spatial discretisation. Therefore in order to establish the reliability of the results from the finite element calculation five different meshes have been used to model one pole-pitch of motor 1, as shown on Fig.6.6a. However in order to simplify the study its yoke is removed and replaced by infinitely permeable iron.

The meshes employed are:

a) Mesh 1: Fig 6.6b, three layers in the airgap;

b) Mesh 2: Fig 6.6c, as Mesh 1, with mesh density along the radius doubled near the tooth tips and in the magnet;

c) Mesh 3: Fig 6.6d, as Mesh 2, with mesh density around the circumference doubled near the tooth tips and in the airgap, as well as in the portion of the magnet nearest the airgap;

d) Mesh 4: Fig 6.6e, as Mesh 3, the only difference being that the discretisation pattern of the elements in the airgap is different;

e) Mesh 5: Fig 6.6f, as Mesh 3, but with the mesh density doubled along the radius through the airgap.

Fig 6.7 shows the flux distributions for different angular positions of the rotor with respect to the stator, whilst Tables 6.3 - 6.7 and Fig 6.8 show the calculated cogging torque. Fig 6.9 shows a comparison of the cogging torque obtained by Maxwell stress integration over a circular path through the middle layer of airgap elements for the different meshes, whilst Fig 6.10 shows the cogging torque obtained by the energy method. The variation of total energy against the total number of nodes and elements is shown in Fig 6.11 and Table 6.6.

With reference to the results from the finest mesh (Mesh 5), the results obtained by Maxwell stress integration are not as good as those obtained by the energy method. Nevertheless when employing Maxwell stress it is always better to integrate through the middle layer of airgap elements in order to get reasonable results. In addition it remains necessary to have a fine mesh discretisation.

Fig 6.12 and Table 6.9 show a comparison of the cogging torque calculated by both the Maxwell stress and energy methods for meshes 3, 4, and 5. They show that the results obtained from both methods converge as the mesh is refined and that the total energy converges to a constant [6.14]. Also given two meshes of the same mesh density but reversed mesh discretisation in the airgap improved results are obtained if the average of the two Maxwell stress values is used.

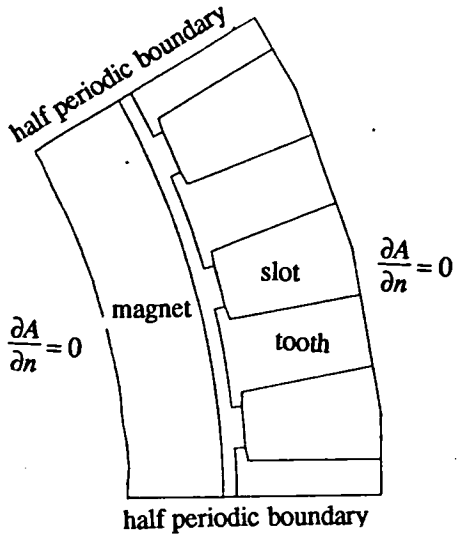

(a) Boundary conditions

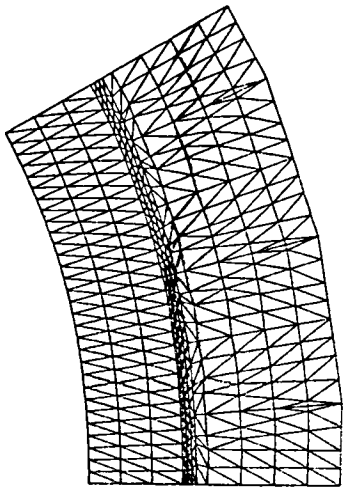

(b) Mesh 1

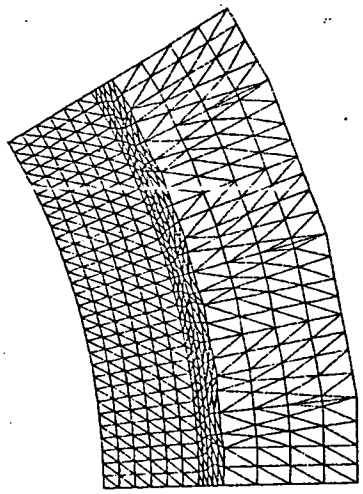

(c) Mesh 2

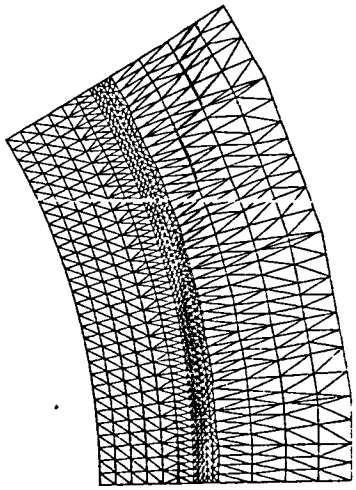

(d) Mesh 3

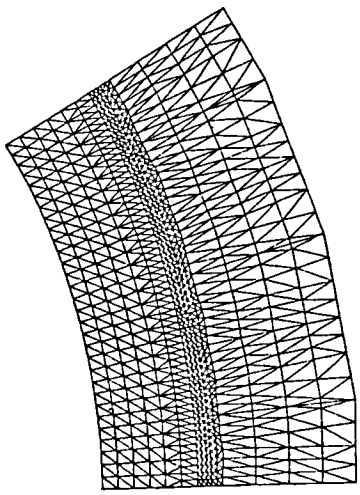

(e) Mesh 4

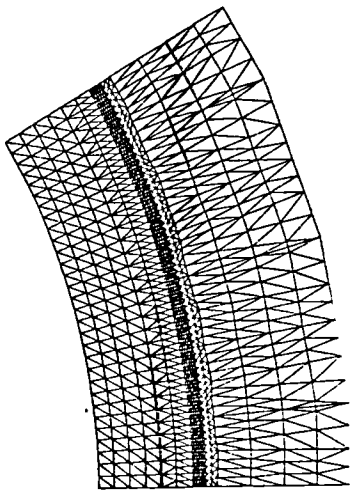

(f) Mesh 5

Fig 6.6 Meshes and boundary conditions of the internal rotor motor

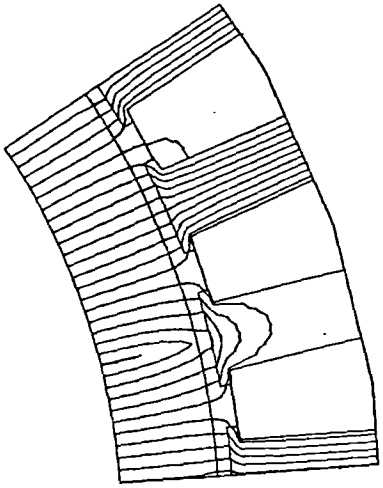

(a) Angular position = 0^o

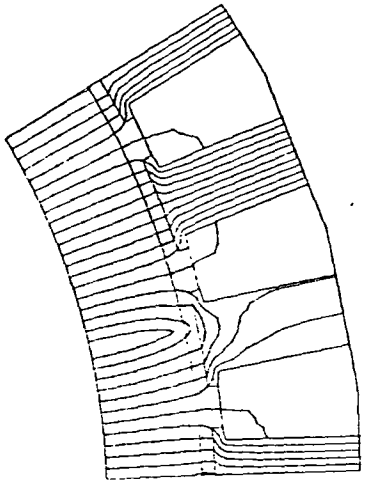

(b) Angular position = 1^o

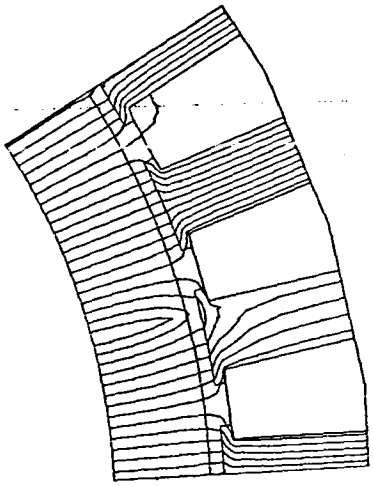

(c) Angular position = 2^o

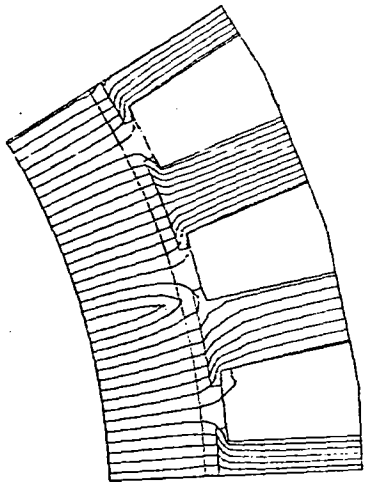

(d) Angular position = 3^o

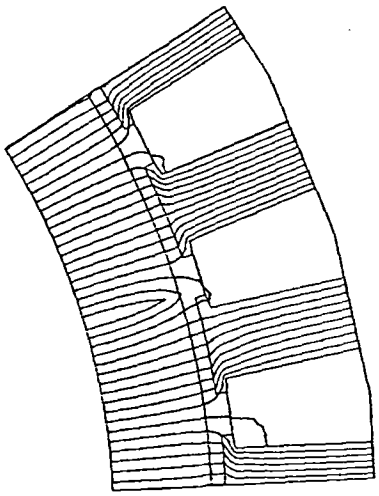

(e) Angular position = 4^o

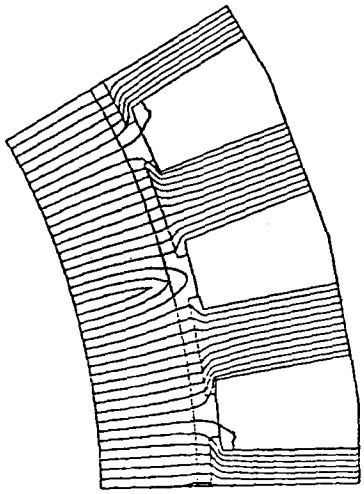

(f) Angular position = 5^o

Fig 6.7 Equi-scalar potential distribution for different angular positions

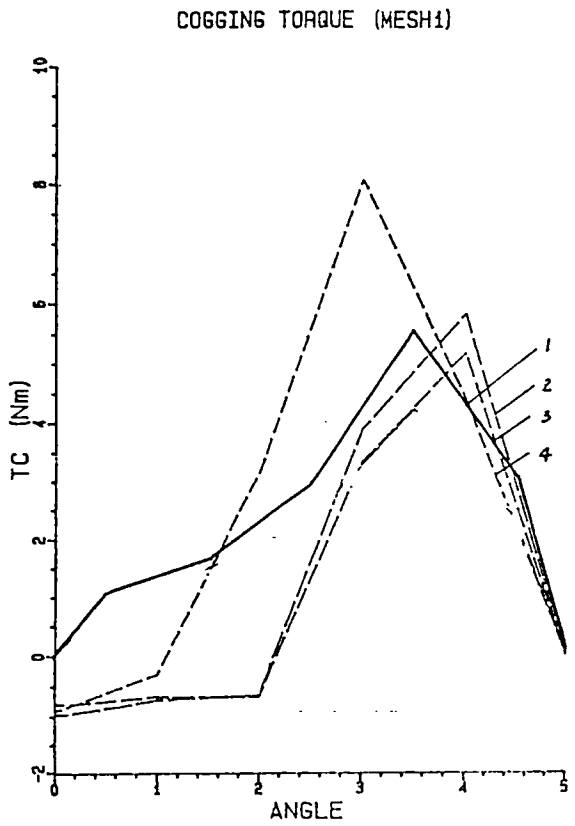

(a) Mesh 1

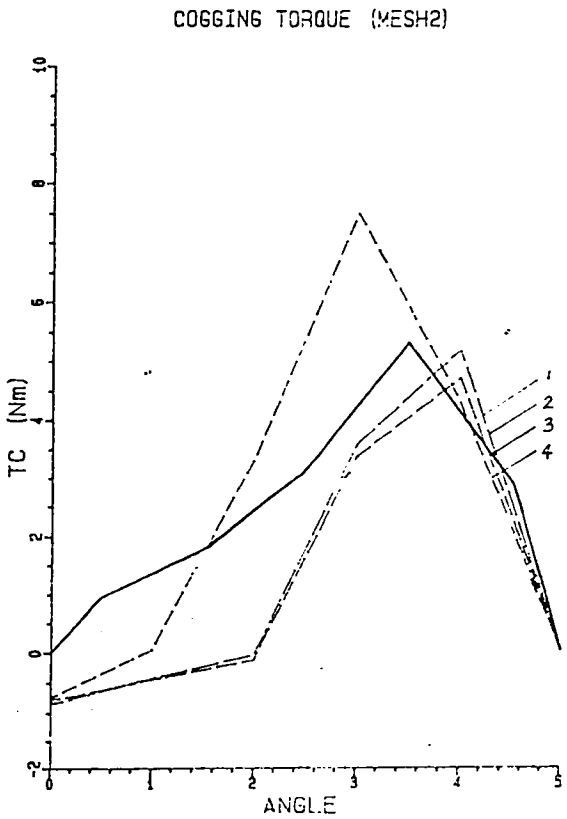

(b) Mesh 2

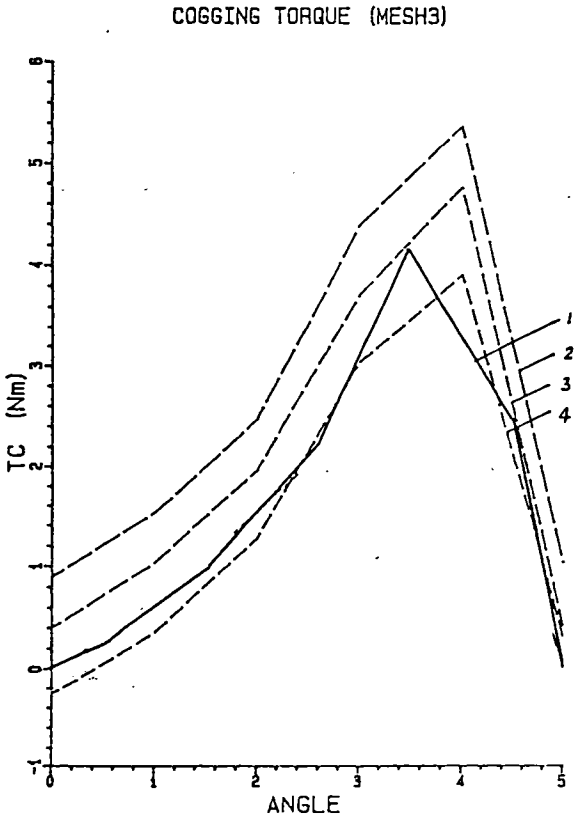

(c) Mesh 3

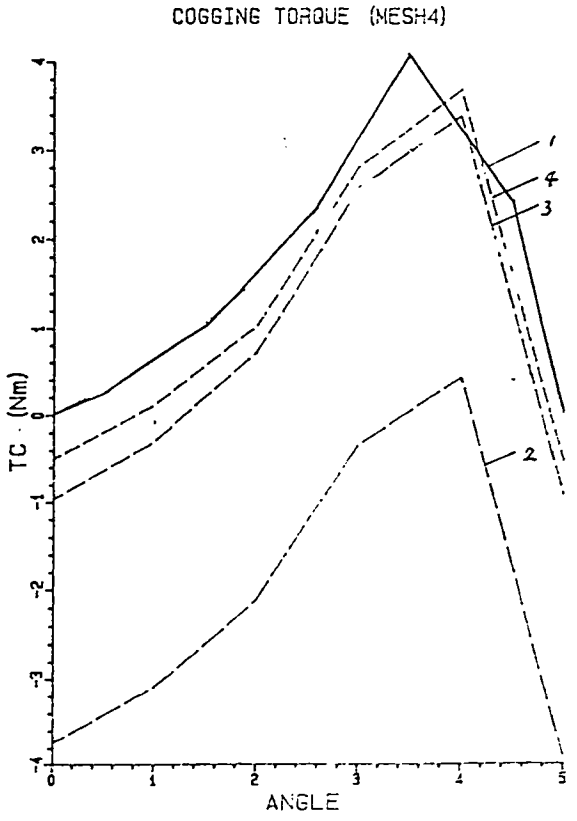

(d) Mesh 4

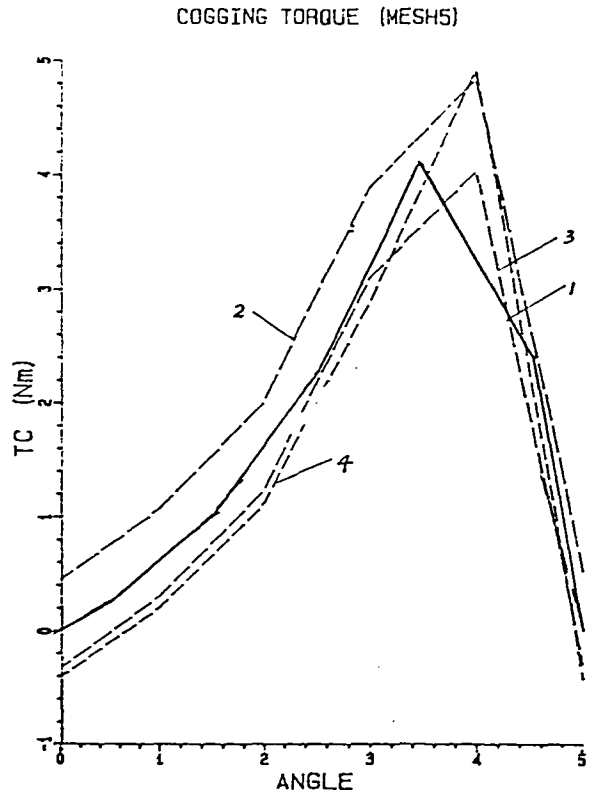

(e) Mesh 5

Fig 6.8 Predicted cogging torque

curve 1: predicted by the energy method
curve 2: predicted by Maxwell stress evaluated for a path through the layer of airgap near magnets
curve 3: predicted by Maxwell stress evaluated for a path through the middle layer of airgap
curve 4: predicted by Maxwell stress evaluated for a path through the layer of airgap near the stator

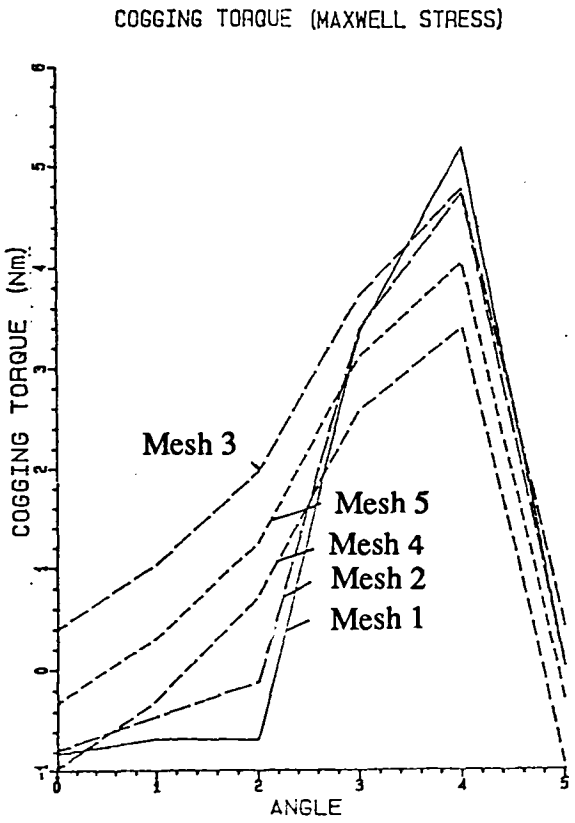

Fig 6.9 Comparison of cogging torque for different meshes by Maxwell stress

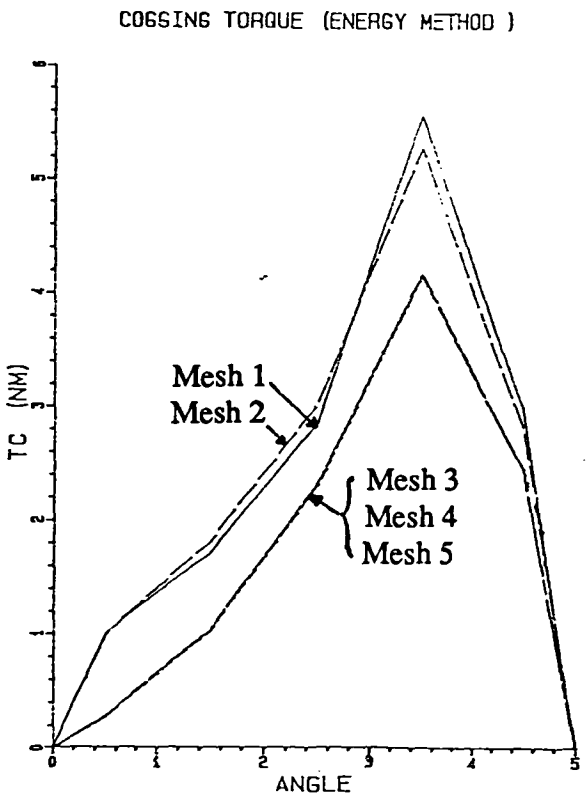

Fig 6.10 Comparison of cogging torque for different meshes by the energy method

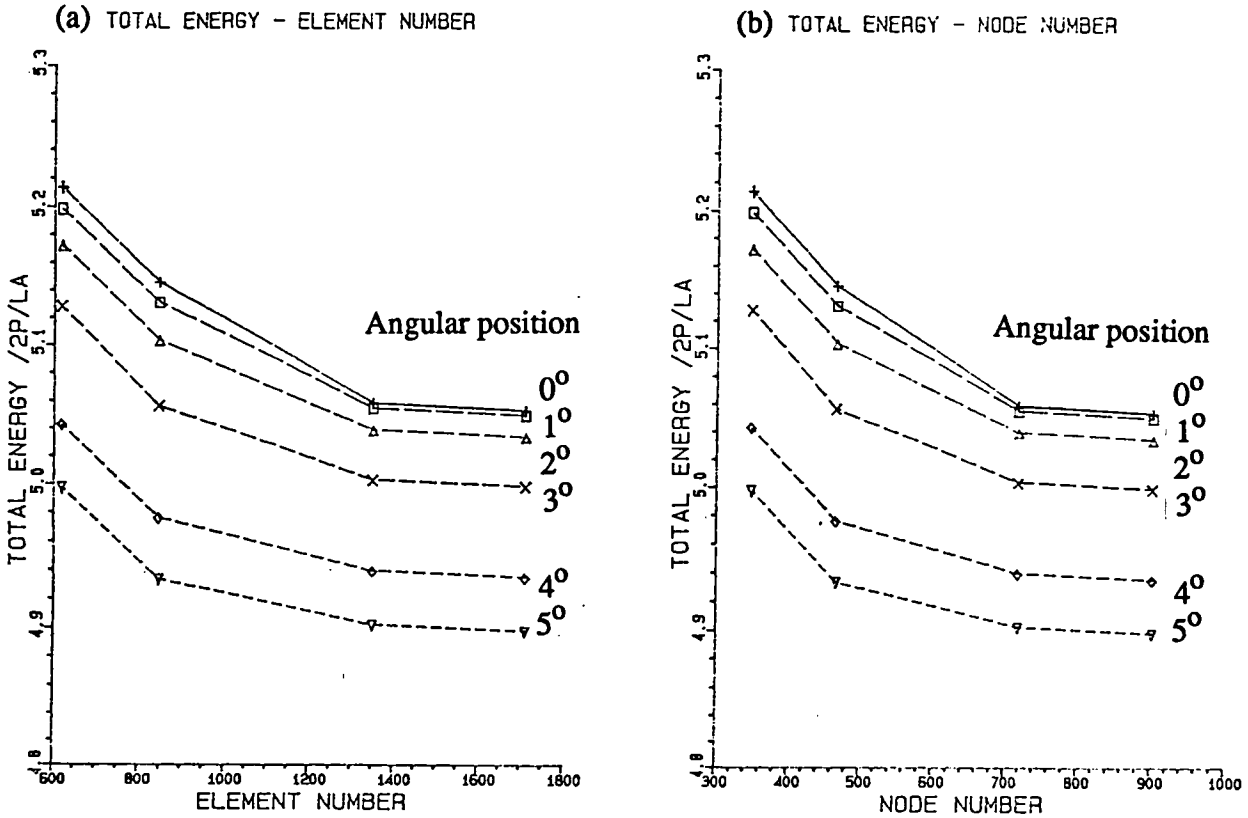

Fig 6.11 Variation of total energy with the number of elementsand nodes for different angular positions
2p is the pole number, l_a is the axial length

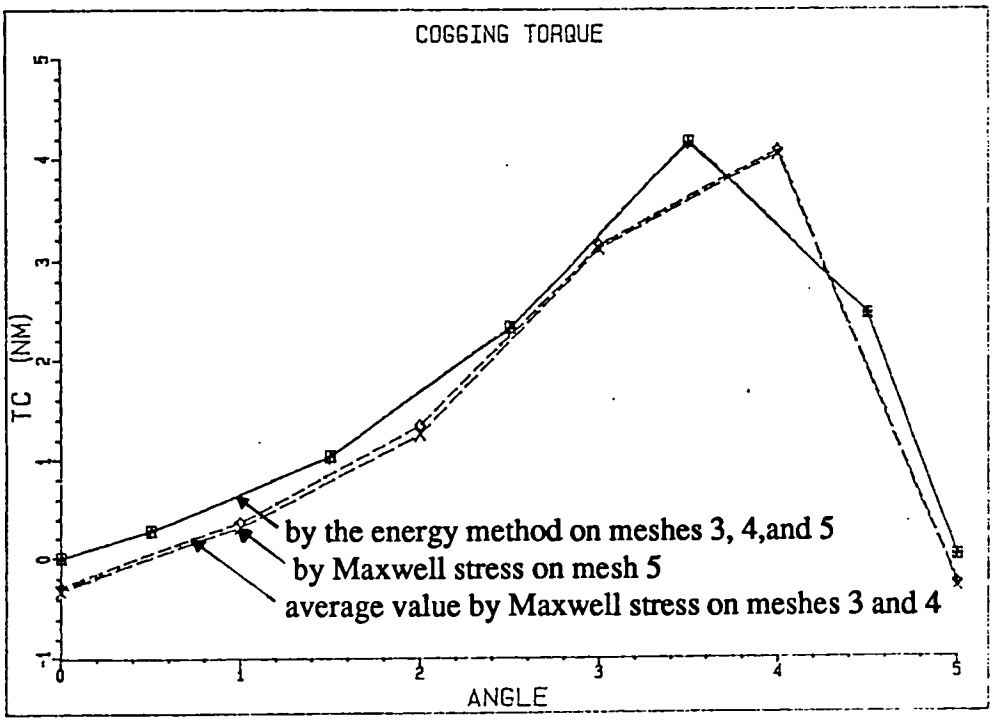

Fig 6.12 Comparison of predicted cogging torque

Table 6.3 Comparison of cogging torque from finite element calculation with Mesh 1 (Nm)

Angular position (degree)	Maxwell stress			Energy method
	Through layer of elements nearest magnet	Through middle of airgap	Through layer of elements nearest stator	
0	-1.000	-0.826	-0.924	0.00
0.5				1.01
1	-0.730	-0.670	-0.304	
1.5				1.72
2	-0.643	-0.689	3.177	
2.5				2.87
3	3.892	3.34	8.07	
3.5				5.57
4	5.836	5.175	4.40	
4.5				2.99
5	0.0032	0.0035	-0.0029	0.00

Table 6.4 Comparison of cogging torque from finite element calculation with Mesh 2 (Nm)

Angular position (degree)	Maxwell stress			Energy method
	Through layer of elements nearest magnet	Through middle of airgap	Through layer of elements nearest stator	
0	-0.853	-0.788	-0.743	0.00
0.5				0.995
1	-0.423	-0.451	0.045	
1.5				1.81
2	-0.038	-0.127	3.34	
2.5				3.03
3	3.588	3.381	7.49	
3.5				5.27
4	5.190	4.71	4.288	
4.5				2.81
5	0.0024	0.0033	-0.0026	0.00

Table 6.5 Comparison of cogging torque from finite element calculation with Mesh 3 (Nm)

Angular position (degree)	Maxwell stress			Energy method
	Through layer of elements nearest magnet	Through middle of airgap	Through layer of elements nearest stator	
0	0.901	0.400	-0.252	0.00
0.5				0.276
1	1.53	1.03	0.357	
1.5				1.035
2	2.47	1.96	1.27	
2.5				2.33
3	4.38	3.71	3.03	
3.5				4.17
4	5.37	4.76	3.91	
4.5				2.45
5	1.02	0.405	0.307	0.00

Table 6.6 Comparison of cogging torque from finite element calculation with Mesh 4 (Nm)

Angular position (degree)	Maxwell stress			Energy method
	Through layer of elements nearest magnet	Through middle of airgap	Through layer of elements nearest stator	
0	-3.74	-0.966	-0.502	0.00
0.5				0.280
1	-3.10	-0.303	0.104	
1.5				1.037
2	-2.12	0.714	1.02	
2.5				2.33
3	-0.348	2.57	2.80	
3.5				4.17
4	0.421	3.39	3.68	
4.5				2.45
5	-3.90	-0.931	-0.539	0.00

Table 6.7 Comparison of cogging torque from finite element calculation with Mesh 5 (Nm)

Angular position (degree)	Maxwell stress			Energy method
	Through layer of elements nearest magnet	Through middle of airgap	Through layer of elements nearest stator	
0	0.455	-0.320	-0.399	0.00
0.5				0.272
1	1.08	0.311	0.211	
1.5				1.023
2	2.03	1.25	1.13	
2.5				2.307
3	3.90	3.11	2.90	
3.5				4.15
4	4.85	4.04	4.93	
4.5				2.45
5	0.522	-0.294	-0.429	0.00

Table 6.8 Energy variation with mesh and angular position

Mesh(node, element)	Energy (J)					
Angular position	0	1	2	3	4	5
Mesh 1 (348,618)	5.21314	5.19770	5.17143	5.12743	5.04222	4.99639
Mesh 2 (466,846)	5.14532	5.13009	5.10246	5.05603	4.97529	4.93232
Mesh 3 (718,1350)	5.05830	5.05408	5.03824	5.00263	4.93884	4.90127
Mesh 4 (718,1350)	5.04437	5.04009	5.02422	4.98858	4.92476	4.88718
Mesh 5 (901,1710)	5.05311	5.04895	5.03329	4.99797	4.93441	4.89690

Table 6.9 Comparison of cogging torque from finite element calculation (Nm)

Angular position (degree)	Energy method			Maxwell stress	
	Mesh 5	Mesh 4	Mesh 3	Mesh 5	(Mesh 3 +Mesh 4)/2
0	0.00	0.00	0.00	-0.320	-0.283
0.5	0.272	0.280	0.276		
1				0.311	0.3635
1.5	1.023	1.037	1.035		
2				1.25	1.337
2.5	2.307	2.33	2.33		
3				3.11	3.14
3.5	4.15	4.17	4.17		
4				4.04	4.075
4.5	2.45	2.45	2.45		
5	0.00	0.00	0.00	-0.294	-0.263

6.5.2 Comparisons

Figs. 6.13 and 6.14 show the comparison of the predicted magnetic field distribution at the stator iron bore for both internal rotor (Motor 1) and external rotor (Motor 2) motors. The predicted results are obtained from either analytical or finite element calculations, whilst in the calculation the stators have been modelled by equivalent slotless topologies as shown in the Figs. 6.13 and 6.14. Furthermore, in the finite element analysis the stator and rotor iron has been modelled by natural Neuman boundary conditions. Hence the effect of saturation has been neglected. It shows that there is excellent agreement between the analytical and the finite element predicted magnetic field distribution produced by the magnets for both motors.

Based on the analytically predicted field distributions, the cogging torque waveform is calculated and compared with that deduced from the finite element analysis, as well as measurement.

6.4.2.1 Internal Rotor Motor

A comparison between the analytically predicted cogging torque variation with rotor position and the results from a finite element calculation for the internal rotor Motor 1 is shown in Fig

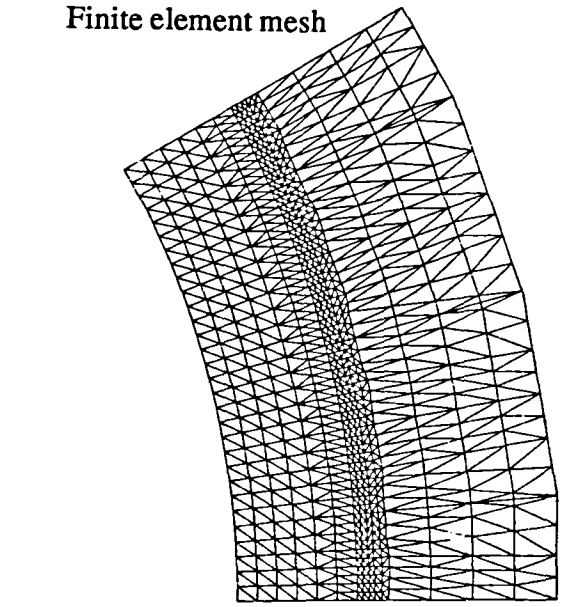

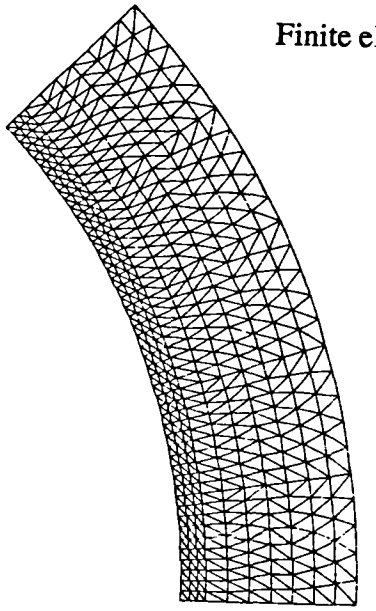

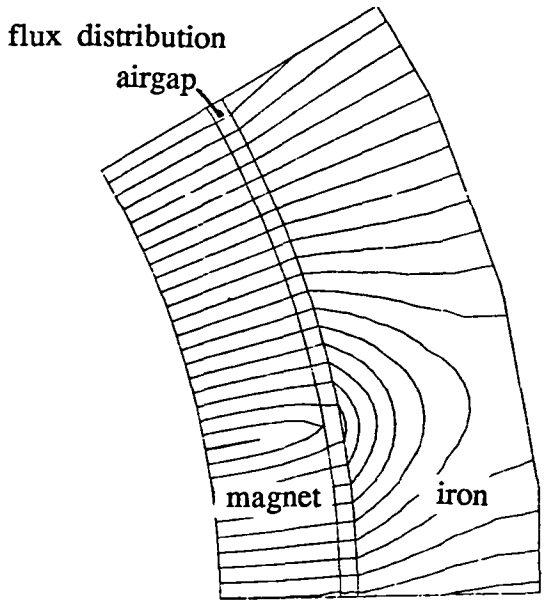

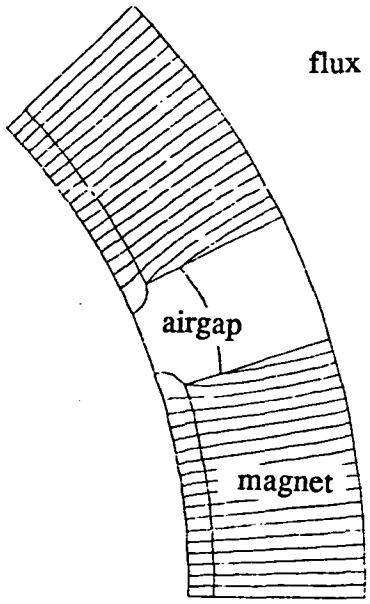

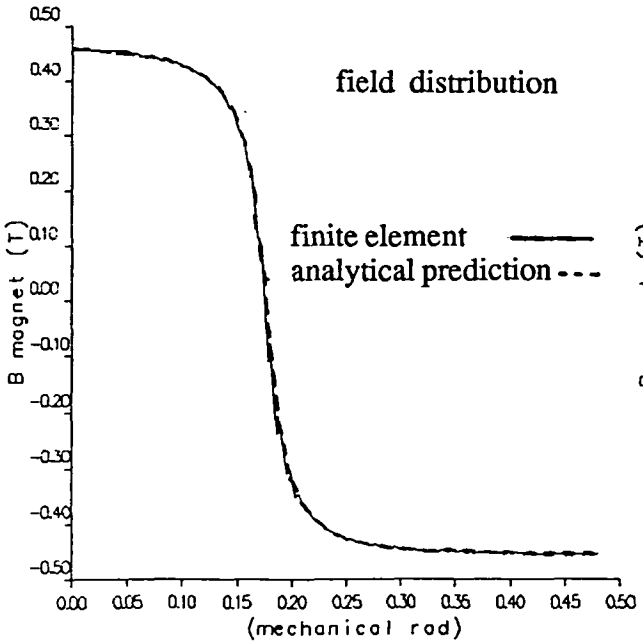

Fig 6.13 Comparison of field distribution at the stator iron bore for internal rotor motor

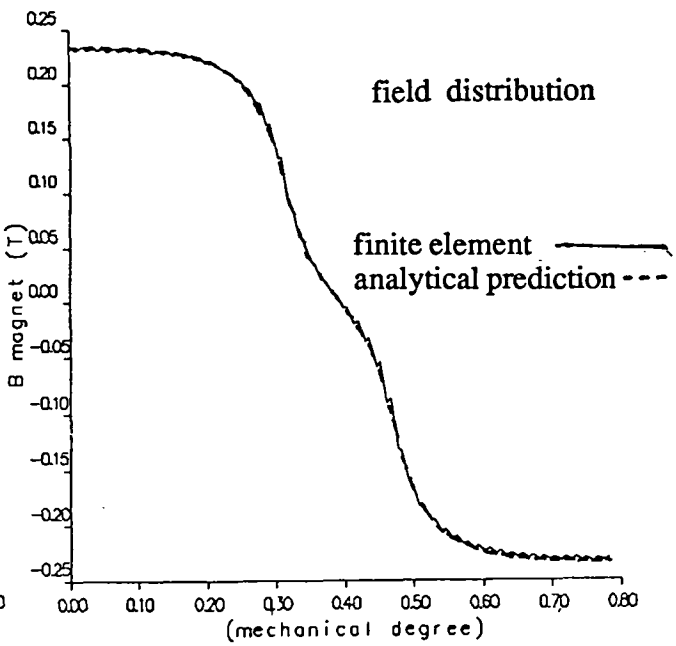

Fig 6.14 Comparison of field distribution at the stator iron bore for external rotor motor

6.15. The finite element results are based on Mesh 3 and calculated by the energy method, and hence are considered to be of high reliability. However in order to obtain the peak value of the cogging torque more points on the cogging torque waveform in Fig 6.13 than those in Fig 6.12 have been calculated.

The prediction of cogging torque by the proposed method is considered good enough to allow the variation of the peak value with the machine design parameters to be established. Also it is worth restating that traditional analytical models based on the energy method would have failed since the predicted cogging torque would be zero when the pole-arc to pole-pitch ratio is unity as was the case in this prototype.

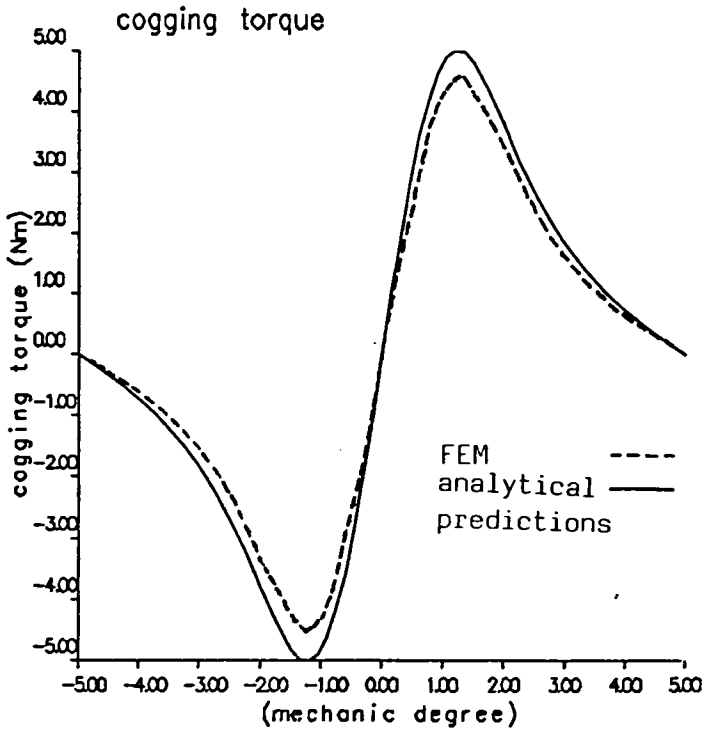

Fig 6.15 Comparison of predicted cogging torque waveforms forinternalrotor motor No 1

6.4.2.2 External Rotor Motor

Comparisons for Motor 2 are shown in Fig 6.16 and Table 6.10 where the measured and finite element predicted results are taken from [6.1]. As can be seen, the fundamental (ie 24th harmonic) component of the cogging torque is a minimum for a particular slot-opening, which by the technique proposed is when $\alpha = 0.647$, ie $b_o = 4.9$mm, which is in excellent agreement with both the measured and finite element results. However for this condition the 48th harmonic attains a negative maximum (see Fig 8 in [6.1]), so that the cogging torque is not actually zero but a small value. For convenience, subsequent results predicted by the technique are the resultant peak values of cogging torque, ie the resultant of all harmonics, and its first two harmonic components, as shown in Table 6.10. However in Fig 6.16 the variation of the peak value of the cogging torque waveforms with the slot openings is plotted only for the fundamental component (ie 24th harmonic). When $\alpha = 0.568$ and $\alpha = 0.647$ the resultant cogging torque is dominated by the 24th and 48th harmonic components respectively, and when $\alpha = 0.683$ it is the resultant of two harmonic components, whilst as far as the 24th harmonic component is concerned, the waveform for $\alpha = 0.712$ is in anti-phase to that for $\alpha = 0.524$, which is indicated by their signs.

In Fig 6.16 the predicted peak value of cogging torque deviated more from the measured results and the finite element predictions as the slot-opening was increased. This may be caused by the finite height of the teeth which in the analytical model are assumed to be longer than half the slot-opening. However as the slot-opening is increased this assumption may no longer be valid, and modifications may be necessary. For example, the permeance given by equation (6.7a) could be modified to:

$$\lambda = \begin{cases} \dfrac{\mu_o}{g + \dfrac{h_m}{\mu_R} + \dfrac{2\pi r_s}{4}} & \text{for and } (k-1)\tau_t + \dfrac{b_o}{2} \le x_i \le (k-1)\tau_t + \dfrac{b_o}{2} + h_{tt} \\ & \qquad\quad (k-1)\tau_t + \dfrac{b_o}{2} - h_{tt} \le x_i \le (k-1)\tau_t + \dfrac{b_o}{2} \\ 0 & \text{for } (k-1)\tau_t - \dfrac{b_o}{2} + h_{tt} \le x_i \le (k-1)\tau_t + \dfrac{b_o}{2} - h_{tt} \end{cases} \tag{6.23}$$

where h_{tt} is the height of a tooth tip. For this prototype motor the height of tooth tips depends on the slot opening, as shown in Fig 6.17. Table 6.10 also shows the predicted results when the modifications are made according to equation (6.23) in which h_{tt} is determined by equation (6.24).

Table 6.10 Variation of cogging torque with slot opening predicted for prototype motor 2

α	slot opening	before modification			height of tooth tip	after modification		
		peak value of cogging torque	24th harmonic	48th harmonic		peak value of cogging torque	24th harmonic	48th harmonic
$(1-b_o/\tau_t)$	b_o (mm)	(mNm)	(mNm)	(mNm)	h_{tt}(mm)	(mNm)	(mNm)	(mNm)
0.712	4.0	0.71	0.70	0.008	1.53	0.63	0.61	0.054
0.697	4.2	0.59	0.57	-0.05	1.57	0.46	0.45	-0.006
0.683	4.4	0.48	0.42	-0.11	1.61	0.3	0.27	-0.041
0.668	4.6	0.37	0.26	-0.16	1.65	0.15	0.08	-0.08
0.654	4.8	0.26	0.09	-0.19	1.68	0.19	-0.096	-0.11
0.64	5.0	0.26	-0.08	-0.20	1.72	0.36	-0.3	-0.12
0.625	5.2	0.38	-0.24	-0.19	1.75	0.55	-0.5	-0.11
0.611	5.4	0.48	-0.39	-0.16	1.78	0.69	-0.67	-0.08
0.6	5.6	0.58	-0.53	-0.12	1.82	0.86	-0.85	-0.043
0.582	5.8	0.66	-0.64	-0.059	1.85	1.02	-1.01	-0.004
0.568	6.0	0.74	-0.73	0.004	1.88	1.12	-1.11	0.006
0.553	6.2	0.81	-0.79	0.062	1.91	1.23	-1.21	0.101
0.539	6.4	0.85	-0.83	0.11	1.93	1.28	-1.25	0.141
0.524	6.6	0.88	-0.83	0.14	1.96	1.33	-1.28	0.15
0.51	6.8	0.86	-0.8	0.15	1.99	1.3	-1.25	0.15
0.496	7.0	0.79	-0.74	0.13	2.01	1.24	-1.21	0.12
0.481	7.2	0.67	-0.65	0.096	2.03	1.13	-1.11	0.077

$$h_{tt} = R_i - \sqrt{x_o^2 + \tfrac{1}{3}(x_o - b_o)^2} \qquad (6.24)$$

where x_o= 11mm.

Clearly when the slot openings are large such effect is very significant and the finer modification is necessary in order to achieve more accurate peak values.

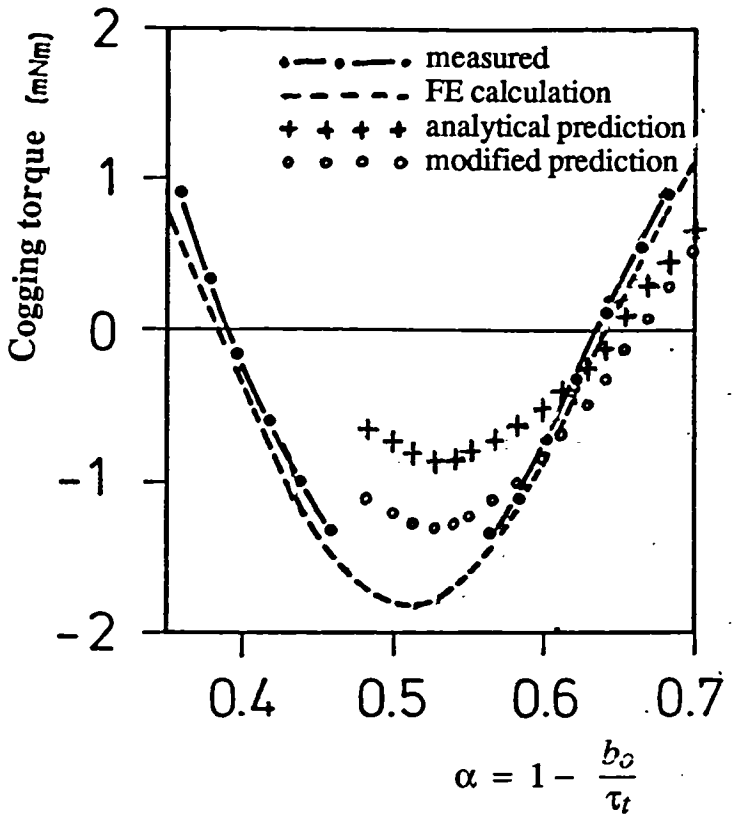

Fig 6.16 Comparison of variation of peak value of cogging torque with slot opening

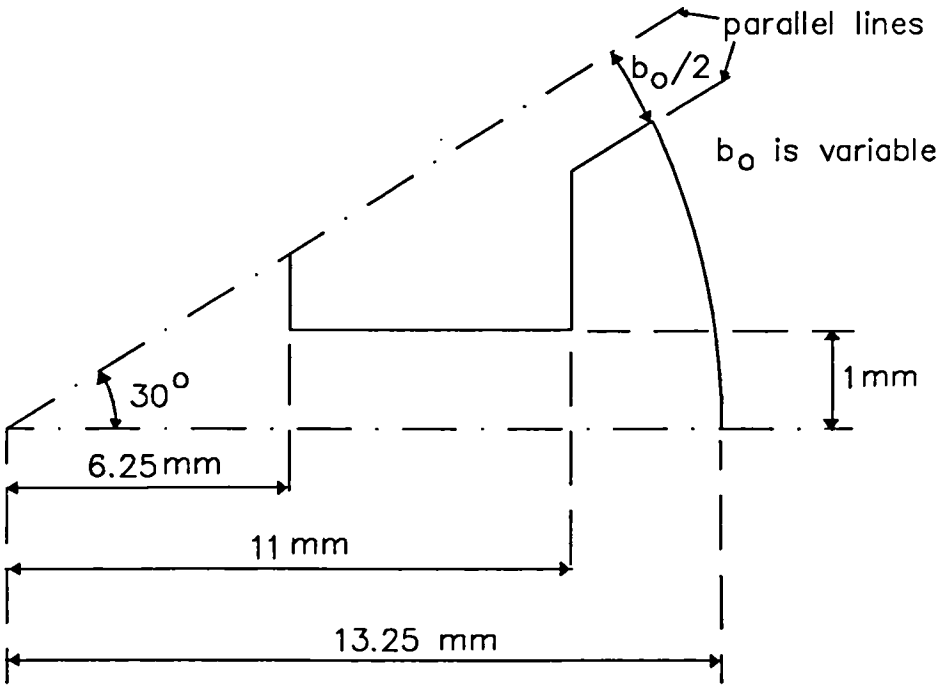

Fig 6.17 Tooth geometry of external rotor motor

Based on the developed analytical model, the effects of the leading design parameters on the cogging torque can be investigated to establish the general rules for minimising the cogging torque to aid the optimum multi-dimensional selection of an appropriate combination of slot number and pole number, auxiliary slots and teeth, slot openings, magnet pole-arc to pole pitch ratio, angle of skew of magnet and/or slots, magnet shift, distribution of slots etc., and hence enable low cogging torque motors to be designed.

Using the basic parameters of the external rotor motor (Motor 2), typical results are shown in Figs 6.18 and 6.19. Fig 6.18 shows the variation of the peak value of the cogging torque with pole-arc to pole-pitch ratio for different combinations of stator slot number and magnet pole number, viz Q_s /2p = 9/8, 6/8, 12/8, and 12/4, whilst Fig 6.19 shows the variation of the peak value of the cogging torque with the slot opening for different pole-arc to pole-pitch ratios, viz α_p = 1.0, 0.8, and 0.7925 when the slot number/pole number is Q_s /2p = 9/8.

6.5 Conclusions

An analytical method for predicting the cogging torque based on the calculation of the field distribution and the lateral forces which act on the stator teeth has been developed and partially validated.

The technique offers acceptable accuracy when predicting the peak value of the cogging torque and its variation with design parameters. It remains valid even when the pole-arc to pole-pitch ratio is unity, which was not the case for existing analytical methods based on the calculation of energy. The technique can cater for both internal and external rotor motors, modelled in either rectangular or cylindrical coordinate systems, and with motor topologies in which the magnets are shifted or the stator have unevenly distributed slots etc.

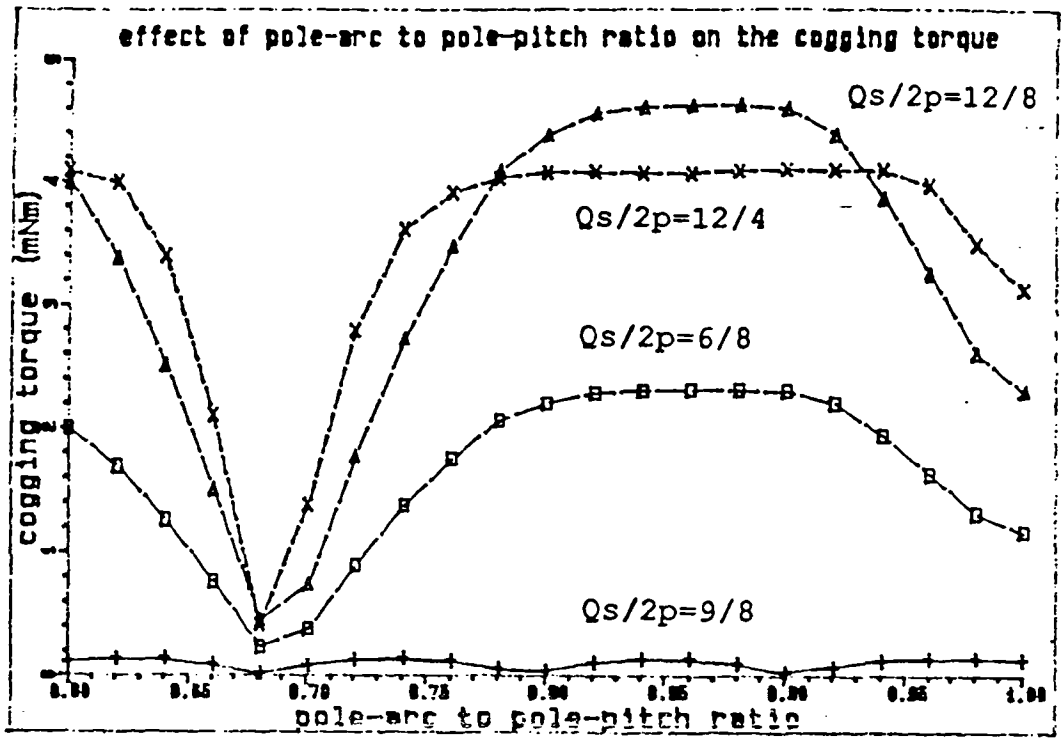

Fig 6.18 Variation of peak value of cogging torque with pole-arc to pole-pitch ratio for different combinations of stator slot number and magnet pole number

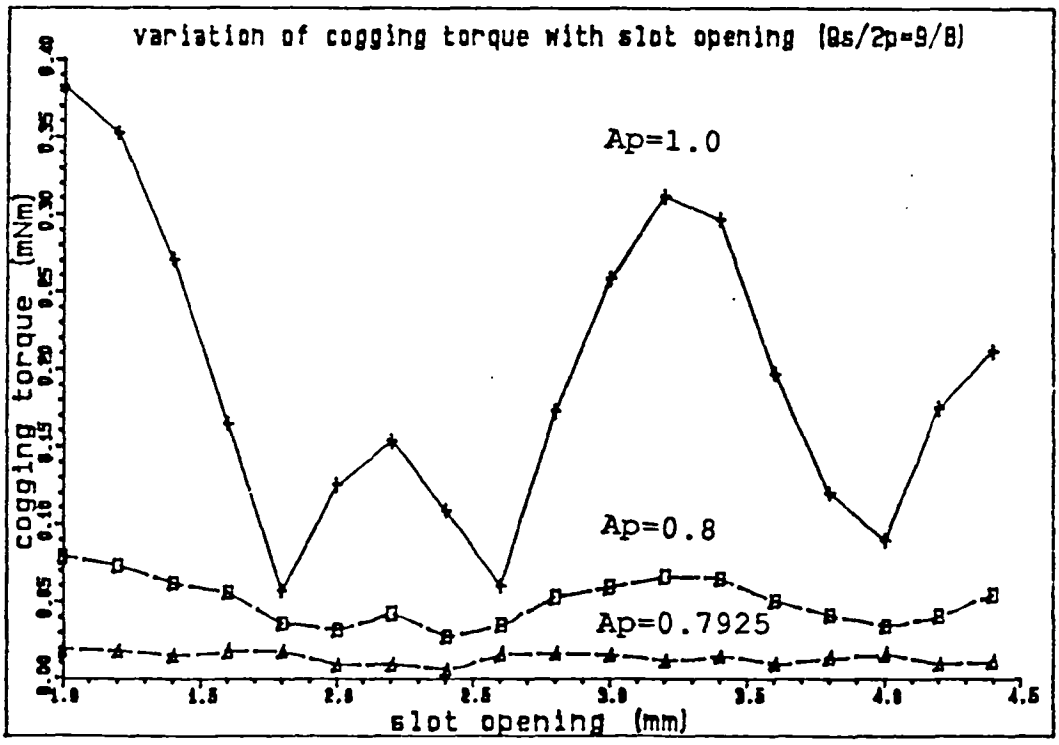

Fig 6.19 Variation of peak value of cogging torque with slot openings for different pole-arc to pole-pitch ratios

6.6 Appendix -Torque Calculation by the Energy Method

Electromagnetic force or torque can be calculated in a variety ways, such as the Maxwell stress method [6.10], the energy method [6.11], and the virtual work method [6.12][6.13][6.15]. However, they require accurate field solutions, and thus a high level of mesh discretisation, since force or torque is dependent upon local field quantities. In this appendix, however, only the energy method is described since its application to permanent magnet machines is somewhat different from that for wound field machines .

In order to calculate the torque at a particular rotor position the method requires that accurate field solutions be calculated for two different rotor positions, displaced by an incremental angle. Therefore the technique is demanding on computing time, and may also suffer from cancellation problems since it relies on the difference between quantities of nearly equal magnitude. However this disadvantage can be overcome by employing the virtual work method [6.13][6.14][6.15] in which the spatial derivative of energy is pre-deduced in formulating the finite element equations and therefore only a single field calculation is required for each force (torque) calculation.

6.6.1 Torque Produced in an Electromagnetic device

By conservation of energy the total system energy change due to an angular displacement can be expressed as:

$$\Delta E_{elec} = \Delta E_{stored} + \Delta E_{mech} \tag{6.25}$$

viz, a variation of the electrical input energy will cause a variation of the stored magnetic energy, and at the same time result in mechanical work given by the product of torque and angular displacement.

In a permanent magnet device, such as a brushless DC motor, the input energy is the electrical energy supplied to the windings from the power supply, whilst the magnetic energy is stored in

(i) Non-magnetic regions, such as air and copper;

(ii)Soft-magnetic regions, viz iron;

(iii)Permanent magnet regions.

Therefore

$$\Delta E_{stored} = \Delta (E_{air} + E_{iron} + E_{magnet}) \tag{6.26}$$

$$\Delta E_{mech} = T \Delta \theta \tag{6.27}$$

Hence the torque produced is given by

$$T = \frac{-1}{\Delta \theta} (\Delta E_{stored} - \Delta E_{elec}) \tag{6.28}$$

6.6.2 Energy Stored in a Magnetic Field

In general the energy stored in a magnetic field can be calculated by:

$$E = \int w \, dv \tag{6.29}$$

$$w = energy / unit\ volume = \int_0^B H \, dB \tag{6.30}$$

which is calculated according to the material properties, viz:

(i) Non-magnetic region

As shown in Fig.6.20a, since B= μ_o H, equation (6.30) becomes

$$w_{air} = \frac{B^2}{2 \mu_o} \tag{6.31}$$

(ii) Soft magnetic region

By modelling the magnetisation characteristic by the function

$$B = \mu_o H + s_1 \arctan (a_1 H) + s_2 \arctan (a_2 H) \tag{6.32}$$

where s1,s2,a1, and a2 are constants for a specific material.

the energy can be calculated according to Fig.6.20b:

$$Energy\ stored = BH - Coenergy\ stored \tag{6.33}$$

and

$$Coenergy = \int_0^H B\, dH = \mu_o \frac{H^2}{2} + H s_1 \arctan (a_1 H) - \frac{s_1}{2 a_1} \ln [1 + (a_1 H)^2]$$
$$+ H s_2 \arctan (a_2 H) - \frac{s_2}{2 a_2} \ln [1 + (a_2 H)^2] \tag{6.34}$$

$$\text{Therefore } w_{iron} = BH - \int_0^H B\, dH \tag{6.35}$$

(iii) Permanent magnet region

Assuming a linear demagnetisation characteristic as shown in Fig.6.20c, then

$$\int_B^{B_R} H\, dB = \frac{(B_R - B)}{2} H = \frac{(B_R - B)^2}{2 \mu_o \mu_R} \tag{6.36}$$

In the finite element calculation the stored energy produced can be considered to be associated with the components of B which are parallel and perpendicular to the magnetisation direction, B_{par} and B_{per} separately, ie. the energy associated with B_{par} is calculated by the above equation, whilst the energy associated with B_{per} by treating the magnet as equivalent to the air. Therefore the total stored energy is given by:

$$w_{magnet} = \frac{1}{2 \mu_o \mu_{par}} \left(B_R - B_{par} \right)^2 + \frac{1}{2 \mu_o \mu_{per}} B_{per}^2 \tag{6.37}$$

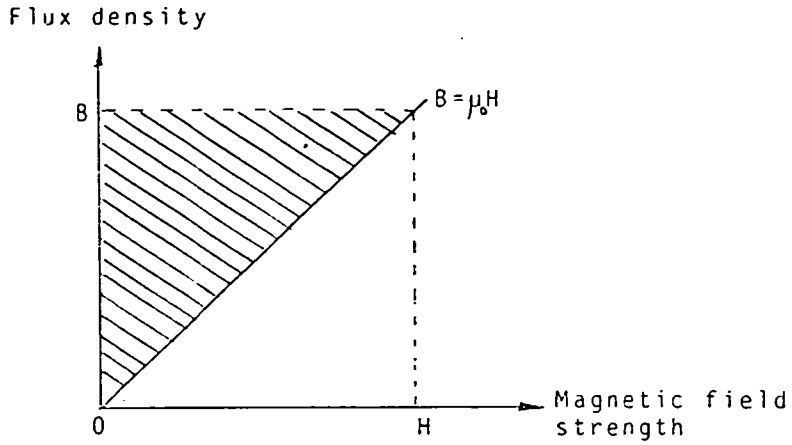

(a) Non-magnetic region

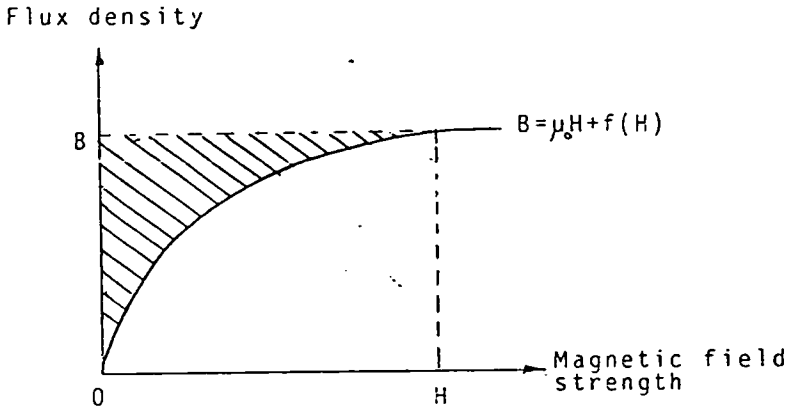

(b) Soft magnetic region

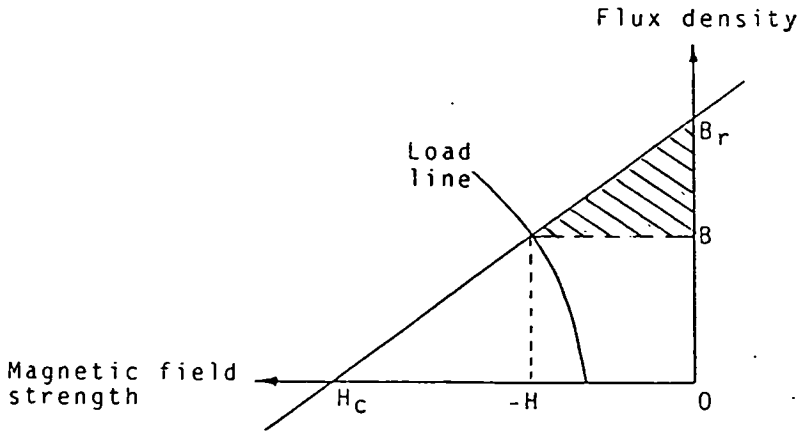

(c) Permanent magnet region

Fig.6.20 Energy calculation

where μ_{par} and μ_{per} are the relative permeabilities parallel and perpendicular to the magnetisation direction and can be approximated by

$$\mu_{par} = \mu_R , \quad \mu_{per} = \mu_o \tag{6.38}$$

6.6.3 Input Electrical Energy

The unit volume input electrical energy corresponding to any rotor position is given by

$$E_{elec} = \int J \,.\, A \, dv \tag{6.39}$$

where J is the specified current density, and A is the vector magnetic potential. However in the calculation of the cogging torque the current density is set as zero.

CHAPTER 7

ANALYTICAL SIMULATION OF DYNAMIC PERFORMANCE OF BRUSHLESS DC DRIVES

7.1. Introduction

The increasing prominance of permanent magnet excited machine drive systems for motion control applications in all market sectors reflects not only the significant improvement in material properties which has occured in recent years, with the tantalising design possibilities which this offers, but also a developing capability in both power and integrated electronics, which is being utilised to control drives for equipment varying in sophistication from machine tools to domestic fans and the like. Of the various permanent magnet machine formats which have evolved it is the brushless dc motor which is the most important emerging category since it offers good reliability and controllability as well as a choice of topologies to suit the size and shape of product for which it provides the drive, such as disc drives and spindle drives for computers and VCR's etc. Many of its applications are extremely sensitive in respect of the permitted levels of speed pulsation and acoustic noise.

However, although the elimination of the commutator has reduced the mechanical noise, the non-sinusoidal phase current waveforms have tended to increase the electromagnetic noise. Furthermore significant torque ripples may result from commutation events as well as cogging etc, which in turn will induce tangential vibrations. Therefore, it is often important to predetermine the dynamic characteristics of the drive system, embracing not only the motor and its load but also the electronic converter and control system, to ensure that a given design can produce the required performance over a wide range of operating conditions. In this respect the effects of winding inductances, as well as other parasitic influences, which may cause the torque-speed characteristic of a drive to deviate substantially from the idealised linear form, as

well as giving rise to unacceptable torque ripple and affecting performance factors such as dynamic response and speed range, may be significant.

Several methods for predicting the dynamic steady-state performance of permanent magnet brushless DC drives have been developed. However, truly numerical methods, despite allowing a high degree of refinement in the system model [7.1], tend to be rather time-consuming and hence unsuitable for routine use as part of an iterative design procedure. In this respect the approaches that have been most successful exploit the symmetry of the machine and its drive inverter, and hence the symmetric waveforms that describe the electrical variables. Such a technique was used initially for analysing the steady-state performance of a triac-controlled single-phase induction motor [7.2]. Subsequently the technique was extended to the analysis of the steady-state performance of three-phase induction motors with voltage control by symmetrically triggered thyristors [7.3], and more recently the technique has been applied to the analysis of permanent magnet brushless DC motors [7.4][7.5]. However previous analyses assumed either sinusoidal [7.4] or trapezoidal [7.5] back-emf waveforms in the stator windings. In practice the actual induced emf will depart more or less from these idealised waveforms, which may, as a consequence, introduce errors - especially in the prediction of torque ripple or when the merits of advanced or retarded commutation are being considered.

In this chapter the technique is also applied to the analysis of permanent magnet brushless DC drives, but it is developed further so that it can account for any induced back-emf waveform. Therefore because it remains based on an analytical model, for which the initial conditions which yield the steady-state solution are generated directly by exploiting the periodicity in the stator winding current waveforms, it provides a rapid means of assessing the important features of motor and drive performance during the early stages of design.

The model includes the following features:

(i) It can account for any induced back-emf waveform.

(ii) The switching devices and freewheel diodes in the inverter drive circuit are represented as an appropriate constant voltage drop behind a series resistance.

(iii) It can cater for normal, advanced, or retarded commutation.

(iv) It can impose a pre-specified current limit.

In addition, the analytical electromagnetic circuit equations can be combined with the motion equation of the rotor. Consequently, a numerical model, i.e., a state-variable model, for predicting the transient and steady-state dynamic performance of 3-phase star-connected brushless DC drives is developed. The converter drive circuit is idealised into two states, according to whether the freewheel diode is conducting or not. These are ALWAYS described by two FIXED groups of state equations for both transient and steady-state dynamic operation. Then the dynamic performance is obtained by introducing the relationship between the state variables and the stator winding currents.

The analysis is validated against measurements on an axial-field, three-phase, 12-pole permanent magnet brushless DC motor, and two prototype radial-field, internal rotor, three-phase, four-pole permanent magnet brushless DC motors. One of the stators has an overlapping stator winding whilst the other has a non-overlapping stator winding. Comparisons are made with predictions from the different models which are developed. The effects of commutation and winding temperature (resistance) on the dynamic performance are investigated, and the integration of the developed model into a more sophisticated system simulation package is then indicated.

7.2. System Model and its Symmetry

Fig 7.1 shows a 3-phase star-connected brushless DC motor together with its bipolar drive, which consists of a transistor bridge inverter with freewheel diodes. Commutation logic ensures that the phase currents are switched in synchronism with the rotor position so as to maintain an average load angle of 90^{o}elec. under normal commutation.

In the ensuing analysis it is assumed that:

(i) The system is operating under a steady-state condition, and moreover that the rotor speed is constant, ie. the motor plus its load present a sufficiently high mechanical time constant such that any torque ripple produces negligible speed fluctuation.

(ii) The six transistors T1 - T6 have identical idealised characteristics, and are switched symmetrically. In the non-conducting state they are modelled as an infinite impedance whilst in the conducting state they are represented by a fixed voltage drop behind a series resistance. Similar assumptions have been made for the freewheel diodes D1 - D6.

(iii) The 3-phase permanent magnet excited motor is entirely symmetric and produces periodic induced back-emf waveforms.

(iv) The parameters of the motor are assumed to be constant, ie. saturation and thermal effects are neglected.

A typical stator phase winding current waveform is illustrated in Fig 7.2.

If the commutation timing is assumed to be spaced correctly by 60^{o}elec, then the current waveform has a symmetrical pattern consisting of three intervals per half-cycle, each interval being sub-divided into two periods whose relative length is determined by the conduction time for a given freewheel diode, as summarised in Table 7.1 and Fig 7.3.

Period 1a ($-\frac{\pi}{6} \leq \theta \leq \theta_1$), when the freewheel diode is conducting. θ_1 is the instant when the freewheel diode switches from a conducting to a blocking state, whilst ($\frac{\pi}{6} + \theta_1$) is the conducting time of the diode. During this period all three phase windings of the stator carry current since there are two distinct paths for current to circulate, as shown in Fig 7.3. The main path is from the power supply and through two phase windings via two transistors, whilst the other is through one of the two windings and the third phase winding, via a transistor and diode.

Period 1b ($\theta_1 \leq \theta \leq \frac{\pi}{6}$), when the freewheel diode is blocking. At the instant θ_1 the circulating current through the diode becomes zero. During this period the only current path is through the two phase windings which are connected to the power supply via two transistors.

Because of symmetry in the waveform only one interval $-\frac{\pi}{6} \leq \theta \leq \frac{\pi}{6}$ (and hence two periods Δ_1 and Δ_2) needs to be analysed, the waveform for each phase then being constructed by a suitable time displacement.

For example, with reference to Fig 7.2:

a) The current of phase A in intervals 4, 5 and 6 is in antiphase to that in intervals 1, 2 and 3.

b) The time periods for intervals 1a, 2a and 3a are the same, viz $\Delta_1 = \frac{\pi}{6} + \theta_1$, and similarly for intervals 1b, 2b and 3b, viz $\Delta_2 = \frac{\pi}{6} - \theta_1$.

c) The value of the current in period 1b is the same as that in period 2b.

d) The value of the current in period 2a is the sum of the currents in periods 1a and 3a.

In summary, in order to obtain the entire current waveform only one sixth of a full cycle, ie., $-\frac{\pi}{6} \leq \theta \leq \frac{\pi}{6}$, needs to be analysed, for which the most important parameters to determine are:

a) the initial value of the current in a phase which is being commutated off at the instant that another phase is being commutated on, eg. with respect to Fig 7.3, the value of i_c at $\theta = -\frac{\pi}{6}$, ie. i_{co} when $i_{ao} = 0$ and $i_{bo} = - i_{co}$.

b) the conducting time ($\theta_1 + \frac{\pi}{6}$) of the freewheel diodes during the commutation process. With respect to Fig 7.3, eg. the conducting time of D_6 as current is commutated from phase C to phase A.

Table 7.1 Commutation period and features

Interval No	Period	Transistors conducting	Diode conducting	Winding conducting	Conditions	Terminal current
1a	$(-\frac{\pi}{6}, \theta_1)$	T_1 T_5	D_6	ABC	$\theta = -\frac{\pi}{6}$, $i_a=0$	$i_t = i_a$
					$\theta = \theta_1$, $i_c=0$	
1b	$(\theta_1, \frac{\pi}{6})$	T_1 T_5	/	AB	$i_c = 0$	$i_t = i_a$
2a	$(\frac{\pi}{6}, \frac{\pi}{6} + \Delta 1)$	T_1 T_6	D_5	ACB	$\theta = \frac{\pi}{6}$, $i_c = 0$	$i_t = - i_c$
					$\theta = \frac{\pi}{6} + \Delta 1$, $i_b = 0$	
2b	$(\frac{\pi}{6} + \Delta 1, \frac{\pi}{2})$	T_1 T_6	/	AC	$i_b = 0$	$i_t = - i_c$
3a	$(\frac{\pi}{2}, \frac{\pi}{2} + \Delta 1)$	T_2 T_6	D_4	BCA	$\theta = \frac{\pi}{2}$, $i_b = 0$	
					$\theta = \frac{\pi}{2} + \Delta 1$, $i_a = 0$	$i_t = i_b$
3b	$(\frac{\pi}{2} + \Delta 1, \frac{5\pi}{6})$	T_2 T_6	/	BC	$i_a = 0$	$i_t = i_b$
4a	$(\frac{5\pi}{6}, \frac{5\pi}{6} + \Delta 1)$	T_2 T_4	D_3	BAC	$\theta = \frac{5\pi}{6}$, $i_a = 0$	$i_t = - i_a$
					$\theta = \frac{5\pi}{6} + \Delta 1$, $i_c = 0$	
4b	$(\frac{5\pi}{6} + \Delta 1, \frac{7\pi}{6})$	T_2 T_4	/	BA	$i_c = 0$	$i_t = - i_a$
5a	$(\frac{7\pi}{6}, \frac{7\pi}{6} + \Delta 1)$	T_3 T_4	D_2	CAB	$\theta = \frac{7\pi}{6}$, $i_c = 0$	$i_t = i_c$
					$\theta = \frac{7\pi}{6} + \Delta 1$, $i_b = 0$	
5b	$(\frac{7\pi}{6} + \Delta 1, \frac{3\pi}{2})$	T_3 T_4	/	CA	$i_b = 0$	$i_t = i_c$
6a	$(\frac{3\pi}{2}, \frac{3\pi}{2} + \Delta 1)$	T_3 T_5	D_1	CBA	$\theta = \frac{3\pi}{2}$, $i_b = 0$	$i_t = - i_b$
					$\theta = \frac{3\pi}{2} + \Delta 1$, $i_a = 0$	
6b	$(\frac{3\pi}{2} + \Delta 1, \frac{11\pi}{6})$	T_3 T_5	/	CB	$i_a = 0$	$i_t = - i_b$

Note : $\Delta 1 = \pi/6 + \theta_1 \therefore \Delta 2 = \pi/3 - \Delta 1$

where θ_1 is the position at which the diode is switched from conducting to being blocked. θ_1 is assumed less than $\pi/6$, which is normal for brushless DC motors. However if $\theta > \pi/6$, then states "b" will not exist and the upper limit of states "a" should be replaced by the upper limit of states "b", eg. in interval 1, state 'a' would exist for the whole period $-\pi/6$ to $+\pi/6$.

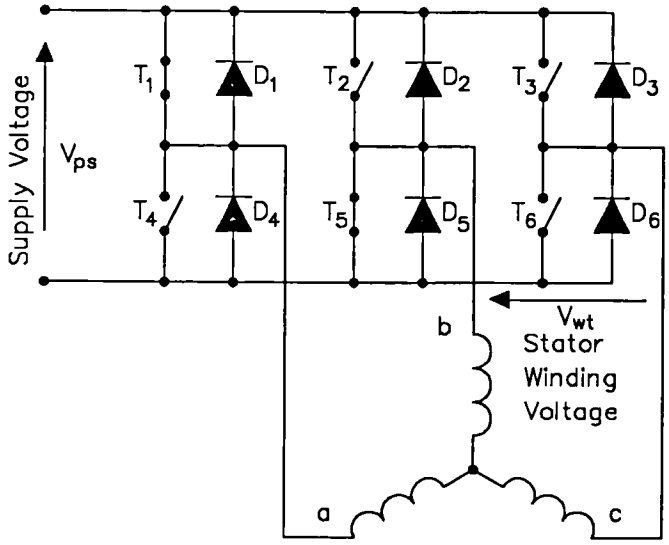

Fig 7.1 Basic elements of brushless DC drive system

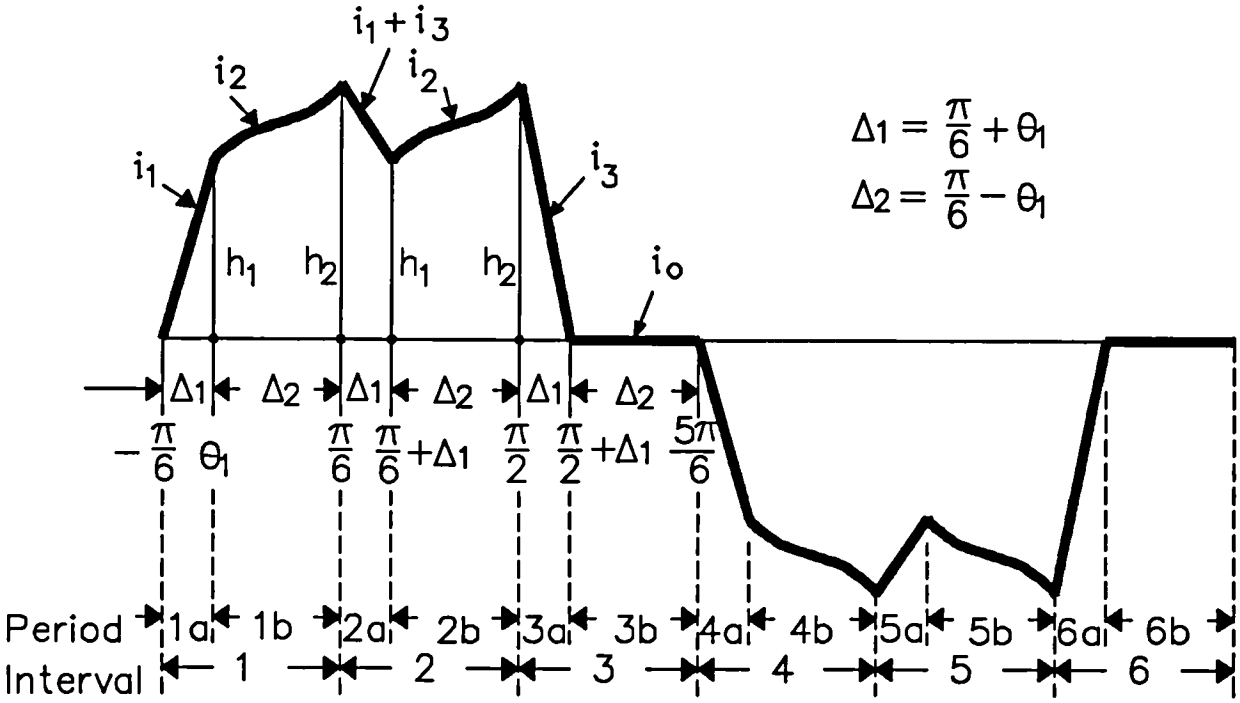

Fig 7.2 Typical stator winding phase current waveform

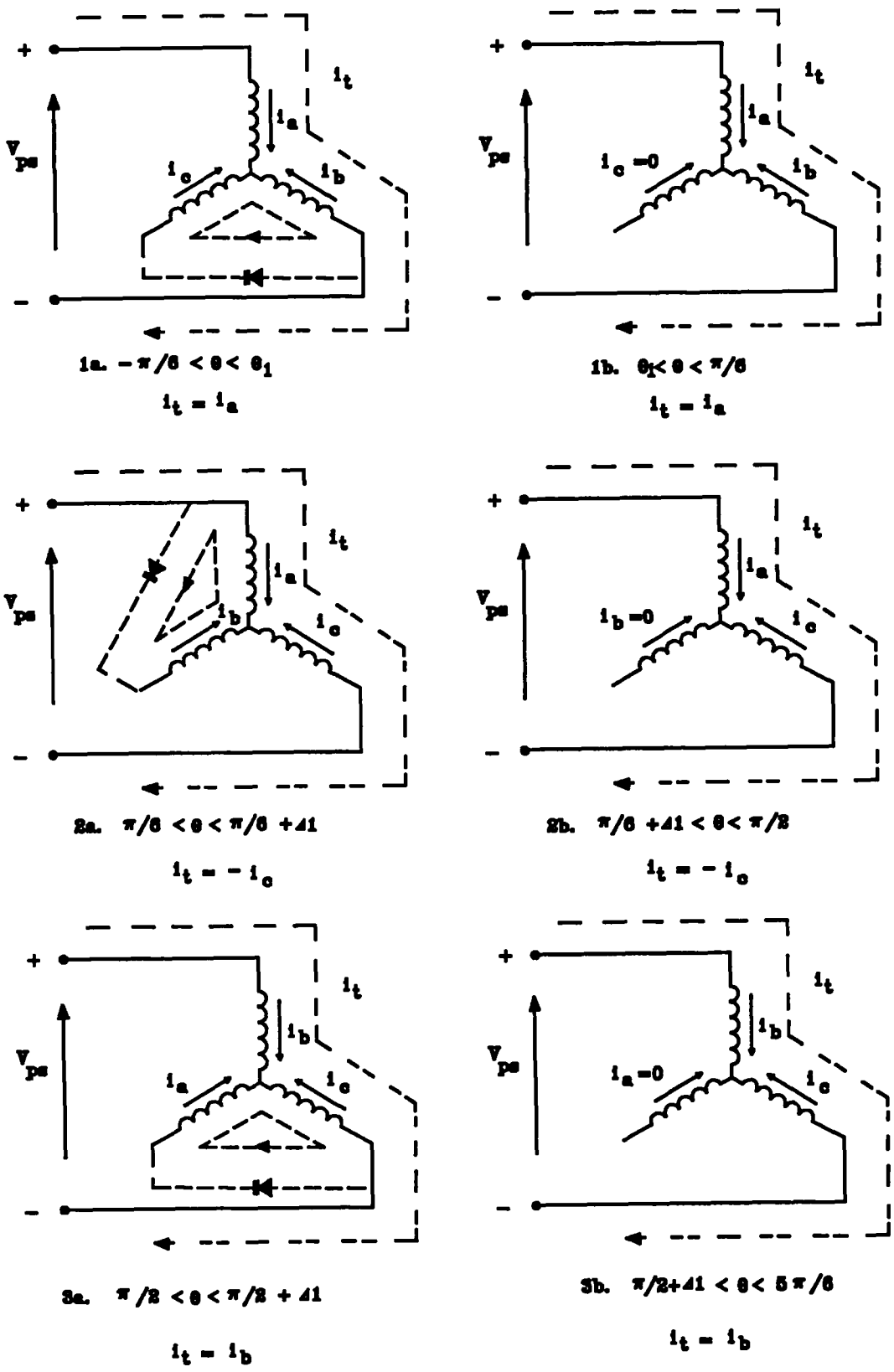

Fig 7.3 Variation of current flow with commutation events

Clearly, Fig 7.2 is only a representative current waveform, and the actual waveform will depend on the motor and drive parameters as well as the load condition, as will be demonstrated later.

7.3. Mathematical Models

7.3.1 Back-emf and Commutation

If the maximum value of the normalised back-emf per phase is 1 it can be expressed as a function of the angular position and the commutation angle in the form:

$$e_a = emf\,(\theta - \alpha + \theta_o)$$
$$e_b = emf\,(\theta - \alpha + \theta_o - 2\pi/3)$$
$$e_c = emf\,(\theta - \alpha + \theta_o - 4\pi/3) \qquad (7.1)$$

where α is the commutation angle, being

<0 for retarded commutation

= 0 for normal commutation

>0 for advanced commutation

Under normal commutation the commutation of the current in a particular phase is time delayed by an angle $\beta = \pi/6$ from the zero crossing of its induced emf waveform, as shown in Fig 7.4. Since, in Fig 7.2, the current starts to flow in phase a at $\theta = -\pi/6$, then, for this case, the angle θ_0 is defined as:

$$\theta_o = \beta + \frac{\pi}{6} = \frac{\pi}{3} \qquad (7.2)$$

Hence, for sinusoidal induced back-emf waveforms,

$$e_a = \sin\,(\theta - \alpha + \frac{\pi}{3})$$

$$e_b = \sin\,(\theta - \alpha - \frac{\pi}{3})$$

$$e_c = \sin\,(\theta - \alpha - \pi) \qquad (7.3)$$

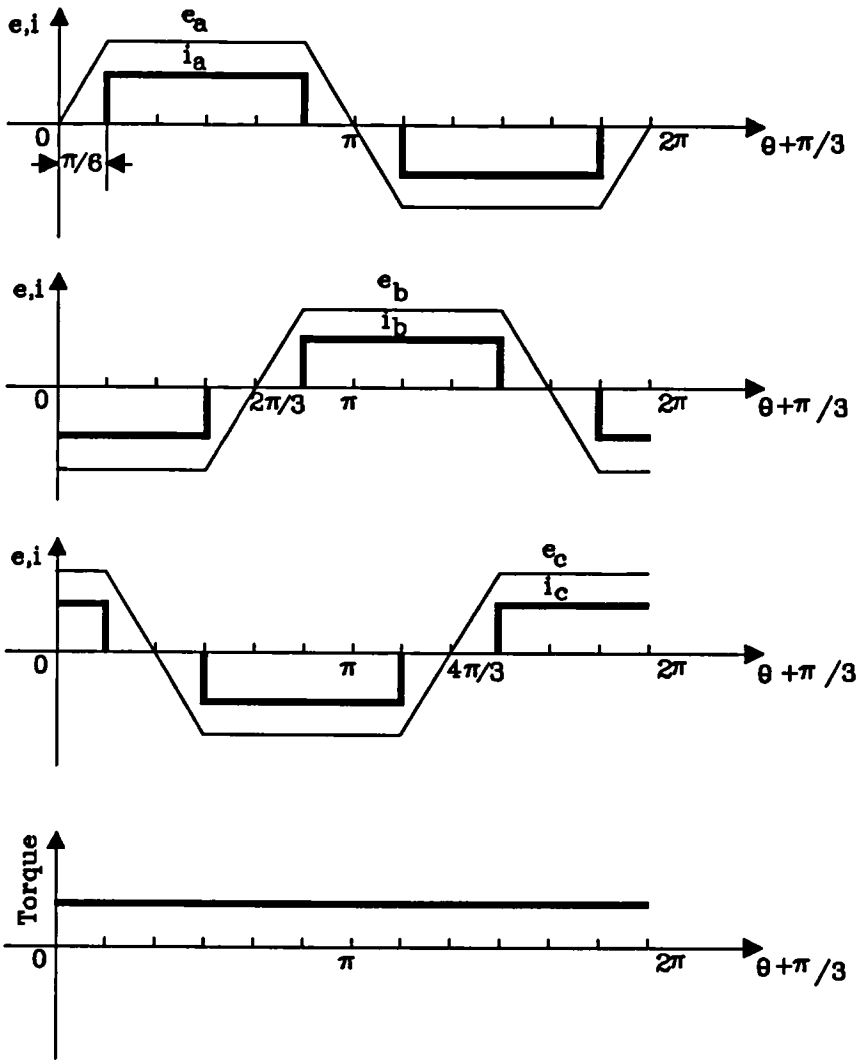

Fig 7.4 Idealised back-emf and current waveforms

Any other back-emf waveform can be discretised numerically in the form:

$emf(I)$ and $\theta(I)$ $I = 1, 2, ..., N$ (7.4)

where N is the total number of data points over a complete cycle. Thus the back-emf at any instant is determined by linear interpolation. For example, the idealised trapezoidal back-emf waveform shown in Fig 7.5 would be discretised as in Table 7.2.

Table 7.2 Idealised trapezoidal back-emf waveform

emf (I)	0	E_o	E_o	$-E_o$	$-E_o$	0
θ (I)	0	θ_o	$\pi - \theta_o$	$\pi+\theta_o$	$2\pi-\theta_o$	2π

Of course, the more complex the waveform the more data points are required to represent it.

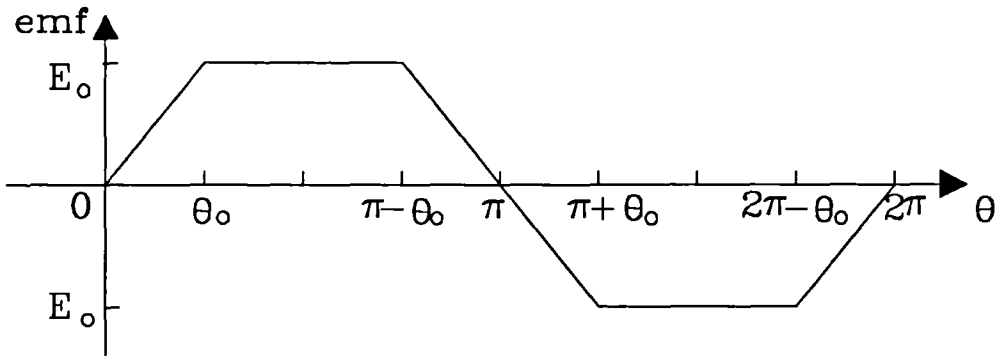

Fig 7.5 Trapezoidal back-emf waveform

7.3.2 Drive Circuit

The drive circuit for a brushless DC motor contains a complex arrangement of transistors, diodes, resistors, and capacitors. However, as regards the main current path from the power supply to the motor the most important are the transistors and freewheel diodes. A typical idealised current/voltage characteristic for a transistor in its conducting state is shown in Fig 7.6a. This can be modelled as a fixed voltage drop behind a series resistance as shown in Fig 7.6b, where ΔV_1 and ΔR are the voltage drop and resistance of one transistor. Hence the total voltage drop V_t is given by:

$$V_t = \Delta V_1 + \Delta R\, i_t \qquad (7.5)$$

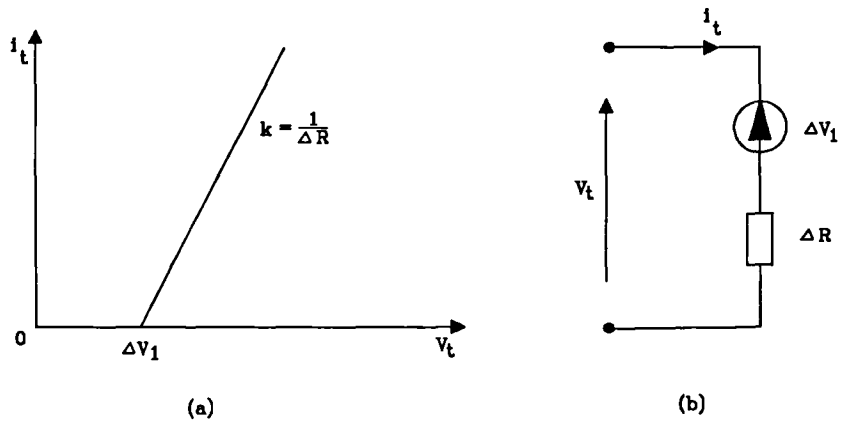

Fig 7.6 Characteristic and equivalent circuit of transistor and diode

The relationship between the power supply voltage V_{ps} and the terminal voltage V_{wt} at the windings, Fig 7.1, is

$$V_{wt} = V_{ps} - 2\,V_t = V_{ps} - \Delta V_{t1} - \Delta R_t\, i_t \tag{7.6}$$

where

$$\Delta V_{t1} = 2\,\Delta V_1 \qquad \Delta R_t = 2\,\Delta R \tag{7.7}$$

For simplicity, when the diode is conducting its resistance is assumed to be the same as that of the transistor, but its fixed voltage drop ΔV_2 is different, ie.

$$V_d = \Delta V_2 + \Delta R\, i_t \tag{7.8}$$

7.3.3 Voltage Equations

In the model, voltage equations for a star-connected three-phase brushless DC motor in the interval $-\pi/6 \le \theta \le \pi/6$ are expressed for the two periods : $-\pi/6 \le \theta \le \theta_1$ when the freewheel is conducting; and $\theta_1 \le \theta \le \pi/6$ when the diode is blocking.

Hence, for $-\pi/6 \le \theta \le \theta_1$

$$R\,(i_a - i_b) + L\,(\frac{d\,i_a}{d\,t} - \frac{d\,i_b}{d\,t}) + M\,(\frac{d\,i_b}{d\,t} - \frac{d\,i_a}{d\,t}) + K_{em}\,\omega_m\,(e_a - e_b) = V_{ps} - \Delta V_{t1}$$

$$R\,(i_c - i_b) + L\,(\frac{d\,i_c}{d\,t} - \frac{d\,i_b}{d\,t}) + M\,(\frac{d\,i_b}{d\,t} - \frac{d\,i_c}{d\,t}) + K_{em}\,\omega_m\,(e_c - e_b) = -\Delta V_{t2}$$

$$i_a + i_b + i_c = 0 \tag{7.9}$$

where $\Delta V_{t2} = \Delta V_1 + \Delta V_2$ (7.10)

and for $\theta_1 \le \theta \le \pi/6$

$$R\,(i_a - i_b) + L\,(\frac{d\,i_a}{d\,t} - \frac{d\,i_b}{d\,t}) + M\,(\frac{d\,i_b}{d\,t} - \frac{d\,i_a}{d\,t}) + K_{em}\,\omega_m\,(e_a - e_b) = V_{ps} - \Delta V_{t1}$$

$$i_c = 0$$

$$i_a + i_b + i_c = 0 \quad (i_b = -i_a) \tag{7.11}$$

where $R = r + \Delta R$

r,L,M are the phase resistance and self-inductance, and the mutual inductance parameters of the motor.

e_a,e_b,e_c are the normalised back-emf waveforms, with unit magnitude corresponding to their peak value.

K_{em} is the normalised back-emf constant, which is related to the normalised back-emfs e_a,e_b,e_c. Since the value of K_{em} is determined by the peak value of the back-emf waveform it is larger than or equal to the back-emf constant, K_e determined by the average value of the back-emf waveform during the conducting period.

ω_m is the mechanical angular velocity of the rotor.

$$\theta = p\,\omega_m\,t$$

and $$\frac{d}{dt} = \frac{d}{d\theta}\frac{d\theta}{dt} = p\,\omega_m\frac{d}{d\theta}$$

where p is the pole-pair number.

The governing equations can be rearranged into the following forms:

for $-\pi/6 \le \theta \le \theta_1$

$$\frac{p\,\omega_m\,(L-M)}{R}\frac{di_a}{d\theta} + i_a + \frac{K_{em}\,\omega_m}{3R}(2e_a - e_b - e_c) = \frac{2(V_{ps} - \Delta V_{t1}) + \Delta V_{t2}}{3R}$$

$$\frac{p\,\omega_m\,(L-M)}{R}\frac{di_c}{d\theta} + i_c + \frac{K_{em}\,\omega_m}{3R}(2e_c - e_a - e_b) = \frac{-2\Delta V_{t2} - (V_{ps} - \Delta V_{t1})}{3R}$$

$$i_b = -i_a - i_c \qquad (7.12a)$$

and for $\theta_1 \le \theta \le \pi/6$

$$\frac{p\,\omega_m\,(L-M)}{R}\frac{di_a}{d\theta} + i_a + \frac{K_{em}\,\omega_m}{3R}(2e_a - e_b - e_c) = \frac{2(V_{ps} - \Delta V_{t1}) + \Delta V_{t2}}{3R}$$

$$i_c = 0$$

$$i_b = -i_a \qquad (7.13a)$$

and then simplified into

for $-\pi/6 \le \theta \le \theta_1$

$$\frac{d\,i_a}{d\,\theta} + C_1\, i_a = Q_a'(\theta)$$

$$\frac{d\,i_c}{d\,\theta} + C_1\, i_c = Q_c'(\theta)$$

$$i_b = -\,i_a - i_c \qquad (7.12b)$$

and for $\theta_1 \le \theta \le \pi/6$

$$\frac{d\,i_a}{d\,\theta} + C_1\, i_a = Q_a''(\theta)$$

$$i_c = 0$$

$$i_b = -\,i_a \qquad (7.13b)$$

where $$C_1 = \frac{R}{p\,\omega_m\,(L-M)}$$

$$C_{21} = \frac{2\,V_{ps} - 2\,\Delta V_{t1} + \Delta V_{t2}}{3\,p\,\omega_m\,(L-M)}$$

$$C_{22} = \frac{-\,V_{ps} + \Delta V_{t1} - 2\,\Delta V_{t2}}{3\,p\,\omega_m\,(L-M)}$$

$$C_{23} = \frac{V_{ps} - \Delta V_{t1}}{2\,p\,\omega_m\,(L-M)}$$

$$C_3 = \frac{K_{em}}{p\,(L-M)}$$

$$Q_a'(\theta) = C_{21} - \frac{C_3}{3}\,(2\,e_a - e_b - e_c)$$

$$Q_c'(\theta) = C_{22} - \frac{C_3}{3}\,(2\,e_c - e_a - e_b)$$

$$Q_a''(\theta) = C_{23} - \frac{C_3}{2}\,(e_a - e_b) \qquad (7.14)$$

7.3.4 Calculation of Phase Currents

As can be seen from the above equations, the variables of one phase have been decoupled from those of another. Therefore, the explicit solutions are:

for $-\pi/6 \le \theta \le \theta_1$

$$i_a' = e^{-C_1\theta}\left[\int_{-\frac{\pi}{6}}^{\theta} Q_a'(\theta)\, e^{C_1\theta}\, d\theta + C_a'\right]$$

$$i_c' = e^{-C_1\theta}\left[\int_{-\frac{\pi}{6}}^{\theta} Q_c'(\theta)\, e^{C_1\theta}\, d\theta + C_c'\right] \qquad (7.15)$$

and for $\theta_1 \le \theta \le \pi/6$

$$i_a'' = e^{-C_1\theta}\left[\int_{\theta_1}^{\theta} Q_a''(\theta)\, e^{C_1\theta}\, d\theta + C_a''\right]$$

$$i_c'' = 0 \qquad (7.16)$$

where the superscripts ' and " refer to periods 1a and 1b respectively, and the constants θ_1, C_a', C_c', C_a " are determined from the continuity conditions:

1) $i_a'|_{\theta = -\frac{\pi}{6}} = 0$ (7.17a)

2) $i_c'|_{\theta = -\frac{\pi}{6}} = i_a''|_{\theta = \frac{\pi}{6}}$ (7.18a)

3) $i_c'|_{\theta = \theta_1} = 0$ (7.19a)

4) $i_a'|_{\theta = \theta_1} = i_a''|_{\theta = \theta_1}$ (7.20a)

which yield:

$$C_c' = -\int_{-\frac{\pi}{6}}^{\theta} Q_c'(\theta)\, e^{C_1\theta}\, d\theta \qquad (7.17b)$$

$$C_a' = 0 \qquad (7.18b)$$

$$C_a'' = C_a' + \int_{-\frac{\pi}{6}}^{\theta_1} Q_a'(\theta)\, e^{C_1\theta}\, d\theta = \int_{-\frac{\pi}{6}}^{\theta_1} Q_a'(\theta)\, e^{C_1\theta}\, d\theta \tag{7.19b}$$

$$e^{C_1\frac{\pi}{3}} \int_{-\frac{\pi}{6}}^{\theta_1} Q_c'(\theta)\, e^{C_1\theta}\, d\theta + \int_{-\frac{\pi}{6}}^{\theta_1} Q_a'(\theta)\, e^{C_1\theta}\, d\theta + \int_{\theta_1}^{\frac{\pi}{6}} Q_a''(\theta)\, e^{C_1\theta}\, d\theta = 0 \tag{7.20b}$$

The above equations can now be used to determine the conducting time of the diode as described in section (7.3.5).

At each instant during the period $-\frac{\pi}{6} \le \theta \le \frac{\pi}{6}$, starting from $\theta = -\frac{\pi}{6}$ when $i_a' = 0$, the phase currents are calculated from the value at the preceeding instant according to:

for $-\frac{\pi}{6} < \theta_i + \Delta\theta \le \theta_1$

$$i_a'\big|_{\theta_i+\Delta\theta} = e^{-C_1(\theta_i+\Delta\theta)} \left[\int_{-\frac{\pi}{6}}^{\theta_i+\Delta\theta} Q_a'(\theta)\, e^{C_1\theta}\, d\theta \right]$$

$$= e^{-C_1\Delta\theta}\, e^{-C_1\theta_i} \left[\int_{-\frac{\pi}{6}}^{\theta_i} Q_a'(\theta)\, e^{C_1\theta}\, d\theta + \int_{\theta_i}^{\theta_i+\Delta\theta} Q_a'(\theta)\, e^{C_1\theta}\, d\theta \right]$$

$$= e^{-C_1\Delta\theta} \left[i_a\big|_{\theta_i} + e^{-C_1\theta_i} \int_{\theta_i}^{\theta_i+\Delta\theta} Q_a'(\theta)\, e^{C_1\theta}\, d\theta \right] \tag{7.21a}$$

$$i_a'\big|_{\theta_o = -\frac{\pi}{6}} = 0 \tag{7.21b}$$

and for $\theta_1 < \theta_i + \Delta\theta \le \frac{\pi}{6}$

$$i_a''|_{\theta_i+\Delta\theta} = e^{-C_1\Delta\theta}\ [\ i_a''|_{\theta_i}\ + e^{-C_1\,\theta_i}\int_{\theta_i}^{\theta_i+\Delta\theta} Q_a''(\theta)\,e^{C_1\theta}\,d\theta\ ] \tag{7.22a}$$

$$i_a''|_{\theta_i=\theta_1} = i_a'|_{\theta_i=\theta_1} \tag{7.22b}$$

and similarly for phase c

for $-\frac{\pi}{6} < \theta_i+\Delta\theta \le \theta_1$

$$i_c'|_{\theta_i+\Delta\theta} = e^{-C_1\Delta\theta}\ [\ i_c'|_{\theta_i}\ + e^{-C_1\,\theta_i}\int_{\theta_i}^{\theta_i+\Delta\theta} Q_c'(\theta)\,e^{C_1\theta}\,d\theta\ ] \tag{7.23a}$$

$$i_c'|_{\theta_o=-\frac{\pi}{6}} = C_c'\ e^{C_1\frac{\pi}{6}} \tag{7.23b}$$

and for $\theta_1 < \theta_i+\Delta\theta \le \frac{\pi}{6}$

$$i_c''|_{\theta_i+\Delta\theta} = 0 \tag{7.24}$$

where

$$C_c' = -\int_{-\frac{\pi}{6}}^{\theta} Q_c'(\theta)\,e^{C_1\theta}\,d\theta$$

$$= -\frac{C_{22}}{C_1}\left(e^{C_1\theta_1} - e^{-C_1\frac{\pi}{6}}\right) + \frac{C_3}{3}\int_{-\frac{\pi}{6}}^{\theta_1}(2\,e_c - e_a - e_b)\,e^{C_1\theta}\,d\theta \tag{7.25}$$

and

$$\int_{\theta_i}^{\theta_i+\Delta\theta} Q_a'(\theta)\,e^{C_1\theta}\,d\theta = \frac{C_{21}}{C_1}\left(e^{C_1(\theta_i+\Delta\theta)} - e^{C_1\theta_i}\right) - \frac{C_3}{3}\int_{\theta_i}^{\theta_i+\Delta\theta}(2e_a - e_b - e_c)\,e^{C_1\theta}\,d\theta \tag{7.26}$$

$$\int_{\theta_i}^{\theta_i+\Delta\theta} Q_a''(\theta)\, e^{C_1\theta}\, d\theta = \frac{C_{23}}{C_1}\left(e^{C_1(\theta_i+\Delta\theta)} - e^{C_1\theta_i}\right) - \frac{C_3}{2}\int_{\theta_i}^{\theta_i+\Delta\theta} (e_a - e_b)\, e^{C_1\theta}\, d\theta \tag{7.27}$$

$$\int_{\theta_i}^{\theta_i+\Delta\theta} Q_c'(\theta)\, e^{C_1\theta}\, d\theta = \frac{C_{22}}{C_1}\left(e^{C_1(\theta_i+\Delta\theta)} - e^{C_1\theta_i}\right) - \frac{C_3}{3}\int_{\theta_i}^{\theta_i+\Delta\theta} (2e_c - e_a - e_b)\, e^{C_1\theta}\, d\theta \tag{7.28}$$

The integration $\int_{\theta_i}^{\theta_i+\Delta\theta} \ldots d\theta$ can be evalulated by any numerical method, such as the Gauss integration method, as described in section (7.3.7).

Hence the initial value of the phase current i_c at $\theta = -\frac{\pi}{6}$ ie. i_{co}' is determined from:

$$i_{co}' = i_c'\Big|_{\theta_o = -\frac{\pi}{6}} = C_c'\, e^{C_1\frac{\pi}{6}} \tag{7.29}$$

The current waveforms then repeat cyclically.

If, however, during the calculation procedure the value of a phase current exceeds a pre-set current limit it assumes this to be a default value for that instant, before continuing with the calculation.

7.3.5 Conducting Time of Freewheeling Diodes

The conducting time of the diodes is obtained by rewriting equation (7.20b) as:

$$F(\theta_1) = 0 \tag{7.30}$$

where

$$F(\theta_1) = \int_{-\frac{\pi}{6}}^{\theta_1} \left[e^{C_1 \frac{\pi}{3}} Q_c'(\theta) + Q_a'(\theta) \right] e^{C_1 \theta} d\theta + \int_{\theta_1}^{\frac{\pi}{6}} Q_a''(\theta) e^{C_1 \theta} d\theta$$

$$= \frac{1}{C_1} (C_{21} + C_{22} e^{C_1 \frac{\pi}{3}}) (e^{C_1 \theta_1} - e^{-C_1 \frac{\pi}{6}}) + \frac{C_{23}}{C_1} (e^{C_1 \frac{\pi}{6}} - e^{C_1 \theta_1})$$

$$-\frac{C_3}{2} \int_{-\frac{\pi}{6}}^{\frac{\pi}{6}} (e_a - e_b) e^{C_1 \theta} d\theta$$

$$-\frac{C_3}{6} (2 e^{C_1 \frac{\pi}{3}} - 1) \int_{-\frac{\pi}{6}}^{\theta_1} (2 e_c - e_a - e_b) e^{C_1 \theta} d\theta \qquad (7.31)$$

Since the diode blocks at instant $\theta = \theta_1$, the conducting time $| \theta_1 + \frac{\pi}{6} |$ can be determined by iteration of θ_1 until equation (7.30) is satisfied.

7.3.6 Torque, Terminal Current, and Efficiency

During the different periods of a cycle the terminal current corresponds to the current in phase A, B or C respectively according to Fig 7.3, ie.

$$\text{i.e.} \quad i_t = \begin{cases} i_a & \text{for } -\frac{\pi}{6} \le \theta \le \frac{\pi}{6} \\ -i_c & \text{for } \frac{\pi}{6} \le \theta \le \frac{\pi}{2} \\ i_b & \text{for } \frac{\pi}{2} \le \theta \le \frac{5\pi}{6} \\ -i_a & \text{for } \frac{5\pi}{6} \le \theta \le \frac{7\pi}{6} \\ i_c & \text{for } \frac{7\pi}{6} \le \theta \le \frac{3\pi}{2} \\ -i_b & \text{for } \frac{3\pi}{2} \le \theta \le \frac{11\pi}{6} \end{cases} \qquad (7.32)$$

However, because of symmetry, the average value of the terminal current need to be calculated only over the period [-π/6, π/6], during which the circulating current through the freewheel diode

is restricted to phases B and C and makes no contribution to the terminal current. Therefore the average terminal current is given by:

$$I_{t_{ave}} = \frac{1}{N} \sum_{j=1}^{N} i_{a_j} \tag{7.33}$$

where N is the number of discretising points over the period (- $\pi/6$, $\pi/6$). The average torque can also be calculated over the same period, but now the contributions of all three phases must be considered. Therefore the instantaneous value of the torque is given by:

$$T_t = K_{em} \left(i_a e_a + i_b e_b + i_c e_c \right) \tag{7.34}$$

whilst the average value is:

$$T_{t_{ave}} = \frac{1}{N} \sum_{j=1}^{N} T_{t_j} \tag{7.35}$$

The efficiencies of the total system and of the motor alone are given by:

$$\eta_s = \frac{T_{t_{ave}} \, \omega_m}{V_{ps} \, I_{t_{ave}}} \tag{7.36}$$

$$\eta_m = \frac{T_{t_{ave}} \, \omega_m}{V_{wt} \, I_{t_{ave}}} \tag{7.37}$$

7.3.7 Numerical Integration

In the previous sections there are a number of integrations of the from:

$$f = \int_{\theta_l}^{\theta_u} e^{-C_1 \theta} \, e(\theta) \, d\theta \tag{7.38}$$

for which five point Gauss numerical integration is adopted. The Gauss integration points and the related weighting factors are:

GK(1) = 0.2369269	GX(1) = - 0.9061798
GK(2) = 0.4786287	GX(2) = - 0.5384693
GK(3) = 0.5688889	GX(3) = 0.0
GK(4) = 0.4786287	GX(4) = 0.5384693
GK(5) = 0.2369269	GX(5) = 0.9061798

(7.39)

Letting $$CA_1 = \frac{(\theta_u - \theta_l)}{2}$$

$$CA_2 = \frac{(\theta_u + \theta_l)}{2} \tag{7.40}$$

and $$\theta = CA_1\ \theta_x + CA_2 \tag{7.41}$$

then $$f = \int_{-1}^{1} e^{-C_1\theta}\ e(\theta)\, CA_1 \mid_{\theta = CA_1\ \theta_x + CA_2}\ d\theta_x$$

$$= \sum_{I=1}^{5} GK(I)\ e^{-C_1\theta}\ e(\theta)\, CA_1 \mid_{\theta = CA_1\ \theta_x + CA_2} \tag{7.42}$$

In general the integration interval can be divided into several sub-intervals and then the Gauss integration is performed over each sub-interval.

7.4 Validation of Mathematical Models

7.4.1 Radial- Field Brushless DC Motors

Fig 7.7 shows two prototype radial-field, internal rotor, three-phase four-pole permanent magnet brushless DC motors on which the analytical model has been validated.

One of the stators has an overlapping stator winding whilst the other has a non-overlapping winding.

(a) stator with overlapping 3-phase winding (b)stator with non-overlapping 3-phase winding (c) rotor with surface mounted ferrite magnets

Fig 7.7 Radial-field brushless DC motors

Both motors use the same rotor, and are supplied from the same drive circuit. Fig 7.8 shows the stator laminations together with their associated normalised back-emf waveforms. The parameters of the motors are given in Table 7.3.

Table 7.3 Parameters of the prototype radial-field motors

parameter	symbol	overlapping winding	nonoverlapping winding	unit
pole-pair number	2p	4	4	
slot number	Q_s	12	6	
winding resistance	r	2.7	1.095	Ω/phase
self-inductance	L	5.63	7.72	mH/phase
mutual-inductance	M	-2.15	-3.25	mH
back-emf constant per phase	K_{em}	0.0987	0.089786	V/rad^{-1}

The motors were supplied from the "Motorola" MC 33034 drive IC which was supplied at V_{ps}=45V. The voltage drop and equivalent resistance for the devices which are used in the drive model are:

ΔV_1=0.163V, ΔV_2=0.7V, and $\Delta R = 0.65\ \Omega$

Fig 7.9 shows the excellent agrement between the predicted and measured phase current waveforms, whilst the predicted torque waveforms are shown in Fig 7.10. Fig 7.11 compares predicted and measured dynamic torque/speed characteristics, which are not linear as would be the case under idealised commutation conditions (ie L = M = 0), the difference in their slopes being mainly due to the neglect of the variation in winding resistance with load, and hence temperature, in the simulation, which will be discussed further in section 7.6.

Fig 7.12 shows the predicted and measured conducting time of the freewheel diode, whilst Fig 7.13 compares predicted and measured phase current waveforms for the non-overlapping winding motor when the instant of commutation is varied from normal, to 14^oelec. advanced, and 14^oelec. retarded. The effect of commutation on the dynamic performance will be discussed in section 7.6.

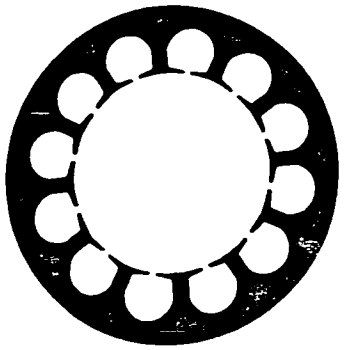

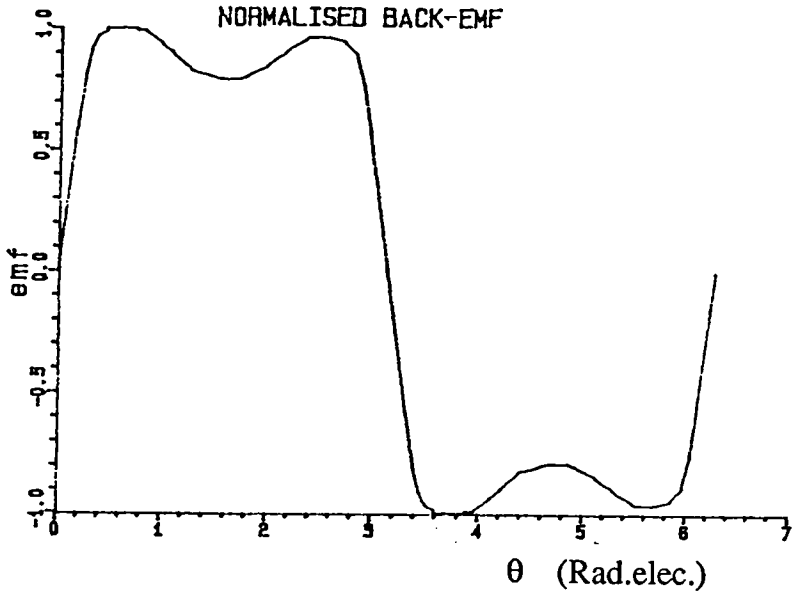

(a) Overlapping winding

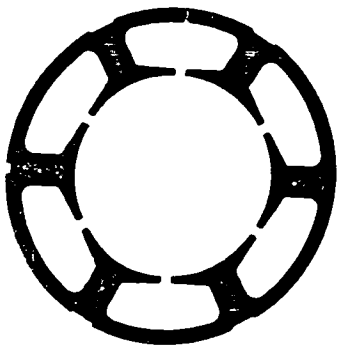

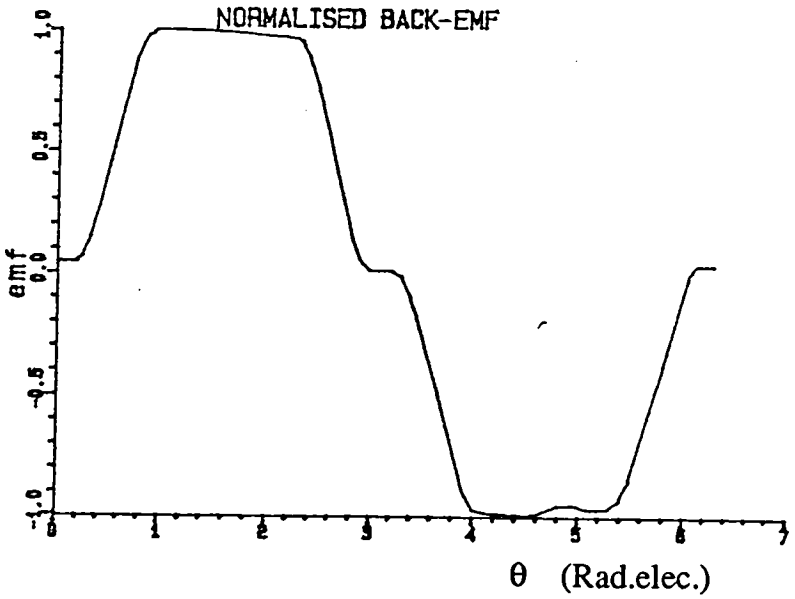

(b) Non-overlapping winding

Fig 7.8 Stator laminations and back-emf waveforms

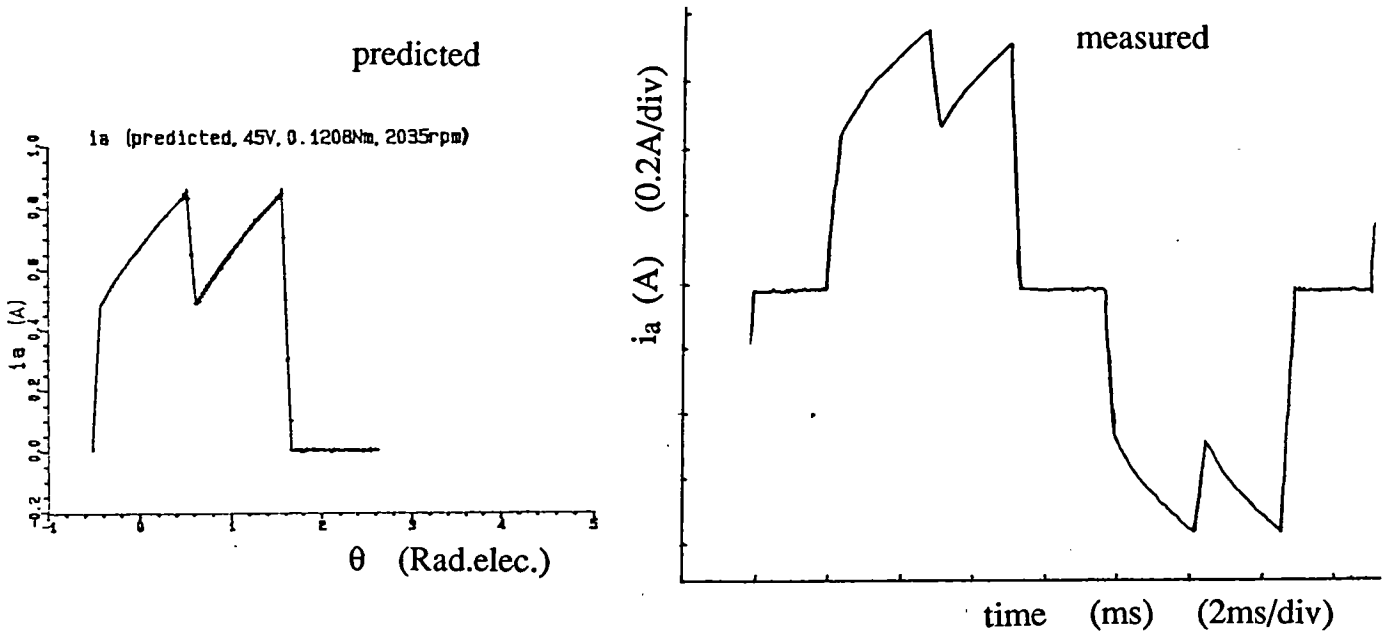

(a) Overlapping winding

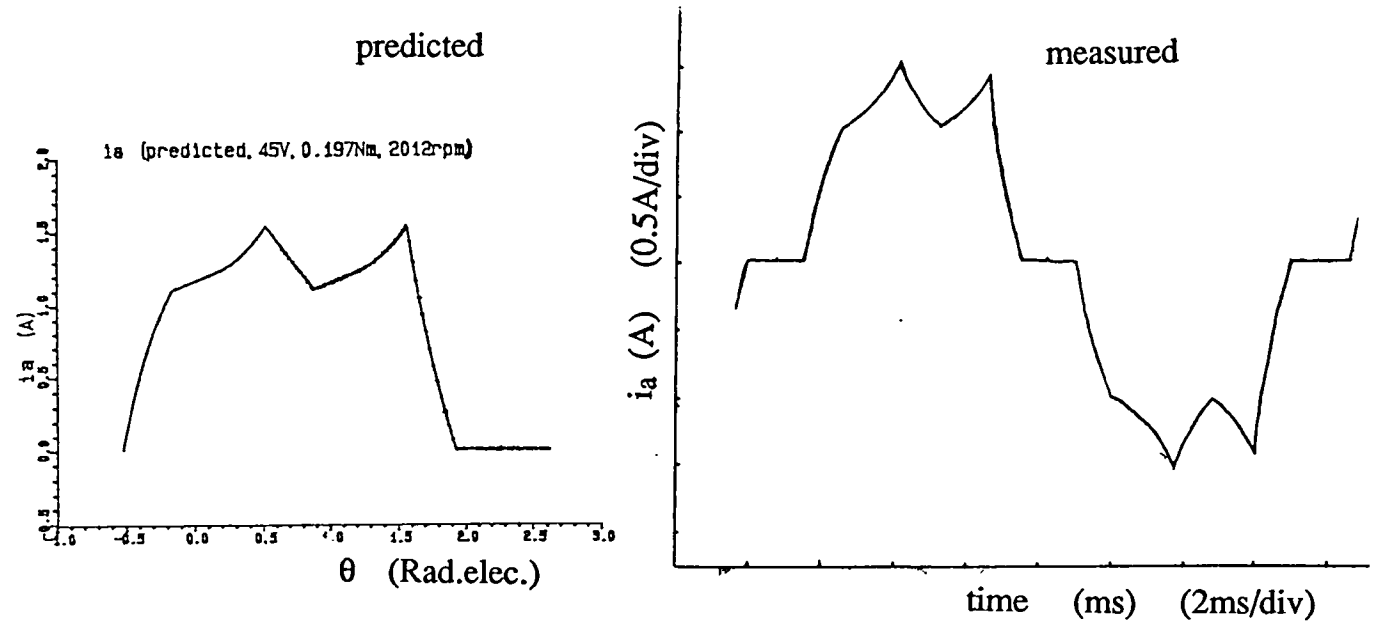

(b) Non-overlapping winding

Fig 7.9 Masured and predicted phase current waveforms

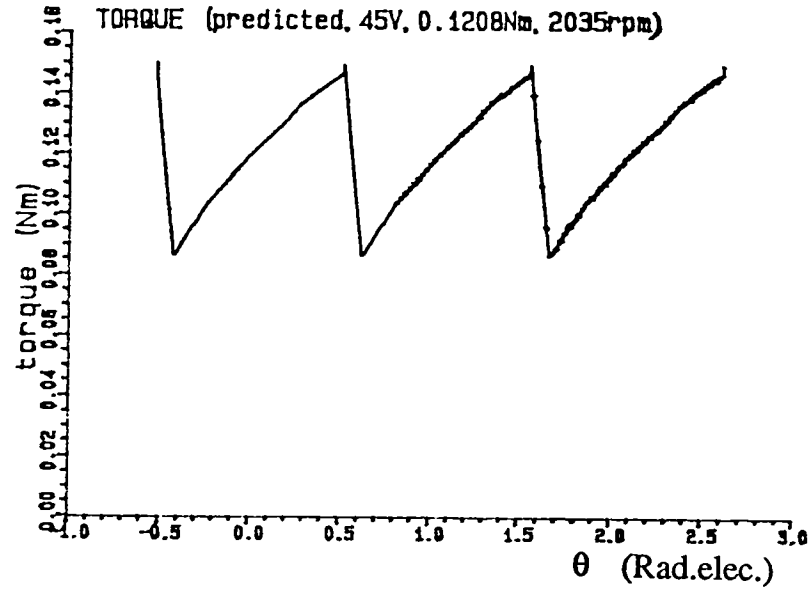

(a) Overlapping winding

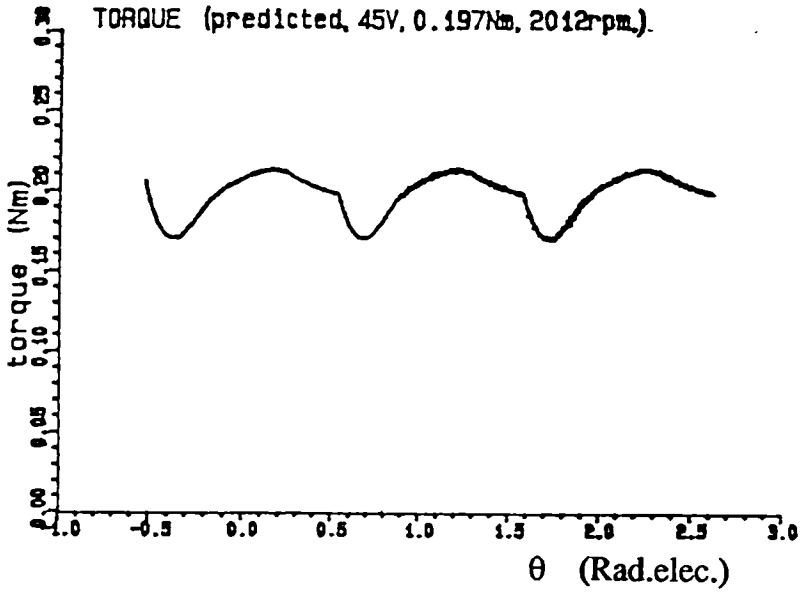

(b) Non-overlapping winding

Fig 7.10 Predicted torque waveforms

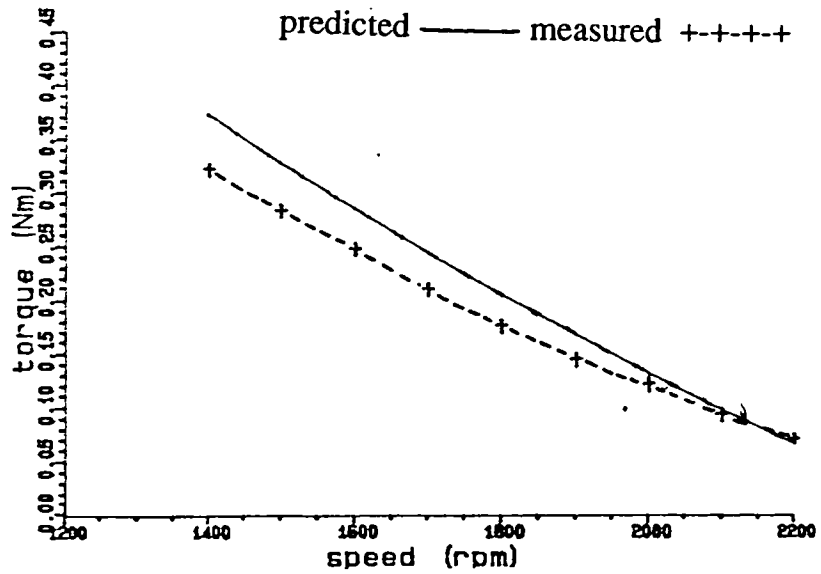

(a) Overlapping winding

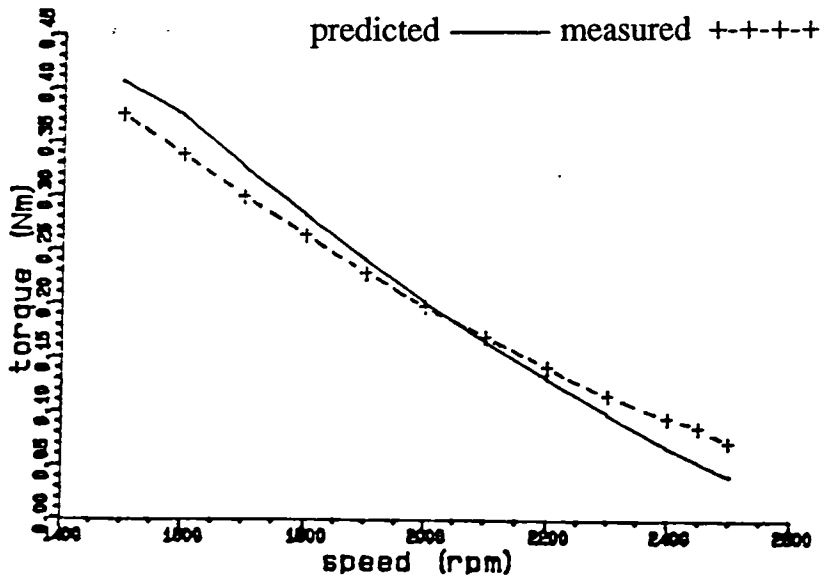

(b) Non-overlapping winding

Fig 7.11 Predicted and measured torque-speed curves

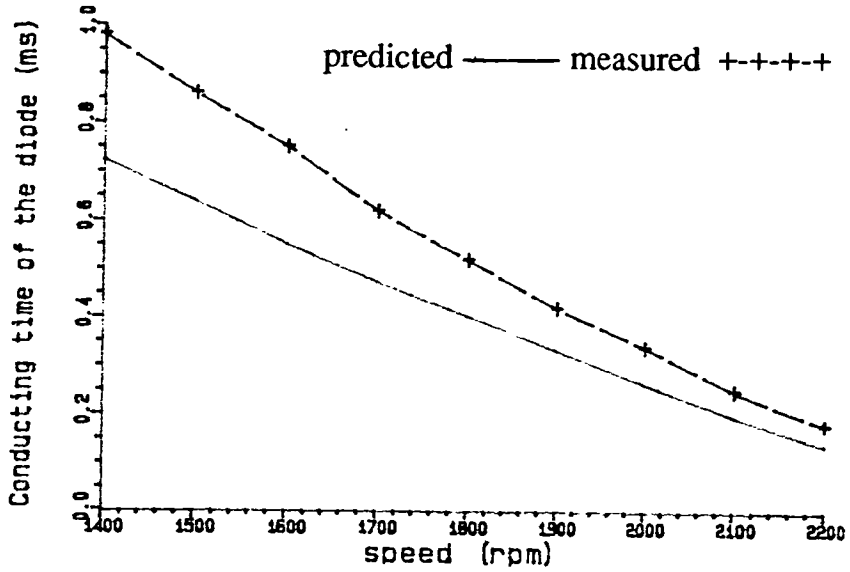

(a) Overlapping winding

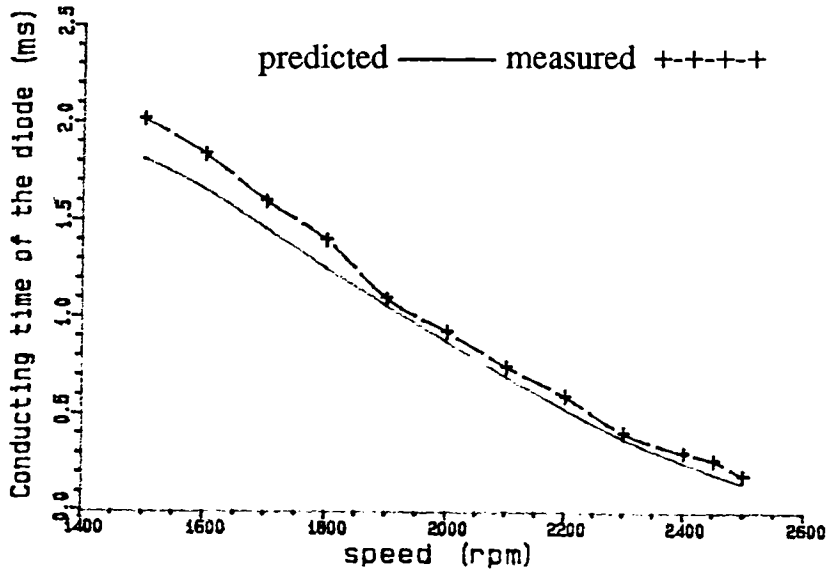

(b) Non-overlapping winding

Fig 7.12 Predicted and measured conducting time of the diode

measured predicted

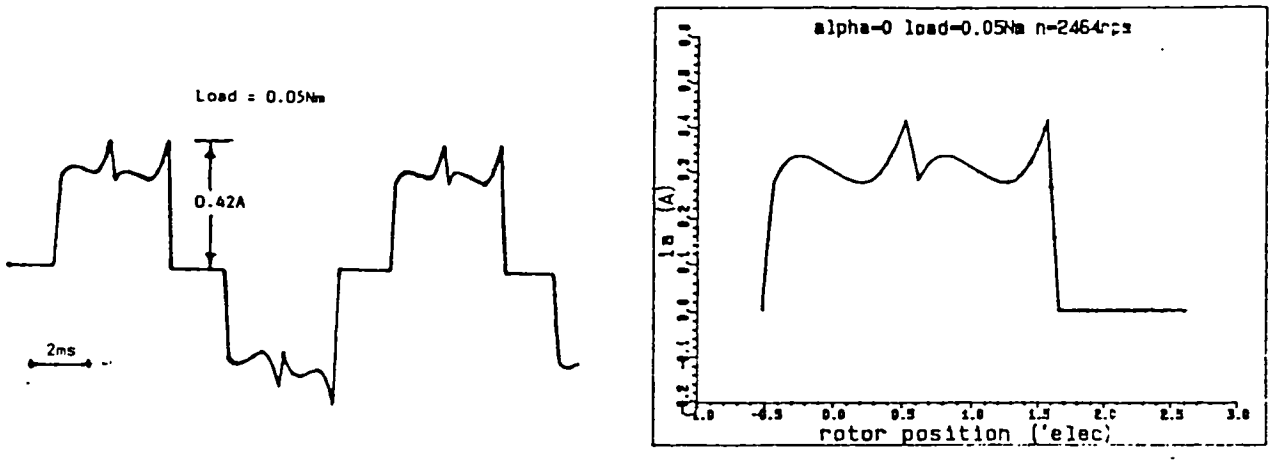

(a) Normal commutation (0^{o} elec.)

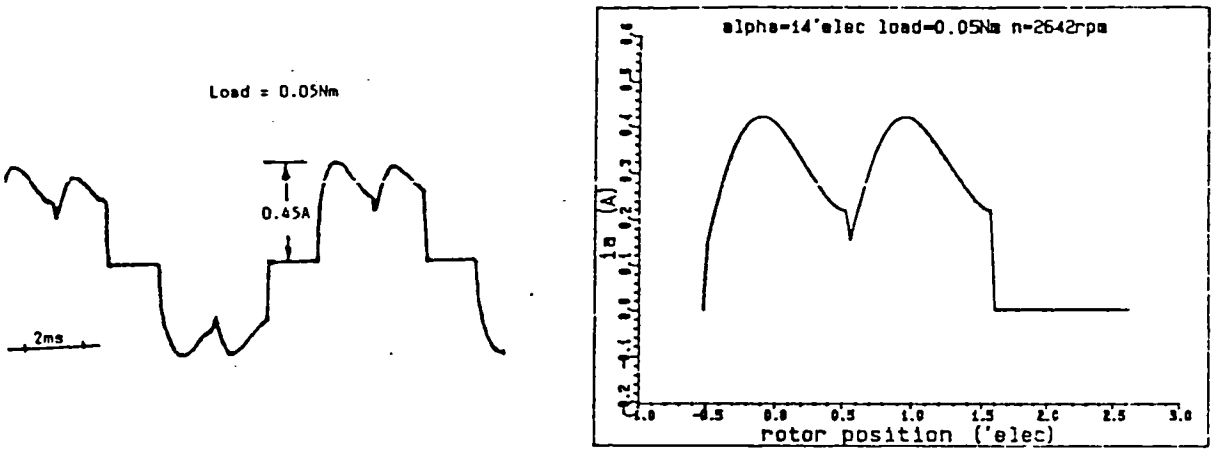

(b) Advanced commutation ($+14^{o}$elec.)

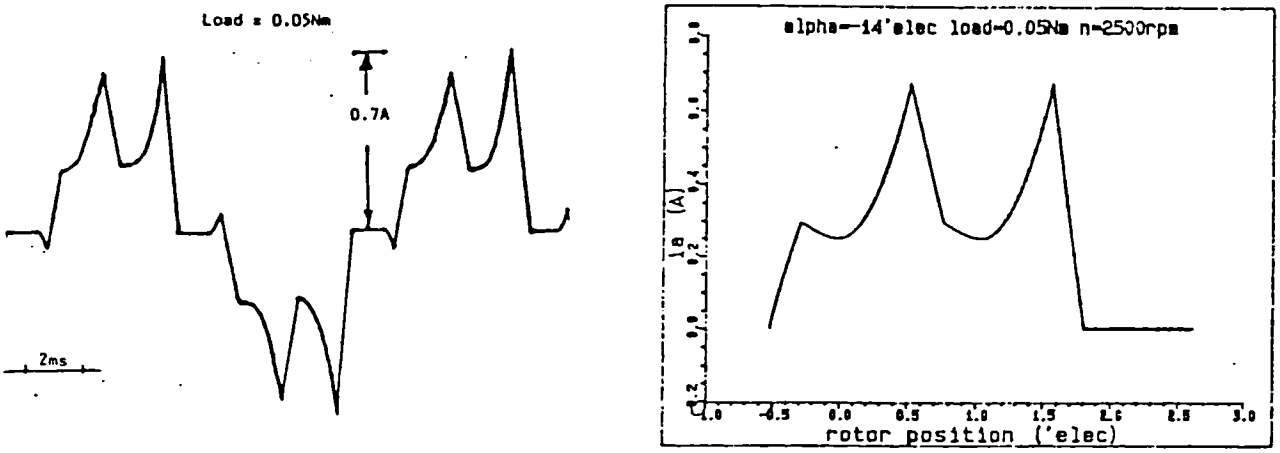

(c) Retarded commutation (-14^{o}elec.)

Fig 7.13 Measured and predicted phase current waveforms of non-overlapping winding motor for normal, advanced, and retarded commutation

7.4.2 Axial-field Brushless DC Motor

The simulation models which have been developed are suitable for both radial-field and axial-field topologies of brushless DC motors. In this section validations are made on the 12-pole, axial-field, brushless permanent magnet DC motor, shown in Fig 7.14, which has a single airgap, three-phase overlapping airgap winding, and sintered NdFeB magnets [7.6]. The parameters of the motor are shown in Table 7.4. The motor is driven by the "Unitrode" UC 3620 integrated circuit, for which the constant voltage drop and series resistance are modelled as:

$\Delta V_1 = 0.8925V$ and $\Delta R = 0.825\,\Omega$

for both the transistor and freewheel diodes.

Table 7.4 Parameters of an axial field motor.

Pole-pair number	$2p = 12$
Pole-arc/pole-pitch ratio	$\alpha_p = 1.0$
Supply voltage	V_{ps} = 12-15V
Speed	n=800 rpm, $\omega = 83.8$ rads/s
Magnet thickness	$l_m = 3$ mm
Airgap length (effective)	$l_g' = 2.77$ mm
External diameter	$D_o = 88.4$ mm
Internal diameter	$D_i = 71.6$ mm
Magnet remanence	$B_R = 1.15$ T
Relative recoil permeability	$\mu_R = 1.02$
Total conductors per phase	N = 528
End winding overhang (average)	$l_{ec} = 1.5$ mm
Measured Parameters:	
Phase resistance (at normal running condition)	$R_{ph} = 0.93\,\Omega$
Self-inductance	L = 0.16 mH
Mutual inductance	M = -0.099 mH
Equivalent resistance from supply voltage to the terminals of windings	1.65 Ω

Fig 7.15 shows the predicted and measured line and phase back-emf waveforms [7.6]. Figs 7.16 and 7.17 show typical comparisons of the predicted and measured phase currents and torque-speed curves when the motor is operated at different supply voltages, whilst Fig 7.18

shows a calculated torque waveform. However, despite inductance having a significant effect on the current waveform, the torque-speed curves are not affected greatly, ie. they are almost linear since the winding inductance of the prototype slotless motor is comparatively small.

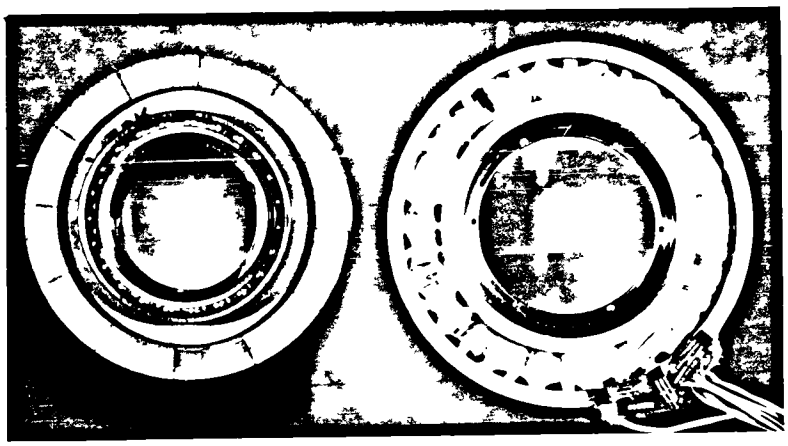

Fig. 7.14 Prototype axial-field brushless DC motor

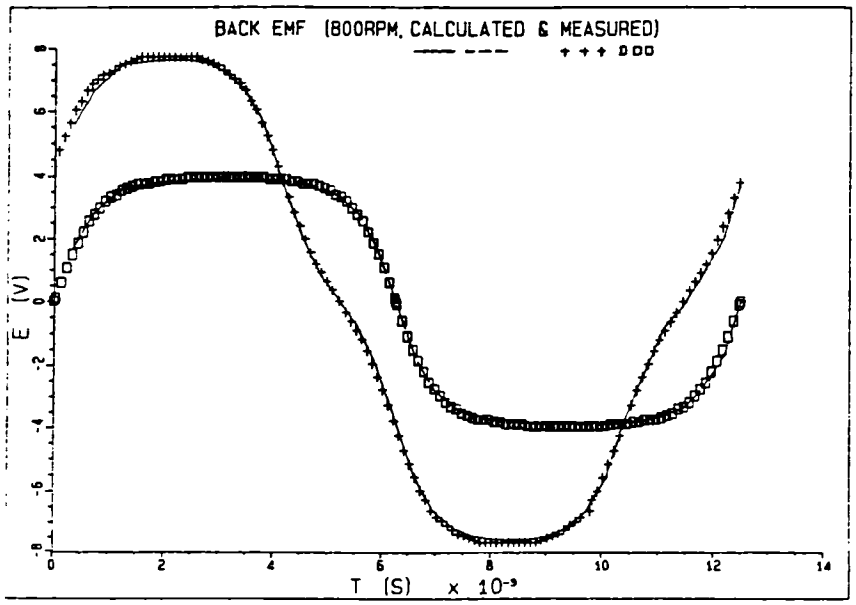

Fig. 7.15 Comparison of predicted and measured line and phase back-emf waveforms

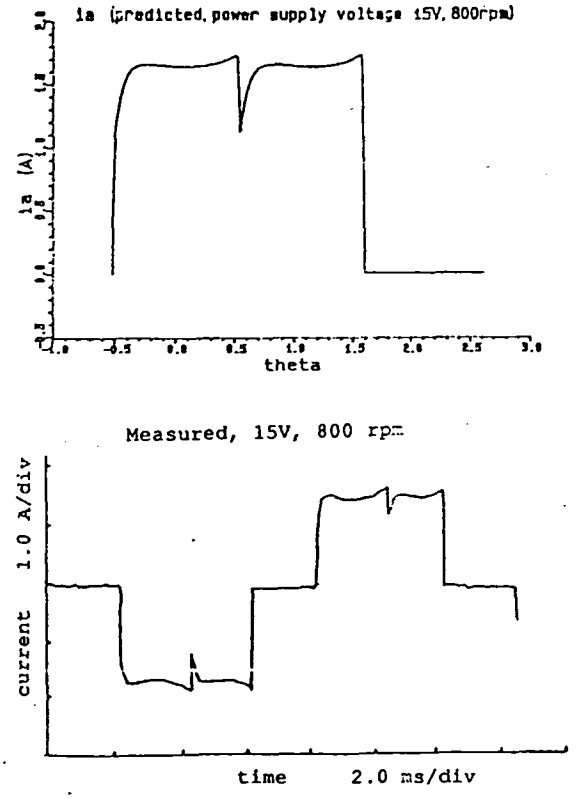

Fig. 7.16 Predicted and measured current waveforms

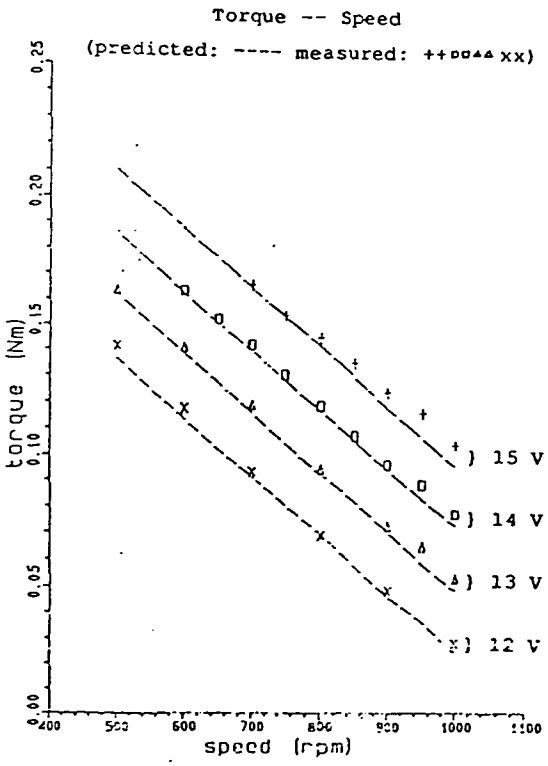

Fig. 7.17 Predicted and measured torque-speed curves

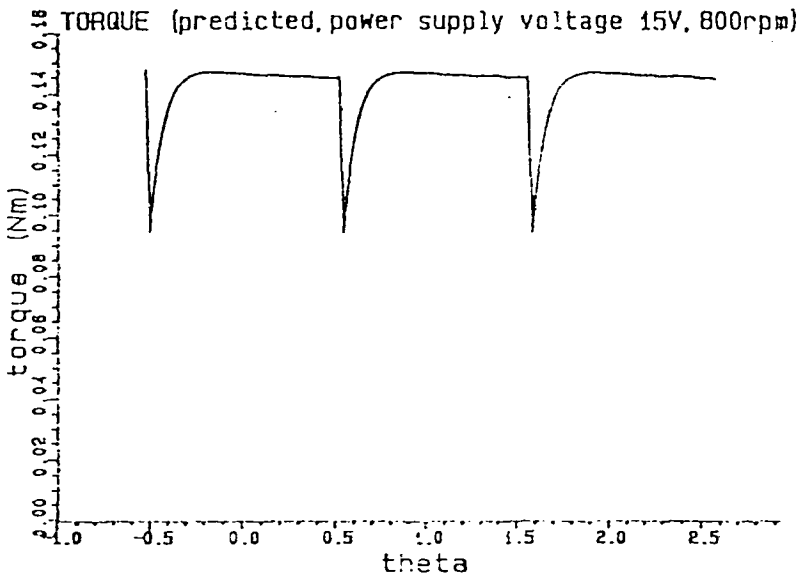

Fig. 7.18 Predicted torque waveform

7.5 Coupling the Rotor Motion Equation into Steady-State Models

In the preceeding sections an analytical method for simulating the steady-state dynamic performance of brushless DC drives was described. However, the transient dynamic performance may also be of major importance. It is then necessary to abandon the assumption of constant speed. However, in this case it becomes unrealistic to use an analytical model. Hence in this section, a numerical model, ie. a state-variable model is developed by extending the models developed in section 7.3 to include the motion equation of the rotor.

The drive is first idealised into two states, which depend on whether the flywheel diode is conducting or not, which are **ALWAYS** described by two **FIXED** groups of state equations in an idealised state-variable model and solved by the Runge-Kutta integration method. The dynamic performance is obtained by introducing the relationship between the idealised state variables and the stator winding currents.

The developed state-variable model includes similar features to those cited for the analytical model, such as the ability to cater for any back-emf waveform, and normal, advanced, or retarded commutation, as well as to impose current limiting. Also it is very easy to integrate the model into a complete system simulation package, as will be shown later.

7.5.1 Idealised State-variables

Although under transient dynamic conditions the speed cannot be assumed to be constant as in the steady-state models described in section 7.3, the relationship between the rotor angular position and the stator commutation periods is still valid. The states of the drive system consist of six uniform intervals of 60^{o}elec per full cycle, each interval being sub-divided into two periods as mentioned in 7.2. Of course, in general the current waveforms of the three phases will no longer be the same in each cycle and have no periodicity. However, it is possible to describe the system if two idealised state current variables are introduced, one being the line current i_l from the dc power supply to the transistors and windings of two excited phases, the other being a

circulating current i_{II} through the diode, transistor and windings of two phases, Fig 7.19. The relationship between the two idealised state variables i_I, i_{II} and the phase currents i_a, i_b, i_c in each interval 1- 6 is shown in Table 7.5. In two periods of every interval (periods (a) and (b)), these relationships are the same. However, because the diode is blocked in period (b), the circulating current through the diode i_{II} is always zero. The start point of period (b) is determined by examining when the current i_{II} becomes zero in period (a), at which time the diode is switched from conducting to being blocked. Hence the system model can be implemented by two idealised states depending on whether the diode is conducting or not, as shown in Fig 7.20.

The equations developed for the steady-state model in section 7.3 are still applicable to the dynamic state as far as the electrical aspects are concerned and can be incorporated with the equation of motion for the rotor. Due to the inductance, the currents cannot change instantaneously, and continuity conditions must be applied when the drive system switches from one interval to another. These conditions are:

$$i_a \,(\, or \;\; i_b, i_c \,) \,|\, \theta = \textit{interval boundary}^{+} \;=\; i_a \,(\, or \;\; i_b, i_c \,) \,|\, \theta = \textit{interval boundary}^{-} \qquad (7.43a)$$

Here "-" means in the previous interval, whilst "+" means in the following interval. Interval boundaries for angular position are $\theta = 0, \pi/3, \pi, \pi/3, 5\pi/3, 2\pi$ etc.

When these boundaries are applied to the two state current variables, they become

$$i_I \,|\, \theta = \textit{interval boundary}^{+} \;=\; i_{II} \,|\, \theta = \textit{interval boundary}^{-} \qquad (7.43b)$$

$$i_{II} \,|\, \theta = \textit{interval boundary}^{+} \;=\; i_I \,|\, \theta = \textit{interval boundary}^{-} \qquad (7.43c)$$

which are shown on Fig 7.20. Whilst the initial values for i_I and i_{II} at time =0 are zero.

Here it is worth mentioning two important aspects:

i) In the analytical approach the angular position is with reference to $\theta = -\pi/6$ in order to simplify the subsequent expressions in the formulae, in which the integration is from $\theta = -\pi/6$ to $\pi / 6$. In the transient state it is usual to define the angular position with reference to $\theta = 0$. Therefore there is an angular difference of $\pi /6$, between the analytical and the numerical models. Hence equation (7.2), ie, θ_o, in the expression for the back-emf waveform now becomes:

$$\theta_o = \beta + 0 = \frac{\pi}{6}$$

ii) The variables in the state-equations of electrical machines are usually assumed to be the phase winding currents, i_a, i_b, and i_c, [7.1][7.7][7.8][7.9] [7.10]. As a consequence the state equations depend on the commutation logic, which change according to the switching sequence of the drive. Due to the cyclic nature of the commutation events the state equations also vary cyclically. In contrast, in this thesis an idealised model of the state variables is introduced in which two **FIXED** groups of state equations, in terms of two idealised state-variables i_I and i_{II}, are **ALWAYS** used to describe the states of a brushless DC drive throughout the transient and steady-state dynamic conditions, irrespective of the commutation events or switching sequences.

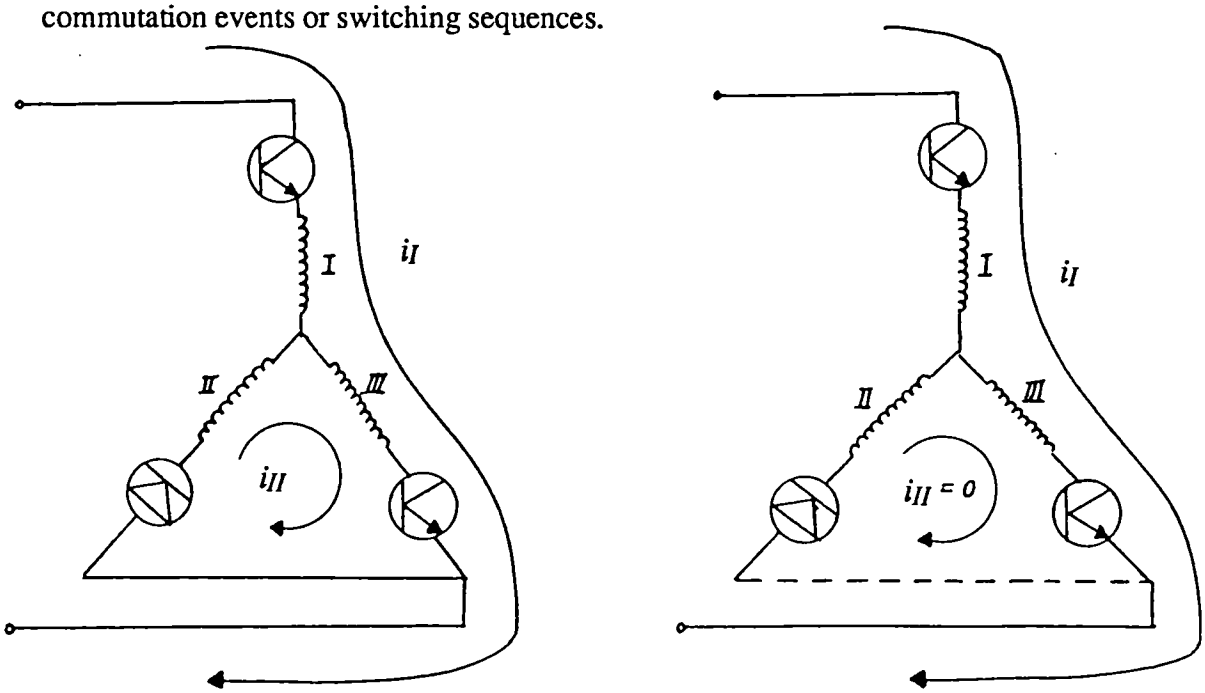

Fig. 7.19 Idealised state-variable model

Table 7.5 Relationship between the state-variables and the winding phase currents

θ	$0 \sim \pi/3$	$\pi/3 \sim 2\pi/3$	$2\pi/3 \sim \pi$	$\pi \sim 4\pi/3$	$4\pi/3 \sim 5\pi/3$	$5\pi/3 \sim 2\pi$
N	1a 1b	2a 2b	3a 3b	4a 4b	5a 5b	6a 6b
i_a	i_I i_I	$i_I + i_{II}$ $i_I + i_{II}$	i_{II} i_{II}	$-i_I$ $-i_I$	$-i_I$ $-i_{II}$ $-i_I-i_{II}$	$-i_{II}$ $-i_{II}$
i_b	$-i_I-i_{II}$ $-i_I-i_{II}$	$-i_{II}$ $-i_{II}$	i_I i_I	$i_I + i_{II}$ i_I+i_{II}	i_{II} i_{II}	$-i_I$ $-i_I$
i_c	i_{II} i_{II}	$-i_I$ $-i_I$	$-i_I-i_{II}$ $-i_I-i_{II}$	$-i_{II}$ $-i_{II}$	i_I i_I	i_I+i_{II} $i_I + i_{II}$
$i_I(y_3)$	i_a	$-i_c$	i_b	$-i_a$	i_c	$-i_b$
$i_{II}(y_4)$	i_c	$-i_b$	i_a	$-i_c$	i_b	$-i_a$
(i_{III})	i_b	i_a	i_c	i_b	i_a	i_c

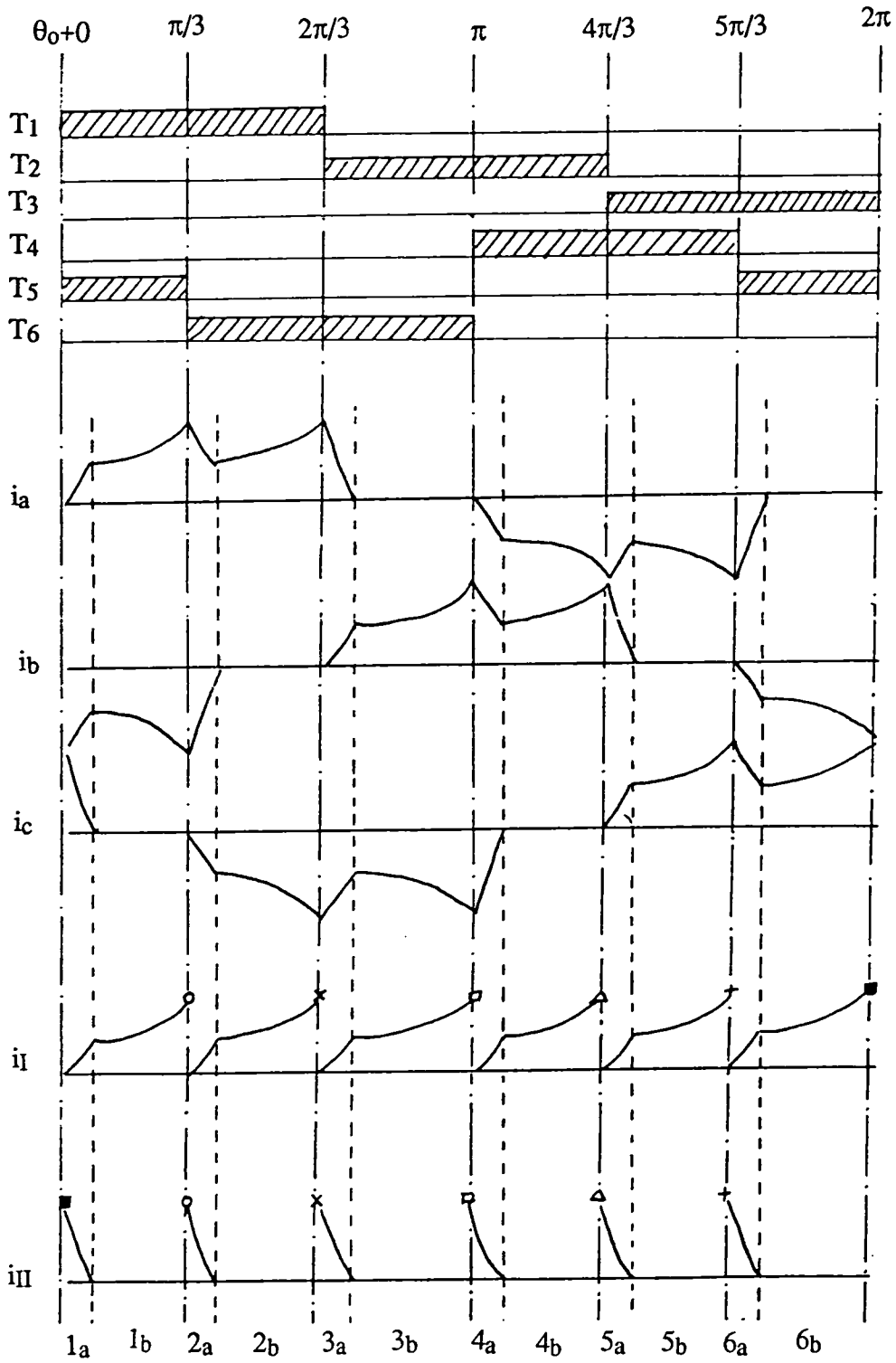

Fig. 7.20 Relationship between the idealised state-variables and the winding phase currents

7.5.2 State-variable Equations

In the same way as for the analytical models described in section 7.3, the switching devices and freewheel diodes in the inverter drive circuit are modelled as a fixed voltage drop and series resistance, as shown in Fig 7.5. According to the idealised state-variable model described in the previous section, the voltage equations for star-connected three-phase brushless DC motors in an interval of $\pi/3$ can be expressed in two periods : period 1 when the diode is conducting, and period 2 when the diode is blocking.

Hence for period 1:

$$R\,(i_I - i_{III}) + L\left(\frac{d\,i_I}{d\,t} - \frac{d\,i_{III}}{d\,t}\right) + M\left(\frac{d\,i_{III}}{d\,t} - \frac{d\,i_I}{d\,t}\right) + K_{em}\,\omega_m\,(e_I - e_{III}) = V_{ps} - \Delta V_{t1}$$

$$R\,(i_{II} - i_{III}) + L\left(\frac{d\,i_{II}}{d\,t} - \frac{d\,i_{III}}{d\,t}\right) + M\left(\frac{d\,i_{III}}{d\,t} - \frac{d\,i_{II}}{d\,t}\right) + K_{em}\,\omega_m\,(e_{II} - e_{III}) = \Delta V_{t2}$$

$$i_I + i_{II} + i_{III} = 0 \qquad (7.44)$$

When i_{II} becomes zero, the diode is blocking, or when the conducting period being to the end of the period, and the state changes from period 1 to period 2, for which

$$R\,(i_I - i_{III}) + L\left(\frac{d\,i_I}{d\,t} - \frac{d\,i_{III}}{d\,t}\right) + M\left(\frac{d\,i_{III}}{d\,t} - \frac{d\,i_I}{d\,t}\right) + K_{em}\,\omega_m\,(e_I - e_{III}) = V_{ps} - \Delta V_{t1}$$

$$i_{II} = 0$$

$$i_I + i_{II} + i_{III} = 0 \quad (i_{III} = -i_I) \qquad (7.45)$$

In a similar way to that in section 7.3, a simplified form of state equation can be deduced, viz:

for period 1:

$$\frac{d\,i_I}{d\,t} + C_1\,i_I = \theta_I'\,(\theta)$$

$$\frac{d\,i_{II}}{d\,t} + C_1\,i_{II} = \theta_{II}'\,(\theta)$$

$$i_{III} = -i_I - i_{II} \qquad (7.46)$$

and for period 2:

$$\frac{d\,i_I}{d\,t} + C_1\,i_I = \theta_I''(\theta)$$

$$i_{II} = 0$$

$$i_{III} = -i_I \qquad (7.47)$$

where

$$\theta_I'(\theta) = C_{21} - \frac{C_3}{3}(2\,e_I - e_{II} - e_{III})\,\omega_m$$

$$\theta_{II}'(\theta) = C_{22} - \frac{C_3}{3}(2\,e_{II} - e_I - e_{III})\,\omega_m$$

$$\theta_I''(\theta) = C_{23} - \frac{C_3}{2}(e_I - e_{III})\,\omega_m$$

$$C_1 = \frac{R}{(L-M)}$$

$$C_{21} = \frac{2\,V_{ps} - 2\,\Delta V_{t1} + \Delta V_{t2}}{3\,(L-M)}$$

$$C_{22} = \frac{-V_{ps} + \Delta V_{t1} - 2\,\Delta V_{t2}}{3\,(L-M)}$$

$$C_{23} = \frac{V_{ps} - \Delta V_{t1}}{2\,(L-M)}$$

$$C_3 = \frac{K_{em}}{(L-M)} \qquad (7.48)$$

Equations (7.46) and (7.47) are used to describe the states of a brushless DC motor drive throughout the transient and steady-state dynamic conditions.

According to Table 7.5, the relationship between the state variables i_I, i_{II}, i_{III} and the phase currents i_a, i_b, i_c in one cycle is

$$\begin{cases} i_a = i_I \\ i_c = i_{II} \\ i_b = -i_a - i_c \end{cases} \qquad \text{for } 0 \le \theta \le \frac{\pi}{3}$$

$$\begin{cases} i_c = -i_I \\ i_b = -i_{II} \\ i_a = -i_b - i_c \end{cases} \quad \text{for } \frac{\pi}{3} \le \theta \le \frac{2\pi}{3}$$

$$\begin{cases} i_b = i_I \\ i_a = i_{II} \\ i_c = -i_a - i_b \end{cases} \quad \text{for } \frac{2\pi}{3} \le \theta \le \pi$$

$$\begin{cases} i_a = -i_I \\ i_c = -i_{II} \\ i_b = -i_a - i_c \end{cases} \quad \text{for } \pi \le \theta \le \frac{4\pi}{3}$$

$$\begin{cases} i_c = i_I \\ i_b = i_{II} \\ i_a = -i_b - i_c \end{cases} \quad \text{for } \frac{4\pi}{3} \le \theta \le \frac{5\pi}{3}$$

$$\begin{cases} i_b = -i_I \\ i_a = -i_{II} \\ i_c = -i_a - i_b \end{cases} \quad \text{for } \frac{5\pi}{3} \le \theta \le 2\pi \qquad (7.49)$$

In the above equation, $\frac{d\theta}{dt} = p\,\omega_m$

For both periods, the torque equations are

$$\begin{cases} T_e = K_{em}(\bar{e}_a i_a + \bar{e}_b i_b + \bar{e}_c i_c) \\ T_e = J\frac{d\omega_m}{dt} + D\,\omega_m + T_l + T_c \end{cases} \qquad (7.50)$$

where T_e is the electromagnetic torque;

T_l is the load torque;

T_c is the cogging torque;

J is the intertia of the rotor, including the inertia of any coupled load;

D is the damping factor.

Therefore the state-variables are chosen as:

$$\begin{cases} y_1 = t \\ y_2 = \omega_m \\ y_3 = i_I \\ y_4 = i_{II} \\ y_5 = \theta \end{cases} \tag{7.51}$$

The state equations are:

For period 1:

$$\frac{dy_1}{dt} = 1$$

$$\frac{dy_2}{dt} = \frac{1}{J}(T_e - D\,y_2 - T_l - T_c)$$

$$\frac{dy_3}{dt} = -C_1\,y_3 + C_{21} - \frac{C_3}{3}y_2\,(2\,e_I - e_{II} - e_{III})$$

$$\frac{dy_4}{dt} = -C_1\,y_4 + C_{22} - \frac{C_3}{3}y_2\,(2\,e_{II} - e_I - e_{III})$$

$$\frac{dy_5}{dt} = p\,y_2 \tag{7.52}$$

For period 2:

$$\frac{dy_1}{dt} = 1$$

$$\frac{dy_2}{dt} = \frac{1}{J}(T_e - D\,y_2 - T_l - T_c)$$

$$\frac{dy_3}{dt} = -C_1\,y_3 + C_{23} - \frac{C_3}{2}y_2\,(e_I - e_{III})$$

$$\frac{dy_4}{dt} = 0$$

$$\frac{dy_5}{dt} = p\,y_2 \tag{7.53}$$

In the above equations e_I, e_{II}, e_{III} are the back-emfs, and

$$\begin{aligned} T_e &= K_{em}(\bar{e}_a\,i_a + \bar{e}_b\,i_b + \bar{e}_c\,i_c) \\ &= K_{em}(e_I\,i_a + e_{III}\,i_b + e_{II}\,i_c) \end{aligned} \tag{7.54}$$

The initial values of all the variables are zero.

7.5.3 Numerical Integration of State-variable Equations

In electrical engineering, the two most popular numerical integration methods for solving the state equations of a system are the Runge-Kutta method and the Adams-Bashforth method.

The state equations are:

$$\dot{y}(t) = F(y, v) \tag{7.55}$$

where y(t) is the state-variable and v is the control variable.

The main requirements of the 4th-order Runge-Kutta method are:

1) Calculate the slopes four times in each integration step;
2) Calculate the weighted average slope;
3) Determine the variable values of the next step by the formulae:

$$y_{i+1} = y_i + \frac{1}{6}(K_1 + 2K_2 + 2K_3 + K_4) \tag{5.56}$$

where

$$K_1 = hF(y_i, t_i)$$

$$K_2 = hF\left(y_i + \frac{K_1}{2}, t_i + \frac{h}{2}\right)$$

$$K_3 = hF\left(y_i + \frac{K_2}{2}, t_i + \frac{h}{2}\right)$$

$$K_4 = hF\left(y_i + \frac{K_3}{2}, t_i + h\right) \tag{7.57}$$

and h is the step length of integration.

The main advantage of the Runge-Kutta method is that when y_{i+1} is calculated only y_i is used. Therefore it is very easy to change the step length of integration because it is a mono-step method. Furthermore its calculation accuracy is quite high (the residue error is $O(h^5)$). However it requires four slopes in order to calculate the slope in one integration step, and thus the calculation time

is high. If a larger integration step is used the calculation accuracy will be reduced, and may lead to unstability.

The Adams-Bashforth method is a multi-step method. At time t_i it estimates the value y'_{i+1} at time t_{i+1} by utilising the variable values and their first-order differential values in the previous steps. Calibration formulae are then used to improve the accuracy of the estimated results.

The estimation and calibration formulae are:

$$y'_{i+1} = y_i + \frac{h}{24}(55\ \dot{y}_i - 59\,\dot{y}_{i-1} + 37\,\dot{y}_{i-2} - 9\,\dot{y}_{i-3})$$

$$y_{i+1} = y_i + \frac{h}{24}(9\,\dot{y}'_{i+1} + 19\,\dot{y}_i - 5\,\dot{y}_{i-1} + \dot{y}_{i-2}) \qquad (7.58)$$

where y'_{i+1} are the estimated values of y at t_{i+1}, whilst y_{i+1} are their calibrated values.

The main advantages of the Adams-Bashforth method are its comparatively high accuracy, which has the same order of residue error as the Runge-Kutta method, and its comparatively high stability. Because it needs to calculate the slope only once, it takes less computer time than the 4th-order Runge-Kutta method. However the estimated results of one step are related to the previous values of several steps, eg. when y_{i+1} is calculated, values y_i, $\dot{y}_i$, $\dot{y}_{i-1}$, $\dot{y}_{i-2}$, and $\dot{y}_{i-3}$ are used.

When the integrated function has a sudden transition, which often occurs in brushless DC drives as the transistors and the conducting windings are commutated, the differential value changes very quickly, and a larger error will be introduced in the Adams-Bashforth method unless special methods are used to compensate for this. In such circumstances it is better to use the Runge-Kutta method.

In this study, therefore, the 4-th order Runge-Kutta method is used.

Fig 7.21 shows the predicted transient phase current, torque, and speed time waveforms during the starting period for the non-overlapping winding radial-field motor referred to earlier. The drive has a current limit of 3A. Therefore when the phase current tends to exceed the current limit when only two phase windings are conducting it is set to the default of 3A. However during the transient period there is a surge in the current waveform which is larger than 3A. This is due to the circulating current which flows when all three phase windings are conducting, but which makes no contribution to the line current.

7.6 Comparison of Predictions from Different Approaches

The analytical steady-state dynamic model and the state-variable transient model for simulating the performance of brushless DC drive systems have been validated against tests as well as against predictions from an earlier numerical model developed at the University of Sheffield [7.7]. The validation is described in this section, and the integration of the state-variable model into a more sophisticated system simulation package is indicated.

Figs 7.21 and 7.23 compare the predicted and measured current waveforms under normal commutation for the radial-field motor having non-overlapping windings, whilst Figs 7.24, 7.25, 7.26 and 7.27 show comparisons for 14 degrees elec. advanced and 14 degrees elec. retarded commutation. In the figures, (a) is the measured waveform, (b) is the predicted waveform from the analytical steady-state simulation model, (c) is the predicted waveform from the state-variable simulation model, and (d) is the predicted waveform from Liu's earlier numerical simulation program [7.7]. Excellent agreement is obtained under different load and commutation conditions.

The analytical simulation technique, though being restricted to the analysis of the steady-state dynamic performance, provides a rapid means of assessing the important features of motor and drive performance during the early stages of design since the initial conditions which yield the

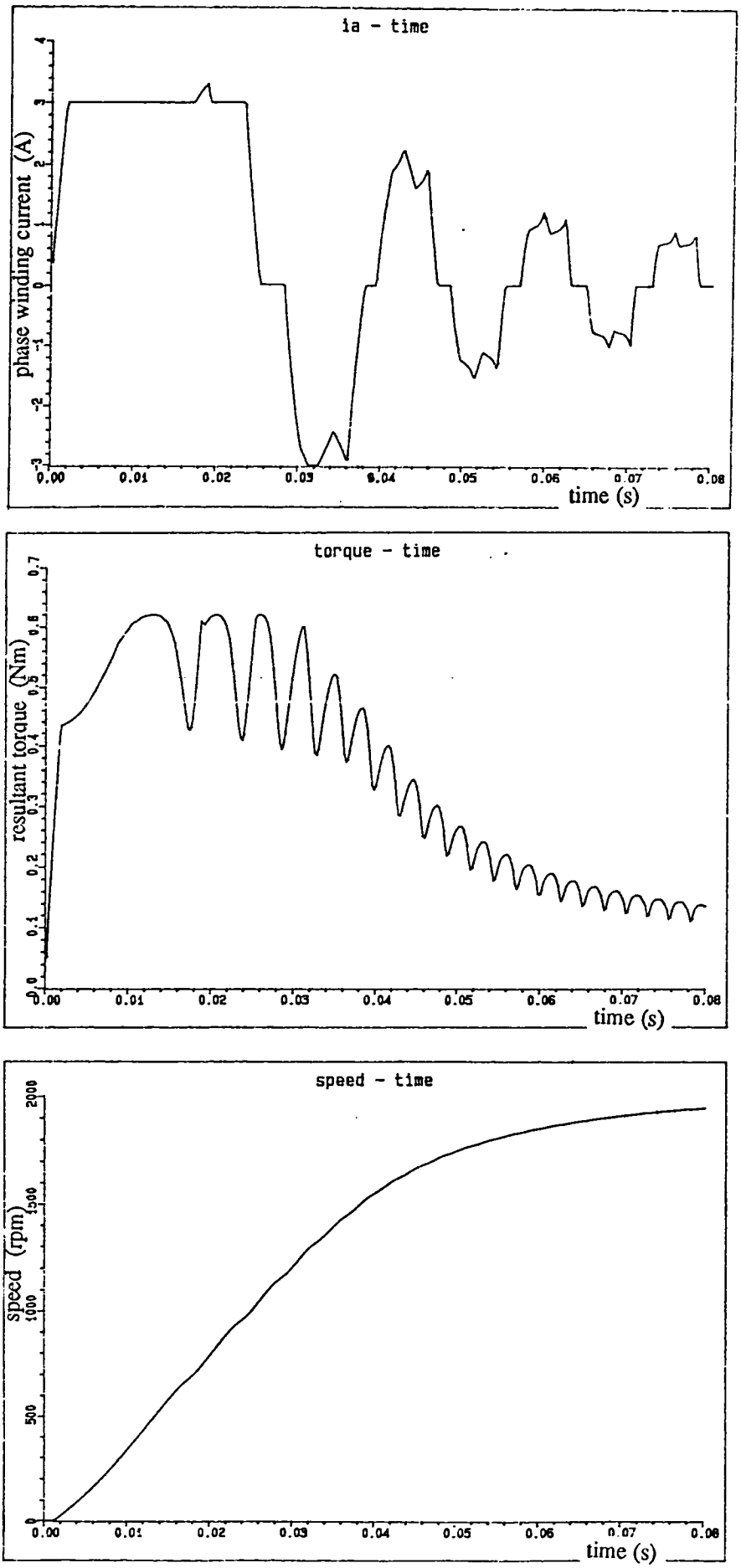

Fig. 7.21 Transient phase current, torque, and speed traces

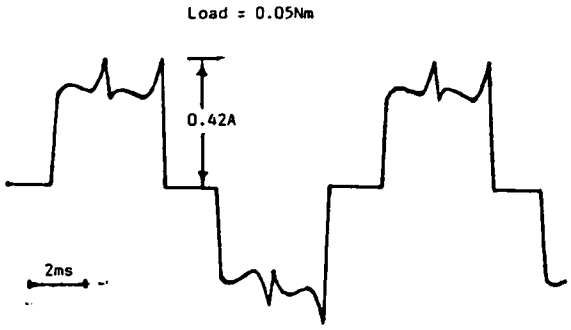

(a) measured

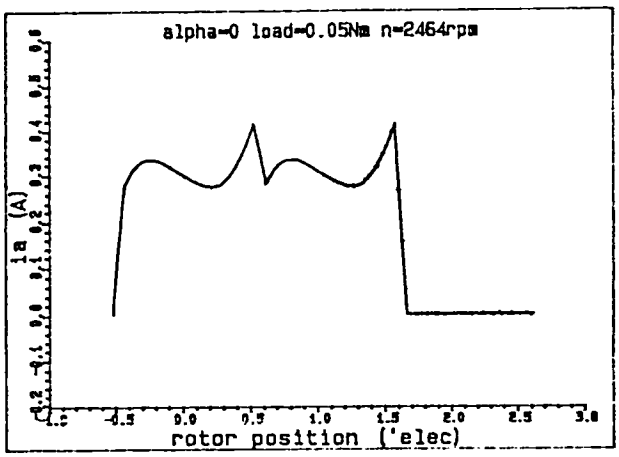

(b) predicted by analytical method

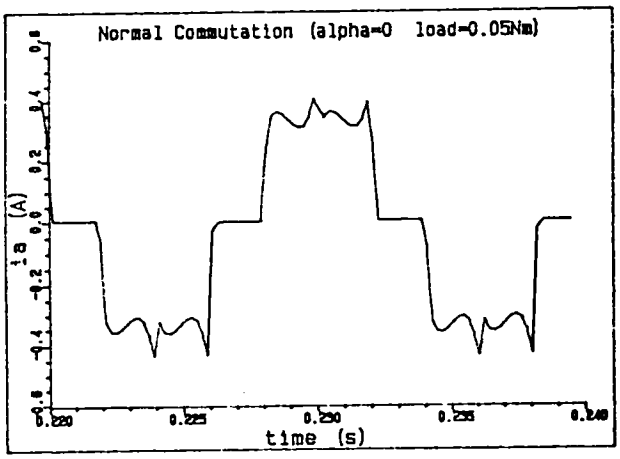

(c) predicted by state-variable method

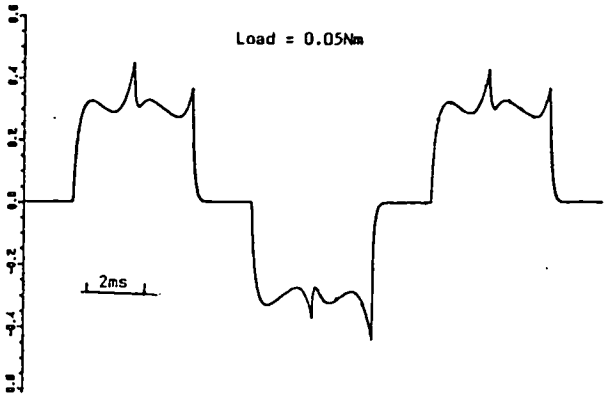

(d) predicted by [7.7]

Fig 7.22 Comparison of stator current waveforms with measurement
Normal commutation, Load = 0.05 Nm

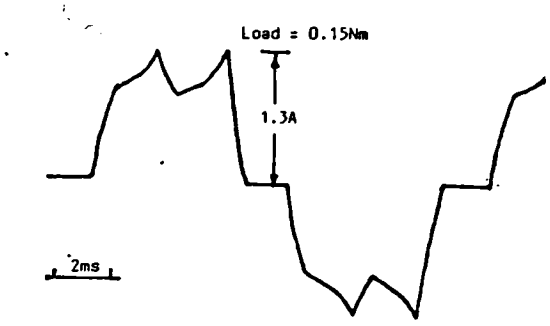

(a) measured

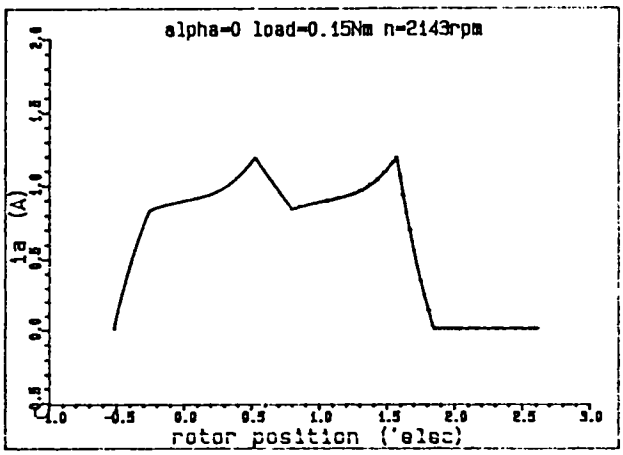

(b) predicted by analytical method

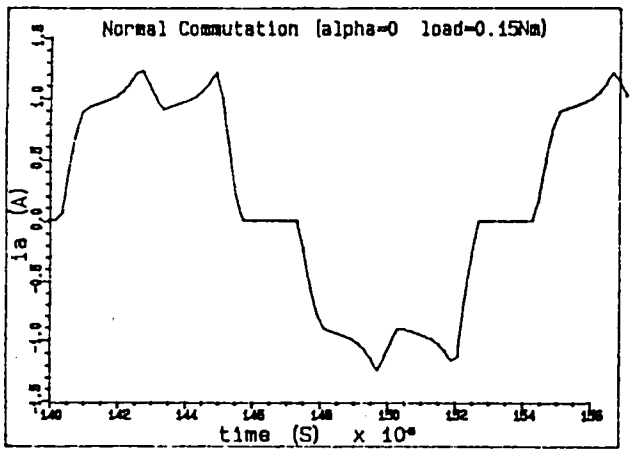

(c) predicted by state-variable method

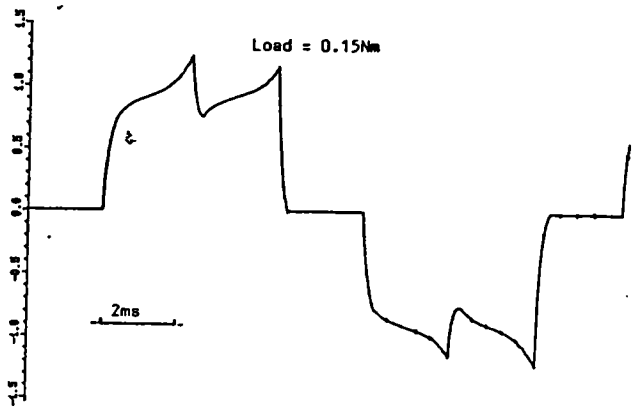

(d) predicted by [7.7]

Fig 7.23 Comparison of stator current waveforms with measurement
Normal commutation, Load = 0.15 Nm

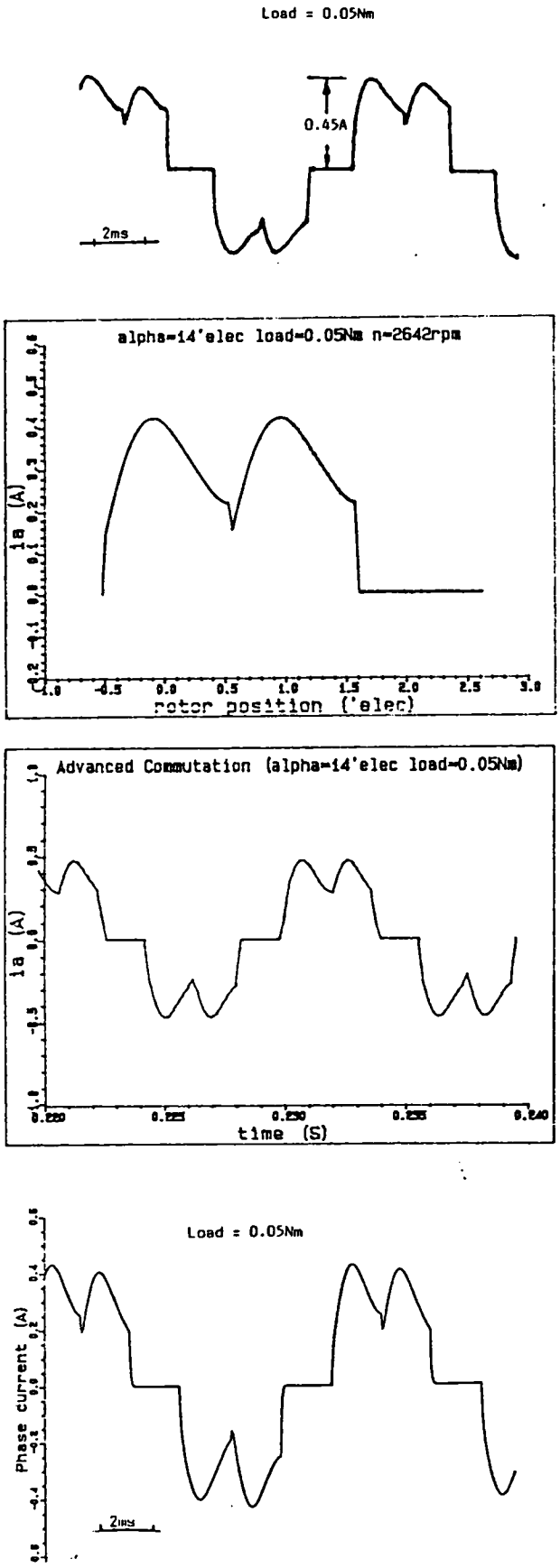

(a) measured

(b) predicted by analytical method

(c) predicted by state-variable method

(d) predicted by [7.7]

Fig 7.24 Comparison of stator current waveforms with measurement
14^{o} elec. advanced commutation, Load = 0.05 Nm

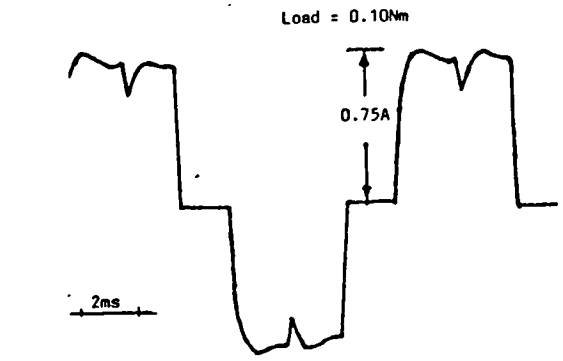

(a) measured

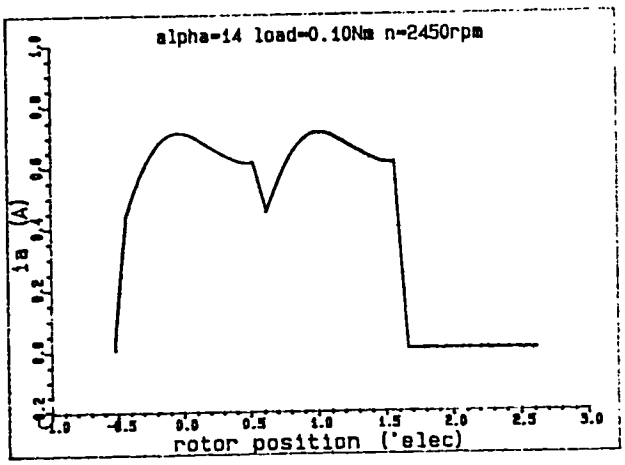

(b) predicted by analytical method

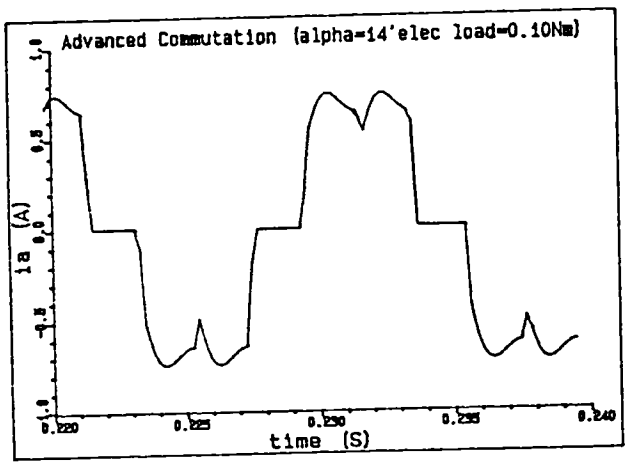

(c) predicted by state-variable method

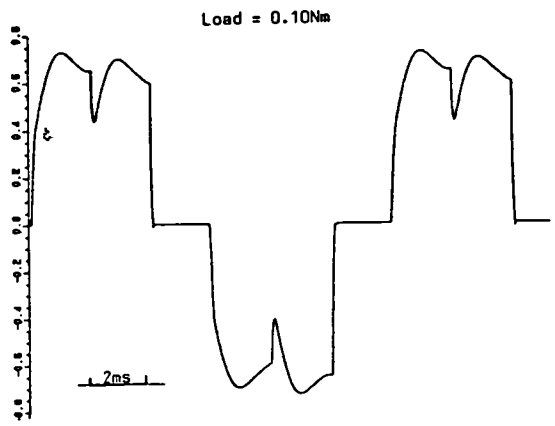

(d) predicted by [7.7]

Fig 7.25 Comparison of stator current waveforms with measurement
14^{o} elec. advanced commutation, Load = 0.10 Nm

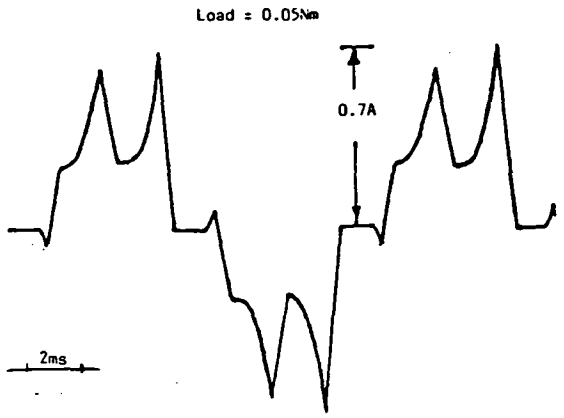

(a) measured

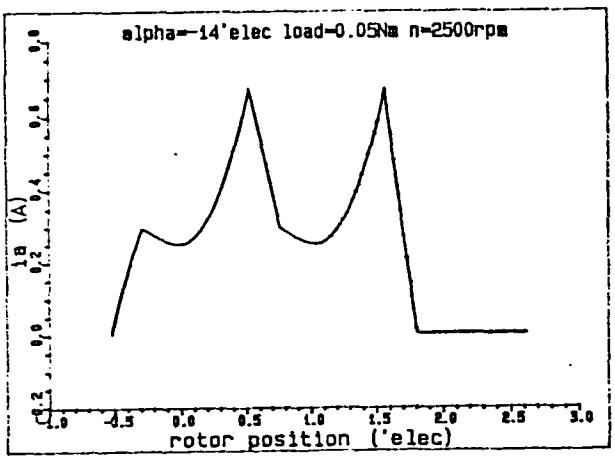

(b) predicted by analytical method

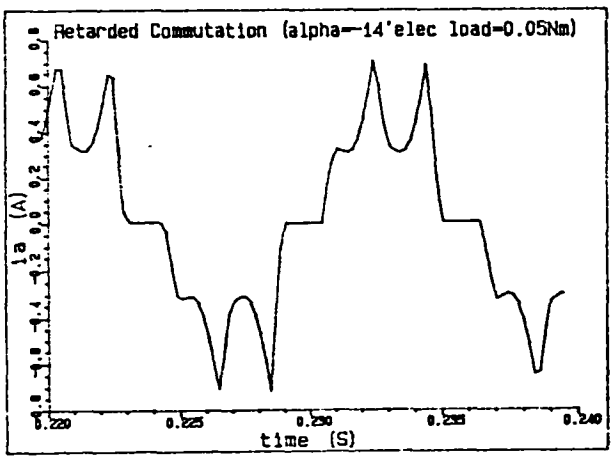

(c) predicted by state-variable method

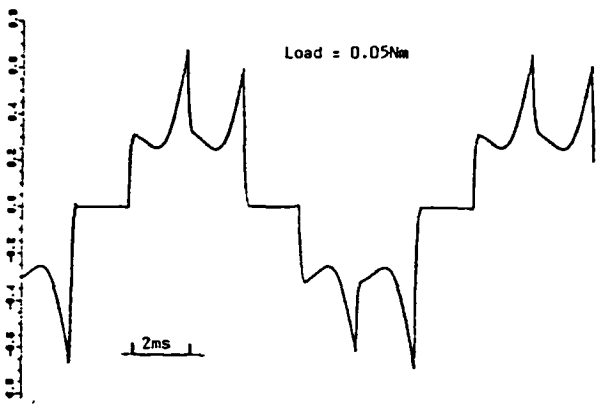

(d) predicted by [7.7]

Fig 7.26 Comparison of stator current waveforms with measurement
14^{o} elec. retarded commutation, Load = 0.05 Nm

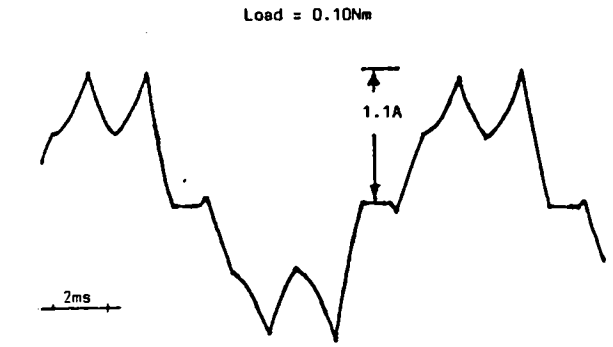

(a) measured

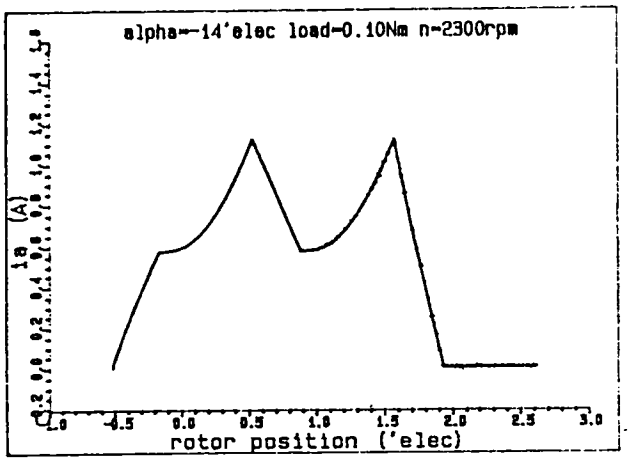

(b) predicted by analytical method

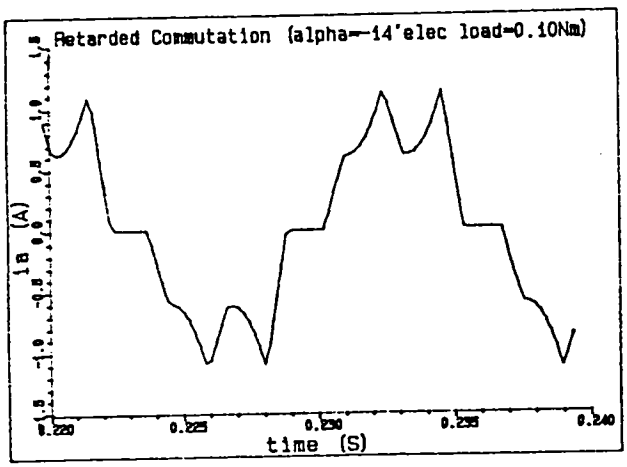

(c) predicted by state-variable method

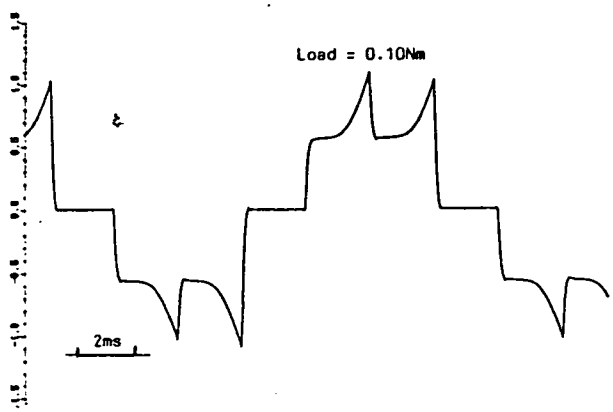

(d) predicted by [7.7]

Fig 7.27 Comparison of stator current waveforms with measurement
14^{o} elec. retarded commutation, Load = 0.10 Nm

steady-state solution are generated directly by exploiting the periodicity in the stator winding current waveforms. The calculation is only necessary for 1/6 of a cycle of a complete current waveform.

In contrast, other numerical techniques for predicting the steady-state performance require computation over about a hundred cycles, depending on the inertia of the rotor. Therefore the angular position increment in the numerical computation is very critical since if it is too small the computing time will increase greatly, whilst if it is too large the conducting time of the diodes will be not predicted to the required accuracy, and a large error will be introduced into the prediction of the current, and hence the torque waveform. Since a typical increment angle is around 0.0001 - 0.00001 electrical rad., computation time will be excessive for predicting the steady-state dynamic performance during the routine design studies. Nevertheless a numerical transient dynamic model is necessary when the speed ripple is likely to be large, and when a brushless DC motor is to be used in a servo or control system. The proposed transient dynamic model, based on the idealised state-variables, offers the following advantages compared to alternative approaches [7.7]:

a) The model is very simple. The electrical state equations are identical to those of the steady-state model.
b) The state equations are in standard forms, and hence do not involve the inversion of the coefficient matrix as in [7.7].
c) Unlike the situation in [7.7] the coefficient matrices of the state equations need not change their values in all of the commutation intervals. This is the major advantage of the proposed idealised model.
d) It has been shown that it is appropriate to use a constant voltage drop and a resistance to represent the characteristics of transistors and diodes when they are conducting. This simple method of the switching devices combined with the Runge-Kutta integration method for solving the state equations has eliminated the disadvantages associated with the Adams-Bashforth integration method [7.7], which requires special models of the devices

so as to avoid large errors in the solution during the commutation period. For example in [7.7] a resistance-inductance model is employed in which the inductance and resistance are selected such that the "off" state impedance of an open-circuited phase has a time constant similar to that of the "on" state phase. By so doing the transition of the differential values of the currents during the switching period is smoothed and numerical instability avoided. However such an approach introduces two disadvantages: the order of the state equations is greatly increased (almost doubled), which greatly increases the simulation time; and an inductance must be specified for the switching devices, which might cause difficulty when different drive systems have to be simulated.

As a result, the developed numerical dynamic model for simulating the transient and steady-state dynamic performance of a brushless DC drive can now be used as a single functional block in a general purpose system simulation package developed at the University of Sheffield, as shown in [7.11].

7.7 Effects of Commutation and Temperature on Dynamic Performances

There are many aspects which affect the dynamic performances of a brushless DC drive. For example, the machine parameters, viz. winding inductances and resistances, the free-wheeling diodes, the back-emf waveforms. Temperature is also another consideration since it affects the properties of magnets as well as the resistance of windings.

Fig 7.28 shows how the demagnetising characteristic of two generic types of permanent magnets vary with temperature. Ferrite magnets have a positive temperature coefficient of intrinsic coercivity, whilst NdFeB magnets have a negative one, both have a negative temperature coefficient of remanence. A temperature rise will therefore affect the open-circuit magnetic field and hence the back-emf waveform, which in turn will cause the dynamic performances to deviate from that at room temperature. In this section, however, attention is focussed on the effects of the commutating instant and the temperature rise of the stator windings.

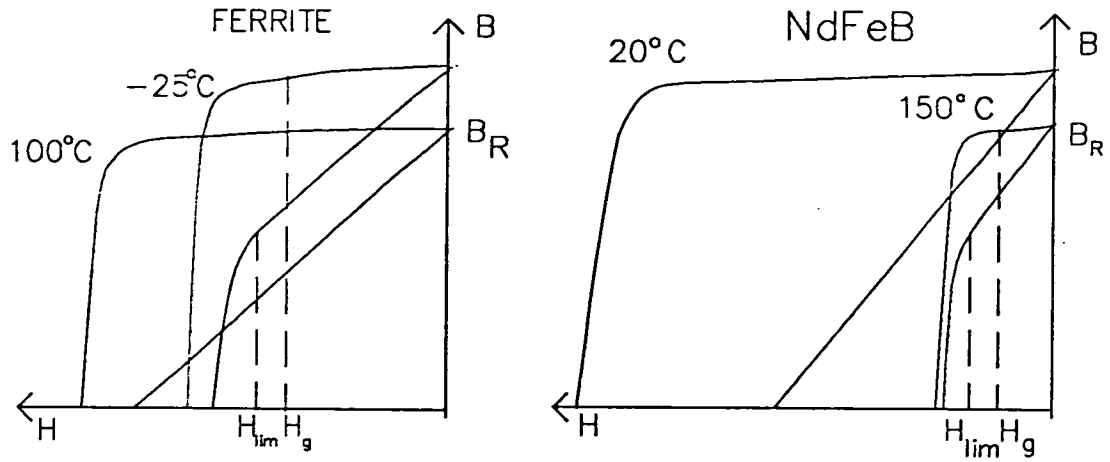

Fig. 7.28 Variation of demagnetising curve with temperature

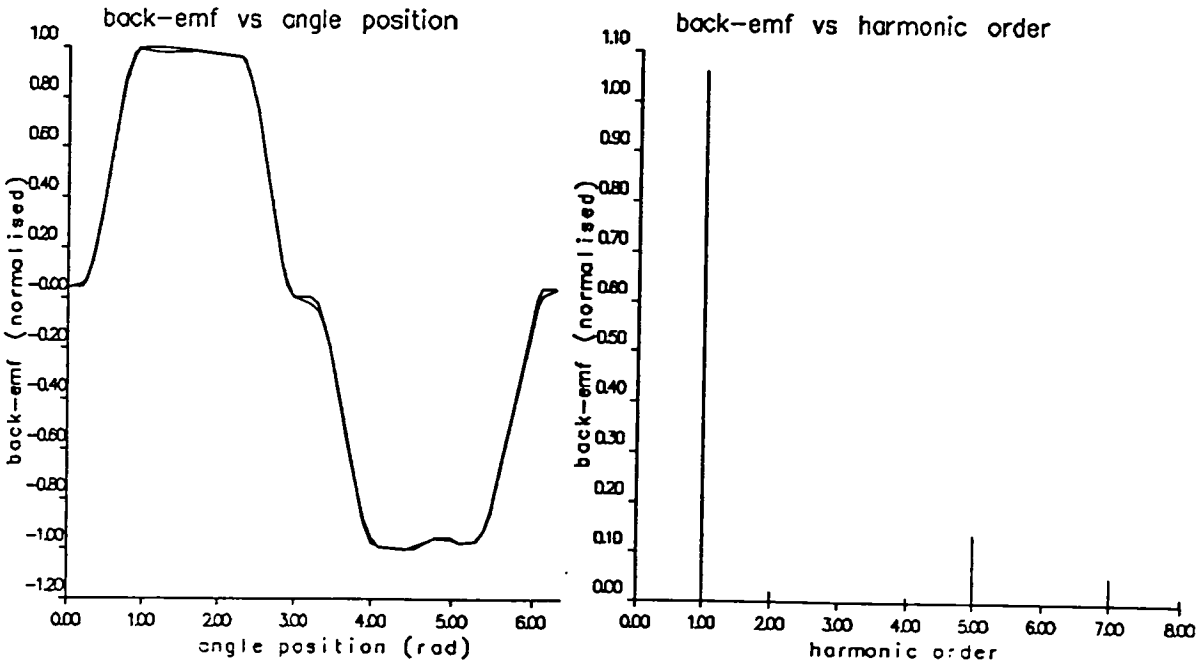

Fig. 7.29 Normalised back-emf waveform and its spectrum

7.7.1 Commutation Effects

In this section the effect of commutation on the current and torque waveforms and their spectra, as well as on the linearity of the torque-speed curve is investigated. The spectrum analysis is based on an analytical approach to Fourier series analysis which will be described in Chapter 8. Fig 7.29 shows the normalised measured back-emf waveform and its spectrum for the prototype non-overlapping winding motor, together with the waveform synthesised from a finite number of terms in the Fourier series, terms being neglected if their amplitude is smaller than 1/100 of the fundamental component. Clearly very good agreement is obtained between the actual and synthesised waveforms.

Figs 7.30 and 7.31 compare the phase current and torque waveforms and their spectra at loads of 0.05Nm and 0.1Nm respectively, whilst Figs 7.32 and 7.33 compare the current and torque waveforms and their spectra the normal, 14 degrees elec. advanced, and 14 degrees elec. retarded commutation. Figs 7.34 and 7.35 compare predicted and measured torque-speed curves for the different commutation conditions. The results show that:

i) The load condition does not affect the shape of the current and torque waveforms significantly, whilst the commutation strategy does have a major effect.

ii) The "flat" top of the 'trapezoidal' back-emf waveform for this non-overlapping winding motor is only around 120 degrees elec. Therefore when operated with 14 degrees elec. advanced commutation, at the instant when a phase is commutated on its back-emf is very small, so that the current rises more rapidly than for normal commutation. However due to the smaller back-emf at the beginning of the conducting period, the torque ripple is increased. However, the average phase current may be increased and hence the average torque is likely to be higher, although this depends on the average value of the product of the instantaneous back-emf and current during the conducting period.

iii) In contrast to ii), when the commutation is retarded by 14 degrees elec. the back-emf at the beginning of the conducting period of a phase winding has a maximum value corresponding to the 'flat top' of the waveform, whilst at the end of the period it has a much lower value.

Hence the phase current waveforms for 14 degrees elec. retarded commutation are initially similar to those for normal commutation but then becomes larger, ie. the peak of the current waveform occurs at the end of the conducting period, and is usually larger than that for normal or advanced commutation. As a consequence, more current harmonics exist. However, due to the smaller back-emf near the end of the conducting period, the torque ripple may remain small.

iv) It is clear that if the back-emf has the ideal symmetrical trapezoidal waveform and its 'flat-top' is wider than 120 degrees elec., then either advancing or retarding the commutation will have no effect on either the current or torque waveforms, as well as the torque-speed characteristic, as long as the whole of the conducting period falls within the period corresponding to the 'flat-top' of the emf. For example, if the 'flat-top' of the back-emf waveform is 150 degrees elec. then advancing or retarding the commutation by up to 15 degrees elec. will have no effect on either the current or torque waveforms, or the torque-speed curve.

v) For a particular back-emf waveform, the phase current and resultant torque may be increased by varying the commutation angle. Normally the commutation of the current in a particular phase is time delayed by an angle $\beta = 30$ degrees elec. from the zero crossing of its back-emf waveform. Therefore the angle by which commutation is advanced or retarded should be within a maximum value of 30 degrees elec., otherwise the efficiency of the motor and drive will decrease significantly due to the back-emf being negative during the part of the conducting period, and the additional copper loss, as shown in Fig 7.36.

vi) Again, by varying the commutation angle the torque-speed curve is modified, as shown in Fig 7.35. For a given operating speed, there is an optimum commutation angle at which the efficiency of the motor or drive is a maximum. Fig 7.36 shows the predicted variation of the average phase current, the torque, and the efficiency of the non-overlapping winding motor with the commutation angle. Clearly the variation will depend largely on the back-emf waveform and the parameters of the motor.

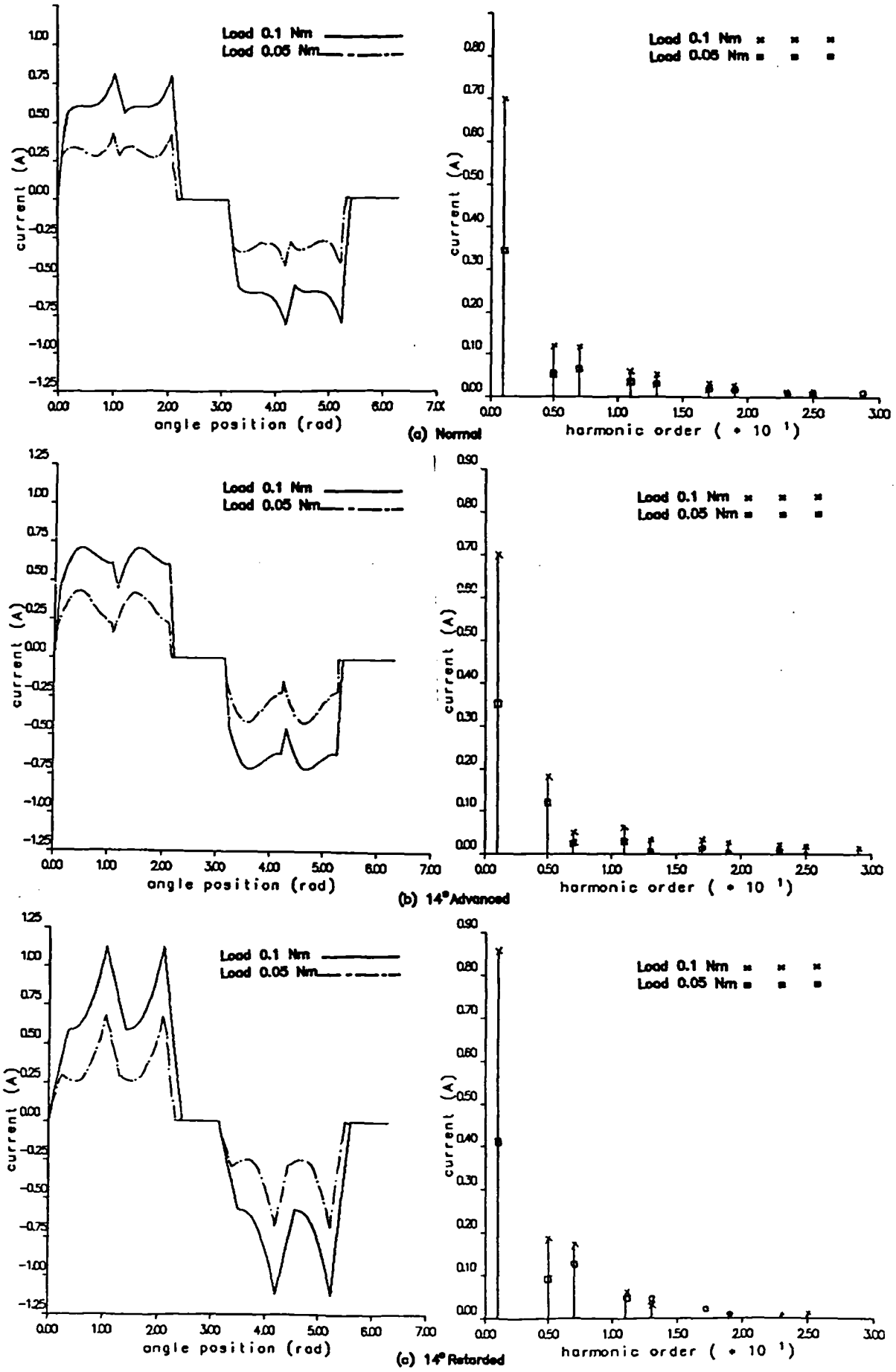

Fig. 7.30 Effects of load/commutation on the current waveform and spectrum

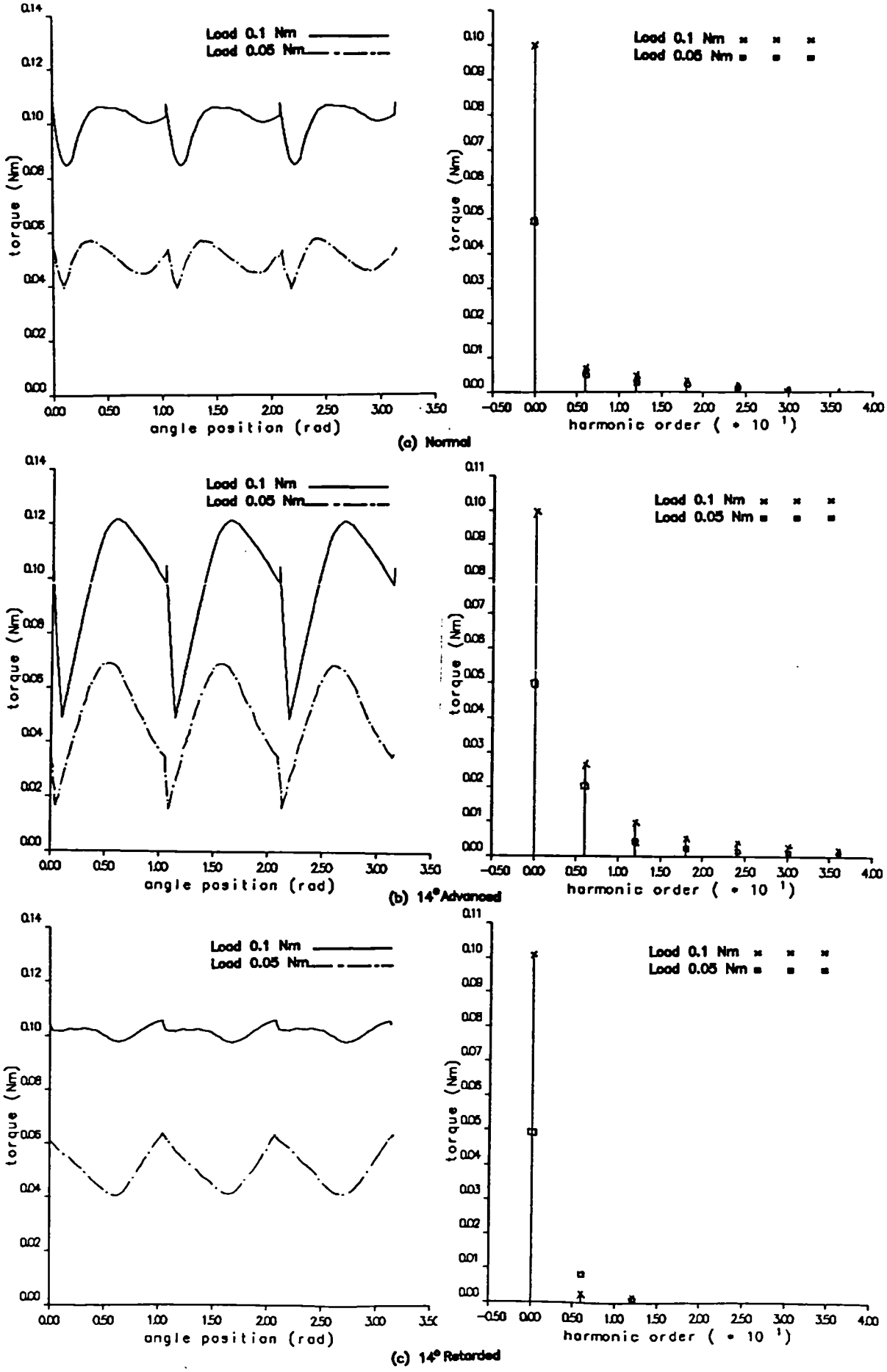

Fig. 7.31 Effects of load/commutation on the torque waveform and spectrum

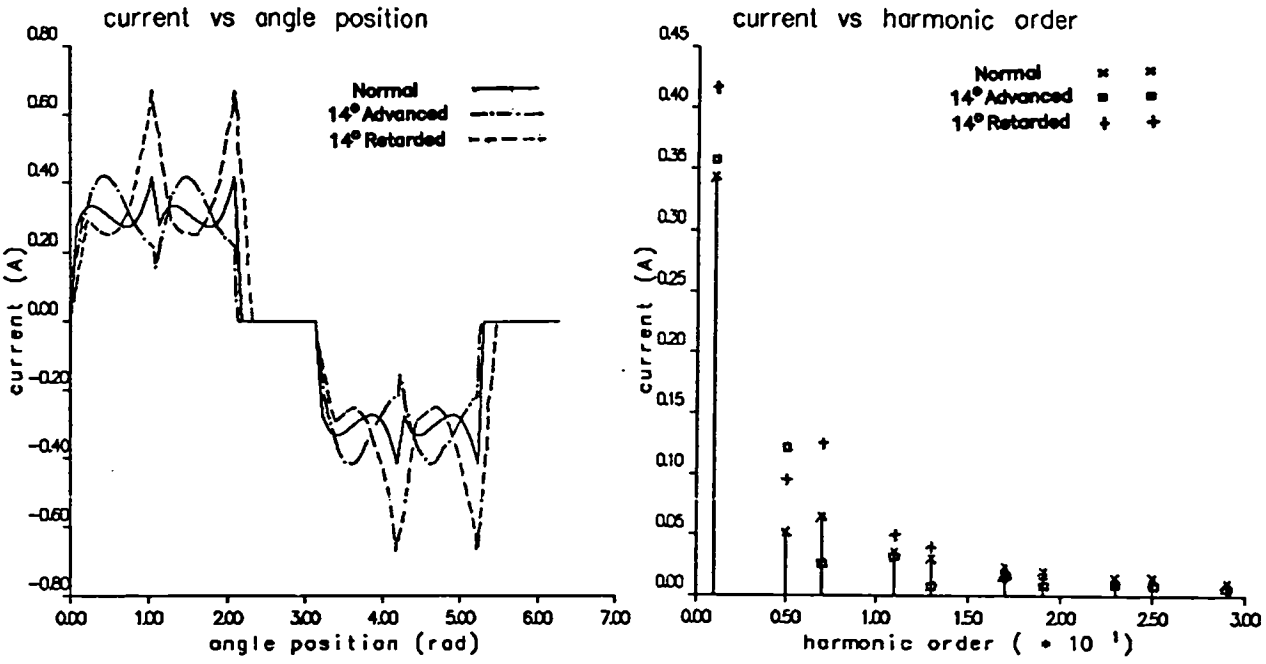

(a) Current

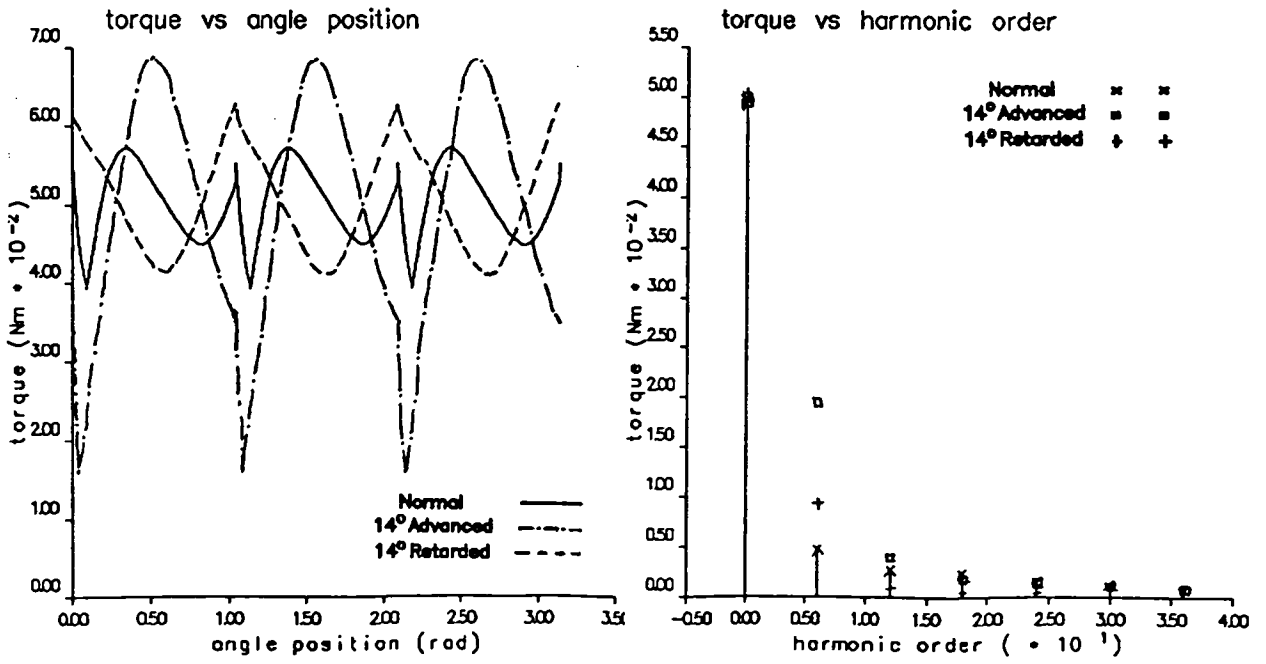

(b) Torque

Fig. 7.32 Commutation effect on the current and torque waveforms and spectra (0.05 Nm)

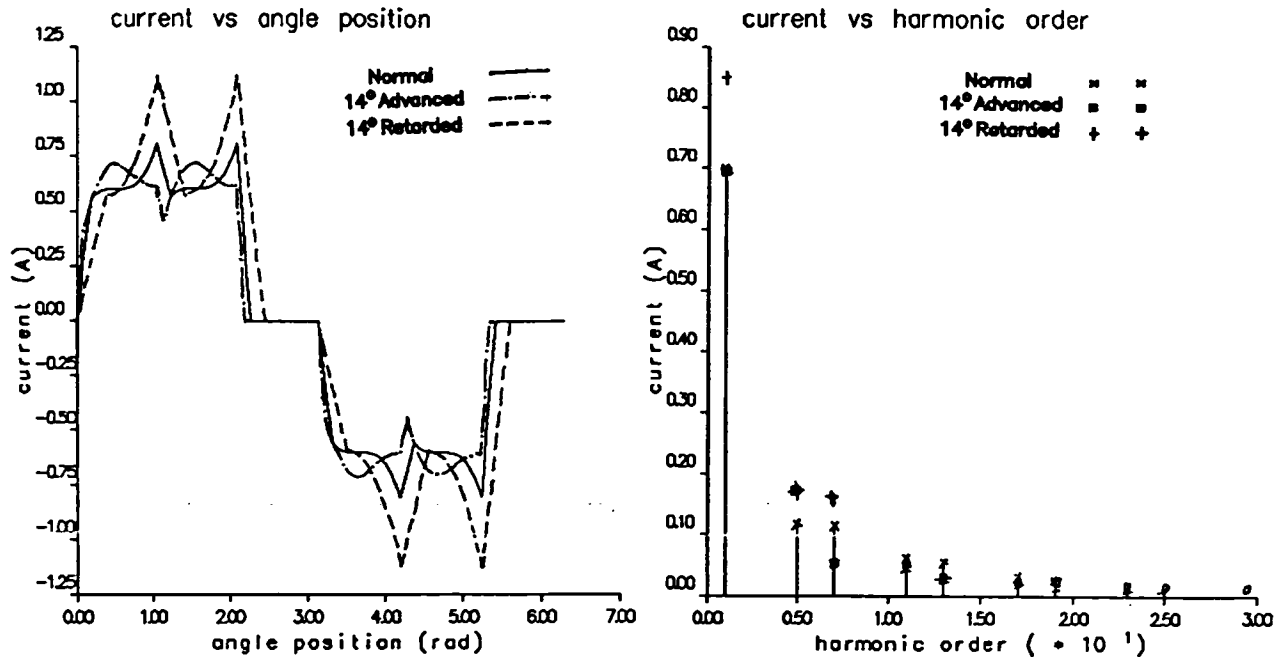

(a) Current

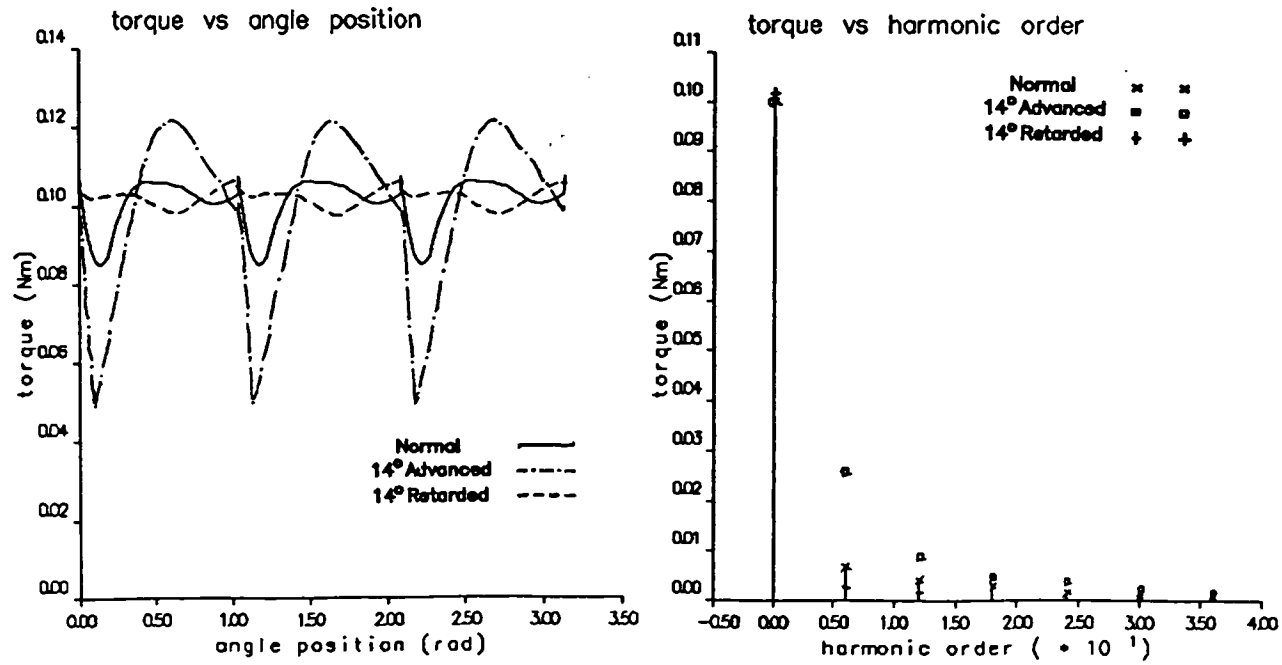

(b) Torque

Fig. 7.33 Commutation effect on the current and torque waveforms and spectra (0.10 Nm)

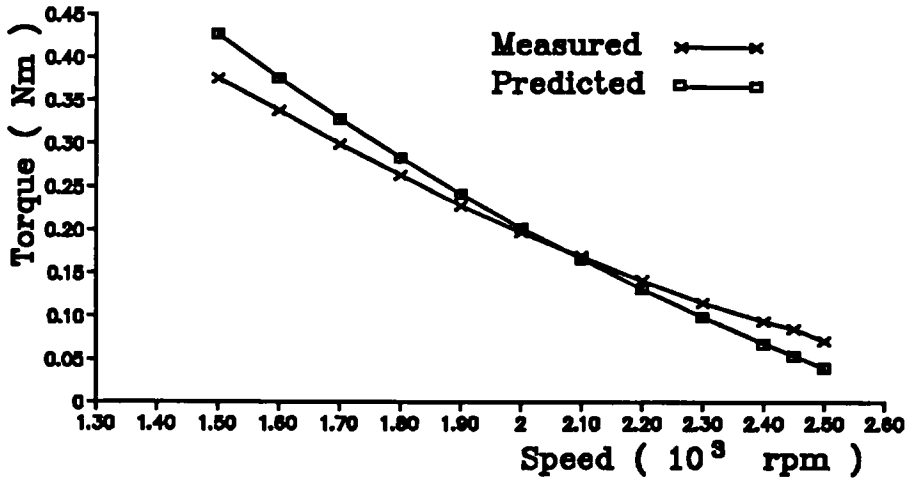

(a) Normal commutation

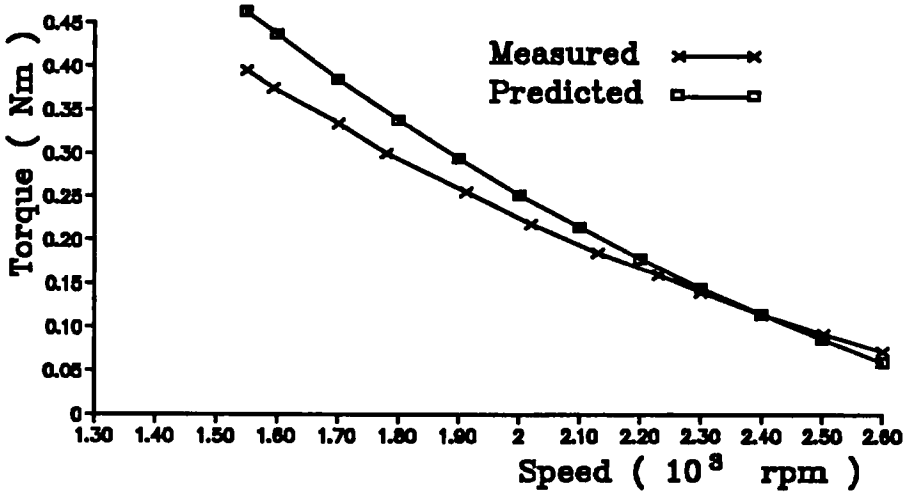

(b) Advanced commutation (14 elec.deg.)

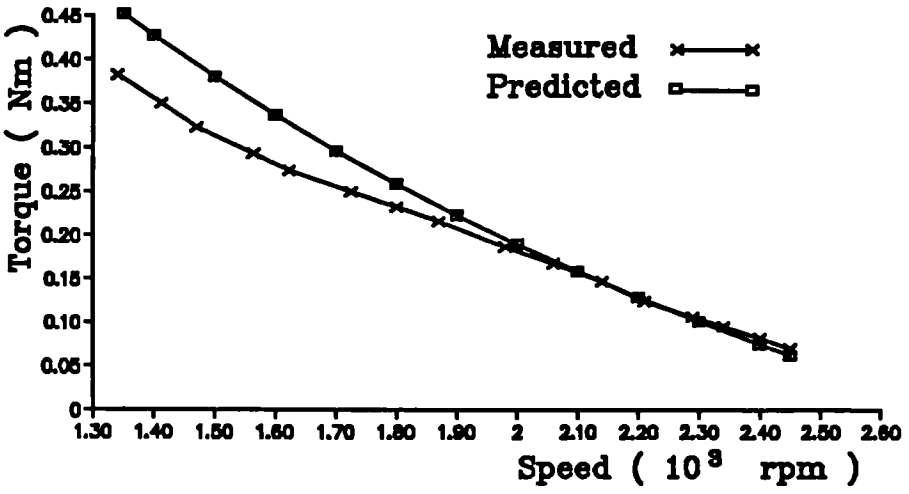

(c) Retarded commutation (14 elec.deg.)

Fig 7.34 Comparison of torque-speed curves

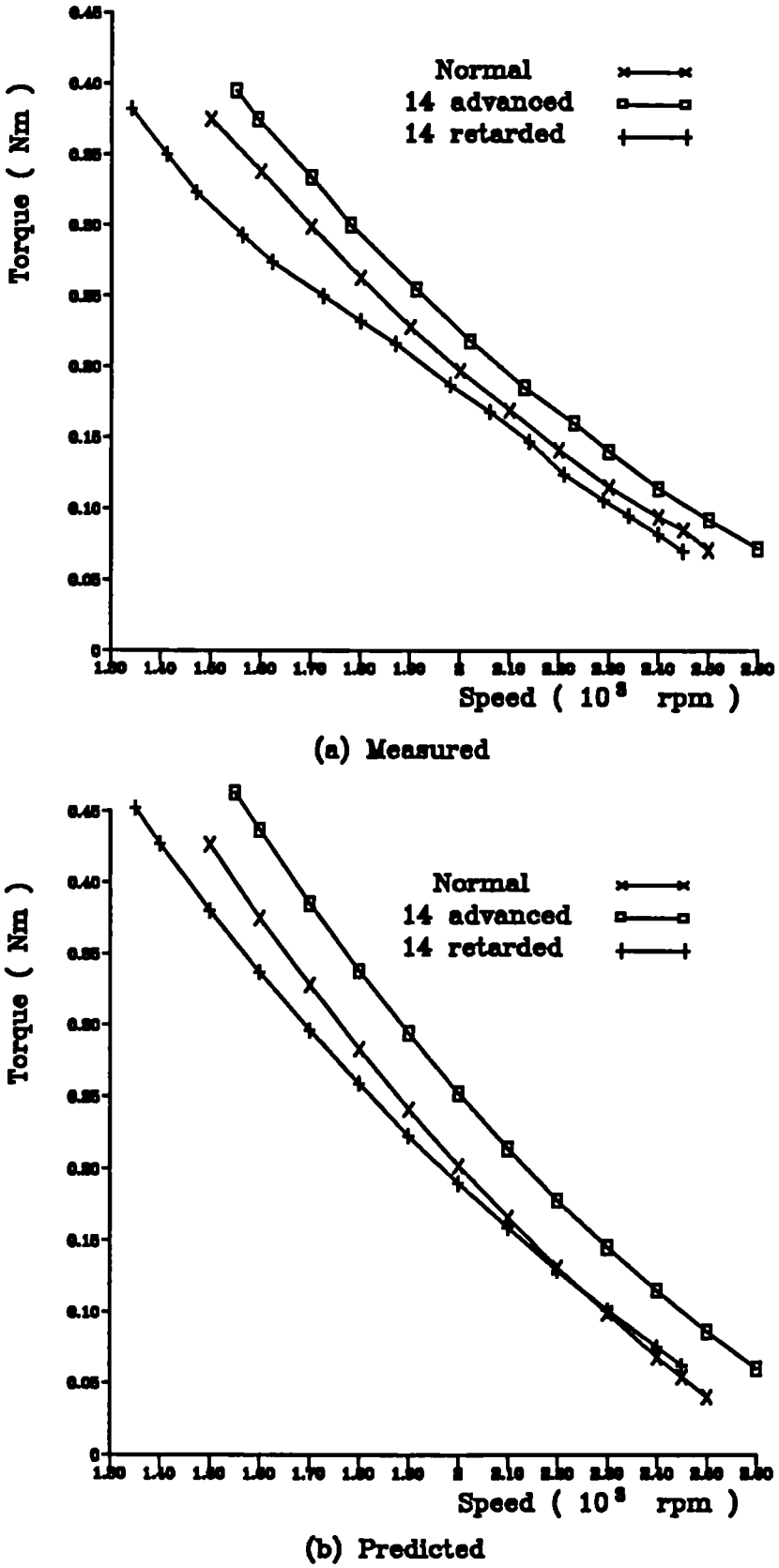

Fig 7.35 Effect of commutation on the torque-speed curves

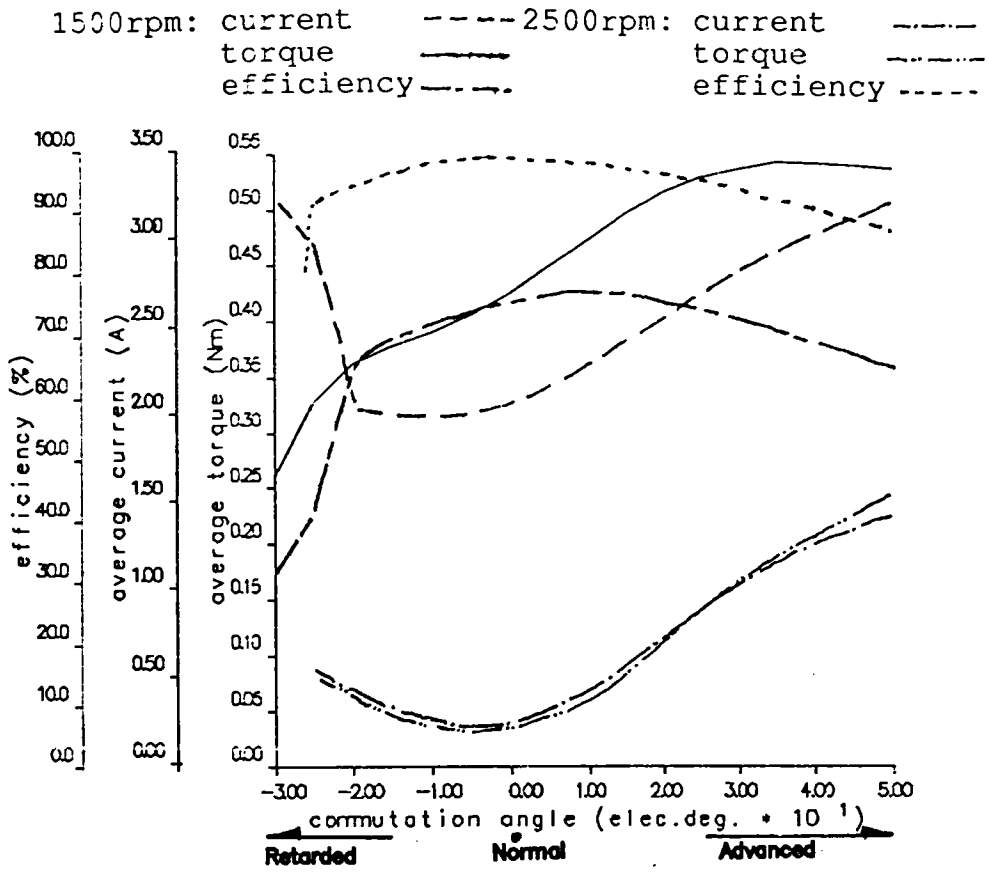

Fig. 7.36 Variation of average current, torque, and efficiency of non-overlapping winding motor with the commutation angle

7.7.2 Temperature Effect

In Fig 7.34 it will be observed that there is a significant difference between the slope of the predicted and measured torque-speed characteristics under normal, advanced, and retarded commutation. However the predicted and measured torques agree quite well on light loads, whereas the predicted torque becomes somewhat higher than the measured value as the load is increased. It will be noted, however, that the predictions assume a constant winding resistance viz. the room temperature value.

The effect of temperature on the winding resistance is the most likely cause of such a deviation.

However the phase winding resistance R_t at any temperature "t" can be estimated from the resistance R_{to} at temperature "t_o" from:

$$R_t = \frac{234.5 + t}{234.5 + t_o} R_{t_o} \qquad (7.59)$$

As a consequence of the increase in phase winding resistance with load and therefore temperature, the winding current, and hence the torque, will be smaller than the value predicted for a constant resistance.

In Fig 7.34 every measured point was obtained under a stable thermal condition, ie. when the motor had run for a reasonably long time, whilst the corresponding predicted values are all calculated assuming a fixed winding resistance (21°C).

Fig 7.37 on the other hand compares the measured torque-speed curves for normal commutation of overlapping and non-overlapping winding motos with those predicted when winding resistances corresponding to temperature of 0 °C or 120 °C are used, as calculated from equation (7.59). The revised values are given in Table 7.6.

Table 7.6 Revised resistances for overlapping/ non-overlapping winding motors

phase winding resistance (Ω)	non-overlapping winding motor	overlapping winding motor
21°C (measured)	1.081	2.67
0°C (calculated)	0.99	2.45
120°C (calculated)	1.5	3.7

The measured torque-speed curve of both motors is now straddled by the predicted curves. However, a more detailed analysis would need a detailed thermal analysis so as to account for the variation of the demagnetising characteristic of the permanent magnet temperature, as well as a prediction of the frictional torque-speed characteristic etc.

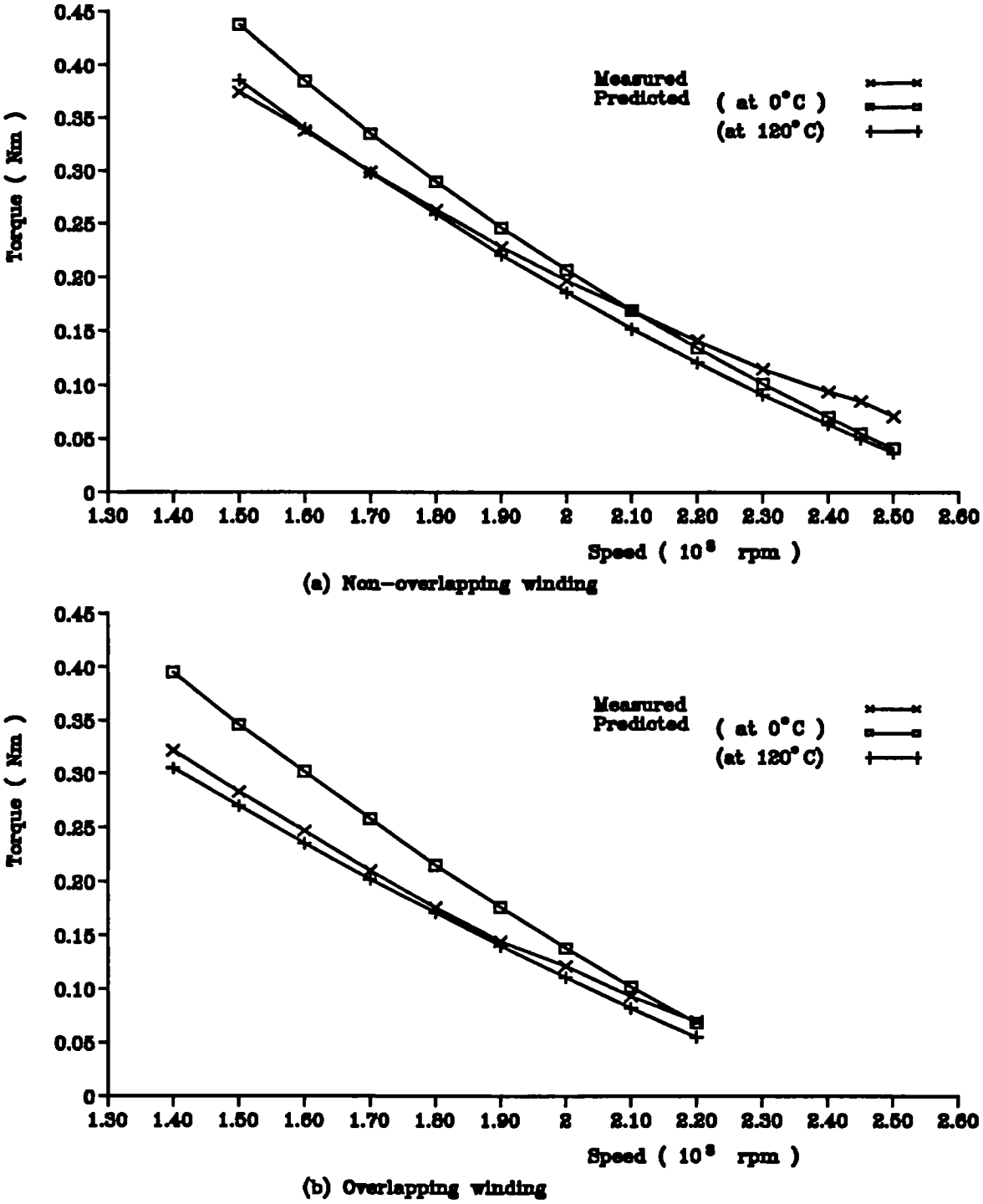

Fig 7.35 Effect of temperature on the torque-speed curves

7.7 Conclusions

It is useful to be able to simulate the steady-state dynamic operation of a brushless DC drive system during the early stages of design. The analytical technique which has been described and validated in this chapter would be eminently suitable for this purpose. The analytical technique presented can account for any induced back-emf waveform, and can model the characteristic of the switching devices and free-wheel diodes in the converter circuit by an appropriate voltage drop behind a series resistance. It can also cater for normal, advanced, or retarded commutation, as well as a pre-specified current limit. However since it is based on an analytical model, for which the initial conditions which yield the steady-state solution are generated directly by exploiting the periodicity in the stator winding current waveforms, it provides a rapid means of assessing some important features of the motor and drive performance, albeit with the assumption of negligible speed ripple.

By introducing two idealised current variables and incorporating the motion equation of the rotor, a more refined state-variable model for predicting both the transient and steady-state dynamic performance of a brushless DC drive has been developed and validated. Both models can be linked to other aspects of the design process, for example finite element analysis for predicting the back-emf waveforms and winding inductances. Further, although the analyses have been restricted to motors having three-phase, star-connected windings, the techniques are applicable equally to delta connected windings as well as to any number of phases.

The simulation models have been used to examine the effects of commutation and temperature (winding resistance) on the dynamic performance, ie. current and torque waveforms and their frequency spectra, torque-speed characteristics etc. It has been shown that the commutation strategy can have a significant effect on the dynamic performance, whilst the variation in phase winding resistance due to temperature changes may also cause a significant variation in the slope of torque-speed characteristics.

CHAPTER 8

MAGNETIC FIELD ANALYSIS IN BRUSHLESS DC MOTORS ON LOAD

8.1 Introduction

One consequence of the adoption of electronically controlled brushless DC drive systems is that the phase current waveforms contain significant harmonics, which, amongst other things, can greatly increase the possibility of resonances between the radial exciting forces and the stator structure as well as the total emitted acoustic noise. In order to predict the electromagnetic, vibrational, and acoustic behaviour it is necessary to analyse the airgap field distribution with the motor on no-load and on load.

Although several papers have been published on the calculation of the airgap magnetic field of a brushless DC motor[8.1[[8.2], none have been concerned with the prediction of the magnetic field on load.

The calculation of magnetic field in a loaded brushless DC motor involves the prediction of the open-circuit field produced by the rotor magnets and the armature reaction field produced by the 3-phase stator windings. The armature reaction field calculation is important not only in the prediction of radial exciting forces, but also in assessing whether the permanent magnets are prone to partial irreversible demagnetisation, as well as in the calculation of self- and mutual-winding inductances.

In Chapter 5 a technique for predicting the open-circuit magnetic field distribution in the airgap/magnet region of permanent magnet motors was presented. The technique was based on

an analytical two-dimensional model in polar coordinates and accounted for the effect of stator slotting on the magnetic field distribution. Excellent agreement with finite element calculations was achieved. In this chapter the analytical calculation is extended to cater for the armature reaction field produced by the stator windings.

The calculation of the armature reaction field in a brushless permanent magnet DC motor differs significantly from that for a conventional motor, such as the induction motor, in the following three aspects. Firstly, due to the low recoil permeability of the permanent magnets - typically μ_m is around $1.1\mu_o$, it has a much larger effective airgap. Secondly, the phase current waveforms contain significant harmonics as a result of the electronic commutation events. Thirdly, the magnetic field of the 3-phase stator winding does not rotate uniformly but in incremental steps at the instant of commutation.

The large effective airgap of a brushless DC motor would lead to a significant error if a conventional 1-d analysis in rectangular coordinates [8.3], such as those used in induction motors [8.4] was employed. Due to flux focussing and interpolar flux leakage a two-dimensional model is required.

This chapter describes a two-dimensional analytical technique, modelled in polar coordinates, which can account for the important features of a brushless DC motor cited above, in particular, the effects of stator winding distribution, the large effective airgap, the stator slot openings, and the winding current harmonics etc on the distribution of magnetic field on load. The predicted armature reaction field, due to the analytically calculated phase current waveform (Chapter 7), together with the open-circuit field produced by the magnets (Chapter 5) make it possible to predict the instantaneous field distribution under any specified load condition and commutation strategy. The predicted open-circuit, armature reaction, and load field distribution are compared with those obtained from corresponding finite element calculations.

8.2 Analytical Calculation of Armature Reaction Field in Brushless DC Motors

In a similar manner to the prediction of the open-circuit magnetic field described in Chapter 5, the armature reaction field is calculated in two steps. Firstly the 2-dimensional magnetic field produced by the windings in a smooth airgap is analysed, then the 2-dimensional relative permeance function, as described in Chapter 5, is introduced to account for the effect of slotting and to obtain the actual armature reaction field.

For simplicity the relative recoil permeability of the magnets is assumed to be unity, which will not introduce any significant error in the calculation of the load field distribution since under normal conditions the armature reaction field is usually only around 10 - 20% of the open-circuit field.

8.2.1 Magnetic Field of a Single Conductor

Fig 8.1 shows a single current carrying conductor in a cylindrical airgap for both internal rotor and external rotor motors. If end effects are neglected, the airgap is uniform, and the permeability of the stator and rotor iron is assumed to be infinite, the magnetic field is obtained by solving the two-dimensional Laplacian equation:

$$\nabla^2\varphi = \frac{1}{r}\frac{\partial}{\partial r}\left(r\frac{\partial \varphi}{\partial r}\right) + \frac{1}{r^2}\frac{\partial^2\varphi}{\partial \alpha^2} = 0 \qquad (8.1)$$

whose general solution is:

$$\varphi(\alpha, r) = \sum_{\nu} (A_\nu r^\nu + B_\nu r^{-\nu})(C_\nu \cos \nu\alpha + D_\nu \sin \nu\alpha) + (A_o \ln r + B_o)(C_o \alpha + D_o) \qquad (8.2)$$

Since the permeability of the iron is infinite, only a radial component of flux density exists on the stator and rotor surfaces, which gives rise to the boundary conditions:

$$\left\{\frac{\partial \varphi}{\partial r}\right\}_{r=R_i} = 0 \tag{8.3}$$

$$\left\{\frac{\partial \varphi}{\partial r}\right\}_{r=R_m} = 0 \tag{8.4}$$

The magnetic potentials on the stator and rotor surfaces can be obtained by integrating the magnetic field intensity on the iron surfaces, ie. for closed paths over the stator or rotor symmetrically enclosing the conductor which, according to Ampere's Law, gives:

$$\varphi|_{r=R_i} = \frac{i}{2}\left(\frac{\alpha}{\pi} - 1\right) = \frac{-i}{2} \sum_{\nu=1,2,3,\ldots}^{\infty} \frac{2}{\nu\pi} \sin \nu\alpha \tag{8.5}$$

$$\varphi|_{r=R_m} = 0 \tag{8.6}$$

for an internal rotor motor, and

$$\varphi|_{r=R_i} = \frac{i}{2}\left(1 - \frac{\alpha}{\pi}\right) = \frac{i}{2} \sum_{\nu=1,2,3,\ldots}^{\infty} \frac{2}{\nu\pi} \sin \nu\alpha \tag{8.7}$$

$$\varphi|_{r=R_m} = 0 \tag{8.8}$$

for an external rotor motor

where R_i is the radius of the stator surface.

$$R_m = R_i - g - h_m \text{ for an internal rotor motor, and}$$
$$R_m = R_i + g + h_m \text{ for an external rotor motor} \tag{8.9}$$

Hence for an internal rotor motor, shown in Fig 8.1(a), the magnetic scalar potential distribution produced by the conductor, obtained from the general solution, equation (8.2), and the boundary conditions, equations (8.3)-(8.6), is

$$\varphi = \frac{-i}{\pi} \sum_{\nu=1,2,3,\ldots}^{\infty} \frac{R_i^{\nu}}{\nu} \left[\frac{1}{R_i^{2\nu} - R_m^{2\nu}} r^{\nu} - \frac{R_m^{2\nu}}{R_i^{2\nu} - R_m^{2\nu}} r^{-\nu}\right] \sin \nu\alpha \tag{8.10}$$

and components of the flux density are then calculated from:

$$B_r = -\mu_o \frac{\partial \varphi}{\partial r}$$

$$B_\alpha = -\mu_o \frac{\partial \varphi}{\partial \alpha} \tag{8.11}$$

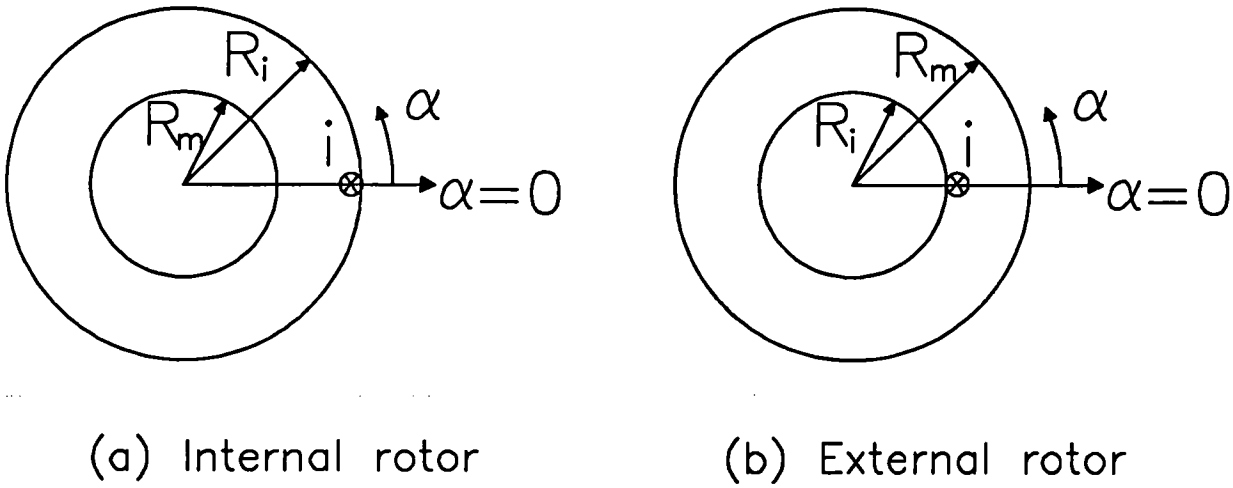

(a) Internal rotor (b) External rotor

Fig 8.1 Magnetic field of a conductor.

For a permanent magnet brushless DC motor it is more important to calculate the radial component of the magnetic field, ie.

$$B_r = \mu_o \frac{i}{\pi} \sum_\nu \frac{R_i^\nu}{R_i^{2\nu} - R_m^{2\nu}} \left[r^{\nu-1} + R_m^{2\nu} r^{-\nu-1} \right] \sin \nu \alpha$$

$$= \mu_o \frac{i}{\pi} \frac{1}{r} \sum_\nu \left(\frac{r}{R_i} \right)^\nu \frac{1 + \left(\frac{R_m}{r} \right)^{2\nu}}{1 - \left(\frac{R_m}{R_i} \right)^{2\nu}} \sin \nu \alpha \tag{8.12}$$

In particular at $r = R_m$, ie. on the rotor surface

$$B_r|_{r = R_m} = \mu_o \frac{i}{2} \frac{4}{\pi} \frac{1}{R_m} \sum_\nu \left(\frac{R_m}{R_i} \right)^\nu \frac{1}{1 - \left(\frac{R_m}{R_i} \right)^{2\nu}} \sin \nu \alpha \tag{8.13}$$

whilst at r = R_i, ie. on the stator surface

$$B_r|_{r=R_i} = \mu_o \frac{i}{2}\frac{4}{\pi}\frac{1}{R_i} \sum_{\nu} \frac{1}{2} \frac{1 + \left(\frac{R_m}{R_i}\right)^{2\nu}}{1 - \left(\frac{R_m}{R_i}\right)^{2\nu}} \sin \nu\alpha \tag{8.14}$$

Similarly the magnetic scalar potential distribution produced by a single conductor can be obtained for the external rotor motor, shown in Fig 8.1(b). However, the only difference between the expressions for the magnetic potential and flux density in an external rotor motor and an internal rotor motor is the sign of the expressions, ie.

$$\varphi^e = -\varphi^i \tag{8.15a}$$

$$B^e = -B^i \tag{8.15b}$$

therefore

$$B_r^e|_{r=R_m} = -B_r^i|_{r=R_m} \tag{8.16a}$$

$$B_r^e|_{r=R_i} = -B_r^i|_{r=R_i} \tag{8.16b}$$

where the superscripts "e" and "i" refer to external rotor motor and internal rotor motors respectively.

8.2.2 Magnetic Field of a Coil

In a similar manner to the 1-d model [8.4] of an induction motor, the two-dimensional field due to a single-turn current carrying coil in a brushless permanent magnet DC motor can be determined as the resultant field of two conductors spaced by the winding pitch angle α_y and carrying equal but opposite currents.

In section 8.2.1 the radial component of the magnetic field due to single conductor was derived as:

$$B = \mu_o \frac{i}{\pi \delta} \sum_{\nu = 1, 2, 3, \ldots}^{\infty} \frac{1}{\nu} F_b(\nu, r) \sin \nu \alpha \tag{8.17}$$

where for simplicity the subscript "r" which refers to the radial component is omitted;

$\delta = g + \frac{h_m}{\mu_R} = g + h_m$ is the effective airgap and

$F_b(\nu,r)$ is a function dependant on the radius and harmonic order, and is given by:

$$F_b(\nu, r) = F_b^i(\nu, r)$$

$$= \delta \frac{\nu}{r} \left(\frac{r}{R_i}\right)^{\nu} \frac{1 + \left(\frac{R_m}{r}\right)^{2\nu}}{1 - \left(\frac{R_m}{R_i}\right)^{2\nu}} \tag{8.18a}$$

for an internal rotor motor and

$$F_b(\nu, r) = F_b^e(\nu, r)$$

$$= -\delta \frac{\nu}{r} \left(\frac{r}{R_i}\right)^{\nu} \frac{1 + \left(\frac{R_m}{r}\right)^{2\nu}}{1 - \left(\frac{R_m}{R_i}\right)^{2\nu}}$$

$$= \delta \frac{\nu}{r} \left(\frac{R_i}{r}\right)^{\nu} \frac{1 + \left(\frac{r}{R_m}\right)^{2\nu}}{1 - \left(\frac{R_i}{R_m}\right)^{2\nu}} \tag{8.18b}$$

for an external rotor motor

where it will be noted that the reference position for the magnetic field is at the position of the conductor, as shown in Fig 8.2(a).

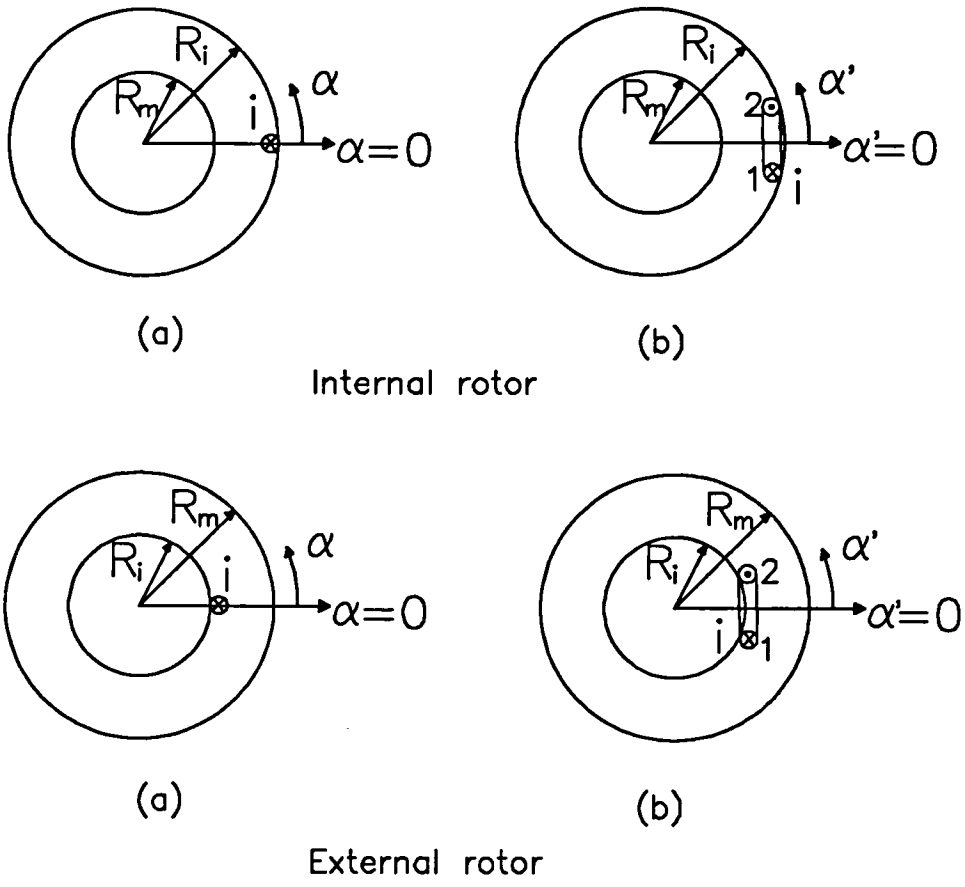

Fig 8.2 Reference positions of magnetic field of a coil.

For simplicity the reference position for the magnetic field of a coil is chosen to be the axis of the coil, as shown in Fig 8.2(b). Therefore,

for conductor 1, letting $\alpha = \alpha' + \frac{\alpha_y}{2}$, $i = i'$, then

$$B_1 = \mu_o \frac{i'}{\pi \delta} \sum_{\nu = 1, 2, 3, \ldots}^{\infty} \frac{1}{\nu} F_b(\nu, r) \sin \nu \left(\alpha' + \frac{\alpha_y}{2} \right) \tag{8.19a}$$

whilst for conductor 2, letting $\alpha = \alpha' - \frac{\alpha_y}{2}$, $i = -i'$, then

$$B_2 = -\mu_o \frac{i'}{\pi \delta} \sum_{\nu = 1, 2, 3, \ldots}^{\infty} \frac{1}{\nu} F_b(\nu, r) \sin \nu \left(\alpha' - \frac{\alpha_y}{2} \right) \tag{8.19b}$$

Therefore for a single-turn coil, the resultant magnetic field is

$$B = B_1 + B_2 = 2\,\mu_o \frac{i'}{\pi\,\delta} \sum_{\nu = 1, 2, 3, \ldots}^{\infty} \frac{K_{d\nu}}{\nu} F_b(\nu, r) \cos \nu\,\alpha' \tag{8.19c}$$

Writing α' as α and i' as i, for a coil the radial component of the magnetic field is

$$B = 2\,\mu_o \frac{i}{\pi\,\delta} \sum_{\nu = 1, 2, 3, \ldots}^{\infty} \frac{K_{d\nu}}{\nu} F_b(\nu, r) \cos \nu\,\alpha \tag{8.19d}$$

where $K_{d\nu} = \sin\nu \frac{\alpha_y}{2}$ is the winding pitch factor. (8.20)

Clearly the magnetic field is symmetrical about the axis of the coil.

8.2.3 Effect of Airgap Length

As mentioned in the introduction due to the large effective airgap, the armature reaction field of brushless permanent magnet DC motors must be calculated by a two-dimensional method. However it is of particular interest to compare the field distributions predicted from both 1-d and 2-d models.

Rewriting the expression for the magnetic field produced by a conductor as:

$$B = \mu_o \frac{i}{\pi\,\delta} \sum_{\nu = 1, 2, 3, \ldots}^{\infty} \frac{1}{\nu} F_b(\nu, r) \sin \nu\,\alpha \tag{8.17}$$

then if the effective airgap δ, and hence the value of $|R_i - R_m|$, is small enough,

$$r \approx R_m \approx R_i\,,\; R_i - R_m = \delta \tag{8.21}$$

Therefore, for the internal rotor motor

$$F_b(\nu, r) = F_b^i(\nu, r)$$

$$= \delta \frac{\nu}{r} \left(\frac{r}{R_i}\right)^{\nu} \frac{1 + \left(\frac{R_m}{r}\right)^{2\nu}}{1 - \left(\frac{R_m}{R_i}\right)^{2\nu}}$$

$$\approx \delta \frac{2\nu}{R_i} \frac{R_i^{2\nu}}{R_i^{2\nu} - R_m^{2\nu}}$$

$$= \delta \frac{2\nu}{R_i} \frac{R_i^{2\nu}}{(R_i - R_m)(R_i^{2\nu-1} + R_i^{2\nu-2} R_m + \ldots + R_m^{2\nu-1})}$$

$$\approx \delta \frac{2\nu}{R_i} \frac{R_i^{2\nu}}{\delta 2\nu R_i^{2\nu-1}}$$

$$= 1 \qquad (8.22a)$$

Similarly, for the external rotor motor:

$$F_b(\nu, r) = F_b^e(\nu, r) \approx 1 \qquad (8.22b)$$

which becomes unity, and therefore independant of the radius.

Therefore for small effective airgaps, the magnetic field produced by a single conductor becomes:

$$B = \mu_o \frac{i}{\pi \delta} \sum_{\nu = 1, 2, 3, \ldots}^{\infty} \frac{1}{\nu} \sin \nu \alpha \qquad (8.23)$$

which is identical with equation (10) in Ref [8.4]. Therefore when the airgap is small enough, the magnetic field distribution predicted from a 2-d model is identical to that from the 1-d model which is widely used in the analysis of the airgap field in induction motors. Furthermore there is no difference between the result predicted for external rotor and internal rotor motors. In both cases the magnetic field is independant of the radius. Hence flux focussing is neglected. However because of their large effective airgap the airgap field produced by stator windings in permanent magnet motors should be analysed by a 2-d method. In a 2-d model the function $F_b(\nu,r)$ describes the effect of the airgap length on the harmonic component of the magnetic field produced by a conductor, and is equally valid for the magnetic field of a coil or a group of coils, eg. a 3-phase winding.

A numerical calculation for the effect of airgap length on the field distribution will be given in section 8.4.3.

Since the difference in the magnetic field in internal rotor and external rotor motors is only in the function $F_b(v,r)$ and the definitions of R_o and R_m , as described by equations (8.9) (8.18a) and (8.18b), the analysis for an internal rotor motor can be easily modified for an external rotor motor. Therefore in the following sections only the analysis of internal rotor motors is described.

8.2.4 Effect of Slot Openings

From various viewpoints, such as the calculation of the self- and mutual-winding inductances, the prediction of the radial force distribution for noise and vibration estimation etc, it is important to calculate the armature reaction field distribution at the stator bore. However in the analyses of sections 8.2.2 and 8.2.3 the current carrying conductors were assumed to be idealised line current sources of zero sectional area. As a consequence, solutions for the magnetic field at the stator bore cannot be obtained numerically since at $r = R_i$ the function $F_b(v,r)$ becomes

$$\left| Fb(v,r) \right|_{r=R_i} = \left| \delta \frac{v}{r} \left(\frac{r}{R_i} \right)^{v} \frac{1+\left(\frac{R_m}{r} \right)^{2v}}{1-\left(\frac{R_m}{R_i} \right)^{2v}} \right|_{r=R_i} = \delta \frac{v}{R_i} \left| \frac{1+\left(\frac{R_m}{R_i} \right)^{2v}}{1-\left(\frac{R_m}{R_i} \right)^{2v}} \right| \tag{8.24}$$

for higher harmonic orders v

$$\left(\frac{R_m}{R_i} \right)^{2v} \approx 0 \qquad \text{for internal rotor motor}$$

and $$\left(\frac{R_i}{R_m} \right)^{2v} \approx 0 \qquad \text{for external rotor motor}$$

Therefore for higher harmonic orders $F_b(v,r)$ is directly proportional to the harmonic order, which causes the solution for the magnetic field on the stator iron surface, ie. equation (8.17) or (8.20), to be a divergent Fourier series. Hence a convergent numerical solution cannot be obtained.

In Chapter 5 the effect of slotting on the open-circuit field distribution was studied by introducing a two-dimensional relative permeance function. Slotting has a similarly important effect on the armature reaction field, as will be shown later in this Chapter by analytical and numerical examples. Therefore an identical 2-d relative permeance function, as the open-circuit field calculation, will be introduced. However, in this section a slot-opening factor, obtained from a 2-dimensional analytical model, is also introduced for the following reasons:

a) To study the effect of slot-openings on the magnetic field produced by the stator windings when the permeance variation is neglected.

b) To eliminate the numerical divergence problem in the solution for the magnetic field produced by a conductor or a coil.

To show the effect of slotting, the 2-d model having a distributed current sheet, shown in Fig.8.3, will be considered.

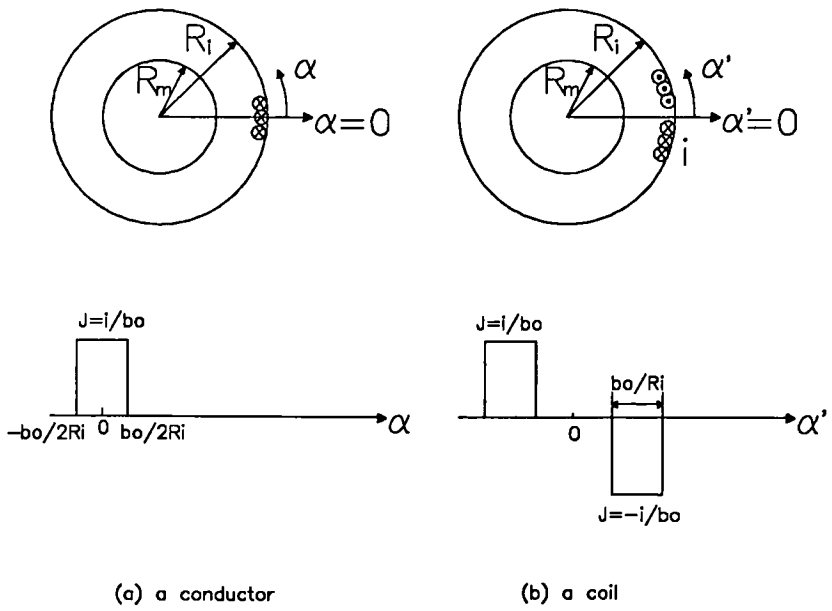

Fig 8.3 Effect of slotting - distributed current sheet.

Figs 8.3(a) and 8.3(b) show the distributed current sheet representation for a conductor and a coil respectively, both being accommodated in slots. The current sheet is so distributed that its current value is uniform along an arc whose length is determined by the slot-openings, b_o. For

simplicity the field distribution of the distributed current conductor, shown in Fig 8.3(b), is solved first.

For Fig 8.3(b) the current density distribution over the slot-openings is given by:

$$J = \begin{cases} \dfrac{i}{b_o} & -\dfrac{b_o}{2R_i} \le \alpha \le \dfrac{b_o}{2R_i} \\ 0 & other\ \alpha \end{cases} \tag{8.25}$$

Therefore the Fourier series expansion is obtained as:

$$J = \frac{i}{2\pi R_i} + \frac{2i}{\pi b_o} \sum_{\nu} \frac{1}{\nu} \sin \nu \frac{b_o}{2R_i} \cos \nu \alpha \tag{8.26}$$

whilst the governing Laplacian equation in polar coordinates is

$$\frac{\partial^2 \varphi}{\partial r^2} + \frac{1}{r}\frac{\partial \varphi}{\partial r} + \frac{1}{r^2}\frac{\partial^2 \varphi}{\partial \alpha^2} = 0 \tag{8.27}$$

The boundary conditions to be imposed are

$$H_\alpha |_{r=R_m} = 0 \tag{8.28}$$

$$H_\alpha |_{r=R_i} = -J \tag{8.29}$$

Since the general solution is

$$\varphi(\alpha, r) = \sum_{\nu} (A_\nu r^\nu + B_\nu r^{-\nu})(C_\nu \cos \nu \alpha + D_\nu \sin \nu \alpha)$$

$$+ (A_o \ln r + B_o)(C_o \alpha + D_o) \tag{8.30}$$

and

$$H_r = -\frac{\partial \varphi}{\partial r} \qquad B_r = -\mu_o \frac{\partial \varphi}{\partial r}$$

$$H_\alpha = -\frac{1}{r}\frac{\partial \varphi}{\partial \alpha} \qquad B_\alpha = -\mu_o \frac{1}{r}\frac{\partial \varphi}{\partial \alpha} \tag{8.31}$$

then the radial component of the magnetic field for a distributed conductor is obtained as

$$B(\alpha, r) = \mu_o \frac{i}{\pi}\frac{1}{r} \sum_{\nu} \left\{ \frac{\sin \nu \dfrac{b_o}{2R_i}}{\nu \dfrac{b_o}{2R_i}} \right\} \left(\frac{r}{R_i}\right)^\nu \frac{1 + \left(\dfrac{R_m}{r}\right)^{2\nu}}{1 - \left(\dfrac{R_m}{R_i}\right)^{2\nu}} \sin \nu \alpha$$

$$+\frac{i\,\alpha}{2\,\pi}\;\frac{1}{\ln\left(\frac{R_i}{R_m}\right)}\left\{\ln\left(\frac{R_m}{r}\right)-1\right\}$$

$$=\frac{\mu_o}{\pi}\frac{i}{\delta}\sum_{v}\frac{1}{v}\left\{\frac{\sin v\frac{b_o}{2R_i}}{v\frac{b_o}{2R_i}}\right\}Fb(v,r)\sin v\,\alpha+\frac{i\,\alpha}{2\,\pi}\;\frac{1}{\ln\left(\frac{R_i}{R_m}\right)}\left\{\ln\left(\frac{R_m}{r}\right)-1\right\} \tag{8.32}$$

where the reference for the angular variable α, ie. $\alpha = 0$, is at the centre of the distributed current conductor. Hence, following a similar deduction to that given in section 8.2.2, the radial component of the airgap flux density due to a distributed current coil is derived as:

$$B(\alpha,r)=\frac{2\,\mu_o}{\pi}\frac{i}{\delta}\sum_{v}\frac{1}{v}\left\{\frac{\sin v\frac{b_o}{2R_i}}{v\frac{b_o}{2R_i}}\right\}K_{dv}\,Fb(v,r)\cos v\,\alpha \tag{8.33}$$

where the reference for the angular variable α, ie. $\alpha = 0$, is at the axis of the distributed current coil.

On comparing equations (8.33) and (8.20) it can be seen that the difference between the magnetic field distribution for a concentrated coil and that for a distributed current coil is in the term

$$K_{sov}=\frac{\sin v\frac{b_o}{2R_i}}{v\frac{b_o}{2R_i}} \tag{8.34}$$

which can be appropriately defined as the slot-opening factor.

Clearly if the slot-opening b_o is very small, ie. $b_o \rightarrow 0$, then the slot-opening factor approaches unity, ie.

$$K_{sov}|_{b_o=0} = 1 \tag{8.35}$$

It can be shown that due to the introduction of the slot-opening factor the solution for the magnetic field of a distributed current conductor or a coil is always convergent, and hence can be calculated numerically, even at the stator surface. Similar results can be obtained for an external rotor motor.

In summary, on the basis of a 2-dimensional analytical model, the magnetic field of a distributed current coil, re-written from equation (8.33), is

$$B(\alpha, r) = \frac{2\,\mu_o}{\pi}\,\frac{i}{\delta}\,\sum_{\nu}\,\frac{1}{\nu}\,K_{so\nu}\,K_{d\nu}\,F_b(\nu, r)\,\cos\nu\alpha \qquad (8.36)$$

This is the radial component of the magnetic field in the airgap. A similar expression can be derived for the tangential component.

8.2.5 Effect of Current Harmonics - Analytical Spectral Analysis

As mentioned in the introduction, the phase winding current waveforms of a brushless DC motor contain significant harmonics as a consequence of the electronic commutation events. Typical phase winding current waveforms have already been shown in Chapter 7, where the waveforms were obtained from a dynamic simulation using either an analytical or a numerical approach. In this section an analytical technique for Fourier series analysis is presented which is based on a linear interpolation and an analytical calculation of the Fourier series coefficients.

The data for a waveform is assumed to be periodic in the interval $(0, 2P_l)$ or may be transformed into that range, where $2P_l$ is the period. Suppose that in the interval $(0,2P_l)$ there are N_p pairs of values of the function (f_r, x_r), not necessarily equi-spaced, but with the particular values f(0) and $f(2P_l)$, as shown in Fig 8.4.

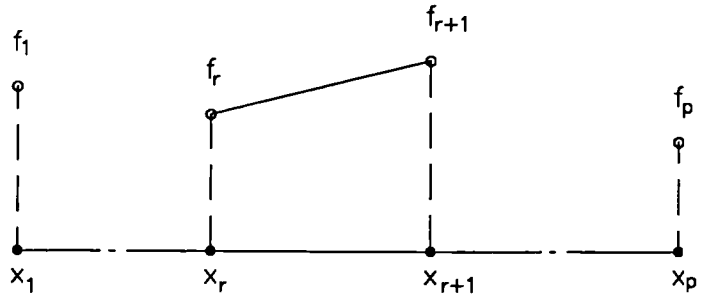

Fig 8.4 Linear interpolation for spectral analysis.

then in one cyclic period $(0, 2P_l)$, the value between two discretised points is obtained by linear interpolation, ie.

$$f(x) = f_r + \frac{x - x_r}{x_{r+1} - x_r}\,(f_{r+1} - f_r)$$

$$= \frac{f_r x_{r+1} - x_r f_{r+1}}{x_{r+1} - x_r} + \frac{f_{r+1} - f_r}{x_{r+1} - x_r}\,x \qquad (8.37)$$

$$\text{for } (x_r < x < x_{r+1}),\ r = 1, 2, \ldots, N_p - 1$$

Based on this linear interpolation, the Fourier series expansion is obtained as:

$$f(x) = a_o + \sum_{n=1}^{\infty} \left\{ a_n \cos\left(n \frac{\pi}{P_l} x\right) + b_n \sin\left(n \frac{\pi}{P_l} x\right) \right\}$$

$$= a_o + \sum_{n=1}^{\infty} \sqrt{a_n^2 + b_n^2}\, \sin\left(n \frac{\pi}{P_l} x + \alpha_n\right) \qquad (8.38)$$

where

$$a_o = \frac{1}{2P_l} \int_o^{2P_l} f(x)\,dx$$

$$= \frac{1}{4P_l} \left[f_p x_p - f_1 x_1 + \sum_{r=1}^{N_p - 1} (f_r x_{r+1} - f_{r+1} x_r) \right] \qquad (8.39)$$

$$a_n = \frac{1}{P_l} \int_o^{2P_l} f(x) \cos\left(n \frac{\pi}{P_l} x\right) dx$$

$$= \frac{1}{n\pi} \left[f_p \sin\left(n \frac{\pi}{P_l} x_p\right) - f_1 \sin\left(n \frac{\pi}{P_l} x_1\right) \right]$$

$$+ \frac{P_l}{n^2 \pi^2} \sum_{r=1}^{N_p - 1} \frac{f_{r+1} - f_r}{x_{r+1} - x_r} \left[\cos\left(n \frac{\pi}{P_l} x_{r+1}\right) - \cos\left(n \frac{\pi}{P_l} x_r\right) \right] \tag{8.40}$$

$$b_n = \frac{1}{P_l} \int_o^{2P_l} f(x) \sin\left(n \frac{\pi}{P_l} x\right) dx$$

$$= \frac{1}{n\pi} \left[f_p \cos\left(n \frac{\pi}{P_l} x_p\right) - f_1 \cos\left(n \frac{\pi}{P_l} x_1\right) \right]$$

$$+ \frac{P_l}{n^2 \pi^2} \sum_{r=1}^{N_p - 1} \frac{f_{r+1} - f_r}{x_{r+1} - x_r} \left[\sin\left(n \frac{\pi}{P_l} x_{r+1}\right) - \sin\left(n \frac{\pi}{P_l} x_r\right) \right] \tag{8.41}$$

$$\text{and } \alpha_n = \arctan\left(\frac{b_n}{a_n}\right) \tag{8.42}$$

Therefore, for the numerically simulated 3-phase current waveforms of Chapter 7, the Fourier series are obtained as:

$$i_a = \sum_u I_u \sin\left[u(p\,\omega_r t) + \theta_u\right]$$

$$i_b = \sum_u I_u \sin\left[u(p\,\omega_r t - 2\pi/3) + \theta_u\right]$$

$$i_c = \sum_u I_u \sin\left[u(p\,\omega_r t - 4\pi/3) + \theta_u\right] \tag{8.43}$$

where $\theta = p\ \omega_r t$, and the current waveform for phase A starts at $\theta = 0$, Fig 8.5, with θ_u being the phase angle for each harmonic.

Fig 8.5 compares an original simulated phase current waveform, for an overlapping winding 3-phase, 4-pole, radial-field brushless DC motor whose parameters are given in Chapters 5 and 7, and running at a speed of 1500 rpm, with one synthesised from its Fourier series. In the Fourier

series expansion harmonic components whose amplitude was smaller than 1/500 of the fundamental component were neglected. It will be seen that excellent agreement has been achieved.

Table 8.1 shows how the amplitude and phase of the harmonic components in this typical current waveform vary. Since the prototype motor had a symmetrical star-connected 3-phase winding, only odd order harmonics exist, since for the steady-state operation $i(\theta) = -i(\theta + 2\pi)$, and there are no triplen harmonic components.

Table 8.1 - Harmonics in the current waveform at 1500 rpm.

Harmonic order, u	Amplitude, I_u ,(A)	Phase angle, θ_u, (rad)
1	0.20628E+01	0.38649E+00
5	0.46674E+00	- 0.14506E+01
7	0.26598E+00	0.25084E+00
11	0.16602E+00	- 0.20073E+01
13	0.12351E+00	- 0.27334E+00
17	0.75471E-01	- 0.25521E+01
19	0.61059E-01	- 0.79823E+00
23	0.31228E-01	- 0.30442E+01
25	0.25372E-01	- 0.12638E+01
29	0.73870E-02	0.30790E+01
31	0.58718E-02	- 0.12936E+01
35	0.67434E-02	- 0.16859E+01
37	0.70265E-02	0.88281E-01
41	0.10564E-01	- 0.19967E+01
43	0.10383E-01	- 0.23149E+00
47	0.98646E-02	- 0.24833E+01
49	0.66259E-02	- 0.29747E+01
53	0.94893E-02	- 0.71258E+00
55	0.62827E-02	- 0.11969E+01

Total harmonics: 19

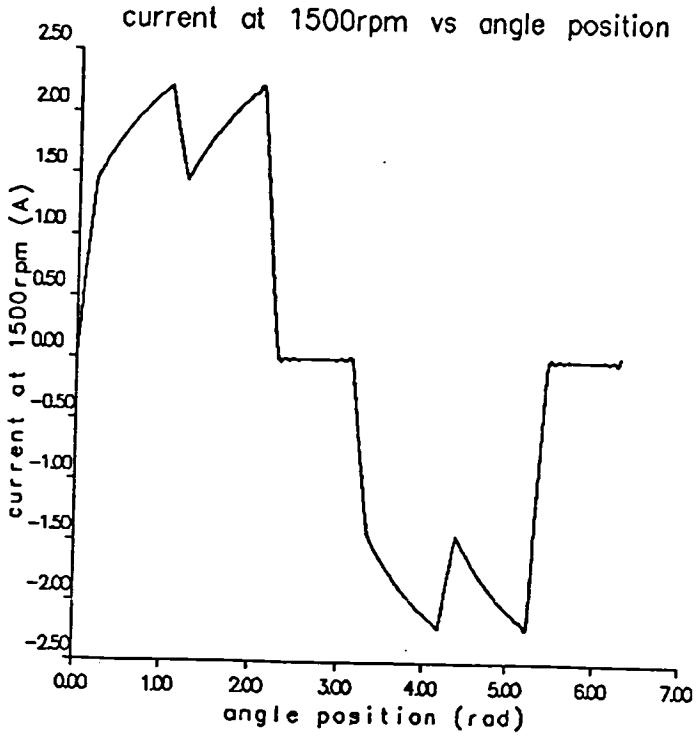

Fig 8.5 - Typical simulated and synthesised phase winding current waveform.

8.2.6 Armature Reaction Field of 3-phase Winding in Brushless DC Motors

In section 8.2.4 the magnetic field distribution due to a current carrying conductor or coil accommodated in the slots of a motor has been obtained by a two-dimensional analytical technique accounting for the effect of the slot openings. The magnetic field of a distributed phase winding can be obtained by introducing a winding distribution factor, in a 1-dimensional analysis, which is commonly applied to induction motors, ie.

$$B(\alpha, r, t) = \mu_o \frac{2W}{\pi} \frac{i}{\delta} \sum_{\nu} \frac{1}{\nu} K_{sov} K_{dpv} F_b(\nu, r) \cos \nu \alpha \qquad (8.44)$$

with reference to the axis of the phase winding, $\alpha = 0$,

where W is the number of series turns per phase;

$K_{dpv} = K_{dv} K_{pv}$

K_{pv} is the winding distribution factor, given by:

$$K_{pv} = \frac{\sin q \frac{v\pi}{Q_s}}{q \frac{v\pi}{Q_s}} \tag{8.45}$$

and $q = Q_s/2pm$ is the number of slots per phase per pole;

Q_s is the total number of stator slots;

p is the pole pair number;

m is the phase number

Hence the magnetic field produced by the 3-phase winding in a brushless DC motor can be deduced from equation (8.44), together with equation (8.43) as

$$\begin{aligned} B_{winding}(\alpha, r, t) &= B_a(\alpha, r) + B_b(\alpha, r) + B_c(\alpha, r) \\ &= \mu_o \frac{2W}{\pi\delta} \sum_v \frac{1}{v} K_{sov} K_{dpv} F_b(v, r) \\ &\quad .[\, i_a \cos v\alpha + i_b \cos v(\alpha - \tfrac{2\pi}{3}) + i_c \cos v(\alpha - \tfrac{4\pi}{3})\,] \\ &= \mu_o \frac{W}{\pi\delta} \sum_u I_u \sum_v \frac{1}{v} K_{sov} K_{dpv} F_b(v, r) \\ &\quad .2\{ \sin[\, u(p\omega_r t) + \theta_u\,] \cos v\alpha \\ &\quad + \sin[\, u(p\omega_r t - 2\pi/3) + \theta_u\,] \cos v(\alpha - \tfrac{2\pi}{3}) \\ &\quad + \sin[\, u(p\omega_r t - 4\pi/3) + \theta_u\,] \cos v(\alpha - \tfrac{4\pi}{3})\,\} \end{aligned} \tag{8.46}$$

where

$$2\{\} = \begin{cases} \sin[\,(up\omega_r t) + \theta_u + v\alpha\,] + \\ + \sin[\,(up\omega_r t) + \theta_u + v\alpha - (\frac{v}{p} + u)2\pi/3\,] + \\ + \sin[\,(up\omega_r t) + \theta_u + v\alpha - (\frac{v}{p} + u)4\pi/3\,] + \end{cases}$$

$$+\left\{\begin{array}{l}\sin\left[\left(up\,\omega_r t\right)+\theta_u-v\alpha\right]+\\ +\sin\left[\left(up\,\omega_r t\right)+\theta_u-v\alpha+\left(\frac{v}{p}-u\right)2\pi/3\right]+\\ +\sin\left[\left(up\,\omega_r t\right)+\theta_u-v\alpha+\left(\frac{v}{p}-u\right)4\pi/3\right]\end{array}\right.$$

$$=\left[1+2\cos\left(\frac{v}{p}+u\right)2\pi/3\right]\sin\left[\left(up\,\omega_r t\right)+\theta_u+v\alpha-\left(\frac{v}{p}+u\right)2\pi/3\right]$$

$$+\left[1+2\cos\left(\frac{v}{p}-u\right)2\pi/3\right]\sin\left[\left(up\,\omega_r t\right)+\theta_u-v\alpha+\left(\frac{v}{p}-u\right)2\pi/3\right]$$

$$=\frac{\sin\left(\frac{v}{p}+u\right)\pi}{\sin\left(\frac{v}{p}+u\right)\pi/3}\sin\left[\left(up\,\omega_r t+\theta_u+v\alpha\right)-\left(\frac{v}{p}+u\right)2\pi/3\right]$$

$$+\frac{\sin\left(\frac{v}{p}-u\right)\pi}{\sin\left(\frac{v}{p}-u\right)\pi/3}\sin\left[\left(up\,\omega_r t+\theta_u-v\alpha\right)+\left(\frac{v}{p}-u\right)2\pi/3\right] \qquad (8.47)$$

whilst

$$\frac{\sin\left(\frac{v}{p}\pm u\right)\pi}{\sin\left(\frac{v}{p}\pm u\right)\pi/3}=\begin{cases}0 & \text{for}\quad \frac{v}{p}\pm u\neq 3c\\ 3 & \text{for}\quad \frac{v}{p}\pm u=3c\end{cases} \qquad (8.48)$$

$c=0,\pm1,\pm2,\ldots$

therefore

$$2\{\}=3\sin\left[\left(up\,\omega_r t+\theta_u\pm v\alpha\right)-\{\pm\}3c\,(2\pi/3)\right]$$

$$=3\sin\left(up\,\omega_r t+\theta_u\pm v\alpha\right) \qquad (8.49)$$

and $\frac{v}{p}\pm u=3c$

ie. $v=p\left(3c-\{\pm\}u\right)$ (8.50a)

However, similar to the case of one-dimensional analytical model (see the note on page 20 in [8.4]), a symmetrical 3-phase winding with equal phase-belts produces only harmonics of the order:

$$v=p\left(6c-\{\pm\}u\right) \qquad (8.50b)$$

Hence based on a two-dimensional analytical model the magnetic field is obtained by combining equations (8.46) (8.49) and (8.50), ie.

$$B_{winding}(\alpha, r, t) = \mu_o \frac{3W}{\pi} \frac{1}{\delta} \sum_u I_u \sum_v \frac{1}{v} K_{sov} K_{dpv} F_b(v, r) \cdot \sin[up\omega_r t \pm v\alpha + \theta_u] \qquad (8.51)$$

where v is any integer larger than zero and is determined by the following equation:

$$v = p(6c - \{\pm\} u) \quad \text{and} \quad c = 0, \pm 1, \pm 2, \ldots$$

u = odd integer not equal to a multiple of three, ie., u = 1, 5, 7, 11, 13, ...

and $\alpha = 0$ corresponds to the axis of phase A winding, whose current is zero at the t = 0, ie. $i_{a|_{t=0}} = 0$, and which is commutated at t = 0.

In a similar manner to the open-circuit calculation, when slotting was taken into account by its permeance effect on the magnetic field produced by the magnet, an identical 2-dimensional analytical relative permeance function, described in section 5.2.3, is introduced. The armature reaction field, $B_{armature\text{-}reaction}(\alpha, r, t)$, is then calculated from the product of the magnetic field produced by the stator windings, $B_{winding}(\alpha, r, t)$, with the effects of the slots neglected and the relation permeance function, $\tilde{\lambda}(\alpha, r)$, ie.

$$B_{armature-reaction}(\alpha, r, t) = B_{winding}(\alpha, r, t)\, \tilde{\lambda}(\alpha, r) \qquad (8.52)$$

where the method of calculating the relative permeance function $\tilde{\lambda}(\alpha, r)$ has already been described in section 5.4.2.

It is worth pointing out that although the above approach is applied specifically to brushless permanent magnet DC motors, the technique is equally applicable to the analysis of the magnetic field produced by the stator windings of any AC variable speed motor, such as a transistor converter controlled induction motor or a brushless permanent magnet AC drive, simply by

customising it to the particular case. For example, by letting the effective airgap δ be the actual physical airgap in an induction motor and $F_b(v, r) = 1$, the analysis can be applied to an inverter controlled induction motor.

8.2.7 Comparison of Predictions with Finite Element Calculations

As was the case for a motor on open-circuit, slotting affects the armature reaction field in two ways. Firstly the airgap flux density is reduced compared with the flux when unslotted, an effect which can be accounted for in a similar way to that described in section 5.4.1. However in a surface-mounted magnet brushless motor, this effect is relatively small. Secondly it affects the armature reaction field distribution in both the airgap and the magnets.

In this section the results obtained from the proposed analytical technique and those from finite element analysis are compared for the case when the effect of slotting is neglected, whilst a comparison when the effect of slotting is included will be described in section 8.4.3.

Fig 8.6 shows the finite element mesh and flux distributions due to the winding excitation alone at different instantaneous rotor positions for the prototype motor whose parameters are given in Table 5.1, and whose instantaneous phase currents are obtained from the dynamic simulation of section 8.2.5, as shown in Fig 8.5. The stator slotting has been neglected and the teeth modelled by a natural Neuman boundary condition, whilst the winding currents are represented as a current sheet distributed over the arc of the slot openings. It can be seen that over a large portion of the airgap the flux paths deviate considerably from the radial direction due to the large effective airgap, and emphasises the need for the two-dimensional analytical technique instead of the simpler one-dimensional method.

Fig 8.7 compares instantaneous field distributions along arcs at different radii in the airgap/magnet region. Since at any radius a contour intersects two layers of finite elements, the results consist of two parts obtained from upper and lower layers of element, as illustrated earlier in Fig 5.17. The analytical predictions are also calculated from two radial positions, whose radii

are given in Table 5.4 for this internal rotor motor. The analytical predictions and the finite element calculations show excellent agreement in both the waveforms and amplitudes, as shown in Table 8.2 and Fig 8.8.

It is interesting to contrast these results with those calculated by the traditional 1-d analytical method and shown in Fig 8.9. Its main features are:

i) The flux density distribution around the circumference has a stepped rectangular waveform, the increments in flux density due to the winding current in the slot being:

$$\Delta B = \frac{\mu_o N_s i}{\delta} \tag{8.53}$$

for full pole-pitch windings

where N_S is the conductors in one slot, δ is the effective airgap length, and i is the instantaneous current value.

For example for this particular prototype motor, at time t = 0, i = 2.15 A, N_S = 150, δ = 5.45mm

$$\Delta B = 0.075 \text{ T}$$

ii) The flux density distribution is independant of the radius.

In contrast the 2-dimensional predictions show that:

a) the flux density distribution along the circumference is not a stepped waveform. Due to the large effective airgap and hence the correspondingly large flux leakage, there is flux focussing at the stator teeth at the sides of the winding current sheets, and flux weakening on the rotor surface.

b) the amplitude of the flux density varies with the radius. On the one hand due to leakage it tends to decrease, with an increase of distance from the current source, whilst on the other hand due to the flux focussing effect it tends to increase as the radius is reduced. As a consequence, for an internal rotor motor in passing from the stator to the rotor hub the flux

density near the current sheets decreases, whilst near the axis of coils it increases, ie. near the current sheets the effect of flux leakage predominates, whilst near the axis of the coils the effect of flux focussing is predominant. Clearly for an external rotor radial-field motor topology the resultant flux density will decrease in moving from the stator to the rotor hub.

c) due to the reasons mentioned above, the flux density distribution varies significantly with the radius, ie. in passing from the stator iron to the rotor iron. As to the apparant oscillations in the predictions, this is due to discretisation effects in the finite element analysis and to the use of a finite number of terms in the Fourier series of the analytical calculation, similar to that which was discussed in the open-circuit field calculation of section 5.5.1.

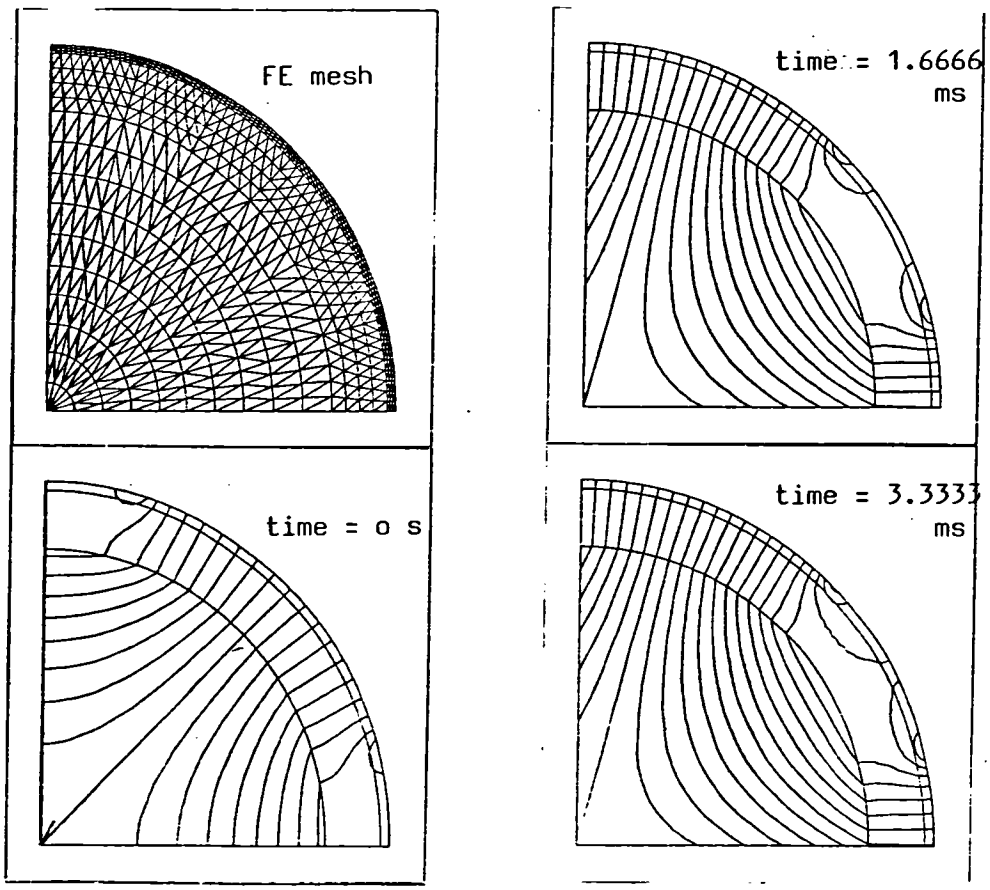

Fig 8.6 Finite element mesh and flux distribution due to the winding excitation alone

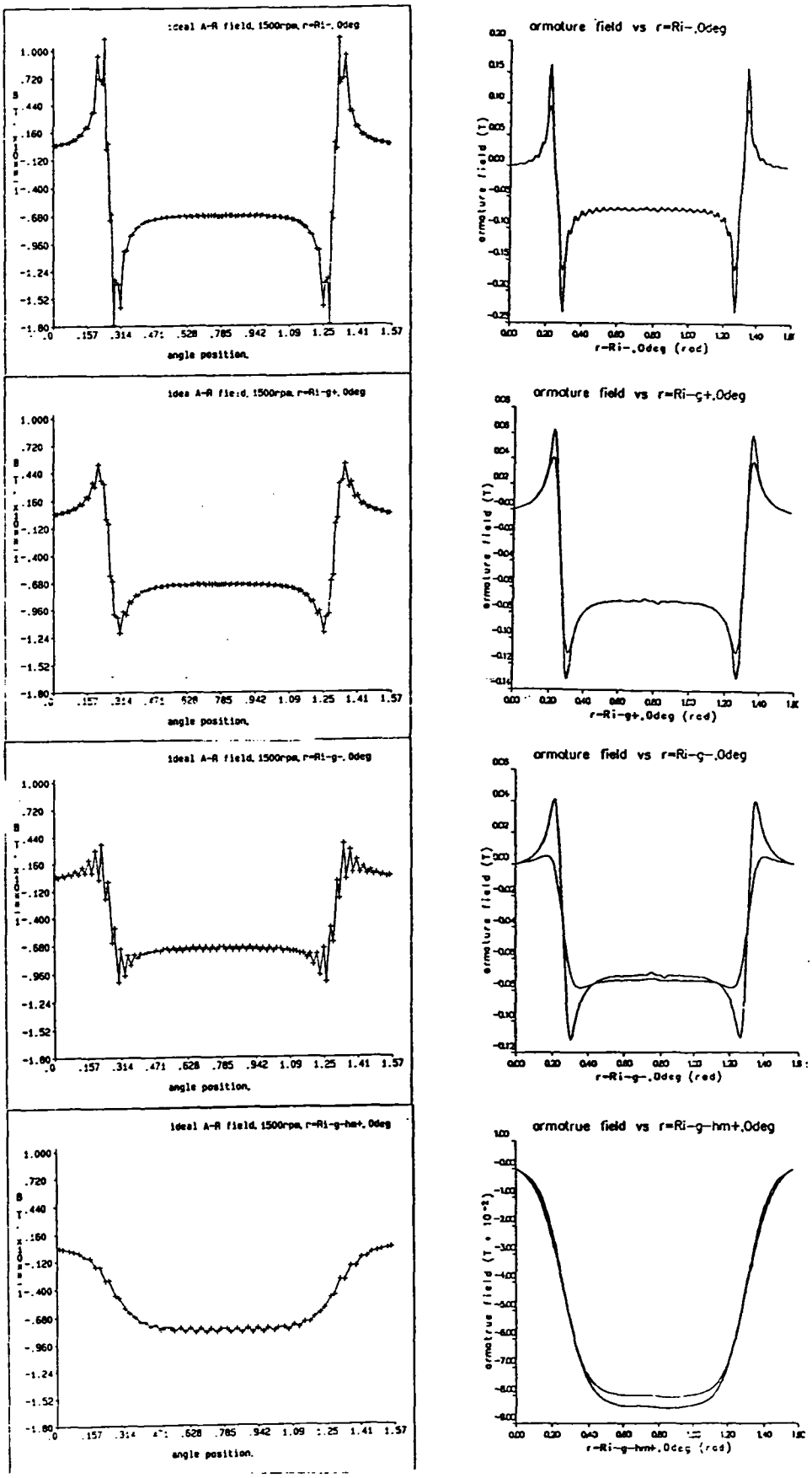

Fig 8.7a Comparison of field distribution produced by the windings at different radii, time=0s

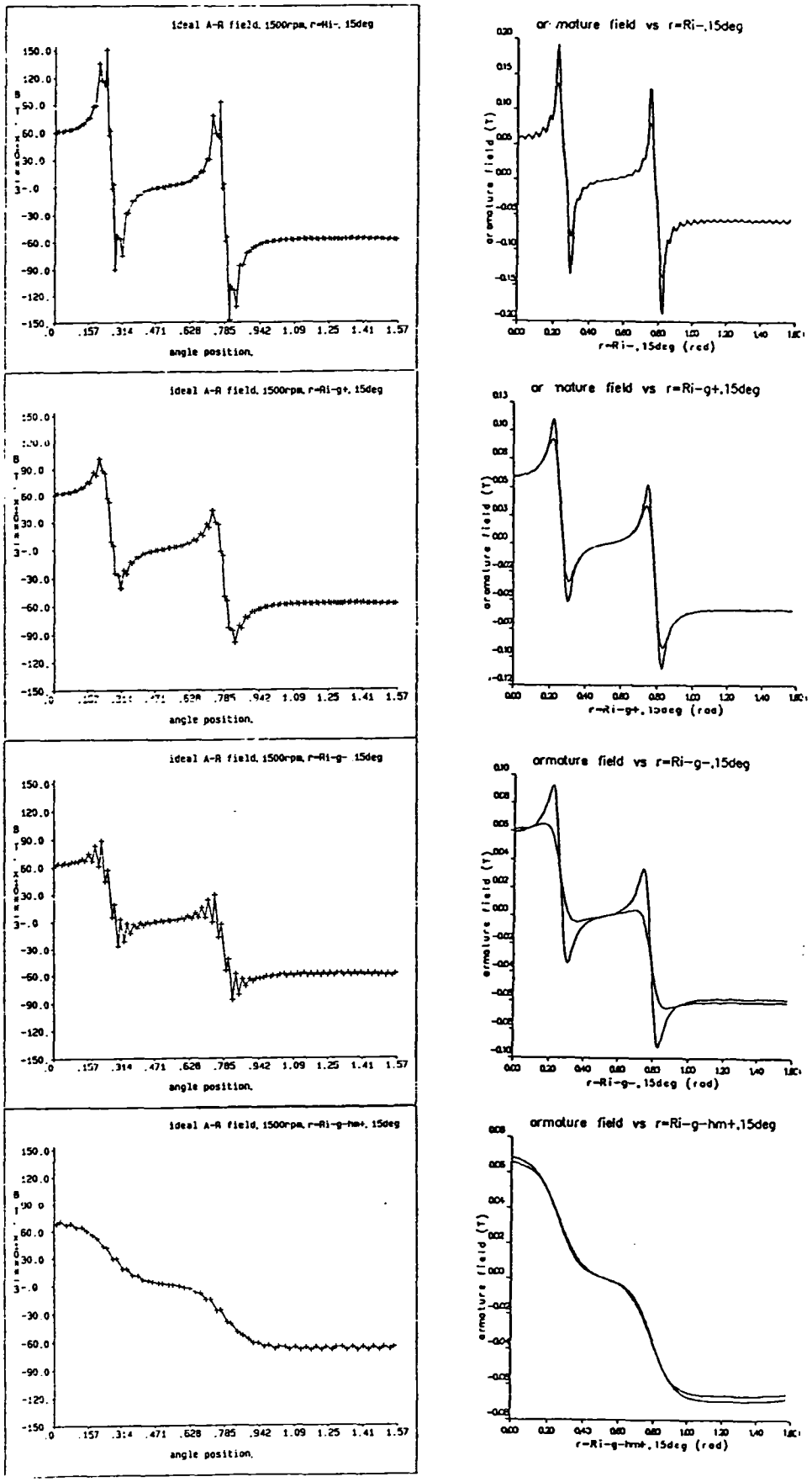

FEM calculation

Analytical prediction

Fig 8.7b Comparison of field distribution produced by the windings at different radii, time=1.66ms

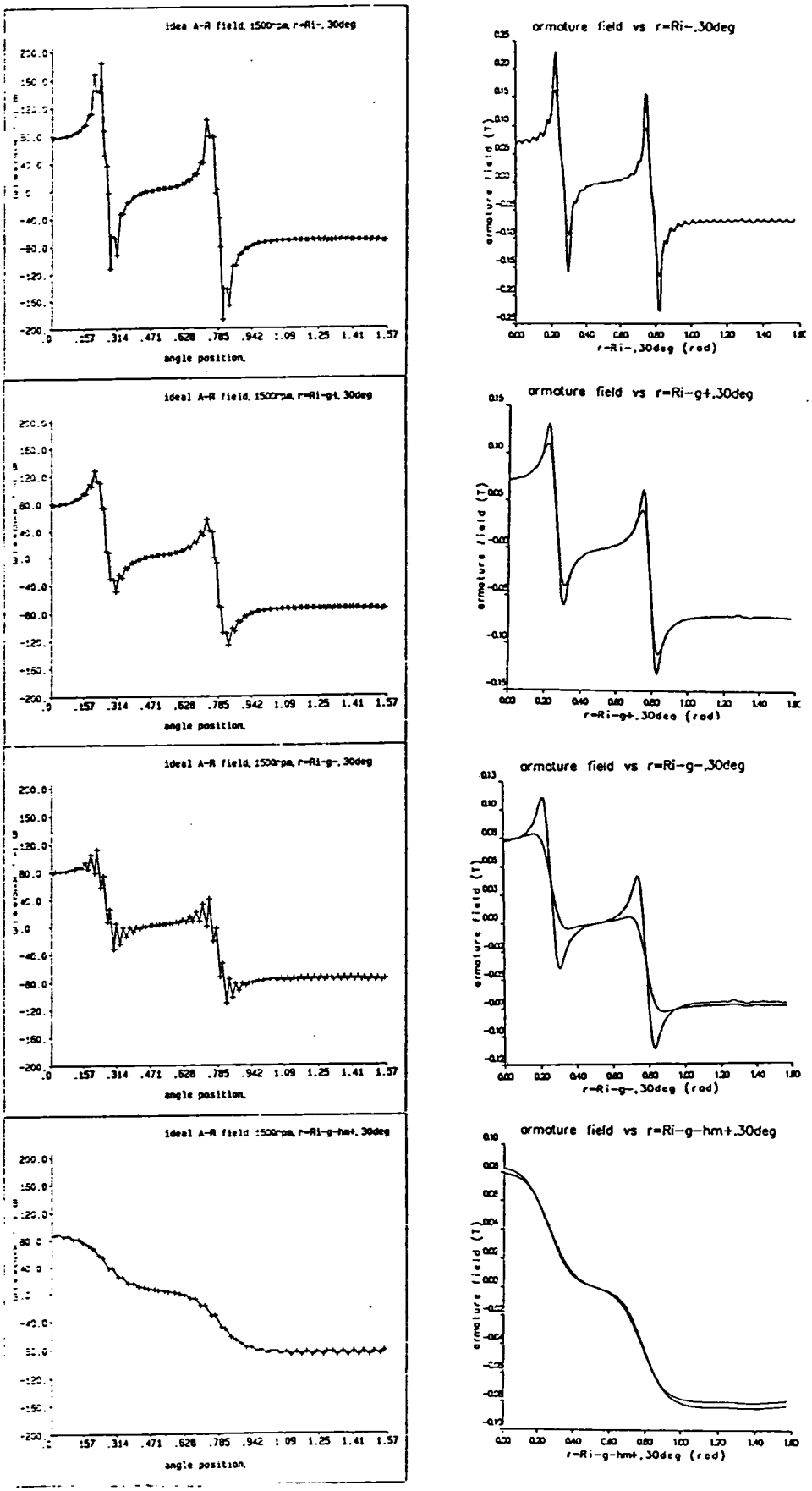

FEM calculation

Analytical prediction

Fig 8.7c Comparison of field distribution produced by the windings at different radii,time=3.33ms

Table 8.2 Comparison of predicted aramature reaction field for a smooth airgap model

Radius	Flux density (FEM)	Flux density (analytical prediction)
m	T	T
0.024685	0.084197	0.0830393
0.025078	0.080448	0.0817772
0.025862	0.080443	0.0793699
0.026254	0.076956	0.0782520
0.027038	0.076952	0.0759657
0.027430	0.073750	0.0750948
0.028214	0.073748	0.0730580
0.028606	0.070874	0.0718571
0.029082	0.070870	0.0706534
0.029167	0.070369	0.0701847
0.029334	0.070372	0.0696459
0.029417	0.069879	0.0693576
0.029585	0.069884	0.0691550

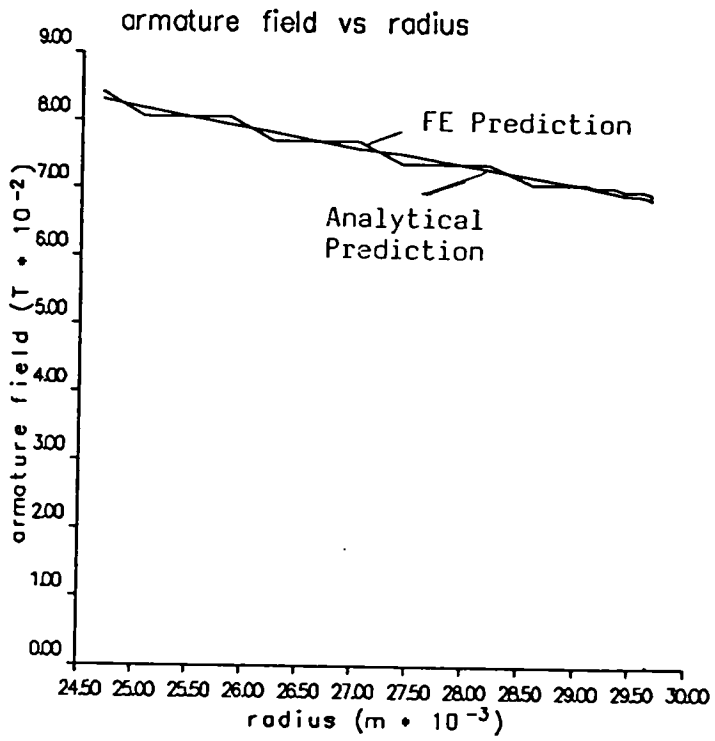

Fig 8.8 Variation of field under a stator tooth due to winding excitation alone

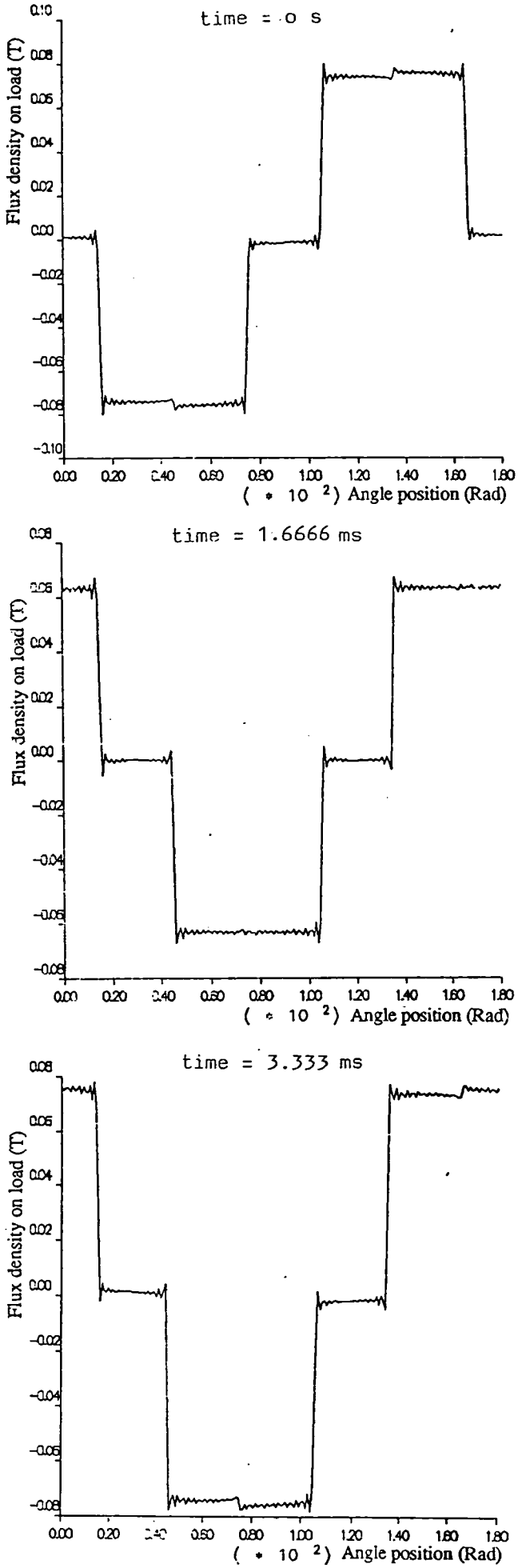

Fig 8.9 Instantaneous field distribution produced by the windings from a traditional 1-d analytical prediction

8.3 Back-emf Induced in Windings of a Brushless DC Motor

The back-emf induced in the windings of a brushless permanent magnet DC motor can be calculated from a knowledge of the open-circuit magnetic field distribution, and the winding distribution.

For a slotless motor topology the open-circuit field is the magnetic field produced by the magnets in a smooth airgap, ie.

$$B_{open\text{-}circuit}(\theta, r) = B_{magnet}(\theta, r) = \sum B_n \cos n p \theta \qquad (8.54)$$

When the motor is slotted an average value of the relative permeance can be used to account for the reduction of the effective flux, ie.

$$B_{open\text{-}circuit}(\theta, r) = B_{magnet}(\theta, r)\, \Lambda_o \qquad (8.55a)$$

$$\text{where } \Lambda_o = \frac{1}{K_c}\left(1 - 1.6\,\beta \frac{b_o}{\tau_t}\right) \qquad (8.55b)$$

which is identical to equation (5.124). Since it is the flux density distribution at the stator bore that induces the back-emf in the windings,

$$B_{open\text{-}circuit}(\theta) = \Lambda_o\, B_{magnet}(\theta, r)\,|_{r=R_i} \qquad (8.56)$$

where $\Lambda_o = 1$ for slotless motors, and

$\theta = \alpha - \alpha_{ma}$

where α and θ are the angular position referred to the stator and the rotor respectively, and α_{ma} is their relative position which depends on the speed of the rotor, ie.

$$\alpha_{ma} = \omega_r t + \theta_o \qquad (8.57)$$

where θ_o is an initial angle depending on the commutation angle.

Therefore

$$B_{open\text{-}circuit}(\alpha, t) = \Lambda_o \sum_n B_n \cos n p (\alpha - \alpha_{ma}) \qquad (8.58)$$

Hence the flux linking a coil is calculated from

$$\psi = \int_{-\frac{\alpha_y}{2}}^{\frac{\alpha_y}{2}} B_{open-circuit}(\alpha, t)\, R_i\, l_{ef}\, d\alpha \tag{8.59a}$$

where α_y is the winding pitch angle, R_i is the radius of the stator bore, l_{ef} is the effective axial length of the stator coil.

Hence

$$\psi = \Lambda_o \sum_n B_n R_i l_{ef} \int_{-\frac{\alpha_y}{2}}^{\frac{\alpha_y}{2}} \cos np(\alpha - \alpha_{ma})\, d\alpha$$

$$= \Lambda_o \sum_n 2 B_n R_i l_{ef} \int_0^{\frac{\alpha_y}{2}} \cos np\,\alpha \cos np\,\alpha_{ma}\, d\alpha$$

$$= \Lambda_o \sum_n \frac{2 B_n R_i l_{ef}}{np} \sin np\frac{\alpha_y}{2} \cos np\,\alpha_{ma}$$

$$= \Lambda_o \sum_n \frac{\Phi_n}{np} K_{dn} \cos np\,\alpha_{ma} \tag{8.59b}$$

where

$$\Phi_n = 2 B_n R_i l_{ef} \Lambda_o \tag{8.60}$$

and $K_{dn} = \sin np\frac{\alpha_y}{2}$

Therefore the voltage induced in each turn of the coil is

$$e = -\frac{d\psi}{dt} = \Lambda_o \sum_n 2 B_n R_i l_{ef} \omega_r K_{dn} \sin np\,\alpha_{ma}$$

$$= \sum_n \omega_r \Phi_n K_{dn} \sin np\,\alpha_{ma} \tag{8.61}$$

Hence for a distributed multi-pole winding, the induced emf per phase is obtained as:

$$e = \sum_n \omega_r \Phi_n W K_{dpn} \sin n p \alpha_{ma} = \sum_n E_n \sin n p \alpha_{ma} \quad (8.62a)$$

where $E_n = \omega_r \Phi_n W K_{dpn}$ (8.62b)

W is the series turns per phase;

and $K_{dpn} = K_{dn}K_{pn}$ is the winding factor, K_{pn} being the winding distribution factor, and K_{dn} being the winding pitch factor, which are the same as for the calculation of the magnetic field produced by the windings, ie. equations (8.20) and (8.45)

$$K_{dn} = K_{dv}|_{v=np} \quad (8.63a)$$

$$K_{pn} = K_{pv}|_{v=np} \quad (8.63b)$$

For a standard inverter fed brushless DC motor under normal commutation the commutation of the current waveform in a particular phase is time-delayed by an angle $\pi/6$ (elec Rad) from the zero crossing of its back-emf waveform, as described in Chapter 7 and shown in Fig 8.10.

Therefore, if the phase current is given by

$$i_a = \sum_u I_u \sin u (p \omega_r t + \theta_u) \quad (8.64)$$

with $i_a|_{t=0} = 0$ as indicated in Fig 8.10, then for a symmetrical back-emf waveform and normal commutation, ie.

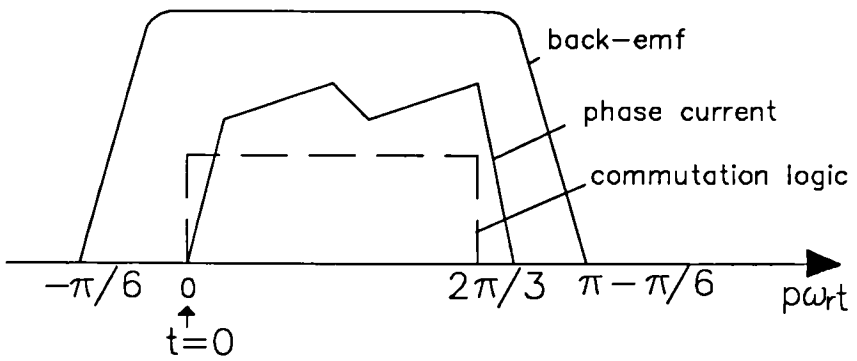

Fig 8.10 Relative position between phase current and back-emf waveforms under normal commutation.

$$e_a = \sum_n E_n \sin n \left(p \, \omega_r \, t + \frac{\pi}{6} \right) \tag{8.65a}$$

For advanced or retarded commutation, the back-emf waveform becomes

$$e_a = \sum_n E_n \sin n \left(p \, \omega_r \, t - \alpha_c + \frac{\pi}{6} \right) \tag{8.65b}$$

where α_c is the commutation angle in electrical radians, where for advanced commutation $\alpha_c > 0$, for retarded commutation $\alpha_c < 0$, whilst for normal commutation $\alpha_c = 0$.

On comparing equations (8.56b) and (8.62), the following relationship holds:

$$\alpha_{ma} = \omega_r \, t - \frac{\alpha_c}{p} + \frac{\pi}{6p} \tag{8.66}$$

Therefore θ_o is determined from equations (8.66) and (8.57) as:

$$\theta_o = -\frac{\alpha_c}{p} + \frac{\pi}{6p} \tag{8.67}$$

Hence re-writing equation (8.62), the back-emf is obtained as

$$e_a = \sum_n E_n \sin n \left(p \, \omega_r \, t - \alpha_c + \frac{\pi}{6} \right) \tag{8.68}$$

where $E_n = \omega_r \, \Phi_n \, W \, K_{dpn} = \omega_r \left(2 \, B_n \, R_i \, l_{ef} \right) W \, K_{dpn} \, \tilde{\Lambda}_o$ (8.69)

8.4 Resultant Magnetic Field on Load

In previous sections solutions for the open-circuit and armature reaction field components have been obtained for a surface-mounted radial-field motor, accounting for the effect of slotting. In this section, these analyses are summarised and the relative positions of the component fields, and the relative permeance, and the back-emf and current waveforms are established so that the resultant instantaneous magnetic field for any load condition and any commutation strategy can be deduced and compared with predictions from finite-element calculations.

8.4.1 Relative Positions of the Open-circuit and Armature Reaction Fields, and the Permeance

In order to obtain a solution for the instantaneous magnetic field under any load condition and commutation strategy it is critical to determine the relative positions of a variety of functions. For example:

1) Reference direction of rotation of the rotor;
2) Reference polarity of current flowing in each phase winding;
3) Reference phase sequence in space;
4) Reference position for the axis of phase A;
5) Reference position for the corresponding phase current;
6) Reference positions for the fields produced by the magnets and the windings, as well as for the permeance function;
7) Relationship between time and angular position;
8) Relative position between the axis of phase A winding and the permeance function;
9) Relative position between the axis of phase A winding and the permanent magnet poles; etc.

All the above items are summarised and discussed in the following:

1) Reference direction of rotation of the rotor

It is assumed that the direction of rotation of the rotor is anti-clockwise, as shown in Fig 8.11.

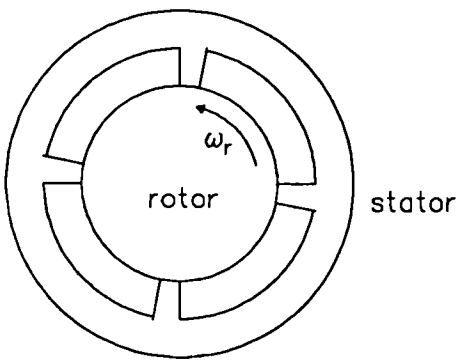

Fig 8.11 Direction of rotation of the rotor.

2) Reference polarity of current flowing in each phase winding

The reference direction of the current flowing in phase A is shown in Fig 8.12.

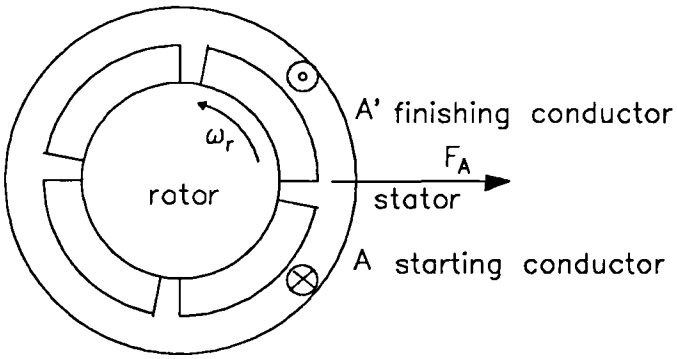

Fig 8.12 Directions of current flowing in phase A.

The direction of current flow is such that:

i) Following the direction of rotation the rotor magnetic field cuts the start conductors A first, and then the finish conductors A' of phase A, as shown in Fig 8.12, and similarly for the other two phases.

ii) The current flowing in the start conductors A is into the plane of the paper, whilst that in the finish conductor A' is out of the plane of the paper.

iii) The direction of the mmf produced by the winding is determined by the right-hand rule.

3) Reference phase sequence in space

Fig 8.13 shows the sequence of phases A, B, and C in space.

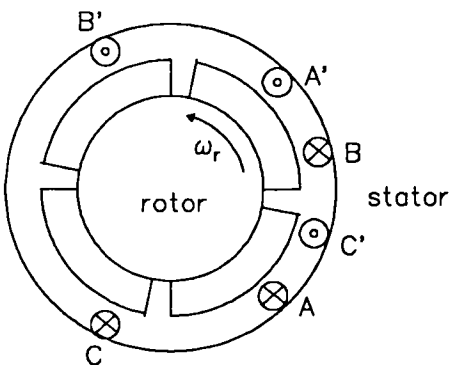

Fig 8.13 Sequence of phases A, B, and C in space.

The sequence is such that following the rotation of the rotor the emf induced in phases B and C are respectively 120 elec retarded and 120 elec advanced in time with respect to the emf induced in phase A. This definition will ensure that the time phase sequence is the same as the spatial phase sequence.

4) Reference position for the axis of phase A

The reference position for the axis of phase A is such that the initial spatial angle position, $\alpha=0$ is defined at the axis of phase A.

5) Reference position for the phase current

The reference position for the phase current is related to the previous definitions. In particular, the current waveform of A is such that at the initial time, t = 0 when the winding of phase A is being commutated on the current flowing in the winding has a positive polarity, as shown in Fig 8.14.

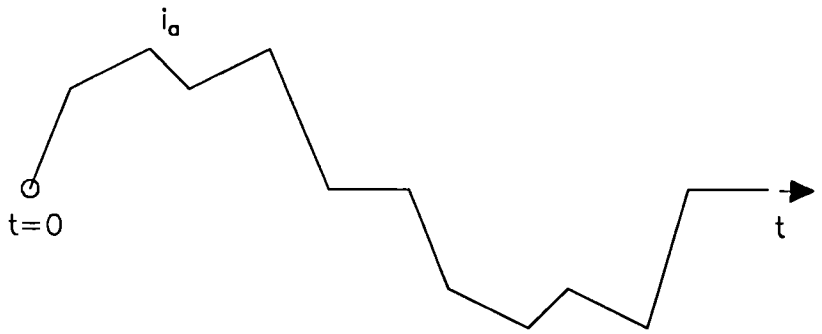

Fig 8.14 Definition of initial time for current waveform

6) Reference positions for magnetic fields produced by the magnets and the windings, and the permeance function

As already mentioned in Chapter 5, the solution for the magnetic field produced by the permanent magnets has a reference position, $\theta = 0$ at the centre of one pole whose direction of magnetisation is coincident with the positive radial direction of the polar coordinate system, ie.

$$B_{magnet}(\theta, r) = \sum_{n} B_n \cos n p \theta \qquad (5.53)$$

The solution obtained in section 8.2 for the magnetic field produced by the windings is with reference to $\alpha = 0$ being at the axis of the phase A winding, ie.

$$B_{winding}(\alpha, r, t) = \sum_{u} \sum_{v} B_{uv} \sin(u p \omega_r t - v_u p \alpha + \theta_u) \qquad (8.51)$$

whereas the reference position $\alpha = 0$ for the relative permeance function obtained in section 5.4 is at the centre of a slot opening, ie.

$$\lambda(\alpha, r) = \sum_{\mu} \Lambda_\mu \cos \mu Q_s \alpha \qquad (5.123)$$

7) Relationship between time and angular position

The relationship between the time and the angular position can be determined from a dynamic simulation, as described in Chapter 7. However for steady-state operation if the speed of the rotor is assumed to be constant, a simple relationship can be obtained from the preceeding definitions for the current waveform and the magnetic field produced by the windings.

since $\alpha = \omega_r t = \frac{2\pi n_r}{60} t$ (mechanical rad.) (8.70)

or $\alpha = \omega_r t = \frac{360 n_r}{60} t = 6 n_r t$ (mechanical degree) (8.71)

hence $t = \frac{\alpha}{6 n_r}$ (8.72)

where n_r is the speed of the rotor (rpm).

8) Relative position between the axis of phase A winding and the permeance function

The definition of the relative position between the permeance and the mmf produced by the windings can be determined according to the particular winding topology of a motor. As defined in 6) above, the reference for the permeance function is at the stator slot axis. However if the angular position $\alpha = 0$ is redefined to be at the axis of phase A stator winding, the physical origin of the permeance function may no longer be at the stator slot axis. In general there are two cases which will determine the physical origin of the permeance function, viz:

Case 1: The winding pitch is an odd integer of the slot pitch, as shown in Fig 8.15(a).

Case 2: The winding pitch is an even integer of the slot pitch, as shown in Fig 8.15(b).

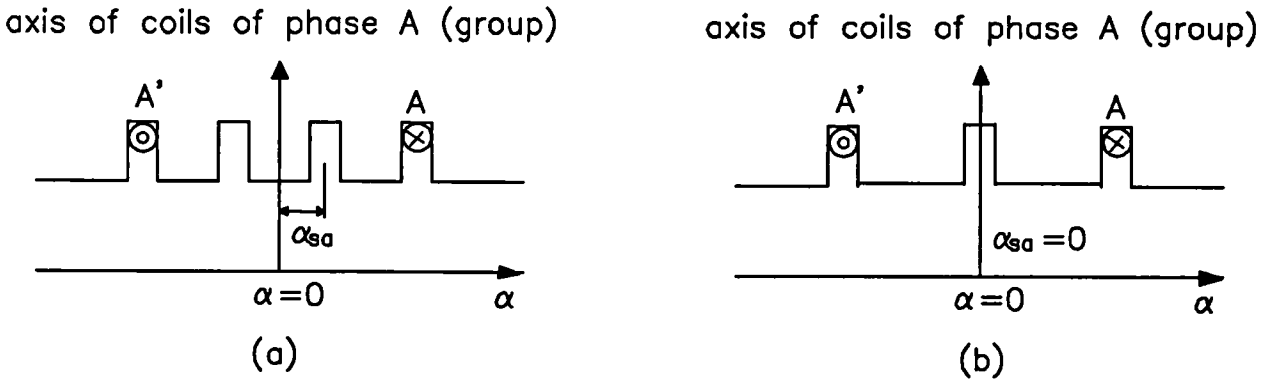

Fig 8.15 Relative positions between axes of phase windings and permeance.

It will be seen that in the case (1) the axis of the coils of phase A coincides with the centre of a stator tooth, whilst in case (2) the axis of phase A coincides with the centre of a stator slot. Therefore if the magnetic field produced by the windings is defined by

$$B_{winding}(\alpha, r, t) = \sum_{u} \sum_{v} B_{uv} \sin(u p \omega_r t - v_u p \alpha + \theta_u) \qquad (8.51)$$

with $\alpha = 0$ being at the axis of phase A windings

and $$i_a = \sum_{u} I_u \sin u(p \omega_r t + \theta_u) \qquad (8.43)$$

then the relative permeance function is given by:

$$\tilde{\Lambda}(\alpha, r) = \sum_{\mu} \Lambda_{\mu} \cos \mu Q_s (\alpha + \alpha_{sa}) \tag{8.73}$$

where

$$\alpha_{sa} = \begin{cases} \textit{half slot pitch} = \dfrac{\pi}{Q_s} & \text{for } \textit{case } 1 \\ 0 & \text{for } \textit{case } 2 \end{cases} \tag{8.74}$$

$$\text{ie. } \tilde{\Lambda}(\alpha, r) = \begin{cases} \sum\limits_{\mu} (-1)^{\mu} \Lambda_{\mu} \cos \mu Q_s \alpha & \text{for } \textit{case } 1 \\ \sum\limits_{\mu} \Lambda_{\mu} \cos \mu Q_s \alpha & \text{for } \textit{case } 2 \end{cases} \tag{8.75}$$

9) Relative position between the axis of phase A winding and the permanent magnet poles

In section 8.3 it was stated that

$$\theta = \alpha - \alpha_{ma} \tag{8.76}$$

where α is the stator angular position with its reference $\alpha = 0$ at the axis of phase A winding, and

α_{ma} is the relative position between the axes of the magnetic fields due to phase A windings and the magnets.

Hence $$\alpha_{ma} = \omega_r t - \frac{\alpha_c}{p} + \frac{\pi}{6p} \tag{8.66}$$

Therefore if the magnetic field produced by the windings is given by equation (8.51), the magnetic field produced by the magnets is now given by:

$$B_{magnet}(\alpha, r, t) = \sum_{n} B_n \cos np (\alpha - \alpha_{ma}) \tag{8.77}$$

8.4.2 Instantaneous Field Distributions

In summary the instantaneous field distribution under any specified load condition can be calculated from

$$B_{load}(\alpha, r, t) = B_{open-circuit}(\alpha, r, t) + B_{armature-reaction}(\alpha, r, t) \tag{8.78}$$

whilst $$B_{open-circuit}(\alpha, r, t) = B_{magnet}(\alpha, r, t)\,\Lambda(\alpha, r) \tag{8.79}$$

and $$B_{armature-reaction}(\alpha, r, t) = B_{winding}(\alpha, r, t)\,\Lambda(\alpha, r) \tag{8.80}$$

where

$$B_{magnet}(\alpha, r, t) = \sum_{n=1,3,5,\ldots}^{\infty} B_n \cos n p \left(\omega_r t - \alpha - \frac{\alpha_c}{p} + \frac{\pi}{6p}\right) \tag{8.81}$$

$$B_{winding}(\alpha, r, t) = \sum_{u=1,2,3,\ldots}^{\infty} \sum_{c=0,\pm 1,\pm 2,\ldots}^{\infty} B_{uv} \sin\left[u(p\,\omega_r t) + \nu_u\,\alpha + \theta_u\right] \tag{8.82}$$

and

$$\Lambda(\alpha, r) = \sum_{\mu=0,1,2,\ldots}^{\infty} \Lambda_\mu \cos \mu Q_s (\alpha + \alpha_{sa}) \tag{8.83}$$

where $$\nu_u = \pm p\,(6c - \{\pm\} u) \tag{8.84}$$

$$\alpha_{sa} = \begin{cases} \dfrac{\pi}{Q_s} & \text{for } \textit{winding pitch = odd integer of slot pitch} \\ 0 & \text{for } \textit{winding pitch = even integer of slot pitch} \end{cases} \tag{8.85}$$

and $$i_a = \sum_{u=1,2,3,\ldots}^{\infty} I_u \sin u(p\,\omega_r t + \theta_u) \tag{8.86}$$

with $i_a|_{t=0}$

θ_u is the phase angle of the current harmonics;

ω_r is the angular speed of rotation of the rotor;

α is the angular position on the stator;

with $\alpha|_{t=0} = 0$ and $\alpha = 0$ at the axis of phase A stator winding.

Fig 8.16 shows instantaneous field distributions from finite element analyses in which the instantaneous current values are obtained from the dynamic simulation in Chapter 7 and shown in Fig 8.5, whilst the relative position is determined by the technique described in the previous section. Again the results relate to the prototype internal rotor radial-field motor whose parameters are described in Table 5.1 and whose mesh discretisation is shown in Fig 5.20. At a rotor speed of 1500 rpm, from time t = 0 to time t = 3.333 ms corresponds to 1/6 of a full cycle,

whilst time t = 0 s, 1.666 ms, and 3.333 ms correspond to the rotor positions 0^o , 15^o , and 30^o mech respectively. As can be seen, since under the assumed steady-state condition the rotor rotates at a constant speed, the magnetic field produced by the magnets also rotates uniformly, whilst the magnetic field produced by the windings rotates in incremental steps between the commutation events. As a result, the magnetic field on load also rotates non-uniformly. To be more specific, in the flux distributions in Fig 8.16, at time t = 0 s, only phases B and C are conducting, since although phase A is just about to be commutated on, its current is still zero. At time t = 1.666 ms phases A and C are conducting, whilst phase B is blocked and the current of phase B is zero. The axis of the magnetic field produced by the windings has rotated by an incremental angle of 30^o elec when the rotor has rotated by 15^o mech. However, in the time interval t = 3.333 ms, no further commutation event occurs, phases A and C continuing to conduct and phase B still being blocked. When the rotor has rotated a further 15^o mech, the axis of the magnetic field produced by the windings at time t = 3.333 ms effectively remains at the same position as that at time t = 1.666 ms, only the magnitude of magnetic field has changed due to the nature of the current waveform resulting from the effect of the winding inductances.

Therefore under a load condition the angle between the axes of the open-circuit field and the armature reaction field effectively varies from 60^o elec, at the beginning of a commutation period to 120^o elec at the end of the period.

The instantaneous field distribution derived from the analytical prediction is described in the next section.

8.4.3 Comparison of Predictions with Finite Element Calculations

In this section predictions from finite element and analytical calculations are compared for the open-circuit field, the armature reaction field, and the net magnetic field on load.

For the internal rotor motor whose parameters are given in Table 5.1, and whose discretisation is shown in Fig 5.20, Figs 8.17, 8.19, 8.21, and Figs 8.18, 8.20, 8.22 compare analytical and

finite element predictions in both circumferential and radial directions for the open-circuit field, the armature reaction field, and the load magnetic field at different instances in time. For each condition a comparison of the variation along a radius through the airgap/magnet region is given in Tables 8.3 - 8.6. The comparisons show that the analytical predictions of the open-circuit, armature reaction, and load field distributions are in excellent agreement with the results from finite element analyses. It will be noted that earlier discussions regarding the effects of finite element discretisation, flux focussing, leakage flux, and oscillations in the predicted field distributions are still relevant.

For this particular prototype motor the magnetic circuit was not highly saturated, as was mentioned earlier in Chapter 5. Hence the armature reaction field predicted from an idealised model, Fig 8.23, in which the teeth have been modelled by a natural Neuman boundary condition (ie. $\mu_{Fe} = \infty$), show excellent agreement with Fig 8.19. Indeed it is usually the case that the airgap flux density due to the armature reaction field is normally less than 20% of that due to the magnets, saturation being dominated by the field of the permanent magnets.

8.5 Calculation of self- and mutual-inductances

It is a relatively simple matter to extend the technique for calculating the armature reaction field, as described in section 8.2, to the calculation of the self- and mutual stator winding inductances of the active length of a motor. In section 8.2.6 the magnetic field of a distributed winding has been obtained as

$$B_{winding}(\alpha, r, t) = \mu_o \frac{2 W i_a}{\pi \delta} \sum_{\nu} \frac{1}{\nu} K_{sov} K_{dpv} F_b(\nu, r) \cos \nu \alpha \qquad (8.44)$$

where $\nu = p\nu'$, $\nu' = 1, 2, 3, \ldots$ for phase A

letting $B_a(\alpha, t) = B_{winding}(\alpha, r, t)|_{r=R_i} = \sum_{\nu} B_{a\nu} \cos \nu \alpha \qquad (8.87)$

then, for each harmonic component, the flux per pole is

$$\Phi_v = \frac{2}{\pi} l_{ef} \frac{\tau}{v} B_{av} \tag{8.88}$$

where τ is the pole pitch and l_{ef} is the effective length of the windings.

The flux linkage between the winding and the harmonic field produced by itself or by another phase winding is

$$\Psi_v^{aa} = \Phi_v W K_{dpv} \tag{8.89a}$$

or

$$\Psi_v^{ab} = \Phi_v W K_{dpv} \cos \frac{v}{p} \frac{2\pi}{3} \tag{8.89b}$$

Hence the self- and mutual stator winding inductances of the active region of either an internal rotor or an external rotor motor are obtained as:

$$L_g = \frac{\sum \Psi_v^{aa}}{i_a}$$

$$= \frac{4}{\pi^2} \frac{\tau l_{ef}}{p} \frac{\mu_o}{\delta} \sum_v \left(\frac{W K_{dpv}}{v} \right)^2 F_b(v, r)|_{r=R_i} \tag{8.90}$$

and

$$M_g = \frac{\sum \Psi_v^{ab}}{i_a}$$

$$= \frac{4}{\pi^2} \frac{\tau l_{ef}}{p} \frac{\mu_o}{\delta} \sum_v \left(\frac{W K_{dpv}}{v} \right)^2 F_b(v, r)|_{r=R_i} \cos \frac{v}{p} \frac{2\pi}{3} \tag{8.91}$$

where $v = p, 2p, 3p, \ldots$

Comparing the above 2-dimensional analysis for calculating the self- and mutual stator winding inductances with the 1-dimensional model as applied to conventional machine formats, such as induction motors [8.4], it will be found that the main difference lies in the term $F_b(v, r)$. Indeed, as has been discussed in section 8.2.3, the function $F_b(v, r)$ accounts for the effect of the airgap in the 2-dimensional analysis.

8.6 Conclusions

In this chapter a comprehensive analytical technique has been presented for predicting the airgap field distribution in radial-field brushless DC motors under any specified load condition, accounting implicitly for the stator winding current waveform and the effects of stator slot openings. It is based on a 2-dimensional analysis, in polar coordinates, of the airgap/permanent magnet region, and combines an analytical calculation of the armature reaction field from an analytical prediction of the current waveforms, with the open-circuit field produced by the magnets to enable the instantaneous field distribution to be predicted under any load condition and specified commutation strategy. The predicted open-circuit, armature reaction, and load field distributions all show excellent agreement with results from finite element analyses.

Fundamental to the calculation is a knowledge of the relative position of factors such as the open-circuit and armature reaction field components, the permeance function, the back-emf and current waveforms etc. This has been analysed and accounted for in the calculation of the instantaneous field distributions.

In addition 2-dimensional analytical methods for calculating the back-emf and the self- and mutual-winding inductances has been developed.

The techniques are suitable for either internal or external rotor surface-mounted permanent magnet brushless dc motor topologies, and should be applicable to the analysis of corresponding topologies of brushless permanent magnet AC motor.

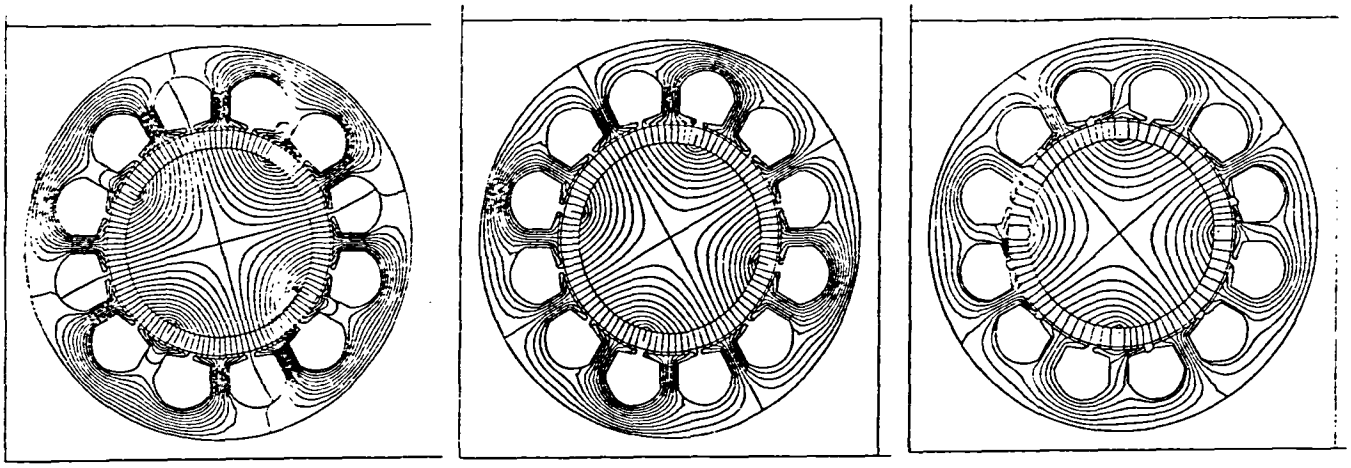

Open-circuit field
time = o s, 0° mech.

Open-circuit field
time = 1.6666 ms, 15° mech.

Open-circuit field
time = 3.333 ms, 30° mech.

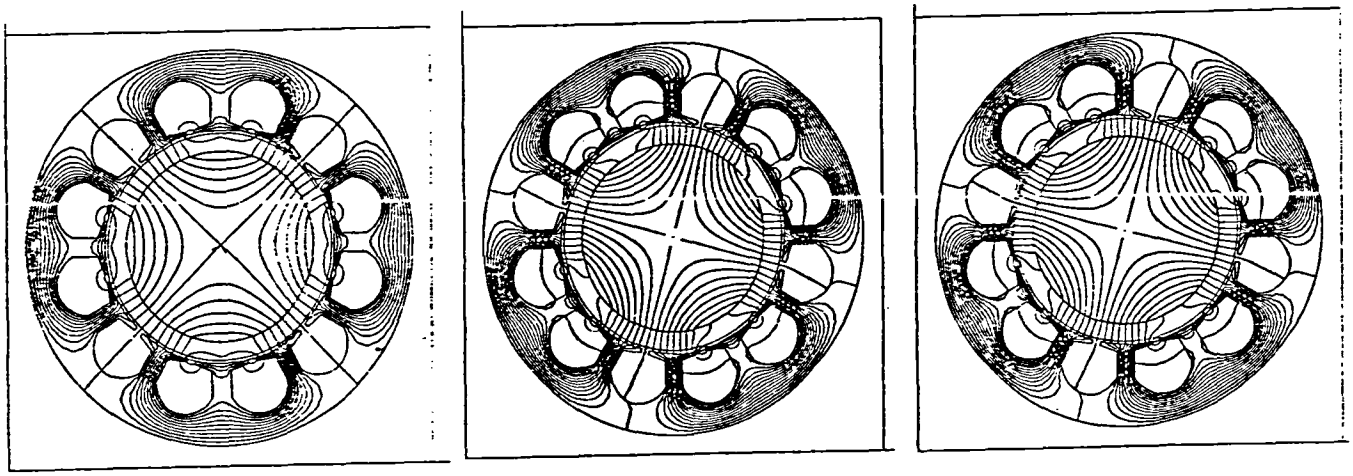

Armature reaction field
time = o s, 0° mech.

Armature reaction field
time = 1.666 ms, 15° mech.

Armature reaction field
time = 3.333 ms, 30° mech.

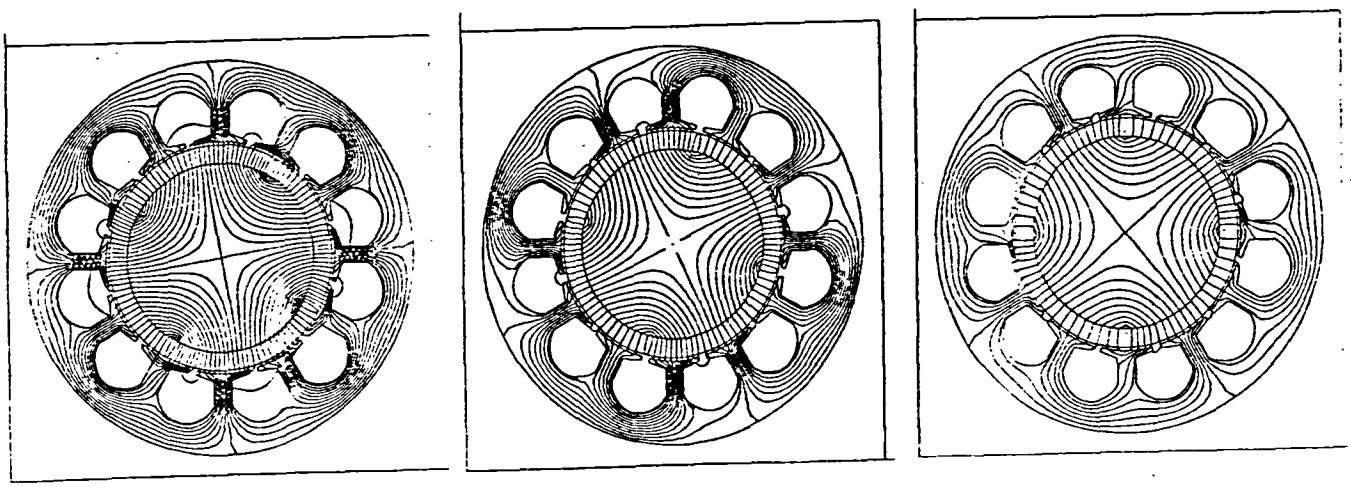

Load field, 1500 rpm
time = os, 0° mech.

Load field, 1500 rpm
time = 1.666 ms, 15° mech.

Load field, 1500 rpm
time = 3.333 ms, 30° mech.

Fig 8.16 Instantaneous field distributions

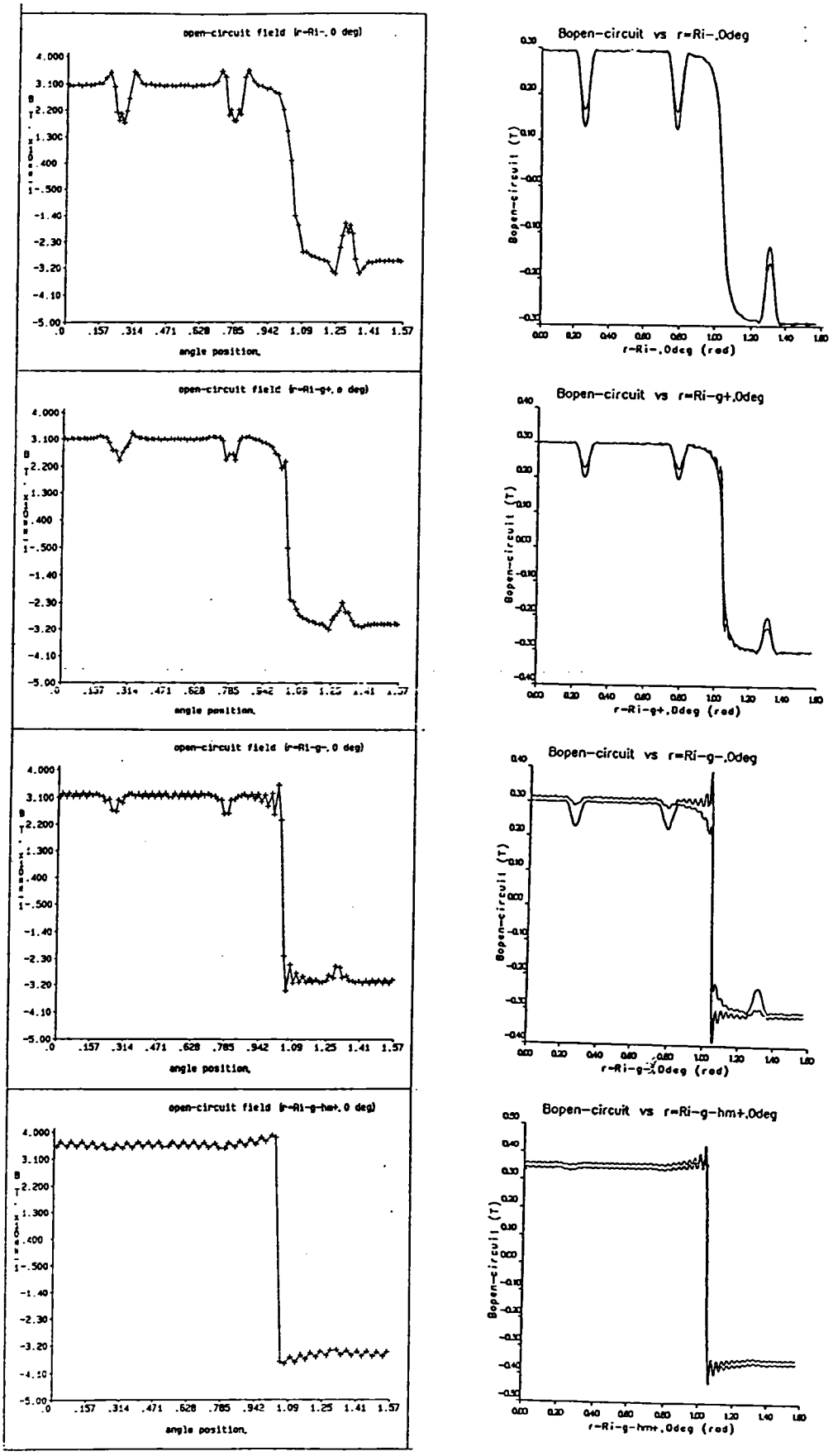

FEM calculation

Analytical prediction

Fig 8.17a Comparison of open-circuit field distribution at different radii, time=0s

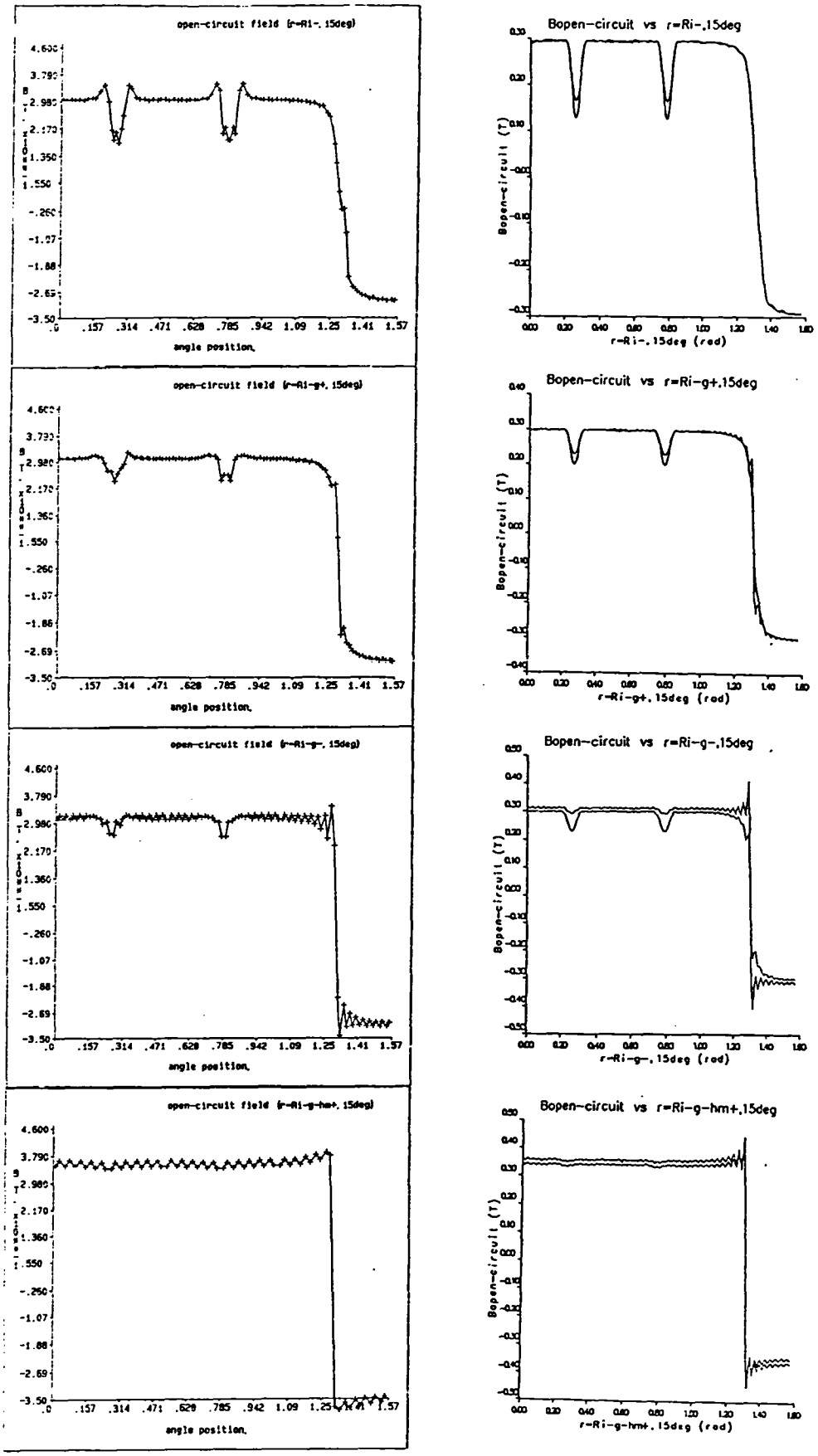

FEM calculation

Analytical prediction

Fig 8.17b Comparison of open-circuit field distribution at different radii, time=1.66ms

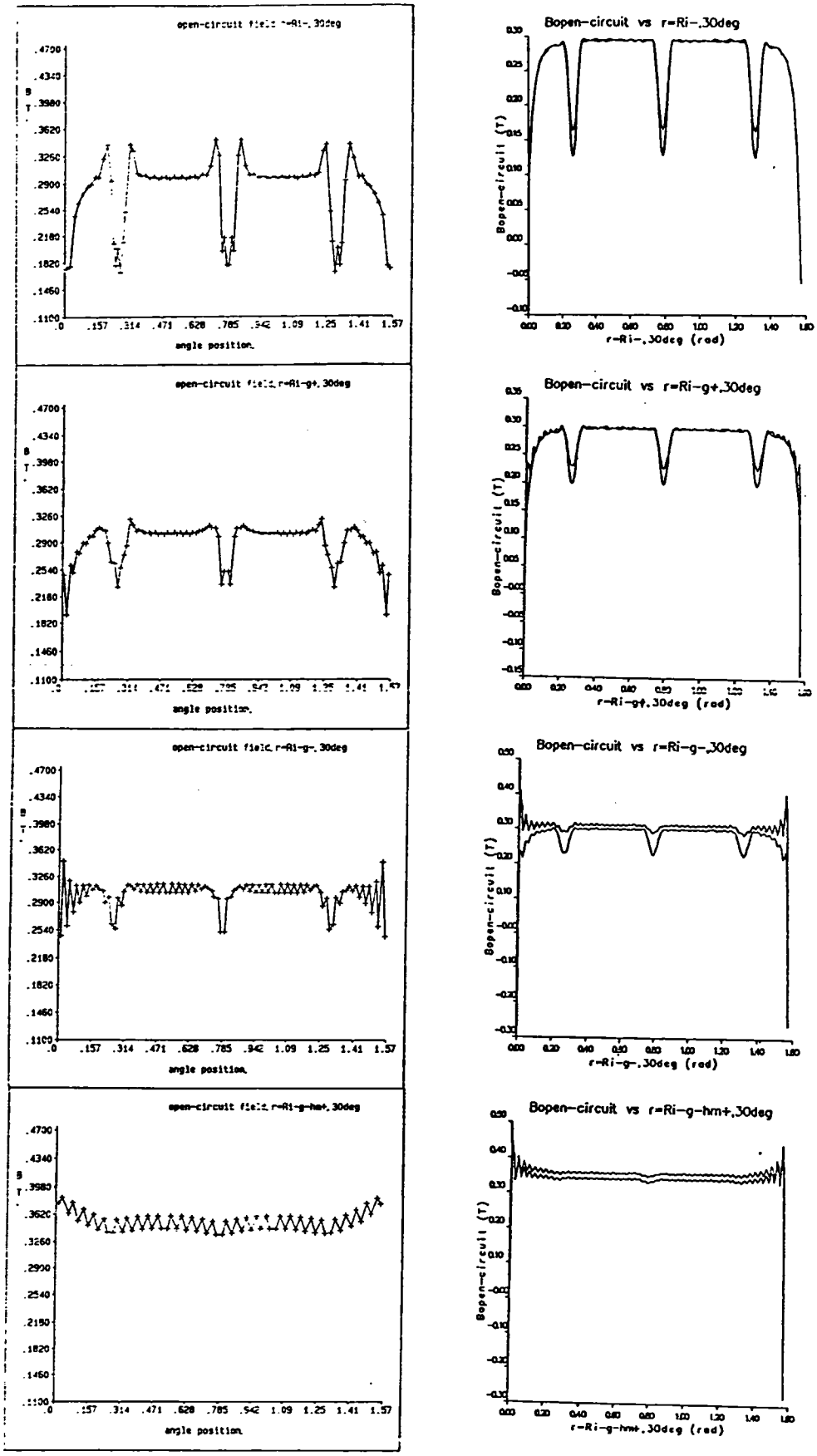

Fig 8.17c Comparison of open-circuit field distribution at different radii, time=3.33ms

Table 8.3 Variation of open-circuit field along a pole axis

Radius	Flux density (FEM)	Flux density (analytical prediction)
m	T	T
0.024685	0.35724	0.353855
0.025078	0.34154	0.348326
0.025862	0.34152	0.337777
0.026254	0.32729	0.332722
0.027038	0.32728	0.323307
0.027430	0.31413	0.319261
0.028214	0.31412	0.310705
0.028606	0.30218	0.305493
0.029081	0.30217	0.299224
0.029164	0.29975	0.298811
0.029331	0.29975	0.296829
0.029414	0.29746	0.295997
0.029580	0.29746	0.295004
0.029662	0.29475	0.295116

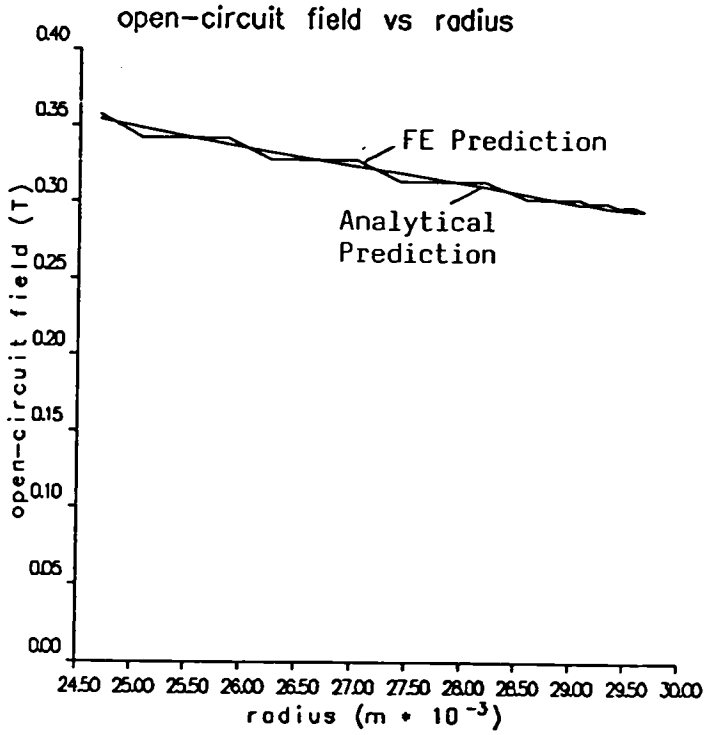

FFig 8.18 Variation of open-circuit field along a pole axis

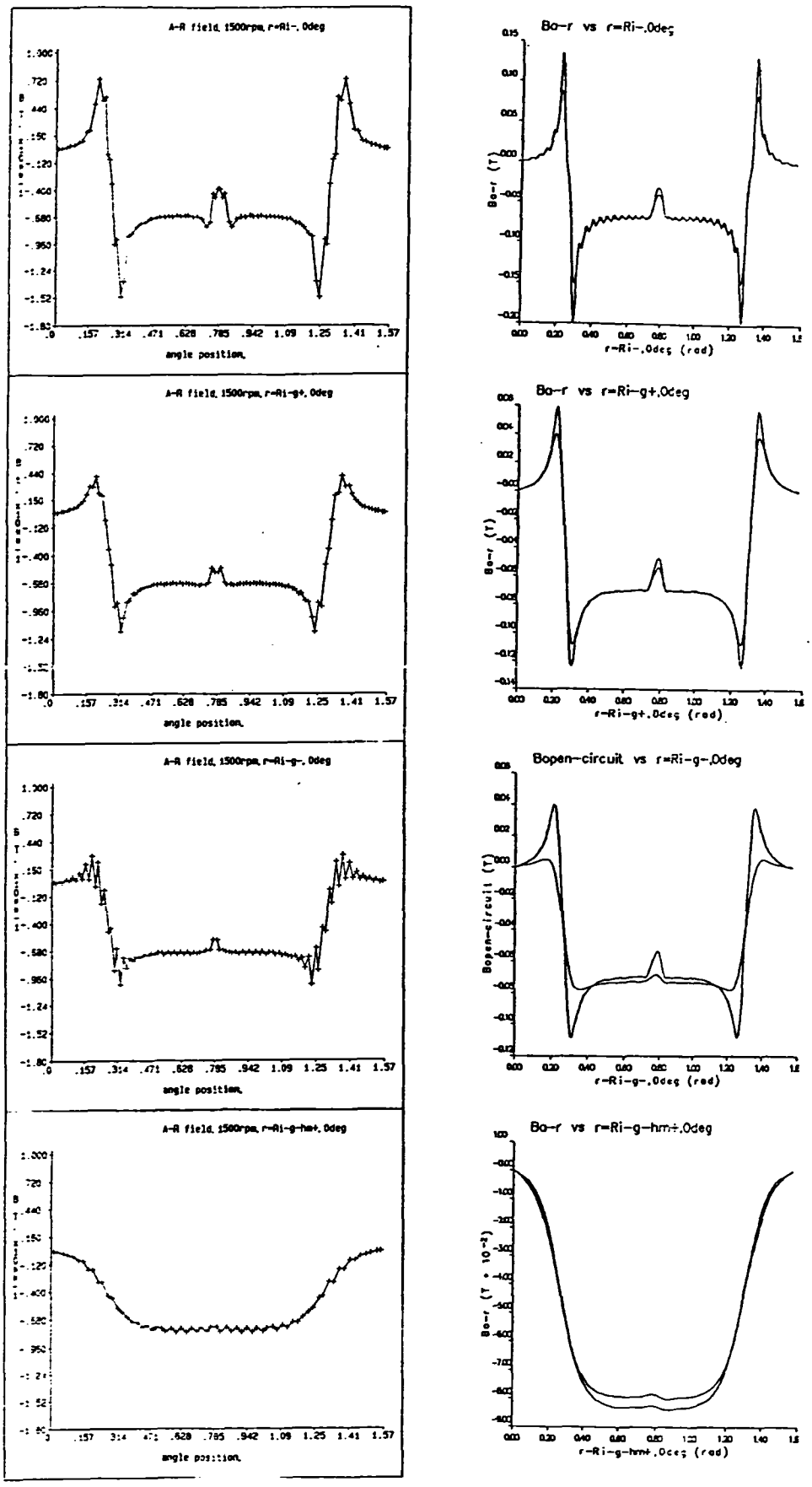

Fig 8.19a Comparison of armature reaction field distribution at different radii, time=0s

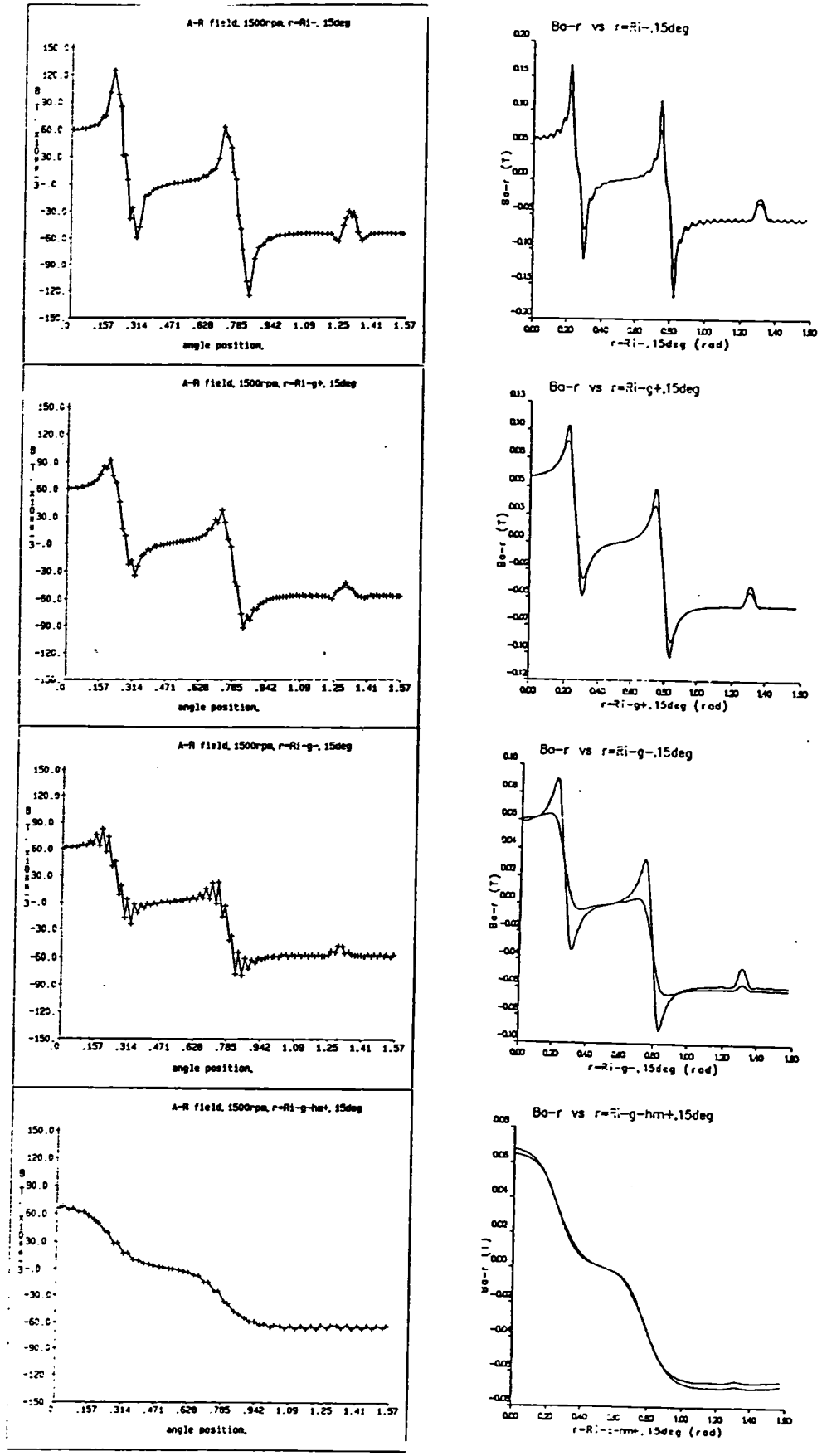

Fig 8.19b Comparison of armature reaction field distribution at different radii, time=1.66ms

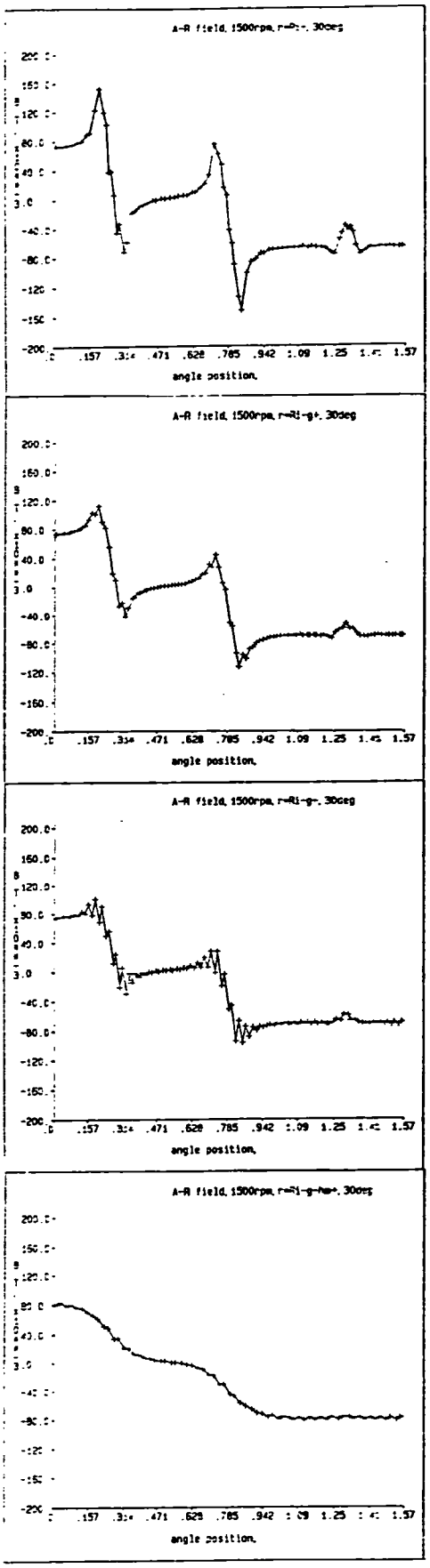

FEM calculation

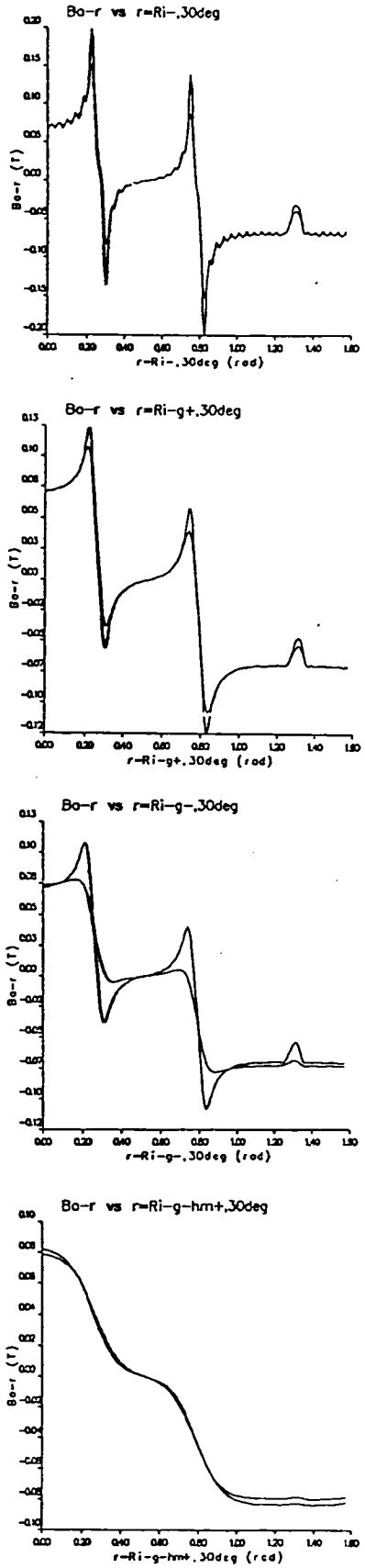

Analytical prediction

Fig 8.19c Comparison of armature reaction field distribution at different radii, time=3.33ms

Table 8.4 Variation of armature reaction field under a stator tooth

Radius	Flux density (FEM)	Flux density (analytical prediction)
m	T	T
0.024685	0.080823	0.0798130
0.025078	0.077467	0.0787963
0.025862	0.077470	0.0770409
0.026254	0.074791	0.0762781
0.027038	0.074800	0.0749410
0.027430	0.072494	0.0746756
0.028214	0.072502	0.0735097
0.028606	0.070233	0.0728534
0.029081	0.070234	0.0718931
0.029331	0.070019	0.0709628
0.029662	0.069298	0.0695147

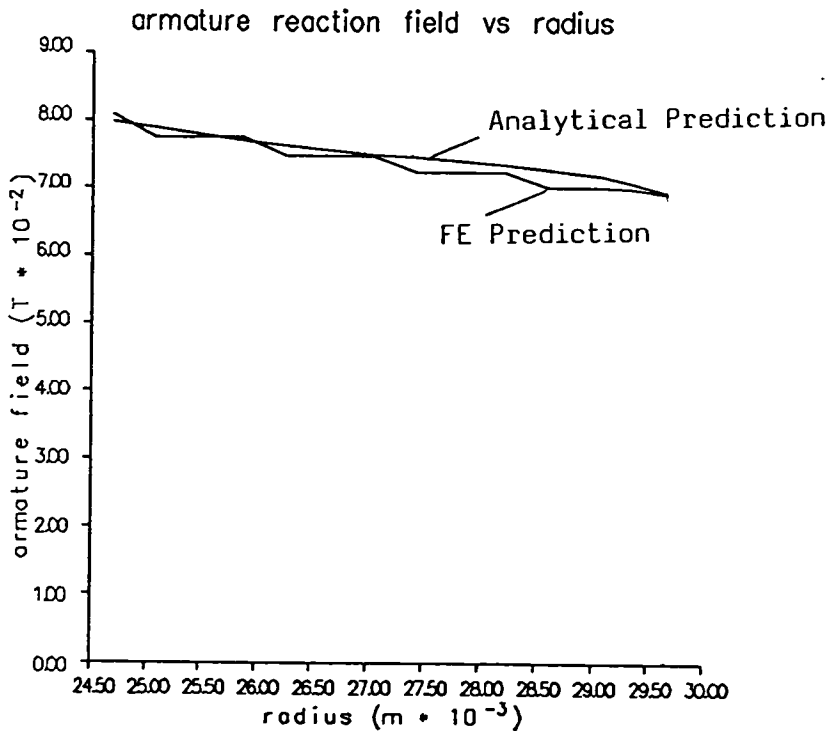

Fig 8.20 Variation of armature reaction field under a stator tooth

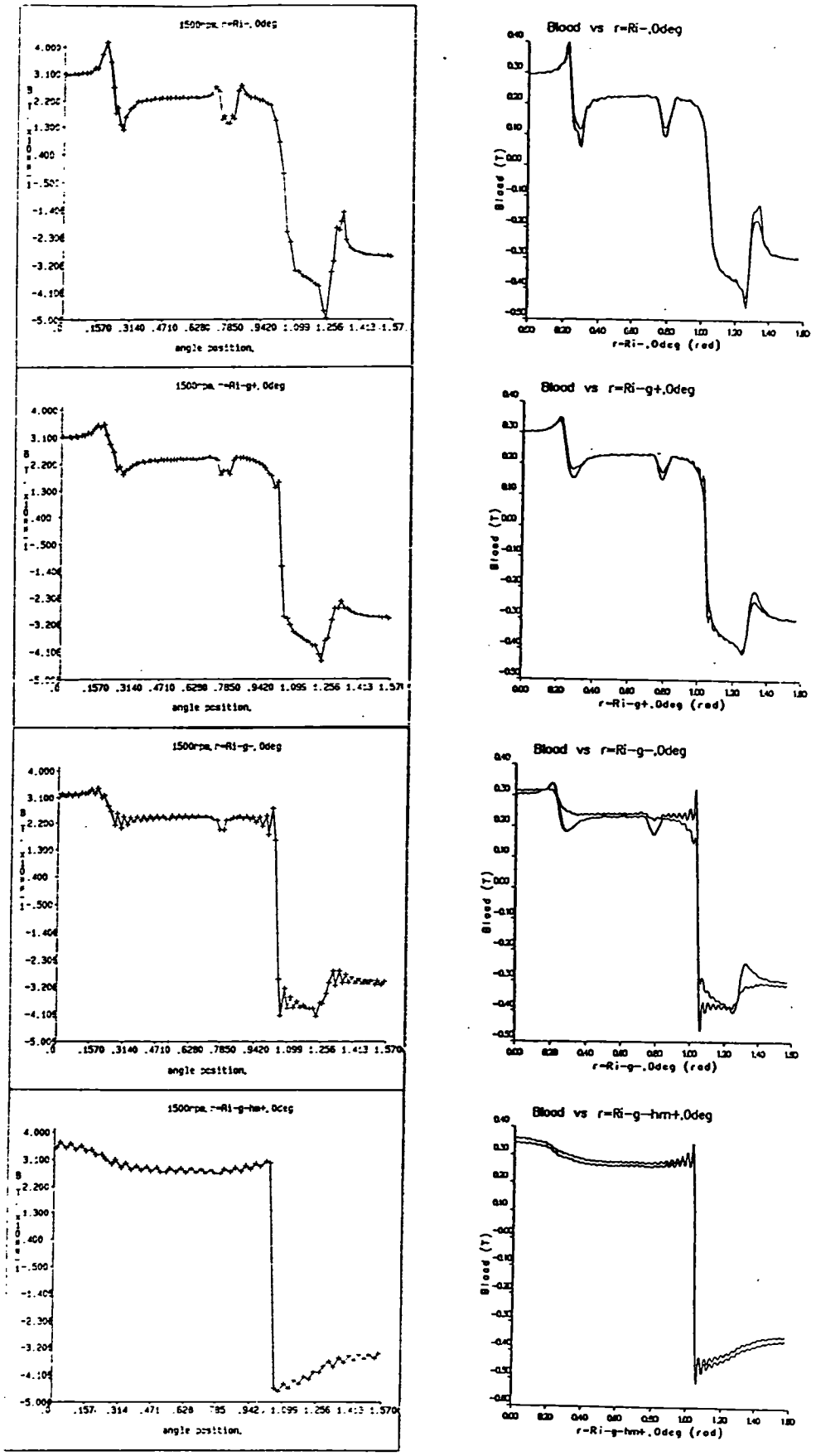

Fig 8.21a Comparison of load field distribution at different radii, time=0s

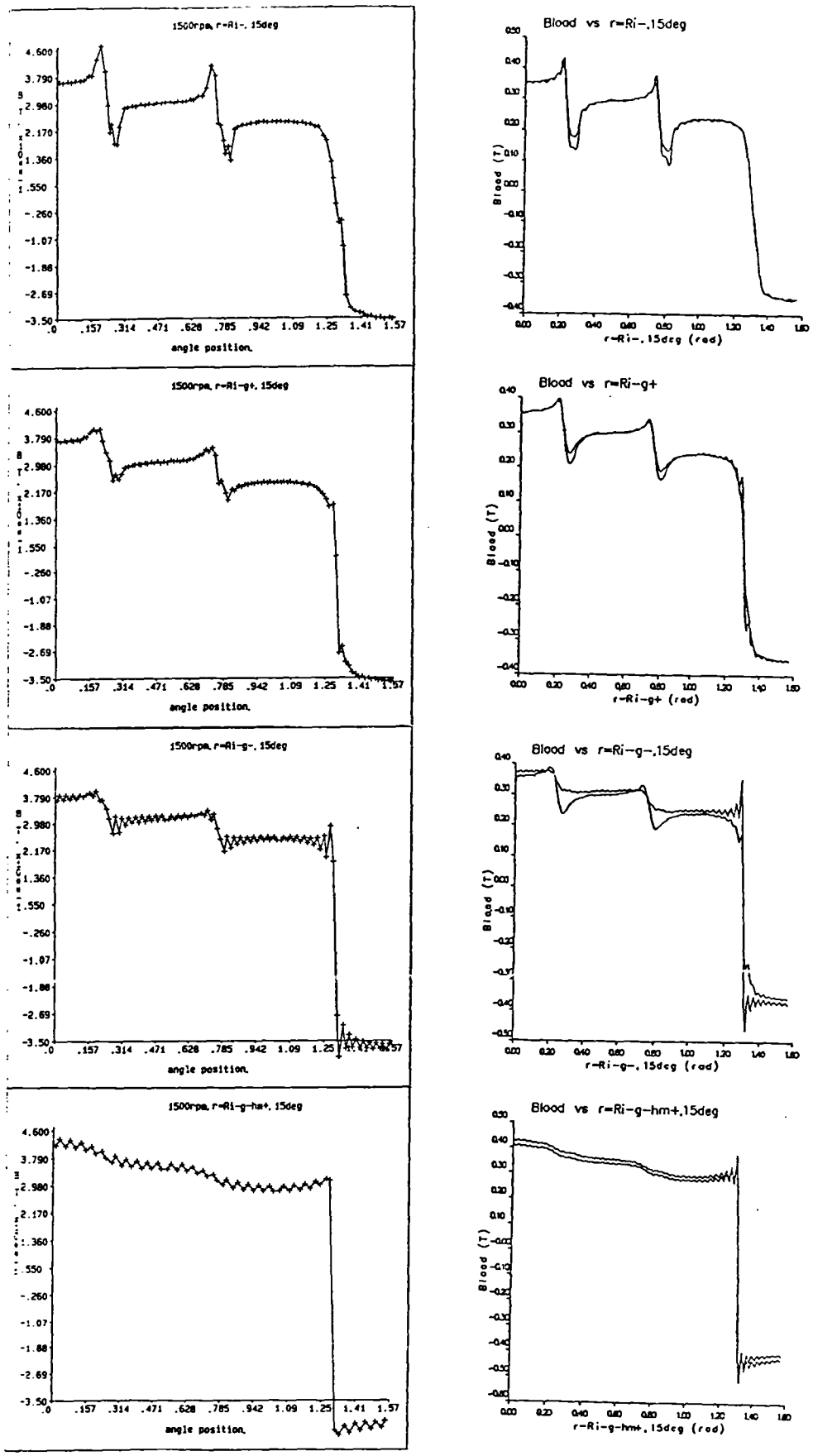

FEM calculation Analytical prediction

Fig 8.21b Comparison of load field distribution at different radii, time=1.66ms

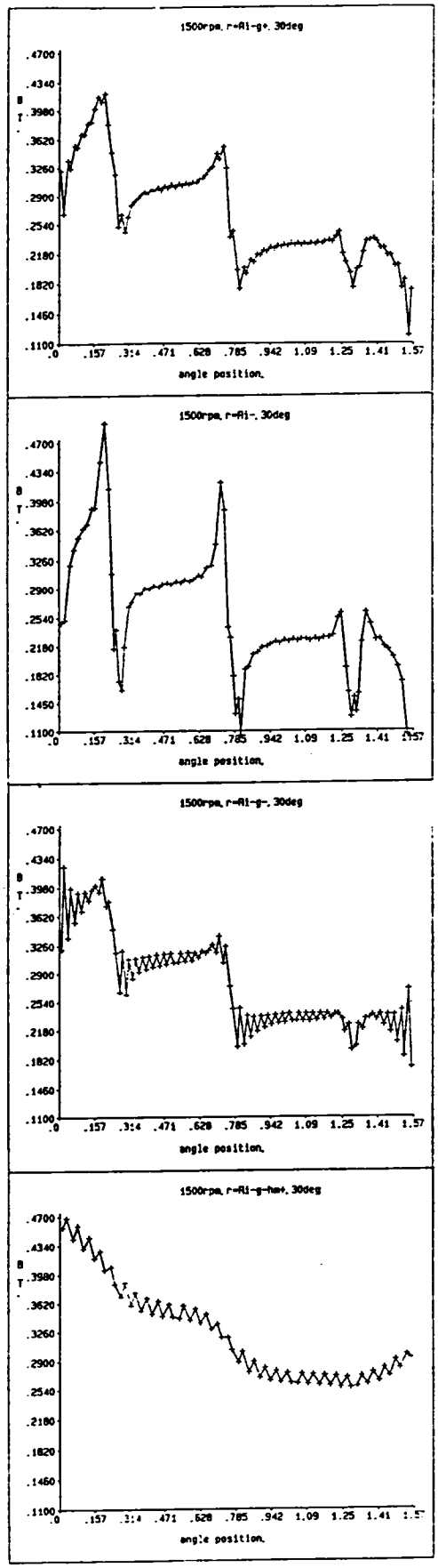

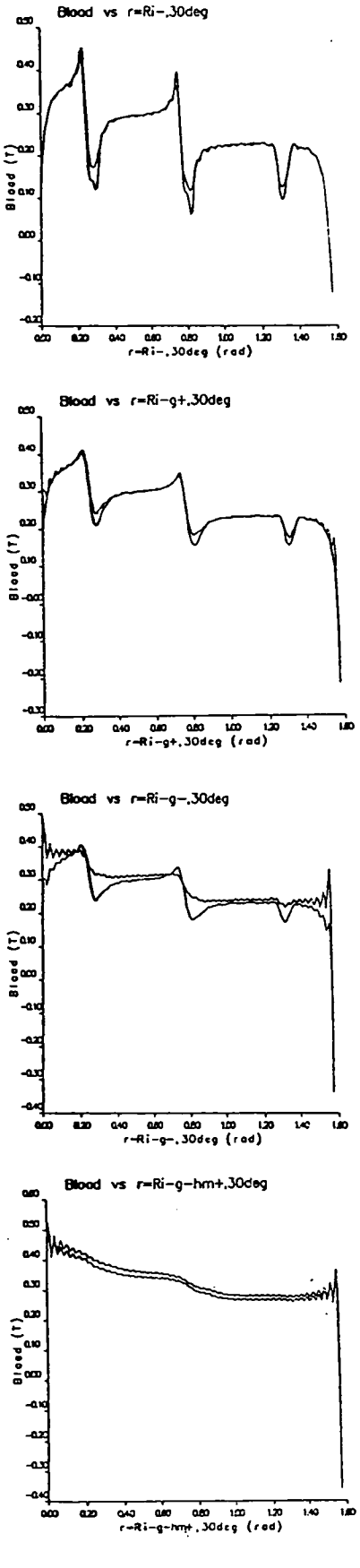

FEM calculation

Analytical prediction

Fig 8.21c Comparison of load field distribution at different radii, time=3.33ms

Table 8.5 Variation of load field under a stator tooth at 0^{o} mech.

Radius	Flux density (FEM)	Flux density (analytical prediction)
m	T	T
0.024685	0.35602	0.351317
0.025078	0.34080	0.345705
0.025862	0.34076	0.336062
0.026254	0.32711	0.330988
0.027038	0.32707	0.320939
0.027430	0.31447	0.316222
0.028214	0.31444	0.308877
0.028606	0.30252	0.302611
0.029081	0.30252	0.300554
0.029164	0.30010	0.299221
0.029330	0.30011	0.297439
0.029413	0.29777	0.296726
0.029580	0.29778	0.295501
0.029662	0.29576	0.293660

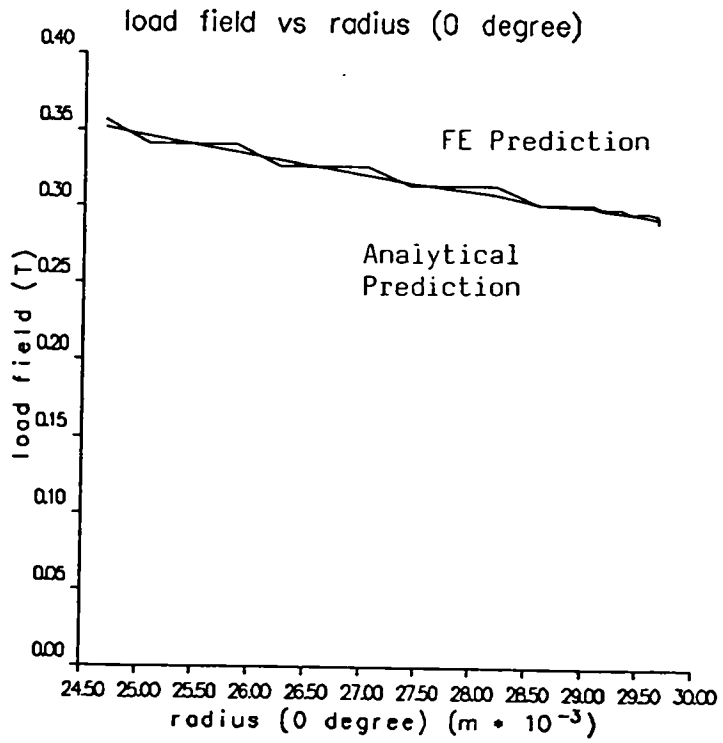

Fig 8.22a Variation of load field under a stator tooth at 0^{o} mech.

Table 8.6 Variation of load field under a stator tooth at 30^{0} mech.

Radius	Flux density (FEM)	Flux density (analytical prediction)
m	T	T
0.024685	0.27314	0.277470
0.025078	0.26098	0.272968
0.025862	0.26098	0.263970
0.026254	0.24938	0.259682
0.027038	0.24936	0.250880
0.027430	0.23884	0.247395
0.028214	0.23883	0.239365
0.028606	0.22931	0.235810
0.029081	0.22929	0.230962
0.029164	0.22751	0.228647
0.029331	0.22751	0.227153
0.029414	0.22542	0.226262
0.029580	0.22542	0.225220
0.029662	0.22373	0.224183

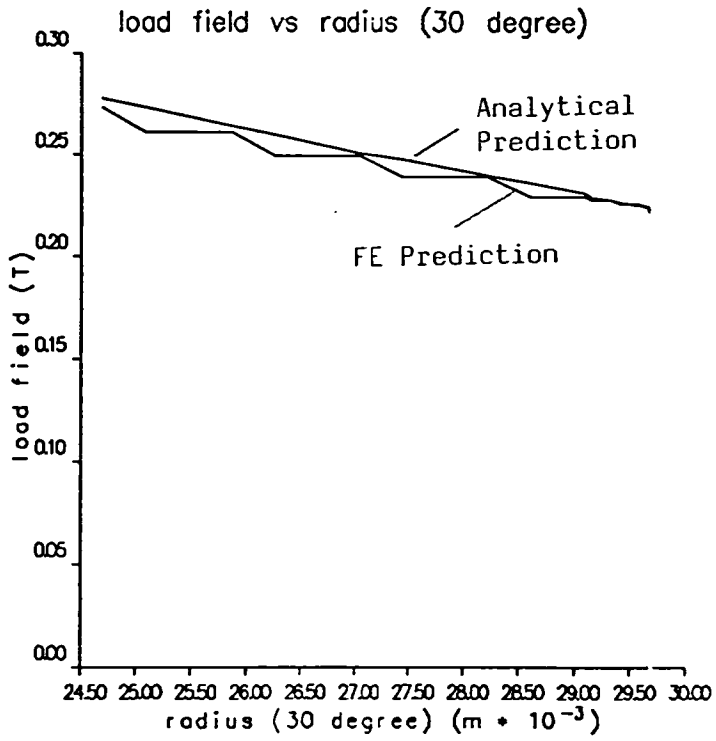

Fig 8.22b Variation of load field under a stator tooth at 30^{0} mech.

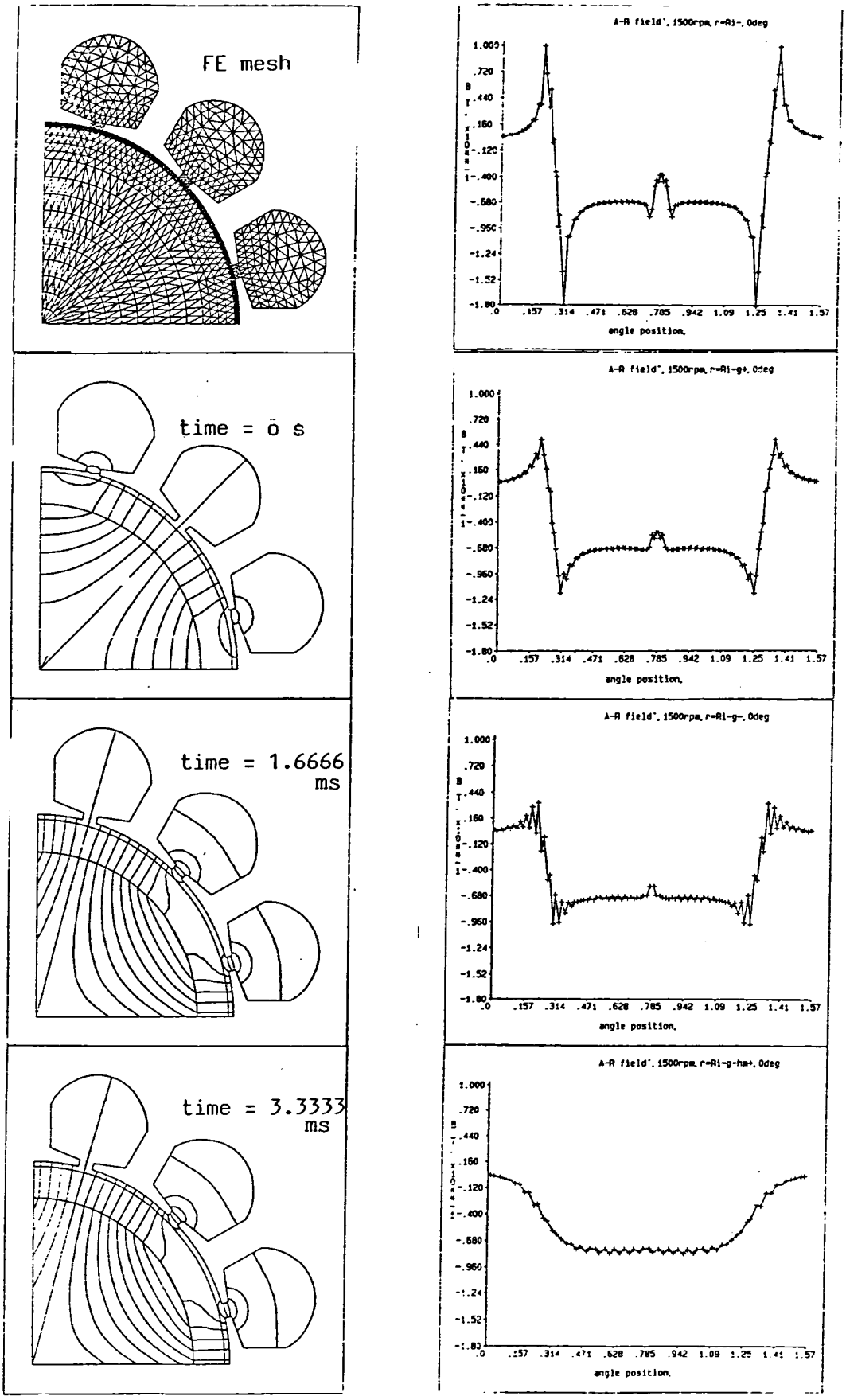

Fig 8.23a Comparison of armature reaction field distribution at different radii, calculated by FE analysis of an idealised model

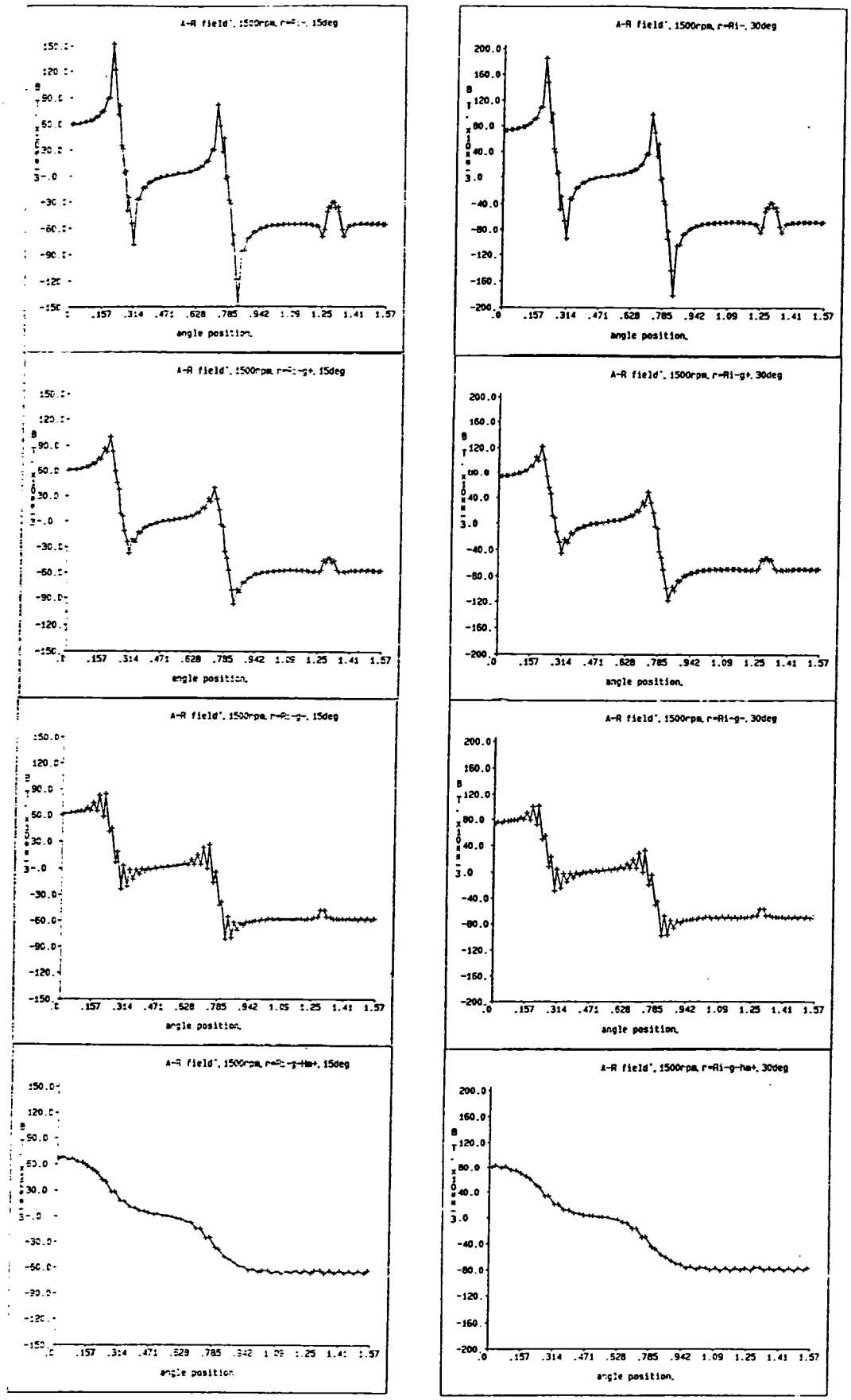

time = 1.6666 ms

time = 3.3333 ms

Fig 8.23b Comparison of armature reaction field distribution at different radii, calculated by FE analysis of an idealised model

CHAPTER 9

ESTIMATION AND ANALYSIS OF ELECTROMAGNETIC FORCE, VIBRATION, AND ACOUSTIC POWER OF BRUSHLESS DC MOTORS

9.1 Introduction

One consequence of the adoption of electronically controlled drive systems is that the phase current waveforms are no longer purely sinusoidal but contain significant harmonics [9.1] which greatly increase the possibility of resonances between the exciting forces and the stator structure, as well as the total level of emitted acoustic noise. Therefore, the study of the emitted acoustic noise cannot be restricted to the motor itself but must consider the complete drive system, including the supply inverter. Although this aspect has been the subject of recent research, much remains to be studied since to date only normal component identification on the noise spectrum from AC adjustable speed drives has been investigated [9.2][9.3][9.4][9.5]. Further, little research has been reported on the prediction of acoustic power radiated from such drives, whilst significant assumptions are usually employed, eg. the current waveform is assumed to contain a fundamental component only [9.6].

Many applications for brushless permanent magnet DC motor drive systems are noise sensitive. However the analysis of noise from brushless DC motors is somewhat different to that for adjustable speed AC drives which are based on induction motors and transistor/thyristor inverters. The vast majority of brushless DC motors have surface-mounted permanent magnet rotors, which leads to a large effective airgap, whilst the armature reaction field results from phase current waveforms which necessarily depart from the ideal rectangular waveform and rotates in incremental steps between commutation events, as described in Chapter 8. Therefore relative to its brushed counterpart, whilst the removal of the commutator can lead to a significant reduction in the mechanical noise, the non-ideal phase current waveforms tend to increase the

electromagnetically generated noise, despite the fact that in surface-mounted topologies the slot harmonic fields are alleviated because of the large effective airgap. Furthermore significant torque ripple can arise due to commutation events as well as cogging, both of which will induce tangential vibrations. However to date no investigations have been reported on the noise emitted from brushless permanent magnet DC motors.

Although the techniques for calculating the airgap field, radial force, vibration, and hence acoustic noise have been applied primarily to induction motors [9.7][9.8][9.9][9.10], the models for predicting the vibration and noise are equally applicable to permanent magnet excited machine formats. However, even for induction motors, existing analytical methods are feasible only for particular forms of stator construction [9.7][9.11], whilst numerical methods are usually difficult to apply because of the movement of the rotor on the one hand [9.12][9.13] and the non-sinusoidal current waveforms on the other.

In Chapters 5, 7, and 8 a comprehensive analytical technique was presented for predicting the airgap field distribution in radial field brushless motors under any load conditions, accounting implicitly for the corresponding stator winding current waveforms, the large effective airgap, and the effects of the stator slot openings. The predicted open-circuit, armature reaction, and load magnetic field distributions have all shown excellent agreement with corresponding results from finite element analyses.

In this chapter an analytical technique for predicting the acoustic power level of a brushless DC motor is developed and compared with the measurements on a prototype radial field internal rotor encased-type motor. The technique calculates the load field distribution analytically, according to the method described in Chapters 5, 7, and 8, whilst the resulting radial force density waves acting on the stator are evaluated by the Maxwell stress, and then used as the input to vibrational response and acoustic radiation models. The acoustic radiation model is based on the cylindrical model of finite length developed in Chapter 3, whilst the vibrational response model accounts for the effects of both the iron core and the frame, as well as damping effects.

The vibrational response model is developed further from the initial lumped parameter model established by the author [9.11][9.9] with due account of the stiffening effect of the frame, whilst according to the results reported in Chapter 2, the modifying effects of the end-shields on the stiffness of the stator is established by experiment.

9.2 Spatial and Time-Dependent Radial Force Calculation

9.2.1 Radial Force Density Wave

The vibrational force waves acting on the stator bore can be calculated by Maxwell stress, neglecting the tangential component of the flux density

$$p(\alpha, t) = \frac{B^2(\alpha, t)}{2\mu_o} \tag{9.1}$$

The general form of the vibrational force waves, in which a large amplitude and low mode number are important from the viewpoint of noise and vibration, is given by:

$$p(\alpha, t) = \sum P_m \cos(\omega_m t + m\alpha + \alpha_{mo}) \tag{9.2}$$

where m is the mode number and ω_m is the angular frequency of the force wave. Both are computed from the orders and angular frequencies of the flux density harmonic components.

As summarised in section 8.4.2, the instantaneous field distribution under any load condition can be calculated from:

$$B_{load}(\alpha, r, t) = B_{open-circuit}(\alpha, r, t) + B_{armature-reaction}(\alpha, r, t) \tag{9.3}$$

whilst $$B_{open-circuit}(\alpha, r, t) = B_{magnet}(\alpha, r, t)\,\tilde{\lambda}(\alpha, r) \tag{9.4}$$

and $$B_{armature-reaction}(\alpha, r, t) = B_{winding}(\alpha, r, t)\,\tilde{\lambda}(\alpha, r) \tag{9.5}$$

Therefore the spatial and time dependent harmonics of the flux density for the prediction of noise and vibration from an internal rotor motor is obtained by setting $r = R_i$, ie., evaluating the flux density at the stator bore.

Since $B(\alpha, t) = B_{load}(\alpha, r, t)|_{r=R_i}$ (9.6a)

Therefore $B(\alpha, t) = \left[B_{magnet}(\alpha, t) + B_{winding}(\alpha, t)\right]\lambda(\alpha)$ (9.6b)

where $B_{magnet}(\alpha, t) = B_{magnet}(\alpha, r, t)|_{r=R_i}$ (9.6c)

$B_{winding}(\alpha, t) = B_{winding}(\alpha, r, t)|_{r=R_i}$ (9.6d)

and $\lambda(\alpha) = \lambda(\alpha, r)|_{r=R_i}$ (9.6e)

Since the evaluation of equations (9.1) and (9.2) involves considerable computation, a CAD program, whose flow-chart is shown in Fig 1.3, has been developed to evaluate:

a) relative permeance waves;
b) magnetic field distribution produced by the magnets (slot openings neglected);
c) open-circuit magnetic field distribution (accounting for slot openings);
d) cogging torque waveforms;
e) steady-state dynamic phase current waveforms;
f) tangential torque waveforms;
g) magnetic field distributions produced by the windings (slot openings neglected);
h) armature reaction field distributions (accounting for slot openings);
i) load magnetic field distributions;
j) radial force waves.

The above calculations involve three basic operations with the spatial and time-dependent Fourier series terms, viz:

If $A = \sum A_1 \cos(A_2 t + A_3 \alpha + A_4)$ (9.7a)

$B = \sum B_1 \cos(B_2 t + B_3 \alpha + B_4)$ (9.7b)

and $C = \sum C_1 \cos(C_2 t + C_3 \alpha + C_4)$ (9.7c)

i) $C = A\,B$

$$C = \sum\sum \frac{A_1 B_1}{2} \cos\left[(A_2 \pm B_2)\, t + (A_3 \pm B_3)\, \alpha + (A_4 \pm B_4) \right] \tag{9.8}$$

ii) $C = A^2$

$$C = \sum\sum \frac{A_1 A'_1}{2} \cos\left[(A_2 \pm A'_2)\, t + (A_3 \pm A'_3)\, \alpha + (A_4 \pm A'_4) \right] \tag{9.9}$$

iii) $C = A + B$

If $A_2 = B_2$ and $A_3 = B_3$ then

$$C_1 = \sqrt{(A_1 \cos A_4 + B_1 \cos B_4)^2 + (A_1 \sin A_4 + B_1 \sin B_4)^2} \tag{9.10a}$$

$$C_4 = \arctan\left\{ \frac{A_1 \cos A_4 + B_1 \cos B_4}{A_1 \sin A_4 + B_1 \sin B_4} \right\} \tag{9.10b}$$

However for the prediction of the noise on open-circuit, it is possible to employ a much simpler approach which is described in [9.14].

The frequencies of the vibration and noise under any load condition are proportional to the pole number, 2p, and the rotor speed n_r, ie.

$$f = 2k \frac{p\, n_r}{60} \qquad k=1,2,3,... \tag{9.11}$$

which is the same as for the open-circuit condition [9.14]. However as the load is applied it will cause the amplitude of the noise spectrum to vary, whilst the frequency will also change with the rotor speed. Clearly the noise spectrum for a brushless DC motor will differ from that for induction motors, synchronous motors, and DC commutator motors etc, as described in section 1.2.

The calculation of the relative permeance and the field produced by the magnets and the windings, ie., $\tilde{\lambda}(\alpha)$, $B_{magnet}(\alpha, t)$ and $B_{winding}(\alpha, t)$ are summarised in sections (9.2.2), (9.2.3), and (9.2.4).

9.2.2 Relative Permeance

The relative permeance is expressed in the form of a Fourier series, viz:

$$\Lambda(\alpha, r) = \sum_{\mu = 0, 1, 2, \ldots}^{\infty} \Lambda_\mu \cos \mu Q_s (\alpha + \alpha_{sa}) \tag{9.12a}$$

$$\text{where } \alpha_{sa} = \begin{cases} \dfrac{\pi}{Q_s} & \text{for } \textit{winding pitch = odd integer of slot pitch} \\ 0 & \text{for } \textit{winding pitch = even integer of slot pitch} \end{cases} \tag{9.12b}$$

therefore

$$\Lambda(\alpha, r) = \begin{cases} \sum_{\mu} (-1)^{\mu} \Lambda_\mu \cos \mu Q_s \alpha & \text{for } \textit{winding pitch = odd integer of slot pitch} \\ \sum_{\mu} \Lambda_\mu \cos \mu Q_s \alpha & \text{for } \textit{winding pitch = even integer of slot pitch} \end{cases}$$

where (9.12c)

$$\Lambda_o = \frac{1}{K_c}\left(1 - 1.6\,\beta \frac{b_o}{\tau_t}\right) \tag{9.13a}$$

$$\Lambda_\mu = -\beta\, G_\mu\left(\frac{b_o}{\tau_t}\right) \tag{9.13b}$$

$$\text{and} \quad G_\mu\left(\frac{b_o}{\tau_t}\right) = \frac{1}{\mu}\frac{4}{\pi}\left[0.5 + \frac{\left(\mu \frac{b_o}{\tau_t}\right)^2}{0.78125 - 2\left(\mu \frac{b_o}{\tau_t}\right)^2}\right] \sin\left(1.6\,\pi\,\mu \frac{b_o}{\tau_t}\right) \tag{9.13c}$$

where K_C is the Carter coefficient, which accounts for the increase of the effective airgap, and b_o and τ_t are the slot opening and the tooth-pitch respectively, Q_s is the number of stator slots, whilst β depends on the radial position along the axis of a slot and is determined bythe conformal transformation. However, at the stator bore surface β is given by:

$$\beta = \frac{1}{2}\left[1 - \frac{1}{\sqrt{1 + \left(\frac{b_o}{2\,g'}\right)^2 (1 + \nu^2)}}\right] \tag{9.14}$$

where ν is determined from:

$$g'\frac{\pi}{b_o} = \frac{1}{2}\ln\left[\frac{\sqrt{a^2+v^2}+v}{\sqrt{a^2+v^2}-v}\right] + \frac{2g'}{b_o}\arctan\frac{2g'}{b_o}\frac{v}{\sqrt{a^2+v^2}} \tag{9.15}$$

where $g' = g + \frac{h_m}{\mu_R}$ is the effective airgap; $a^2 = 1+\left(\frac{2g'}{b_o}\right)^2$

9.2.3 Magnetic field produced by magnets

For an internal rotor topology the magnetic field produced by the magnets is given by equations (5.62), (5.57), and (8.81), ie.

$$B_{magnet}(\alpha, r, t) = B_{rI}(r, \theta) = \sum_{n=1,3,5,\ldots}^{\infty} B_n \cos np\left(\omega_r t - \alpha - \frac{\alpha_c}{p} + \frac{\pi}{6p}\right)$$

where (9.16a)

$$B_n = \frac{M_1}{2\mu_R}\left\{\frac{\left(\frac{R_o}{R_i}\right)^2 - \left(\frac{R_m}{R_i}\right)^2 + \left(\frac{R_m}{R_i}\right)^2 \ln\left(\frac{R_o}{R_m}\right)^2}{\frac{\mu_R+1}{\mu_R}\left[1-\left(\frac{R_m}{R_i}\right)^2\right] - \frac{\mu_R-1}{\mu_R}\left[\left(\frac{R_o}{R_i}\right)^2 - \left(\frac{R_m}{R_o}\right)^2\right]}\right\}\left[1+\left(\frac{R_i}{r}\right)^2\right]$$

for $np = 1$ and (9.16b)

$$B_n = \frac{M_n}{\mu_R}\frac{np}{(np)^2-1}$$
$$\cdot\left\{\frac{(np-1)+2\left(\frac{R_m}{R_o}\right)^{np+1} - (np+1)\left(\frac{R_m}{R_o}\right)^{2np}}{\frac{\mu_R+1}{\mu_R}\left[1-\left(\frac{R_m}{R_i}\right)^{2np}\right] - \frac{\mu_R-1}{\mu_R}\left[\left(\frac{R_o}{R_i}\right)^{2np} - \left(\frac{R_m}{R_o}\right)^{2np}\right]}\right\}$$
$$\cdot\left[\left(\frac{r}{R_i}\right)^{np-1}\left(\frac{R_o}{R_i}\right)^{np+1} + \left(\frac{R_o}{r}\right)^{np+1}\right] \tag{9.16c}$$

for $np \neq 1$

$$\text{whilst } M_n = 2B_R\,\alpha_p\frac{\sin\frac{n\pi\alpha_p}{2}}{\frac{n\pi\alpha_p}{2}} \tag{9.17}$$

$$R_o = R_i - g \quad \text{and} \quad R_m = R_i - g - h_m \tag{9.18}$$

Therefore at the stator bore, ie., $r = R_i$, the flux density distribution is obtained as:

when np=1

$$B_{magnet}(\alpha, t) = \frac{M_1}{\mu_R}\left\{\frac{\left(\frac{R_o}{R_i}\right)^2 - \left(\frac{R_m}{R_i}\right)^2 + \left(\frac{R_m}{R_i}\right)^2 \ln\left(\frac{R_o}{R_m}\right)^2}{\frac{\mu_R+1}{\mu_R}\left[1 - \left(\frac{R_m}{R_i}\right)^2\right] - \frac{\mu_R-1}{\mu_R}\left[\left(\frac{R_o}{R_i}\right)^2 - \left(\frac{R_m}{R_o}\right)^2\right]}\right\}$$

$$\cos\left(\omega_r t - \alpha - \frac{\alpha_c}{p} + \frac{\pi}{6}\right) \tag{9.19a}$$

and when $np \neq 1$

$$B_{magnet}(\alpha, t) = \sum 2\frac{M_n}{\mu_R}\frac{np}{(np)^2 - 1}\left(\frac{R_o}{R_i}\right)^{np+1}$$

$$\cdot\left\{\frac{(np-1) + 2\left(\frac{R_m}{R_o}\right)^{np+1} - (np+1)\left(\frac{R_m}{R_o}\right)^{2np}}{\frac{\mu_R+1}{\mu_R}\left[1 - \left(\frac{R_m}{R_i}\right)^{2np}\right] - \frac{\mu_R-1}{\mu_R}\left[\left(\frac{R_o}{R_i}\right)^{2np} - \left(\frac{R_m}{R_o}\right)^{2np}\right]}\right\}$$

$$\cos np\left(\omega_r t - \alpha - \frac{\alpha_c}{p} + \frac{\pi}{6p}\right) \tag{9.19b}$$

9.2.4 Magnetic Field Produced by Windings

The magnetic field produced by the windings is given by equations (8.51) and (8.82), ie. by letting r = Ri, ie.

$$B_{winding}(\alpha, t) = \mu_o \frac{3W}{\pi\delta} \sum_{u=1,2,3,\ldots}^{\infty} I_u \sum_{c=0,\pm1,\pm2,\ldots}^{\infty} \frac{1}{v} K_{sov} K_{dpv} F_b(v, r)|_{r=R_i}$$

$$\sin\left[u(p\,\omega_r t) + v_u\,\alpha + \theta_u\right] \tag{9.20a}$$

(9.20b)

where $$F_b(v, r)|_{r=R_i} = \delta\frac{v}{R_i}\frac{1 + \left(\frac{R_m}{R_i}\right)^2}{1 - \left(\frac{R_m}{R_i}\right)^2}$$

$$\delta = g + h_m \approx g' \tag{9.20c}$$

$$v_u = \pm p(6c - \{\pm\}u) \tag{9.20d}$$

(9.20e)

and $$i_a = \sum_{u=1,2,3,\ldots}^{\infty} I_u \sin u(p\,\omega_r t + \theta_u) \quad (i_a|_{t=0})$$

whilst K_{dpv} is the winding factor determined by equations (8.23a) and (8.45); K_{sov} is the slot opening factor given by equation (8.34).

9.3 Analytical Model for Vibrational Response Estimation

9.3.1 Vibrational Response of the Stator

As was mentioned earlier, due to the complexity of the stator structure existing analytical calculations of the dynamic mechanical response of a machine to the electromagnetically induced exciting forces is usually restricted to a single ring model of the stator core. Hence it cannot account for the effect of the frame etc. In this section an analytical model for calculating the vibrational response of the stator is also presented. It employs an equivalent lumped force [9.9], and utilises the measured damping ratio which was obtained independently by Yang and Hubner [9.7], the method for estimating the natural frequencies of a single ring type core developed by Jordan, Frohne, and Uner and summarised by Yang [9.7] is extended to calculate the vibrational response of the encased type stator by introducing the lumped stiffness and mass [9.9], whilst an approximation to the effect of the frame is obtained by modifying the radial thickness of the core yoke. Further, the increase in the stiffness of the stator due to the restricting effect of the end-shields, which was studied in Chapter 2, is studied further and accounted for by experimental modal analysis.

For an encased stator type motor, and assuming the radial vibration of the core and the frame to be identical, the radial vibrational displacement can be calculated from:

$$A_{rd} = \frac{P'_m}{K_m} \frac{1}{\sqrt{\left[1 - \left(\frac{f}{f_m}\right)^2\right]^2 + \left(2\zeta \frac{f}{f_m}\right)^2}} \tag{9.21}$$

where P'_m is the equivalent lumped force [9.9], given by

$$P'_m = 2\pi R_i l_c P_m \tag{9.22}$$

where R_i is the inner radius of the stator bore, l_c is the axial length of the core, P_m and f are the amplitude and frequency of the excitation radial force density wave, from equation (9.2), f_m is the m^{th} order natural frequency of the stator, which can be determined from:

$$f_m = \frac{1}{2\pi}\sqrt{\frac{K_m}{M_m}} \tag{9.23}$$

K_m and M_m are the lumped stiffness and mass of the stator.

ζ is the damping ratio of the stator, which can be determined experimentally. For a stator with windings the measured results obtained by Yang and Hubner [9.7] for small and medium sized machines are almost identical, and therefore can be utilised in the calculation. It is modelled approximately as:

$$2\pi\zeta = 2.76\times 10^{-5} f + 0.062 \tag{9.24}$$

9.3.2 Effect of the Frame

Most small motors normally have an encased type stator, the core of which is simply pressed into a frame. As a consequence the frame has a significant effect on the vibrational response of the stator. Further, as mentioned in Chapter 2, the end-shields significantly increase the stiffness of the stator. Hence their modifying effect must also be considered.

For a mode order m = 0 or 1 the stiffness of a single thin ring is directly proportional to its radial thickness, h, axial length, l, and modulus of elasticity, E, and inversely proportional to its mean radius, R, ie:

$$K \quad \text{proportional to} \quad \frac{E\,h\,l}{R} \tag{9.25}$$

Since the frame may have a different axial length and material from rest of the core, as an approximation it is reasonable to simply let

$$\frac{E_f h_f l_f}{R_{cf}} = \frac{E_c h'_f l_c}{R_{cf}} \tag{9.26}$$

$$\text{hence } h'_f = \frac{E_f l_f}{E_c l_c} h_f \tag{9.27}$$

where R_{cf} is the modified mean radius of the stator and h'_f is the equivalent radial thickness of the frame when the frame is converted to the same material and axial length as the core yoke.

Similarly for $m \geq 2$ since

$$\text{K proportional to } \frac{E h^3 l}{R^3} \tag{9.28}$$

then letting

$$\frac{E_f h_f^3 l_f}{R_{cf}} = \frac{E_c h'^3_f l_c}{R_{cf}} \tag{9.29}$$

$$\text{gives } h'_f = \left(\frac{E_f l_f}{E_c l_c}\right)^{1/3} h_f \tag{9.30}$$

Therefore the radial thickness, the mean radius, and the weight of the core yoke are modified according to:

$$h_{cf} = h_c + h'_f \tag{9.31a}$$

$$R_{cf} = R_c + \tfrac{1}{2} h'_f \tag{9.31b}$$

$$G_{cf} = G_c + G_f \tag{9.31c}$$

With this simple approach if the material and axial length of the frame are identical to those of the core, ie:

$$E_f = E_c, \quad l_f = l_c \tag{9.32a}$$

Then for m = 0, 1, and $m \geq 2$

$$h'_f = h_f \tag{9.32b}$$

and

$$h_{cf} = h_c + h_f \tag{9.32c}$$

$$R_{cf} = R_c + \tfrac{1}{2} h_f \tag{9.32d}$$

$$G_{cf} = G_c + G_f \tag{9.32e}$$

which are physically correct since the frame effectively acts as a portion of the core.

9.3.3 Lumped Stiffness and Mass of the Stator

The lumped stiffness and mass of the stator can then be calculated by the method given in [9.9]. When the vibrational mode order m = 0, ie. for the pulsating vibration mode

$$K_o = \frac{2\pi E_c h_{cf} l_c}{R_{cf}} \tag{9.33a}$$

$$M_o = \frac{G_{cf}}{g} \Delta \tag{9.33b}$$

whilst for m=1

$$K_1 = \frac{2\pi E_c h_{cf} l_c}{R_{cf}} \tag{9.34a}$$

$$M_1 = \frac{G_{cf}}{g} \frac{\Delta}{F_1^2} \tag{9.34b}$$

when the vibration of mode order $m \geq 2$

$$K_m = \frac{2\pi E_c I_c}{R_{cf}^3} (m^2 - 1)^2 F_{em}^2 \tag{9.35a}$$

$$M_m = \frac{G_{cf}}{g} \frac{\Delta}{F_m^2} \frac{m^2 + 1}{m^2} \tag{9.35b}$$

where F_{em} is the ratio of the natural frequencies of the complete assembled motor to those of the stator alone, and is introduced to account for the increase of the stator stiffness due to the restriction effect of the end-shields, and can be determined experimentally or by finite element analysis; F_1 and F_m are determined from [9.7]:

$$F_1 = \left\{ \frac{2}{1 + i^2 \frac{\Delta_m}{\Delta}} \right\}^{1/2} \tag{9.36a}$$

$$F_m = \left\{ 1 + \frac{i^2 (m^2 - 1)[m^2 (4 + \Delta_m/\Delta) + 3]}{m^2 + 1} \right\}^{-1/2} \tag{9.36b}$$

where $$i = \frac{1}{\sqrt{12}} \frac{h_{cf}}{R_{cf}} \tag{9.37}$$

$$I_c = \frac{h_{cf}^3 l_c}{12} \tag{9.38}$$

I_c is the moment of inertia of the cross-section, whilst Δ and Δ_m are the mass addition factors for displacement and rotation respectively, and are defined as:

$$\Delta = 1 + \frac{G_f + G_{wi} + G_{vr}}{G_{cf}} \tag{9.39}$$

$$\Delta_m = 1 + \frac{Q_s \theta_t}{2 \pi I_c R_{cf}} + \frac{Q_{vr} \theta_{vr}}{2 \pi I_c R_{cf}} \tag{9.40}$$

$$\text{where } \theta_{vr} = S_{vr} h_{vr}^3 \left[\frac{1}{3} + \left(\frac{h_{cf}}{2 h_{vr}} \right) + \left(\frac{h_{cf}}{2 h_{vr}} \right)^2 \right] \tag{9.41}$$

and

$$\theta_t = S_t^* h_t^3 \left[\frac{1}{3} + \left(\frac{h_{cf}}{2 h_t} \right) + \left(\frac{h_{cf}}{2 h_t} \right)^2 \right] \tag{9.42}$$

$$S_t^* = S_t \frac{G_t + G_{wi}}{G_t} \tag{9.43}$$

where S_t and S_{vr} are the mean sectional area of a tooth and a ventilating rib, respectively; G_c, G_f, G_t, G_{wi}, and G_{vr} are the weight of the core yoke, frame, teeth, winding including the insulation, and the ventilating ribs respectively; G_{cf}, h_{cf}, R_{cf} are the modified weight, radial thickness, and mean radius of the core yoke, with due account for the effect of the frame by equations (9.27)(9.30)(9.31); R_c, h_c are the mean radius and radial thickness of the yoke, and h_t, h_{vr} are the radial height of a tooth and a ventilating rib; Q_s, Q_{vr} are the number of teeth and ventilating ribs; E_c is the modulus of elasticity of the core material; $g = 9.8$ m/s .

9.4 Analytical Model for Acoustic Power Level Prediction

In the cylindrical model of finite length, the ends of the machine are replaced by infinitely long cylindrical stiffening baffles, such that the vibration of the stator is not transmitted into the extensions. The relative sound intensity I_l has already been obtained in Chapter 3 and is given by equation (3.13), ie.

$$I_l = \frac{2\,k\,a\,b}{\pi^2} \int_{-k}^{+k} \frac{\dfrac{1}{a^2(k^2-x^2)}}{J_n{}'^2(a\sqrt{k^2-x^2}) + Y_n{}'^2(a\sqrt{k^2-x^2})} \left(\frac{\sin b\,x}{b\,x}\right)^2 dx \tag{9.44}$$

where $b = l_f/2$; $K = \omega/c$, $\omega = 2\pi f$, c is the speed of sound; and a is the outer radius of the frame. J'_n and Y'_n are the differentials of Bessel functions of the 1st and 2nd kind.

Knowing the relative sound intensity and the vibration the acoustic power radiated by an electrical machine is calculated from:

$$W = \frac{1}{2}\rho\,c\,(\omega A_{rd})^2 . 4\pi\,a\,b . I_l = 2\rho\,c\,\pi^2 f^2 A_{rd}{}^2 . 4\pi\,a\,b . I_l \tag{9.45}$$

where $\rho c = 415$ kg/m and ρc is the sound resistance in air.

Hence the acoustic power level is obtained from:

$$L_w = 10 \log_{10} \frac{W}{W_o} \tag{9.46}$$

where $W_o = 10^{-12}$ (W).

9.5 Validations

In this section the predicted acoustic power spectrum of a brushless DC motor is compared with the measured acoustic power spectrum obtained from the measurement of the sound pressure spectra around the motor when it is placed in an anechoic chamber, whilst the analytical model for predicting the vibrational response of the stator is partially validated by comparing its

predicted natural frequencies with those derived from finite element analysis and measurements. Further confirmation of the conclusions cited in Chapter 2 regarding the effect of the end-shields on the natural frequencies of a small motor is obtained. In addition the calibration of a noise measurement system is proposed and described.

9.5.1 Description of Experiments

i) Experimental machine

The experimental machine is the 4-pole, 12-slot, 3-phase, overlapping winding, surface-mounted magnet, radial-field brushless DC motor, the electromagnetic parameters of which are listed in Table 5.1. The open-circuit, armature reaction, and load field distributions, as well as the dynamic performance have already been studied in Chapters 5, 7, and 8. The dimensions required for the calculation of the vibrational behaviour and acoustic power are as follows:

Weight of frame	0.322 Kg
Weight of core	0.341 Kg
Weight of teeth	0.121 Kg
Weight of winding, including insulation	0.92 Kg
Total stator weight	1.72 Kg
Outside diameter of frame	0.11 m
Inside diameter of frame (ie. outside diameter of core)	0.101 m
Equivalent height of core yoke	
(circular slot bottom equivalent to rectangular bottom)	0.008 m
Height of teeth	0.01325 m
Width of teeth	0.00486 m
Axial length of frame	0.08 m
Axial length of core	0.02 m

ii) Experimental apparatus

The main component of the measurement system is a dynamic signal analyser, HP 35660A. For the noise measurement a precision integrating sound level meter, B & K 2221, is used, whose

AC output is input to the HP 35660A for spectral analysis of the sound pressure level, as shown in Fig 9.1. Both the B & K 2221 and the HP 35660A are calibrated by the sound level calibrator B & K 4230. A modally tuned impact hammer which incorporates a force transducer, PCB 086B03, an accelerometer, PCB 303A03, and two battery power units, PCB 480B02, is used in the measurement of the natural frequencies of the stator as shown in Fig 9.2. For both the noise and natural frequency measurements, the motor is placed on sponge, as shown in Figs 9.1 and 9.2.

iii) Anechoic chamber

An anechoic chamber, Fig 9.3, which was originally designed for microwave measurements was utilised for the noise measurement of the test motor. Although the anechoic chamber, whose height, length, and width are 2.5 m, 3.5 m, and 2.0 m respectively, was smaller than the standard for machinery noise measurement, it was found to be suitable due to the small dimensions (0.11m x 0.08m - diameter x axial length) of the test motor.

In order to simulate a semi-free acoustic field the acoustic absorbing material on the floor was removed and replaced by polystyrene, whose thickness was around 5 mm, so that sound waves could be fully reflected from this surface.

Meanwhile in order to minimise background noise, which may be introduced by fans etc, the dynamic signal analyser and the DC power supply were both placed in an adjacent room, as shown in Fig 9.4.

iv) Background noise

In order to demonstrate the acoustic characteristic of the anechoic chamber the background noise was measured and analysed.

Fig 9.5 shows the background noise spectrum measured inside the anechoic chamber, as well as the comparison of the noise spectrum when the test motor (with ball-bearings) is running on

Fig 9.1 Noise measurement system

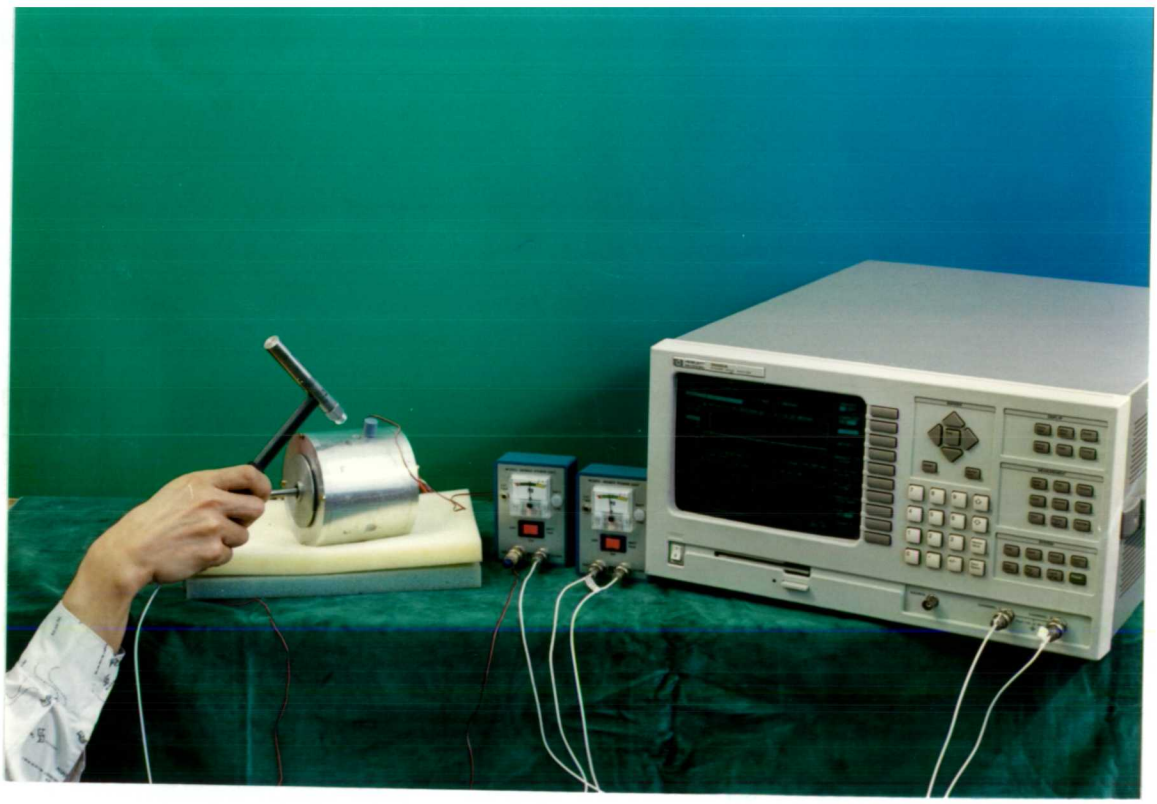

Fig 9.2 Vibrational behaviour measurement system

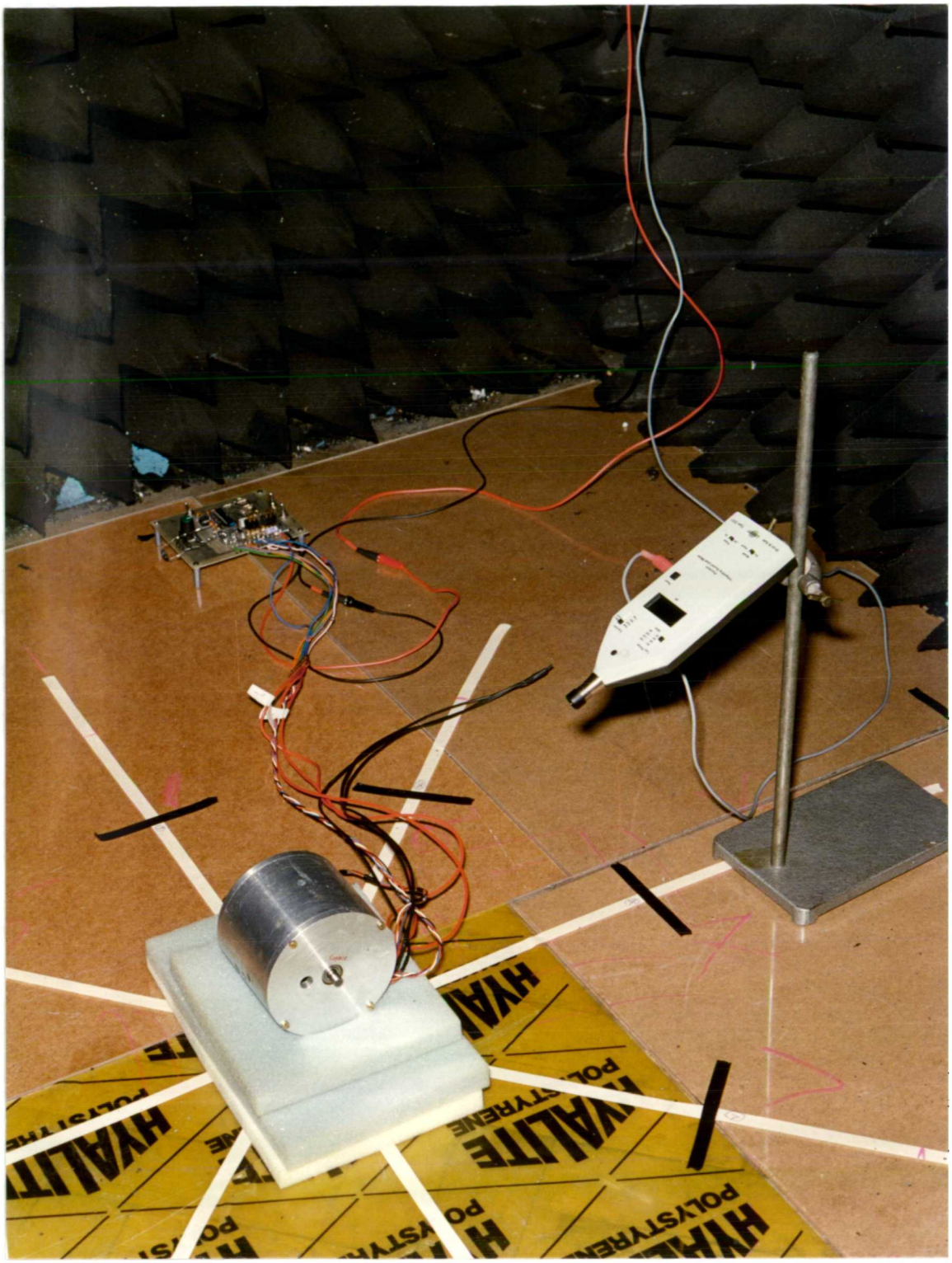

Fig 9.3 Noise measurement in an anechoic chamber

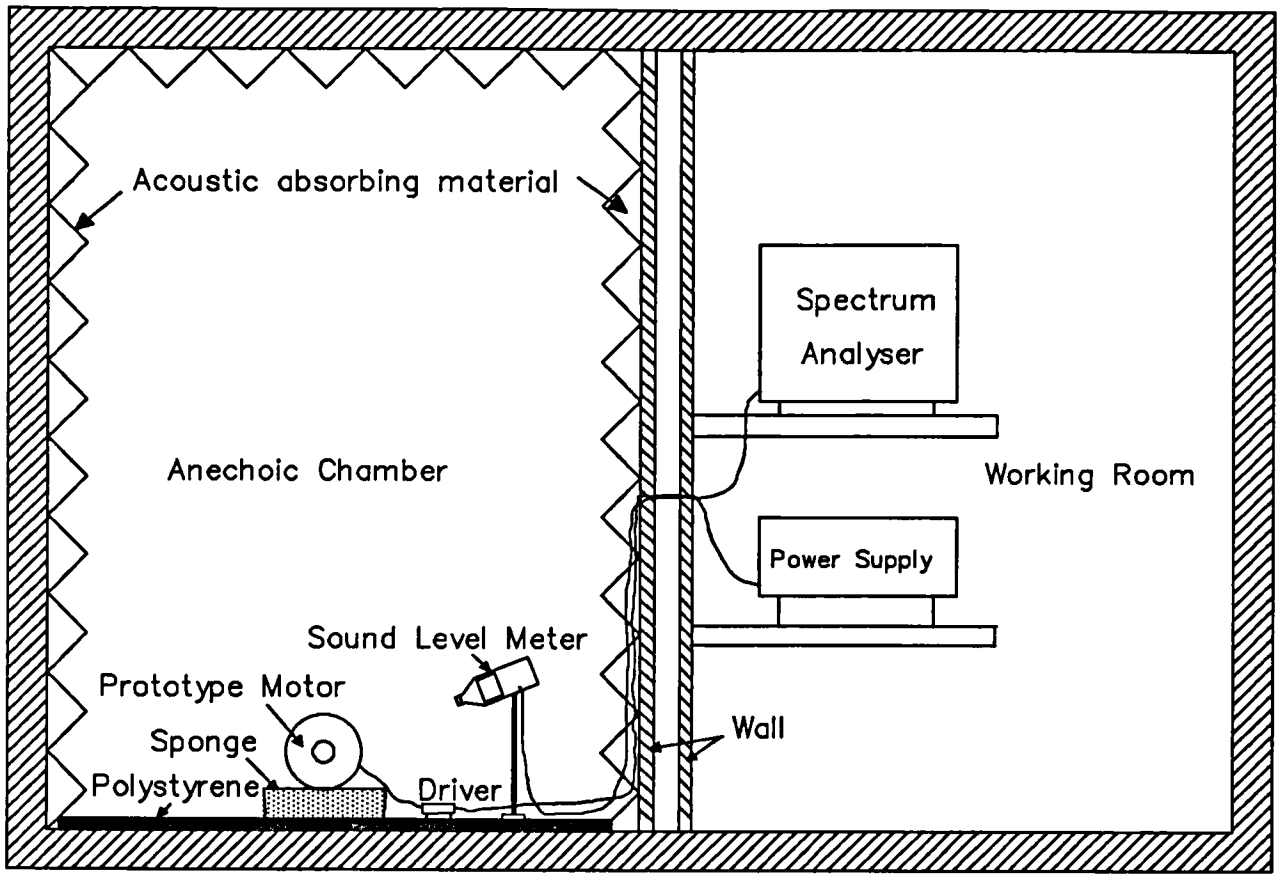

Fig 9.4 Schematic of noise measurement

no-load and at stand-still (the measurement point being located at a central radial position, 0.4m from the centre of the motor). It shows that whilst the background noise is very low at higher frequency, the anechoic chamber is subjected to a large background noise at low frequencies, below 242 Hz. As a consequence, when the motor is running on no-load in the frequency range 10 - 242Hz the noise spectrum is dominated by the background noise. However at other discrete frequencies the components of the no-load motor noise are normally higher than the background noise by 20 - 40 dB, which is considered to be good enough for the motor noise measurement.

In order to analyse the low frequency background noise the sound level meter was moved to the adjacent room and placed near the analyser and power supply, as shown in Fig 9.6, and the sound

pressure spectrum measured. Fig 9.7 shows the resulting spectrum, together with the background noise spectrum measured inside the anechoic chamber. It can be seen that the 242Hz noise component, which is produced by the cooling fan inside the analyser, is significant on both spectra, and that below this frequency almost every frequency component on the measured noise spectrum corresponding to one on the background noise spectrum. Since at low frequency the sound waves can easily penetrate through the wall, due to their long wavelength and low absorbing coefficient of the wall to low frequency sound waves, it is clear that although located in an adjacent room, the analyser and the power supply are the main cause of the low frequency background noise inside the anechoic chamber. Fortunately, however, most of the noise components produced by the test motor have a higher frequency and the measurements of most interest are the higher frequency components due to the low-frequency attenuation of A-weighted sound level in the standard of noise measurement.

9.5.2 Comparison of Natural Frequencies of Stators

In this section the predicted natural frequencies of the stators, from the analytical model developed for predicting its vibrational response, are compared with those from finite element analysis and measurements. Also, the increase of the natural frequencies of the stator due to the restricting effect of the stator end-shields is observed in the measurements.

i) Annular ring

This simple model is a solid ring of mild steel [9.15], the inside and outside diameters of which are 0.386m and 0.4762m respectively. Table 9.1 compares the measured natural frequencies obtained by Girgis and Verma [9.15], as well as by the author [9.16], and predictions from a finite element analysis [9.16] and from the analytical model described in section 9.3. As expected for this simple annular ring, the analytically predicted results are in good agreement with both the measured and the finite element results.

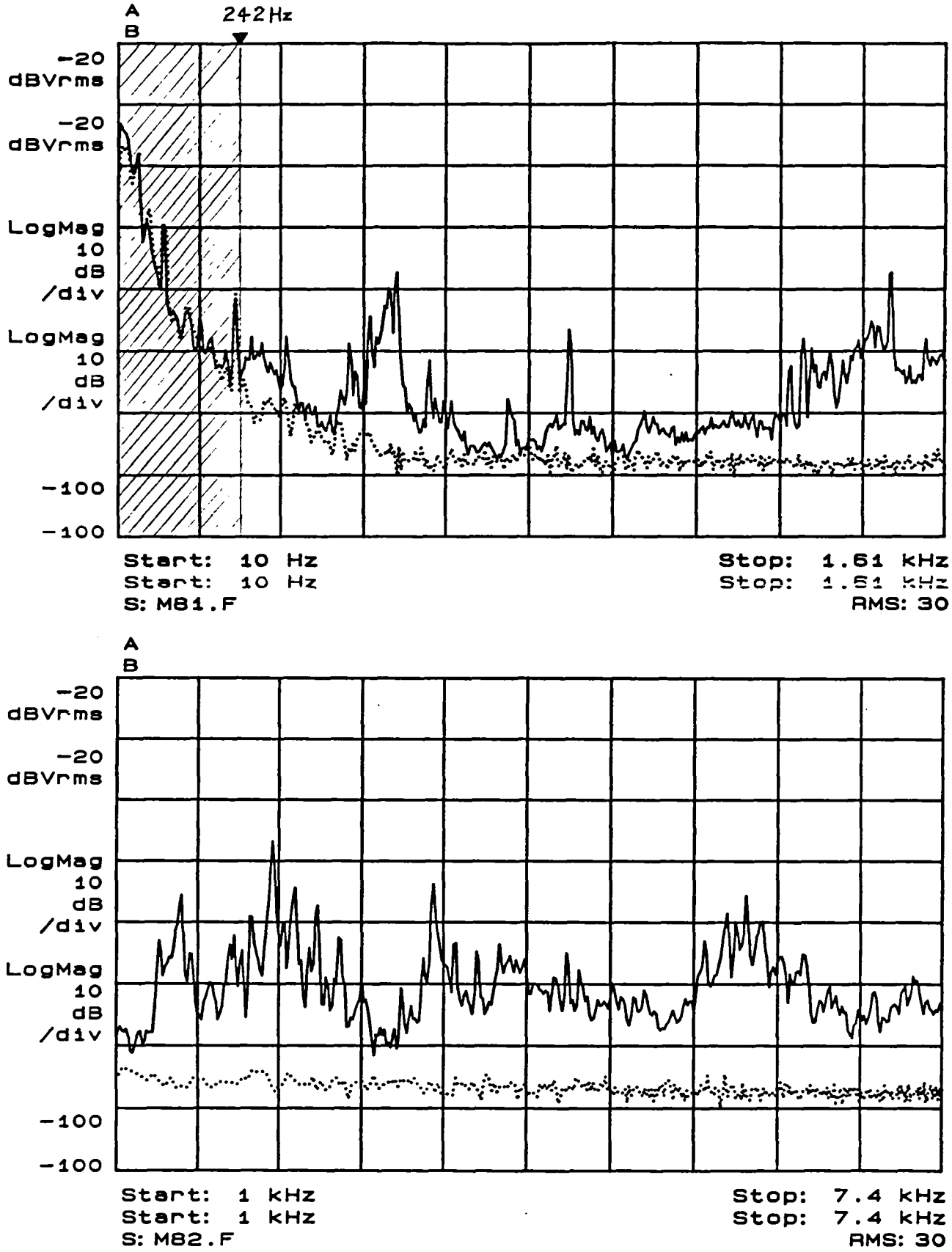

Fig 9.5 Comparison of noise spectra when the motor is at stand-still and no-load conditions

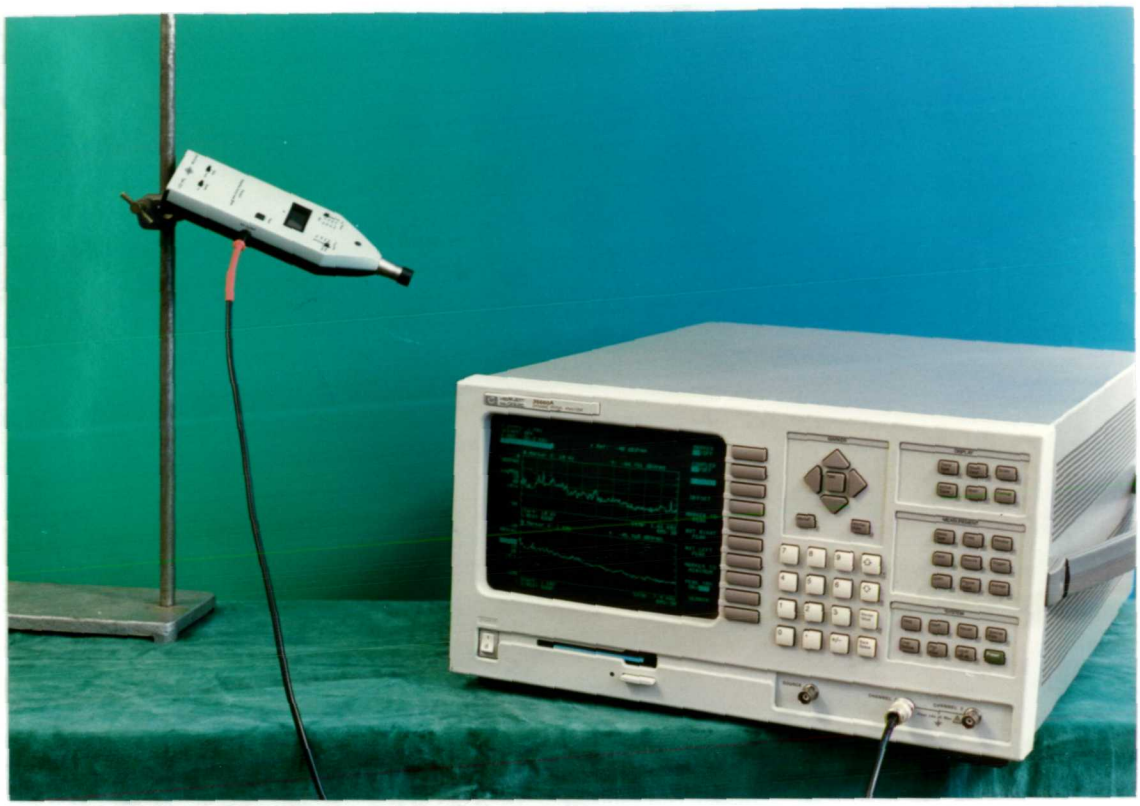

Fig 9.6 Measurement of fan's noise of the analyser

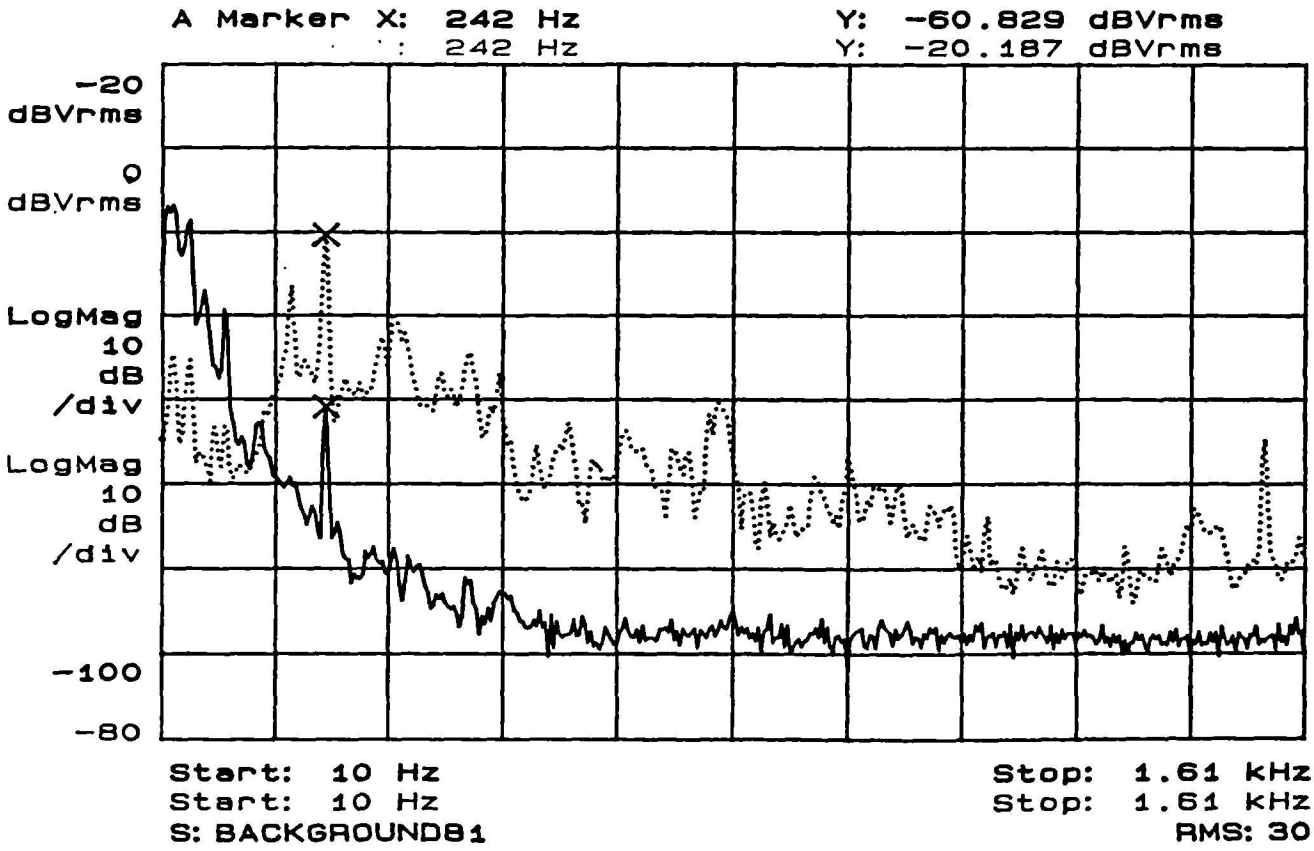

Fig 9.7 Effect of analyser's noise on the background noise of the anechoic chamber

Table 9.1 Comparison of natural frequencies of an annular ring

Mode order	0	2	3	4	5
Girgis & Verma's measured results, Hz,[9.15]		599	1652	3067	4687
Author's measured results, Hz,[9.16]		593	1593	3025	
Author's finite element results, Hz,[9.16]	3806	602	1641	3007	4664
Analytical prediction, Hz	3793	600	1628	2961	4507

ii) Core without winding

The core has 36 slots [9.17], and its inside and outside radii are 0.0625m ans 0.1025m respectively, whilst the radius at the bottom of the slots is 0.0875m. The weights of the yoke and the teeth are 7.7Kg and 4.65Kg respectively. Table 9.2 compares the measured natural frequencies obtained by Verma and Girgis [9.17], and the analytically predicted results, as well as finite element predictions [9.18].

Table 9.2 Comparison of natural frequencies of the core without winding

Mode order	0	2	3	4	5	6
Verma& Girgis's measured results, Hz,[9.17]	6620	770	2025	3550	4880	5630
Author's finite element results, Hz,[9.18]	6680	776	2048	3577	5017	5948
error (%)	0.91	0.78	1.14	0.75	4.52	5.64
Analytical prediction, Hz, error (%)	6630	780	2080	3640	5070	6070
	0.15	1.9	2.7	2.5	5.6	7.8

Again, the analytically predicted results are of high accuracy. It will be noted that Frohne's analytical formula [9.7] for calculating the natural frequencies of the stator with teeth and winding is a particular case for the developed analytical model for predicting the vibrational response of the stator. Further validations of Frohne's formula, which can be found in [9.17],

can be used to validate the analytical model of this chapter only when the core itself is modelled.

iii) Stator with winding and frame

This is the test motor refered to in section 9.5.1 which has a cast aluminium frame with a different axial length from the core. The effect of the frame on the natural frequencies, as well as the vibrational response of the stator, has been accounted for according to the method described in section 9.3.

Table 9.3 compares measured and predicted natural frequencies, whilst its excitation impulse force applied by the hammer and the corresponding frequency response (transfer function) are shown in Fig 9.8.

As a comparison the analytically predicted natural frequencies of the core with the winding only, ie., the stator frame being neglected, are also listed in Table 9.3. Clearly for this particular motor the effect of the frame is very significant, as is likely to be the case in general [9.7]. Therefore a large error will be introduced if its effect is neglected, as it is normally assumed in the analytical prediction [9.7]. The good agreement between the analytically predicted and measured results indicates that the method proposed in section 9.3 can be used to account for the effect of the frame.

Table 9.3 Comparison of natural frequencies of the stator with winding and frame

Mode order	0	1	2	3	4	5
Measured results,Hz	10040		1920	4608	7488	
Analytical prediction, Hz, error (%)	10425	14386	1891	4681	7767	10913
	3.8	/	-1.5	1.6	3.7	/
Analytical prediction,neglecting the frame, Hz	8970	12427	1125	2878	4915	7059
error (%)	-10.7	/	-41.4	-39.5	-34.4	/

iv) Effect of end-shields

As mentioned in Chapter 2, because of their stiffening effect, the end-shields significantly increase the values of the natural frequencies of the stator. Therefore the change of the natural frequencies before and after the end-shields were bolted to the stator has been measured and a similar conslusion to that given in Chapter 2 was obtained. Fig 9.9 shows the excitation impulse force signal and the measured frequency response (transfer function) of the assembled motor, whilst the effect of the end-shields on the natural frequencies and modes are shown in Table 9.4 and Fig 9.10.

From the measured results, the modifying coefficients of the end-shields on the natural frequencies of the stator are obtained as:

$$F_{em} = \frac{f_m\ (\ assembled\ motor\ )}{f_m\ (\ stator\ only\ )} \tag{9.47}$$

hence $$F_{e2} = \frac{3500}{1920} = 1.82$$

$$F_{e3} = \frac{6130}{4608} = 1.33$$

$$F_{e4} = \frac{9920}{7488} = 1.32$$

Table 9.4 Effect of end-shields on the natural frequencies of a brushless DC motor

Mode order	2	3	4
Stator only, Hz	1920	4608	7488
Whole motor assembling, Hz	3500	6130	9920
Ratio of increasement, F_{em}	1.82	1.33	1.32

9.5.3 Calibration for Noise Measurement

In this section the calibration procedure for the noise measurement system is proposed and described.

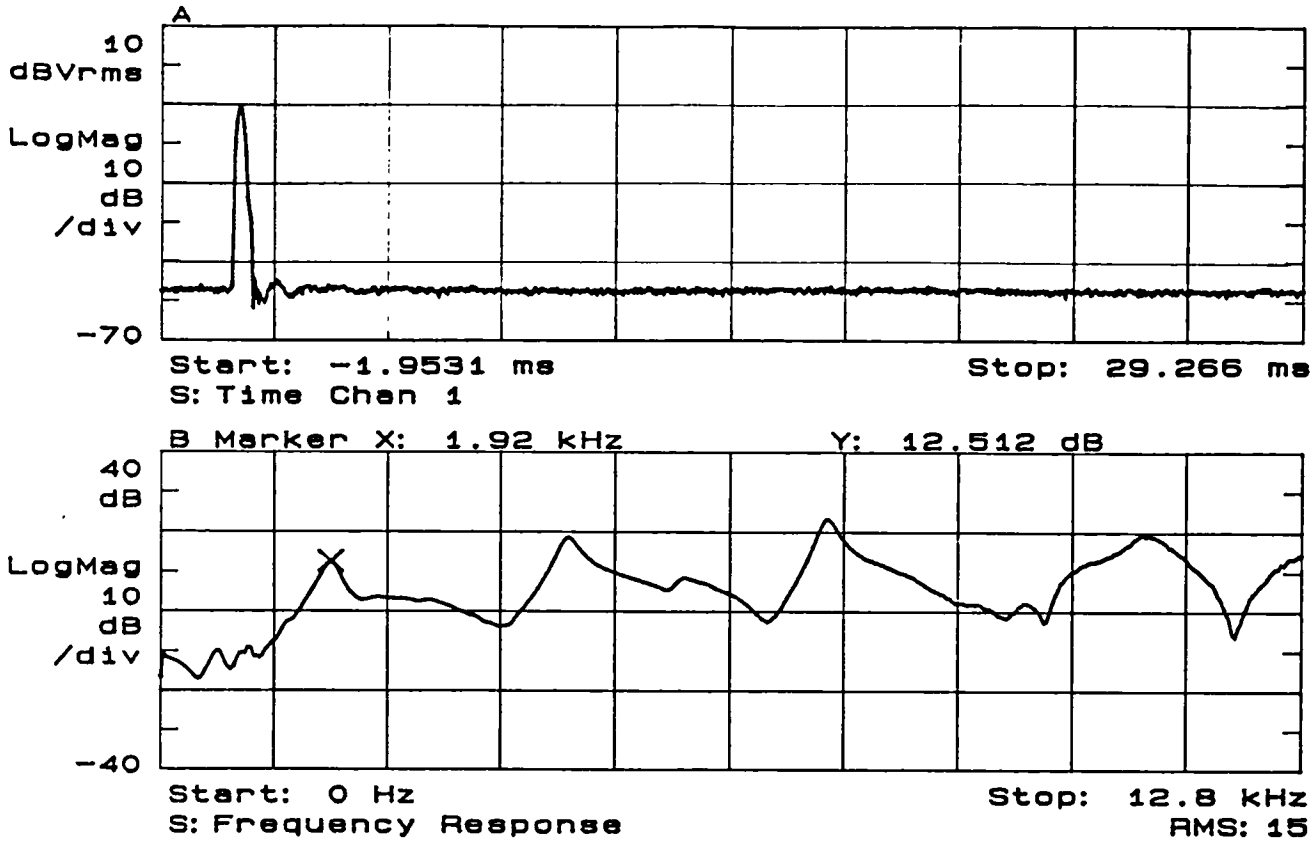

Fig 9.8 Excitation force signal and frequency response of the stator with winding and frame

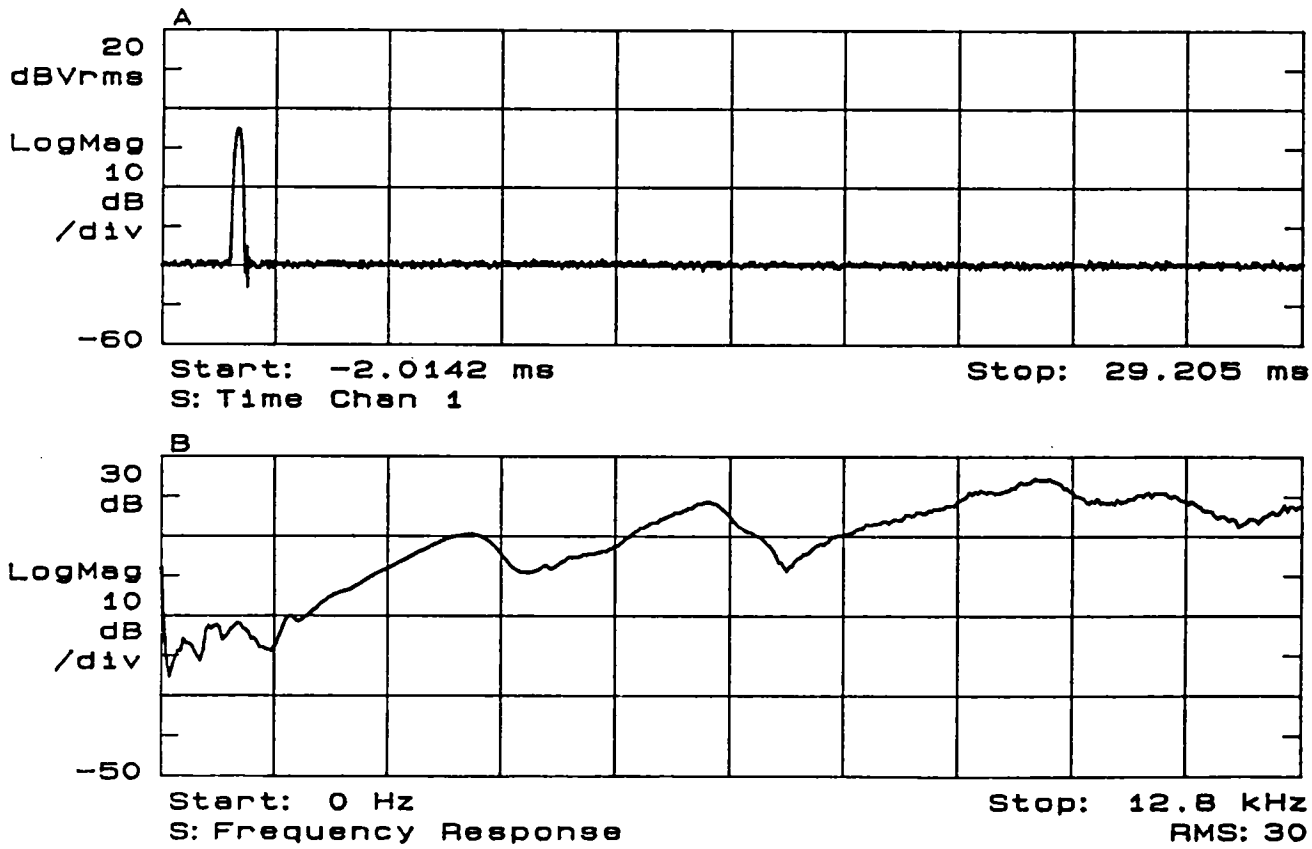

Fig 9.9 Excitation force signal and frequency response of a brushless DC motor

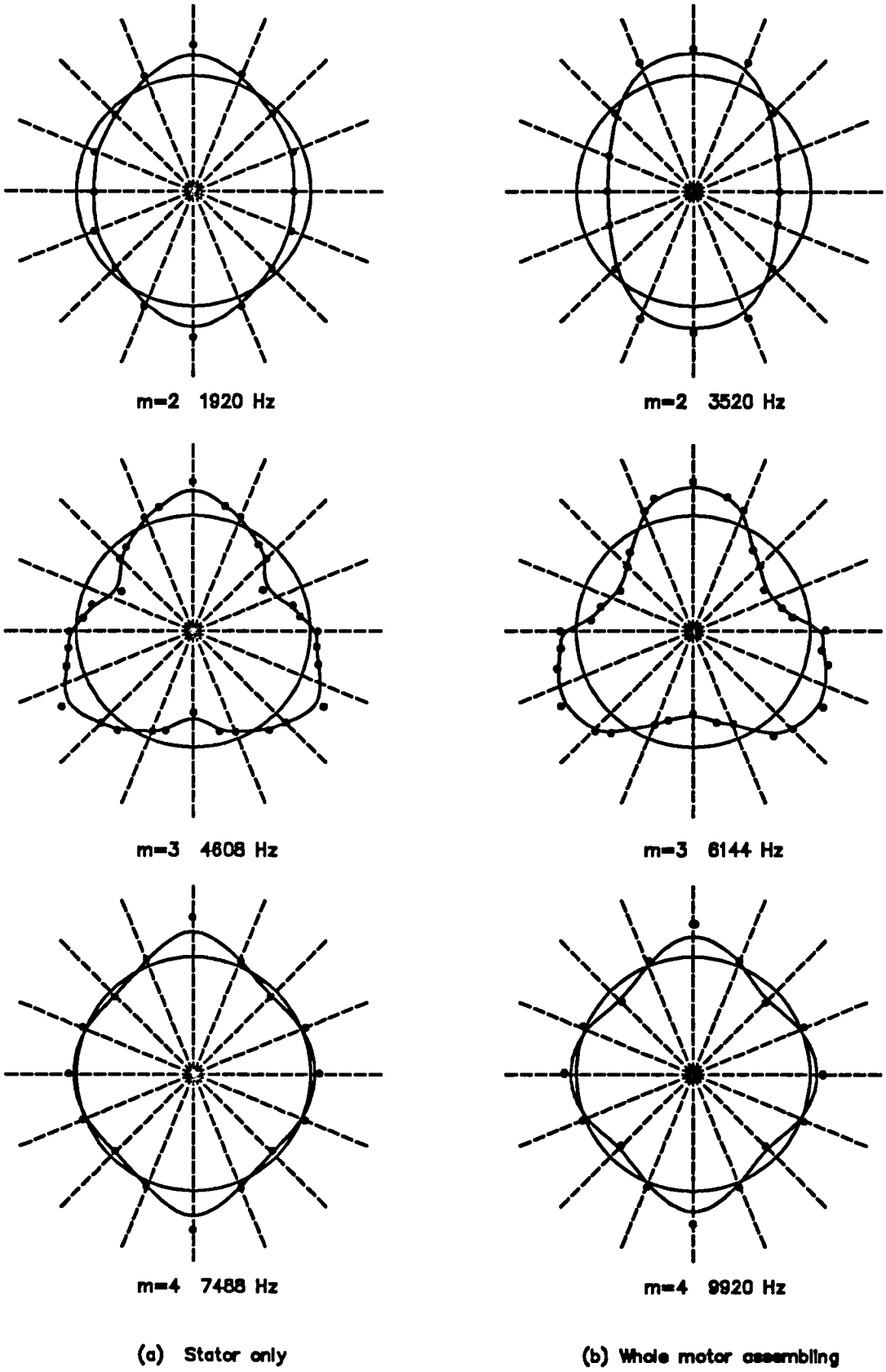

Fig 9.10 Natural frequencies and modes of a motor stator with/without end-shields & rotor

(Note: measurements are carried out in a quadrant region and results are presented according to the symmetry of the modes)

i) Calibration of sound level meter

The calibration of the sound level meter, B&K 2221, was undertaken strictly according to the instruction mannual [9.19] by using the sound level calibrator, B&K 4230, which generates a pure sinusoidal 1KHz, 94dB sound wave.

ii) Calibration of noise measurement system

As mentioned earlier in section 9.5.1, the noise measurement system consists of the sound level meter, B&K 2221, and the dynamic signal analyser, HP35660A. However, since the dB value on the dynamic analyser is the dBVrms, which is the dB value of the input voltage signal, it must be calibrated and converted into the dB value of the sound pressure. Therefore the following calibrations have been adopted in the sound pressure level spectrum analysis:

a) connect the AC output of the sound level meter, B&K 2221, to the channel one input of the analyser, HP 35660A, as shown in Fig 9.11.
b) set the control on the sound level meter to Functions: 'Peak'; Range: '45-105', Mode: 'Run', and Power: 'On'.
c) fit the sound level calibrator, B&K 4230, over the microphone, as shown in Fig 9.11.
d) start the sound level calibrator and press 'Reset' on the sound level meter.
e) set the analyser to Function: 'Channel one spectrum'; Average: 'On', and Number: '10'; Window: 'Hanning'; Frequency range: '800-1200Hz'; Scale: 'Auto'.
f) start the real-time average on the signal analyser so that its frequency spectrum is measured, as shown in Fig 9.12.
g) values of 488.31 mVrms and - 6.226 dBVrms are measured from the spectra, which correspond to the sound pressure level 94dB (1KHz) when the sound level meter is set to the measurement range 45-105.

From the calibrated results the following calibration constants are calculated:

a) The reference voltage value in the analyser, HP 35660A

Since $L'_p = 20 \log_{10} \frac{V}{V_o}$ (9.48)

Fig 9.11 Calibration of noise measurement system

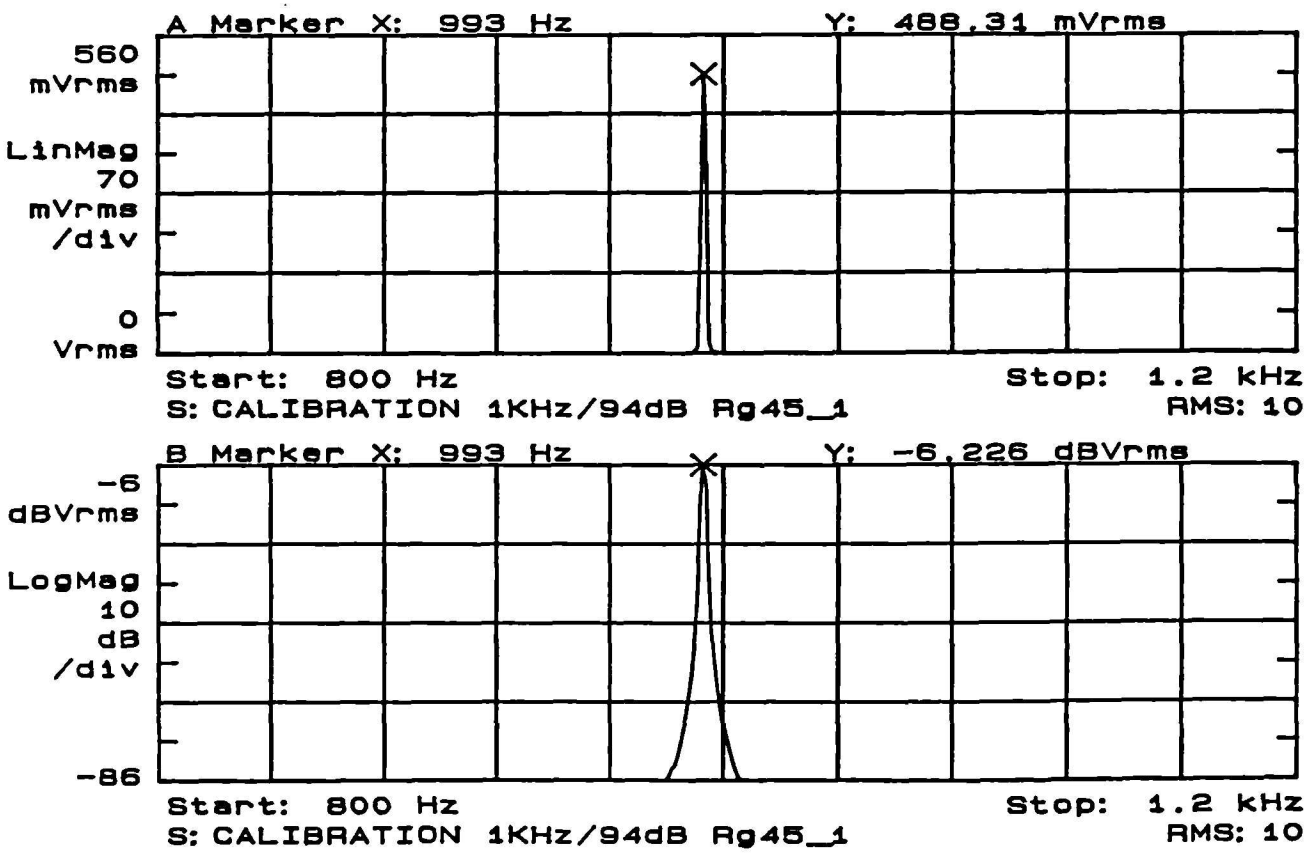

Fig 9.12 Calibrated results of noise measurement system

where L'_p is the dB value of the voltage on the analyser, HP35660A, corresponding to its absolute value V.

Since $V = 0.48831$ Vrms, $L'_p = -6.226$ dBrms

therefore $V_o = 1$ Vrms

b) The relationship between dB values of voltage and sound pressure is

$$L_p = L'_p - \Delta L_{pa} + C$$

where L_p is the dB value of the sound pressure level; C is the calibration constant; ΔL_{pa} is the dB attenuation of the sound level meter, B&K 2221. If ΔL_{pa} is chosen as zero for its range '25-105', it can be obtained from other ranges, as given in Table 9.5.

Table 9.5 Relative attenuation of the sound level meter

Range, dB	V_{pa} (times of Vrms)	ΔL_{pa} (dBVrms)
25 - 85	1	0
45 - 105	1/10	- 20
65 - 125	1/100	- 40
85 - 145	1/100	- 60

Since according to the above calibration when the measurement range of the sound level meter is set to '45-105', and the sound level calibrator generates 94 dB sound pressure level, ie.

$L_p = 94$dB, $L'_p = -6.226$ dBVrms, $\Delta L_{pa} = -20$ dBVrms

ie. $94 = -6.226 + 20 + C$

therefore $C = 80.226$ dB

Hence $L_p = L'_p - \Delta L_{pa} + 80.226$ (dB) (9.50)

In the later measurement of noise from the brushless DC motor, the range of the sound level meter is always set to '25-85' due to the low noise level being measured, therefore, $\Delta L_{pa} = 0$ dB

$L_p = L'_p - \Delta L_{pa} + 80.226$ (dB) (9.51)

9.5.4 Sound Pressure Level Spectrum Measurement

i) Distribution of measurement points

In order to effectively estimate the acoustic power emitted from the test motor, eight measurement positions, at which the sound pressure spectra are to be analysed, are chosen to lie on a hemispherical array. The schematic rangement and coordinates of the microphone positions are shown in Fig 9.13 and Table 9.6. The microphone is at a height of z=0.6r, whilst the radius of the hemispherical array was chosen as r=0.4m so that the area of the hemispherical surface is unity ($s = 2\pi r^2 \approx 1\ m^2$). Hence the measured average sound pressure level over eight measurement points will be simply the same as the numerical acoustic power level.

Table 9.6 Coordinates of microphone positions (m)

Measurement position number	x	y	z
1	0.32	0	0.24
2	0	0.32	0.24
3	- 0.32	0	0.24
4	0	- 0.32	0.24
5	0.226	0.226	0.24
6	- 0.226	0.226	0.24
7	- 0.226	- 0.226	0.24
8	0.226	- 0.226	0.24

ii) Measured sound pressure spectra

The brushless DC motor was run under a no-load condition and placed on sponge in the anechoic chamber, as shown in Fig 9.3, the sound pressure spectra being measured over the eight measurement points, as shown in Fig 9.14, and summarised in Table 9.7. The results were obtained with the range of the sound level meter set to '25-85', and a 'Hanning' window was employed to reduce the numerical bias and leakage errors of the finite sample. In Table 9.7 the average sound pressure level for each significant frequency component is calculated and calibrated according to equation (9.50).

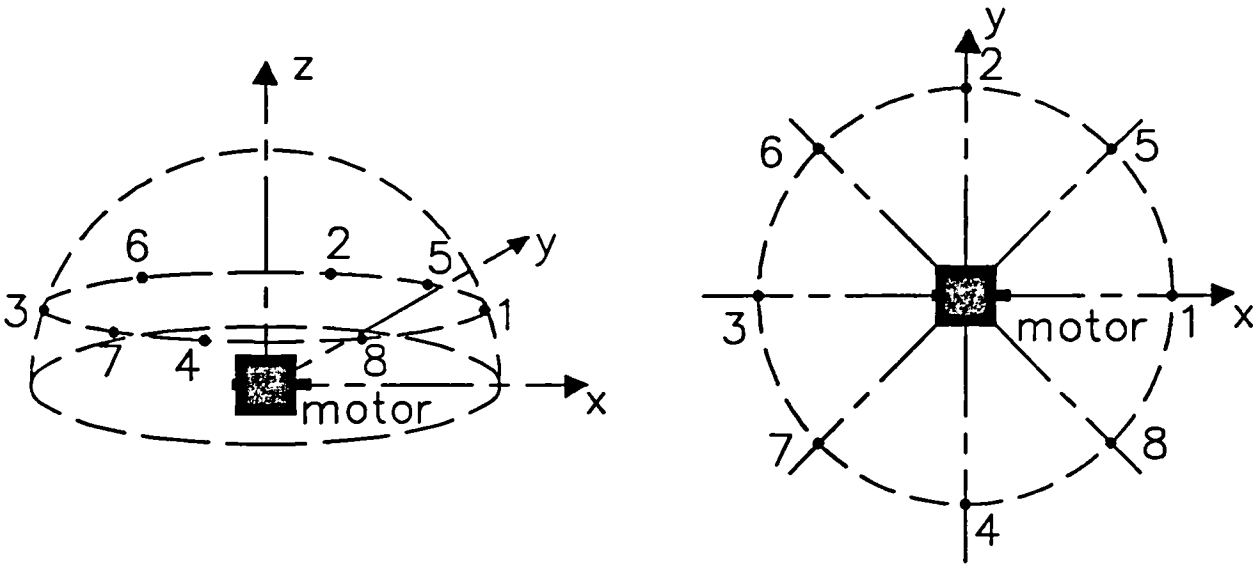

Fig 9.13 Microphone array on the hemisphere

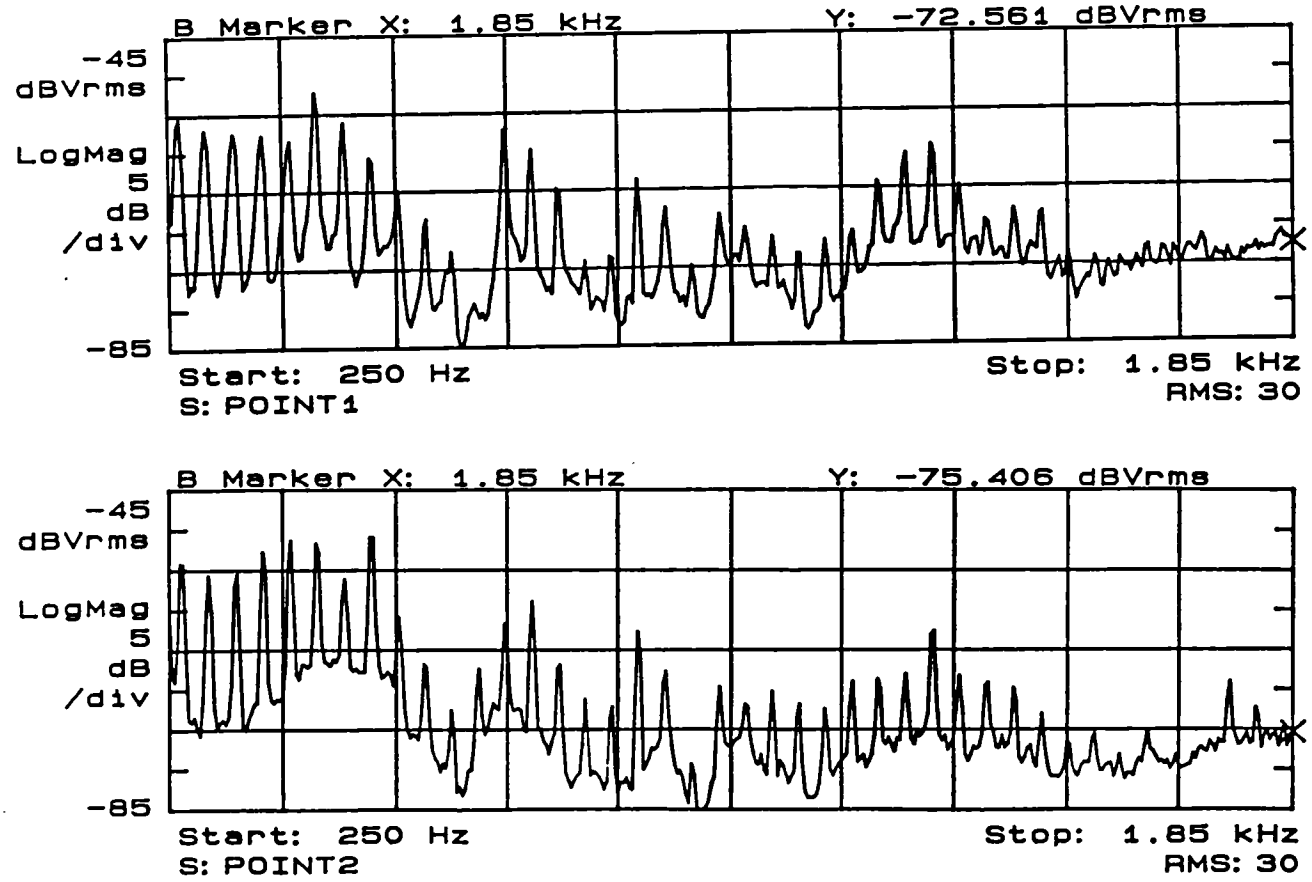

Fig 9.14 Measured sound pressure spectra (before calibration)

Table 9.7 Measured and calibrated sound pressure level of a brushless DC motor

Frequency	Average values of 8-point sound pressure measurement		Calibrated results of average sound pressure level
Hz	V_{rms}	dBV_{rms}	dB (Linear)
302	1.20	- 58.4	21.8
342	1.15	- 58.8	21.5
382	1.23	- 58.2	22.0
422	1.61	- 55.9	24.3
458	2.17	- 53.3	27.0
498	1.82	- 54.8	25.4
534	1.54	- 56.2	24.0
574	0.78	- 62.1	18.1
614	0.52	- 65.7	14.6
650	0.29	- 70.7	9.5
682	0.36	- 68.9	11.4
726	1.226	- 58.2	22.0
766	1.04	- 59.6	20.6
802	0.485	- 66.3	14.0
842	0.25	- 72.0	8.2
878	0.256	- 71.9	8.4
918	0.576	- 64.8	15.4
958	0.494	- 66.1	14.1
994	0.127	- 77.9	2.3
1034	0.399	- 68.0	12.2
1070	0.259	- 71.7	8.5
1110	0.26	- 71.7	8.5
1146	0.255	- 71.9	8.3
1186	0.198	- 74.1	6.2
1226	0.268	- 71.4	8.8
1262	0.41	- 67.8	12.4
1302	0.64	- 63.9	16.4
1338	0.85	- 61.4	18.8
1378	0.496	- 66.1	14.1
1414	0.348	- 69.2	11.1
1454	0.342	- 69.3	11.0
1494	0.283	- 71.0	9.2

Note: error in frequency readings on the analyser = 4 Hz.

It was observed from the sound pressure measurements that for most of the frequency components the measured levels at the radial positions (points 2 & 4) were larger than those at the axial positions (positions 1 & 3), except for the 726Hz, 1302Hz, and 1338Hz components, which, according to the direction of noise radiation and by the method of noise identification from the measurement position [9.9], indicates that the noise spectrum of the motor is dominated by the radial vibration of the stator, whilst the 726Hz, 1302, and 1338Hz components are due to the axial vibration of the end-shields. Indeed, the test motor has negligible aerodynamic noise, whilst the bearing noise was also negligible since a pair of oiled bush bearings were used. Therefore the discretised frequency components on the noise spectrum are all generated by electromagnetically induced vibration.

9.5.5 Analysis of Acoustic Power Radiated by the Test Motor

Table 9.8 compares the predicted and measured acoustic power level for the dominant frequency components, ie., 458 Hz, 918 Hz, and 1378 Hz, for the test motor. It is discussed further in the following sections:

Table 9.8 Comparison of predicted and measured acoustic power level

Frequency	Acoustic power level from 8-point sound pressure measurement	Predicted acoustic power level
Hz	dB	dB
458	27.0	11.9
918	15.4	17.5
1378	14.1	17.7

i) Acoustic power measurement

As mentioned in Chapter 4, although near-field noise measurement techniques, such as the sound intensity method, have been extensively studied over the last few years, existing standards, either national or international, e.g., ISO/DIS 1680, ISO 3740-3748, for acoustic power measurement are all based on the sound pressure measurement over an array of points around the machine, but neglecting the phase angle difference between the sound pressure and the particle velocity.

Since the phase angle difference reduces with the distance between the measurement point and the motor, the measurement becomes more accurate when the measurement distance increases. However according to the standard for noise measurement a measurement distance of 0.4m (or 0.5m) is normally suggested for small motors, and 1m for large motors. Due to the dimensional restrictions imposed by the anechoic chamber which was available for the measurements, as well as the low noise level from the test motor, a distance of 0.4m was chosen for the measurement. At a radial position of r=0.4m (z=0m) at the mid-plane of the motor the phase angle difference between the sound pressure and the particle velocity for the 458Hz component was found to be $\theta_{pv}=98.37^{o}$ by applying the cylindrical acoustic model of Chapter 3. This indicates that if the phase angle difference is constant on the spherical surface at radius r=0.4m, it will introduce an error around $10\log_{10}\left(\frac{1}{\cos\theta_{pv}}\right) = 8.4$ dB. In fact, the phase angle difference varies from point to point and there is no general, easy, or accurate method of estimating the error which may be introduced in the measurement. As a result, the measured results for acoustic noise are only of reference value. However the prediction has accounted for the phase angle difference. Hence it is worth noting the limitation of the current method for measuring acoustic power. At the same time developements are occurring with regard to the sound intensity measurement technique, especially concerning the feasibility for its application to the acoustic power measurement from electrical machines since only such kinds of experimental investigation will make it possible to account for the phase angle difference between the sound pressure and the particle velocity [9.20].

ii) Noise spectrum of brushless DC motors

From section 9.1 it can be seen that the radial electromagnetic force in a brushless DC motor can be subdivided into three components, ie.,

a) Forces produced by the open-circuit magnetic field

ie. $$\frac{1}{2\mu_o}\left[B_{magnet}(\alpha, t)\,\tilde{\lambda}(\alpha, t)\right]^2 \qquad (9.52)$$

b) Forces produced by the armature reaction field

ie. $$\frac{1}{2\mu_o}\left[B_{winding}(\alpha, t)\,\tilde{\lambda}(\alpha, t)\right]^2 \qquad (9.53)$$

c) Forces produced by the interaction between the open-circuit magnetic field and the armature reaction field

ie. $$\frac{2}{2\mu_o}\left[B_{winding}(\alpha, t)\,B_{magnet}(\alpha, t)\,\tilde{\lambda}^2(\alpha, t)\right] \qquad (9.54)$$

which are the same as the expressions for a conventional machine. However a brushless DC motor has the following features:

1) As given in eqn (9.11), the noise frequency is proportional to the pole number and the rotor speed. Hence the spectrum depends on the load condition, since this may alter both the amptitudes and frequencies.
2) There are a lot of components of mode order zero which dominate the noise spectrum, whilst in induction and synchronous motors, it is the components of mode two or three which are dominant.
3) Since the full-load armature reaction field in a brushless DC motor is normally less than about 20% of the open-circuit magnetic field, and under a no-load condition it is very much smaller, the effect of components (b) and (c) on the no-load noise is minimal, ie., the harmonics in the open-circuit magnetic field have a very important role in the electromagnetically generated noise;
4) Due to 3) those features which affect the field harmonics on open-circuit are also important in noise generation. These include the magnetisation and magnet arrangement, the static and dynamic rotor eccentricity etc.

ii) Asymmetry in brushless DC motors

The following sources of asymmetry, which will commonly exist in a brushless DC motor, may affect the acoustic characteristic:

a) MMF source

1) Unsymmetrical magnetisation (or partial demagnetisation) which may introduce even order harmonics in the open circuit magnetic field;
2) Unsymmetrical phase winding current waveform, due to unsymmetrical back-emf waveform because of (1) and non-uniformly distributed Hall sensor positions or unsymmetrically disposed 3-phase windings. The unsymmetrical phase winding current waveform may contain harmonics other than 1, 5, 7, 11, 13, ...

b) Permeance source

1) Static rotor eccentricity;
2) Dynamic rotor eccentricity;
3) Saturation in the magnetic circuit.

As mentioned in ii) under a no-load condition the effect of asymmetry in the winding current waveform is insignificant.

iv) Methods of accounting for asymmetry

Sources of asymmetry in the MMF can be accounted for simply by introducing the relevant harmonics of magnetisation in the open-circuit magnetic field calculation and the simulated current waveform in the armature reaction field prediction. Additional harmonics due to asymmetry in the permeance sources are considered in the calculation of the permeance function, which is given by:

$$\Lambda(\alpha, t) = \Lambda_{symmetry}(\alpha) + \Lambda_{ad}(\alpha, t) \tag{9.55}$$

where $\Lambda_{symmetry}$ is given by equation (9.12).

$$\Lambda_{ad}(\alpha, t) = \Lambda_{ecs} \cos\alpha + \Lambda_{ecd} \cos(\omega_{ec} t - \alpha) + \Lambda_{sa} \cos p(\omega_r t - \alpha) \tag{9.56}$$

and $\omega_{ec} = \omega_r$ is the angular rotor speed.

$$\Lambda_{ecs,d} = 2 \frac{1 - \sqrt{1 - e_{s,d}^2}}{e_{s,d} \sqrt{1 - e_{s,d}^2}} \tag{9.57}$$

$$e_{s,d} = \frac{d_{ecs,d}}{g + h_m / \mu_R} \tag{9.58}$$

d_{ecs}, d_{ecd} are the static and dynamic rotor eccentricities respectively, $g + h_m/\mu_R$ being the effective airgap.

In equation (9.56) the first and second terms are the fundamental components accounting for the rotor static and dynamic eccentricities, whilst the third term accounts for magnetic saturation which must be estimated by a more complicated method, such as finite element analysis. However for the test motor saturation was negligible, as was discussed earlier in Chapters 5 and 8.

v) Identification of origins on noise spectrum

As has been observed in Fig 9.14 and Table 9.7, in addition to the most dominant predicted noise components, ie., 458Hz, 918Hz, and 1378Hz which are generated by the radial vibration of the stator, a number of other substantial components have been measured. According to the above analysis, they can be identified by 'isolating' the different possible causes and executing the developed software, as summarised by the results given in Table 9.9. It is important to note that the analysis predicts 458Hz, 918Hz, and 1378Hz as being the most dominant components in the relevant frequency bands, and 682Hz and 1146Hz, as well as 650Hz, 1110Hz, and 1186Hz as being the most insignificant, and this is confirmed by the measurements, as shown in Table 9.7. This is due to the fact that the components are of higher mode order, 5, and the 682Hz and 1146Hz components are produced purely by the interaction between the harmonics due to asymmetry in the MMF and the permeance, ie., due to rotor eccentricity, as well as due to the partial demagnetisation which is observed in the test motor - as evidenced by the measured back-emf waveform of Fig 7.8. Other components on the other hand are generated by the harmonics produced by the modulation between the main harmonics (asymmetry being neglected) and the harmonics due to asymmetry, with the exception of the 726Hz, 1302Hz, and 1338Hz components, as explained earlier.

Table 9.9 Identification of components on noise spectrum, at rotor speed = 2293 rpm

Frequency	symmetrical condition(a)	rotor eccentricity (1st-order in permeance)		asymmetry open-circuit field (d)	All (a)+(b)+ (c)+(d)	Note
Hz		static (b)	dynamic (c)			
302	* (4)	* (3,4,5)	* (4)		* (3,4,5)	
342			* (3)		* (3)	
382				* (2)	* (1,2,3)	
422			* (1)		* (1)	resonance (1)of whole motor
458	* (0)	* (-1,0,1)	* (0)		* (-1,0,1)	
498			* (-1)		* (-1)	
534				* (-2)	* (-3,-2,-1)	
574			* (-3)		* (-3)	
614	* (-4)	* (-5,-4,-3)	* (-4)		* (-5,-4,-3)	
650			* (-5)		* (-5)	small dB
682					* (-5,5)	small dB
726			* (5)		* (5)	due to 1 end shield
766	* (4)	* (3,4,5)	* (4)		* (3,4,5)	
802			* (3)		* (3)	
842				* (2)	* (1,2,3)	
878			* (1)		* (1)	
918	* (0)	* (-1,0,1)	* (0)		* (-1,0,1)	
958			* (-1)		* (-1)	
994				* (-2)	* (-3,-2,-1)	
1034			* (-3)		* (-3)	
1070	* (-4)	* (-5,-4,-3)	* (-4)		* (-5,-4,-3)	
1110			* (-5)		* (-5)	small dB
1146					* (-5,5)	small dB
1186			* (5)		* (5)	small dB
1226	* (4)	* (3,4,5)	* (4)		* (3,4,5)	
1262			* (3)		* (3)	
1302				* (2)	* (1,2,3)	due to 2 end shields
1338			* (1)		* (1)	
1378	* (0)	* (-1,0,1)	* (0)		* (-1,0,1),	
1414			* (-1)		* (-1)	
1454				* (-2)	* (-3,-2,-1)	
1494			* (-3)		* (-3)	

Note: Signs ± of mode order given in ( ) indicate the force waves rotate in the opposite direction.

9.6 Conclusions

An analytical technique for predicting the acoustic noise and vibration of brushless permanent magnet DC motors has been presented and compared with measurements. The technique utilises all the information generated from previous chapters to calculate the instantaneous field distribution on load, and hence the spatial and time dependent radial force waves by applying the Maxwell stress formula. The developed vibrational response model is based on the lumped parameter model and has accounted for the modifying effect of the frame, and the damping effects, as well as the effect of the end-shields, whilst the developed acoustic radiation model can account for the effect of the ratio of diameter to axial length since it is based on a cylindrical model of finite length developed in Chapter 3 when the effect of end-shield vibration has been neglected. The spectrum of the noise has been analysed and it has been shown that unlike more conventional motors, such as induction and synchronous machines, and brushed DC machines, the frequencies of the emitted noise are proportional to pole number and the rotational speed of the rotor, and that in general the most important mode order is zero.

CHAPTER 10
GENERAL CONCLUSIONS

10.1 Introduction

The prominance of permanent magnet motor drives for motion control systems in all market sectors reflects not only the improvements in material properties which has occurred in recent years, with the tantalising design possibilities which this offers, but also a developing capability in both power and integrated electronics, which is being utilised to control drives for applications varying in sophistication from machine tools to video cassette players, many of which are noise sensitive. Arguably the most significant emerging category of motor is the brushless dc type, the vast majority of which have surface-mounted magnet rotors, which in turn leads to a large effective airgap as far as armature reaction effects are concerned. Further, unlike more traditional machine formats, such as the induction motor, the armature reaction field results from phase current waveforms which contain significant harmonics as a consequence of commutation events, between which the rotor rotates in incremental steps.

A comprehensive investigation, accounting for the features cited above, has been undertaken, and methods for analysing various aspects of the electromagnetic performance of a brushless permanent magnet DC motor have been developed, with particular reference to the acoustic noise and vibration. These are summarised in Figs 1.2 - 1.4. Original contributions reported in the thesis embrace the calculation of the open-circuit, armature reaction, and load magnetic fields, the prediction of force and torque, the dynamic simulation of drives, the analysis of mechanical vibrations and acoustic radiation, and the calculation of the slot permeance, winding inductances, and back-emf waveform of brushless permanent magnet DC motors. Most of the techniques developed in the thesis are based on 2-dimensional analyses. Throughout the predictions of magnetic field and torque, the dynamic performance, and the acoustic behaviour have been compared with measurements and/or finite element analyses, and all have shown good agreement.

Table 10.1 Application scope of developed techniques

Methods		chapter	Main features	Applications
1	Open-circuit magnetic field	5	2-d, analytical	Surface-mounted radial-field PM DC/AC motors, including brushed/brushless & internal/external rotor topologies
2	Armature reaction field	8	2-d, analytical	All radial-field motor topologies, including asynchronous/synchronous, brushless DC/AC, internal/external rotors
3	Magnetic field on load	8	2-d, analytical	Surface-mounted brushless, internal/external rotor, radial-field PM DC/AC motors
4	Permeance	5	"2-d", analytical	All radial-field motor topologies, including conventional DC/AC machines & brushed/brushless PM motors, as well as stepping motors etc.
5	Dynamic simulation	7	analytical & numerical	Brushless, internal/external rotor, radial/axial-field PM DC/AC motors
6	Cogging torque	6	2-d, analytical & numerical	Brushed/brushless, internal/external rotor, radial-field PM DC/AC motors
7	Inductances	8	2-d, analytical	All radial-field motors, particularly useful for brushless internal/external rotor, radial-field PM DC/AC motors
8	Back-emf	8	2-d, analytical	Brushless, internal/external rotor, radial-field PM DC/AC motors
9	Spectrum analysis	8	analytical	Harmonic analysis of waveforms, e.g., cogging torque, back-emf, phase winding current, field distribution, & torque ripple etc.
10	Vibrational behaviour	2	"3-d", experimental modal analysis	All small internal rotor, radial-field motors
11	Acoustic behaviour	3 & 4	"3-d", analytical & FEM	All internal rotor, radial-field motors having a cylindrical external surface
12	Vibrational response & noise level estimation	9	analytical	All internal rotor, radial-field, encased type stator motors

Although the techniques have been applied to radial-field topologies of motor, many would be equally applicable to other topologies and machine formats, as indicated in Table 10.1.

10.2 Magnetic Fields in Brushless DC Motors

10.2.1 Effect of Stator Slotting

It has been shown that slotting affects the magnetic fields in a brushless permanent magnet DC motor in the following ways:

i) The effect of slotting in reducing the airgap flux can be accounted for by the use of a Carter coefficient, ie. by modifying the effective airgap length. However in the calculation of the open-circuit, armature reaction, and load magnetic fields the effect of slotting in machines equipped with surface-mounted permanent magnet rotors is much smaller than in other types of machine due to the larger effective airgap, except in the case when a very large slot opening is employed, in an attempt to reduce the cogging torque for example.

ii) Slotting affects the magnetic field distribution in both the airgap and the magnets. Hence 2-dimensional techniques, based on the conformal transformation and a 2-dimensional relative permeance function, have been used in the calculation of the field distributions. It has been shown that:

   a) The conventional 1-dimensional method used in the analysis of induction motors is no longer suitable for permanent magnet motors due to their large effective airgap;

   b) Whilst the effect of slotting on the field distribution at the stator iron surface is significant it has little effect on the distribution at the rotor iron surface;

   c) The 2-dimensional relative permeance model which has been developed can account for the variation of the flux density with radius. As a consequence when it is coupled with the analytical models for calculating the magnetic field produced by the magnets and windings, the resulting analytical predictions all show excellent agreement with finite element calculations.

iii) Slotting requires that the stator winding current distribution in the 2-dimensional analytical models be represented as current sheets distributed over the slot openings. This eliminates problems of numerical divergence in 2-dimensional analyses based on models having

discrete conductors on the surface of the stator, and again shows good agreement with finite element calculations.

10.2.2 Open-circuit Magnetic Field

A general analytical method has been established to calculate the open-circuit magnetic field distribution of permanent magnet motors. It can cater for slotless and slotted, and internal and external rotor, radial-field motors modelled in either polar or rectangular coordinate systems. The technique is based on a 2-dimensional analytical model to calculate the magnetic field produced by the magnets in the airgap/magnet regions, and utilises the concepts of mmf and permeance, ie. the field produced by the magnets and a relative permeance function. It involves the solution of the governing Laplacian/Poissonian field equation in the airgap/magnet regions without the assumption of unity relative recoil permeability of the magnet, but with due account for stator slot openings by the application of the conformal transformation method and the introduction of a "two-dimensional" relative permeance function.

Therefore it permits the analytical calculation of the open-circuit magnetic field distribution in all topologies of radial-field surface-mounted permanent magnet motor. Predicted results have been compared with predictions from finite element calculations for both an internal rotor motor and an external rotor motor, and excellent agreement has been achieved. Based on the developed technique the effects of slot-openings and flux focussing have been investigated.

10.2.3 Armature Reaction Field

A systematic analysis of the armature reaction field in a brushless permanent magnet DC motor has been presented. It has the following features:

i) It originates from the 2-dimensional analysis, in polar coordinates, of the magnetic field produced by a single conductor or coil, and can account for the effect of the large effective airgap in brushless permanent magnet DC motors.

ii) It accounts for the harmonics in the phase current waveforms deduced from the simulation described in Chapter 7 by the application of an analytical spectrum analysis.

iii) It is based on the 2-dimensional analysis of an analytical model in which the stator winding current is represented by current sheets distributed over the slot-openings, and for which a slot-opening coefficient has been introduced to overcome the problem of numerical divergence which is experienced in the solution of a concentrated conductor model.

iv) The effect of slotting is accounted for by using a 2-dimensional relative permeance function, which is identical to that used in the analysis of the open-circuit magnetic field.

v) The technique is based on an entirely general analysis of the winding mmf, and hence is suitable for any winding topology.

vi) It is applicable to both external and internal rotor motors.

10.2.4 Instantaneous Magnetic Field on Load

A comprehensive analytical technique for predicting the airgap field distribution in radial-field, internal/external rotor, brushless DC motors under any load condition, accounting implicitly for the corresponding stator windiing current waveforms and the effect of stator slot-openings has been developed. It is based on a 2-dimensional analysis, in polar coordinates, of the airgap/magnet regions, and combines the analytical calculation of the armature reaction field in Chapter 8, with the analytical prediction of the current waveforms from Chapter 7 and the open-circuit magnetic field produced by the magnets from Chapter 5, to permit the instantaneous field distribution, and hence the radial force distribution, to be predicted under any load condition and specified commutation strategy.

The relationship between the various quantities involved, such as the open-circuit and the armature reaction component fields, the permeance, the back-emf and current waveforms etc, has been determined analytically. Instead of having a constant 90 degrees elec between the axes of the open-circuit field and the armature reaction field, as normally assumed in a finite element calculation of the magnetic field distribution on load, the load angle varies from 60 degrees elec at the beginning of a commutation period to 120 degrees elec at the end, whilst the exact instantaneous angle can be determined precisely according to the analytical method proposed.

10.2.5 Back-emf and Winding Inductances

Based on the developed 2-dimensional analytical technique for calculating the open-circuit magnetic field distribution, a 2-dimensional analytical method for calculating the back-emf waveforms in the windings of a brushless permanent DC motor has been developed.

Since the existing analytical calculation of the winding inductances is essentially based on a 1-d technique, which is appropriate for induction motors, it cannot account for the large effective airgap in a brushless permanent magnet DC motor. In the thesis, therefore, the 2-dimensional analytical technique for predicting the armature reaction field is also applied to the calculation of the self- and mutual-winding inductances.

The developed techniques are suitable for both internal and external rotor surface-mounted permanent magnet brushless DC motors, and as well as for any winding distribution. In addition they are equally applicable to the analysis of brushless AC motors.

10.3 Cogging Torque and the Dynamic Performance of Brushless DC Motors

10.3.1 Cogging Torque

The accuracy of the torque predicted from a finite element calculation is determined largely by the level of discretisation employed, as well as the evaluation method. In general, a high accuracy requires a very fine discretisation. On the other hand analytical methods for predicting the cogging torque, such as those based on calculation of energy, are successful only in certain circumstances, and are likely to fail in others.

An analytical method for predicting the cogging torque, based on the calculation of the field distribution and the net lateral forces which act on the stator teeth, has been developed and partially validated.

The technique is capable of predicting the cogging torque in internal and external rotor motors modelled in either a rectangular or a polar coordinate system. Also it is able to deal with motor topologies in which the magnets are shifted, have an uneven slot distribution etc, design features which are sometimes employed in an attempt to reduce the cogging torque. It offers acceptable accuracy when predicting the peak value of the cogging torque and its variation with the motor design parameters. It remains valid even when the pole-arc to pole-pitch ratio is unity, which is not the case for existing analytical methods based on the calculation of energy.

A comprehensive list of possible methods for reducing the cogging torque is given in the thesis, and a detailed finite element analysis of cogging torque prediction by the energy method and Maxwell stress integration, based on different mesh discretisations, has been described. The investigation utilises the relationship between the total stored energy and the mesh density, to provide a useful means of gauging the adequacy of the meshing density in a finite element model of a permanent magnet excited motor. It shows that the results obtained from both the energy method and Maxwell stress integration converge as the mesh is refined, and that the total energy eventually converges to a constant value. However with the same accuracy requirement for torque prediction, a coarser discretisation can be used in the energy method rather than for Maxwell stress integration, for which it is always better to integrate through a central layer of airgap elements.

10.3.2 Dynamic Simulation

An analytical model for predicting the steady-state dynamic performance of a 3-phase brushless DC drive has been developed and validated. In the model, which assumes a constant speed, the initial conditions which yield the steady-state solution are generated directly by exploiting the periodicity in the stator winding voltage and current waveforms and hence it provides a rapid means of assessing the important features of the motor and drive performance during the early stages of design.

The model includes the following features:

(i) It can account for any induced back-emf waveform.

(ii) The switching devices and freewheel diodes in the inverter drive circuit are represented as an appropriate constant voltage drop behind a series resistance.

(iii) It can cater for normal, advanced, or retarded commutation.

(iv) It can impose a pre-specified current limit.

A numerical model was developed further by coupling in the equation of motion of the rotor so as to enable the transient and steady-state dynamic performance of brushless DC drives to be predicted. The drive circuit is idealised into two states, which depend on whether the freewheel diode is conducting or not, and are always described by two fixed groups of state equations. The dynamic performance is obtained by introducing a relationship between the state variable and the stator winding currents.

The analyses have been validated against measurements on an axial-field, and two radial-field permanent magnet brushless DC motors.

Both the analytical and numerical models can be linked to other aspects of the design process, for example to finite element analyses for predicting the back-emf waveforms and winding inductances, and can be used as functional blocks in a more sophisticated system simulation package. Further, although the analyses have been restricted to motors having three-phase, star-connected windings, the techniques are applicable equally to delta-connected windings as well as to any number of phases.

10.3.3 Dynamic Performance

The developed simulation models have been used to examine the effects of commutation and temperature (winding resistance) on the dynamic performance, ie. current and torque waveforms and their frequency spectra, torque-speed characteristics etc.

It has been shown that:

i) The commutation strategy can have a significant effect on the dynamic performance, particularly on the current and torque waveforms.

ii) The load condition does not significantly alter the shape of current and torque waveforms.

iii) The winding inductances (or the ratio of winding inductance to resistance) are the main cause of the departure of the torque-speed characteristic from the ideal linear relationship. However the variation in winding resistance due to temperature changes may also cause a significant variation in the slope of the torque-speed characteristic.

iv) Since the back-emf waveform has a significant effect on the harmonics in the current and torque waveforms, it should be possible to minimise the torque ripple and current harmonics by careful design of the winding arrangement and the magnetic circuit, as well as the magnetisation of the magnets.

10.4 Vibrational and Acoustic Behaviour

10.4.1 Modal Analysis of Vibrational Behaviour

In small motors, the length-to-diameter ratio of the stator is usually not very large. As a consequence their end-shields, which are bolted to the stator frame, have a relatively large stiffness. The rotor, which is supported by the end-shields and the bearings, will also restrict and affect the vibrational behaviour of the stator. However previous investigations on the vibrational behaviour concern only the stator itself, neither the end-shields nor the rotor and the running conditions being taken into account, which is the case even for experimental investigations and three-dimensional analysis.

The effect of end-shields, the rotor, and the running conditions on the natural frequencies and modes of the stator have been investigated, for the first time, by the modern modal analysis technique. It has been shown that:

i) Because of their restricting effects, the end-shields significantly increase the values of the natural frequencies of the stator.

ii) Although in comparison the effect of the rotor is much smaller, it does cause important new natural frequencies to be introduced, in particular the first-order mode.

iii) The modifying effects of load are small, even up to rated load.

The study has provided data which should assist future investigations, particularly in regard to the effects of mounting feet on the natural frequencies and modes of stators, in developing vibrational models based on finite elements, as well as acoustic models.

10.4.2 Analytical Acoustic Model

A knowledge of the relationship between the vibration and acoustic noise of an electrical machine is critical to the calculation of its acoustic power and to the analysis and control of noise from electrical machines. Hence the acoustic radiation efficiency (relative sound intensity coefficient) is studied in the thesis, both analytically and numerically.

In the cylindrical model of finite length which has been employed the main dimensional characteristics have been included as far as electromagnetic noise is concerned. In addition the effect of the axial length-to-diameter ratio has been considered, the solutions being obtained analytically. Consequently the analytical prediction of acoustic power has extended the earlier research carried out by Erdelyi, Alger, Ellison and Yang.

An improved technique for calculating the acoustic power radiated by an electrical machine has been presented. It is based on the sound pressure and the stator vibration velocity at the vibrating surface, and results in a much simpler formula for calculating the relative sound intensity, and eliminates the need for calculating the sound pressure and the particle velocity distributions around a machine. Hence the computing time is greatly reduced. Also it has the advantage of a much simpler form, making it easier to use for routine design. Subsequently the sound pressure distribution is investigated, and its variation in three-dimensions is calculated and measured.

10.4.3 Finite Element Analysis of Acoustic Behaviour

Existing analytical models for acoustic radiation assume that the stator has either a unity aspect ratio or infinite axial length and infinite stiffening baffles. Hence they cannot accout for the effects of the end-shields. In the thesis, the finite element method is used to study the radiated acoustic power with particular emphasis on machines having an axisymmetric construction. It is combined with a Fourier series analysis, the Fourier series being used to represent the circumferential variation of the sound pressure, whilst finite elements are used to interpolate and discretise the variation in the radial-axial plane. The combination of both methods allows the acoustic radiation of electrical machines to be predicted with due account of the effect of end-shields, which is not possible with existing analytical methods. Calculation methods for the acoustic power using finite elements in various acoustic fields, from two-dimensional and axisymmetric to three-dimensional, are described, and corresponding formulae deduced. Based on this approach a suite of planar, axisymmetric, and harmonic axisymmetric finite element programs have been developed and the effects of the far-field boundary condition on the calculation studied. It has been shown that in the calculation of emitted acoustic power it is proper to use the local spherical wave boundary condition and to place the far-field boundary at 0.75 times the outside radius of the machine. Predictions of the acoustic power from the harmonic axisymmetric finite element method are validated against measurements on a three-phase induction motor.

The technique has been applied to Jordan's spherical model of acoustic radiation. It has been shown that when Jordan's method is used to calculate the radiated acoustic power, it is necessary to express the vibrations of the machine in the form of a Legendre series, otherwise large errors are introduced. The relative sound intensity coefficients of the spherical model, in which the vibration of the machine is expressed in the form of a Fourier series, have been obtained by finite element analysis which makes it possible to use Fourier series analysis throughout. However, it has also been shown that predictions from the spherical acoustic model are very close to those from the analytical cylindrical acoustic model of finite length when its ratio of length-to-diameter

is unity. Hence instead of using a spherical acoustic model it is preferable to employ a cylindrical acoustic model of finite length since the latter can account for the length-to-diameter ratio.

10.5 Acoustic Noise of Brushless DC Motors

10.5.1 Vibrational Response Model

An analytical model for calculating the vibrational response of small motors having an encased type stator has been proposed. It differs from conventional ones in that it can account not only for the iron core but also the frame, as well as the damping effects, for which the damping ratios are obtained from measurements. Based on a lumped parameter model of the stator vibration, the effects of the frame, as well as the teeth and windings, have been accounted for analytically. With due account of the modifying effect of the frame, the analytically calculated natural frequencies of the stators have been shown to be in good agreement with both the measured and finite element predicted results. However, at present the modifying effects of the end-shields on the stiffness of the stator are deduced by experiment. In the future, these may be obtained from three-dimensional finite element calculations.

10.5.2 Acoustic Noise of Brushless DC Motors

Based on the developed analytical techniques for predicting the instantaneous open-circuit, armature reaction, and load field distributions, as well as the analytical simulation of the dynamic performance of a radial-field brushless DC motor, the vibrational radial force and tangential torque waves can be calculated, whilst the resulting vibration and acoustic power are also estimated analytically. Hence not only can the acoustic noise be predicted under any load condition and any commutation strategy, using analytical techniques throughout, but possible causes of the noise spectrum, such as rotor eccentricity, partial demagnetisation of the magnets, or asymmetry of the field distribution, as well as harmonics in the current waveform can be investigated. It has been shown, by both the analysis and measurements, that unlike the more conventional machine formats, such as induction motors, synchronous machines, and

direct-current machines, the noise spectrum of a brushless DC motor is directly proportional to pole number and the rotational speed of the rotor. In addition, the vibrational mode of zero-order plays an important role, at least as significant as modes of two- or three-order. Due to the large effective airgap and the fact that the full-load armature reaction field in a brushless DC motor is normally only 10% - 20% of the open-circuit magnetic field, it is the open-circuit magnetic field distribution which dominates the noise spectrum. However, if there is no speed control loop in the drive system, the rotational speed of the rotor decreases with an increase of load, which results in a reduction in the frequencies of the radial force waves. Therefore, the noise spectrum and emitted acoustic power will also change with the load.

10.6 Possible Future Work

Although the electromagnetic performance of brushless permanent magnet DC motors, with particular reference to their noise and vibration, has been studied comprehensively, due to the time restriction and the need to fulfill other commitments under the BRITE research project it was not possible to take all the aspects to their logical conclusion. Therefore the following topics are suggested as being worthy of future research:

i) Three-dimensional finite element analysis of the vibrational behaviour of electrical machines in general;

ii) A more thorough comparison of analytical predictions of the winding inductances and back-emf waveforms with finite element calculations and measurements (currently being carried out);

iii) A more detailed investigation into the effects of design parameters on the cogging torque, and the establishment of general design rules for minimising the cogging torque;

iv) The integration of the analytical magnetic field calculation, analytical dynamic simulation, and analytical prediction of winding inductances and back-emf waveform etc developed in the thesis, into a comprehensive CAD package having an appropriate architecture to permit

ease of data transfer and various routes to evolving an optimum design (currently being carried out by the author and colleagues);

v) A study of the effects of the magnetisation, the commutation strategy, and the current waveform on the acoustic noise emitted from brushless DC motors;

vi) The application and extension of the achievements reported in the thesis to other machine formats.

REFERENCES

CHAPTER 1

1.1 Ellison, A.J., and Moore, C.J., 1968, "Acoustic noise and vibration of rotating electric machines", Proc. IEE, 115, 1633-1640.

1.2 Harris, C.M., 1971, "Handbook of noise control", 2nd ed., McGraw-Hill, New York.

1.3 Campbell, J., 1963, "Electric-motor noise", Machine Design, 35, 137-158.

1.4 Talaat, M.E., 1957, "Calculation of windage-noise power level in large induction motors", Trans.AIEE, 76, 46-55.

1.5 Brozen, R.J., 1973, "No-load to full-load airborne noise level change on high-speed polyphase induction motors", Trans.IEEE-IA, 9, 180-200.

1.6 Ploner, B., 1976, "Aerodynamic noise in medium-sized asynchronous motors", Brown Bover Rev., 63, 493-499.

1.7 Yang, S.J., 1970, "The measurement and calculation of acoustic noise from electrical machines", PhD thesis, University of London.

1.8 Yang, S.J., 1981, "Low-noise electrical motors", Clarendon Press, Oxford.

1.9 Erdelyi, E., 1955, "Predetermination of sound pressure levels of magnetic noise of polyphase induction motors", Trans. AIEE, 74, 1269-1280.

1.10 Шубов, И.Г., 1974, "Noise and vibration in electrical machines", «Энергия», Ленинградское отделение.

1.11 Chen, Y.X., and Zhu, Z.Q., 1987, "Analysis and control of noises from electrical machines", Zhejiang University Press. (in Chinese)

1.12 Heller, B., and Hamata, V., 1977, "Harmonic field effects in induction machines", Elsevier Scientific Publishing Company, Amsterdam, Oxford, New York.

1.13 Alger, P.L., 1964, "The nature of induction machines", Gordonk Breach, New York.

1.14 King, A.J., 1965, "The measurement and suppression of noise", Chapman and Hall.

1.15 Liwschitz-Garik, M., and Whipple, C.C., 1961, "Alternating current machines", D.Van Nostrand.

1.16 Hamata, V., 1966, "Magnetic noise of d.c. machines", Acta Tech.CSAV, 2, 202-226.

1.17 Stanka, V., 1964, "Magneticky hluk stejnosmernych stroju", Elektrotech Obzor, 53, 247-251.

1.18 Mikina, S.J., 1934, "The effect of skewing and pole spacing on magnetic noise in electric machinery", Trans.ASME, 5, 711-720.

1.19 Dovoracek, A.I., 1963, "Forces on the teeth in d.c. machines", Trans. AIEE, 82, ptIII, 1054-1061.

1.20 Fritz, H., 1921, "Uber die Gerauschbildung bei elektrischen maschinen", Arch. Elektrotech. 10, 73-95.

1.21 Chapman, F.T., 1923, "The production of noise and vibration by certain squirrel-cage induction motors", J.IEE, 61, 39-48.

1.22 Graybeal, T.D., 1944, "The nature of vibration in electrical machinery", Trans.AIEE, 63, 712-718.

1.23 Hildebrand, L.E., 1930, "Quiet induction motors", Trans.AIEE, 49, 848-852.

1.24 Appleman, W.R., 1937, "The cause and elimination of noise in small induction motors", Trans.AIEE, 56, 1359-1367.

1.25 Morrill, W.J., 1940, "Harmonic theory of noise in induction motors", Trans.AIEE, 59, 474-480.

1.26 Muster, D.F., and Wolfert, G.L., 1955, "Single phase induction motor noise due to dissymmetry harmonics", Trans.AIEE, 74, ptIII, 1189-1192.

1.27 Summers, E.W., 1955, "Vibrations in 2-pole induction motors related to slip frequency", Trans.AIEE, 74, ptIII, 69-72.

1.28 Magyar, L.W., 1959, "Sources of electromagnetic vibration in single phase induction motors", Trans.AIEE, 78, ptII, 81-85.

1.29 Graham, Q., Beckwith, S., and Milliken, F.H., 1931, "Magnetic noise in synchronous machines", Trans.AIEE, 50, 1056-1062.

1.30 Penniman, A.C., and Taylor, H.D., 1941, "Suppression of magnetic vibration and noise in 2-pole turbine generators", Trans.AIEE, 60, 283-388.

1.31 Walker, J.H., and Kerruish, N., 1960, "Open-circuit noise in synchronous machines", Proc.IEE, 107A, 505-512.

1.32 Walker, J.H., and Kerruish, N., 1961, "Noise in salient-pole machines", AEI Engrg, 1, 428-435.

1.33 Ridley, G.K., 1963, "Computer analysis of open-circuit noise in synchronous machines", AEI Engrg.(Computation- in-engineering supplement), 3, 29-35.

1.34 Fu, Z.Q., 1988, "Analysis of electromagnetic vibration and noise in hydroelectric generators", Proc.ICEM88, Italy, 93-98.

1.35 Chen, Y.X., Zhu, Z.Q., 1982, "Estimation and control of the noise of TSWN 85/31-8, 250kW electric generator", Conference of noise control, CES.1982.(in Chinese)

1.36 Imhoff, J.F. et al, 1989, "Spectral analysis of electromagnetic vibrations in d.c. machines through the finite element method", Trans.IEEE-MAG, 25, 3590-3592.

1.37 Lefevre, Y., et al, 1989, "Determination of synchronous motor vibrations due to electromagnetic force harmonics", Trans. IEEE-MAG, 25, 2974-2976.

1.38 Subramanyan, V., 1971, "Axial forces in induction motors with skewed slots", Proc.IEE, 118, 1759-1760.

1.39 Subramanyan, V., 1975, "Axial magnetic forces in induction motors with skewed slots", Proc. IEE, 122, 149-153.

1.40 Bradford, C.E., and Rhudy, R.G., 1953, "Axial magnetic forces on induction machine rotors", Trans.AIEE, 72, ptIII, 488-494.

1.41 Fruchtenicht, J. et al, 1978, "Calculation of axial forces in three-phase induction motors.I.theory of the stationary state;II.influence of slot skew, front fields, tangential field components and saturation", Siemens Forsch-& Entwicklungsber, 7, 102-107.& 132-137.

1.42 Slavik, C.J., 1989, "Axial magnetic forces in induction machines at twice line frequency", Proc.Int.Conf.on Electrical Machines and Drives, IEE Conf.Pubn No 310, 237-240

1.43 Binns, K.J., 1968, "Cogging torques in induction motors", Proc.IEE, 115, 1783-1790.

1.44 Hamata, V., Heller, B., 1983, "The influence of tangential forces upon magnetic noise of an induction machines", Acta Technica, CSAV, 28, 338-344.

1.45 Hamata, V., Heller, B., 1982, "New aspects of magnetic noise in induction machines", Acta Technica, CSAV, 30, 389-397.

1.46 Binns, K.J., and Kahan, P.A., 1981, "Effect of load on the tangential-force pulsations and harmonic torques of squirrel-cage induction motors", Proc.IEE, 128, ptB, 207-211.

1.47 Binns, K.J., and Rowlands-rees, G., 1975, "Main flux pulsations and tangential tooth-ripple forces in induction motors", Proc.IEE, 122, 273-277.

1.48 Binns, K.J., and Kahan, P.A., 1980, "Effect of load on the flux pulsations and radial-force pulsations of induction motors teeth", Proc.IEE, 127, ptB, 223-230.

1.49 Heller, B., and Jokl, A.L., 1969, "Tangential forces in squirrel-cage induction motors", Trans.IEEE-PAS, 88, 484-492.

1.50 Kimball, Jr.A.L., and Alger, P.L., 1924, "Single phase motor torque pulsations", Trans.AIEE, 43, 730-739.

1.51 Morrill, W.J., 1929, "The revolving field theory of the capacitor motor", Trans.AIEE, 48, 614-632.

1.52 Williamson, S., 1981, "Twice-line-frquency pulsating torques in shaded-pole motors", Electric machines and Electromechanics, 6, 67-78.

1.53 Hamata, V., 1984, "The analysis of basic causes of noise generation of single-phase induction motors", Acta Technica, CSAV, 29, 26-31.

1.54 Zhu, Z.Q., and Chen, Y.X., 1987, "Analysis and control of tangential vibration and noise of single phase induction machines", Journal of Zhejiang University, 21, 95-106.(in Chinese)

1.55 Ellison, A.J., and Yang, S.J., 1971, "Effects of rotor eccentricity on acoustic noise from induction machines", Proc.IEE, 118, 174-184.

1.56 Bose, B.K.(editor), 1980, "Adjustable speed AC drive systems", IEEE Press, New York.

1.57 Yang, S.J., and Timar, P.L., 1980, "The effect of harmonic currents on the noise of a three-phase induction motor", Trans.IEEE-PAS, 99, 307-310.

1.58 Williamson, S., Pearson, D., and Rugege, A.M., 1981, "Acoustic noise and pulsating torques in a triac-controlled permanent-split- capicitor fan motor", Proc.IEE, 128, ptB, 201-206.

1.59 Takahashi, I., and Mochikawa, H., 1986, "Optimum PWM waveforms of an inverter for decreasing acoustic noise of an induction motor", Trans.IEEE-IA, 22, 828-834.

1.60 Belmans, R.J., et al, 1987, "Analysis of the audible noise of three-phase squeirrel-cage induction motors supplied by inverters", Trans.IEEE-IA, 23, 842-847.

1.61 Giessler, F., and Sattler, P.K., 1988, "Magnetic noise of induction machines by inverter supply", Proc.ICEM88, Italy, 611-616.

1.62 Nishimura, T., Nakaoka, M., and Maruhashi, T., 1989, "Reduction of vibration and acoustic noise in induction motor driven by three phase PWM AC chopper using static induction transistors", Trans.IEEE-Power Electronic, 4, 625-631.

1.63 Wallace, A.K., Spee, R., and Martin, L.G., 1990, "Current harmonics and acoustic noise in AC adjustable-speed drives", Trans.IEEE- IA, 26, 267-273.

1.64 Courtier, G.A.C., and Hunnabll, P.J., 1990, "Acoustic suitablity of variable speed drives for use with fans in the H & V environment", Proc.of Institute of Acoustics, 10.

1.65 Timar, P.L., and Hallenius, K.E., 1988, "Some notes on the necessity to extend the vib-acoustic tests of rotating electrical machines used in variable-speed drives", Conf. Rec.of Industry Applications Society Annual Meeting, 124-128.

1.66 Patel, H.S., and Hoft, R.G., 1973, " Generalized techniques of harmonic elimination and voltage control in thyristor inverters: Part I - harmonic elimination and Part II - voltage control techniques", Trans.IEEE-IA, 9, 310-317, and 10, 666-673.

1.67 Taleb, M., and Ortmeyer, T.H., 1990, "Modified current injection technique", Electric Machines and Power Systems, 18, 13-27.

1.68 Kenjo, T., and Nagamori, S., 1985, "Permanent-magnet and brushless DC motors", Clarendon Press, Oxford.

1.69 Miller, T.J.E., 1989, "Permanent magnet brushless drives and reluctance motors", Clarendon Press, Oxford.

1.70 Le-huy, H, Perret, R., and Feuiliet, R., 1986, "Minimization of torque ripple in brushless dc motor drives", Trans.IEEE-IA, 22, 748-755.

1.71 Murai, Y., et al , 1989, "Torque ripple improvement for brushless DC miniature motors", Trans.IEEE-IA, 25, 441-450.

1.72 Kovacs, K.P., 1977, "Two-pole induction motor vibrations caused by homopolar alternating fluxes", Trans.IEEE-PAS, 96, 1105-1108.

1.73 Williamson, S., and Mirzaian, K., 1985, "Analysis of cage induction motors with stator winding faults", Trans.IEEE-PAS, 104, 1838-1842.

1.74 Cameron, J.R., Thomson, W.T., and Dow, A.B., 1986, "Vibration and current monitoring for detecting airgap eccentricity in large induction motors", Proc.IEE, 133, ptB, 155-163.

1.75 Ding, F.L., and Trutt, F.C., 1988, "Calculation of frequency spectra of electromagnetic vibration for wound-rotor induction machines with winding faults", Electricmachines and Power System, 14, 137-150.

1.76 Penman, J., and Thian, B.M., 1990, "Relationship between alternative methods of monitoring the condition of electrical machines", Proc.of Institute of Acoustics, 12, 9-18

1.77 Tavner, P.J., and Penman, J., 1987, "Condition monitoring of electrical machines", Research Studies Press Ltd, England.

1.78 Yang, S.J., and Ellison, A.J., 1985, "Machinery noise measurement", Oxford University Press, New York.

1.79 ISO Standards No 3744, 3745, 3746, 6926.

1.80 Ellison, A.J., Moore, C.J., and Yang, S.J., 1969, "Methods of measurement of acoustic noise radiated by an electric machine", Proc.IEE, 116, 1419-1431.

1.81 Ellison, A.J., and Yang, S.J., 1970, "Acoustic noise measurements on nominally identical small electric machines", Proc.IEE, 117, 555-560.

1.82 Shen, P.Y., 1986, "Sound intensity measurement of acoustic power emitted by an machine", MSc.thesis, Zhejiang University. (in Chinese)

1.83 Kron, G., 1931, "Slot combinations of induction motors", Trans.AIEE, 50, 757-767.

1.84 Jordan, H., and Rothert, H., 1953, "Rules of slot numbers and their relationship with the magnetic noise of induction machines", Elektrotech Z(ETZ)A, 74, 637-642.

1.85 Jordan, H., and Muller-Tomfelde, H., 1961, "Akustische Wirkung der Schrangung bei Drehstrom-Asynchronmaschinen mit Kafiglaufern", Elektrotech.Z.ETZ-A, 82, 788-792.

1.86 Sperling, Von P.G., 1969, "Erfahrungen bei der Vorausberechnumg elektromagnetisch erzeugter Maschinengerausche", Simens Z. 43, 894-898.

1.87 Jordan, H., 1950, "Der gerauscharme Elektromotor", Girardet, Essen.

1.88 Zhu, Z.Q., Chen, Y.X., Shang, Q.Y., 1988, "Theory and design of low noise induction motors", Special and Micro Motors, CES. No.3, 13-17.(in Chinese)

1.89 Bolte, E., and Gerling, D., 1990, "Noise Analysis of Inverter-fed variable-speed industion motor drives", Proc.of Int. Conf. on Electrical machines, Boston.

1.90 Shapiro, H., and Fallon, W.H., 1960, "Low-noise motor design", Elec.Manufacturing, May, 265-273.

1.91 Tsivitse, P.J., and Weishmann, P.R., 1971, "Polyphase induction motor noise", Trans.IEEE-IGA, 7, 339-358.

1.92 Yang, S.J., and Ellison, A.J., 1987, "Noise and vibration", Chapter 14 in "Handbook of electric machines", Edited by Nasar, S.A., McGraw-Hill, New York.

1.93 Yang, S.J., 1975, "Acoustic noise from small 2-pole single- phase induction machines", Proc.IEE, 122, 1391-1396.

1.94 Jordan, H., and Frohne, H., 1957, "Ermittlung der eigenfrequenzen des standers von drehstrommotoren", Larmbekampfung, 7, 137-140.

1.95 Frohne, H., 1959, "Uber die primaren bestismmungsgrossen der lautstarke bei asynchronmaschinen", Dr.Ing.thesis, Technical University of Hanover.

1.96 Uner, Z., and Jordan, H., 1964, "Berechnung der eigenfrequenzen der blechpakete von drehstrommaschinen", Konstruktion, 16, 108-111.

1.97 Erdelyi, E., and Horvay, G., 1957, "Vibration modes of stators of induction motors", Trans.ASME-E, 24, 39-45.

1.98 Ellison, A.J., and Yang, S.J., 1971, "Natural frequencies of stators of small electric machines", Proc.IEE, 118, 185-190.

1.99 Verma, S.P., and Girgis, R.S., 1973, "Resonant frequenies of electrical machine stators having encased constructure. Pt1, Pt2", Trans.IEEE-PAS, 92, 1573-1585.

1.100 Verma, S.P., and Girgis, R.S., 1975, "Considerations in the choice of main dimensions of stators of electrical machines in related to their vibration characteristics", Trans.IEEE-PAS, 94, 2151-2159.

1.101 Girgis, R.S., and Verma, S.P., 1979, "Resonant frequencies and vibration behaviour of stators of electrical machines as affectted by teeth, winding, frame and laminations", Trans. IEEE-PAS, 98, 1446-1455.

1.102 Girgis, R.S., and Verma, S.P., 1981, "Method for accurate determination of resonant frequencies and vibration behaviour of stators of electrical machines", Proc.IEE, 128, 1-11.

1.103 Verma, S.P., and Girgis, R.S., 1981, "Experimental verification of resonant frequencies and vibration behaviour of stators of electrical machines", Proc.IEE-B, 128, 22-32.

1.104 Verma., S.P., Singal, R.K., and Williams, K., 1987, "Vibration behaviour of stators of electrical machines, part 1: theoretical study", J.Sound & Vib., 115, 1-12.

1.105 Singal, R.K., and Williams, K., Verma, S.P., 1987, "Vibration behaviour of stators of electrical machines, part 2: experimental study", J.Sound & Vib., 115, 13-23.

1.106 Verma, S.P., Williams, K., and Singal, R.K., 1989, "Vibrations of long and short laminated stators of electrical machines.part 1:theory, experimental models, procedure and set-up", J.Sound & Vib., 129, 1-13.

1.107 Williams, K., and Singal, R.K., Verma, S.P., 1989, "Vibrations of long and short laminated stators of electrical machines.part 2:results for long stators", J.Sound & Vib., 129, 15-29.

1.108 Singal, R.K., Verma, S.P., and Williams, K., 1989, "Vibrations of long and short laminated stators of electrical machines.part 3:results for short stators and validity of simplified frequency equation", J.Sound & Vib., 129, 31-44.

1.109 Holzmann, F., 1972, "Eigenfrequenzen des blechpaketes von drehstrum maschinen unter berucksicktigung des schwingungsverhaltens derzahne", ETZ-A, 93, 82-85.

1.110 Chen, Y.X., Zhu, Z.Q, 1986, "Analysis of natural frequencies and modes of electrical machines with square stators", Proceedings of conference on noise and vibration of electrical machines, CES.(in Chinese)

1.111 Den Hartog, J.P., 1928, "Vibration of frames of electrical machines", Trans. ASME-APM, 50, 1-6, 9-11.

1.112 Voronetskii, B.B., 1956, "Natural frequencies of a.c. electrical machine stators", Vest.Elektromprom., 7, 52-57.

1.113 Lubcke, E., 1956, "Korperschall probleme in elektromaschinenbau", VDI-Ber., 8, 65-70.

1.114 Seidel, B.S., and Erdelyi, E.A., 1964, "On the vibration of a thick ring in its own plane", Trans.ASME-B, 86, 240-244.

1.115 Chen, Y.X., Zhu, Z.Q., 1985, "Mechanical and electrical analogs for the analysis of vibration in electrical machines", Electrical Machinery Technology, 3, 29-32.(in Chinese)

1.116 Zhu, Z.Q., Chen, Y.X., 1986, "Vibration analysis of double-ring and encased stator electrical machines by mechanical and electrical analogs", Proceedings of conference on noise and vibration of electrical machines, CES.(in Chinese), 117-124.

1.117 Yang, S.J., 1978, "Finite element method in evaluating the stator natural frequencies of small machines", Proc. ICEM'78, Brussels, G3/8-1-G3/8-8.

1.118 Zhu, Z.Q., 1984, "Study of vibrational behaviour of stators of electrical machines", MSc.thesis, Zhejiang University. (in Chinese)

1.119 Chen, Y.X., and Zhu, Z.Q., 1986, "Study on the natural frequencies and modes of stators of electrical machines", Proc.ICEM86, Munchen, F.R.Germany.pt1, 301 -304.

1.120 Zhu, Z.Q., Chen, Y.X., 1987, "The basis of finite element method for the analysis of natural frequencies and modes of electrical machine stators", Trans.Chinese Electrotechnical Society, 2, 25-31.(in Chinese)

1.121 Zhu, Z.Q., and Chen, Y.X., 1987, "Analysis of natural frequencies and modes of electrical machine stators by finite element method", Trans.Chinese Electrotechnical Society, 4, 39-46. (in Chinese)

1.122 Watanabe, S., Kenjo, S., et al, 1983, "Natural frequencies and vibration behaviour of motor stators", Trans.IEEE-PAS, 102, 949-956.

1.123 Noda, S., Mori, S., Ishibashi, F., and Itomi, K., 1987, "Effect of coils on natural frequencies of stator cores in small induction motors", Trans.IEEE-EC, 93-99.

1.124 Belmans, R., et al, 1987, "Theoretical and experimental analysis of the stator natural frequencies of induction motors", Proc. BICEM'87, Beijing, Part 1, 336-339.

1.125 Belmans, R., et al, 1986, "CAD-finite element conbination for calculating natural frequencies of machine stators", Proc.of Int.Conf.on Evolution and Modern Aspects of Induction Motors, Turino, Italy, 219-223.

1.126 Baudry, R.A., Heller, P.A., and Curtis, L.P., 1954, "Magnetic vibrations in a.c. generator stators", Trans.AIEE, 73, 508-516.

1.127 Chen, Y.X., Zhu, Z.Q., 1986, "An experimental investigation into the natural frequencies and modes of electrical machine stators", Large Electrical Machines and Hydraulic Turbines, CES, 2, 16-21.(in Chinese)

1.128 Ewins, D.J., 1984, " Modal testing, theory and practice", Letchworth, Research Studies.

1.129 Kako, F., Tsuruta, T., Nagaishi, K., and Kohmo, H., 1983, "Experimental study on magnetic noise of large induction motors", Trans.IEEE-PAS, 102, 2805-2810.

1.130 Yu, X.C., Zhang, T.Y., Zhang, W.X., 1986, "The modal analysis of the stator vibration of electrical machines by signal processor", Proc.ICEM'86, Muchen, Part 1, 336-339.

1.131 Zhu, Z.Q., and Howe, D., 1989, "Effects of end-shields and rotor on the natural frequencies and modes of the stator an electrical machine", Proc.Int.Conf.on Electrical Machines and Drives, IEE Conf.Pubn no 310, 232-236.

1.132 Garvey, S.D., 1989, "Vibrational behaviour of laminated components in electrical machines", Proc.Int.Conf.on Electrical Machines and Drives, IEE Conf.Pubn no 310, 226-231.

1.133 Carter, F.W., 1932, "Magnetic noise in dynamo-electric machines", Engineering, 134, 548-551 and 579-581.

1.134 Jordan, H., 1949, "Approximate calculation of the noise produced by squirrel cage motors", Eng.Dig., 10, 222-226.

1.135 Ellison, A.J., and Moore, C.J., 1969, "Calculation of acoustic power radiated by an electric machine", Acustica, 25, 28-34.

1.136 Zhu, Z.Q., Howe, D., 1990, "Finite element analysis of acoustic power radiated by electrical machines", Proc. of institue of acoustics, 12, 29-36.

1.137 Alger, P.L., 1954, "Magnetic noise in polyphase-induction motors", Trans.AIEE, 73, pt.IIIA, 118-125.

1.138 Zhu, Z.Q., Chen, Y.X., 1987, "On the acoustic power radiated by an electrical machine", Large Electrical Machines and Hydraulic Turbines, CES, 1, 23-27.(in Chinese)

1.139 Alger, P.L., and Erdelyi, E., 1956, "Calculation of the magnetic noise of polyphase induction motors", J.Acoust.Soc.Am.28, 1063-1067.

1.140 Ellison, A.J., and Yang, S.J., 1971, "Calculation of acoustic power radiated by an electric machine", Acustica, 25, 28-34.

1.141 Yang, S.J., 1975, "Effect of length-diameter ratio on noise radiation from an electrical machine", Acustica, 32, 255-261.

1.142 Zhu, Z.Q., and Chen, Y.X., 1987, "On the calculation of acustic power radiated by an electrical machine", Proc. Int. Conf. on Electrical Machines and Drives, IEE Conf. Pubn. 282, 118-121.

1.143 Timar, P.L., and Poloujadoff, M., 1984, "Method of comparative measurement as a survey process to determine the A-weighted sound power level of rotating electrical machines", Trans.IEEE-PAS, 103, 1816-1821.

1.144 Junger, M.C., and Feit, D., 1972, "Sound, structures, and their interaction", The MIT Press.

1.145 Morse, P.M., and Ingard, K.U., 1968, "Theoretical acoustics", McGraw-Hill Book Co., New York.

1.146 Schenck, H.A., 1968, "Improved integral formulation for acoustic radiation problems', J.Acoust.Soc.Am., 44, 41-58.

1.147 White, R.C., and Walker, J.G., 1982, "Noise and vibration", Ellis Horwood Ltd.

1.148 Junger, M.C., 1953, "The physical interpretation of the expression for an outgoing wave in cylindrical coordinates", J.Aoust.Soc.Am., 25, 40-47.

CHAPTER 2

2.1 Yang, S.J., 1981, "Low-noise electrical motors", Oxford University Press, New York.

2.2 Zhu, Z.Q., and Chen, Y.X., 1987, "On the calculation of acustic power radiated by an electrical machine", Proc. Int. Conf. on Electrical Machines and Drives, IEE Conf. Pubn. 282, 118-121.

2.3 Baudry, R.A., Heller, P.A., and Curtis, L.P., 1954, "Magnetic vibrations in a.c. generator stators", Trans.AIEE, 73, 508-516.

2.4 Girgis, R.S., and Verma, S.P., 1981, "Method for accurate determination of resonant frequencies and vibration behaviour of stators of electrical machines", Proc.IEE, 128, 1-11.

2.5 Verma, S.P., and Girgis, R.S., 1981, "Experimental verification of resonant frequencies and vibration behaviour of stators of electrical machines", Proc.IEE-B, 128, 22-32.

2.6 Erdelyi, E., and Horvay, G., 1957, "Vibration modes of stators of induction motors", Trans.ASME-E, 24, 39-45.

2.7 Ellison, A.J., and Yang, S.J., 1971, "Natural frequencies of stators of small electric machines", Proc.IEE, 118, 185-190.

2.8 Watanabe, S., Kenjo, S., et al, 1983, "Natural frequencies and vibration behaviour of motor stators", Trans.IEEE-PAS, 102, 949-956.

2.9 Noda, S., Mori, S., Ishibashi, F., and Itomi, K., 1987, "Effect of coils on natural frequencies of stator cores in small induction motors", Trans.IEEE-EC, 93-99.

2.10 Belmans, R., et al, 1987, "Theoretical and experimental analysis of the stator natural frequencies of induction motors", Proc. BICEM'87, Beijing, Part 1, 336-339.

2.11 Belmans, R., et al, 1986, "CAD-finite element conbination for calculating natural frequencies of machine stators", Proc.of Int.Conf.on Evolution and Modern Aspects of Induction Motors, Turino, Italy, 219-223.

2.12 Verma, S.P., Williams, K., and Singal, R.K., 1989, "Vibrations of long and short laminated stators of electrical machines.part 1:theory, experimental models, procedure and set-up", J.Sound & Vib., 129, 1-13.

2.13 Williams, K., and Singal, R.K., Verma, S.P., 1989, "Vibrations of long and short laminated stators of electrical machines.part 2:results for long stators", J.Sound & Vib., 129, 15-29.

2.14 Singal, R.K., Verma, S.P., and Williams, K., 1989, "Vibrations of long and short laminated stators of electrical machines.part 3:results for short stators and validity of simplified frequency equation", J.Sound & Vib., 129, 31-44.

2.15 Zhu, Z.Q., and Chen, Y.X., 1987, "Analysis of natural frequencies and modes of electrical machine stators by finite element method", Trans.Chinese Electrotechnical Society, 4, 39-46.

2.16 Yang, S.J., and Ellison, A.J., 1985, "Machinery noise measurement", Clarendon Press, Oxford.

2.17 Zhu, Z.Q., Chen, Y.X., Shang, Q.Y., 1988, "Theory and design of low noise induction motors", Special and Micro Motors, CES. No.3, 13-17.(in Chinese)

2.18 Chen, Y.X., and Zhu, Z.Q., 1987, "Analysis and control of noises from electrical machines", Zhejiang University Press.(in Chinese)

Chapter 3

3.1 Carter, F.W., 1932, "Magnetic noise in dynamo-electric machines", Engineering, 134, 548-551 and 579-581.

3.2 Jordan, H., 1949, "Approximate calculation of the noise produced by squirrel cage motors", Eng.Dig., 10, 222-226.

3.3 Ellison, A.J., and Moore, C.J., 1969, "Calculation of acoustic power radiated by an electric machine", Acustica, 25, 28-34.

3.4 Alger, P.L., 1954, "Magnetic noise in polyphase-induction motors", Trans.AIEE, 73, pt.IIIA, 118-125.

3.5 Alger, P.L., 1964, "The nature of induction machines", Gordonk Breach, New York.

3.6 Erdelyi, E., 1955, "Predetermination of sound pressure levels of magnetic noise of polyphase induction motors", Trans. AIEE, 74, 1269-1280.

3.7 Alger, P.L., and Erdelyi, E., 1956, "Calculation of the magnetic noise of polyphase induction motors", J.Acoust.Soc.Am.28, 1063-1067.

3.8 Ellison, A.J., and Yang, S.J., 1971, "Calculation of acoustic power radiated by an electric machine", Acustica, 25, 28-34.

3.9 Yang, S.J., 1975, "Effect of length-diameter ratio on noise radiation from an electrical machine", Acustica, 32, 255-261.

3.10 Yang, S.J.,1981, "Low-noise electrical motors", Oxford University Press, Oxford.

3.11 Kaemmer, N, and Crocker, M.J., 1983, "Sound power determination from surface intensity measurements on a vibrating cylinder", J. Acoust Soc. Am., 73, 856-866.

3.12 Ellison, A.J., and Yang, S.J., 1971, "Effects of rotor eccentricity on acoustic noise from induction machines", Proc.IEE, 118, 174-184.

3.13 Zhu, Z.Q., Chen, Y.X., 1987, "On the acoustic power radiated by an electrical machine", Large Electrical Machines and Hydraulic turbines, CES, 1, 23-27.(in Chinese)

Chapter 4

4.1 Yang, S.J.,1981, "Low-noise electrical motors", Oxford University Press, Oxford.

4.2 Fenlon, F.H., 1969, "Calculation of the acoustic radiation field at the surface of a finite cylinder by the method of weighted residual", Proc.IEEE, 57, 291-306.

4.3 White, R.C., and Walker, J.G., 1982, "Noise and Vibration", Ellis Horwood Ltd.

4.4 Hunt, J., Knittel, M.R., and Barach, D., 1974, "Finite element approach to acoustic radiation from elastic structures', J. Acoust Soc. Am., 55, 269-280.

4.5 Astley, R.J., and Eversman, W., 1983, "Finite element formulation for acoustic radiation", J. Sound and Vib., 88, 47-64.

4.6 Kagawa,Y., et al, 1980, "A finite element approach to a coupled structure-acoustic radiation system with application to loudspeaker characteristic calculation", J. Sound & Vib., 69, 229-243.

4.7 Schenck, H.A., 1968, "Improved integral formulation for acoustic radiation problems", J. Acoust. Soc. Am., 44, 41-58.

4.8 Niwa, Y., Kobayashi, S., and Kilahara, M., 1982, "Determination of eigenvalues by boundary element methods" Developments in Boundary Element Method-2, Applied Science Publishers, London, 143-176.

4.9 Zhu, Z.Q., and Chen,Y.X., 1987, "On the calculation of acoustic power radiated by an electrical machine", Proc. 3rd Int. Conf. on Elec. Machines & Drives, IEE Conf. Pubn., 282, 118-121.

4.10 Jordan, H., 1949, "Approximate calculation of the noise produced by squirrel cage motors", Eng. Dig., 10, 222-226.

Chapter 5

5.1 Heller, B., and Hamata, V., 1977, "Harmonic field effects in induction machines", Elsevier Scientific Publishing Company.

5.2 Wavre, N., "Servo brushless DC motor - study of torque ripple through induced voltage", 583-586.

5.3 Evans, P.D., and Brown, D., 1990, " Simulation of brushless DC drives", Proc. IEE-B, 137, 299-308.

5.4 Ree, J. D. L., and Boules, N., 1987, "Torque production in permanent magnet synchronous motors", IEEE Industry Application Society conference record, 87, CH2499-2, 15-20.

5.5 Eid, G., and Mouillet, A., 1984,"Transistorized DC brushless micromotor with rare-earth permanent magnets", Proc ICEM '84, 2, Lausanne (Switzerland), 570-573.

5.6 Gu, Q., and Gao, H., 1985, "Airgap field for PM electrical machines", Electrical Machines and Power Systems, 10, 459-470.

5.7 Boules,N., 1984, "Two-dimensional field analysis of cylindrical machines with permanent magnet excitation", Trans.IEEE-IA, 20, 1267-1277.

5.8 Boules, N., 1985, "Prediction of no-load flux density distribution in PM machines", Trans.IEEE-IA, 21, 633-643.

5.9 Xiong, G., and Nasar,B. A., 1989, "Analysis of fields and forces in a permanent magnet linear synchronous machine based on the concept of magnetic charge", Trans.IEEE-MAG,25, 2713-2719.

5.10 Gu, Q., and Gao, H.,1985, "Effect of slotting in PM electrical machines", Electrical Machines and Power Systems, 10, 273-284.

5.11 Kramer,C., 1980, "The effect of slotting in permanentic synchronous machines", Proc. of ICEM, Athens, Greece, 1, 287-294.

5.12 Gu, Q., and Gao, H., 1986, "The fringing effect in PM electrical machines", Electrical Machines and Power Systems, 11, 159-169.

5.13 Freeman,G. M., 1962, "Calculation of harmonics, due to slotting, in the flux density waveform of a dynamo-electric machine", Proc IEE, 109C, 581-588.

5.14 Pohl, R., 1946, "Theory of pulsating field machines", Journal IEE, 93B.

Chapter 6

6.1 Ackermann, B., Sottek,R., Janssen,J.H.H., and Steen, R.I., 1989, "A new technique for reducing the cogging torque in a class of brushless DC motors", Philips Research Report.

6.2 Wagner, J.A., 1975, "Numerical analysis of cogging torque in a brushless DC motor", IEEE Industry Applications Society Conference record, Vol 75, CHO 999-31A, 669-674.

6.3 Li,T., and Slemon, G., 1988, "Reduction of cogging torque in permanent magnet motors", Trans.IEEE-MAG, 24, 2901-2903.

6.4 Goto, M., and Kobayashi, K., 1983, "An analysis of the cogging torque of a DC motor and a new technique of reducing the cogging torque", Electrical Eng. in Japan, 103, 113-120.

6.5 Kobayashi, K., and Goto, M., 1985, "A brushless DC motor of a new structure with reduced torque fluctuations", Electrical Eng. in Japan, 105, 104-112.

6.6 Zhu, Z.Q., 1990, "Analytical prediction of cogging torque in permanent magnet motor based on energy method", Research report, University of Sheffield.

6.7 Bolton, H.R., Liu, Y.D., and Mallinson, N.M., 1986, "Investigation into a class of brushless DC motor with quasi-square voltage and currents", Proc.IEE-B, 133, 103-111.

6.8 Ree, J.D.L., and Boules, N., 1987, "Torque production in permanent magnet synchronous motors", IEEE Industry Application Society conference record, 87, CH2499-2, 15-20.

6.9 Ree, J.D.L., and Latorre, J., 1988, "Permanent magnet machines torque considerations", IEEE Industry Applications Society conference record, 88, CH 2565-32.

6.10 Mizia, J., Adamiak, K., Eastham, A.R., and Dawson,G.E., 1988, "Finite element force calculation : comparison of methods for electrical machines", Trans.IEEE-MAG, 24, 447-450.

6.11 Marinescu, M., and Marinescu, N., 1988, "Numerical computation of torques in permanent magnet motors by Maxwell stress and energy method", Trans.IEEE-MAG, 24, 463-46.

6.12 Aronson, E.A., and Brauer, J.R., 1989, " Magnetic torque or force calculation by direct differentiation of finite element coenergy",Trans.IEEE-MAG, 25, 3578-3580.

6.13 Coulomb,J.L., 1983, "A methodology for the determination of global electromechanical quantities from a finite element analysis and its application to the evaluation of magnetic forces, torques and stiffness",Trans.IEEE-MAG, 19, 2514-2519.

6.14 Penman, J., and Grieve, M.D.,1986, "Efficient calculation of force in electromagnetic devices",Proc.IEE-B, 133, 212-216.

6.15 Coulomb, J.L., and Meunier, G., 1984, "Finite element implementation of virtual work principle for magnetic or electric force and torque computation",Trans.IEEE-MAG, 20, 1894-1896.

Chapter 7

7.1 Evans, P.D., and Brown, D., 1990, " Simulation of brushless DC drives",Proc. IEE-B, 137, 299-308.

7.2 Novotny, D., and Fath, A.F., 1968, "The analysis of induction machines controlled by series connected semiconductor switches", Trans.IEEE-PAS, 87, 597-605.

7.3 Lipo, T.A., 1971, "The analysis of induction motors with voltage control by symmetrically triggered thyristors", Trans.IEEE-PAS, 90, 515-525.

7.4 Nucera,R.R., Sudhoff, S.D., and Krause, P.C., 1989, "Comparison of steady-state performance of an electronically commutated motor", Trans.IEEE-IA, 25, 1110-1117.

7.5 Huth, G., 1989, "Grenzkennlinien von Drehstrom-servoantrieben in block- stromlechnik", Archiv ETZ, 11, 401-408, (in German).

7.6 Zhu,Z.Q., and Howe, D., 1990, "Design and analysis of axial-field permanent magnet brushless DC motors", Proc. 11th. Workshop on REPM, Pittsburgh, 596-610.

7.7 Liu, Y.,P., Howe, D., Birch, T.S., and Matthews, D.M.H.,1989, "Dynamic modelling and performance prediction of brushless permanent magnet drive systems", Proc 4th Int Conf on Electrical Machines and Drives, IEE Conf Pubn No 310, 95-99.

7.8 Murai,Y., et al, 1989, "Torque ripple improvement for brushless DC miniature motors ", Trans.IEEE-IA, 25, 441-450.

7.9 Nehl,T.W., et al, 1982, "Dynamic simulation of radially oriented permanent magnet-type elctronically operated synchronous machines with parameters obtained from finite element field solutions", Trans. IEEE-IA, 18, 172-182.

7.10 Pillay,P., and Krishnan,R., 1989, "Modeling, simulation, and analysis of permanent-magnet motor drives, part II: The brushless DC motor drive", Trans.IEEE-IA, 25, 274-279.

7.11 Howe,D., Jenkins,M.K., Zhu,Z.Q.,1991, "Simulation of permanent magnet motor drives", Chapter 28, NATO-ASI, "Supermagnets-Hard Magnetic Materials", Kluwer Academic Publishers, 706-737.

Chapter 8

8.1 Boules, N., 1985, "Prediction of no-load flux density distribution in permanent magnet machines", Trans.IEEE-IA, 21, 633-643.

8.2 Boules, N., 1984, "Two-dimensional field analysis of cylindrical machines with permanent magnet excitation", Trans.IEEE-IA, 20, 1267-1277.

8.3 Boldea, I., Nasar, S.A., and Fu, Z., 1988, "Fields, forces, and performance equations of air-core linear self-synchronous motor with rectangular current control", Trans.IEEE-MAG, 24, 2194-2203.

8.4 Heller, B., and Hamata, V., 1977, "Harmonic field effects in induction machines", Elsevier Scientific Publishing Company.

Chapter 9

9.1 Bose, B.K.(editor), 1980, "Adjustable speed AC drive systems", IEEE Press, New York.

9.2 Yang, S.J., and Timar, P.L., 1980, "The effect of harmonic currents on the noise of a three-phase induction motor", Trans.IEEE-PAS, 99, 307-310.

9.3 Belmans, R.J., et al, 1987, "Analysis of the audible noise of three-phase squeirrel-cage induction motors supplied by inverters", Trans.IEEE-IA, 23, 842-847.

9.4 Giessler, F., and Sattler, P.K., 1988, "Magnetic noise of induction machines by inverter supply", Proc.ICEM88, Italy, 611-616.

9.5 Wallace, A.K., Spee, R., and Martin, L.G., 1990, "Current harmonics and acoustic noise in AC adjustable-speed drives", Trans.IEEE- IA, 26, 267-273.

9.6 Bolte, E., and Gerling, D., 1990, "Noise Analysis of Inverter-fed variable-speed industion motor drives", Proc.of Int. Conf. on Electrical machines, Boston.

9.7 Yang, S.J.,1981, "Low-noise electrical motors", Oxford University Press, Oxford.

9.8 Timar, P.L., and Hallenius, K.E., 1988, "Some notes on the necessity to extend the vib-acoustic tests of rotating electrical machines used in variable-speed drives", Conf. Rec.of Industry Applications Society Annual Meeting, 124-128.

9.9 Chen, Y.X., and Zhu, Z.Q., 1987, "Analysis and control of noises from electrical machines", Zhejiang University Press. (in Chinese)

9.10 Zhu, Z.Q., and Chen, Y.X., 1987, "On the calculation of acustic power radiated by an electrical machine", Proc. Int. Conf. on Electrical Machines and Drives, IEE Conf. Pubn. 282, 118-121.

9.11 Zhu, Z.Q., Chen, Y.X., Shang, Q.Y., 1988, "Theory and design of low noise induction motors", Special and Micro Motors, CES. No.3, 13-17.(in Chinese)

9.12 Imhoff, J.F. et al, 1989, "Spectral analysis of electromagnetic vibrations in d.c. machines through the finite element method", Trans.IEEE-MAG, 25, 3590-3592.

9.13 Zhu, Z.Q., Howe, D., 1990, "Finite element analysis of acoustic power radiated by electrical machines", Proc. of institue of acoustics, 12, 29-36.

9.14 Zhu, Z.Q., Howe, D., 1990, "Analytical models for predicting noise and vibration in brushless permanent magnet DC motors", UPEC'90, 277-280.

9.15 Girgis, R.S., and Verma, S.P., 1979, "Resonant frequencies and vibration behaviour of stators of electrical machines as affectted by teeth, winding, frame and laminations", Trans. IEEE-PAS, 98, 1446-1455.

9.16 Zhu, Z.Q., Chen, Y.X., 1987, "The basis of finite element method for the analysis of natural frequencies and modes of electrical machine stators", Trans.Chinese Electrotechnical Society, 2, 25-31.(in Chinese)

9.17 Verma, S.P., and Girgis, R.S., 1973, "Resonant frequenies of electrical machine stators having encased constructure. Pt1, Pt2", Trans.IEEE-PAS, 92, 1573-1585.

9.18 Zhu, Z.Q., and Chen, Y.X., 1987, "Analysis of natural frequencies and modes of electrical machine stators by finite element method", Trans.Chinese Electrotechnical Society, 4, 39-46. (in Chinese)

9.19 Bruel & Kj er, 1982, "Instruction manual for precision integrating sound level meters Type 2221 and 2222".

9.20 Yang, S.J., and Ellison, A.J., 1985, "Machinery noise measurement", Oxford University Press, New York.

Appendix 1: Chapters of the book entitled:

ANALYSIS AND CONTROL OF NOISES FROM ELECTRICAL MACHINES

by Chen Y.X. Zhu Z.Q. Ying S.C.

published by Zhejiang University Press, 1987. 378pages + v

Contents

Chapter 1. **Introduction**
- by Chen Y.X. pp 1-17

Chapter 2. **Mechanical and electrical analog in the analysis of vibration of electrical machines**
- by Zhu Z.Q. pp 18-34

Chapter 3. **Vibrational behaviour and response of stators of electrical machines**
- by Zhu Z.Q. pp 35-57

Chapter 4. **Acoustic power radiated by an electrical machine**
- by Zhu Z.Q. pp 58-68

Chapter 5. **Magnetic vibration and noise of asynchronous induction machines**
- by Zhu Z.Q. pp 69-115

Chapter 6. **Tangential vibration and noise from single-phase induction motors**
- by Zhu Z.Q. pp 116-134

Chapter 7. **Vibration and noise from synchronous induction machines and direct-current electrical machines**
- by Zhu Z.Q. pp 135-170

Chapter 8. **Control of electromagnetic noises**
- by Zhu Z.Q. pp 171-212

Chapter 9. **Aerodynamic noise**
- by Chen Y.X. pp 212-244

Chapter 10. **Bearing noise**
- by Ying S.C. pp 245-286

Chapter 11. **Identification of noises from electrical machines**
- by Chen Y.X. pp 287-302

Chapter 12. **Measurement of noise and vibration of electrical machines**
- by Zhu Z.Q. and Ying S.C. pp 303-350

Appendices

Appendix 2.1

CAD OF ELECTRICAL MACHINES -- A STUDY OF ELECTROMAGNETIC, VIBRATIONAL, AND ACOUSTIC BEHAVIOUR

by Zhu Z.Q. June 1989

ABSTRACT

The electromagnetic, vibrational, and acoustic behaviour of electrical machines has been studied in this thesis. It embraces 1) vibrational behaviour of stators; 2) acoustic behaviour of stators; 3) analysis and control of tangential vibration and noise of single-phase induction machines; 4) design synthesis of low noise three-phase induction motors.

The concept of a generalised tooth / slot is introduced to study the vibrational behaviour of stators. According to this concept the principles for selecting the exciting/picking-up points are established and validated both theoretically and experimentally. A finite element package, in which the high-order curved isoparametric elements and the lumped mass matrix are adopted, and the reduced order integration technique is used, has been developed to investigate the natural frequencies and modes of various types of stators, taking into account the effects of winding and frame. Good agreement between calculated and measured results has been achieved. The effects of the end-shields, rotor and running conditions on the natural frequencies and modes of the stator have, for the first time, been investigated by the modern modal analysis technique.

New formulae for the calculation of the acoustic power radiated by a cylindrical stator of finite length, using an analytical method, are presented. A technique which combines the finite element method and Fourier series analysis to account for the effects of end-shields on the acoustic radiation has been developed. Based on the developed technique a suite of planar, axisymmetric and harmonic axisymmetric finite element programs, which are capable of calculating the radiated acoustic field and power in a 3-dimensional field, have been developed and validated on a test motor. Furthermore the spherical model of the acoustic radiation of motors has been improved by the application of finite elements. In addition the techniques developed are applied to the analysis of acoustic modes and natural frequencies by introducing the lumped acoustic mass matrix into the acoustic finite element.

The tangential vibration and noise produced by single-phase induction machines are analysed. General formulae for asynchronous torques, synchronous torques, and vibrational torques are developed by the compound current method. These allow analysis of tangential vibrations at any frequency without the limitation of twice-line frequency as commonly reported in the literature. The frequencies of the tangential vibration are verified by measurement and analysis of the noise spectra of electric fans. Using the developed method the fan motors have been re-designed to reduce the tangential vibration and noise without changing the electromagnetic or aerodynamic performances.

A systematic approach to the design synthesis of low noise three-phase induction machines is presented.The model established can estimate the noise level of encased type motors. It differs from conventional methods in that the model can consider not only the iron core but also the frame, as well as their damping effects. Based on the developed design synthesis, a range of three-phase induction motors, rated from 180W-550W, have been designed successfully to a low noise specification, and have been put into mass production.

Appendix 2.2

CAD OF ELECTRICAL MACHINES

- A Study of Electromagnetic,Vibrational & Acoustic Behaviour

by Z.Q. Zhu June 1989

CONTENTS

ABSTRACT

CHAPTER 1. INTRODUCTION 1
1.1 Introduction 1
1.2 Review of electromagnetic noise and vibration 2
1.3 Review of previous work on vibrational behaviour 5
1.4 Review of previous work on acoustic behaviour 8
1.5 Main research in the thesis 9

CHAPTER 2. BASIS OF FINITE ELEMENT METHOD FOR PREDICTING NATURAL FREQUENCIES AND MODES OF STATORS 14
2.1 Introduction 14
2.2 Vibrational eigenvalue equation 15
2.3 Stiffness matrix and lumped mass matrix of high order isoparametric elements 17
2.4 Reduced order integration technique and verifications 18
2.5 Conclusions 21
2.6 Appendices 21
2.6.1 Kinetic energy and potential energy of elements
2.6.2 Shape functions of isoparametric elements

CHAPTER 3. ANALYSIS OF NATURAL FREQUENCIES AND MODES OF STATORS 25
3.1 Introduction 25
3.2 Generalised tooth/slot and generalised tooth symmetrical /antisymmetrical modes 26
3.3 Study of natural frequencies and modes of different kinds of stators 27
3.3.1 Circular ring
3.3.2 Effects of magnetic poles - DC machine stators
3.3.3 Effects of teeth/slots
3.3.4 Effects of swallow-tail slots
3.3.5 Effects of winding
3.3.6 Effects of frame and feet - encased type stators
3.3.7 Effects of ribs - double ring type stators
3.3.8 Square type stators
3.4 Conclusions 59
3.5 Appendix 59
Model parameters

CHAPTER 4. EXPERIMENTAL STUDY OF NATURAL FREQUENCIES AND MODES OF STATORS 61
4.1 Theoretical basis 61
4.2 Measurement methods 63
4.2.1 Sinusoidal force excitation
4.2.2 Impulse or random force excitation
4.3 Selection of exciting point and picking up point 69
4.4 Comparison of different methods 72

4.5 Classification of stator modes 74
4.6 Conclusions 75
4.7 Appendix 75
4.7.1 Model test

CHAPTER 5. EFFECTS OF END-SHIELDS AND ROTOR ON NATURAL FREQUENCIES AND MODES OF STATORS 77
5.1 Introduction 77
5.2 Modern experimental modal analysis technique 78
5.3 Experimental method 81
5.4 Modal analysis of the machine 85
5.4.1 Measured results
5.4.2 Modal analysis of the stator
5.4.3 Effects of end-shields
5.4.4 Effects of the rotor
5.4.5 Effects of running conditions
5.5 Conclusions 97
5.6 Appendix 98
5.6.1 Analysis of vibration spectrum

CHAPTER 6. STUDY OF ACOUSTIC FIELD AND POWER RADIATED BY AN ELECTRICAL MACHINE USING ANALYTIC METHOD 99
6.1 Introduction 99
6.2 Derivation of formulae 100
6.3 Comparison of relative sound intensity coefficients 103
6.4 Measurement and calculation of acoustic field 105
6.5 Conclusions 110
6.6 Appendix 111
6.6.1 S.J.Yang's formula of relative sound intensity coefficients

CHAPTER 7. ANALYSIS OF ACOUSTIC BEHAVIOUR OF ELECTRICAL MACHINES BY FINITE ELEMENT METHOD (PART 1) 113
7.1 Introduction 113
7.2 Calculation of acoustic power 114
7.2.1 Three dimensional finite element of acoustic radiation
7.2.2 Planar and axisymmetric fields
7.2.3 Harmonic axisymmetric field
7.2.4 Element matrices and acoustic power in different fields using triangular elements
7.3 Experimental verifications and effects of far-field boundary conditions 127
7.4 Conclusions 134
7.5 Appendices 134
7.5.1 Boundary conditions and acoustic field radiated by an electrical machine
7.5.2 Three dimensional isoparametric element
7.5.3 Detection of standing waves and travelling waves

CHAPTER 8. ANALYSIS OF ACOUSTIC BEHAVIOUR OF ELECTRICAL MACHINES BY FINITE ELEMENT METHOD (PART 2) 139
8.1 Introduction 139
8.2 Conventional spherical model using Lagendre series 140
8.3 Improved spherical model using Fourier series 144
8.4 Conclusions 146

CHAPTER 9. A FINITE ELEMENT METHOD FOR ANALYSING ACOUSTIC MODES AND NATURAL FREQUENCIES 149
9.1 Introduction 149
9.2 Lumped acoustic mass matrix 150

9.3 Axisymmetric structure 154
9.4 Case studies 155
9.5 Conclusions 160

CHAPTER 10. ANALYSIS AND CONTROL OF TANGENTIAL VIBRATION AND NOISE OF SINGLE-PHASE INDUCTION MOTORS **162**
10.1 Introduction 162
10.2 Vibration torques and " compound current " analysis 164
10.3 Tangential vibrations 174
10.4 Verification and noise reduction 176
10.5 Conclusions 183

CHAPTER 11. THEORY AND DESIGN OF LOW NOISE INDUCTION MACHINES **184**
11.1 Introduction 184
11.2 Establishment of design theory 185
11.3 Design of low noise induction machines 188
11.4 Conclusions 191
11.5 Appendices 192
11.5.1 Measured results of low noise induction machines
11.5.2 Comparisons of new design and existing design

CHAPTER 12. CONCLUSIONS **194**
12.1 Vibrational behaviour of electrical machines 194
12.2 Acoustic behaviour of electrical machines 196
12.3 Tangential vibration of electrical machines 197
12.4 Design of low noise induction machines 198

REFERENCES **199**

Appendix 3

PUBLICATIONS FROM THE RESEARCH IN THE THESIS

1. Zhu, Z.Q., Howe, D.,1989, Effect of end shields and rotor on the natural frequencies and modes of stator of an electrical machine, Proc. of 4th Int. Conf. on Electrical Machines and Drives, IEE, London, UK, IEE Pubn. No. 310, 232-236.

2. Zhu, Z.Q., Chen Y.X., 1987,On the calculation of acoustic power radiated by an electrical machine, Proc. of 3rd Int. Conf. on Electrical Machines and Drives, IEE, London,UK, IEE Pubn. No. 282, 118-121.

3. Zhu, Z.Q., Howe, D. ,1990 , Finite element analysis of acoustic power radiated by electrical machines, Proc. of Institute of Acoustics, Vol.12(6), 29-36.

4. Zhu, Z.Q., Howe, D., 1991, Analytical prediction of the airgap field distribution in permanent magnet motors accounting for the effect of slotting, accepted to present at Int. Symp. on Electromagnetic Fields in Electrical Engineering, ISEF'91, Sept.18-20,1991, Southampton, UK.

5. Howe, D., Zhu, Z.Q. ,1991, The influence of finite element discretisation on the prediction of cogging torque in permanent magnet excited motors, accepted to present at COMPUMAG, IEEE, Sorrento, Italy, July 7-11, 1991.

6. Zhu, Z.Q., Howe, D. ,1991, Analytical prediction of the cogging torque in radial-field permanent magnet brushless motors, accepted to present at COMPUMAG, IEEE, Sorrento, Italy, July 7-11, 1991.

7. Howe, D., Jenkins M.K., and Zhu, Z.Q.,1991, Simulation of permanent magnet motor drives. Chapter 28, NATO-ASI Series, 'Supermagnets-Hard Magnetic Materials', (edited by G.J. Long and F. Grandjean). Kluwer Academic Publishers ,1991, 757-789.

8. Zhu, Z.Q., Howe, D., 1990, Design and analysis of axial-field permanent magnet brushless DC motors, Proc. of 11th Int. Workshop on Rare-earth Magnets and Their Applications, Pittsburgh, USA, 596-610.

9. Zhu, Z.Q.,Howe, D. ,1990, Analytical models for predicting noise and vibration in brushless permanent magnet DC motors, Proc. of 25th Universities Power Engineering Conf., 277-280.

10. Zhu, Z.Q., Howe, D., 1991, Analytical determination of the instantaneous airgap field in a brushless permanent magnet DC motor, accepted to present at Int. Conf. on Computation in Electromagnetics, IEE, Nov. 26-27,1991.

11. Bolte, E., Ackermann, B., Halfmann, J., Howe, D., Zhu, Z.Q., Jenkins, M.K., Evison, P.R.,Mitchell, J.K., 1991, Computer-aided design and analysis of permanent magnet brushless drive systems, accepted to present at 6th Int. Forum on CAD,UK, Sept.1991.